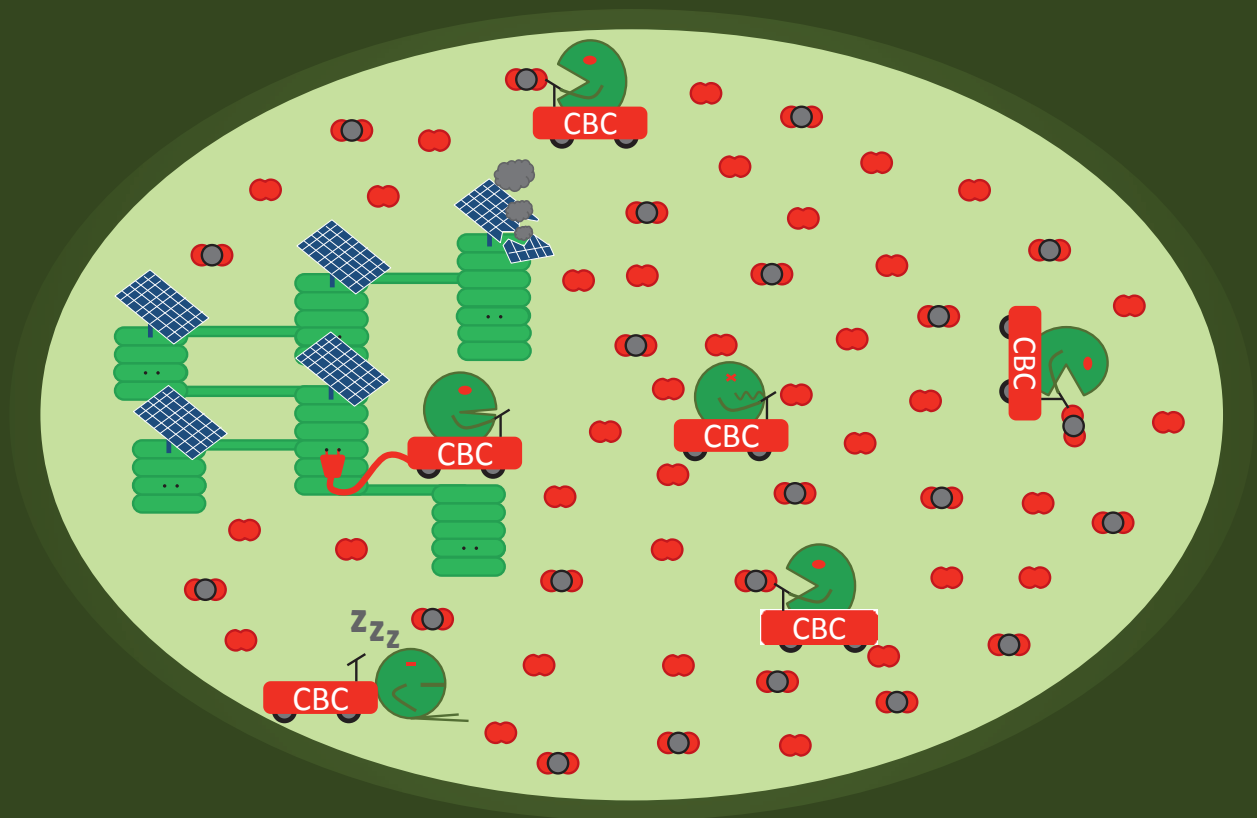


Dynamic photosynthesis under a fluctuating environment: a modelling-based analysis



Alejandro Morales Sierra

**Dynamic photosynthesis under a fluctuating environment:
a modelling-based analysis**

Alejandro Morales Sierra

Thesis committee

Promotors

Prof. Dr P. C. Struik
Professor of Crop Physiology
Wageningen University

Prof. Dr J. Molenaar
Professor of Applied Mathematics
Wageningen University

Co-promotors

Dr X. Yin
Senior scientist, Centre for Crop System Analysis
Wageningen University

Dr J. Harbinson
Assistant professor, Horticulture and Product Physiology
Wageningen University

Other members

Prof. Dr H van Amerongen, Wageningen University
Prof. Dr B.M. Nicolai, KU Leuven, Belgium
Dr C. Fleck, Wageningen University
Dr T. L. Pons, Utrecht University

This research was conducted under the auspices of the C.T. de Wit Graduate School for Production Ecology and Resource Conservation

**Dynamic photosynthesis under a fluctuating environment:
a modelling-based analysis**

Alejandro Morales Sierra

Thesis

submitted in fulfilment of the requirements for the degree of doctor

at Wageningen University

by the authority of the Rector Magnificus

Prof. Dr A.P.J. Mol,

in the presence of the

Thesis Committee appointed by the Academic Board
to be defended in public

on Tuesday 21 March 2017

at 4 p.m. in the Aula.

Alejandro Morales Sierra

Dynamic photosynthesis under a fluctuating environment: a modelling-based analysis,
282 pages.

PhD thesis, Wageningen University, Wageningen, NL (2017)
With references, with summary in English

ISBN: 978-94-6343-045-6

DOI: 10.18174/400729

Table of contents

Chapter 1	General introduction	1
Chapter 2	Dynamic photosynthesis in different environmental conditions	17
Chapter 3	Metabolic and diffusional limitations of photosynthesis in fluctuating irradiance in <i>Arabidopsis thaliana</i>	33
Chapter 4	An in silico analysis of the biochemical and diffusional limitations to C3 CO ₂ assimilation under fluctuating light conditions at the leaf and canopy level	61
Chapter 5	An in silico analysis of the metabolic regulation of the photosynthetic electron transport chain in C3 plants	128
Chapter 6	General discussion	208
	References	227
	Summary	271
	Acknowledgements	275
	PE & RC Training and Education Statement	277
	Curriculum vitae	279
	List of Publications	281
	Funding	282

Chapter 1

General introduction

“I observed that plants not only have a faculty to correct bad air in six to ten days, by growing in it... but that they perform this important office in a complete manner in a few hours; that this wonderful operation is by no means owing to the vegetation of the plant, but to the influence of light of the sun upon the plant”

Jan Ingenhousz, 1779

More than two centuries ago, the Dutch-born physician Jan Ingenhousz observed that green organs of plants, when exposed to light, were able to restore a property to the air that was destroyed by animals, and by the same plants in darkness (Ingenhousz, 1779). This property was described as the ability of air to sustain a flame, and would later be identified as molecular oxygen. This early description of light-dependent O₂ evolution of leaves led to general interest among scientists and was followed by a series of discoveries throughout the 19th century and first half of the 20th century that established the fundamental principles of oxygenic photosynthesis in plants (Tanaka and Makino, 2009). In the 21st century, photosynthesis remains an important area of research and it is considered one of the most important processes of life on Earth.

1.1 Photosynthesis and the challenges of the 21st century

Photosynthesis is a fundamental process in the biosphere, as it is responsible for the growth and maintenance of the lowest trophic levels across all ecosystems, with the exception of some deep-water habitats and microbial communities within the Earth's crust that rely on chemosynthesis (Kiel and Tyler, 2010; Lever et al., 2013). Rates of photosynthesis are related to the maximum productivity of an ecosystem (Melillo et al., 1993) and physiological adaptations of photosynthesis may contribute to biodiversity (Sage and Stata, 2015).

Photosynthesis also plays an important role in regulating the climate on Earth. The assimilation of CO₂ into biomass and stabilization of this biomass results in sequestration of atmospheric CO₂, which aids in the reduction of the greenhouse effect (Bonan, 2008). Indeed, in the 1990s, forests represented a sink equivalent to 30% of anthropogenic CO₂ emissions (Pan et al., 2011). Also, as an important component of the global carbon cycle, photosynthesis has a strong impact on predictions of future climate (Booth et al., 2012). Despite its importance, the predictive modelling of photosynthesis is limited by the quality of the models used to describe it (Rogers et al., 2014).

As part of the biosphere, humans rely ultimately on photosynthesis for nurture. The global population is expected to increase in the future, with current estimations for 2050 placed at 9.7 billion under a medium-growth scenario (U.N. , 2015). Covering the demands of such a population will require to increase agricultural production from 60% (Alexandratos and Bruinsma, 2012) to 110% (Tilman et al., 2002) with respect to current levels, with uncertainties in the estimations originating from uncertainties in the demographic projections, changes in diets, and future increases in average income. These projections indicate that food security is one of the main challenges of the 21st century.

Humanity is also facing a major energy crisis, because of the non-renewable nature of the main sources of energy (WEC, 2016), and the negative aspects that the use of fossil fuels has on the climate, via the greenhouse effect (IPCC, 2007). In the search for alternative sources of energy, bioenergy (i.e., biofuels, forestry and agricultural residues) has emerged as an important alternative, and was responsible for 10% of the global energy supply in 2016 (WEC, 2016). However, it remains a challenge to avoid competition with

food production while achieving a sustainable production of bioenergy (Tilman et al., 2009).

Increasing the global production of biomass for food and energy may be achieved by increasing the total area cultivated or by increasing the yields of plant production systems. It has been estimated that there are 1.4 billion ha of good land for rain-fed food and bioenergy production, compared to the current total of 1.6 billion ha under agricultural use (Alexandratos and Bruinsma, 2012). Tapping into additional land would conflict with other land usages, such as conservation of biodiversity, regulation of the hydrological cycle, or carbon sequestration (Balmford et al., 2005). Between 1961 and 2013, the total area of land under cultivation only increased by 10.5% (according to the database FAOSTAT, accessed on 14th November 2016) so there might be some practical limitations to how fast the agricultural land area can increase (Alexandratos and Bruinsma, 2012). The increasing water scarcity may also limit the expansion of agricultural land area (Falkenmark, 2013). In addition, it has been suggested that raising crop yields in existing lands may be a more sustainable approach to maintaining high levels of food production in the future (Foley et al., 2011), especially if the world's population will continue to increase beyond 2050 (U.N., 2015).

If the extension of current agricultural land is not sufficient or desirable to cover the global demand for food and bioenergy in the future, yields per unit land should be increased. Part of the increase may be achieved by closing the gap between actual and potential yields by means of improvements in management (van Ittersum et al., 2013). A study by Pradhan et al. (2015) indicated that closing yield gaps was sufficient for several countries to meet their food demand by 2050. However, these estimations should be taken with care, due to the limited accuracy of models and methods of calculation, and the lack of suitable input data (van Ittersum et al., 2013). Furthermore, the law of diminishing returns may keep individual farmers from fully closing the gap, as it could result in suboptimal economic performance (Lobell et al., 2009), although historical trends in yield and nitrogen use efficiency indicate that technological development and synergies among different agronomic factors may lead to higher efficiencies at higher yields (de Wit, 1992).

Finally, the third option is to use genetic improvement to raise the yield of cultivated systems under different soil, climate and management options. The yields of the main four crops for food and feed (i.e., maize, rice, wheat and soybean), responsible for 66% of the food calories consumed globally (Ray et al., 2013), have increased progressively in the last decades. However, their current rate of growth (0.9–1.6% per year) would be insufficient to cover future global food and feed demand, which would require an average annual increase of 2.4% (Ray et al., 2013). The recent improvements in crop yields is, in many cases, associated with increases in the fraction of total biomass allocated to grains, especially in wheat and rice (Hay, 1995), whereas in maize, the improvements are associated to exploitation of hybrid vigour and adaptation of the crop to high plant density (Duvick, 2005). Thus, improvements in photosynthesis have had a marginal role in increasing the yields of the main cereal crops (Zhu et al., 2010) and maximum rates of leaf photosynthesis are poorly correlated with yield across historical series of cultivars (Long et al., 2006b).

On the other hand, theoretical analyses predict that significant improvements in crop yield and bioenergy production could be achieved by improving photosynthesis (Long et al., 2006b; Zhu et al., 2010; Yin and Struik, 2015). In addition, experiments show that

elevated CO₂ levels result in increases of yields in wheat, rice and soybean (Long et al., 2006a), which suggests that photosynthesis may limit crop yields under field conditions. These results indicate that further improvements of yields could be achieved via genetic improvement of photosynthesis. Some success has already been achieved in this respect, by manipulating the properties and content of photosynthetic enzymes in leaves (Woodrow, 2009; Raines, 2011; Rosenthal et al., 2011; Carmo-Silva et al., 2015; Simkin et al., 2015; Kromdijk et al., 2016), although many of these improvements have not yet been transferred to economically relevant crops and/or tested under agronomically relevant conditions. In addition, within a species, there may be a natural variation in leaf photosynthesis that could be translated into higher biomass production, as is the case in *Oryza sativa* (Gu et al., 2012b) and *Triticum aestivum* (Driever et al., 2014)

Achieving improvements in bioenergy and food production through enhancements of photosynthesis would benefit from (i) identification of targets for improvement, and (ii) extrapolation of knowledge on photosynthesis physiology to agronomically relevant conditions. Simulation models based on systems thinking can play a fundamental role in this process (Yin and Struik, 2010; Keurentjes et al., 2011; Zhu et al., 2012) as they are capable of integrating knowledge from multiple disciplines and areas of research, and make quantitative connections between individual components of a biological system and its overall behaviour. For example, such models can be used to link specific molecular components of the system to overall performance under different environments (Yin and Struik, 2010).

It is in this context that this dissertation proposes novel simulation models of photosynthesis that are used to analyse the performance of leaf and canopy photosynthesis under environmental conditions closer to those experienced in the field, with the aim of (i) providing new tools for photosynthesis research *in silico*, and (ii) quantifying the role of different photosynthetic processes in limiting photosynthesis under different environmental conditions. To support the modelling effort, a review of the literature, as well as a comprehensive experiment tailored to the needs of the models are also presented. In the rest of this introductory chapter, the relevant background knowledge on photosynthesis is provided, as well as an overview of the historical evolution and current state-of-the-art in photosynthesis modelling.

1.2 The physiology of photosynthesis in plants

Photosynthesis in plants is a process by which a fraction of the solar energy absorbed by a photosynthetic organ (in most cases a leaf) is converted into sucrose and starch, which can be used for synthesis of new biomass. Photosynthesis may also be used for assimilation into organic form of nitrogen and sulfur (Foyer and Noctor, 2002; Takahashi et al., 2011), and it plays an important role in oxidative stress (Foyer and Shigeoka, 2011) and redox balance (Taniguchi and Miyake, 2012). In this dissertation, the focus is on CO₂ assimilation, while other roles of photosynthesis are considered to the extent that they may affect CO₂ assimilation.

Photosynthesis takes place inside plastids called chloroplasts, which were incorporated into early eukaryotes via endosymbiosis of photosynthetic cyanobacteria (Yoon et al., 2004). Chloroplasts are separated from the cellular medium (cytosol) by a double membrane (chloroplast envelope). The envelope of the chloroplast contains numerous transporters that allow the exchange of specific metabolites with the cytosol (Pottosin and Shabala, 2016). Inside the chloroplasts, there is a membrane of complex structure

called thylakoid. The thylakoid membrane separates the inner space of the chloroplast into two compartments: the lumen of the thylakoid and the stroma of the chloroplast (hereafter, lumen and stroma, respectively). Embedded in the thylakoid membrane, a series of proteins form a light harvesting and electron transport chain responsible for absorbing radiative energy (irradiance) and using that energy to drive the phosphorylation of ADP and reduction of NADP^+ in the stroma (Figure 1.1). These molecules are used by the Calvin cycle (Figure 1.2) to assimilate molecules of CO_2 into simple sugar phosphates, a process that begins with the carboxylation of ribulose-1,5-bisphosphate (RuBP) in a reaction catalysed by RuBP carboxylase/oxygenase (Rubisco). These sugar phosphates are then used for sucrose synthesis in the cytosol, or are converted into starch in the stroma. CO_2 diffuses from the air surrounding the leaf into the chloroplasts, resulting in gradients of CO_2 mole fractions ($[\text{CO}_2]$) across the different compartments of the leaf (Figure 1.3). Some species possess special mechanisms to concentrate $[\text{CO}_2]$ in the chloroplasts (Furbank et al., 1989), but this dissertation will only focus on the so-called C3 species, which lack any special mechanisms for concentrating $[\text{CO}_2]$.

Irradiance is absorbed by two photosystems: Photosystem I (PSI) and Photosystem II (PSII). The absorption of irradiance occurs in a series of protein complexes associated to PSI and PSII, known as the antenna complexes of PSI and PSII (PSI_{ac} and PSII_{ac} , respectively). The antenna complexes are composed of proteins and pigments (chlorophylls and carotenoids) located in the core and periphery of the photosystems. The distinction between inner and outer (or core and peripheral) antenna complexes is often used (Croce and van Amerongen, 2013; van Amerongen and Croce, 2013; Papageorgiou and Govindjee, 2014). While this distinction is important when studying energy transfer among the different components of PSI_{ac} and PSII_{ac} , these processes may be assumed to be in rapid equilibrium at the scales of seconds (Croce and van Amerongen, 2013; van Amerongen and Croce, 2013). The energy absorbed by PSII_{ac} is used to oxidise a molecule of chlorophyll in the reaction centre, which drives the oxidation of water into O_2 , H^+ and electrons, through a series of intermediate reactions that constitute the oxygen evolving complex, located on the luminal side of the thylakoid membrane. The electrons are ultimately transported to a pool of plastoquinone (PQ) molecules that can diffuse through the thylakoid membrane acting as electron carriers. PQ is reduced into plastoquinol (PQH_2), taking two electrons from PSII and two protons (H^+) from the stroma.

PQH_2 diffuses through the thylakoid membrane to the oxidase site at the cytochrome b_6f complex (cyt b_6f). There, it is oxidised and its two electrons are divided over two electron transport chains: the high and low potential chains. The former uses the electron to reduce a molecule of plastocyanin (Pc) on the luminal side. The latter reduces a molecule of PQ bound on the reductase site (complete reduction to PQH_2 requires two turnovers of cyt b_6f). The two H^+ of the PQH_2 being oxidised are released into the lumen. The low potential chain is also known as the Q cycle and its physiological function is to double the number of H^+ released into the lumen for every electron produced by PSII.

Reduced Pc is then oxidised by PSI. The irradiance absorbed by PSI is used to reduce ferredoxin (Fd), extracting the charge from Pc. Reduced Fd can reduce different metabolites in the stroma (Figure 1.1). Under normal physiological conditions, most of the electrons will be used for NADPH synthesis by ferredoxin-NADP⁺ reductase. However, there are also alternative forms of electron transport that either do not lead to NADPH production or result in the oxidation of NADPH by acceptors outside the Calvin cycle and

photorespiration. One possibility is that Fd reduces PQ, in what is known as cyclic electron flow around PSI. Also, Fd or NADPH may be oxidised by alternative electron sinks, which include the reduction of O_2 (Asada, 2000), reduction of NO_2^- and assimilation of NH_4^+ into an organic form (Foyer and Noctor, 2002), and reduction of oxaloacetate into malate, coupled to export of malate out of the chloroplast (Fridlyand et al., 1998). In addition, Fd may reduce different forms of thioredoxin which are involved in the regulation of the activity of several enzymes in the stroma (see below).

An excess of energy occurs whenever the rate of excitation of $PSII_{ac}$ exceeds the capacity of the electron transport chain at that moment. This excess can cause photoinhibition of the reaction centres of PSII (Allahverdiyeva and Aro, 2012). While photoinhibition is reversible, full recovery may take hours (Campbell and Tyystjärvi, 2012) and can inhibit CO_2 assimilation (Hikosaka et al., 2004). Different strategies may be used by the system to reduce photoinhibition (Allahverdiyeva and Aro, 2012), of which non-photochemical quenching (NPQ) is considered one of the most important (Kramer et al., 2004a). NPQ consists of a regulated increase in the dissipation of excitations as heat in $PSII_{ac}$, such that a smaller fraction of the energy reaches the reaction centre. The mechanisms responsible for regulation of NPQ are still unclear, although, under many circumstances, NPQ is dominated by the so-called qE mechanism that is regulated (indirectly) by the pH of the lumen, thus establishing a link with the fluxes of H^+ across the thylakoid membrane (Strand and Kramer, 2014). Photoinhibition may also contribute to NPQ, as there is evidence that photoinhibited PSII units remain highly quenched, though the mechanism is still not understood (Krause, 1988; Šetlík et al., 1990; Renger et al., 1995; Gilmore et al., 1996; Matsubara and Chow, 2004). Also, multiple forms of slowly reversible NPQ with similar kinetics to photoinhibition have been proposed (Ruban and Belgio, 2014).

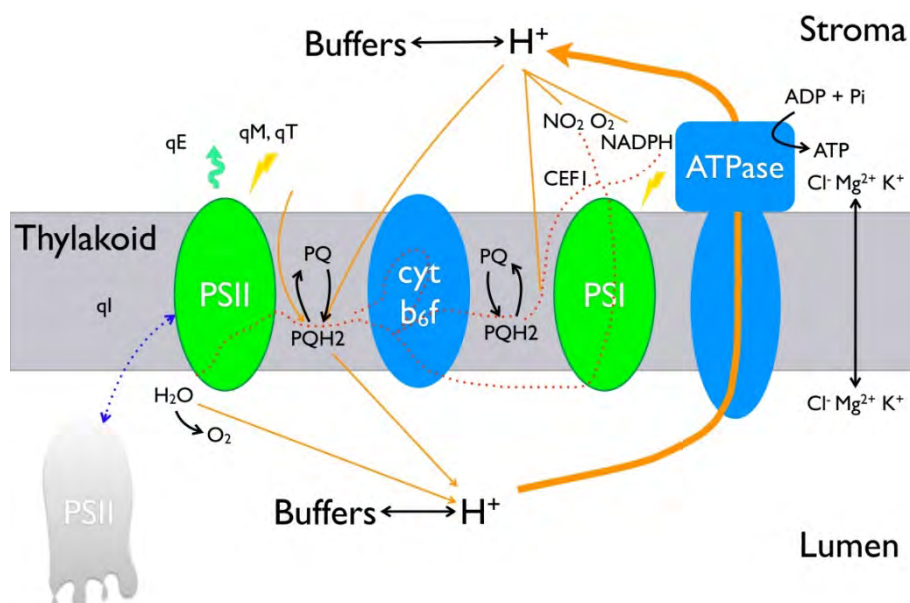


Figure 1.1: Schematic representation of the photosynthetic electron transport chain in plants. “PSII” and “PSI” stand for Photosystem II and I, respectively, including the associated antenna complexes. “cyt b_6f ” stands for the cytochrome b_6f complex, whereas “ATPase” stands for the ATP synthase. The red, dotted lines describe the different fluxes of electrons: linear electron flux, Q cycle within cyt b_6f , cyclic electron flux around PSI and reduction of alternative electron sinks (NO_2^- , O_2). The orange, solid lines describe the different fluxes of H^+ across the thylakoid membrane. “ qE ” stands for energy-dependent, non-photochemical quenching, “ qM ” for chloroplast movement, “ qT ” for state transitions, and “ qI ” for photoinhibition of PSII reaction centres.

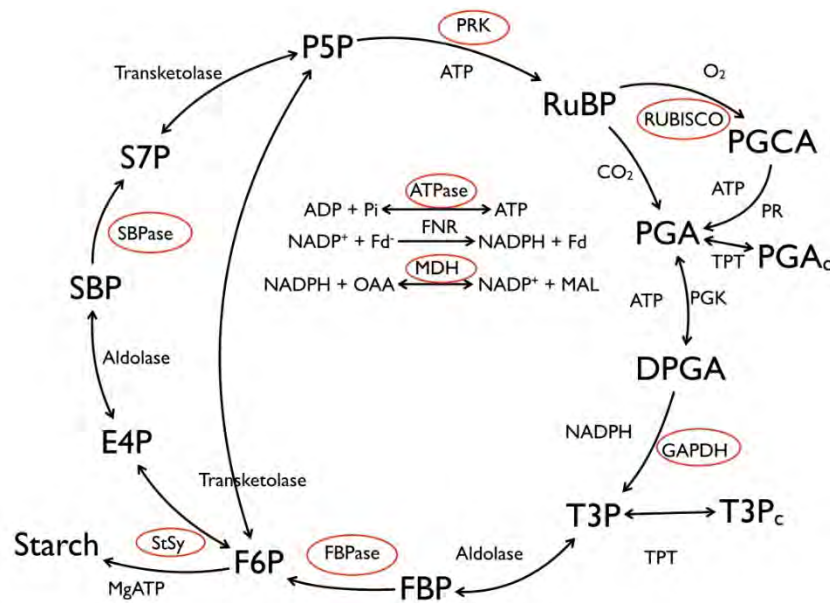


Figure 1.2: Schematic representation of the Calvin cycle. Enzymes inside red ellipses are regulated indirectly by irradiance. "PR" stands for photorespiration. The subscript "c" is used to denote metabolites in the cytosol. Additional reactions included in the diagram are ATP synthesis, NADPH synthesis, and malate dehydrogenase (MDH).

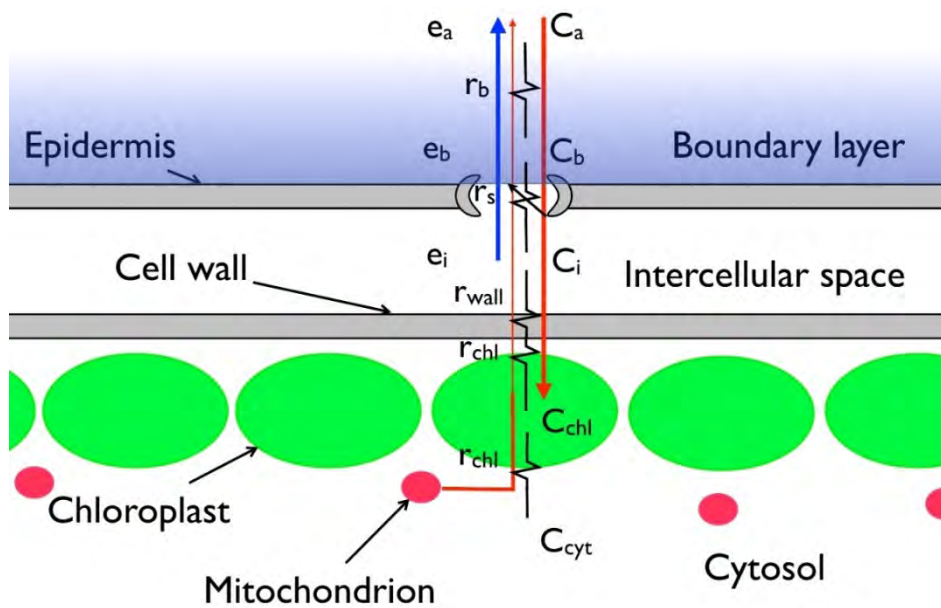


Figure 1.3: Schematic representation of CO_2 diffusion into a leaf, coupled to the flux of water vapour out of the leaf. The red lines represent fluxes of CO_2 , whereas the blue line represents the flux of water vapour. Each diffusion barrier is represented as an electrical resistance. The mole fractions of CO_2 and partial pressures of water vapour for each compartment are represented by the symbols "C" and "e", respectively, with subscripts that denote the compartment ("a" = air, "b" = boundary layer, "i" = intercellular spaces within the leaf, "cyt" = cytosol, and "chl" = chloroplast).

Other mechanisms may also contribute to a reduction of photoinhibition. One of such mechanisms is the movement of chloroplasts in response to blue irradiance. This results in changes of the optical properties of leaves (Haupt and Scheuerlein, 1990; Davis et al., 2011). Its effects in reducing photoinhibition have been demonstrated for *Arabidopsis thaliana* (Kasahara et al., 2002; Davis and Hangarter, 2012), but chloroplast movements are not significant in many species (Davis et al., 2011). Another mechanism consists of the so-called state transitions, which involve transfer of some of the protein complexes in PSII_{ac} to PSI_{ac}, thus adjusting the relative distribution of irradiance between the two photosystems. This is achieved by changes in the phosphorylation levels of PSII_{ac}, and this phosphorylation is ultimately dependent on the redox state of the pools of PQ/PQH₂ and thioredoxin (Rintamäki et al., 2000). Because of these interactions, state transitions operate mainly at low irradiance (Mekala et al., 2015) or in response to changes in the spectrum of irradiance (Hogewoning et al., 2012). In any case, the fraction of protein complexes affected by state transitions appears to be small (Dietzel et al., 2008).

As H⁺ accumulate in the lumen, a H⁺ electrochemical gradient is formed across the thylakoid membrane. According to the chemiosmotic theory (Mitchell, 2011), this gradient represents a H⁺ motive force (pmf) that drives ATP synthesis. That is, as H⁺ flows into the stroma through the ATP synthase (ATPase), the energy released in this transport is used to drive ATP synthesis. In addition to the pmf, the rate of ATP synthesis is also regulated by the concentrations of substrates and products in the stroma (Pänke and Rumberg, 1996), and reduction by thioredoxins (Schwarz et al., 1997). Additionally, the electrical component of the pmf affects the internal electron transport through PSII (Lebedeva et al., 2002), whereas the pH component of pmf regulates the kinetics of PQH₂ oxidation by cyt b₆f as well as qE. In addition to H⁺, other ions (Mg²⁺, Cl⁻, and K⁺, among others) may also move across the thylakoid membrane through different channels (Pottosin and Shabala, 2016) and alter the partitioning of pmf into its electrical and pH component (Cruz et al., 2001).

In the stroma, CO₂ is assimilated into organic form by Rubisco, which converts a molecule of RuBP (5C) into two molecules of phosphoglycerate (3C, PGA). Rubisco may also assimilate a molecule of O₂ producing a molecule of PGA and a molecule of phosphoglycolate (2C, PGCA). Two molecules of PGCA are converted into one molecule of PGA, with the release of a molecule of CO₂. This conversion consists of several steps that take place in different cellular compartments and it is known as photorespiration. Experimental results (Harley and Sharkey, 1991) suggest that part of the flux through photorespiration may be diverted towards other metabolic pathways, such that less than half of PGCA may be converted into PGA.

In addition to Rubisco, the Calvin cycle consists of several enzymes responsible for regenerating RuBP from PGA and allocating some of the intermediate metabolites towards sucrose and starch synthesis (Figure 1.2). ATP and NADPH are consumed in some of these reactions, where the Calvin cycle is coupled to the electron transport chain. Although only 1.5 PGA is produced per oxygenation (instead of the 2 PGA per carboxylation), the reduction of PGCA into PGA consumes additional ATP and NADPH, such that an increase in the ratio of oxygenation over carboxylation results in an increase of the consumption of ATP relative to NADPH in the stroma (Farquhar et al., 1980). Assuming that the stoichiometry of the different reactions in the electron transport chain does not change with physiological conditions, an increase in the stromal demand of ATP

relative to NADPH requires an increase in alternative electron transport in order to increase the flux of H^+ released into the lumen.

Several of the enzymes in the Calvin cycle are redox sensitive and their activities increase when reduced by thioredoxins (Nikkanen and Rintamäki, 2014). As thioredoxins become increasingly reduced at higher irradiances, the activities of the redox-sensitive enzymes in the Calvin cycle increase with irradiance, allowing for a better coupling between the electron transport chain and the Calvin cycle. The activities of enzymes may also be co-regulated, as for the case of GAPDH and PRK (Figure 1.2), which are controlled by binding to the CP12 protein, which itself is also redox sensitive (Howard et al., 2008). In addition, the activities of enzymes like FBPase and SBPase (Figure 1.2) are also affected by stromal pH and concentration of Mg^{2+} ions (Gardemann et al., 1986; Cadet and Meunier, 1988).

The activity of Rubisco is also dependent on irradiance, as well as CO_2 (von Caemmerer and Edmondson, 1986). The catalytic sites of Rubisco are not active until they bind a molecule of CO_2 and Mg^{2+} , in a process called carbamylation (Mate et al., 1996). When RuBP binds a carbamylated site, it will become carboxylated or oxygenated. However, if RuBP binds an inactive site, catalysis is not possible and the RuBP molecule will remain tightly bound to the site, effectively acting as an inhibitor by preventing carbamylation. Under physiologically relevant conditions, Rubisco becomes inhibited in the presence of RuBP (Mate et al., 1996). In addition, there are some specific Rubisco inhibitors that do not take part in catalysis, and some others that are the result of catalytic misfires during carboxylation or oxygenation (McNevin et al., 2006; Parry et al., 2013). In order to restore activity to the catalytic sites, the tightly bound inhibitors must be released, and this is achieved by a chaperone called Rubisco activase. Although the details on how Rubisco activase operates are still unclear, it is known that its activity depends on reduction by thioredoxin and the concentrations of ATP and ADP in the stroma (Hazra et al., 2015).

To maintain the rates of CO_2 assimilation, a rapid supply of CO_2 to Rubisco is required. Transport across membranes may be facilitated by aquaporins (Flexas et al., 2008), but it is assumed to be energetically passive (i.e., no energy is consumed directly to transport CO_2 across barriers). A passive diffusion requires the creation of a gradient of $[CO_2]$ between the carboxylation sites and the air surrounding the leaf. The magnitude of such a gradient depends on the diffusivity of CO_2 molecules through the different barriers within the leaf. Using an electrical circuit as analogy, these barriers may be grouped into two components: the stomatal and mesophyll conductances. The former refers to the diffusion of CO_2 through the stomatal pores on the surface of the leaf. The opening and closing of these pores is highly regulated and responds to environmental conditions as well as internal physiological signals (Mott, 2009; Lawson et al., 2011; Lawson et al., 2014). The mesophyll conductance refers to the internal barriers, between the intercellular space (which is air-filled) and the vicinity of Rubisco in the stroma. Mesophyll conductance is highly dependent on leaf anatomy (Berghuijs et al., 2015) and appears to respond to environmental conditions (Flexas et al., 2008), although some of these apparent responses may be the result of methodological artefacts (Tholen et al., 2012; Gu and Sun, 2014).

1.3 Photosynthesis in its natural environment

As part of a canopy, a leaf may be exposed to strong temporal fluctuations in incident irradiance. The best-known type of fluctuations are so-called “sunflecks”, which consist of brief increases in irradiance on a low background irradiance (Way and Pearcy, 2012).

Chapter 1

Generally, a sunfleck is associated with direct exposure to the sun of a leaf that was previously in the shade. This is possible because of gaps in the structure of canopies, either permanent or created transiently by wind (Roden, 2003). Some general characterization of sunflecks has been performed, in terms of amplitude, duration and frequency (Pearcy, 1990; Smith and Berry, 2013), and general patterns have emerged from these analyses: (i) for a given leaf, sunflecks tend to be clustered in time, separated by longer periods of no sunflecks, (ii) sunflecks are usually short (< 10 seconds), and (iii) tend to increase irradiance by at least $100 \mu\text{mol m}^{-2} \text{s}^{-1}$. The study of sunflecks is further complicated by the penumbra effect (Denholm, 1981), and by non-isotropic scattering of irradiance by leaves (Grant, 1987).

Another source of fluctuations in irradiance that has received comparatively less attention is the transient shading of a leaf that was previously exposed to the sun because of passing clouds or the structure of the canopy. Whereas shading by canopy structure can be seen as a phenomenon complementary to sunflecks (i.e., the creation of a sunfleck in one point results in shading of another location), shading by clouds (“cloudflecks”) should be treated separately as (i) cloudflecks are less dependent on the structure of the canopy, (ii) cloudflecks can affect leaves on the top of the canopy, and (iii) may result in very different temporal distributions. For example, Knapp and Smith (1988) observed that, on days with intermittent cloudiness on a subalpine meadow, the average length of a cloudfleck was 3.8 minutes, an order of magnitude longer than a typical sunfleck. While the effect of sunflecks on CO_2 assimilation has been studied extensively in the last decades (Pearcy and Way, 2012), few studies are available on the effect of intermittent cloudiness on CO_2 assimilation (see Fay and Knapp 1995, and references therein).

Osterhout and Haas (1918) reported one of the earliest studies on dynamic photosynthesis, by measuring the rate at which the pH of a medium increased in the presence of filaments of *Ulva rigida* after a change in irradiance from darkness to a direct exposure to the sun. This experiment revealed that changes were slow (in the scale of minutes) and followed (approximately) first-order kinetics. Soon after, experiments were published where dynamic CO_2 assimilation and chlorophyll fluorescence were measured (Warburg, 1920; Kautsky and Hirsch, 1931; McAlister and Myers, 1940). The behaviour of photosynthesis during these dark-to-light transients became known as “induction phenomena” (van der Veen, 1949). It was proposed that the “induction state” of photosynthesis determined how fast it could reach the steady-state, and that this induction state decreased with exposure to darkness (Warburg, 1920; van der Veen, 1949). Measurements of photosynthetic induction have played an important role in elucidating the mechanisms of photosynthesis, and in the development of dynamic models (Walker, 1973; Govindjee, 1995; Pearcy et al., 1996). It is now generally accepted that induction of photosynthesis (at the scale of minutes) is, at least, limited by activation of Rubisco (Mott and Woodrow, 2000) and opening of the stomata (Allen and Pearcy, 2000a; Vialet-Chabrand et al., 2016). Other potential effects may be associated with activation of other enzymes in the Calvin cycle (Sassenrath-Cole et al., 1994), build-up of metabolites in the Calvin cycle (Walker, 1973), and activation of sucrose phosphate synthase (Stitt and Grosse, 1988).

Under natural conditions, leaves are not exposed to darkness during the diurnal period. Hence, when the research objective is to understand the dynamics of photosynthesis under the natural environment, low irradiance instead of darkness should be used to study induction phenomena (McCree and Loomis, 1969). Much of the induction

phenomena are still observed when using low irradiance (McCree and Loomis, 1969; Pearcy et al., 1985; Sharkey et al., 1986b; Yamori et al., 2012), but the magnitude of the effects tends to be lower as the induction state increases with irradiance.

With the development of gas exchange measurement systems for leaves, additional phenomena were observed after decreases in irradiance. Decker (1955) observed that the apparent rates of leaf respiration in darkness were transiently larger after illumination than in the steady-state. A more complex pattern has been revealed for CO₂ assimilation after a transition from high to low irradiance, whereby (i) CO₂ assimilation remains transiently higher than in the final steady-state for a few seconds (Chazdon and Pearcy, 1986), followed by (ii) values transiently lower than in the final steady-state for a few minutes (Vines et al., 1982). Multiple hypotheses have been postulated to explain these phenomena, including delays in CO₂ release by photorespiration (Vines et al., 1983), enhancement of mitochondrial respiration after illumination (Azcón-Bieto et al., 1983), an overshoot in sucrose synthesis (Prinsley et al., 1986b), and relaxation of non-photochemical quenching (Armbruster et al., 2014; Kromdijk et al., 2016).

Other processes in photosynthesis are known to respond dynamically to changes in irradiance, such as the movement of chloroplasts (Haupt and Scheuerlein, 1990) that affect leaf optical properties (Davis et al., 2011), and changes in apparent mesophyll conductance (Flexas et al., 2007a). However, to my knowledge, the potential effects of these phenomena on CO₂ assimilation under fluctuating irradiance have not been tested experimentally or analysed *in silico*.

As indicated in the previous sections, the photosystems need to be protected from any excess of energy that could result in photoinhibition. During photosynthetic induction, the excess of energy is higher than in the steady-state, due to lower activity of enzymes in the Calvin cycle. In addition, the effects of photoinhibition on rates of CO₂ assimilation are higher at low irradiance (Hikosaka et al., 2004), such that the slow reversibility of photoinhibition may limit time-integrated CO₂ assimilation under fluctuating conditions (Zhu et al., 2004). Indeed, evidence shows that leaves become significantly photoinhibited during the day (Long et al., 1994; Murchie et al., 1999), and experiments with mutants deficient in qE display higher rates of photoinhibition and have lower biomass production under fluctuating irradiance compared to their wildtype (Külheim et al., 2002; Hubbart et al., 2012).

Another difficulty faced by photosynthesis when exposed to fluctuating irradiance is how to efficiently couple the production and consumption of ATP and NADPH. Furthermore, the dynamic decoupling of CO₂ diffusion and CO₂ assimilation results in strong fluctuations of [CO₂] within leaves (Allen and Pearcy, 2000a; Vialet-Chabrand et al., 2016), which will affect the ratio at which ATP and NADPH are consumed, due to alteration of the ratio between rates of oxygenation and carboxylation. Hence, the electron transport chain requires a high degree of flexibility to dynamically alter the rate of H⁺ release in the lumen relative to production of NADPH (Kramer et al., 2004a). In addition, alternative electron sinks may act as a safety valve to dissipate transient excess of energy and to acidify the lumen to induce NPQ, especially during photosynthetic induction (Igamberdiev et al., 1998; Makino et al., 2002; Fan et al., 2007).

1.4 Modelling of photosynthesis

The word “model” is perhaps one of the most ambiguous and abused terms in plant sciences. A model may be a diagram of a metabolic pathway, a verbal hypothesis on how a biological mechanism works, a species that is used in multiple experiments and considered a reference in the field, a digital or physical representation of a plant or protein, a statistical algorithm that captures relationships between variables in a dataset, or a set of equations that describes how a biological system may work at a certain level of abstraction. It is only the last definition that is of interest for this dissertation.

Even after narrowing the definition of the term model, there is still a wide range of models of photosynthesis, depending on the spatial and temporal scales being described, the type of research questions being addressed, and the level of detail at which the underlying mechanisms are described. A detailed review of all these models is beyond the scope of this introduction, but an overview is given of the main types of models that are relevant for this dissertation, in the form of a historical perspective leading to the current state-of-the-art.

1.4.1 Steady-state models of photosynthesis

One of the earliest mathematical models of photosynthesis that included the effect of environmental conditions was proposed by Blackman (1905). He challenged the dominant paradigm, in his time, that there was an optimal irradiance and $[\text{CO}_2]$ for photosynthesis. Instead, he proposed that the rate of CO_2 assimilation “is conditioned as to its rapidity by a number of separate factors [...], the rate of the process is limited by the pace of the ‘slowest’ factor” (Blackman, 1905). This statement became known as the “law of limiting factors” and has influenced many of the models of CO_2 assimilation published afterwards.

Decades later, a model of Rubisco kinetics was proposed by Farquhar (1979) which remains fundamental to all modern models of CO_2 assimilation. A year later, Farquhar et al. (1980) applied the law of limiting factors to couple a simplification of this Rubisco model to an empirical expression that calculated the potential rate of RuBP regeneration as limited by the production of NADPH or ATP. This model (hereafter “FvCB model”) is one of the most important models in the history of photosynthesis research, and it gave rise to an entire family of models of CO_2 assimilation with a broad range of applications (von Caemmerer, 2013).

Notable extensions of the FvCB model include the coupling to resistance-based models of CO_2 diffusion (Farquhar and Sharkey, 1982; Berghuijs et al., 2015), the inclusion of a third limiting factor associated with availability of free phosphate in the chloroplast (Sharkey, 1985), the generalization of the stoichiometries assumed in the coupling of the electron transport chain to the Calvin cycle (Yin et al., 2006), or the extension of the model to C_4 metabolism (von Caemmerer, 2000; Yin and Struik, 2012).

However, under natural conditions, photosynthesis is not always in steady state, and predictions made with models that assume a quasi-steady state (i.e., that photosynthesis responds instantly to changes in environmental conditions), result in overestimations of measured CO_2 assimilation (Pearcy et al., 1997; Stegemann et al., 1999; Naumburg et al., 2001a; Naumburg and Ellsworth, 2002). Therefore, dynamic models of photosynthesis are required.

1.4.2 Dynamic models of photosynthesis

Several simple, phenomenological models of photosynthesis were constructed in the 1980s and 1990s to quantify the effect of enzyme activation and stomatal conductance kinetics on CO₂ assimilation. The general approach was to use an analytical, steady-state model of photosynthesis, and to modify some of the parameters during the simulation according to phenomenological descriptions of their dynamics. This approach was successful in reproducing experimental observations and useful in generating a consistent paradigm that explained CO₂ assimilation under sunflecks in terms of a few processes. Gross (1982) modelled CO₂ assimilation by Rubisco, which activity was dependent on irradiance and changed in time with first-order kinetics. This approach was extended by Woodrow and Mott (1989), who distinguished between two components with different kinetics, the slowest of which was associated to Rubisco and its rate constant of activation was proportional to the amount of Rubisco activase. Gross et al. (1991) linked the fast component to activation of other enzymes in the Calvin cycle, and combined this approach with the FvCB model by explicitly simulating the amounts of triose phosphate and RuBP in leaves. This model was later refined by Pearcy et al. (1997) and Kirschbaum et al. (1998). The model by Pearcy et al. (1997) has been used in several studies (Naumburg et al., 2001a; Naumburg and Ellsworth, 2002; Roden, 2003; Montgomery and Givnish, 2008) and may be considered a reference model for studies of dynamic CO₂ assimilation under fluctuating irradiance.

Other dynamical models have focused on understanding the Calvin cycle by describing each reaction according to its kinetics *in vitro* (Pettersson and Ryde-Pettersson, 1988; Laisk et al., 1989; Woodrow and Mott, 1993; Fridlyand and Scheibe, 1999b; Poolman et al., 2000; Zhu et al., 2007). Most of these models were analysed under steady-state conditions with the objective of quantifying the effect of the different enzymes in the Calvin cycle on the rate of CO₂ assimilation. The approach followed, which is known as “metabolic control analysis” (Heinrich and Rapoport, 1974), assumes that there is no rate-limiting step in a pathway, but rather that all enzymes share different degrees of control on the flux through the pathway. This approach is generally considered more realistic than the law of limiting factors. However, to my knowledge, none of these models have been tested with measurements of CO₂ assimilation under different environmental conditions. One important limitation of these models is the large number of kinetic parameters that have to be determined. In addition, it is not clear whether *in vivo* kinetics can be predicted by models based on *in vitro* kinetics (Harris and Königer, 1997).

Regarding the electron transport chain, there is a long tradition of modelling the kinetics of energy transfer and electron transport associated to PSII. Much of the early work focused on modelling sub-components of the network of reactions within PSII, including the oxygen evolving complex (Kok et al., 1970), the two electron-gate model of Q_B reduction (Velthuys and Amesz, 1974), and the exciton-radical-pair equilibrium model (Lavergne and Trissl, 1995). Recent models aim at integrating these approaches into comprehensive models, often used to analyse fluorescence induction at the scale of microseconds to seconds (Stirbet et al., 1998; Lebedeva et al., 2002; Lazár, 2003; Zhu et al., 2005; Xin et al., 2013).

The rest of the components of the electron transport chain are generally not modelled in isolation but as parts of models of the whole electron transport chain. Simplified representations, usually in the form of rate equations, are used to describe them. Notable exceptions include the modelling of cyt b₆f to study possible bypass reactions of the Q

cycle (Berry and Rumberg, 2001; Schumaker and Kramer, 2011), and kinetic models of ATPase built to understand the effects of pmf, reduction by thioredoxin, and concentration of substrates on ATP synthesis (Kramer et al., 1990; Pänke and Rumberg, 1996). Although some early work was published by Laisk and Walker (1989), most detailed models of the electron transport chain are rather recent (Berry and Rumberg, 2001; Lebedeva et al., 2002; Laisk et al., 2009a; Ebenhöh et al., 2011; Zaks et al., 2012; Zhu et al., 2013; Tikhonov and Vershubskii, 2014; Matuszyńska et al., 2016). The models by Zhu et al. (2013) and Laisk et al. (2009a) also include detailed descriptions of the reactions in the stroma and cytosol, which makes them the two most comprehensive dynamic models of photosynthesis published so far.

1.4.3 Scaling photosynthesis to the canopy

Although photosynthesis takes place within chloroplasts, calculations of biomass production require to scale it up to the canopy level. Scaling photosynthesis to the canopy usually focuses on modelling the spatio-temporal distribution of irradiance within the canopy, although in principle the whole microclimate (i.e., wind velocity, temperature, humidity and [CO₂]) should be taken into account (Baldocchi et al., 2002; Zhu et al., 2012). The first model of canopy photosynthesis is attributed to Monsi and Saeki (1953), who proposed the use of the Lambert-Beer law to describe the distribution of irradiance within a canopy, where the extinction coefficient is determined by the distribution of leaf angles. This approximation is known as the “turbid medium” approach (Chelle and Andrieu, 2007). This model was later expanded into more detailed multi-layer models of irradiance distribution within canopies (Norman and Jarvis, 1975; Goudriaan, 1977), taking into account the optical properties of the leaves and separating irradiance into direct, diffuse and scattered components.

These multilayer models were later extended to 3D canopies, such as the crowns of trees (Norman and Welles, 1983; Wang and Jarvis, 1990; Cescatti, 1997), and 2D canopies, such as row crops (Gijzen and Goudriaan, 1989). De Pury and Farquhar (1997) demonstrated that, for calculations of steady-state canopy photosynthesis, the multilayer model by Goudriaan (1977) could be simplified into a two-leaf model that only considered sunlit and shaded fractions of the total leaf area. These different canopy models based on the assumption of turbid medium have been used in the simulation of canopy photosynthesis and plant biomass production (Baumann et al., 2002; Yin and van Laar, 2005; Morales et al., 2016).

One important limitation of models based on the concept of turbid medium is that they cannot track in time the irradiance absorbed by individual leaves. When CO₂ assimilation is assumed to be in quasi-steady state, this does not affect the results, provided that the integration over time and space is performed accurately. However, as soon as it is assumed that CO₂ assimilation depends on the past values of irradiance, due to the effects on enzyme activity, NPQ, photoinhibition, etc., the assumption of turbid medium is no longer useful. Therefore, simulations of dynamic canopy CO₂ assimilation make use of ray-tracers (Chelle and Andrieu, 2007) and 3D canopies where the individual leaves are described explicitly (Percy and Yang, 1996; Naumburg et al., 2001b; Roden, 2003; Retkute et al., 2015).

1.5 Goals and outline of this dissertation

This dissertation aims to answer the following questions:

Q1. How does CO₂ assimilation respond to fluctuating irradiance, under different temperature, [CO₂] and air humidity?

Q2: What is the importance of different photosynthetic processes in limiting dynamic CO₂ assimilation at the leaf and canopy level?

Q3: How is the electron transport chain, coupled to the Calvin cycle, regulated under steady-state and fluctuating irradiance?

Q4: What are potential targets for improvement of photosynthesis under fluctuating irradiance?

Chapter 2 reviews the existing literature on how different environmental conditions modulate CO₂ assimilation of leaves under fluctuating irradiance. The review also identifies those areas where more effort is needed in terms of experimental research and modelling.

Chapter 3 describes an experiment in which several photosynthetic mutants of *Arabidopsis thaliana* are used to test the effects of some of the processes identified in Chapter 2 on dynamic CO₂ assimilation. The diffusional and biochemical limitations to dynamic CO₂ assimilation are also quantified, using different indices adapted from previous studies.

Chapter 4 proposes a novel dynamic model of CO₂ assimilation at the leaf level that takes into account the different photosynthetic processes discussed in Chapters 2 and 3. The model is calibrated and validated with published data as well as the data presented in Chapter 3. The use of photosynthetic mutants allows testing whether the model captures the effect of different processes in a realistic manner. After calibration and validation of the model, simulations are performed to quantify the limitations, at the leaf and canopy levels, imposed by the different photosynthetic processes, under different environmental conditions.

Chapter 5 goes deeper into the mechanisms of photosynthesis and focuses on the electron transport chain, while still conserving most of the processes from Chapter 4. The objective of this model is to study the metabolic regulation of electron transport under steady-state and fluctuating irradiance. The model is calibrated and validated with published data, and simulations are performed to quantify the potential contributions of different mechanisms to the regulation of electron transport.

Finally, Chapter 6 summarises the findings in this dissertation and answers the research questions formulated above. Potential applications and extensions of the models are also discussed, and knowledge gaps are identified.

Chapter 2

Dynamic photosynthesis in different environmental conditions*

* Kaiser E, **Morales A**, Harbinson J, Kromdijk J, Heuvelink E, Marcelis LFM (2015) Dynamic photosynthesis in different environmental conditions. *Journal of Experimental Botany* 66 (9):2415-2426. doi:10.1093/jxb/eru406

Abstract

Irradiance incident on plant leaves often fluctuates, causing dynamic photosynthesis. Whereas steady-state photosynthetic responses to environmental factors have been extensively studied, knowledge of dynamic modulation of photosynthesis remains scarce and scattered. This review addresses this discrepancy by summarizing available data and by identifying the research questions necessary to advance our understanding of interactions between environmental factors and dynamic behaviour of photosynthesis, using a mechanistic framework. Firstly, dynamic photosynthesis is separated into sub-processes related to proton and electron transport, non-photochemical quenching, control of metabolite flux through the Calvin cycle (activation states of Rubisco and RuBP regeneration, post-illumination metabolite turnover) and control of CO₂ supply to Rubisco (stomatal and mesophyll conductance changes). Secondly, the modulation of dynamic photosynthesis and its sub-processes by environmental factors is described. Increases in ambient CO₂ concentration and temperature (up to approx. 35 °C) enhance rates of photosynthetic induction and decrease its loss, facilitating more efficient dynamic photosynthesis. Depending on the sensitivity of stomatal conductance, dynamic photosynthesis may additionally be modulated by air humidity. Major knowledge gaps exist regarding environmental modulation of loss of photosynthetic induction, dynamic changes in mesophyll conductance, and the extent of limitations imposed by stomatal conductance for different species and environmental conditions. The study of mutants or genetic transformants for specific processes under various environmental conditions could provide significant progress in understanding the control of dynamic photosynthesis.

2.1 Introduction

Photosynthesis is mostly studied using controlled, steady-state conditions. In nature, steady states are rare, and environmental factors, especially irradiance, change rapidly. Assimilation rates in nature result from those factors that limit steady-state photosynthesis as well as those that constrain the speed of response to environmental fluctuations (Naumburg and Ellsworth, 2002; Way and Pearcy, 2012). So, to understand photosynthesis in natural conditions we need to understand photosynthesis in fluctuating irradiance, i.e. dynamic photosynthesis.

Previous research on dynamic photosynthesis has focused on kinetics of underlying processes and interspecific variation in response to fluctuating irradiance (Pearcy and Way, 2012). In contrast, no clear picture of the effects of ambient CO₂ concentration ([CO₂]), temperature and leaf-to-air vapour pressure deficit (VPD_{leaf-air}) on dynamic photosynthesis exists (Way and Pearcy, 2012). These environmental factors influence the rate constants and rates of processes that limit the response of photosynthesis to fluctuating irradiance. As leaf temperature and VPD_{leaf-air} often change in parallel with irradiance (Peak and Mott, 2011; Schymanski et al., 2013), transient photosynthesis rates are affected by simultaneous changes in several factors. Atmospheric [CO₂] changes more slowly, currently rising by approx. 2 μmol mol⁻¹ year⁻¹ (IPCC, 2013). Apart from influencing photosynthesis on its own, this increase in [CO₂] is likely to affect air temperature and humidity (IPCC, 2013). Knowledge of dynamic photosynthesis is solid with respect to responses to changing irradiance, but much less developed regarding the modulation of dynamic photosynthesis by other environmental factors, even when these

factors are held constant while irradiance fluctuates. This weakness impacts upon photosynthetic models.

Vegetation and crop science relies heavily on models to predict photosynthesis. Steady-state photosynthesis models are often sophisticated and useful, but tend to overestimate integrated photosynthesis in fluctuating irradiance (Naumburg and Ellsworth, 2002; Timm et al., 2004). The degree of overestimation depends on average irradiance intensity and species-specific responses to fluctuating irradiance (Pearcy et al., 1997; Naumburg et al., 2001a; Naumburg and Ellsworth, 2002), but can be as much as 35% per day (Naumburg and Ellsworth, 2002). Dynamic photosynthesis models, on the other hand, account for the kinetics of photosynthesis as it responds to fluctuating light. Of the dynamic models that exist, none account for all environmental factors mentioned, while some account for the effects of $[\text{CO}_2]$ (Kirschbaum et al., 1998; Naumburg et al., 2001a; Vico et al., 2011), leaf temperature (Pepin and Livingston, 1997; Ozturk et al., 2012) and air humidity (Pepin and Livingston, 1997; Vico et al., 2011). To improve dynamic photosynthesis models, we need better understanding of how environmental factors other than irradiance, even when they are constant, modulate the kinetics of responses to changes in irradiance.

Patterns of fluctuating irradiance can be classified as lightflecks and sunflecks. While lightflecks are artificial increases in irradiance with defined intensity, duration and spectrum (Pearcy et al., 1996), sunflecks are natural increases in irradiance above a threshold intensity, with great temporal, spatial and spectral heterogeneity (Smith and Berry, 2013).

Steady-state responses of photosynthesis to $[\text{CO}_2]$, leaf temperature and $\text{VPD}_{\text{leaf-air}}$ are well understood, which makes analysing gas exchange dynamics in response to fluctuating irradiance easier. In this review, we consider environmental factors besides irradiance to be constant when we look at their role as modulators of dynamic photosynthesis, because a) there are empirical data available on this situation and b) considering two or more factors as changing dynamically would make this already complex process overly complicated. We review the modulation of dynamic photosynthesis by $[\text{CO}_2]$, leaf temperature and $\text{VPD}_{\text{leaf-air}}$, by a) building a framework of all processes that may affect dynamic photosynthesis on the levels of electron transport, flux of metabolites through the Calvin cycle and leaf CO_2 diffusion and b) examining the effects of $[\text{CO}_2]$, leaf temperature and $\text{VPD}_{\text{leaf-air}}$ on underlying processes and on dynamic gas exchange parameters. Using this structure, the reader is first introduced to the “machinery” of dynamic photosynthesis in a mechanistic way, making the following analysis of modulation of dynamic photosynthesis by environmental factors much simpler to understand.

2.2 Dynamic control of photosynthetic gas exchange

The complex process of dynamic photosynthesis can be deconstructed into three major processes: photosynthetic induction, post-illumination CO_2 fixation and post-illumination CO_2 burst (Figure 2.1). Photosynthetic induction itself is driven by sub-processes such as RuBP regeneration, Rubisco activation and stomatal movement. Changes of mesophyll conductance (g_m) and non-photochemical quenching (NPQ) in response to irradiance may further modulate dynamic photosynthesis, and are affected by $[\text{CO}_2]$ and leaf temperature. All of these processes are described below, in a framework (Figure 2.2) that will help

understand modulation of dynamic photosynthesis by $[CO_2]$, leaf temperature and $VPD_{leaf-air}$.

2.2.1 Control of electron transport

2.2.1.1 Electron and proton transport

Light driven charge separation in the reaction centres of photosystems (PS) I and II initiates an electron transport process that results in the oxidation of water on the lumenal side and reduction of ferredoxin on the stromal side of the thylakoid, reducing $NADP^+$ to NADPH (Cruz et al., 2001; Foyer et al., 2012). Electron transport processes are coupled to proton transport across the thylakoid membrane. Proton transport builds up the proton motive force (pmf), which after dark-light transitions mainly consists of a trans-thylakoid electrical potential ($\Delta\Psi$), but partitions into $\Delta\Psi$ and a pH gradient across the thylakoid membrane (ΔpH) after several seconds (Cruz et al., 2001). The pmf affects 1) ATP synthesis, 2) NPQ via ΔpH , 3) maximum electron transport rates (ETR) through the cytochrome b_6/f complex and 4) movement of Mg^{2+} -ions across the thylakoid membrane into the stroma due to $\Delta\Psi$ (Cruz et al., 2001; Foyer et al., 2012). Regulatory mechanisms of electron and proton transport currently receive much attention due to their pivotal role in protecting the photosynthetic apparatus and in balancing ATP/NADPH ratios in fluctuating light. They are dealt with in great detail in recent reviews (Kramer and Evans, 2011; Foyer et al., 2012; Tikkanen et al., 2012; Kono and Terashima, 2014; Shikanai, 2014). In the context of this review, electron and proton transport are mostly important in regulating NPQ and the thioredoxin-ferredoxin system, which in turn activates several of the light-regulated Calvin cycle enzymes.

2.2.1.2 Non-photochemical quenching

Protecting PSII from damage by absorbed excess energy, NPQ is the result of up to four processes that operate at different time scales. These processes include energy-dependent quenching (qE), state transitions, zeaxanthin-dependent quenching, and photoinhibition (Nilkens et al., 2010; Jahns and Holzwarth, 2012; Ruban et al., 2012). The most important process with regards to fluctuating irradiance is qE, as it responds most quickly to changes in irradiance. Additionally, it normally accounts for the largest fraction of NPQ (Ruban et al., 2012). The formation of qE is strictly dependent on the build-up of ΔpH and its sensing by the PSII protein PsbS (Li et al., 2000b; Li et al., 2004). PsbS is most likely a catalyst of qE (Goral et al., 2012; Hubbart et al., 2012). Furthermore, qE is modulated by the amount of zeaxanthin and antheraxanthin (Johnson et al., 2011), carotenoids that are formed from violaxanthin in the xanthophyll cycle; the exact role of the xanthophyll cycle in qE is still under debate (Jahns and Holzwarth, 2012).

Half-times for induction and relaxation of qE are between 15 and 60 seconds (Walters and Horton, 1991; Nilkens et al., 2010; Peguero-Pina et al., 2013). Because relaxation kinetics of qE are slower than the rate of change of irradiance, qE transiently competes with ETR after lightflecks and could decrease integrated daily photosynthesis by 13-32%, compared to the hypothetical situation of instant relaxation of qE (Zhu et al., 2004). Relative losses due to downregulated ETR are greater in low irradiance (Tausz et al., 2005). Furthermore, Zhu et al. (2004) assumed qE to be strongly affected by leaf temperature, making it a process that could impact on dynamic photosynthesis and be modulated by other environmental factors. In transgenic *Oryza sativa* plants overexpressing PsbS, photosynthetic induction was slower because of decreased ETR (Hubbart et al., 2012). Unfortunately, no data were presented that linked qE relaxation

kinetics after decreases in irradiance to photosynthesis rates. Considering the extent of hypothesized effects of slow qE relaxation kinetics on plant productivity (Zhu et al., 2004), it seems worthwhile to underpin those with experimental evidence.

2.2.2 Control of metabolite flux through the Calvin cycle

2.2.2.1 RuBP regeneration activation state

At low irradiance, pools of RuBP and its precursors are small (Sassenrath-Cole and Pearcy, 1992), but increase in higher irradiance. It is assumed that RuBP concentrations are non-limiting when they are 1.5-2 times the active site concentration of Rubisco (Woodrow and Mott, 1989; Sassenrath-Cole and Pearcy, 1992; Pearcy et al., 1996), a level which is reached or exceeded one minute after illumination (Sassenrath-Cole and Pearcy, 1992). Measured half-times of activation and deactivation of RuBP regeneration are in the range of 2-3 minutes (Kirschbaum et al., 1988; Sassenrath-Cole and Pearcy, 1994a). In dark-adapted leaves, the overall limitation due to inactive RuBP regeneration is small, compared to limitations imposed by inactive Rubisco and closed stomata. However, because RuBP regeneration deactivates more quickly in low irradiance than Rubisco (Sassenrath-Cole and Pearcy, 1992), it can impose large limitations on integrated photosynthesis rates in naturally fluctuating irradiance.

Chloroplast FBPase (fructose-1,6-bisphosphatase) and SBPase (sedoheptulose-1,7-bisphosphatase) activity limit RuBP-regeneration activation (Stitt et al., 1980; Prinsley et al., 1986b; Sassenrath-Cole and Pearcy, 1992; Sassenrath-Cole and Pearcy, 1994a). Also, PRK (phosphoribulokinase) may limit the activation of RuBP-regeneration (Sassenrath-Cole and Pearcy, 1992; Sassenrath-Cole and Pearcy, 1994a). Activation of PRK saturated at much lower irradiance than FBPase (Sassenrath-Cole and Pearcy, 1994a). Also, PRK

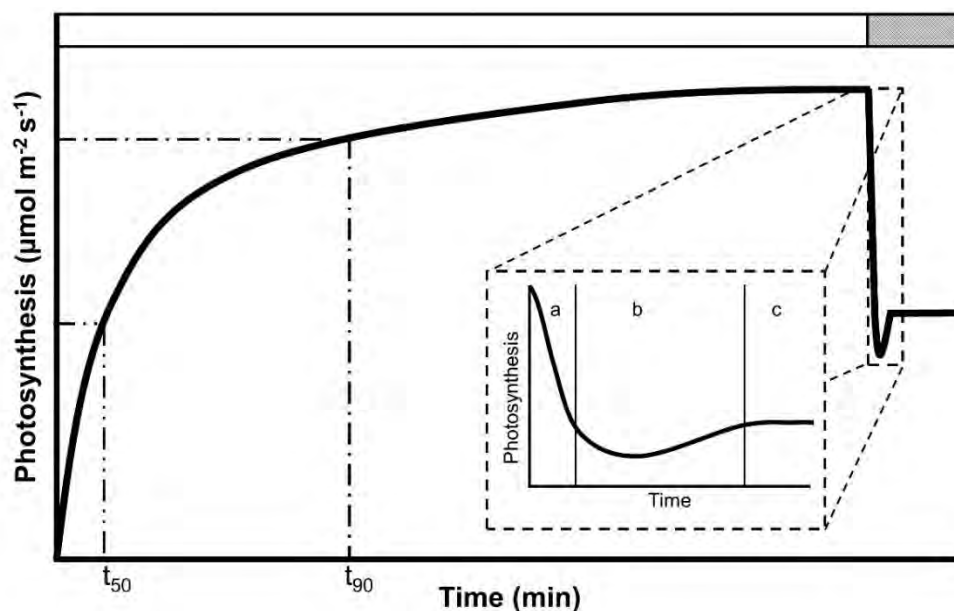


Figure 2.1: Schematic of transient net photosynthesis phenomena upon increase and decrease in irradiance: Photosynthetic induction in a dark-adapted leaf during lightfleck (high irradiance, e.g. $1000 \mu\text{mol m}^{-2} \text{s}^{-1}$, white bar), followed by post-illumination CO_2 fixation and post-illumination CO_2 burst after lightfleck (low irradiance, e.g. $200 \mu\text{mol m}^{-2} \text{s}^{-1}$, grey bar). t_{50} , t_{90} : time required to reach 50 and 90% of full photosynthetic induction, respectively. Inset: a) post-illumination CO_2 fixation, b) post-illumination CO_2 burst and c) new steady-state photosynthesis after lightfleck.

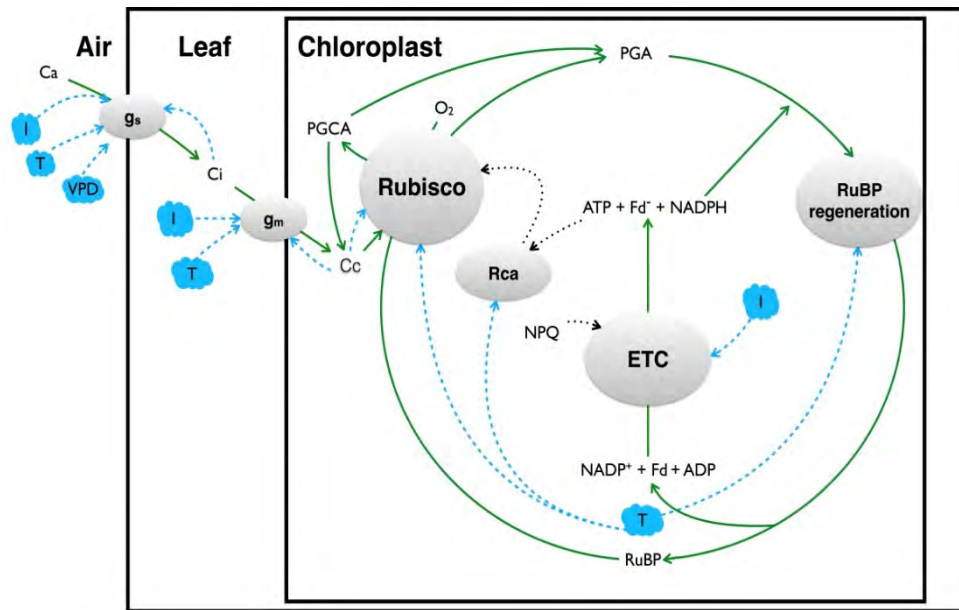


Figure 2.2: Depiction of major components and processes of dynamic photosynthesis (grey circles), and main effects of environmental factors (blue clouds). Material flows are shown as green solid arrows, information flows between processes as dotted arrows and information flows from environmental factors towards processes as blue, dashed arrows. Depending on its location, CO_2 is named either C_a (ambient CO_2 concentration), C_i (substomatal cavity CO_2 concentration) or C_c (chloroplast CO_2 concentration). Further abbreviations: ADP, adenosine diphosphate; ATP, adenosine triphosphate; ETC, electron transport chain; Fd, ferredoxin; g_m , mesophyll conductance; g_s , stomatal conductance; I, irradiance; NADPH, nicotinamide adenine dinucleotide phosphate; NPQ, non-photochemical quenching; O_2 , oxygen; PGA, 3-phosphoglycerate; PGCA, 2-phosphoglycolate; Rca, Rubisco activase; Rubisco, ribulose-1,5-bisphosphate carboxylase oxygenase; RuBP, ribulose-1,5-bisphosphate; T, temperature; VPD, leaf-to-air vapour pressure deficit.

activated more quickly than FBPase and SBPase in lightflecks (Champigny and Bismuth, 1976; Laing et al., 1981; Kobza and Edwards, 1987) and deactivated comparably slowly thereafter (Avron and Gibbs, 1974). Altogether, FBPase and SPBase limit the activation of RuBP regeneration more strongly than PRK.

FBPase and SBPase are directly regulated by the thioredoxin-ferredoxin system (Raines et al., 1999; Ruelland and Miginiac-Maslow, 1999). They are oxidized, and therefore inactive, in the dark. Upon illumination, reducing power is transferred from PSI via ferredoxin to thioredoxin, which reduces and thus activates the enzymes (Ruelland and Miginiac-Maslow, 1999). FBPase is further stabilised and positively regulated by its substrate FBP (fructose-1,6-bisphosphate; Scheibe, 2004), stromal pH and Mg^{2+} (Ishijima et al., 2003), and inhibited by glycerate and its product fructose-6-phosphate (Gardemann et al., 1986; Schimkat et al., 1990). Also, SBPase activity is positively regulated by Mg^{2+} , stromal pH and its substrate sedoheptulose-1,7-bisphosphate (Schimkat et al., 1990), and negatively by inorganic phosphate, glycerate, RuBP and its product sedoheptulose-7-phosphate (Schimkat et al., 1990; Ishijima et al., 2003).

PRK can form a complex with the enzyme glyceraldehyde-3-phosphate dehydrogenase (GAPDH) and a chloroplast protein, CP12, in darkness (Wedel et al., 1997; Howard et al., 2008). In *Pisum sativum* leaves, the complex dissociated within minutes of illumination; the extent of dissociation increased with irradiance between up to $300 \mu\text{mol m}^{-2} \text{s}^{-1}$ (Howard et al., 2008), providing flexible regulation of PRK. However, in dark-adapted leaves of other species (*Vicia faba*, *Solanum tuberosum*, *Solanum lycopersicum* and

Spinacia oleracea), enzymes existed both bound by the PRK/GAPDH/CP12 complex and as free enzymes, while in others (*Phaseolus vulgaris*, *Nicotiana tabacum* and *Arabidopsis thaliana*) the enzymatic complex was almost absent (Howard et al., 2011). Thus, the regulation of PRK and GAPDH activity by CP12 is far from universal among species. It is not clear whether the interspecific differences in PRK regulation impact on RuBP regeneration activation.

2.2.2.2 Rubisco activation state

To fix carbon, Rubisco must be carbamylated, i.e. Rubisco (E) needs to form a complex (ECM) with CO₂ and Mg²⁺ (Woodrow et al., 1996). For carboxylation, RuBP (R) and another CO₂ molecule need to bind to ECM. Several inhibitory sugar phosphates can bind to Rubisco, preventing ECM formation, or to ECM, preventing carboxylation (Salvucci and Crafts-Brandner, 2004): Firstly, RuBP can bind to uncarbamylated Rubisco and form a stable but inactive ER complex (Salvucci and Crafts-Brandner, 2004); it may also bind to EC (McNevin et al., 2006). Secondly, by misprotonation of RuBP during carboxylation or oxygenation, inhibitory sugar phosphates such as PDBP (D-glycero-2,3-pentodiulose-1,5-bisphosphate), 3KABP (3-ketoarabinitol bisphosphate) or XuBP (xylulose-1,5-bisphosphate; collectively abbreviated as 'X') are formed, which can bind to carbamylated Rubisco (Salvucci and Crafts-Brandner, 2004; Andralojc et al., 2012). They might also bind to E and EC complexes (McNevin et al., 2006). Thirdly, CA1P (2-carboxy-D-arabinitol 1-phosphate) can bind to ECM instead of RuBP in low irradiance or darkness (Parry et al., 2013). CA1P is probably present in most species, but not always in concentrations high enough to take effect (Andralojc et al., 2012). In darkness, the activation state of Rubisco can be strongly [CO₂]-dependent, as long as Rubisco is unaffected by CA1P. Namely, the Rubisco activation state can be higher in darkness than in low irradiance, since newly formed RuBP in low irradiance can bind to uncarbamylated Rubisco sites, while in darkness no RuBP is formed and CO₂ binds instead, keeping Rubisco carbamylated (Carmo-Silva and Salvucci, 2013).

To keep ECM catalytically competent and to free inactive ER, EX, ECR and ECX complexes, the chaperone Rubisco activase (Rca) is required (Salvucci et al., 1985; Portis et al., 1986). Rca is inactive in darkness and is activated on illumination (Portis, 2003). Alternative splicing of the Rca gene results in two isoforms: The α -isoform in *A. thaliana* is regulated by the thioredoxin-ferredoxin system, while regulation of the smaller β -Rca is unclear and differs across species (Portis, 2003; Carmo-Silva and Salvucci, 2013). When both isoforms are present, α -Rca controls β -Rca (Zhang and Portis, 1999). Rca requires ATP for catalytic activity and is inhibited by ADP (Zhang and Portis, 1999; Portis, 2003). However, in a recent study using *A. thaliana* mutants, plants containing only β -Rca did not exhibit ADP sensitivity, and kept Rubisco almost fully activated in low irradiance (Carmo-Silva and Salvucci, 2013). Consequently, photosynthetic induction was much faster. In transgenic *N. tabacum* plants with substantially decreased Rca levels, no decreases in steady-state Rubisco activation state were found (Mate et al., 1993). It was inferred that theoretically, a concentration of Rca 200 times lower than Rubisco could suffice to keep Rubisco activated (Mate et al., 1993), although this would slow down the rate of activation significantly. Naturally occurring Rca concentrations are much higher than that, which may help to use fluctuating irradiance more efficiently. The optimal allocation of nitrogen between Rubisco and Rca could therefore depend on a plant's microclimate (Mott and Woodrow, 2000). For more extensive reviews of Rubisco activation, see Parry et al.

(2013) and (Tcherkez, 2013). For kinetics of Rubisco activation and deactivation, see Pearcy et al. (1996).

Generally, the irradiance-dependent regulation of Rubisco is pivotal to dynamic photosynthesis. The activation state of Rubisco is strongly dependent on the functioning of Rca and is further modulated by $[\text{CO}_2]$ and temperature.

2.2.2.3 Post-illumination CO_2 fixation

After decreases in irradiance, it can be observed in rapid gas exchange measurements that assimilation rates do not directly “fall” to a new steady state, but that their decrease lags behind for a few seconds (Figure 2.1a). This phenomenon, termed post-illumination CO_2 fixation, increases integrated carbon assimilation of a lightfleck and can substantially increase average photosynthesis rates of leaves in sunfleck environments (Pons et al., 1992; Roden and Pearcy, 1993; Roden, 2003). Post-illumination CO_2 fixation is driven by pools of Calvin cycle intermediates as well as NADPH, ATP and the pmf (Laisk et al., 1984; Sharkey et al., 1986b). These pools build up within seconds (Sharkey et al., 1986b) and their size increases with irradiance intensity in parallel to photosynthesis rates (Laisk et al., 1984), creating a linear relationship between photosynthesis rates and post-illumination CO_2 fixation (Kirschbaum et al., 2005). Integrated post-illumination CO_2 fixation has been shown to correlate well with RuBP pools over various $[\text{CO}_2]$ levels (Ruuska et al., 1999), and has been used to estimate RuBP pools (Osmond et al., 1988; Kirschbaum et al., 1998). As metabolite pool sizes are often proportional to photosynthetic capacity, so are rates of post-illumination CO_2 fixation (Sharkey et al., 1986b; Osmond et al., 1988; Pearcy et al., 1996). Effects of post-illumination CO_2 fixation on integrated photosynthesis are often negligible (Pearcy et al., 1996). However, as its fraction of integrated dynamic photosynthesis is inversely related to lightfleck length (Roden and Pearcy, 1993), it could increase photosynthesis in species with strongly fluttering leaves (by 5-15%, as estimated by Roden, 2003), as leaf flutter can facilitate extremely short lightflecks.

2.2.2.4 Post-illumination CO_2 burst

After post-illumination CO_2 fixation, a dip in net photosynthesis rates, termed post-illumination CO_2 burst (Decker, 1955) may be visible in gas exchange data (Figure 2.1b). Post-illumination CO_2 bursts of different kinetics occur in C_3 , CAM and some C_4 plants. Different origins of these bursts, related to photorespiration in C_3 and CAM plants (Crews et al., 1975; Vines et al., 1983), overshoots in sucrose synthesis in C_3 plants (Prinsley et al., 1986b), phosphoenolpyruvate carboxykinase activity in CAM plants (Crews et al., 1975), and differences in the activity of malate dehydrogenase in C_4 plants (Downton, 1970) have been reported. In this review, only the photorespiratory CO_2 burst will be considered, as it is most pronounced and most strongly modulated by $[\text{CO}_2]$ and temperature.

The photorespiratory post-illumination CO_2 burst is caused by a transient rise in photorespiratory CO_2 production (Vines et al., 1983; Prinsley et al., 1986b). This is usually explained by a lag-time between adjustment of photorespiratory 2-phosphoglycolate (PGCA) recycling relative to Calvin cycle cycling. After lightflecks, PGCA is recycled into 3-phosphoglycerate (PGA) at a rate which is temporarily higher than at steady state; the corresponding consumption of ATP and reductant as well as CO_2 evolution during glycine decarboxylation cause the burst (Rawsthorne and Hylton, 1991). In *Pelargonium x hortorum*, lightflecks of at least 5 minutes duration were required to maximise the burst

(Vines et al., 1983). Further, a positive correlation of photosynthesis rates after lightflecks and burst magnitude suggests that this phenomenon requires energy (Vines et al., 1983).

2.2.3 Control of CO₂ supply to Rubisco

2.2.3.1 Stomatal conductance

Stomatal conductance (g_s) often decreases in low irradiance, which, together with slow stomatal opening during lightflecks, may limit dynamic photosynthesis. Stomatal limitation during induction can be calculated by correcting assimilation rates for the change in concentration of CO₂ in the substomatal cavity (C_i) (Woodrow and Mott, 1989; Tinoco-Ojanguren and Pearcy, 1993b; Allen and Pearcy, 2000b). It is often assumed that g_s always limits induction, despite reports to the contrary (Ögren and Sundin, 1996; Tausz et al., 2005; Tomimatsu and Tang, 2012). There may be two reasons for this. Firstly, stomatal limitations have often not been analysed, even though the necessary data (dynamic CO₂ exchange and g_s) were available (Chazdon and Pearcy, 1986; Roden and Pearcy, 1993; Pearcy et al., 1997; Pepin and Livingston, 1997; Naumburg and Ellsworth, 2000; Leakey et al., 2002; Leakey et al., 2003). Secondly, many studies focus on forest understory species, which may not be representative of other plant functional types. Re-evaluation of published datasets and genotypes with contrasting stomatal behaviour (Tomimatsu and Tang, 2012) may help to quantify stomatal limitations on dynamic photosynthesis.

Rates of stomatal opening and closure after changes in irradiance are highly heterogeneous between species, environmental conditions and plant functional types. In several closely related *Banksia* trees, smaller stomata opened and closed faster in response to lightflecks than larger stomata, possibly due to their larger membrane surface area to volume ratio (Drake et al., 2013). Two meta-analyses found that on average, stomatal opening in lightflecks was faster than stomatal closure after lightflecks (Ooba and Takahashi, 2003; Vico et al., 2011). However, there was large variation in these traits. In fact, several datasets showed faster stomatal closure than opening (Ooba and Takahashi, 2003; Vico et al., 2011), which could be due to different environmental conditions between experiments.

Stomata respond to a myriad of intrinsic and extrinsic factors, among them all environmental factors discussed in this review. For changes in a single factor, the response is often well known. Far less work has been done on the kinetics of the response (Lawson and Blatt, 2014) or simultaneous changes in several factors, which are likely in nature (e.g. increase in irradiance and leaf temperature, decrease in C_i and $VPD_{\text{leaf-air}}$). Recently, Merilo et al. (2014) have shown that effects of different environmental factors on g_s are non-multiplicative, rarely predictable and strongly species-dependent. This challenges the often-held model assumption that effects of single factors are multiplicative and uniform across species (Damour et al., 2010).

2.2.3.2 Mesophyll conductance

Mesophyll conductance (g_m), mediating CO₂ diffusion from the substomatal cavity to chloroplast, can be a substantial limitation to photosynthesis. It can vary within minutes, and is affected by changes in irradiance, [CO₂] and temperature (Flexas et al., 2007a; Flexas et al., 2008; Tholen et al., 2008; Evans and Von Caemmerer, 2013), making it a potentially important process within the framework of this review. The possible components of g_m , its short-term variability in response to environmental factors and

possible artefacts of methods used for its estimation are under ongoing discussion (Tholen et al., 2012; Griffiths and Helliker, 2013). Relevant factors that may potentially contribute to variations in g_m are carbonic anhydrase, aquaporins, anatomical properties of leaves and cells (Flexas et al., 2012) and the area of chloroplasts facing intercellular spaces (Tholen et al., 2008). Of these, all but the basic anatomical properties of leaves and cells may be affected by short-term changes in environmental factors. Estimating g_m correctly is difficult, and every method has different drawbacks and underlying assumptions. Therefore, using at least two methods simultaneously is recommended (Flexas et al., 2013). Two methods are currently available for measuring rapidly changing g_m : the 'variable J method', using simultaneous gas exchange and chlorophyll fluorescence (Harley et al., 1992a) and online carbon isotope discrimination, using tunable diode laser absorption spectroscopy (Evans and Von Caemmerer, 2013). Combining these methods under various environmental factors should be of great use to determine the dynamics of g_m in fluctuating irradiance and to underpin theories regarding its regulation.

2.3 Environmental factors influencing dynamic photosynthesis

In the remainder of this review, the effects of $[CO_2]$, leaf temperature and $VPD_{\text{leaf-air}}$ on the processes driving dynamic photosynthesis are discussed; they are summarized in Table 2.1. While changes in $[CO_2]$ are normally gradual, leaf temperature and $VPD_{\text{leaf-air}}$ fluctuate almost as rapidly as irradiance itself. Thus, findings with regards to $[CO_2]$ effects presented here may be used for future climate change scenarios, while findings regarding the other two factors can be used with regards to current natural conditions.

2.3.1 CO_2 concentration

Increased $[CO_2]$ generally stimulates rates of photosynthetic induction, and enhances photosynthesis and growth in fluctuating irradiance (Leakey et al., 2002). In previous work, $[CO_2]$ was manipulated either during measurements (Chazdon and Pearcy, 1986) or continuously during plant growth (Naumburg and Ellsworth, 2000; Leakey et al., 2002; Holišová et al., 2012; Tomimatsu and Tang, 2012). In three out of five studies, elevated $[CO_2]$ led to faster photosynthetic induction (Chazdon and Pearcy, 1986; Leakey et al., 2002; Tomimatsu and Tang, 2012). Naumburg and Ellsworth (2000) found no differences in induction rates, while Holišová et al. (2012) reported faster induction for one of two species in elevated $[CO_2]$. The difference in outcomes between studies may be explained by $[CO_2]$ treatment levels (Naumburg and Ellsworth (2000) and Holišová et al. (2012) used the narrowest range between $[CO_2]$ treatments of the studies mentioned), experimental procedures or species differences.

Combining data from several experiments (Chazdon and Pearcy, 1986; Leakey et al., 2002; Tomimatsu and Tang, 2012) revealed that the time required to reach 90% of full induction (t_{90} , visualized in Figure 2.1) decreased with increasing $[CO_2]$ (Figure 2.3; $R^2=0.51$). This effect was more pronounced between 200 and 600 $\mu\text{mol mol}^{-1}$. Because average t_{90} was 16 minutes, this indicates positive effects of $[CO_2]$ on stomatal limitations. No trend was observed for the time to reach 50% of full induction (t_{50} ; Figure 2.3). As average t_{50} was 3 minutes, a time range in which Rubisco activity is normally most limiting, this suggests that $[CO_2]$ did not affect this limitation. The overall effect of $[CO_2]$ on t_{90} was visible for every dataset in Figure 2.3, suggesting that decreasing t_{90} with increasing $[CO_2]$ is a general response among plants. Induction data from Naumburg and Ellsworth (2000) and

Holišová et al. (2012) were not included here, as they were not provided in the original studies.

In *S. oleracea* leaves, after small increases in irradiance, Rubisco activation was highly sensitive to $[\text{CO}_2]$. However, after large irradiance increases, it was $[\text{CO}_2]$ -insensitive ($[\text{CO}_2]$ range: 100-300 $\mu\text{mol mol}^{-1}$; Woodrow et al. (1996)). Woodrow and colleagues assumed that $[\text{CO}_2]$ -sensitive activation reflected a limitation by Rubisco carbamylation, while $[\text{CO}_2]$ -insensitive activation reflected Rca limitation. Elevated $[\text{CO}_2]$ reduced the loss of induction (i.e. the deactivation of Calvin cycle enzymes and stomatal closure) in low irradiance after 5 (Leakey et al., 2002), 6 and 12 minutes (Naumburg and Ellsworth, 2000), probably slowing down Rubisco deactivation. The relationship between low irradiance and $[\text{CO}_2]$ affecting the loss of induction needs further exploration, as deactivation of Rubisco can be different between low irradiance and darkness.

High $[\text{CO}_2]$ generally reduces g_s . However, effects of $[\text{CO}_2]$ on g_s dynamics in fluctuating irradiance are less clear: While stomatal opening rates during lightflecks in elevated $[\text{CO}_2]$ were increased in Naumburg et al. (2001a) and Leakey et al. (2002), they were decreased in Tomimatsu and Tang (2012). Stomata closed faster after lightflecks in elevated $[\text{CO}_2]$ (Naumburg et al., 2001a). Elevated $[\text{CO}_2]$ also appears to decrease g_m in various plant species (Flexas et al., 2007b; Flexas et al., 2008), however this apparent change may be due to changes in re-assimilation of CO_2 emitted from the mitochondria (Tholen et al., 2012). Elevated $[\text{CO}_2]$ decreased steady-state NPQ at various irradiance levels in *Quercus ilex* (Arena et al., 2005), and during long-term exposure in *Betula pendula* (Riikonen et al., 2005). Additionally, elevated $[\text{CO}_2]$ increased the overall efficiency of electron transport through PSII (Riikonen et al., 2005), which should lead to smaller transient limitations of ETR after decreases in irradiance. Increasing $[\text{CO}_2]$ decreases post-illumination CO_2 fixation (Laisk et al., 1984; Ruuska et al., 1999; Sun et al., 1999) and suppresses photorespiration and associated post-illumination CO_2 burst (Vines et al., 1983; Leakey et al., 2002).

To summarize, elevated $[\text{CO}_2]$ increases photosynthetic induction rates in C_3 plants, and leads to slower loss of induction. More work is needed to confirm prior data on g_m dynamics as affected by both irradiance and $[\text{CO}_2]$ (Flexas et al., 2007b), and to quantify interactions between irradiance and $[\text{CO}_2]$ during loss of induction.

2.3.2 Temperature

The temperature response of net photosynthesis generally follows a parabolic curve, often with an optimum at the growth temperature (Yamori et al., 2014). Leaf temperature affects dynamic photosynthesis on many levels, due to temperature sensitivity of Rca and of the enzymes involved (Rubisco, FBPase, SBPase and PRK). Between 5 and 30 °C, net photosynthesis rates (Bernacchi et al., 2013) and enzyme turnover generally increase. Increased turnover possibly reduces limitations due to the activation of RuBP-regeneration and Rubisco.

Combining data from photosynthetic induction experiments with various leaf temperatures during measurements (Küppers and Schneider, 1993; Pepin and Livingston, 1997; Leakey et al., 2003; Yamori et al., 2012; Carmo-Silva and Salvucci, 2013) revealed that the response of t_{90} and t_{50} to leaf temperature was best described by parabolic relationships (Figure 2.4), albeit with strong scatter. The optimum temperature for rate of photosynthetic induction was approx. 30 °C (Figure 2.4). However, some

datasets did not follow this trend (e.g. increasing t_{90} between 15 and 25 °C, closed diamonds in Figure 2.4), leading to a less uniform response of induction rates to temperature than to $[CO_2]$ (Figure 2.3). Interestingly though, the parabolic effects of temperature on induction rates found here matched those for rates of Rubisco activation by Rca for *A. thaliana*, *Camelina sativa*, *N. tabacum* and *Gossypium hirsutum* (Carmo-Silva and Salvucci, 2011). At 38 °C compared to 28 °C, *S. leprosula* showed faster loss of photosynthetic induction, and photosynthesis was more strongly reduced in fluctuating (59% reduction) than in constant irradiance (40% reduction) (Leakey et al., 2003).

At moderately high temperatures (above 30-35 °C), Rubisco activity decreases (Eckardt et al., 1997), due to lowered Rca activity and faster formation of inhibitory sugar phosphates (Feller et al., 1998; Salvucci and Crafts-Brandner, 2004; Yamori et al., 2006). In most species, Rca forms high-molecular-weight aggregates that are catalytically incompetent above 30-35 °C (Feller et al., 1998). However, examples of functioning photosynthesis at higher temperatures exist: The desert plant *Rhazya stricta* maintained irradiance- and CO_2 -saturated net photosynthesis rates up to 43 °C, which may be due to differences between the two isoforms of the plant's Rca (Lawson et al., 2014). Transgenic *O. sativa* plants with increased Rca contents showed faster photosynthetic induction at 15, 25 and 40 °C due to higher Rubisco activation state at low irradiance (Yamori et al., 2012). Thus, increased Rca contents or different Rca isoforms can enhance (dynamic) photosynthesis greatly in a large temperature range.

Table 2.1: Effects of environmental factors on processes controlling dynamic photosynthesis after increases or decreases in irradiance. Environmental factors considered are: ambient CO_2 concentration ($[CO_2]$), leaf temperature and leaf-to-air vapour pressure deficit ($VPD_{leaf-air}$)

		Environmental factor			
		$[CO_2]$	Temperature		$VPD_{leaf-air}$
Change in irradiance	Process		Medium ^a	High ^b	
Increase	RuBP-regeneration activation	- ^c	↑	↗	-
	Rubisco activation	~	↑	↓	↗
	Stomatal opening	~	~	~	↓
	qE buildup	↘	↘	↘	-
	Mesophyll conductance increase	?	↑	~	~
Decrease	RuBP-regeneration deactivation	-	?	?	-
	Rubisco deactivation	↓	?	↑	↗
	Stomatal closure	↑	?	?	↑
	Post-illumination CO_2 fixation	↓	↑	↓	?
	Post-illumination CO_2 burst	↓	↑	↑	?

^a Temperature range: 5 to approx. 30 °C

^b Temperature range: >30 °C

^c Symbols: ↑, ↓: increase or decrease in rate of the process when environmental factor increases; ↗, ↘: hypothesized increase and decrease; - : no effect; ~ : conflicting relationship throughout literature; ?: unknown relationship

Photorespiration, and hence the post-illumination CO₂ burst, increases with temperature (Peterson, 1983), because the ratio [CO₂]/[O₂] in the chloroplast decreases, and because Rubisco specificity for O₂ increases (Foyer et al., 2009). In *O. sativa*, post-illumination CO₂ fixation showed a parabolic response to leaf temperature, increasing in the range 10-30 °C and decreasing at higher leaf temperatures (Sun et al., 1999).

No straightforward relationship exists between g_s and temperature. While rising temperatures increase net photosynthesis rates and guard cell metabolic activity (stimulating stomatal opening), increased C_i from higher respiration and photorespiration may have a diminishing effect on stomatal opening (Willmer and Fricker, 1996). Additionally, VPD_{leaf-air} increases concomitantly with leaf temperature, which is likely to decrease g_s . Thus, there is strong variation in optimum temperatures for maximum g_s (Willmer and Fricker, 1996). Mesophyll conductance, on the other hand, increases in many plant species between 5 and 20 °C and is either constant or decreases at higher temperatures (Flexas et al., 2008). However, in *N. tabacum*, g_m and temperature were linearly correlated up to 40 °C (Evans and Von Caemmerer, 2013).

In irradiance above 1000 $\mu\text{mol m}^{-2} \text{s}^{-1}$, there was no relationship between NPQ and temperature (Bilger et al., 1991; Clarke and Johnson, 2001), while in lower irradiances, steady-state NPQ decreased with increasing temperature (Clarke and Johnson, 2001). Furthermore, relaxation of NPQ after light-dark transitions was severely slowed down at temperatures below 20 °C (Bilger et al., 1991; Gilmore and Björkman, 1995). Overall, this suggests small initial and quickly relaxing NPQ with increasing temperatures, and therefore reduced limitation of ETR after lightflecks.

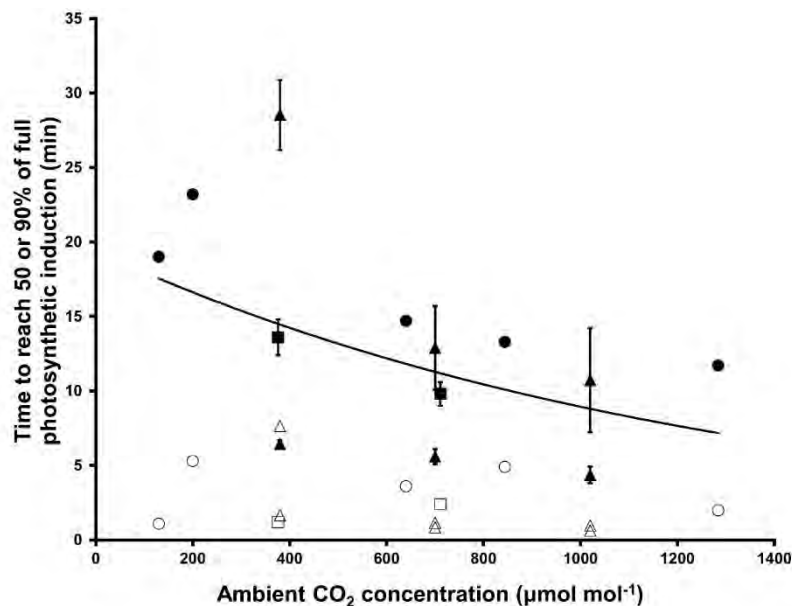


Figure 2.3: Time (minutes) required to reach 50% (t_{50} , open symbols) and 90% (t_{90} , closed symbols) of full photosynthetic induction after a step increase in irradiance, as affected by ambient CO₂ concentration ($\mu\text{mol mol}^{-1}$). Data by Chazdon and Pearcy (1986) (circles); Leakey et al. (2002) (squares) and Tomimatsu and Tang (2012) (triangles). Species included *Alocasia macrorrhiza* (circles), *Shorea leprosula* (squares) and *Populus koreana* x *trichocarpa* as well as *Populus euramericana* (triangles). Error bars ($\pm\text{SE}$) are shown if supplied in the original publication. The negative exponential relationship ($R^2 = 0.51$) between t_{90} and $[\text{CO}_2]$ is described by: $t_{90} = 22.7e^{-7E-04[\text{CO}_2]}$. No relationship between t_{50} and $[\text{CO}_2]$ was found.

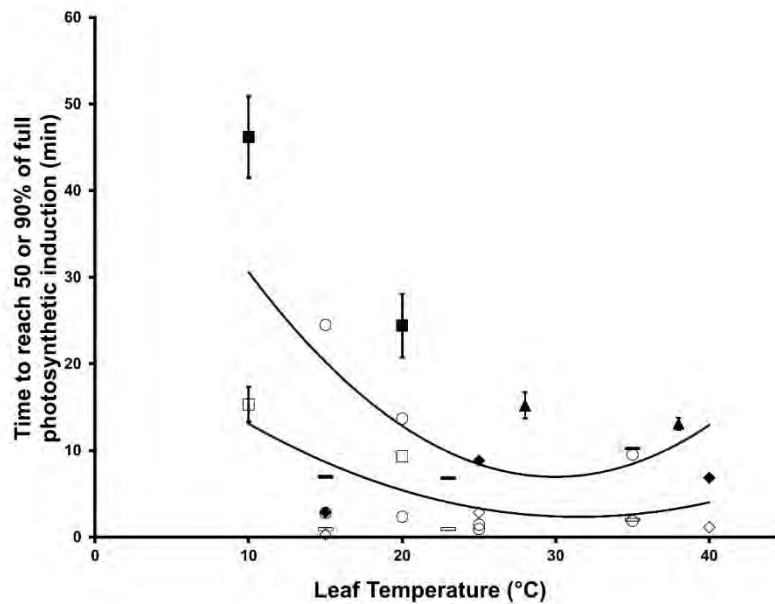


Figure 2.4: Time (min) required to reach 50% (t_{50} , open symbols) and 90% (t_{90} , closed symbols) of full photosynthetic induction after a step increase in irradiance, as affected by leaf temperature (T , °C). Data by Küppers and Schneider (1993) (circles); Pepin and Livingston (1997) (squares); Leakey et al. (2003) (triangles); Yamori et al. (2012) (diamonds) and Carmo-Silva and Salvucci (2013); (Lever et al., 2013) (bars). Species included *F. sylvatica* (circles), *Thuja plicata* (squares), *Shorea leprosula* (triangles), *Oryza sativa* (diamonds) and *Arabidopsis thaliana* (bars). Error bars ($\pm SE$) are shown if supplied in the original publication. 2nd order polynomials were fitted. $t_{90} = 0.06T^2 - 3.55T + 60.19$; $R^2 = 0.34$ and $t_{50} = 0.023T^2 - 1.47T + 25.41$; $R^2 = 0.19$.

Currently, knowledge lacks on how Rubisco deactivation, and decreases in g_s and g_m after lightflecks, are influenced by temperature. Furthermore, it is unclear how activation of RuBP regeneration and Rubisco are affected and which of these processes might consequently limit dynamic photosynthesis more strongly at a given temperature. This knowledge is especially important between 10 and 30 °C, as in this temperature range most global plant productivity takes place.

To summarize, photosynthetic induction rates follow a parabolic response to temperature, with the fastest induction occurring around 30 °C, despite large variation between studies. Above 35 °C, photosynthesis suffers more from high temperature in fluctuating than in constant irradiance. Knowledge is lacking regarding the effects of temperature on the loss of photosynthetic induction and the temperature dependencies of RuBP-regeneration activation and Rubisco activation in fluctuating irradiance.

2.3.3 Air Humidity

Air humidity can affect photosynthesis indirectly through C_i , as stomata tend to close in dry air. Even though g_s generally decreases with increasing VPD_{air} , the extent of stomatal control over transpiration rates differs strongly between species (Monteith, 1995). Whether changes in VPD_{air} affect rates of dynamic photosynthesis depends on the extent to which g_s , and consequently C_i , change in response to VPD_{air} , which in turn depends on species and leaf water status. The only study on $VPD_{leaf-air}$ in dynamic photosynthesis (using *Piper aequale* and *Piper auritum*) showed that decreases in g_s and C_i in elevated $VPD_{leaf-air}$ coincided with lowered photosynthetic induction rates, and increased stomatal limitation during induction (Tinoco-Ojanguren and Pearcy, 1993a). Of course, this may not be representative for all plants and growth conditions. Upon illumination, stomata of

P. aequale and *P. auritum* in elevated $VPD_{\text{leaf-air}}$ exhibited longer lag times in opening, and shorter lag times for closure, thus following a ‘water conservation’ response (Tinoco-Ojanguren and Pearcy, 1993b; Tinoco-Ojanguren and Pearcy, 1993a). In *Sambucus nigra* and *Aegopodium podagraria* leaves, stomata both opened and closed faster in elevated $VPD_{\text{leaf-air}}$; additionally, stomatal aperture showed stronger oscillations during lightflecks in elevated $VPD_{\text{leaf-air}}$ (Kaiser and Kappen, 2000, 2001).

Decreased C_i between subsequent lightflecks might reduce Rubisco activation state, which would lead to slower Rubisco activation during lightflecks, as well as reduced carboxylation rates due to lower substrate availability. Very little is known about $VPD_{\text{leaf-air}}$ effects on g_m , and some of the existing data are inconsistent (Flexas et al., 2008). We hypothesize that $VPD_{\text{leaf-air}}$ does not affect the other sub-processes in our framework.

In summary, elevated $VPD_{\text{leaf-air}}$ lowers g_s to a variable extent, which might decrease C_i , affecting both carboxylation rates and Rubisco activation in fluctuating irradiance. Knowledge is most strongly lacking on sensitivity of dynamic g_s changes to $VPD_{\text{leaf-air}}$ between species and its consequences for dynamic photosynthesis.

2.4 Conclusions

The sub-processes of dynamic photosynthesis are differently affected by the climate: the activation state of RuBP-regeneration is only influenced by temperature, while the activation state of Rubisco is directly affected by $[CO_2]$ and temperature, and indirectly (via C_i) by $VPD_{\text{leaf-air}}$. Steady-state g_s is affected by all environmental factors. However, reported $[CO_2]$ effects on g_s in fluctuating light are contradictory. In the case of temperature and $VPD_{\text{leaf-air}}$ effects on dynamic g_s , almost no knowledge exists. Additionally, understanding the roles of g_m and NPQ in dynamic photosynthesis needs more work.

Leaf temperature and $[CO_2]$ affect dynamic photosynthesis rates more strongly than $VPD_{\text{leaf-air}}$, however leaf temperature and $[CO_2]$ effects have been studied more often, such that this conclusion may shift with more experimental evidence. Data comparison revealed similar directionality for $[CO_2]$ effects across studies (Figure 2.3), while leaf temperature effects were more scattered and non-uniform (Figure 2.4). $VPD_{\text{leaf-air}}$ may affect dynamic photosynthesis indirectly through C_i . However, its relative impact on photosynthetic gas exchange likely depends on the sensitivity of g_s to $VPD_{\text{leaf-air}}$. Further, in order to fully understand and quantify dynamic photosynthesis, loss is just as important as gain of photosynthetic induction. Much less literature is available on the former, as loss of induction studies are more time consuming. Loss of induction was diminished in elevated $[CO_2]$, and enhanced in elevated temperatures, while effects of $VPD_{\text{leaf-air}}$ have not been reported.

Large leaps in knowledge were recently made by using genetic transformants or mutants of underlying processes of dynamic photosynthesis, e.g. Rubisco activation by Rca (Yamori et al., 2012; Carmo-Silva and Salvucci, 2013) and the regulation of NPQ (Hubbart et al., 2012; Suorsa et al., 2012). Affecting one sub-process of dynamic photosynthesis at a time, as can be done using mutants or genetic transformants, can help understand the regulation of the system and quantify the effects that one sub-process has on dynamic photosynthesis, possibly in various environmental conditions.

2.5 Acknowledgements

This work was supported in part by the BioSolar Cells open innovation consortium, supported by the Dutch Ministry of Economic Affairs, and in part by Powerhouse. Andreas Savvides and Nikolaos Ntagkas are gratefully acknowledged for highly useful discussions and comments on the manuscript.

Chapter 3

Metabolic and diffusional limitations of photosynthesis in fluctuating irradiance in *Arabidopsis thaliana**

* Kaiser E[†], **Morales A**[†], Harbinson J, Heuvelink E, Prinzenberg AE, Marcelis LFM (2016) Metabolic and diffusional limitations of photosynthesis in fluctuating irradiance in *Arabidopsis thaliana*. Scientific Reports 6:31252.
doi:10.1038/srep31252

[†] These authors contributed equally.

Abstract

A better understanding of the metabolic and diffusional limitations of photosynthesis in fluctuating irradiance can help identify targets for improving crop yields. We used different genotypes of *Arabidopsis thaliana* to characterise the importance of Rubisco activase (Rca), stomatal conductance (g_s), non-photochemical quenching of chlorophyll fluorescence (NPQ) and sucrose phosphate synthase (SPS) on photosynthesis in fluctuating irradiance. Leaf gas exchange and chlorophyll fluorescence were measured in leaves exposed to stepwise increases and decreases in irradiance. *rwt43*, which has a constitutively active Rubisco enzyme in different irradiance intensities (except in darkness), showed faster increases than the wildtype, Colombia-0, in photosynthesis rates after step increases in irradiance. *rca-2*, having decreased Rca concentration, showed lower rates of increase. In *aba2-1*, high g_s increased the rate of change after stepwise irradiance increases, while in C24, low g_s tended to decrease it. Differences in rates of change between Colombia-0 and plants with low levels of NPQ (*npq1-2*, *npq4-1*) or SPS (*spsa1*) were negligible. In Colombia-0, the regulation of Rubisco activation and of g_s were therefore limiting for photosynthesis in fluctuating irradiance, while levels of NPQ or SPS were not. This suggests Rca and g_s as targets for improvement of photosynthesis of plants in fluctuating irradiance.

3.1 Introduction

In physiological research, plants are often studied under constant environmental conditions. However, plants grow in a variable environment, with changes occurring in the time range of seconds or less (Percy et al., 1990). Of the factors important for net photosynthesis (A_n), irradiance changes most quickly (Percy, 1990), causing a lag between changes in irradiance and changes in A_n , due to the slower regulation of photosynthesis (Percy et al., 1996). This lag decreases light-use efficiency relative to the steady state and transiently increases excess irradiance, possibly harming the photosynthetic apparatus (Kono and Terashima, 2014). Leaves engage various mechanisms in response to fluctuating irradiance. Among the best known mechanisms are the regulation of enzymes of carbon fixation and sucrose metabolism, non-photochemical energy dissipation and stomatal conductance, g_s (Percy et al., 1996; Kaiser et al., 2015). Although difficult to measure, cyclic electron transport may be another important mechanism (recently reviewed by Yamori and Shikanai (2016)), due to a potential regulatory role and the balance of ATP versus NADPH production. During induction of photosynthesis in leaves adapted to darkness or low irradiance, the slow regeneration of ribulose-1,5-bisphosphate (RuBP) is typically most limiting until 60 seconds after illumination (Sassenrath-Cole and Percy, 1992). Thereafter, both the slow carboxylation due to partially inactive Rubisco (time to full activation: ~10 minutes) and slow stomatal opening (10-60 minutes) can limit the rate at which photosynthesis increases (Way and Percy, 2012). Thus, the slow rate of change of these mechanisms results in the lag between changes in irradiance and A_n and the resulting reduction of plant productivity (Küppers and Pfiz, 2009). Reductions in assimilation due to these physiological limitations can be up to 35% per day, subject to light environment and genotype (Naumburg and Ellsworth, 2002), and understanding them better may pave the road towards higher yields (Murchie and Niyogi, 2011; Carmo-Silva et al., 2015).

Our understanding of the metabolic constraints of photosynthesis in fluctuating irradiance (hereafter: 'dynamic photosynthesis') have mainly come from biochemical

studies (Seemann et al., 1988; Stitt and Grosse, 1988; Sassenrath-Cole and Pearcy, 1992), with less use being made of genetic diversity. Naturally occurring ecotypes, mutations, cultivars and genetically modified accessions offer a range of genotypes with specific properties, that could be used to study dynamic photosynthesis (Kaiser et al., 2015). *Arabidopsis thaliana* possesses a wide, well documented genotypic diversity, which has been extended by selecting for mutations and by transgenic modifications.

Rubisco catalyses CO₂ assimilation and its activation limits A_n after irradiance increases (Seemann et al., 1988; Woodrow and Mott, 1989). In the chloroplast stroma, several inhibitory compounds are present and bind to Rubisco. To maintain sufficient Rubisco activity, these inhibitors must be removed from the active sites by the ATPase Rubisco activase, Rca (Salvucci et al., 1985). In *Arabidopsis thaliana*, there are two isoforms of Rca, the larger α -isoform and the smaller β -isoform (Salvucci et al., 1987). In plants containing both isoforms, redox-regulation of the α -isoform affects the ADP sensitivity of the holoenzyme, composed of both isoforms (Zhang and Portis, 1999; Zhang et al., 2002). In low irradiance (i.e. high ADP/ATP ratio), the α -isoform is less active and the rate of overall Rubisco activation is low. Since Rca is a central regulator of Rubisco activity, how these isoforms, or their concentration affect dynamic photosynthesis is an important yet unresolved question.

After CO₂ assimilation by Rubisco, a fraction of the triose phosphates leaves the chloroplast in exchange for orthophosphate (P_i) from the cytosol. In the cytosol, triose phosphate is converted to sucrose, and sucrose phosphate synthase (SPS) plays a central role in this pathway (Stitt et al., 2010). In certain circumstances, such as photosynthetic induction in saturating CO₂, irradiance-dependent activation of SPS can be slower than that of Calvin cycle enzymes, making the Calvin cycle transiently P_i-limited (Stitt and Grosse, 1988). Furthermore, after irradiance decreases, an overshoot in sucrose synthesis can transiently drain metabolites from the Calvin cycle, transiently decreasing A_n (Prinsley et al., 1986b). Plants with reduced SPS concentration may therefore exhibit slower increases in A_n after irradiance increases, and a smaller transient dip in A_n after irradiance decreases.

Leaves protect themselves from absorbed irradiance that is in excess of the capacity of photochemistry using non-photochemical quenching (NPQ). This protection, however, may come at a price. Sustained high levels of NPQ after irradiance decreases may result in transient limitations of the quantum efficiency of photosystem II for electron transport (Φ_{PSII}). Model calculations indicate that slow relaxation of NPQ could decrease canopy photosynthesis by ~13-24% (Zhu et al., 2004). NPQ has been shown to limit A_n in genotypes with faster NPQ buildup after irradiance increases (Hubbart et al., 2012) or slower NPQ relaxation after irradiance decreases (Armbruster et al., 2014). Thus, genotypes with constitutively low NPQ may have increased dynamic photosynthesis rates, principally as a result of less limitation on A_n following a decrease in irradiance.

In many plants, stomata open when irradiance increases. Typically, stomatal opening is slow, transiently limiting A_n during the irradiance increase (Vico et al., 2011). Genotypes with constitutively high g_s may not experience this limitation (Allen and Pearcy, 2000b), and may therefore be more productive in environments with a high proportion of fluctuating irradiance, provided that water is not limiting.

We used several genotypes, i.e. plants containing point mutations, transformants, T-DNA insertion lines (SALK lines (Alonso et al., 2003)) and naturally occurring accessions of *A.*

thaliana, to analyse how metabolic (Rubisco activation, sucrose synthesis, NPQ) and diffusional (g_s) limitations affect dynamic photosynthesis. In addition to measuring their steady-state photosynthetic irradiance and CO₂ responses, we exposed these genotypes to stepwise increases and decreases in irradiance, while measuring gas exchange and chlorophyll fluorescence. To investigate the effects of Rca regulatory properties or concentrations, we used the transformant *rwt43* that lacks the α -isoform of Rca and is therefore ADP-insensitive (Zhang et al., 2002) and the mutant *rca-2*, which is due to a leaky allele mutation that decreases Rca concentration (Shan et al., 2011). To analyze the effect of SPS, we studied the T-DNA mutant line *spsa1* with 80% reduction in maximum SPS activity (Sun et al., 2011). The effect of low NPQ was investigated by using *npq4-1* that lacks PsbS, greatly diminishing NPQ (Li et al., 2000b)) and *npq1-2* that lacks zeaxanthin deepoxidase and therefore violaxanthin, diminishing NPQ (Niyogi et al., 1998). Effects of high and low g_s were analyzed by using *aba2-1* with impaired abscisic acid (ABA) synthesis, leading to constitutively high g_s (Léon-Kloosterziel et al., 1996) and the natural accession C24 with low g_s (Brosche et al., 2010), respectively. The accession Col-0 is the wildtype background to all mutants and transformants used in this study and acts as a control line. This study indicates that wildtype isoform composition and amount of Rca, as well as g_s limit dynamic photosynthesis in *A. thaliana*, while wildtype levels of SPS and NPQ do not.

3.2 Results

3.2.1 Steady-state responses to irradiance and CO₂ confirm genotypic effects on Rubisco activation state, sugar metabolism and stomatal conductance

To characterize the steady-state behaviour of the different *A. thaliana* genotypes we measured their responses to irradiance and leaf internal CO₂ concentration (C_i). Rates of A_n in Col-0 were comparable to studies using plants grown under similar conditions (Veljovic-Jovanovic et al., 2001; Flexas et al., 2007b; Xing et al., 2011; Bates et al., 2012). In the mutant containing less Rca, *rca-2*, irradiance-saturated A_n was lower than for Col-0, and saturation occurred around 600 $\mu\text{mol m}^{-2} \text{s}^{-1}$ (Figure 3.1a). The lower C_i response on A_n in *rca-2* (Figure 3.1b) resulted in significantly decreased maximum carboxylation rate by Rubisco (V_{cmax} ; -23%), maximum rate of electron transport (J_{max} ; -14%) and maximum rate of triose phosphate utilisation (TPU; -7%) compared to Col-0 (Table 3.1). Assimilation in the transformant lacking the α -isoform of Rca, *rwt43*, exhibited similar irradiance and C_i responses as in Col-0 (Figure 3.1). In the mutant with less SPS (*spsa1*), A_n did not differ from Col-0 in its irradiance response (Figure 3.1a), but was strongly reduced at high C_i (Figure 3.1b), resulting in decreased J_{max} (-14%) and TPU (-23%). The ABA-deficient mutant, *aba2-1*, showed larger irradiance- and CO₂-saturated photosynthesis rates compared to Col-0, while the accession C24 showed the opposite (Figure 3.1c, d). Some parameters derived from C_i response curves were therefore larger in *aba2-1* (J_{max} : +18%, TPU: +19%), while they were smaller in C24 (V_{cmax} : -17%, J_{max} : -20%, TPU: -22%). The supply lines (Farquhar and Sharkey, 1982) (Figure 3.1d) emphasize differences in g_s between C24, Col-0 and *aba2-1*: the steeper the slope, the smaller the difference between external CO₂ concentration (C_a) and C_i , and the larger g_s . Irradiance and C_i responses of photosynthesis of low-NPQ mutants (*npq1-2*, *npq4-1*) were similar to Col-0 (Figure 3.1e, f), except for lower J_{max} in *npq4-1* (-7%). The response of quantum yield of photosystem II (ϕ_{PSII}) to C_i largely paralleled that of A_n , with the

Table 3.1: Parameters derived from C_i response curves of A_n . V_{cmax} , maximum carboxylation rate by Rubisco ($\mu\text{mol CO}_2 \text{ m}^{-2} \text{ s}^{-1}$); J_{max} , maximum rate of electron transport in the absence of regulation ($\mu\text{mol electrons m}^{-2} \text{ s}^{-1}$); TPU, maximum rate of triose phosphate utilisation ($\mu\text{mol CO}_2 \text{ m}^{-2} \text{ s}^{-1}$). The root mean squared error (RMSE, $\mu\text{mol CO}_2 \text{ m}^{-2} \text{ s}^{-1}$) of the differences between measurement and model during curve fitting (Sharkey et al., 2007) is shown as an estimation of the overall goodness of fit. Averages \pm SEM, $n = 5-15$. Stars within columns denote significance levels compared to Col-0: *** = $P < 0.0001$, ** = $P < 0.01$, * = $P < 0.05$. Absence of stars denotes lack of significant difference with Col-0 ($P > 0.05$).

	V_{cmax}	J_{max}	TPU	RMSE
Col-0	53 \pm 1	100 \pm 2	7.1 \pm 0.1	0.93 \pm 0.04
<i>rca-2</i>	40 \pm 1 ***	86 \pm 2 ***	6.7 \pm 0.1 n.s.	0.95 \pm 0.11 n.s.
<i>rwt43</i>	57 \pm 3 n.s.	105 \pm 5 n.s.	7.5 \pm 0.2 n.s.	0.98 \pm 0.07 n.s.
<i>spsa1</i>	54 \pm 4 n.s.	86 \pm 5 **	5.5 \pm 0.3 ***	0.85 \pm 0.06 n.s.
<i>aba2-1</i>	58 \pm 3 n.s.	118 \pm 6 ***	8.5 \pm 0.6 **	1.12 \pm 0.11 n.s.
C24	44 \pm 2 **	79 \pm 4 ***	5.5 \pm 0.4 ***	0.76 \pm 0.07 *
<i>npq1-2</i>	52 \pm 3 n.s.	101 \pm 5 n.s.	7.4 \pm 0.4 n.s.	0.95 \pm 0.08 n.s.
<i>npq4-1</i>	53 \pm 1 n.s.	92 \pm 2 *	6.8 \pm 0.2 n.s.	0.98 \pm 0.03 n.s.

exception that ϕ_{PSII} decreased at high C_i in many genotypes (except *rca-2* and *npq4-1*; see Figure 3.S1). This decrease in ϕ_{PSII} was most marked, and started at a lower C_i , in *spsa1* (Figure 3.S1a).

3.2.2 Larger Rubisco activation state and g_s accelerate photosynthetic induction, while lower NPQ does not

Next, we characterised the dynamic behaviour of leaf gas exchange by inducing photosynthesis in dark-adapted leaves using a stepwise increase to saturating irradiance ($1000 \mu\text{mol m}^{-2} \text{ s}^{-1}$). Rates of photosynthetic induction were initially similar between all genotypes (except *rwt43*) until $\sim 60\%$ induction was reached (Figure 3.2). *rwt43* reached 50% of photosynthetic induction (t_{A50}) significantly faster than Col-0 (Table 3.2). Induction remained faster in *rwt43* until it reached $\sim 80\%$ (Figure 3.2a). In *rca-2*, the rate of induction slowed after 60% completion and then increased in a nearly linear fashion rather than the more exponential increase shown by all other genotypes (Figure 3.2a). This increased the time to reach 90% of photosynthetic induction (t_{A90}) by ~ 10 minutes compared to Col-0. *spsa1* showed slightly slower induction rates (Figure 3.2a), increasing t_{A90} by ~ 5 min compared to Col-0. *aba2-1* exhibited faster induction, halving the t_{A90} of Col-0, while induction in C24 was identical to that of Col-0 (Figure 3.2b). Induction in *npq1-2* and *npq4-1* was identical to Col-0 (Figure 3.2c).

To explain the differences between genotypes affecting Rubisco activation and g_s , we looked at the time courses of C_i , diffusional limitation and biochemical limitation. While C_i in Col-0 and *rwt43* dropped by ~ 130 ppm within 10 minutes and then increased by 30-40 ppm following stomatal opening, in *rca-2* it never dropped below its final value (Figure 3.3a). Diffusional limitation reached its maximum within ~ 10 minutes in Col-0 and *rwt43* and then relaxed, while in *rca-2* its increase was much slower and levelled off after ~ 30 minutes (Figure 3.3c). Biochemical limitation during induction relaxed almost completely within ~ 10 minutes in Col-0 and *rwt43*, while in *rca-2* it was generally greater and the same extent of relaxation took ~ 40 minutes (Figure 3.3e). Comparing Col-0 and C24, the

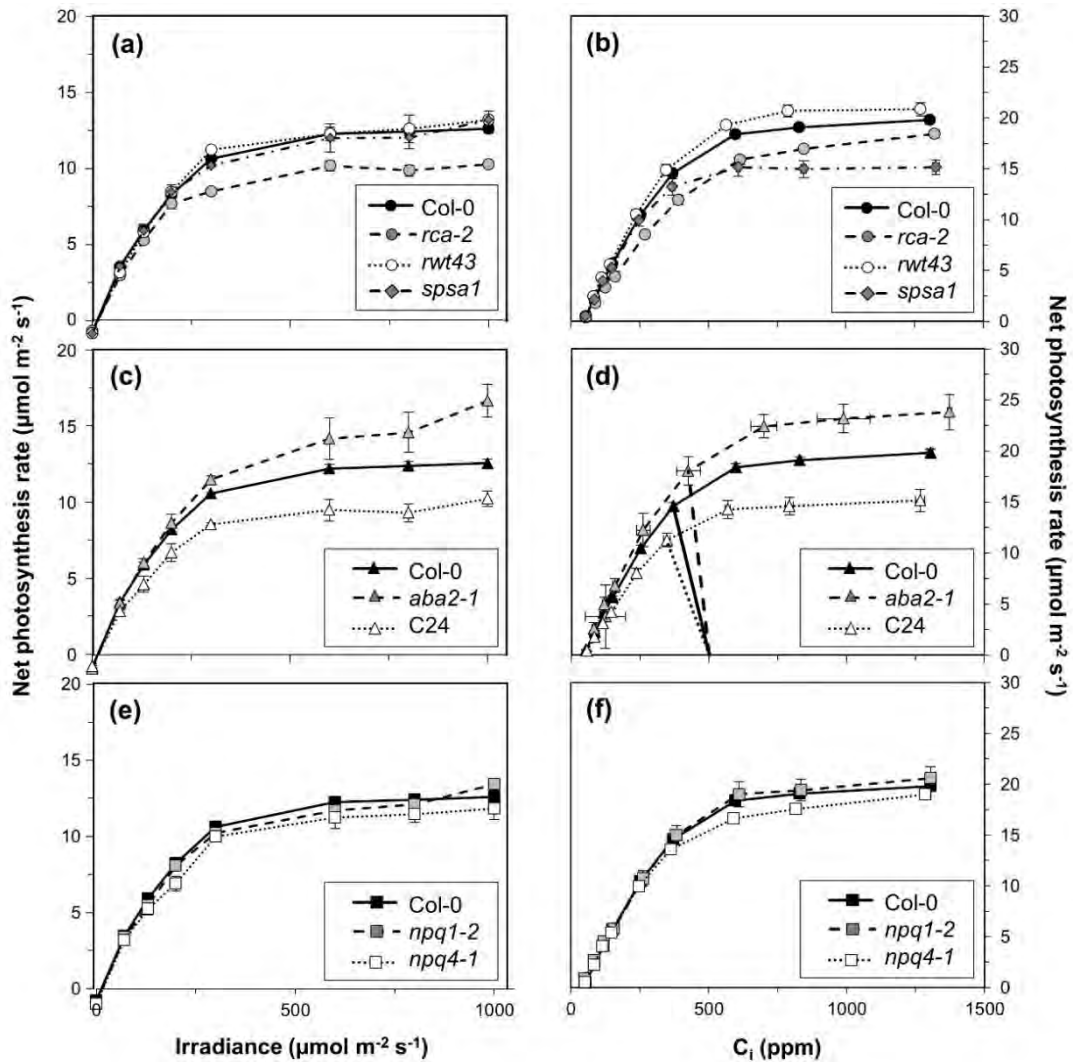


Figure 3.1: Irradiance and CO₂ response of net photosynthesis rates in *rca-2*, *rwt43* and *spsa1* (a, b), *aba2-1* and C24 (c, d) and *npq1-2* and *npq4-1* (e, f). Col-0 is included in each panel for ease of comparison. In d), supply lines (Farquhar and Sharkey, 1982) between C_a = 500 and the corresponding C_i response curve of A_n are shown to emphasize stomatal effects of *aba2-1*, C24 and Col-0 on C_i. Averages ± SEM, n = 5-15.

responses of C_i were almost indistinguishable, while in *aba2-1* the initial decrease in C_i was smaller, ranging from 50-60% of that found in Col-0 (Figure 3.3b). Buildup and relaxation of diffusional limitation were much smaller in *aba2-1* (Figure 3.3d), while relaxation of biochemical limitation was similar between Col-0, *aba2-1* and C24 (Figure 3.3f).

Next to the dark-light transition discussed above, we also exposed leaves that had been adapted to low irradiance (hereafter: background irradiance) to stepwise increases in irradiance, namely 70→800 and 130→600 μmol m⁻² s⁻¹. The responses of A_n to these increases were qualitatively similar to those seen after the dark-light transition (Figure 3.S2). *rwt43* exhibited a faster increase, and *rca-2* a much slower increase than Col-0 (Figure 3.S2a, b). This reduced t_{A50}, but not t_{A90}, in *rwt43*, while t_{A50} and t_{A90} in *rca-2* were larger than Col-0 (Table 3.2). C24 tended to increase photosynthesis more slowly compared to Col-0 (Figure 3.S2c, d), leading to a larger t_{A50} after the 70→800 μmol m⁻² s⁻¹ step increase and larger t_{A50} and t_{A90} after the 130→600 μmol m⁻² s⁻¹ step increase.

Table 3.2: Time (minutes) to reach 50 and 90% of steady-state photosynthesis rates (t_{A50} , t_{A90}) after step increases in irradiance. Averages \pm SEM, $n = 5-15$. Stars within columns denote significance levels compared to Col-0: *** = $P < 0.0001$, ** = $P < 0.01$, * = $P < 0.05$. Absence of stars denotes lack of significant difference with Col-0 ($P > 0.05$).

Genotype	0→1000 $\mu\text{mol m}^{-2} \text{s}^{-1}$		70→800 $\mu\text{mol m}^{-2} \text{s}^{-1}$		130→600 $\mu\text{mol m}^{-2} \text{s}^{-1}$	
	t_{A50}	t_{A90}	t_{A50}	t_{A90}	t_{A50}	t_{A90}
Col-0	1.6 \pm 0.1	14.7 \pm 1.2	1.3 \pm 0.1	10.2 \pm 1.1	0.6 \pm 0.0	9.0 \pm 2.2
<i>rca-2</i>	1.5 \pm 0.2	25.5 \pm 1.5 ***	6.3 \pm 0.4 ***	30.9 \pm 2.0 ***	4.0 \pm 0.7 ***	29.8 \pm 1.7 ***
<i>rwt43</i>	1.2 \pm 0.1 **	14.2 \pm 2.6	0.5 \pm 0.0 ***	16.2 \pm 6.1	0.3 \pm 0.0 ***	18.8 \pm 6.1
<i>spsa1</i>	1.6 \pm 0.1	19.5 \pm 1.3 *	1.3 \pm 0.1	14.1 \pm 7.2	0.6 \pm 0.1	13.7 \pm 6.9
<i>aba2-1</i>	1.4 \pm 0.1	7.3 \pm 0.5 **	1.3 \pm 0.1	7.7 \pm 2.6	0.8 \pm 0.1	15.1 \pm 5.8
C24	1.9 \pm 0.1	15.0 \pm 3.2	1.7 \pm 0.3 *	13.3 \pm 2.7	0.9 \pm 0.2 *	29.4 \pm 5.1 ***
<i>npq1-2</i>	1.4 \pm 0.1	11.7 \pm 1.7	1.3 \pm 0.1	10.7 \pm 2.9	0.7 \pm 0.0	14.6 \pm 8.6
<i>npq4-1</i>	1.5 \pm 0.1	14.8 \pm 2.6	1.1 \pm 0.1	6.1 \pm 0.7	0.6 \pm 0.0	15.3 \pm 11.0

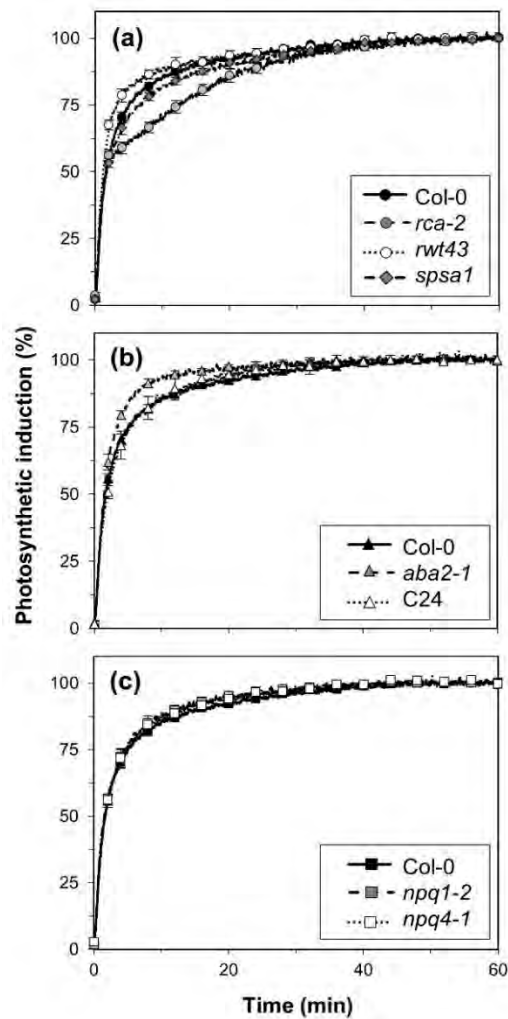


Figure 3.2: Photosynthetic induction after a step increase in irradiance from 0 to 1000 $\mu\text{mol m}^{-2} \text{s}^{-1}$ in *rca-2*, *rwt43* and *spsa1* (a), *aba2-1* and C24 (b) and *npq1-2* and *npq4-1* (c). Col-0 is included in each panel for ease of comparison. Averages \pm SEM, $n = 5-15$.

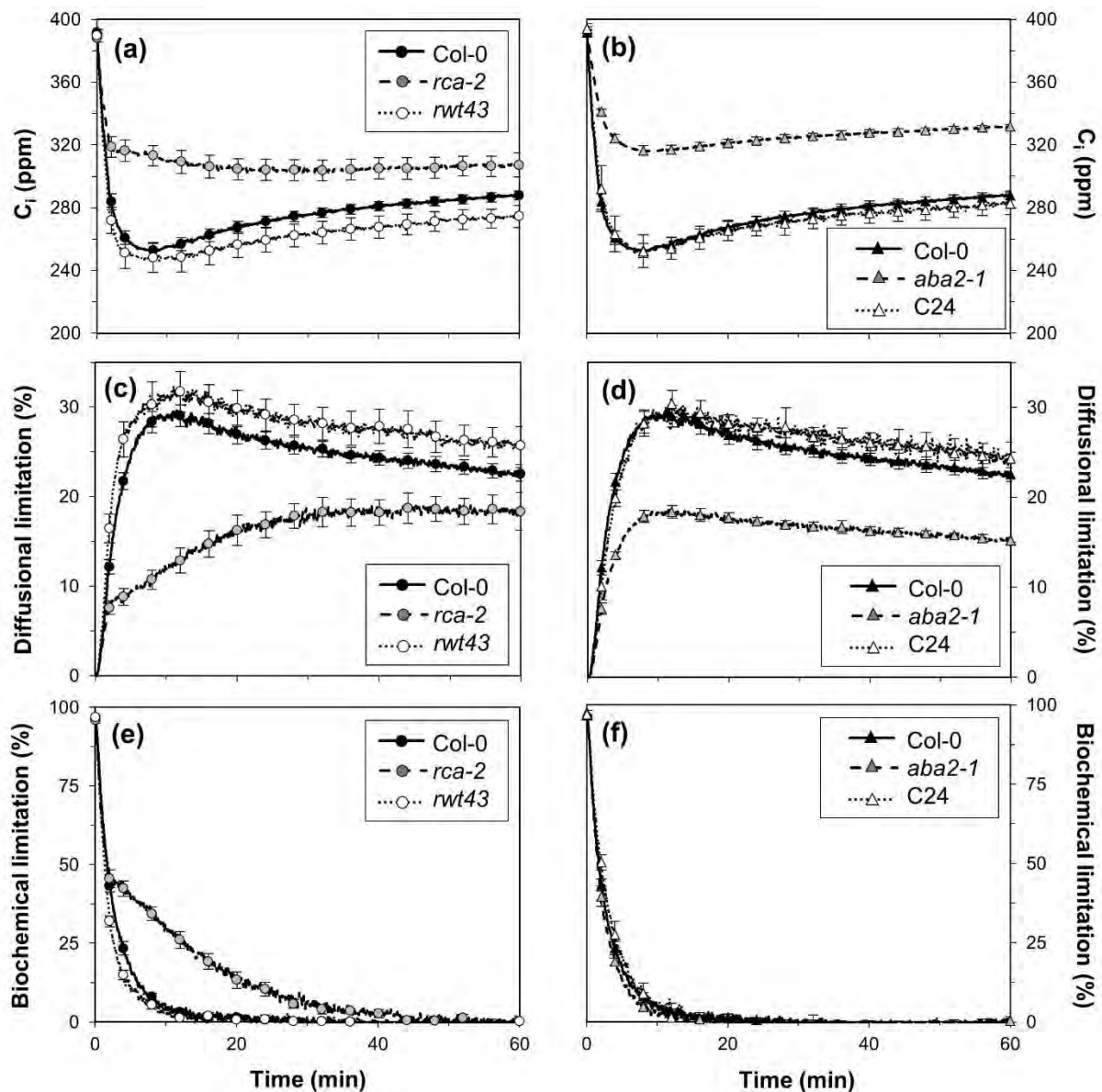


Figure 3.3: Leaf internal CO₂ concentration (C_i), diffusional limitation and biochemical limitation after a step increase in irradiance from 0 to 1000 $\mu\text{mol m}^{-2} \text{s}^{-1}$ in Col-0, *rca-2* and *rwt43* (a, c, e) and Col-0, *aba2-1* and C24 (b, d, f). Averages \pm SEM, $n = 5-15$.

Assimilation responses in NPQ and SPS mutants to those intermediate irradiance increases were similar to Col-0.

Apart from gas exchange dynamics, we also characterised changes in electron transport parameters after the stepwise 0-1000 $\mu\text{mol m}^{-2} \text{s}^{-1}$ transition. Changes in ϕ_{PSII} largely paralleled those of A_n (Figure 3.4). In *rwt43*, the increase in ϕ_{PSII} was slightly faster than in Col-0, while in *rca-2*, it was slower and steady-state ϕ_{PSII} was lower (Figure 3.4a), paralleling its lower steady-state A_n (Figure 3.1a). Despite slightly larger ϕ_{PSII} throughout induction in *spsa1*, final values were not significantly different from Col-0 ($P = 0.09$, Figure 3.4a). *aba2-1* showed increased steady-state ϕ_{PSII} levels, while in C24 they were reduced compared to Col-0 (Figure 3.4c), similar to the differences in steady-state assimilation (Figure 3.1c). In *npq4-1*, ϕ_{PSII} was slightly lower during induction than in *npq1-2* and Col-0 (*npq1-2* had similar ϕ_{PSII} trends and values during induction as Col-0; Figure 3.4e). NPQ in *rca-2* increased more quickly to its steady-state level, which was larger than that of Col-0, *spsa1* and *rwt43* (Figure 3.4b). NPQ in *aba2-1* was lower than in Col-0 and C24 (which

were not significantly different from each other, Figure 3.4d). As expected, *npq1-2* and *npq4-1* developed much lower NPQ levels than Col-0, and NPQ buildup was slower compared to Col-0, but similar in both *npq1-2* and *npq4-1* (Figure 3.4f). Dark-adapted Fv/Fm was 0.805 ± 0.002 (Avg \pm standard error of the mean, SEM) in Col-0. In *rca-2*, C24 and *npq4-1*, Fv/Fm was marginally, but significantly, smaller, possibly due to photoinhibition that was not completely removed by dark adaptation. In *spsa1*, it was slightly but significantly higher than in Col-0 (Figure 3.S3).

3.2.3 Isoform, amount and initial activation state of Rca affect the rate of Rubisco activation

The apparent time constants of Rubisco activation (τ_R , the time to reach 63% of total change in Rubisco activation state), decreased with increasing background irradiance (Figure 3.5). Genotypes differing in g_s , NPQ and SPS did not differ from Col-0 in τ_R . However, τ_R tended to be 17-28% larger in *spsa1* than in Col-0; *P*-values ranged from 0.07 to 0.09. Of the genotypes affecting Rca regulation, *rca-2* exhibited the biggest differences in τ_R , both compared with Col-0 ($P < 0.001$ in all cases) and between background irradiances, with a τ_R of ~ 22 minutes in dark-adapted leaves decreasing to ~ 4 minutes in leaves adapted to an irradiance of $130 \mu\text{mol m}^{-2} \text{s}^{-1}$ (Figure 3.5a). In *rwt43*, τ_R of dark-adapted leaves (2.3 min) was not significantly different to that of Col-0 (3.0 min; $P = 0.08$), but was significantly ($P < 0.001$) smaller at 70 and $130 \mu\text{mol m}^{-2} \text{s}^{-1}$ background irradiance (Figure 3.5b).

3.2.4 Increases in initial g_s up to a threshold value accelerate photosynthetic induction

Before and after stepwise increases in irradiance, g_s was considerably higher in *aba2-1* than in Col-0 and C24 (Figure 3.S4). In dark-adapted leaves of Col-0 and C24, g_s was similar, but in leaves adapted to 70 or $130 \mu\text{mol m}^{-2} \text{s}^{-1}$, it was almost twice as high in Col-0 compared to C24. This spread in g_s was used to explore the threshold between a limiting and a non-limiting initial g_s for the subsequent rates of A_n increase. For example, after the $0 \rightarrow 1000 \mu\text{mol m}^{-2} \text{s}^{-1}$ increase, t_{A90} was lower in plants with initially higher g_s up to $\sim 0.13 \text{ mol m}^{-2} \text{s}^{-1}$, but above $0.13 \text{ mol m}^{-2} \text{s}^{-1}$ there was no further decrease in t_{A90} (Figure 3.6). This shows that an initial $g_s > 0.13 \text{ mol m}^{-2} \text{s}^{-1}$ was non-limiting in this case. We also looked at various time points (t_{A10} , t_{A20} , etc.) after different low-to-high irradiance transitions (i.e. $0 \rightarrow 1000$, $70 \rightarrow 800$ and $130 \rightarrow 600 \mu\text{mol m}^{-2} \text{s}^{-1}$) and found that the threshold between limiting and non-limiting initial g_s was between 0.09 and $0.17 \text{ mol m}^{-2} \text{s}^{-1}$, with no discernible trend between time points or background irradiance levels.

Apart from the effect of initial g_s on the rate of A_n increase, we also analysed the effects of g_s increase after stepwise increases in irradiance (Figure 3.S4). In C24 and Col-0, the increase in g_s after the $0 \rightarrow 1000 \mu\text{mol m}^{-2} \text{s}^{-1}$ increase (until 60 minutes after the start of illumination) and t_{A90} correlated positively (Figure 3.S5). Because initial g_s in *aba2-1* was high, it was non-limiting to rates of increase in photosynthesis after irradiance increases, and stomatal opening did not correlate with t_{A90} (data not shown).

3.2.5 Lower NPQ and SPS do not increase transient photosynthesis after a decrease in irradiance

After step decreases in irradiance ($600 \rightarrow 200$, $800 \rightarrow 130 \mu\text{mol m}^{-2} \text{s}^{-1}$), relative changes in A_n were similar for all genotypes (Figure 3.S6), and there were no significant differences

in either post-illumination CO₂ fixation or the post-illumination CO₂ burst, including the NPQ mutants and *spsa1* (Figure 3.S7).

3.3 Discussion

Making use of the genetic diversity available for *A. thaliana*, we explored several possible physiological limitations of dynamic photosynthesis. This analysis revealed that altered Rubisco activation kinetics or stomatal conductance affect photosynthesis in a dynamic irradiance environment greatly, while alterations in non-photochemical quenching or sucrose synthesis do not.

Changes affecting Rca concentration (*rca-2*) or regulation (*rwt43*) had strong effects on dynamic photosynthesis. The observed effects were likely caused by different kinetics of Rubisco activation, as the initial increase in assimilation after dark-light transitions (first minute in Figure 3.2a) was similar between genotypes, implying a similar limitation due to activation of RuBP regeneration (Sassenrath-Cole and Pearcy (1992) provided

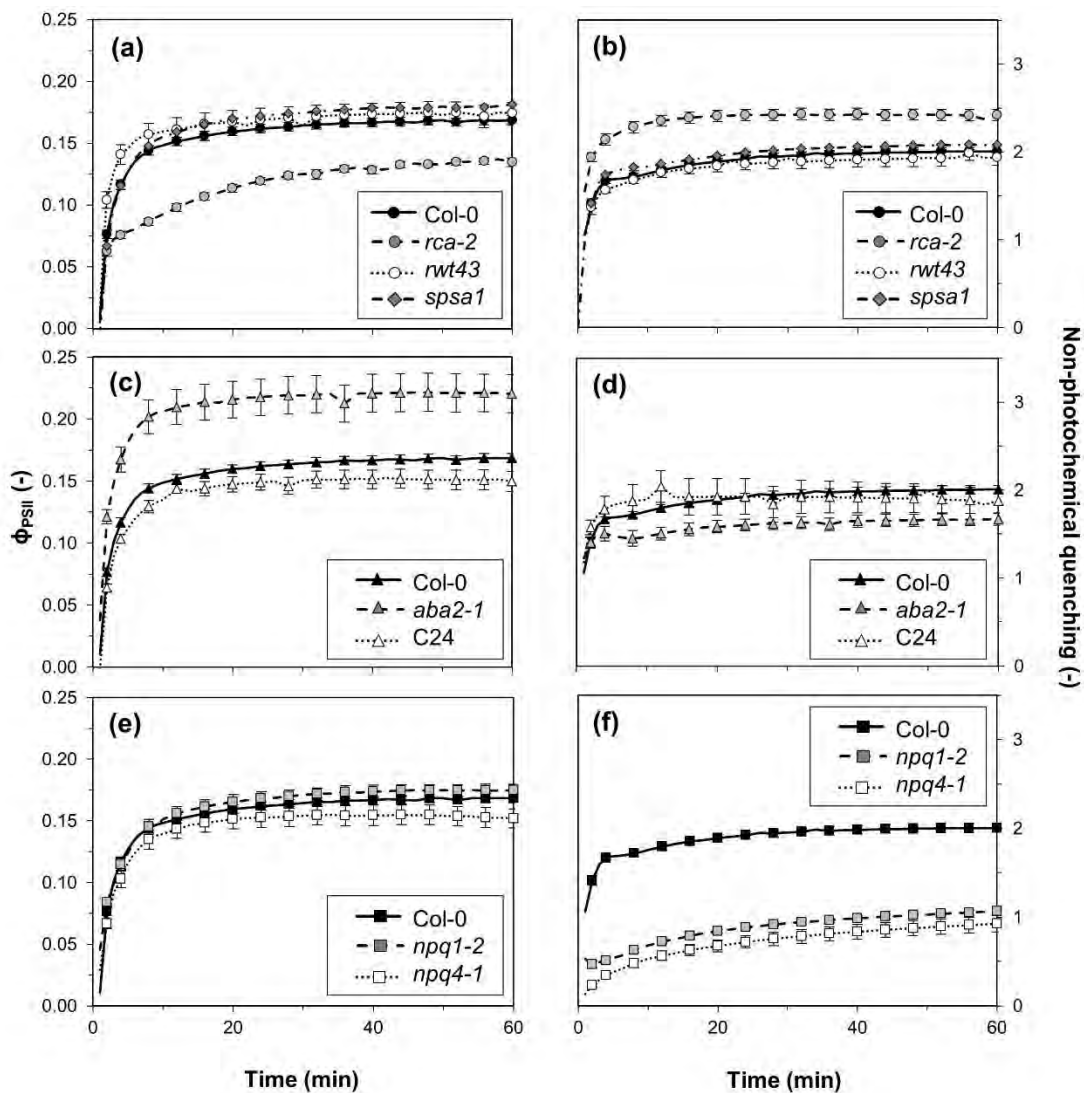


Figure 3.4: Quantum yield of photosystem II (ϕ_{PSII}) and non-photochemical quenching (NPQ) after a step increase in irradiance from 0 to 1000 $\mu\text{mol m}^{-2} \text{s}^{-1}$ in *rca-2*, *rwt43* and *spsa1* (a, b), *aba2-1* and C24 (c, d) and *npq1-2* and *npq4-1* (e, f). *Col-0* is included in each panel for ease of comparison. Averages \pm SEM, $n = 5-15$.

biochemical evidence for this). Furthermore, these genotypes had similar g_s (Figure 3.S8). Lower steady-state irradiance and CO₂ responses in *rca-2* may have been caused by a reduced steady-state activation of Rubisco (Mate et al., 1993). Based on the dependency between maximum Rubisco activation state and Rca concentration reported by Mott and Woodrow (2000) and our estimation of V_{cmax} for *rca-2* (Table 3.1), we estimate that *rca-2* contains ~22% of wildtype Rca levels (Supplementary Text). The effects on the rate of Rubisco activation of such low Rca content are apparent. In antisense or overexpressors of Rca in rice, a positive linear relationship between Rca concentration and the rate of photosynthetic induction was shown for various temperatures (Yamori et al., 2012), demonstrating the role of Rca concentration in controlling dynamic photosynthesis. Intriguingly, in our study τ_R decreased with background irradiance (Figure 3.5). While this decrease was linear in Col-0, it resembled a negative exponential in *rwt43*. This is in agreement with data of Carmo-Silva and Salvucci (2013) (Figure 3.5b). Previous studies have shown that Rubisco activation in Col-0 increased linearly with irradiance (Brooks et al., 1988; Carmo-Silva and Salvucci, 2013; Scales et al., 2014), while in *rwt43*, Rubisco activation state did not change with increasing irradiance (Carmo-Silva and Salvucci, 2013); it was similar to Col-0 in dark-adapted leaves, but close to full activation in low irradiance (Zhang et al., 2002; Carmo-Silva and Salvucci, 2013; Scales et al., 2014). Most likely differences in the activation state of Rca, rather than that of Rubisco, caused τ_R to decrease with background irradiance. Rca activity increased linearly between 0 and 300 $\mu\text{mol m}^{-2} \text{s}^{-1}$ in intact spinach leaves (Lan et al., 1992), and should be high in *rwt43* except in darkness (see above).

Compared to natural fluctuations in irradiance, stomata open and close slowly (Fay and Knapp, 1993). Low initial g_s can become a limitation to carbon fixation after a step change in irradiance (Percy, 1990), because of comparably rapid activation of RuBP regeneration and Rubisco. The peak of this limitation is typically reached within ~10 minutes due to Rubisco activation without similarly large increases in g_s , after which it relaxes due to stomatal opening (Figure 3.3d). We note that the index of diffusional limitation should be refined with respect to changes in Rubisco activation during photosynthetic induction, as well as possible changes in mesophyll conductance (g_m) during transients. With respect to g_m , contrasting responses to irradiance have been reported (Flexas et al., 2008; Tholen et al., 2008); we therefore refrain from speculations on how it may have changed in our measurements but note that it may have affected the index of diffusional limitation. Nevertheless, we believe that diffusional limitation provides a useful qualitative tool to analyse the differences between the genotypes affecting Rubisco activation kinetics and g_s .

The mutant with high initial g_s (*aba2-1*) did not show such large differences in stomatal opening (i.e. difference between initial and final g_s ; Figure 3.S4), but still had much higher rates of A_n increases when irradiance was raised. Therefore, we argue that increasing the initial g_s is a simpler route to increasing dynamic photosynthesis than is increasing the rate of stomatal opening. Stomatal closure in low irradiance is an adaptive response to changing water supply and logical under non-irrigated field conditions, however for crops in well-watered situations, increasing g_s at the expense of water use may be a reasonable target to increase rates of dynamic photosynthesis. Also, the threshold between limiting and non-limiting g_s for rates of photosynthesis increase could be used as a phenotypic marker for breeding of cultivars with non-limiting g_s in fluctuating irradiance. In our analysis, this threshold proved to be consistent independent of the time point after stepwise increases in irradiance and level of background irradiance. Previous findings

indicate that this threshold shows no diurnal variation (Allen and Pearcy, 2000b), and that it is unchanged by water stress (Allen and Pearcy, 2000b) or growth light conditions (Valladares et al., 1997). An open question that remains is whether the threshold is species-specific (Allen and Pearcy, 2000b) or not (Valladares et al., 1997). It is likely that a high initial g_s correlates with constitutively high g_s (i.e. stomata are more open and less sensitive to changes in irradiance), and faster responses of A_n to an increasing irradiance could be reached at the expense of lower intrinsic water use efficiency. Rapid screening for high g_s could be achieved by thermal imaging (McAusland et al., 2013).

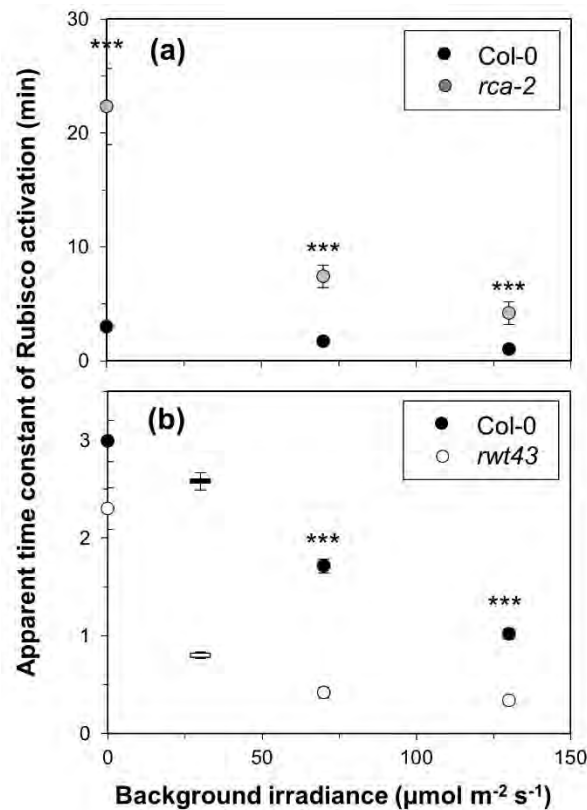


Figure 3.5: Apparent time constant of Rubisco activation in *rca-2* (a) and *rwt43* (b), compared to *Col-0*. Note the different scales of Y-axes in a) and b). Averages \pm SEM, $n = 5-15$. Bars in b) at $30 \mu\text{mol m}^{-2} \text{s}^{-1}$ background irradiance included from Carmo-Silva and Salvucci (2013). Stars denote significance levels of single genotypes compared to *Col-0*: *** = $P < 0.001$.

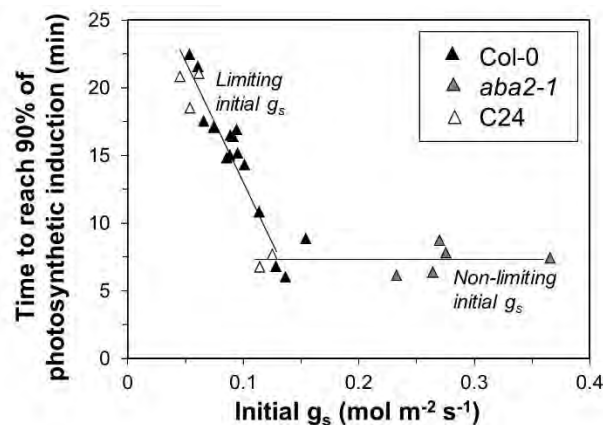


Figure 3.6: Relationship between initial g_s and the time to reach 90% of final photosynthesis rates after a step increase in irradiance ($0-1000 \mu\text{mol m}^{-2} \text{s}^{-1}$) in single replicates of *Col-0*, *aba2-1* and *C24*.

In Col-0, rates of NPQ buildup after a dark-light transition were similar to those seen in previous studies (Li et al., 2002; Nilkens et al., 2010), while mutants *npq1-2*, lacking violaxanthin de-epoxidase (Niyogi et al., 1998) and *npq4-1*, lacking PsbS (Li et al., 2000b) exhibited a much lower buildup of NPQ. However, they showed negligible differences in gas exchange to Col-0, neither in their steady-state responses to irradiance and CO₂ (Figure 3.1e, f) nor in their responses to step increases in irradiance (Figure 3.2c, Figure 3.S2e, f). Similar to our findings, reduced PsbS content in transgenic rice plants strongly reduced NPQ but had limited effects on carbon gain during a 5-min induction period (Hubbart et al., 2012). In contrast, overexpressors with 2-4 fold increases in PsbS showed ~15% lower A_n during induction, demonstrating that increased energy dissipation can have adverse effects on assimilation (Hubbart et al., 2012). Antisense mutants with reduced thylakoid membrane K⁺ flux capacities showed less rapid relaxation of NPQ after irradiance decreases, reducing electron transport and assimilation (Armbruster et al., 2014). Our data revealed no differences between *npq1-2*, *npq4-1* and Col-0 with respect to post-illumination CO₂ fixation (Figure 3.S7), and therefore show that unlike the rate of NPQ relaxation (Zhu et al., 2004; Armbruster et al., 2014), an initially low level of NPQ does not increase carbon gain directly after decreases in irradiance.

Irradiance-dependent activation of SPS is genotype-specific, and *A. thaliana* belongs to a group of species without low light/dark modulation of the enzyme (Huber et al., 1989). This suggests that in the wildtype, SPS activity does not limit photosynthetic induction - however, in a plant with strongly reduced SPS concentration it might. We tested this possibility in the T-DNA mutant *spsa1*, which has a 80% lower maximum SPS activity than Col-0 (Sun et al., 2011). Similar to our findings, Sun et al. (2011) found no photosynthetic differences between *spsa1* and Col-0, except for a strong reduction in CO₂-saturated A_n (-23%). Importantly, the decrease in SPS hardly affected photosynthetic responses to fluctuating irradiance. The only significant difference was a longer time to reach 90% of full induction after dark-light transitions (Table 3.2). However, no such differences were observed in transitions from low to higher irradiance. *spsa1* would probably show decreased rates of dynamic photosynthesis in elevated CO₂ concentrations. Furthermore, it may be that the absence of a measurable effect of *spsa1* on the post-illumination CO₂ burst, which is partly affected by the rate of sucrose synthesis (Prinsley et al., 1986b), was masked by the photorespiratory portion of the CO₂ burst, which is most pronounced in C₃ plants (Kaiser et al., 2015). Also, reduced levels of SPS in species that exhibit strong light/dark modulation of SPS (e.g. barley, maize, spinach and sugarbeet (Huber et al., 1989)) would probably have a stronger negative effect on photosynthetic induction than shown here for *A. thaliana*.

The relationship between ϕ_{PSII} and C_i in C₃ photosynthesis contains three phases: When A_n is a) limited by Rubisco, ϕ_{PSII} increases with C_i ; when A_n is b) limited by RuBP regeneration, ϕ_{PSII} is constant with increases in C_i and when A_n is c) limited by TPU, ϕ_{PSII} decreases with increasing C_i (Long and Bernacchi, 2003; Sharkey et al., 2007). Most genotypes in our study did not show the plateau in ϕ_{PSII} that would signify a phase of RuBP regeneration limitation, with *spsa1* showing an extreme form of that behaviour (Figure 3.S1). This suggests that a) TPU occurs at a lower C_i than visible from gas exchange, b) different limitations occur simultaneously within different layers of the leaf, c) changes in the rate of cyclic electron transport around photosystem I and/or strength of alternative electron sinks or d) with increasing C_i during the phase of limitation by RuBP regeneration photosynthetic electron transport is sometimes restricted, and ϕ_{PSII} is reduced, due to the increased inhibition of starch synthesis following the inhibition of

phosphoglucosomerase by phosphoglycerate (Sharkey, 2015). However, these results have to be interpreted with caution because the number of data points between the end of Rubisco limitation and the onset of TPU was limited and more data may lead to different conclusions.

In conclusion, in *A. thaliana*, the presence of the redox-regulated α -isoform of Rca in the wildtype, and wildtype levels of g_s , are limiting for dynamic photosynthesis. Furthermore, reductions in Rca strongly decrease (dynamic) photosynthesis. We also show that wildtype levels of NPQ and SPS are not limiting in *A. thaliana*. This suggests Rca and g_s as targets for improvement of photosynthesis in fluctuating irradiance.

3.4 Methods

3.4.1 Plant material

Seeds of *npq4-1*, *spsa1* (SALK_148643C) and *rca-2* (SALK_003204C) were obtained from NASC (University of Nottingham, Loughborough, UK (Scholl et al., 2000)). C24 (CS76106) was obtained from the Arabidopsis Biological Resource Center (ABRC, Ohio State University, USA). Seeds of Col-0 and *aba2-1* were obtained from Corrie Hanhart (Wageningen University, the Netherlands), *npq1-2* was obtained from Dr. Shizue Matsubara (Forschungszentrum Jülich, Germany) and *rwt43* was obtained from Dr. Elizabete Carmo-Silva (Rothamsted Research, UK).

3.4.2 Growth conditions

Plants were grown in 0.37 L pots using soil with a 4:1 peat:perlite mixture. Pots were placed on irrigation mats, and mats were saturated daily to full capacity. Plants were fertilized weekly using a nutrient solution especially developed for Arabidopsis (van Rooijen et al., 2015). To inhibit algal growth, the soil was covered with black plastic film. Plants were grown in a growth chamber in short-day conditions (8 hours of light) to delay flowering (Gibeaut et al., 1997) and thus ensure that leaves were large enough for gas-exchange measurements. Irradiance was $172 \pm 4 \mu\text{mol m}^{-2} \text{s}^{-1}$ as supplied by LED lights (GreenPower LED production module deep red/white 120; Philips, Eindhoven, the Netherlands). Temperature was 23/18 °C (day/night) and relative humidity was 70%. Mutants lacking ABA (*aba2-1*) were sprayed with an aqueous solution containing $10 \mu\text{mol mol}^{-1}$ ABA (Sigma, St. Louis, U.S.A.) when plants were 2, 4 and 6 weeks old. This increases rosette growth compared to untreated *aba2-1* plants (data not shown). There was a period of 15 days between the last application of ABA and the first measurements on *aba2-1* plants.

Single genotypes were grown sequentially (approx. one batch per week). Five plants per batch were used for measurements. To monitor the quality of the growth system over time, Col-0 was grown in three batches, each batch separated by several weeks. The number of replicates was therefore 15 for Col-0, and 5 for all other genotypes. The growth system produced very reproducible photosynthetic phenotypes of Col-0 (Figure 3.S10).

3.4.3 Measurements

Measurements were performed using the LI-6400 portable photosynthesis system (Li-Cor Biosciences, Lincoln, Nebraska, USA) equipped with the leaf chamber fluorometer (Part No. 6400-40) on single leaves of plants that were 6-8 weeks old. Leaves large enough to cover the leaf chamber gasket (area: 2 cm^2 , diameter: 1.6 cm) were used. Conditions in

the cuvette were as follows: 23 °C air temperature, 70% relative humidity, 90/10% red/blue light mixture and 500 $\mu\text{mol s}^{-1}$ air flow rate. The choice of flow rate was a compromise between getting a fast time response of the measuring system (necessary in dynamic gas exchange studies), and the difference in CO₂ concentration between sample and reference air stream. Except for the CO₂-response curves, the external CO₂ mole fraction was kept at 400 ppm. The oxygen mole fraction was always 21%.

3.4.3.1 Stepwise increases in irradiance

Leaves were adapted to several background irradiances (0, 70 or 130 $\mu\text{mol m}^{-2} \text{s}^{-1}$) for 30-60 minutes (until A_n and g_s had visibly reached a steady state), and then exposed to single-step increases in irradiance, namely 0→1000, 70→800 and 130→600 $\mu\text{mol m}^{-2} \text{s}^{-1}$. These intensities were chosen, after preliminary irradiance-response curves on Col-0 had shown that all but the highest (1000 $\mu\text{mol m}^{-2} \text{s}^{-1}$) intensity were in the sub-saturating range (Figure 3.S11). Gas exchange was logged nominally every second. Logging was stopped when g_s reached a new steady state (this was assessed visually, and took a minimum of 30 minutes after the step increase), or 60 minutes after switching to 1000 $\mu\text{mol m}^{-2} \text{s}^{-1}$. Before and after the 0→1000 $\mu\text{mol m}^{-2} \text{s}^{-1}$ increase, ϕ_{PSII} and NPQ were measured, using a measuring beam intensity of $\sim 1 \mu\text{mol m}^{-2} \text{s}^{-1}$ and a saturating pulse of $\sim 7600 \mu\text{mol m}^{-2} \text{s}^{-1}$ intensity and 1 s duration. In preliminary measurements on Col-0, the saturating pulse was sufficient to saturate F_m' in leaves adapted to 1000 $\mu\text{mol m}^{-2} \text{s}^{-1}$ (assessed following the manufacturer's recommendations for calibrating the saturating pulse: F_m' was not increased when using saturating pulses of intensity higher than 7600 $\mu\text{mol m}^{-2} \text{s}^{-1}$). The F_o and F_m relative fluorescence yields were measured in dark-adapted leaves. After the increase in irradiance, the F_m' relative fluorescence yield was measured every minute for the first ten minutes, and every two minutes thereafter. The regular application of saturating flashes transiently increased the leaf temperature by 0.4 - 0.7 °C across genotypes (temperature traces of Col-0 are representative of all genotypes, Figure 3.S12). Also, our data (Kaiser *et al.*, unpublished) indicate that the regular application of saturating flashes of similar intensity and frequency in tomato (*Lycopersicon esculentum*) had no effects on leaf gas exchange during photosynthetic induction. The steady-state relative fluorescence yield, F_s , was measured continuously. Dark-adapted F_v/F_m , ϕ_{PSII} and NPQ were calculated as $F_v/F_m = (F_m - F_o)/F_m$, $\phi_{\text{PSII}} = (F_m' - F_s)/F_m'$ and $\text{NPQ} = (F_m - F_m')/F_m'$, respectively.

During transients, g_m and mitochondrial respiration (R_d) were assumed to be constant because, to our knowledge, changes in g_m and R_d have never been assessed for irradiance transients. R_d in the light was considered similar to genotype-specific steady-state respiration in the dark; this assumption is supported by measurements on several species (Yin *et al.*, 2011). For g_m , a value of 0.2 $\text{mol m}^{-2} \text{s}^{-1}$ was assumed for all genotypes, which is an average of three values determined on Col-0 of comparable photosynthetic capacity (Flexas *et al.*, 2007b; Walker *et al.*, 2013).

The time to reach 50 and 90% (i.e. t_{50} and t_{90}) of steady-state A_n was calculated for each irradiance increase. To increase robustness of these indices to experimental noise and outliers, time series were smoothed using a local polynomial regression (Cleveland *et al.*, 1992) with a span of 5%. This means that, for each point in the time series, a polynomial of degree two was fitted using weighted least squares to a data window of size equal to 5% of the total size of the time series; the weight assigned to each point decreases with the distance from the central point.

3.4.3.2 Calculation of diffusional limitation, biochemical limitation and the apparent time constant of Rubisco activation

To calculate several parameters, A_n was corrected for transient changes in chloroplast CO_2 concentration (C_c). For diffusional limitation, A_n was multiplied by the relative rate by which A_n would increase if C_c during induction was equal to ambient CO_2 concentration, C_a ($A_{n_{C_a}}^*$):

$$A_{n_{C_a}}^* = A_n * \frac{f(C_a)}{f(C_c)}, \quad (3.1)$$

Where $f(C_a)$ is the steady-state value of A_n at C_a (i.e. at 400 ppm), and $f(C_c)$ is the steady-state value of A_n at C_c . The relative effects of C_c on A_n were taken from steady-state A_n/C_c response curves by fitting local polynomial regressions (LOESS) in the range 50-500 ppm (Figure 3.S13). Diffusional limitation was then determined as:

$$\text{Diffusional limitation} = \frac{A_{n_{C_a}}^* - A_n}{A_{n_{C_a}}^* - A_{ni}} \cdot 100, \quad (3.2)$$

Where $A_{n_{C_a}}$ is the steady-state value of A_n at C_a and A_{ni} is the initial steady-state rate of A_n . Diffusional limitation is therefore a combination of possible limitations due to g_s and g_m during induction and in the steady state (i.e. it does not decrease to 0% at the end of the time course). For biochemical limitation and τ_R , A_n was multiplied ($A_{n_{C_c}}^*$) by the relative rate by which A_n would increase if transient C_c was equal to final, steady-state C_c (C_{cf}), following Woodrow and Mott (1989):

$$A_{n_{C_c}}^* = A_n * \frac{f(C_{cf})}{f(C_c)}, \quad (3.3)$$

Where $f(C_{cf})$ is the solution for A_n at C_{cf} . Biochemical limitation was calculated after Allen and Percy (2000a):

$$\text{Biochemical limitation} = \frac{A_{nf} - A_{n_{C_c}}^*}{A_{nf} - A_{ni}} \cdot 100, \quad (3.4)$$

Throughout induction, biochemical limitation decreases from 100 to 0%, and therefore indicates the additional limitation imposed on A_n due to incomplete activation of several enzymes. Biochemical and diffusional limitations do not sum up to 100%, and are distinct. The apparent time constant of Rubisco activation (τ_R) was calculated after Woodrow and Mott (1989):

$$\tau_R = \frac{\Delta \text{time}}{\Delta \ln \cdot (A_{nf} - A_{n_{C_c}}^*)}, \quad (3.5)$$

The range of timepoints (Δtime) for calculating τ_R differed between background irradiances (Figure 3.S14), and in some cases between genotypes. This was due to differences in the rate of change of photosynthesis, and included 120 data points in the case of $0 \rightarrow 1000 \mu\text{mol m}^{-2} \text{s}^{-1}$ (all genotypes) and 40 (for *rwt43*) or 60 (all other genotypes) in the case of $70 \rightarrow 800$ and $130 \rightarrow 600 \mu\text{mol m}^{-2} \text{s}^{-1}$. These ranges were selected by visual inspection. The average root mean squared error of the linear fits was $1.2 \mu\text{mol m}^{-2} \text{s}^{-1}$ (range: $1.0 - 3.0 \mu\text{mol m}^{-2} \text{s}^{-1}$).

3.4.3.3 Stepwise decreases in irradiance

Irradiance was decreased in the following steps: 800→130 and 600→200 $\mu\text{mol m}^{-2} \text{s}^{-1}$. From the CO₂ exchange data, post-illumination CO₂ fixation (Pons et al., 1992) and post-illumination CO₂ bursts (Vines et al., 1983) were quantified. The former implies that photosynthesis is above the final steady-state value during the transient, while the latter implies a lower assimilation rate than at steady state. Values were estimated by integrating the difference between time series of photosynthesis and the final steady-state value (Tomimatsu et al., 2014).

3.4.3.4 Irradiance response curves

When A_n was at a steady state, i.e. before step changes in irradiance or at the end of a measurement sequence, 120 data points were used to extract average A_n at a given irradiance. The resulting values were used to construct steady-state irradiance response curves.

3.4.3.5 CO₂ response curves

Leaves were adapted to 1000 $\mu\text{mol m}^{-2} \text{s}^{-1}$ for ~30 min and 500 ppm C_a . C_a was then decreased stepwise until 50 ppm, each step taking 2-3 minutes. Thereafter, C_a was raised to 500 ppm, and after waiting for ~15 minutes, leaves were exposed to stepwise increases in C_a until 1500 ppm, each step taking ~4 minutes. Values were logged every 5 s and the last 60 s of every CO₂ step used to calculate average \pm SEM of C_i and A_n . ϕ_{PSII} was determined at the end of each step as described above. Photosynthesis in all genotypes was corrected for CO₂ leaks using dried leaves of Col-0 (Long and Bernacchi, 2003). Parameters V_{cmax} , J_{max} , and TPU were calculated after Sharkey et al. (2007).

3.4.4 Statistical analysis

Each genotype was compared to Col-0 using a Student's *t*-test (Microsoft Excel, function *t.test*, assuming 2-tailed distribution and two-sample equal variance).

3.5 Acknowledgements

We thank the Nottingham Arabidopsis Stock Centre, Corrie Hanhart, Elizabete Carmo-Silva and Shizue Matsubara for providing *A. thaliana* seeds. Also, we thank Sasan Aliniaiefard for help with the growth system. We thank Shizue Matsubara and Tom Sharkey for helpful discussions. This work was carried out within the BioSolar Cells programme. It was funded by the Dutch Ministry of Economic Affairs and Powerhouse.

3.6 Supplementary Material

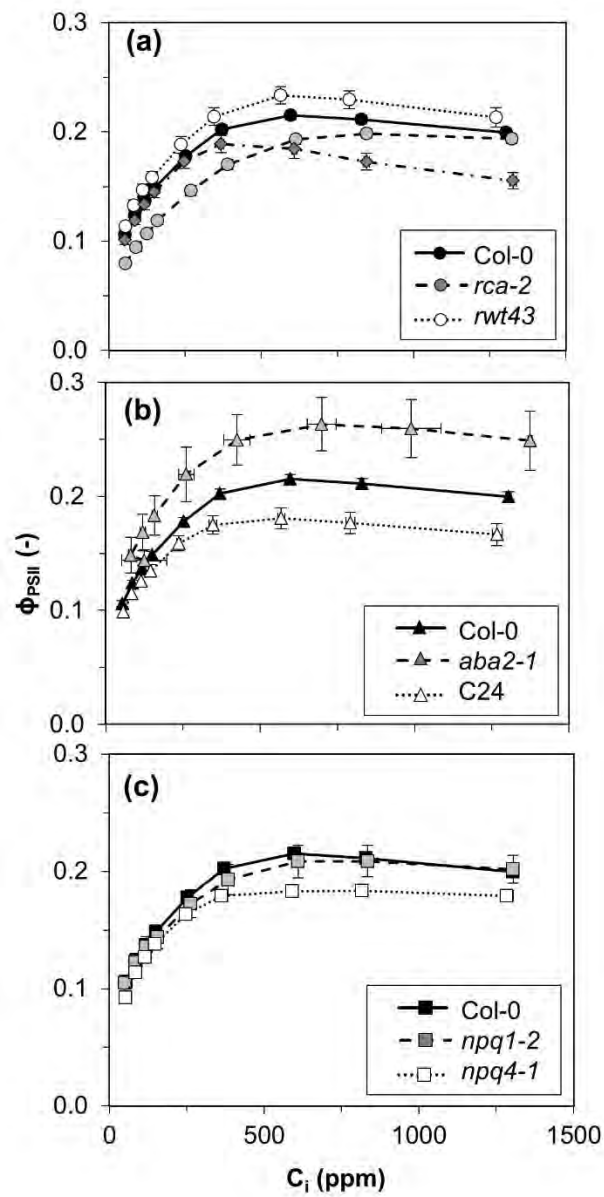


Figure 3.S1: CO₂ response of ϕ_{PSII} in Arabidopsis genotypes. Averages \pm SEM, n = 5-15.

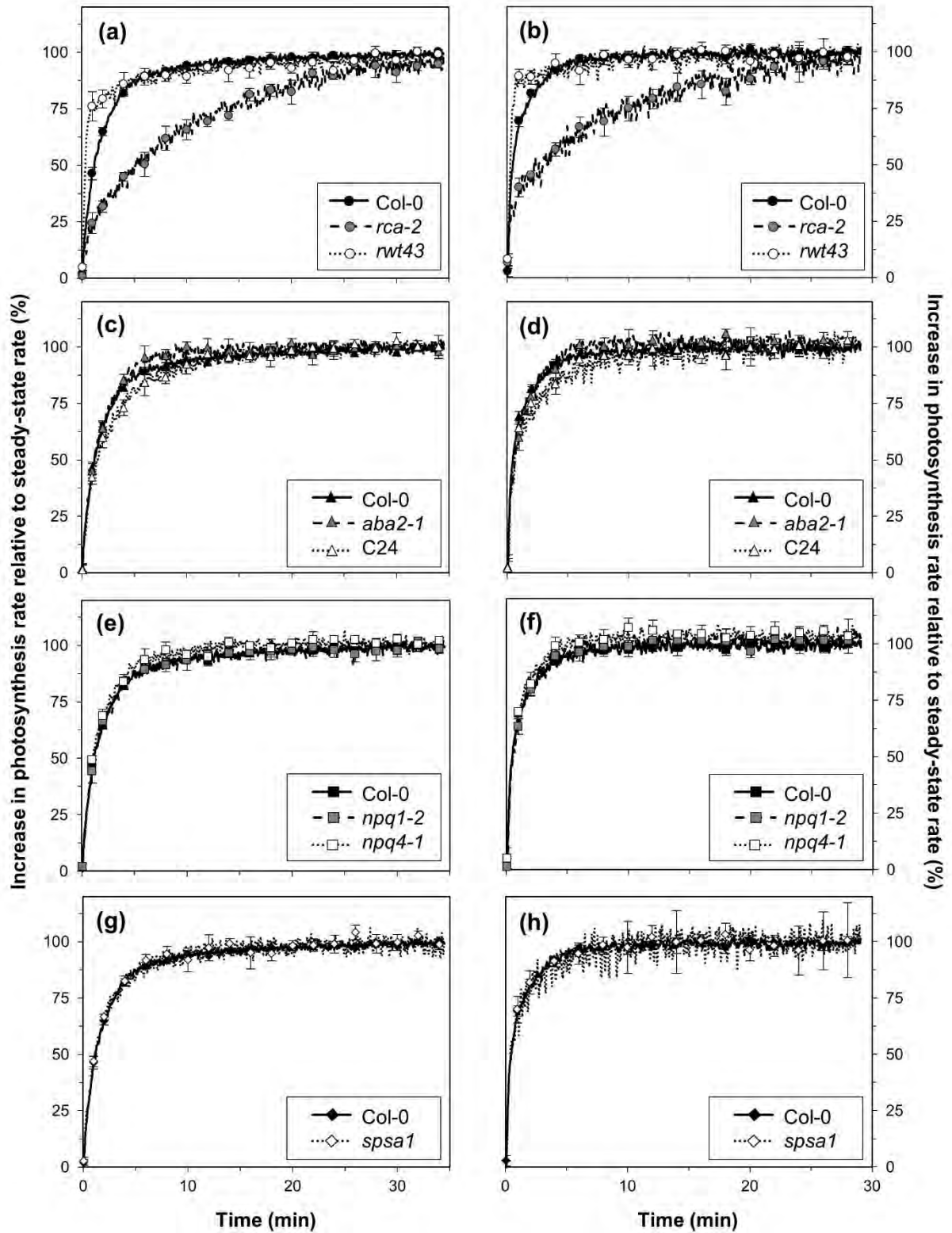


Figure 3.S2: Relative responses of net photosynthesis rates to increases in irradiance, from 70 to 800 (left panel: a, c, e, g) and from 130 to 600 $\mu\text{mol m}^{-2} \text{s}^{-1}$ (right panel: b, d, f, h). Averages \pm SEM, $n = 5-15$.

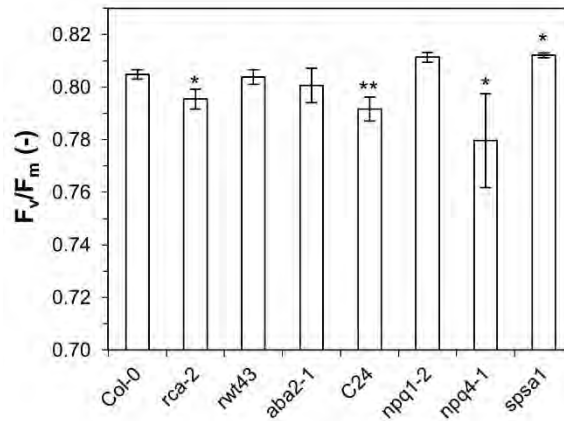


Figure 3.S3: Dark-adapted F_v/F_m in Arabidopsis genotypes after 60 minutes of dark adaptation. Stars denote significant difference from Col-0, as $P < 0.05$ (*) and $P < 0.01$ (**). Averages \pm SEM, $n = 5-15$.

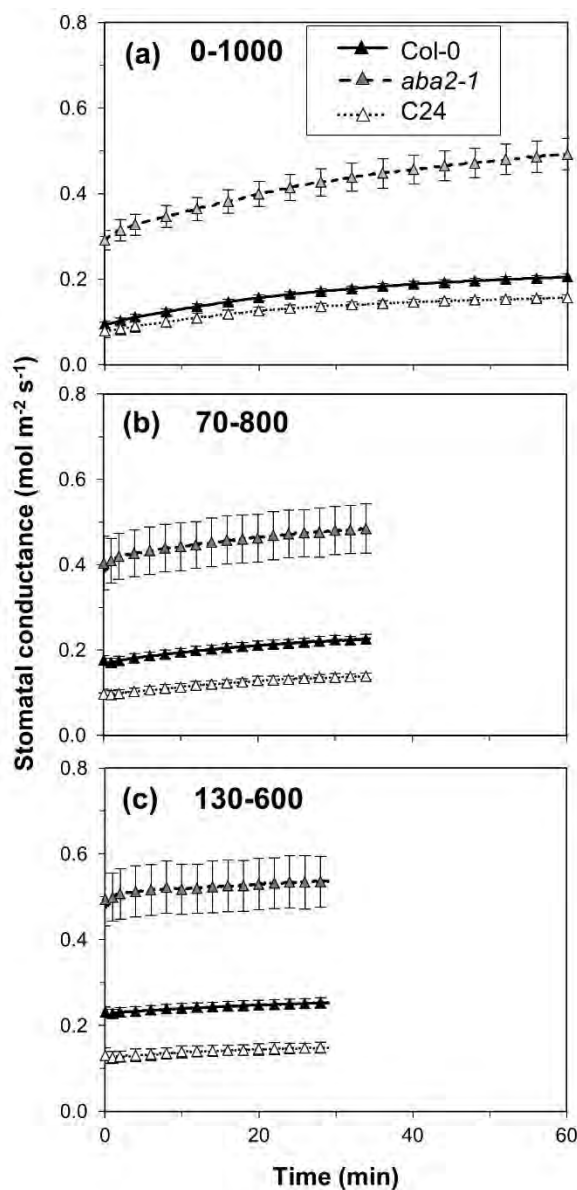


Figure 3.S4: Increases in stomatal conductance in Col-0, aba2-1 and C24 after step increases in irradiance, a) $0 \rightarrow 1000$, b) $70 \rightarrow 800$ and c) $130 \rightarrow 600 \mu\text{mol m}^{-2} \text{s}^{-1}$. Averages \pm SEM, $n = 5-15$.

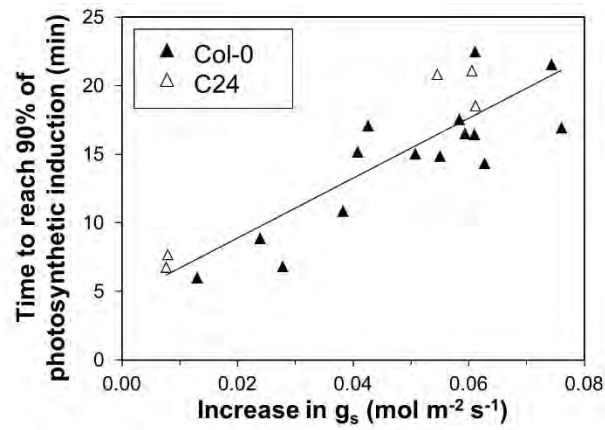


Figure 3.S5: Relationship between the increase in g_s and the time to reach 90% of final photosynthesis rates after a step increase in irradiance ($0-1000 \mu\text{mol m}^{-2} \text{s}^{-1}$) in single replicates of Col-0 and C24 ($R^2 = 0.75$).

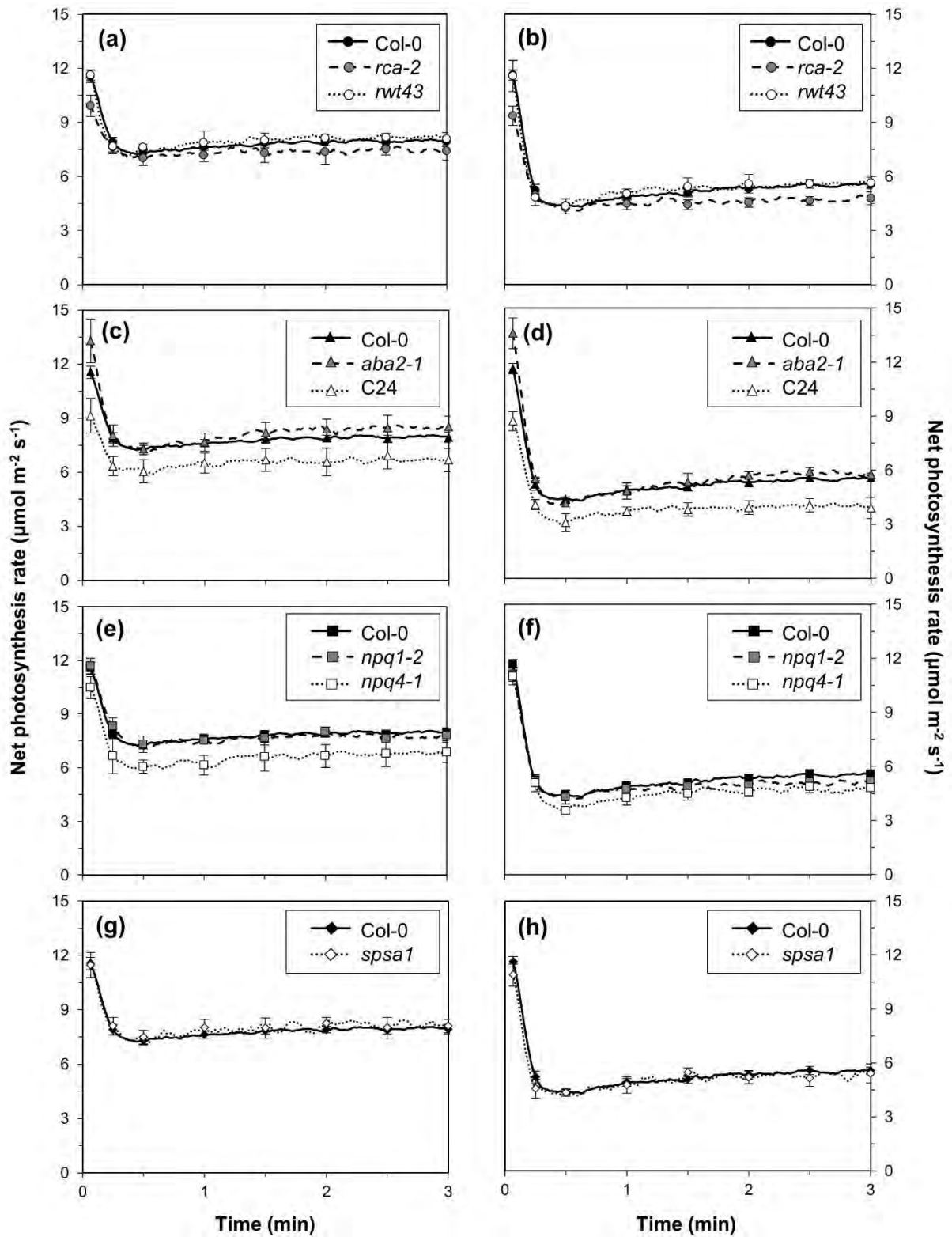


Figure 3.S6: Responses of net photosynthesis rates to step decreases in irradiance, from 600 to 200 (left panel: a, c, e, g) and from 800 to 130 $\mu\text{mol m}^{-2} \text{s}^{-1}$ (right panel: b, d, f, h). Averages \pm SEM, $n = 5-15$.

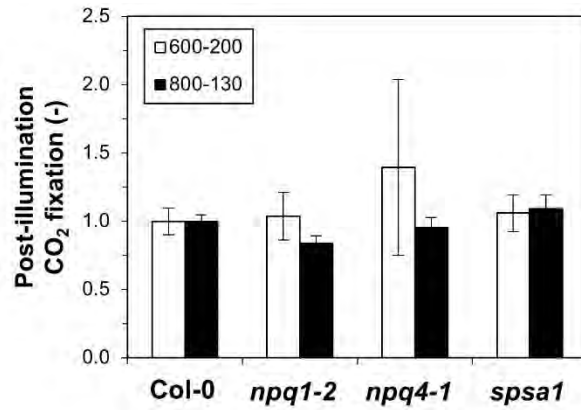


Figure 3.S7: Relative post-illumination CO₂ fixation in Col-0, npq1-2, npq4-1 and spsa1. Values are expressed relative to Col-0, which was $52 \pm 5 \mu\text{mol m}^{-2}$ after $600 \rightarrow 200 \mu\text{mol m}^{-2} \text{s}^{-1}$ step decreases (white bars) and $76 \pm 3 \mu\text{mol m}^{-2}$ after $800 \rightarrow 130 \mu\text{mol m}^{-2} \text{s}^{-1}$ step decreases (black bars). Averages \pm SEM, $n = 5-15$.

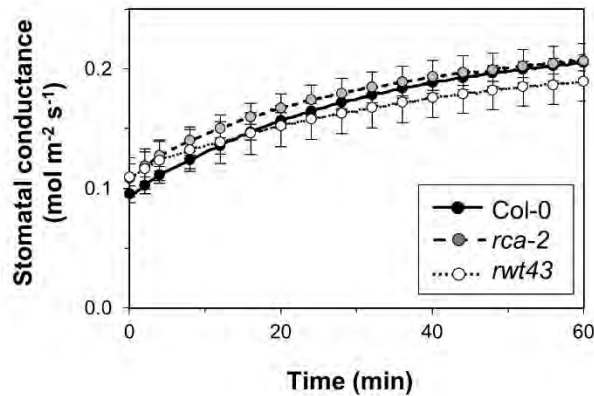


Figure 3.S8: Increases in stomatal conductance in genotypes differing in Rubisco activation rate after a $0-1000 \mu\text{mol m}^{-2} \text{s}^{-1}$ step increase.

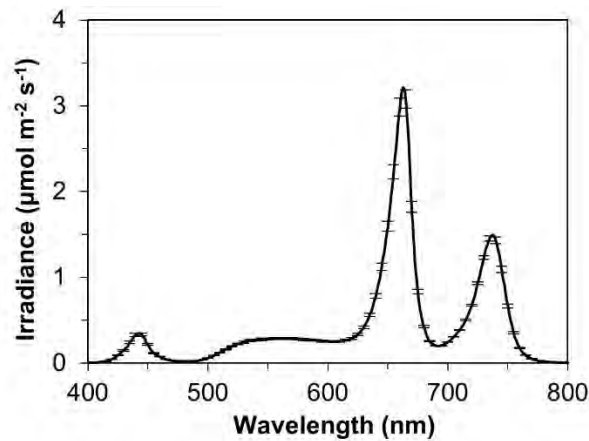


Figure 3.S9: Irradiance spectrum in the growth chamber. Average \pm SEM, $n = 4$.

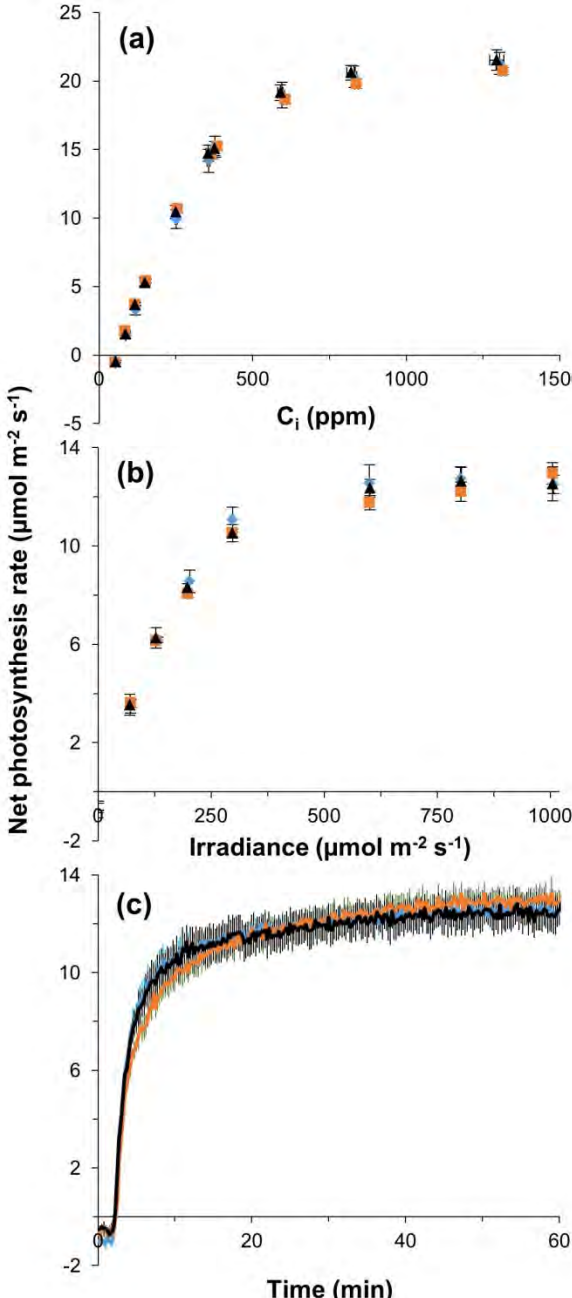


Figure 3.S10: CO_2 response (a), irradiance response (b) and photosynthetic induction (c) in three batches of *Col-0*, grown sequentially in the same growth system. Batch 1, blue symbols; batch 2, orange symbols; batch 3, black symbols. Average \pm SEM, $n = 5$.

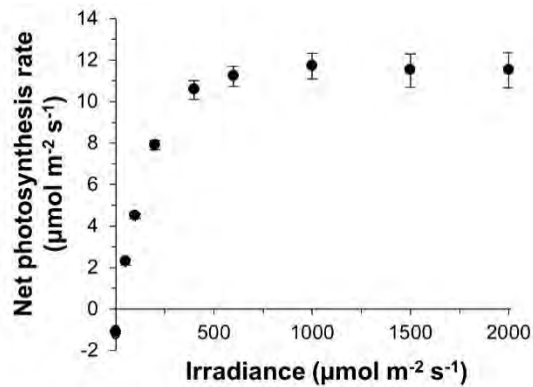


Figure 3.S11: Irradiance response curves of net photosynthesis rate determined on leaves of Col-0 prior to starting the main experiment. These data were used to determine the irradiance levels to be used during for stepwise increases and decreases in irradiance.

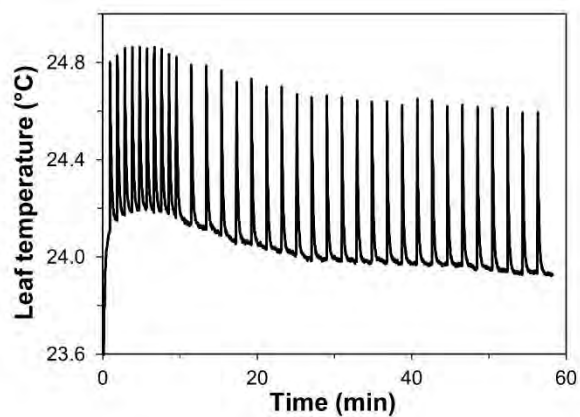


Figure 3.S12: Time course of leaf temperature on a leaf of Col-0 after a stepwise increase from 0 to 1000 $\mu\text{mol m}^{-2} \text{s}^{-1}$. The spikes in leaf temperature are the results of the regular application of saturating flashes used to determine F_m' , and are representative of all genotypes tested.

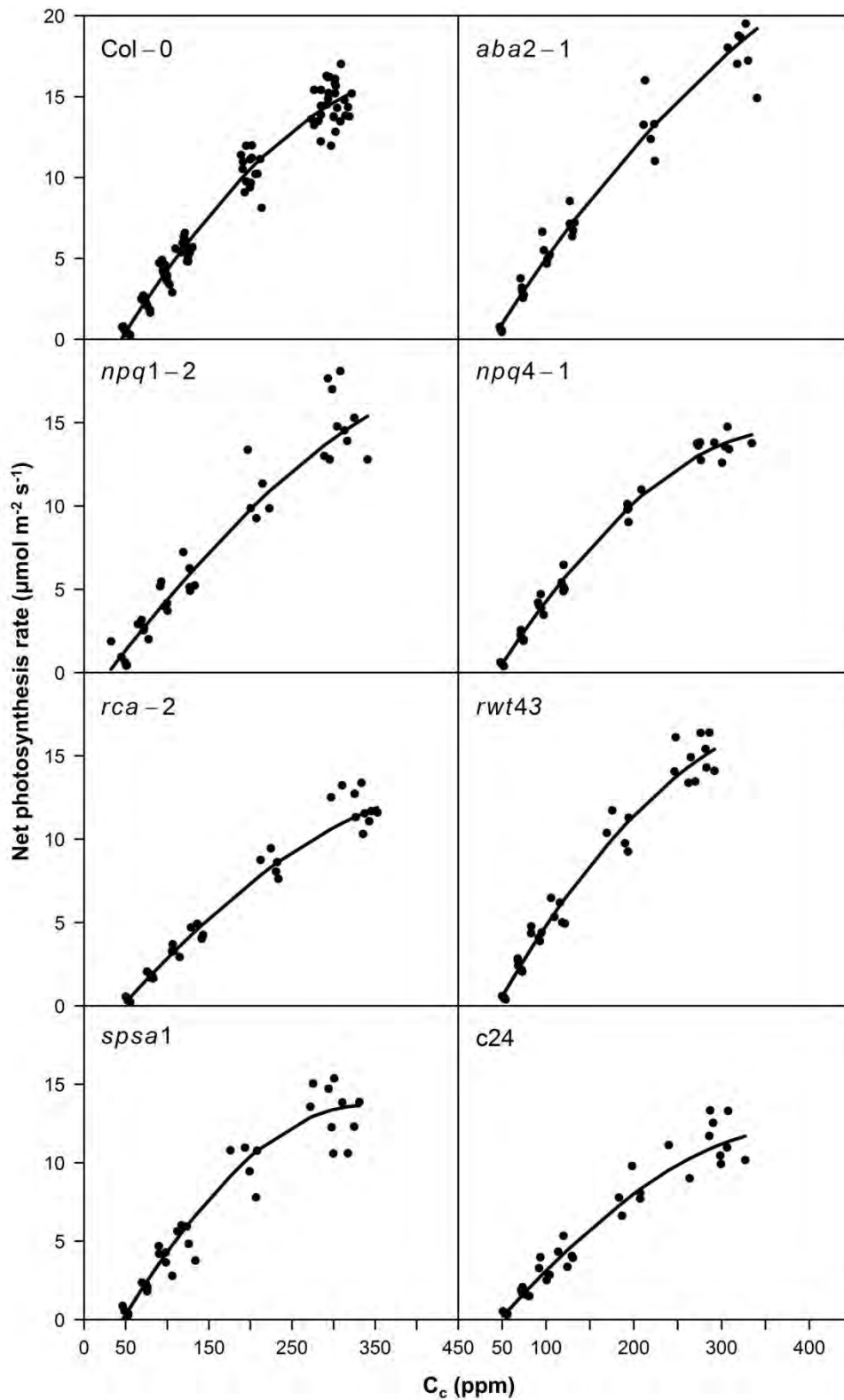


Figure 3.S13: Local polynomial regression fits through data depicting the steady-state A_n/C_c response. The fits were used for correcting the effects of changes in C_c during photosynthetic induction.

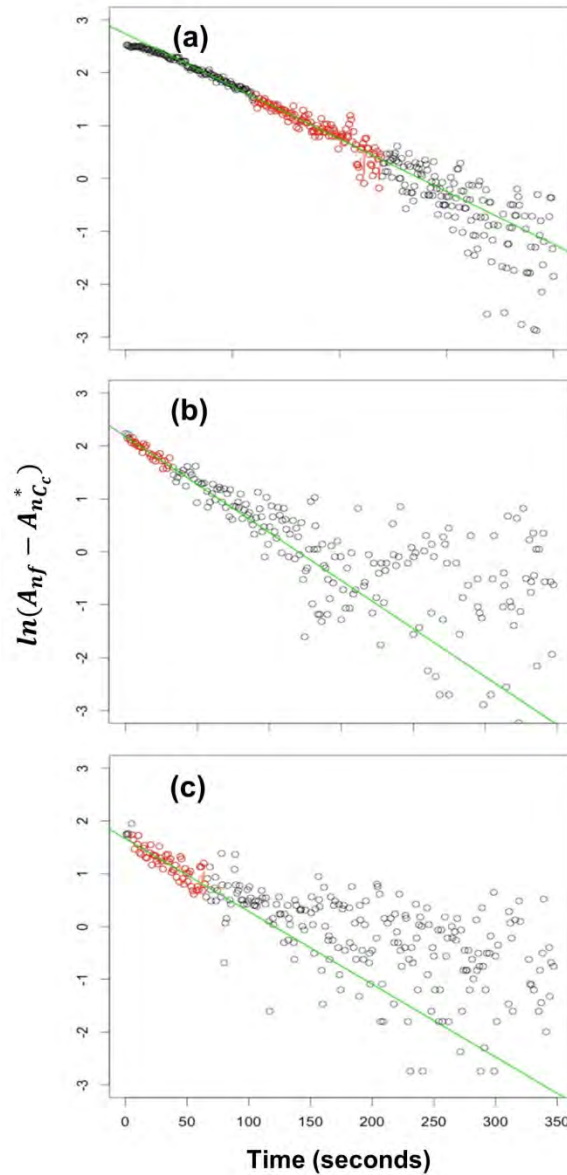


Figure 3.S14: Example of data used to calculate the apparent time constant of Rubisco activation (τ_R) after step increases in irradiance a) $0 \rightarrow 1000$, b) $70 \rightarrow 800$ and c) $130 \rightarrow 600 \mu\text{mol m}^{-2} \text{s}^{-1}$. Red dots indicate the data points used to calculate τ_R , which is equal to the inverse of the slope of the green line. Explanation of abbreviations on Y-axis: \ln , natural logarithm; A_{nf} , steady-state net photosynthesis rate at full photosynthetic induction; $A_{nc_c}^*$, transient net photosynthesis rate during induction, corrected for changes in C_c .

3.7 Supplementary Text: Calculation of Rubisco activase content

Mott and Woodrow (2000) calculated the maximum fraction of Rubisco activation (f_{RB} , achieved at ambient CO₂ concentration and saturating irradiance) from the amount of Rca (mg m⁻²) in a non-linear manner as follows:

$$f_{RB} = \frac{Rca}{Rca + K_A^{Rca}}, \quad (3.6)$$

where K_A^{Rca} (mg m⁻²) is the amount of Rubisco activase at which half of the maximum fraction of Rubisco activation is achieved. Carmo-Silva and Salvucci (2013) reported, for leaves of *A. thaliana* Col-0, grown at similar conditions to the plants in our experiments, a maximum fraction of Rubisco activation of 0.91 (i.e. Rubisco is never fully activated). With the value of $K_A^{Rca} = 12.3$ mg m⁻² reported by Mott and Woodrow (2000) we can derive that the amount of Rubisco activase in Col-0 is 124.4 mg m⁻². Assuming that the total amount of Rubisco in Col-0 and *rca-2* is the same, we deduce the amount of Rubisco activase using Equation 3.6 and our values of V_{cmax} in Col-0 (53 ± 1 $\mu\text{mol m}^{-2} \text{s}^{-1}$) and *rca-2* (40 ± 1 $\mu\text{mol m}^{-2} \text{s}^{-1}$), which results in a value of 27 mg m⁻², that is, 22% of the wildtype level.

Chapter 4

An in silico* analysis of the biochemical and diffusional limitations to C3 CO₂ assimilation under fluctuating light conditions at the leaf and canopy level

* **Morales A**[†], Kaiser E[†], Yin X, Harbinson J, Molenaar J, Struik PC An *in silico* analysis of the biochemical and diffusional limitations to C3 CO₂ assimilation under fluctuating light conditions at the leaf and canopy level. *In preparation*

[†] These authors contributed equally.

Abstract

A dynamic model of leaf CO₂ assimilation was developed as an extension of an existing steady-state model of CO₂ assimilation, by adding the effects of energy-dependent non-photochemical quenching (qE), chloroplast movement, photoinhibition, enzyme activities, metabolite concentrations in the stroma, and dynamic CO₂ diffusion. The model was calibrated to published data, including a comprehensive experiment on *Arabidopsis thaliana* ecotype Columbia-0 (Col-0), and associated mutants in Rubisco activase (*rca-2*), qE (*npq4-1*), abscisic acid (*aba2-1*) and sucrose-phosphate synthase (*spsa1*). The model reproduced the measurements on Col-0 accurately, as well as the effects of mutants by only adjusting the values of the parameters specifically affected by the mutations. Furthermore, predictions of CO₂ assimilation under fluctuating irradiance were successfully validated with measurements from the same experiment. The limitations on dynamic CO₂ assimilation by different photosynthetic processes were analysed at the leaf and canopy level. The analysis showed that several processes can be limiting, depending on whether irradiance is increased or decreased, the most relevant being the kinetics of Rubisco activation, photoinhibition, qE, chloroplast movement, and stomatal and mesophyll conductance. The regulation of electron transport chain and enzymes in the Calvin cycle and the dynamics of stomatal conductance decreased canopy CO₂ assimilation between 5.0% and 9.2% for different diurnal weather conditions.

Table of contents

4.1 Introduction	63
4.2 Model description	64
4.2.1 Rubisco and RuBP regeneration	66
4.2.2 CO ₂ diffusion	87
4.2.3 Leaf energy balance	95
4.2.4 Irradiance and leaf optical properties	96
4.2.5 Open gas exchange systems	100
4.3 Model calibration with photosynthetic mutants	105
4.3.1 Experiment and calibration protocol	105
4.3.2 Results of calibration	106
4.4 Model validation	112
4.5 Factors limiting dynamic CO₂ assimilation at the leaf level	113
4.6 Factors limiting dynamic CO₂ assimilation at the canopy level	118
4.7 Conclusions	123

Abbreviations

ABA: Abscisic acid, A_{can} : Canopy CO₂ assimilation, ADP: Adenosine diphosphate, ATP: Adenosine triphosphate, DOY: Day of year, FBPase: Fructose-1,6-bisphosphatase, FvCB model: Model by Farquhar et al., (1980), g_{sw} : Stomatal conductance to fluxes of water vapour, IRGA: Infrared gas analyser, LAI: Leaf area index, NADPH: Nicotinamide adenine dinucleotide phosphate, NIR: Near infrared, NPQ: Non-photochemical quenching, NSPD: Normalized spectral photon distribution, PAR: Photosynthetically active radiation, PGA: Phosphoglycerate, PRK: Phosphoribulokinase, PSI: Photosystem I, PSII: Photosystem II, Q_A : Quinone A, qE : Energy-dependent non-photochemical quenching, Rca: Rubisco activase, RMSE: Root mean square error, Rubisco: Ribulose-1,5-bisphosphate carboxylase oxygenase, RuBP: Ribulose-1,5-bisphosphate, SBPase: Sedoheptulose-1,7-bisphosphatase, SPS: Sucrose phosphate synthase, TPU: Triose phosphate utilisation, UV: Ultraviolet, VPD: Vapour pressure difference.

4.1 Introduction

Most published models of CO₂ assimilation in C3 plants focus on steady-state behaviour and are derived from the equations proposed by Farquhar et al. (1980). These models have proven to be successful and have been used for a wide range of applications (von Caemmerer, 2013). However, inside a canopy, most leaves are exposed to fluctuating irradiance due to transient exposure to the sun caused by gaps in the canopy and leaf movement by wind and transient shading by clouds (Pearcy, 1990). Although much of the research on CO₂ assimilation under fluctuating irradiance has focused on the understorey of forests (Way and Pearcy, 2012), it is also relevant to annual plants growing at high densities such as crops (Pons et al., 1992). Under these fluctuating conditions, the rate at which CO₂ assimilation responds to changes in the physical environment, as well as the temporal uncoupling of the different processes involved in photosynthesis (due to differences in their time response) can have a strong impact on CO₂ assimilation (Pearcy, 1990). Integration of this effect over time and space requires the use of models specifically designed for this purpose, since steady-state models tend to overestimate measurements under fluctuating irradiance and have lower predictive power than dynamic models (Pearcy et al., 1997; Stegemann et al., 1999; Naumburg et al., 2001a; Naumburg and Ellsworth, 2002).

Mechanistic models that describe in detail the metabolism of C3 photosynthesis have been published (Laisk et al., 2009a; Zhu et al., 2013), but, to best of our knowledge, these models have not been used to study CO₂ assimilation under fluctuating irradiance. While these models are useful for gaining insight into the mechanisms of photosynthesis, the large number of parameters involved has obstructed their calibration against specific genotypes or growth conditions and these models thus remain largely theoretical. This prevents their application to problems such as scaling of CO₂ fluxes to the canopy level, plant growth modelling, or studies on interactions between genotype and environment.

Several phenomenological dynamic models of CO₂ assimilation have been published, including the model by Gross et al. (1991), later improved by Pearcy et al. (1997) and Kirschbaum et al. (1998), as well as the simpler models by Stegemann et al. (1999) and Noe and Giersch (2004). These models contain fewer parameters than in mechanistic models, most of which can be estimated from leaf-level measurements of gas exchange. Of these models, the one by Pearcy et al. (1997) has been used in several studies

(Naumburg et al., 2001a; Naumburg and Ellsworth, 2002; Roden, 2003; Montgomery and Givnish, 2008).

However, the model by Pearcy et al. (1997) ignores some relevant processes including, among others, energy-dependent non-photochemical quenching (qE), chloroplast movement, and mesophyll conductance. Recent studies indicate that qE can limit CO₂ assimilation under fluctuating irradiance (Hubbart et al., 2012; Armbruster et al., 2014; Ikeuchi et al., 2014; Kromdijk et al., 2016). Similar effects have been proposed for non-photochemical quenching associated with photoinhibition based on a modelling study (Zhu et al., 2004). In addition, chloroplast movements may also affect CO₂ assimilation, by decreasing the irradiance absorbed by leaves (Davis et al., 2011), reducing the rates of photoinhibition (Kasahara et al., 2002) and affecting CO₂ diffusion (Tholen et al., 2008; Ho et al., 2016).

Other studies have revealed the need to include additional processes into models of CO₂ assimilation, such as the limitation due to phosphate recycling (Sharkey, 1985) or mesophyll conductance to fluxes of CO₂ (Flexas et al., 2008). Furthermore, leaf temperature also needs to be taken into account because of it affects photoinhibition (Greer et al., 1986), Rubisco activity (Yamori et al., 2012), electron transport (Yamori et al., 2008) and stomatal and mesophyll conductances (von Caemmerer and Evans, 2015). Calculating the temperature of a leaf requires a complete energy balance (Gutschick, 2016).

In this study, a novel, phenomenological, dynamic model of CO₂ assimilation is proposed. It is similar to the model by Pearcy et al. (1997), but includes additional processes (i.e., qE, chloroplast movement, photoinhibition, phosphate recycling, mesophyll conductance, effects of leaf temperature and energy balance). It also improves some of the equations used by Pearcy et al. (1997), specifically, on the regulation of Rubisco activity and coupling of the Calvin cycle to the electron transport chain.

The parameters of the model were estimated by fitting the individual equations or subsets of equations in the model to published data, with an emphasis on *A. thaliana*. In addition, the model was fitted to an extensive dataset published by Kaiser et al. (2016), which includes measurements of CO₂ assimilation and chlorophyll fluorescence of *A. thaliana* Col-0 and several associated photosynthetic mutants. The use of mutants allowed testing some of the assumptions in the model regarding the role of the different photosynthetic processes in constraining CO₂ assimilation under fluctuating conditions. In addition, unpublished measurements from the same experiment described by Kaiser et al. (2016) were used to validate predictions of CO₂ assimilation under fluctuating irradiance. Once the model was properly calibrated and validated, several *in silico* scenarios were simulated at the leaf and canopy level in order to quantify the relative importance of the different processes in limiting CO₂ assimilation.

4.2 Model description

This model is an extension of the steady-state model of CO₂ assimilation for C3 plants proposed by Farquhar et al. (1980). In that model, the rates of carboxylation and oxygenation were calculated according to a mechanistic model of Rubisco (Farquhar, 1979) under the assumption that RuBP concentration is saturating *in vivo*. In addition, it is considered that carboxylation could also be limited by the potential rate of RuBP regeneration which itself would be limited by NADPH or ATP production and thus by the

potential rate of electron transport. Sharkey (1985) proposed a third limitation due to the release of free phosphate associated with the consumption of triose phosphates (this limitation is generally known as “triose phosphate utilisation” or TPU). The approach of calculating CO₂ assimilation as the minimum of several potential rates resembles Blackman’s law of limiting factors (Blackman, 1905) and allows a strong predictive power under steady-state conditions without having to consider explicitly the metabolic regulation of photosynthesis.

Because the model by Farquhar et al. (1980), with the addition of TPU, focuses on steady-state CO₂ assimilation, it does not consider how CO₂ assimilation changes during transitions between steady states, nor what happens to processes that are not limiting in the steady state. To incorporate these aspects into the model, several assumptions were made. Under fluctuating conditions, and when potential electron transport limits CO₂ assimilation, the actual rate of carboxylation by Rubisco is assumed to be adjusted such that production and consumption of NADPH and ATP are equal. This may occur by downregulating Rubisco or by sub-saturating RuBP concentrations. Similarly, NADPH and ATP production are assumed to be down-regulated when their metabolic demand is lower than their potential production, as otherwise the enzymes responsible for their production (i.e., Ferredoxin-NADP⁺ reductase and ATP synthase) would run out of substrate (Noctor and Foyer, 2000). These adjustments do not occur instantaneously and the dynamics of these regulatory mechanisms are assumed to limit CO₂ assimilation under fluctuating conditions (Figure 4.1). Therefore, the first step in constructing the model was to incorporate dynamic changes in the potential rates of each process (see equations in Section 4.2.1). In addition, there is empirical evidence that the rate at which enzymes in the regeneration phase of the Calvin cycle are activated after an increase in irradiance can limit CO₂ assimilation (Sassenrath-Cole and Pearcy, 1992; Sassenrath-Cole et al., 1994). There is also evidence that, in the steady-state, some of these enzymes have a high control coefficient on CO₂ assimilation (Raines, 2003; Woodrow, 2009). These two effects are achieved by reducing the concentration of RuBP (Section 4.2.1).

In order to scale CO₂ assimilation to the leaf level, CO₂ diffusion into the chloroplasts must be taken into account. The diffusion of CO₂ from the air into the chloroplast is modelled in analogy with an electrical circuit that obeys Ohm’s law. The net flux of CO₂ between the leaf and its environment is also dependent on mitochondrial respiration and photorespiration. The equations describing CO₂ diffusion and the calculation of the net flux of CO₂ are described in Section 4.2.2.

Additionally, several processes in photosynthesis are sensitive to temperature. Leaf temperature is the result of the balance between net absorbed solar and thermal radiation and its dissipation as latent and sensible heat fluxes (Gutschick, 2016). Stomatal conductance affects this balance through its effect on leaf transpiration. The equations for the dynamic leaf energy balance are given in Section 4.2.3. The absorption of incident irradiance and the different spectral responses of photosynthesis and leaf energy balance are detailed in Section 4.2.4.

Finally, when comparing simulations of dynamic CO₂ assimilation with measurements performed with an open gas exchange system, it is important to take into account artefacts introduced into the measurements due to the time response of the instrument. To account for this, the physical processes within the measurement system that gives

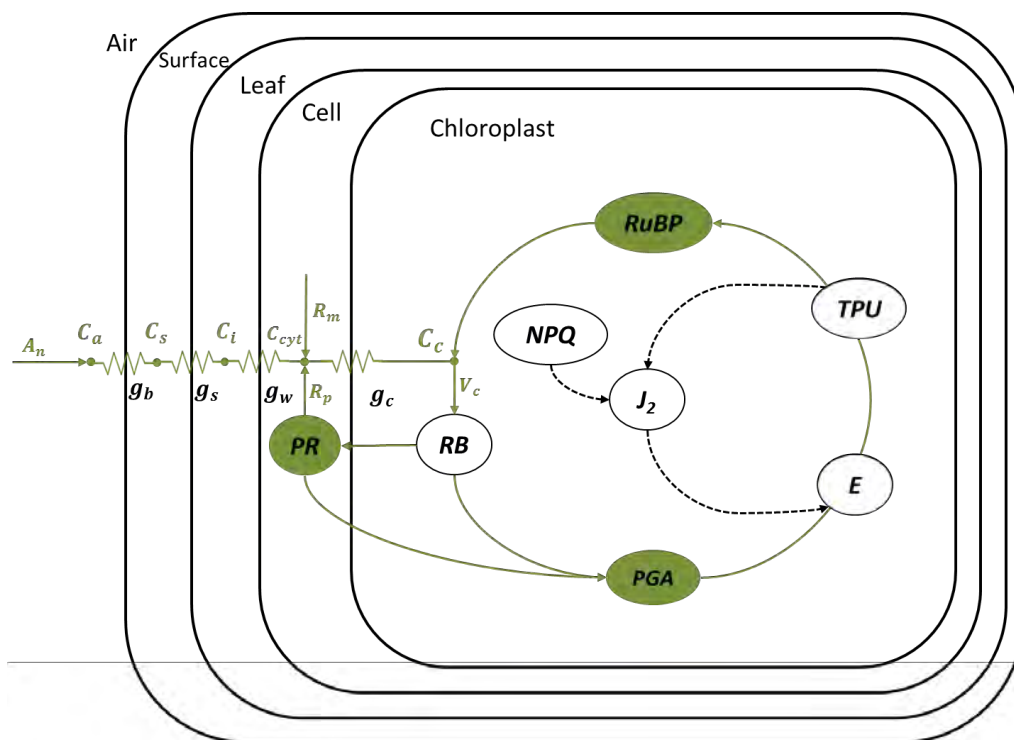


Figure 4.1: Conceptual diagram of the model. The rate of carboxylation is limited by Rubisco kinetics (RB) and the rate of PGA conversion into RuBP is limited either by the activity of enzymes in the regeneration phase of the Calvin cycle (E), triose phosphate utilization (TPU) or the potential rate of electron transport passing Photosystem II (J_2). Non-photochemical quenching (NPQ) is calculated from irradiance (I) and actual electron transport, which may be limited by metabolic demand. CO_2 diffuses from the air (C_a), into the chloroplast (C_c) as mediated by the conductances of the leaf boundary-layer (g_b), the stomata (g_s), cell walls (g_w) and chloroplast (g_c). CO_2 emitted due to consumption of photorespiratory intermediates (PR) is assumed to be delayed with respect to their production by RuBP oxygenation.

rise to these artefacts was simulated, and the output was calculated according to the equations used to derive fluxes and conductances from gas exchange measurements. Details on these corrections are given in Section 4.2.5.

The equations given in the following sections are sufficient to implement the model in any programming language or simulation software. All simulations were performed using the CVODE numerical solver provided by the Sundials library (Hindmarsh et al., 2005) wrapped by the R package RcppSundials (source code available upon request). Other ODE solvers may be used, however the model is a stiff system of differential equations (i.e., the time constants associated to the different processes span several timescales) and thus ODE solvers suitable for stiff problems are required.

4.2.1 Rubisco and RuBP regeneration

The rate of RuBP regeneration (V_R , $\text{mol m}^{-2} \text{s}^{-1}$) is calculated as:

$$V_R = \min(V_{R,J}, V_{R,TPU}, V_{R,E}), \quad (4.1)$$

where $V_{R,J}$, $V_{R,TPU}$ and $V_{R,E}$ are the potential rates ($\text{mol m}^{-2} \text{s}^{-1}$) of RuBP regeneration limited by the potential rate of electron transport (Section 4.2.1.2), low concentrations of stromal free phosphate, as affected by the rate of triose phosphate utilisation

(Sharkey and Vanderveer, 1989), described in Section 4.2.1.3, and the maximum activity of enzymes in the regeneration phase of the Calvin cycle (Section 4.2.1.4), respectively.

In order to couple the reactions of carboxylation and oxygenation with the rest of the Calvin cycle, the amounts of PGA and RuBP per unit of leaf area are simulated dynamically as:

$$\frac{dPGA}{dt} = V_C(2 + 1.5\phi) - V_R, \quad (4.2)$$

$$\frac{dRuBP}{dt} = V_R \frac{1 + \phi}{2 + 1.5\phi} - V_C(1 + \phi), \quad (4.3)$$

where ϕ is the ratio between oxygenation and carboxylation and V_C is the rate of carboxylation ($\text{mol m}^{-2} \text{s}^{-1}$). The coefficient $(2 + 1.5\phi)$ is the stoichiometric ratio between the rates of PGA production and RuBP carboxylation, taking into account that ϕ oxygenations occur per carboxylation. The coefficient $(1 + \phi)$ is the ratio between the rates of RuBP consumption and carboxylation. Thus, the terms $V_C(2 + 1.5\phi)$ and $V_C(1 + \phi)$ represent total production and consumption of PGA and RuBP, respectively. The value of ϕ can be calculated as:

$$\phi = \frac{K_{mc}k_oO_2}{K_{mo}k_cC_c}, \quad (4.4)$$

where k_o and k_c (s^{-1}) are the rate constants of oxygenation and carboxylation, respectively, C_c (mol mol^{-1}) is the CO₂ mole fraction ($[\text{CO}_2]$) inside the chloroplast, O_2 (mol mol^{-1}) is the O₂ mole fraction, and K_{mc} (mol mol^{-1}) and K_{mo} (mol mol^{-1}) are the Michaelis-Menten constants of Rubisco with respect to CO₂ and O₂, respectively.

4.2.1.1 Kinetics of carboxylation and oxygenation

4.2.1.1.1 Potential rate of carboxylation

The rate of carboxylation (V_C , $\text{mol m}^{-2} \text{s}^{-1}$) is calculated by modifying the equations proposed by Farquhar (1979), such that in addition to the effects of $[\text{CO}_2]$, O₂ and RuBP on Rubisco kinetics, the effect of partially active Rubisco is also included:

$$V_C = \frac{k_c C_c RB}{C_c + K_{mc} \left(1 + \frac{O_2}{K_{mo}}\right)} f_{RB} f_{RuBP}, \quad (4.5)$$

$$f_{RuBP} = \frac{\frac{RB + RuBP}{V_{st}} + K_{mapp,RuBP} - \sqrt{\left(\frac{RB + RuBP}{V_{st}} + K_{mapp,RuBP}\right)^2 - \frac{4RB RuBP}{V_{st}^2}}}{2 \frac{RB}{V_{st}}}, \quad (4.6)$$

$$K_{mapp,RuBP} = K_{m,RuBP} \left(1 + \frac{PGA}{V_{st} K_{I,PGA}}\right), \quad (4.7)$$

where RB is the amount of Rubisco catalytic sites per unit of leaf area (mol m^{-2}), f_{RB} is the fraction of Rubisco catalytic sites that are carbamylated and not occupied by inhibitors, V_{st} (m) is the volume of the stroma per unit of leaf area, $K_{m,RuBP}$ (mol m^{-3}) is

the Michaelis-Menten constant of Rubisco with respect to free RuBP, $K_{I,PGA}$ (mol m⁻³) is the competitive inhibition constant of PGA against RuBP binding, and $RuBP$ (mol m⁻²) and PGA (mol m⁻²) are the total RuBP and PGA content per unit of leaf area.

When calibrated with the parameters reported by Farquhar (1979), Equation 4.6 resulted in saturation of Rubisco kinetics when RuBP/Rubisco > 1 and this is well supported by experimental results (Figure 4.2). However, values of steady-state RuBP/Rubisco ratios *in vivo* are sometimes higher (von Caemmerer and Edmondson, 1986; Sharkey, 1989) possibly due to chelation of RuBP with Mg²⁺ ions (von Caemmerer and Edmondson, 1986) or regulation of phosphoribulokinase (Servaites et al., 1991). These processes are not taken into account in the model, with the effect that simulations may underestimate the RuBP/Rubisco ratio.

An increase in leaf temperature (T_L , K) affects the values of k_c , k_o , K_{mc} , and K_{mo} . This effect is well described by the so-called Arrhenius law normalized by the value at 25 °C (Figures 4.3 and 4.4):

$$k_c = k_{c,25} e^{\left(\frac{(T_L-298.15)H_{a,kc}}{298.15RT_L}\right)}, \quad (4.8)$$

$$k_o = k_{o,25} e^{\left(\frac{(T_L-298.15)H_{a,ko}}{298.15RT_L}\right)}, \quad (4.9)$$

$$K_{mc} = K_{mc,25} e^{\left(\frac{(T_L-298.15)H_{a,Kmc}}{298.15RT_L}\right)}, \quad (4.10)$$

$$K_{mo} = K_{mo,25} e^{\left(\frac{(T_L-298.15)H_{a,Kmo}}{298.15RT_L}\right)}, \quad (4.11)$$

where $k_{c,25}$ (s⁻¹), $k_{o,25}$ (s⁻¹), $K_{mc,25}$ (mol mol⁻¹) and $K_{mo,25}$ (mol mol⁻¹) are the values of k_c , k_o , K_{mc} , and K_{mo} at 25 °C (298.15 K), respectively, $H_{a,kc}$ (J mol⁻¹), $H_{a,ko}$ (J mol⁻¹), $H_{a,Kmc}$ (J mol⁻¹), and $H_{a,Kmo}$ (J mol⁻¹) are the activation energies of k_c , k_o , K_{mc} , and K_{mo} , respectively, and R is the universal gas constant (8.31 J mol⁻¹ K⁻¹).

4.2.1.1.2 Regulation of Rubisco activity

The values of f_{RB} are simulated dynamically, assuming that Rubisco activation follows first-order kinetics with different rates of activation and deactivation (Figure 4.5). The rate constant of activation is assumed to be proportional to the amount of Rubisco activase (Figure 4.6) such that:

$$\frac{df_{RB}}{dt} = \begin{cases} (f_{RBSS} - f_{RB})k_{RCA}Rcaf_{Rca} & \text{if } f_{RB} < f_{RBSS} \\ (f_{RBSS} - f_{RB})k_{dRB} & \text{if } f_{RB} \geq f_{RBSS} \end{cases}. \quad (4.12)$$

Here, f_{RBSS} is the steady state value of f_{RB} , k_{Rca} (m² g⁻¹ s⁻¹) is a second-order rate constant of Rubisco activation by Rubisco activase, Rca (g m⁻²) is the amount of Rubisco activase per unit of leaf area, f_{Rca} is a factor capturing the effect of temperature on Rca activity, and k_{dRB} (s⁻¹) is the rate constant of Rubisco deactivation. The value of f_{RBSS} is computed as:

$$f_{RBSS} = \min(f_{RBSS,r}, f_{RBSS,nr}), \quad (4.13)$$

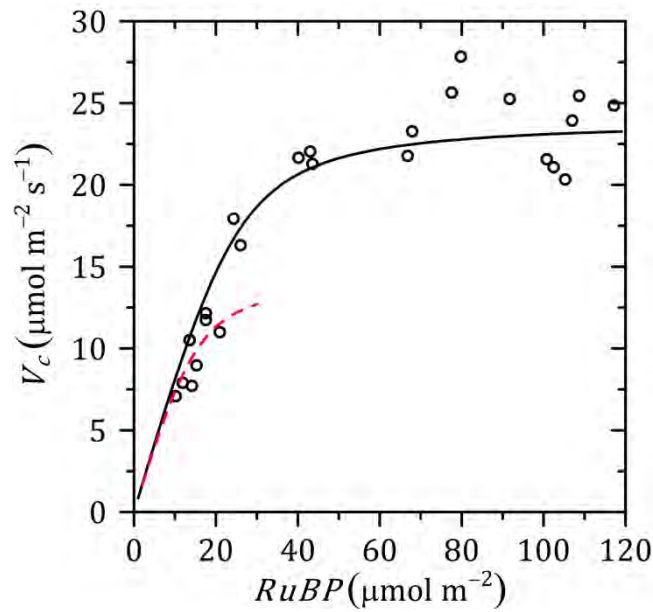


Figure 4.2: Measured (symbols) and predicted (lines) effect of RuBP content on the rate of carboxylation (V_c). Measurements from Price et al. (1995) for GAPDH antisense *Nicotiana tabacum* transformants. Predictions made with Equations 4.5– 4.7. The black, solid line was calculated with $RB = 2.5 \times 10^{-5} \text{ mol m}^{-2}$ (i.e., average measurement at high RuBP levels) and the red, dashed line was calculated with $RB = 1.5 \times 10^{-5} \text{ mol m}^{-2}$ (i.e., average measurement at low RuBP levels). Additional inputs were $K_{I,PGA} = 8.4 \times 10^{-4} \text{ mol m}^{-3}$, $K_{m,RuBP} = 2.2 \times 10^{-2} \text{ mol m}^{-3}$, $V_{st} = 1.8 \times 10^{-5} \text{ m}$, and $PGA = 10^{-4} \text{ mol m}^{-2}$. $R^2 = 0.88$ and $RMSE = 2.37 \text{ } \mu\text{mol m}^{-2} \text{ s}^{-1}$.

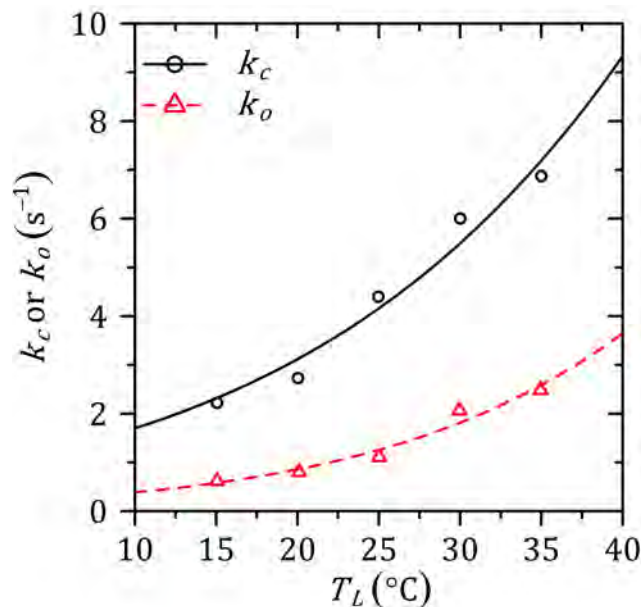


Figure 4.3: Measured (symbols) and predicted (lines) effect of leaf temperature (T_L) on rate constants of carboxylation (k_c) and oxygenation (k_o). Measurements from Walker et al. (2013) for *Arabidopsis thaliana*. Predictions made with Equations 4.8 and 4.9 assuming $k_{c,25} = 4.16 \text{ s}^{-1}$, $H_{a,kc} = 4.18 \times 10^4 \text{ J mol}^{-1}$, $k_{o,25} = 1.26 \text{ s}^{-1}$, and $H_{a,ko} = 5.51 \times 10^4 \text{ J mol}^{-1}$. $R^2 = 0.96$ (k_c) and 0.96 (k_o) and $RMSE = 0.38 \text{ s}^{-1}$ (k_c) and 0.16 s^{-1} (k_o).

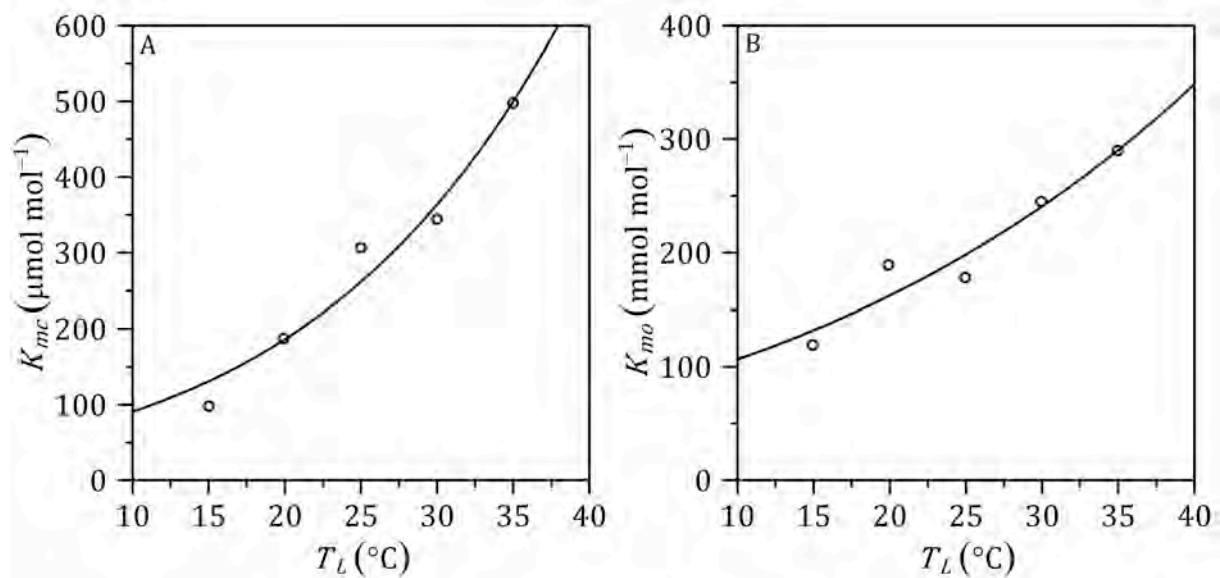


Figure 4.4: Measured (symbols) and predicted (lines) effect of leaf temperature (T_L) on the Michaelis-Menten constants of Rubisco with respect to CO_2 (A) and O_2 (B). Measurements from Walker et al. (2013) for *Arabidopsis thaliana*. Predictions made with Equations 4.10 and 4.11 assuming $K_{mc,25} = 2.62 \times 10^{-4} \text{ mol mol}^{-1}$, $H_{a,Kmc} = 4.94 \times 10^4 \text{ J mol}^{-1}$, $K_{mo,25} = 1.98 \times 10^{-1} \text{ mol mol}^{-1}$, and $H_{a,Kmo} = 2.91 \times 10^4 \text{ J mol}^{-1}$. $R^2 = 0.96$ (A) and 0.92 (B), and $\text{RMSE} = 29.4 \mu\text{mol mol}^{-1}$ (A) and $18.1 \text{ mmol mol}^{-1}$ (B).

where $f_{RBSS,r}$ is the steady-state value of f_{RB} when carboxylation is limited by NADPH production or TPU and $f_{RBSS,rr}$ quantifies the reduction of Rubisco activity at low CO_2 due to reduced carbamylation. $f_{RBSS,r}$ is calculated by inverting Equation 4.5 (see below for details) under conditions where the potential rates of electron transport or TPU limit the regeneration of RuBP:

$$f_{RBSS,r} = \begin{cases} f_{RB,m} & \text{if } I_p = 0 \\ \min \left[\frac{f_{Rca} \min(V_{RJ}, V_{R,TPU}) \left(C_C + K_{mc} \left(1 + \frac{O_2}{K_{mo}} \right) \right)}{(2 + 1.5\phi)k_C C_C R B}, f_{RB,M} \right] & \text{if } I_p > 0 \end{cases} \quad (4.14)$$

Here, V_{RJ} and $V_{R,TPU}$ are the potential rates of PGA conversion into RuBP (mol m^{-2}) limited by potential electron transport and TPU, respectively. $f_{RB,m}$ and $f_{RB,M}$ are the fractions of Rubisco that remain active in darkness and the maximum fraction of Rubisco that can be activated *in vivo*, respectively, and I_p ($\text{mol m}^{-2} \text{ s}^{-1}$) is the irradiance absorbed by the leaf that may be used for photosynthesis.

The reasoning behind Equation 4.14 is as follows. First, it is assumed that Rubisco activity is determined by the activity of Rubisco activase. This activity is itself regulated by changes in the ratio between ATP and ADP in the stroma of the chloroplast and, in some species, reduction by thioredoxin (Zhang et al., 2002; Carmo-Silva and Salvucci, 2013). It is assumed that when there is a deficit of electron transport relative to the potential demand of stromal metabolism (if Rubisco was fully active), the ATP/ADP ratio will fall, which leads to a decrease in the activity of Rubisco activase and, with it, the activation state of Rubisco. The potential demand of stromal metabolism is, by definition, independent of RuBP concentration (Farquhar et al., 1980), hence the

exclusion of this term in the derivation of Equation 4.14. There is empirical evidence indicating that when RuBP regeneration is limited by TPU, the activation state of Rubisco decreases (Sharkey et al., 1986a; Sharkey, 1989). This is also assumed to occur due to a reduction in the ATP/ADP ratio occurring as a result of the decrease in free phosphate that characterizes TPU-limited conditions (Sharkey et al., 1986a; Sharkey, 1989).

The activity of Rubisco activase changes with temperature, displaying an optimum (Carmo-Silva and Salvucci, 2011). As no published formula was found to describe this relationship, the following general expression was used, as it reproduced accurately existing measurements (Figure 4.7):

$$f_{Rca} = \frac{H_{d,Rca} e^{\left(\frac{(T_L - T_{o,Rca})H_{a,Rca}}{T_{o,Rca}RT_L}\right)}}{H_{d,Rca} - H_{a,Rca} \left(1 - e^{\frac{(T_L - T_{o,Rca})H_{d,Rca}}{T_{o,Rca}RT_L}}\right)}, \quad (4.15)$$

where $T_{o,Rca}$ (K) is the optimal temperature for Rca activity, $H_{a,Rca}$ (J mol⁻¹) is an apparent activation energy of Rca activity, and $H_{d,Rca}$ (J mol⁻¹) is an apparent deactivation energy of Rca activity.

For a catalytic site of Rubisco to be active, it has to bind a molecule of CO₂ and a molecule of Mg²⁺, undergoing structural changes (Stec, 2012). The effects of Mg²⁺ on Rubisco activity is beyond the scope of this model, but the effects of CO₂ as an activator are included in an empirical manner. Using data from von Caemmerer and Edmondson (1986), the following linear relationship was deduced (Figure 4.8):

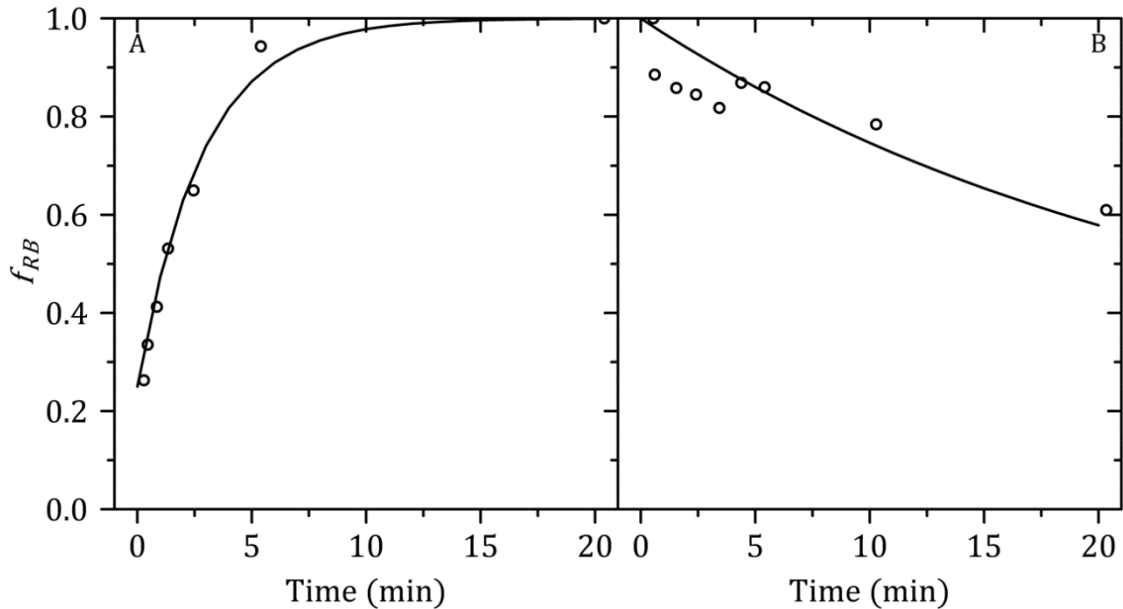


Figure 4.5: Measured (symbols) and predicted (line) dynamics of the fraction of active Rubisco after a stepwise increase in irradiance (A, 35 → 1500 $\mu\text{mol m}^{-2} \text{s}^{-1}$) or a stepwise decrease in irradiance (B, 1500 → 35 $\mu\text{mol m}^{-2} \text{s}^{-1}$). Measurements from Sassenrath-Cole and Percy (1994b) for Glycine max. Predictions made with Equation 4.12 assuming $Rca = 6.76 \times 10^{-2} \text{ g m}^{-2}$, $k_{Rca} = 8.72 \times 10^{-2} \text{ m}^2 \text{ g}^{-1} \text{ s}^{-1}$, and $k_{dRB} = 6.80 \times 10^{-4} \text{ s}^{-1}$. $R^2 = 0.95$ (A) and 0.67 (B), and RMSE = 0.07 (panel A) and 0.07 (panel B).

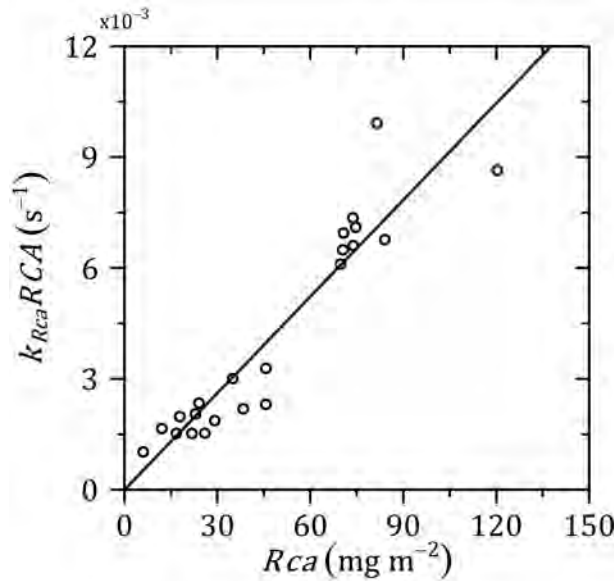


Figure 4.6: Measured (symbols) and predicted (line) dependency of the rate constant of Rubisco activation ($k_{Rca}Rca$) to Rubisco activase content (Rca). Measurements from Mott and Woodrow (2000) using Rca antisense *Nicotiana tabacum* transformants. Predictions made with Equation 4.12 assuming $k_{Rca} = 8.72 \times 10^{-2} \text{ m}^2 \text{ g}^{-1} \text{ s}^{-1}$, $R^2 = 0.96$ and $RMSE = 9.64 \times 10^{-4} \text{ s}^{-1}$.

$$f_{RBSS,nr} = \min(1, a_c + b_c C_c), \quad (4.16)$$

where a_c and b_c (mol mol^{-1}) are empirical coefficients. The value of $f_{RB,M}$ is determined by the amount of Rubisco activase (RCA , g m^{-2}) according to the following hyperbolic relationship (Figure 4.9):

$$f_{RB,M} = \frac{f_{RCA}Rca}{f_{Rca}Rca + K_{A,Rca}}, \quad (4.17)$$

where $K_{A,Rca}$ (g m^{-2}) is the amount of Rubisco activase at which $f_{RB,M} = 0.5$.

4.2.1.2 Electron transport chain

According to the paradigm of limiting factors, the electron transport chain only limits CO_2 assimilation when it reaches its potential rate of electron transport given a certain temperature and irradiance (see Section 4.2.1.2.1). However, the rate of electron transport *in vivo* is highly regulated in order to (i) couple the rate of NADPH and ATP production to the metabolic demand and (ii) to protect the photosystems in the thylakoid from excess energy that results in photoinhibition. The equations to calculate photoinhibition are described in Section 4.2.1.2.4. Part of the excess energy may be dissipated as heat to protect the reaction centres from excessive excitation. Under steady-state conditions, this energy-dependent non-photochemical quenching of energy (qE) is assumed not to limit the potential rate of electron transport as the loss of quantum yield in the antenna complexes can be compensated by increasing the fraction of open reaction centres. Evidence of this compensation comes from measurements of CO_2 assimilation on non-photochemical quenching (NPQ) mutants. However, experimental evidence shows that, after a stepwise decrease in irradiance, excessive qE can transiently limit the rates of electron transport (Armbruster et al., 2014; Kromdijk et al., 2016). The equations employed to simulate qE are given in Section 4.2.1.2.2.

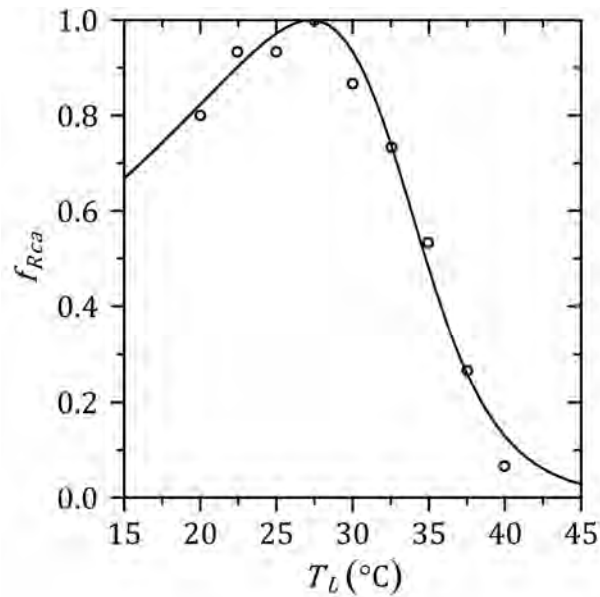


Figure 4.7: Measured (symbols) and predicted (line) effect of leaf temperature on the activity of Rubisco activase. Measurements from Carmo-Silva and Salvucci (2011) for *Arabidopsis thaliana*. Predictions made with Equation 4.15 assuming $T_{o,Rca} = 300.4$ K, $H_{a,Rca} = 3.00 \times 10^4$ J mol⁻¹, and $H_{d,Rca} = 2.90 \times 10^{-5}$ J mol⁻¹. $R^2 = 0.98$ and $RMSE = 0.04$.

The absorbance of irradiance by a leaf in the photosynthetically active region of the spectrum varies with blue irradiance, due to the movements of chloroplasts (Haupt and Scheuerlein, 1990). This phenomenon is included in the model using an empirical approach described in Section 4.2.1.2.3.

Section 4.2.1.2.5 describes how to calculate the maximum rate of RuBP regeneration limited by potential electron transport as well as the actual rate of electron transport when the potential demand of stromal metabolism is limiting. In Section 4.2.1.2.6, the Stern-Volmer NPQ coefficient and other fluorescence coefficients are calculated to facilitate comparisons of simulations with measurements of fluorescence on leaves.

4.2.1.2.1 Potential rate of electron transport

The following non-rectangular hyperbola is used to calculate the potential rate of electron transport (J_p , mol m⁻² s⁻¹) as a function of absorbed irradiance:

$$J_p = \frac{I_{p2} + J_{max} - \sqrt{(I_{p2} + J_{max})^2 - 4I_{p2}J_{max}\theta}}{2\theta}, \quad (4.18)$$

where I_{p2} is the value of J_p at low irradiance (mol m⁻² s⁻¹), J_{max} (mol m⁻² s⁻¹) is the maximum value that J_p can achieve, and θ is a parameter that characterises the curvature of the transition from I_{p2} to J_{max} . Equation 4.18 was proposed by Farquhar and Wong (1984) as a simplification of the analytical model of steady-state potential electron transport derived from first principles by Farquhar and von Caemmerer (1981). The concept of J_p is empirical (von Caemmerer, 2013) and should not be interpreted mechanistically. I_{p2} represents the rate of electron transport through Photosystem II (PSII) at low irradiance and moderate lumen pH. J_{max} is a theoretical value that can only be reached when irradiance is infinite and for an uncoupled

thylakoid (Farquhar and von Caemmerer, 1981), that is, when the electron transport is not downregulated by low lumen pH. In a coupled thylakoid system (i.e., *in vivo*), as irradiance increases, the electron transport chain becomes increasingly more regulated by decreases in lumen pH, even when metabolism is not limiting. This is captured, empirically, by the term θ in Equation 4.18. Although mechanistic models of electron transport exist (see Chapter 5 of this dissertation), Equation 4.18 has been used successfully to calculate CO₂ assimilation as part of the FvCB model under a wide range of environmental conditions and species (von Caemmerer, 2013) and it is highly parsimonious. Whereas the parameter θ remains largely empirical, the variable I_{p2} can be related to underlying physiological processes as proposed by Yin and Struik (2009):

$$I_{p2} = \sigma_2 \phi_{IIp} I_p, \quad (4.19)$$

where σ_2 is the fraction of absorbed irradiance by photosynthetic and accessory pigments associated with the antenna complexes of PSII and ϕ_{IIp} is the maximum quantum yield of PSII in the presence of photoinhibition. Equation 4.19 implies that, at low irradiances and ambient CO₂, when CO₂ assimilation is limited by potential rates of electron transport, the apparent quantum yield of CO₂ assimilation decreases proportionally to ϕ_{IIp} . This linear relationship has been observed in several species, using measurements of CO₂ assimilation and O₂ evolution (Demmig-Adams et al., 1989; Somersalo and Krause, 1989; Hikosaka et al., 2004). The effective maximum quantum yield of the population of PSII in the leaf is calculated as:

$$\phi_{IIp} = \frac{F_{m,app} - F_{o,app}}{F_{m,app}}, \quad (4.20)$$

where $F_{m,app}$ and $F_{o,app}$ are apparent maximum and minimum fluorescence yields of PSII

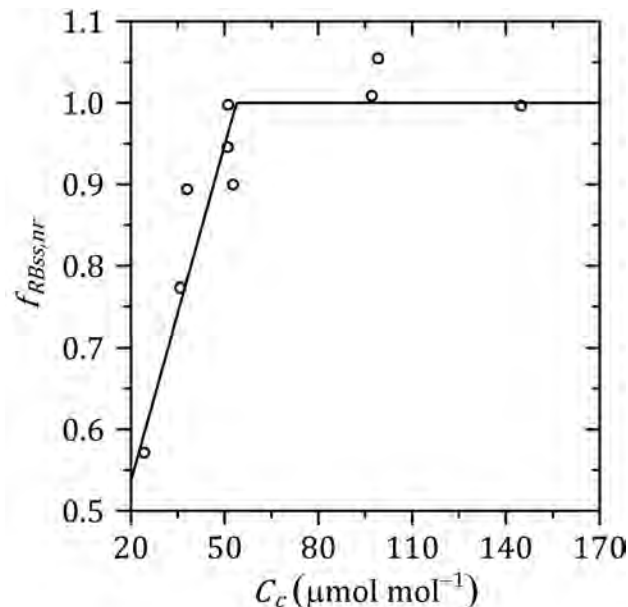


Figure 4.8: Measurements (symbols) and predicted (line) effect of chloroplast CO₂ (C_c) on Rubisco activity due to carbamylation ($f_{RBSS,nr}$). Measurements from von Caemmerer and Edmondson (1986) corrected by mesophyll conductance measured by von Caemmerer and Evans (1991) using *Raphanus sativus*. Predictions made with Equation 4.16 assuming $a_c = 0.27$ and $b_c = 1.4 \times 10^4 \text{ mol mol}^{-1}$. $R^2 = 0.92$ and $RMSE = 0.05$.

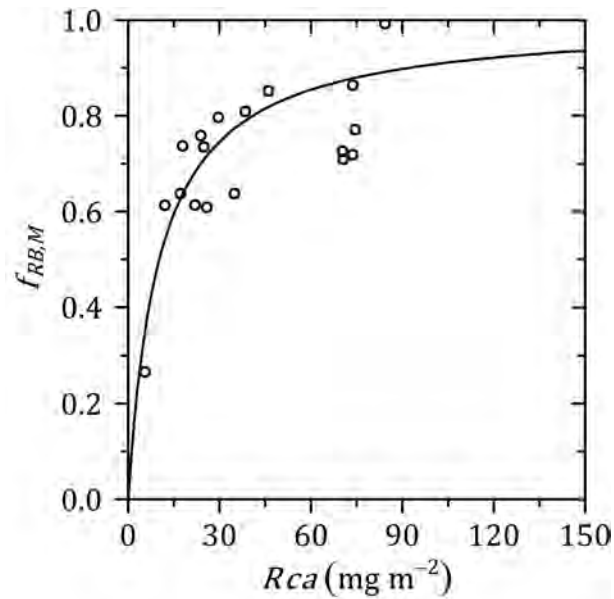


Figure 4.9: Measured (symbols) and predicted (line) effect of Rubisco activase content (Rca) on the maximum fraction of active Rubisco ($f_{RB,M}$). Measurements from Mott and Woodrow (2000) using Rca antisense *Nicotiana tabacum* transformants. Predictions made with Equation 4.17 assuming $K_{A,RCA} = 1.02 \times 10^{-2} \text{ g m}^{-2}$, $R^2 = 0.59$ and $RMSE = 0.12$.

at the leaf level in the absence of qE and chloroplast movement. These apparent fluorescence yields are the result of weighting the contributions of functional and photoinhibited PSII units as:

$$F_{m,app} = F_m(1 - f_{IId}) + F_{md}f_{IId}, \quad (4.21)$$

and

$$F_{o,app} = F_o(1 - f_{IId}) + F_{od}f_{IId}, \quad (4.22)$$

where f_{IId} is the fraction of PSII units that are photoinhibited, F_m and F_o are the maximum and minimum fluorescence yields of functional PSII units and F_{md} and F_{od} are the maximum and minimum fluorescence yields of photoinhibited PSII units. Experimental results indicate that photoinhibited PSII units remain in a highly quenched state and thus have relatively lower maximum fluorescence yields than expected from reaction centres that cannot perform photochemistry (Krause, 1988; Šetlík et al., 1990). This phenomenon has also been confirmed by measurements of fluorescence lifetime (Renger et al., 1995; Gilmore et al., 1996; Matsubara and Chow, 2004). These fluorescence yields are defined as:

$$F_m = \frac{k_f}{k_f + k_{D0}}, \quad (4.23)$$

$$F_o = \frac{k_f}{k_f + k_{D0} + k_p}, \quad (4.24)$$

$$F_{md} = \frac{k_f}{k_f + k_{Dinh}}, \quad (4.25)$$

and

$$F_{od} = \frac{k_f}{k_f + k_{Dinh}}, \quad (4.26)$$

where k_f (s^{-1}) is a rate constant of energy dissipation as fluorescence, k_{D0} (s^{-1}) is a basal rate constant of energy dissipation as heat, k_p (s^{-1}) is a rate constant of energy quenching by net charge separation in the reaction centre and k_{Dinh} (s^{-1}) is a rate constant of heat dissipation associated to photoinhibited PSII units. $F_{md} = F_{od}$ as photoinhibited PSII units are, by definition, not capable of performing photochemistry.

This model explicitly does not take into account the effect of charge recombination within PSII reaction centres (de Wijn and van Gorkom, 2002; Laisk et al., 2012) or contributions from Photosystem I to fluorescence yield (Pfündel et al., 2013). The variable ϕ_{IIP} should be taken as an apparent quantum yield that includes, implicitly, these effects. Despite such simplifications, Equations 4.18 and 4.19 have proven to be highly useful in predicting CO_2 assimilation at low irradiance and at the leaf level (von Caemmerer, 2000; Farquhar et al., 2001; Yin and Struik, 2009) and is considered sufficient for the purpose of this model.

This model does not consider changes in the value of σ_2 due to state transitions (Dietzel et al., 2008). State-transitions become suppressed at high irradiance due to reduction of thioredoxin (Rintamäki et al., 2000; Breitholtz et al., 2005; Nikkanen and Rintamäki, 2014). Also, state transitions can become significant when a leaf is exposed to changes in the irradiance spectrum that excites preferentially one type of photosystem (Hogewoning et al., 2012), but not when only irradiance intensity changes (Mekala et al., 2015). Furthermore, measurements on the state transition mutant *stn7* of *A. thaliana* show similar fluorescence parameters compared with the wildtype (Nilkens et al., 2010; Dall'Osto et al., 2014). Therefore, state transitions may play a more important role in response to changes in the spectrum of irradiance, like a reduction in the red:far-red ratio by shading (McTavish, 1988), than in response to changes in irradiance levels. Such changes in the spectrum are beyond the scope of this model.

The photosynthetically active irradiance absorbed by a leaf (I_p) is calculated as:

$$I_p = \alpha_r (I_b \alpha_{bp} + I_g \alpha_{gp} + I_r \alpha_{rp}), \quad (4.27)$$

where α_r is the relative absorptance with respect to a dark-adapted leaf due to chloroplast movement, I_b , I_g and I_r are the irradiances incident on the leaf surface for blue, green and red wavebands (400 – 500 nm, 500 – 600 nm and 600 – 700 nm, respectively), and α_{bp} , α_{gp} , and α_{rp} are the leaf-level fractions of irradiance that are available for photosynthesis for blue, green and red irradiance, respectively (see Section 4.2.4 for details).

The value of J_{max} is assumed to vary with temperature (Medlyn et al., 2002; Bernacchi et al., 2003) according to the expression (Figure 4.10):

$$J_{max} = \frac{J_{max,25} e^{\left(\frac{(T_L - 298.15)H_{a,Jmax}}{298.15RT_L}\right)} \left[1 + e^{\left(\frac{298.15S_{Jmax} - H_{d,Jmax}}{298.15R}\right)}\right]}{1 + e^{\left(\frac{T_L S_{Jmax} - H_{d,Jmax}}{RT_L}\right)}}, \quad (4.28)$$

where $J_{max,25}$ is the value of J_{max} at 25 °C (298.15 K), $H_{a,Jmax}$ (J mol⁻¹) is an apparent activation energy of J_{max} , S_{Jmax} (J mol⁻¹ K⁻¹) is the apparent entropy coefficient of J_{max} , and $H_{d,Jmax}$ (J mol⁻¹) is an apparent deactivation energy of J_{max} .

4.2.1.2.2 Energy-dependent non-photochemical quenching

It is known that qE increases with protonation of the PsbS protein (Niyogi et al., 2005) and de-epoxidation of xanthophyll pigments (Demmig-Adams and William III, 1996), both of which depend on lumen pH (Zaks et al., 2013). These two processes appear to be regulators of the pH sensitivity of qE and are not strictly required to induce qE if lumen pH is sufficiently low (Johnson and Ruban, 2011; Johnson et al., 2012). However, the exact mechanisms underlying qE are still under debate (Horton et al., 2008; Zaks et al., 2013). Given these uncertainties a mechanistic description of qE is not used in this model. Instead, a “teleonomic” (i.e. goal-seeking) approach is followed, where it is assumed that the goal of qE is achieved if, for the same rate of electron transport, the first stable electron acceptor (i.e., Q_A) becomes more oxidised, as this reduces the probability of acceptor-side photoinhibition (Tyystjärvi et al., 2005). As a proxy for oxidised Q_A , the so-called qP parameter was used, calculated as

$$qP = \frac{\min(J_p, J_m)}{\phi_{IIp} I_{p2}}, \quad (4.29)$$

where J_m (mol m⁻² s⁻¹) is the rate of electron transport limited by metabolism (Section 4.2.1.2.5). qP is not equal to the redox state of Q_A (Kramer et al., 2004b), but it is an useful index, as it is a monotonic function of the Q_A redox state (i.e., as Q_A becomes more oxidised, qP increases), and it is equal to Q_A at the extremes (i.e., 0 and 1). It is assumed that, in the steady state, the increase in qP due to qE is proportional to the difference between qP (in the absence of qE) and the theoretical maximum value. Since qP varies between 0 and 1, its steady-state value as affected by qE (qP_{ss}) can be written as:

$$qP_{ss} = qP + f_{qE}(1 - qP), \quad (4.30)$$

where f_{qE} , which also varies between 0 and 1, is an empirical parameter. The steady-state maximum PSII quantum yield (ϕ_{IIss}), for the same rate of electron transport, assuming qP_{ss} , is defined as:

$$\phi_{IIss} = \frac{\min(J_p, J_m)}{qP_{ss} I_{p2}}. \quad (4.31)$$

Therefore, the reduction in maximum PSII quantum yield can be calculated as:

$$\phi_{qEss} = \min(\phi_{IIp} - \phi_{IIss}, \phi_{qEm}), \quad (4.32)$$

where ϕ_{qEm} is the maximum loss of maximum PSII quantum yield that can be achieved by qE. The equations in the above result in an increase of qE with irradiance and a decrease with CO₂ and the patterns obtained from the simulations (Figure 4.11) are in agreement with those obtained experimentally on *A. thaliana* and *Nicotiana tabacum* (Kanazawa and Kramer, 2002; Avenson et al., 2005; van Rooijen et al., 2015).

Changes in the loss of maximum PSII quantum yield due to qE are assumed to follow first-order kinetics:

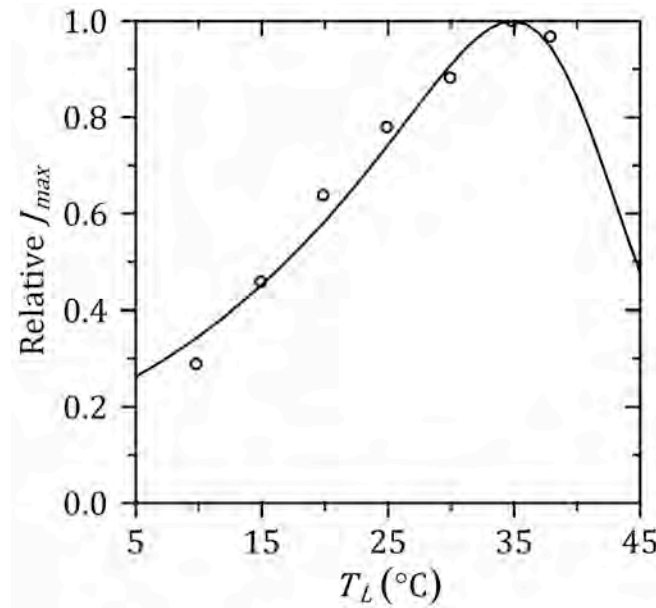


Figure 4.10: Measured (symbols) and predicted (line) values of J_{max} as a function of leaf temperature (T_L). Measurements from Yamori et al. (2008) for *Spinacia oleracea*. Predictions made with Equation 4.28 assuming $H_{a,J_{max}} = 3.62 \times 10^4 \text{ J mol}^{-1}$, $S_{J_{max}} = 690 \text{ J mol}^{-1} \text{ K}^{-1}$, and $H_{d,J_{max}} = 2.16 \times 10^5 \text{ J mol}^{-1}$. $R^2 = 0.98$ and $RMSE = 3.75 \times 10^{-2}$.

$$\frac{d\phi_{qE}}{dt} = \begin{cases} (\phi_{qEss} - \phi_{qE})k_{iqE} & \text{if } \phi_{qEss} > \phi_{qE} \\ (\phi_{qEss} - \phi_{qE})k_{dqE} & \text{if } \phi_{qEss} \leq \phi_{qE} \end{cases}, \quad (4.33)$$

where k_{iqE} and k_{dqE} (s^{-1}) are the rate constants of induction and relaxation of qE. The actual maximum PSII quantum yield, once qE and photoinhibition are taken into account, becomes:

$$\phi_{II} = \phi_{IIp} - \phi_{qE}. \quad (4.34)$$

As described in the previous section, qE is assumed not to limit the actual rate of electron transport under steady-state conditions. However, there is evidence that, after a stepwise decrease in irradiance, qE can be transiently limiting (Armbruster et al., 2014; Kromdijk et al., 2016). This phenomenon has been implemented by assuming that, whenever the actual maximum PSII quantum yield (ϕ_{II}) is higher than in the steady-state (ϕ_{IIss}), the rate of electron transport will be reduced proportionally as:

$$J_{qE} = \begin{cases} J_p & \text{if } \phi_{IIss} > \phi_{II} \\ [1 - (\phi_{IIss} - \phi_{II})/\phi_{IIss}]J_p & \text{if } \phi_{IIss} \leq \phi_{II} \end{cases}, \quad (4.35)$$

where J_{qE} is the potential rate of electron transport taking into account the possible limitation by excess qE. This equation does not imply that photosynthesis is always reduced whenever $\phi_{IIss} > \phi_{II}$. This will only occur if J_{qE} becomes low enough that it limits the rate of RuBP regeneration (Equation 4.44).

4.2.1.2.3 Chloroplast movement

Chloroplast movement is the mechanism by which chloroplasts respond to irradiance in the blue region of the spectrum by moving towards the anticlinal walls of the mesophyll

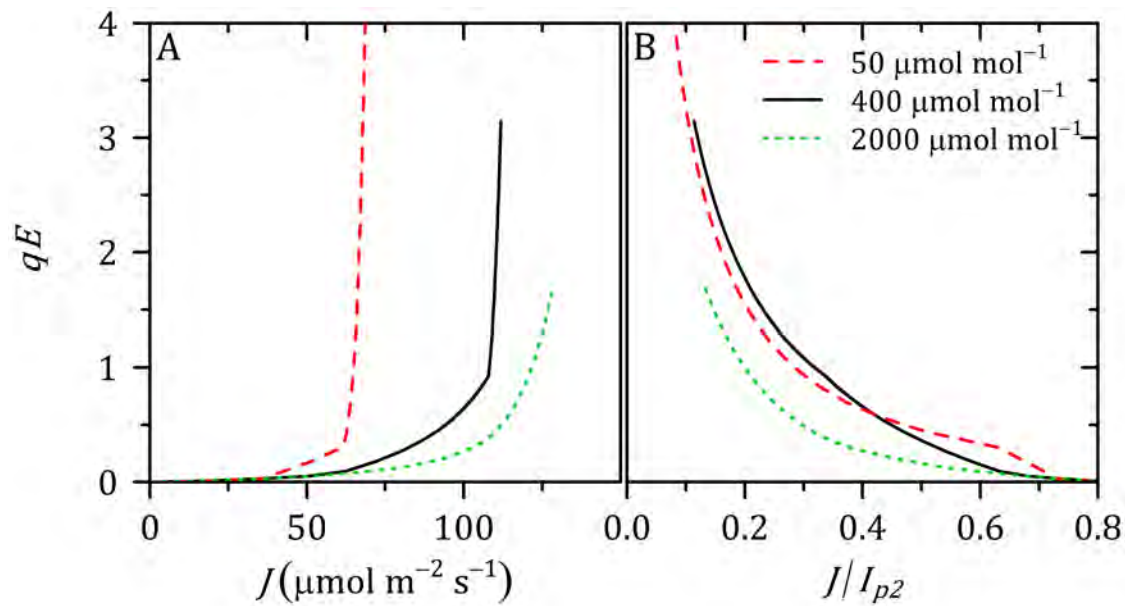


Figure 4.11: Simulated steady-state qE as a function of the actual rate of electron transport (A) and the ratio between actual rate of electron transport and irradiance absorbed by PSII, equivalent to the operational efficiency of PSII (B) for different air $[\text{CO}_2]$. Simulation performed with the whole model with parameters as in Table 4.7.

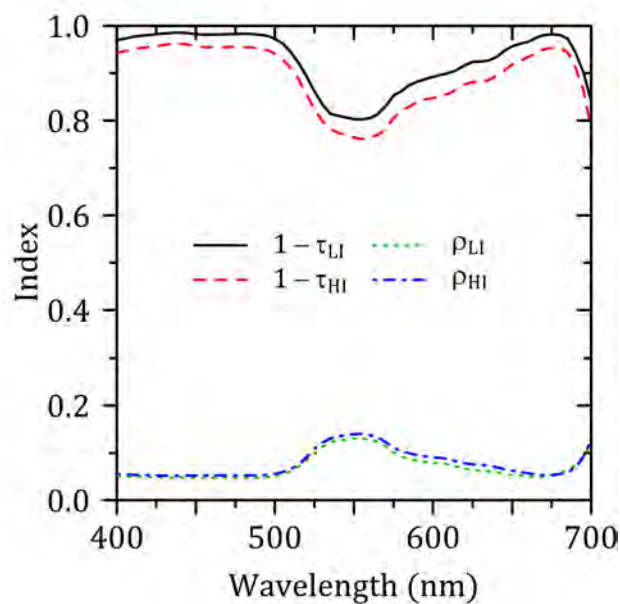


Figure 4.12: Measured fraction of irradiance that is transmitted (τ) or reflected (ρ) at the leaf level, at high and low irradiance (HI and LI, respectively) as a function of wavelength in the photosynthetically active region of the spectrum. Measurements from Davis et al. (2011) for *Arabidopsis thaliana*.

cells at high blue irradiance and periclinal walls at low blue irradiance (Haupt and Scheuerlein, 1990). This movement results in changes of the optical properties of the leaves (Davis and Hangarter, 2012), with an increase in the absorptance of irradiance at the leaf level at low blue irradiance (chloroplast accumulation response) and a net decrease at higher levels (chloroplast light avoidance response). Measurements of the spectral distribution of absorptance of leaves in different species (Brugnoli and Björkman, 1992; Davis et al., 2011) indicate that the relative spectral distribution of absorptance of the leaf does not change significantly with chloroplast movement (Figure

4.12). In some species and/or growth conditions, changes in absorptance due to chloroplast movement are negligible (Davis et al., 2011; Higa and Wada, 2016). For such species, the effect of chloroplast movement can be “turned off” by setting adequate values to the relevant parameters in the equations below.

Based on published results (Brugnoli and Björkman, 1992; Kasahara et al., 2002; Davis and Hangarter, 2012; Łabuz et al., 2015), the following empirical expression was constructed (Figure 4.13):

$$\alpha_{r_{ss}} = \begin{cases} 1 + \frac{I_b}{I_{ac}} \alpha_{rac} & \text{if } I_b \leq I_{ac} \\ 1 + \alpha_{rac} - \frac{\alpha_{ar} I_b + \alpha_{rav} - \sqrt{(\alpha_{ar} I_b + \alpha_{rav})^2 - 4\alpha_{ar} I_b \theta_{ar} \alpha_{rav}}}{2\theta_{ar}} & \text{if } I_b > I_{ac} \end{cases}, \quad (4.36)$$

where $\alpha_{r_{ss}}$ is the steady-state absorptance of irradiance at the leaf level relative to the dark-adapted state, I_{ac} ($\text{mol m}^{-2} \text{s}^{-1}$) is the blue irradiance at which the chloroplast accumulation response is maximised, α_{rac} is the maximum relative increase in absorptance due to the chloroplast accumulation response, α_{rav} is the difference between maximum (accumulation response) and minimum (avoidance response) relative absorptance of the leaf, and α_{ar} ($\text{mol}^{-1} \text{m}^2 \text{s}$) and θ_{ar} are the apparent initial slope and curvature of the dependency of $\alpha_{r_{ss}}$ on irradiance, respectively. From measurements by Łabuz et al. (2015), it can be deduced that the value of α_{ar} increases with leaf temperature (Figure 4.13) and the Arrhenius law is used to describe this dependency as:

$$\alpha_{ar} = \alpha_{ar,25} e^{\left(\frac{(T_L - 298.15)H_{a,\alpha_{ar}}}{298.15RT_L}\right)}, \quad (4.37)$$

where $\alpha_{ar,25}$ is the value of α_{ar} at 25 °C (298.15 K) and $H_{a,\alpha_{ar}}$ (J mol^{-1}) is an apparent activation energy of α_{ar} . Changes in absorptance due to chloroplast movement are assumed to follow first-order kinetics (Figure 4.13):

$$\frac{d\alpha_r}{dt} = \begin{cases} (\alpha_{r_{ss}} - \alpha_r)k_{i\alpha} & \text{if } \alpha_{r_{ss}} > \alpha_r \\ (\alpha_{r_{ss}} - \alpha_r)k_{d\alpha} & \text{if } \alpha_{r_{ss}} \leq \alpha_r \end{cases}, \quad (4.38)$$

where $k_{i\alpha}$ and $k_{d\alpha}$ (s^{-1}) are the rate constants at which absorptance increases and decreases, respectively. Based on published experiments (Brugnoli and Björkman, 1992; Łabuz et al., 2015), these rate constants are calculated as a function of leaf temperature (Figure 4.14), and the following expressions are used:

$$k_{i\alpha} = \frac{k_{i\alpha,25} e^{\left(\frac{(T_L - 298.15)H_{a,k\alpha}}{298.15RT_L}\right)} \left[1 + e^{\left(\frac{298.15S_{k\alpha} - H_{d,k\alpha}}{298.15R}\right)} \right]}{1 + e^{\left(\frac{T_L S_{k\alpha} - H_{d,k\alpha}}{RT_L}\right)}}, \quad (4.39)$$

$$k_{d\alpha} = \frac{k_{d\alpha,25} e^{\left(\frac{(T_L - 298.15)H_{a,k\alpha}}{298.15RT_L}\right)} \left[1 + e^{\left(\frac{298.15S_{k\alpha} - H_{d,k\alpha}}{298.15R}\right)} \right]}{1 + e^{\left(\frac{T_L S_{k\alpha} - H_{d,k\alpha}}{RT_L}\right)}}, \quad (4.40)$$

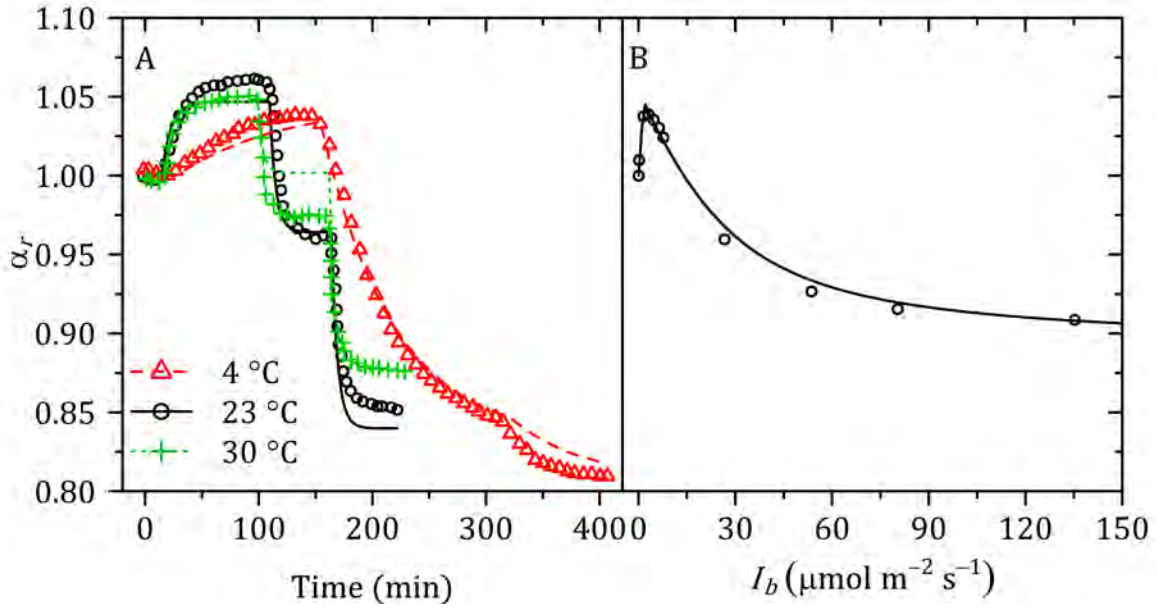


Figure 4.13: Measured (symbols) and predicted (lines) changes in red light absorptance as a function of time (A) for three different constant leaf temperatures (see legend) and three blue irradiance levels applied consecutively (1.6, 20 and 120 $\mu\text{mol m}^{-2} \text{s}^{-1}$), and changes in steady-state red light absorptance as a function of blue irradiance at 25 °C (B). Measurements in panel A from Łabuz et al. (2015) and in panel B from Davis and Hangarter (2012), in both cases for *Arabidopsis thaliana* at 25 °C. Predictions made with Equations 4.36 – 4.40 assuming $I_{ac} = 1.60 \mu\text{mol m}^{-2} \text{s}^{-1}$, $\alpha_{rac} = 0.05$, $\alpha_{rav} = 0.24$ (A) or 0.15 (B), $\theta_{ar} = 0.36$, $\alpha_{ar,25} = 4.35 \times 10^{-3} \text{ mol}^{-1} \text{ m}^2 \text{ s}$, $H_{a,\alpha_{ar}} = -7.46 \times 10^4 \text{ J mol}^{-1}$, $k_{i\alpha,25} = 2.50 \times 10^{-3} \text{ s}^{-1}$, $k_{d\alpha,25} = 3.84 \times 10^{-3} \text{ s}^{-1}$, $H_{a,k\alpha} = 9.05 \times 10^4 \text{ J mol}^{-1}$, $S_{k\alpha} = 1.08 \times 10^3 \text{ J mol}^{-1} \text{ K}^{-1}$, and $H_{d,k\alpha} = 3.28 \times 10^5 \text{ J mol}^{-1}$. $R^2 = 0.99$ (A) and 0.99 (B), and RMSE = 1.29×10^{-2} (A) and 4.62×10^{-3} (B).

where $k_{i\alpha,25}$ and $k_{d\alpha,25}$ (s^{-1}) are the values of $k_{i\alpha}$ and $k_{d\alpha}$ at 25 °C, $H_{a,k\alpha}$ (J mol^{-1}) is the apparent activation energy of both $k_{i\alpha}$ and $k_{d\alpha}$, $S_{k\alpha}$ ($\text{J mol}^{-1} \text{ K}^{-1}$) is the apparent entropy coefficient of both $k_{i\alpha}$ and $k_{d\alpha}$, and $H_{d,k\alpha}$ (J mol^{-1}) is the apparent deactivation energy of both $k_{i\alpha}$ and $k_{d\alpha}$.

4.2.1.2.4 Photoinhibition

Photoinhibition is the process in which PSII reaction centres become damaged, cannot perform photochemistry and have to be repaired in order to recover their functionality. There are several mechanisms that can contribute to photoinhibition of PSII reaction centres (Tyystjärvi et al., 2005) and several biochemical steps to repair a damaged PSII reaction centre (Aro et al., 1993). However, empirical evidence indicates that the rate of photoinhibition is proportional to incident irradiance (Figure 4.15), with corrections due to changes in absorptance (Kasahara et al., 2002; Davis and Hangarter, 2012) and photoprotection by qE (Li et al., 2002). This proportionality allows defining a quantum efficiency of photodamage (k_{inh} , $\text{m}^2 \text{ mol}^{-1}$). The repair process of photodamaged reaction centres is also assumed to follow first-order kinetics (k_{rep} , s^{-1}), as originally proposed by Kok (1956). Thus, the dynamics of f_{IIa} are determined by the balance between photodamage and repair of PSII units according to the expression:

$$\frac{df_{IIa}}{dt} = (1 - f_{IIa})k_{inh}I_p - f_{IIa}k_{rep}. \quad (4.41)$$

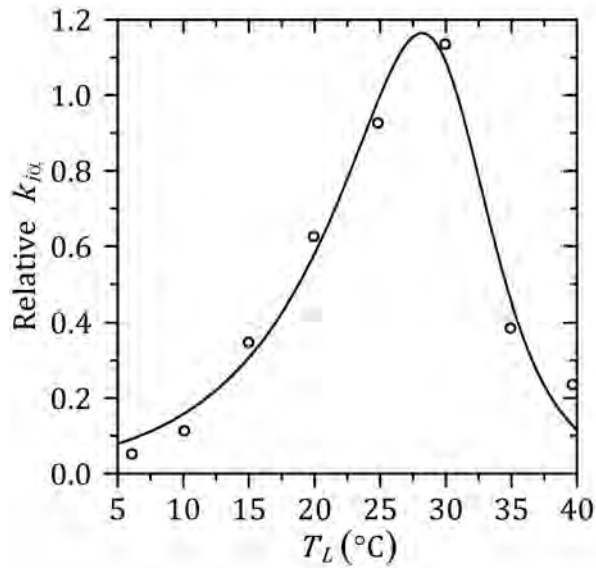


Figure 4.14: Measured (symbols) and predicted (line) changes in the rate constant of chloroplast movement ($k_{i\alpha}$) relative to the value at 25 °C. Measurements from Brugnoli and Björkman (1992) for *Oxalis oregana*. Predictions made with Equation 4.39 assuming $H_{a,k\alpha} = 9.05 \times 10^4 \text{ J mol}^{-1}$, $S_{k\alpha} = 108 \text{ J mol}^{-1} \text{ K}^{-1}$, and $H_{d,k\alpha} = 3.28 \times 10^5 \text{ J mol}^{-1}$.

The quantum efficiency of photodamage decreases with increasing photoprotection, and a linear relationship with ϕ_{qE} is assumed:

$$k_{inh} = \max(k_{inh0} - f_{prot}\phi_{qE}, 0), \quad (4.42)$$

where k_{inh0} ($\text{m}^2 \text{ mol}^{-1}$) is the quantum yield of photoinhibition in the absence of photoprotection and f_{prot} is an empirical coefficient that measures the efficiency of qE in protecting the PSII reaction centres from photoinhibition. Temperature has a significant effect on the rate of PSII repair (Figure 4.16). This effect is calculated as proposed by Yu et al. (2001):

$$k_{rep} = \frac{k_{rep,25} e^{\left(\frac{(T_L - 298.15)H_{a,krep}}{298.15RT_L}\right)} \left[1 + e^{\left(\frac{298.15S_{krep} - H_{d,krep}}{298.15R}\right)} \right]}{1 + e^{\left(\frac{T_L S_{krep} - H_{d,krep}}{RT_L}\right)}}, \quad (4.43)$$

where $k_{rep,25}$ (s^{-1}) is the rate of repair at 25 °C (298.15 K), $H_{a,krep}$ (J mol^{-1}) is an apparent activation energy of k_{rep} , S_{krep} ($\text{J mol}^{-1} \text{ K}^{-1}$) is the apparent entropy coefficient of k_{rep} , and $H_{d,krep}$ (J mol^{-1}) is an apparent deactivation energy of k_{rep} .

4.2.1.2.5 Coupling of electron transport chain to Calvin cycle

When the rate of electron transport through PSII achieves the maximum rate supported by the photosynthetic system, the rate of RuBP regeneration can no longer increase, as further increases in ATP or NADPH production are not possible (Farquhar et al., 1980).

It is possible to calculate the rate of RuBP regeneration either from ATP or NADPH production. Both methods differ in the stoichiometric coefficients used to calculate the number of RuBP molecules that can be produced per electron. When modelling C_3 photosynthesis, it is common to assume NADPH limitation because some of the

stoichiometric coefficients involved in ATP synthesis (e.g., the fraction of linear electrons that engage in the Q cycle of the cytochrome b₆f complex and the effective H⁺/ATP ratio of the ATP synthase) remain uncertain (von Caemmerer, 2000). These calculations also include the fact that a certain fraction of the electrons will be consumed by alternative electron sinks, or cycled around Photosystem I (PSI). These alternative forms of electron transport are incorporated following the approach by Yin and Struik (2009). The rate of RuBP regeneration limited by potential electron transport ($V_{R,J}$, mol m⁻² s⁻¹) is thus calculated as:

$$V_{R,J} = \frac{\min(J_p, J_{qE}) \left(1 - \frac{f_{pseudo}}{1 - f_{cyc}}\right) (2 + 1.5\phi)}{4 + 4\phi}, \quad (4.44)$$

where f_{pseudo} and f_{cyc} are the fractions of electron transport through PSI that are allocated to alternative electron sinks and cyclic electron transport, respectively.

When the potential rate of electron transport does not limit the flux through the Calvin cycle (i.e., the actual rate of electron transport is below its potential), the electron transport chain has to be down-regulated such that the production and consumption of ATP and NADPH match. Under such conditions, the potential rate of electron transport limited by metabolism (J_m , mol m⁻² s⁻¹) can be calculated by inverting Equation 4.44 combined with Equation 4.1 and replacing $\min(J_p, J_{qE})$ by J_m :

$$J_m = \frac{\min(V_{R,E}, V_{R,TPU}) (4 + 4\phi)}{\left(1 - \frac{f_{pseudo}}{1 - f_{cyc}}\right) (2 + 1.5\phi)}. \quad (4.45)$$

No assumptions are made regarding the mechanism by which the electron transport chain is down-regulated except that this mechanism must be sufficiently fast, such that it can be considered to be in quasi-steady state at the time scale of seconds. The actual rate of electron transport (J , mol m⁻² s⁻¹) is calculated as:

$$J = \min(J_p, J_{qE}, J_m) = \min(J_{qE}, J_m). \quad (4.46)$$

4.2.1.2.6 Components of non-photochemical quenching

To compare simulations with experimental data, it is necessary to compute the coefficients that are generally reported by fluorimeters. The exact values of fluorescence yields are not important (they are often reported in “arbitrary units”) and the relevant coefficients are always relative indices (Maxwell and Johnson, 2000; Kramer et al., 2004b).

The maximum and minimum fluorescence yields of functional PSII units in the presence of chloroplast movement and qE (F'_{ma} and F'_{oa}) are calculated as:

$$F'_{ma} = \frac{\alpha_r k_f}{k_f + k_D}, \quad (4.47)$$

$$F'_{oa} = \frac{\alpha_r k_f}{k_f + k_D + k_p}, \quad (4.48)$$

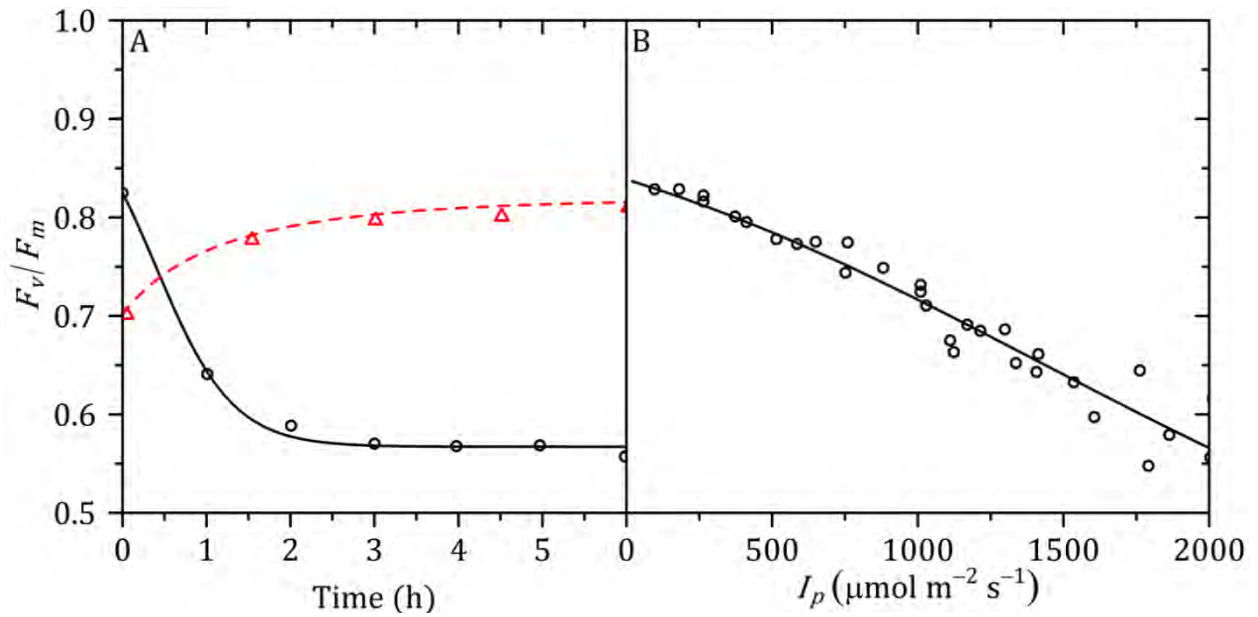


Figure 4.15: Measured (symbols) and predicted (lines) quantum yield of PSII after 30 minutes in darkness as a function of time for constant irradiance (A) or after 1 hour exposure to different irradiance levels of a dark-adapted leaf (B). The time series corresponds to a dark-adapted leaf exposed to $1400 \mu\text{mol m}^{-2} \text{s}^{-1}$ (open circles, solid black line) or a leaf exposed to $70 \mu\text{mol m}^{-2} \text{s}^{-1}$ after 1 hour exposure to $1400 \mu\text{mol m}^{-2} \text{s}^{-1}$ (triangles, dashed red line). Measurements from Kasahara et al. (2002) for *Arabidopsis thaliana* at 25°C . Predictions made with Equations 4.20 – 4.26 and Equations 4.41 – 4.43 with $k_{inh} = 0.36 \text{ m}^2 \text{ mol}^{-1}$, $k_{rep,25} = 1.10 \times 10^{-4} \text{ s}^{-1}$, $k_f = 6.9 \times 10^7 \text{ s}^{-1}$, $k_{D0} = 4.5 \times 10^8 \text{ s}^{-1}$, and $k_{Dinh} = 5.0 \times 10^9 \text{ s}^{-1}$. $R^2 = 1.00$ (A) and 0.94 (B), and $\text{RMSE} = 5.84 \times 10^{-3}$ (A) and 2.01×10^{-2} (B).

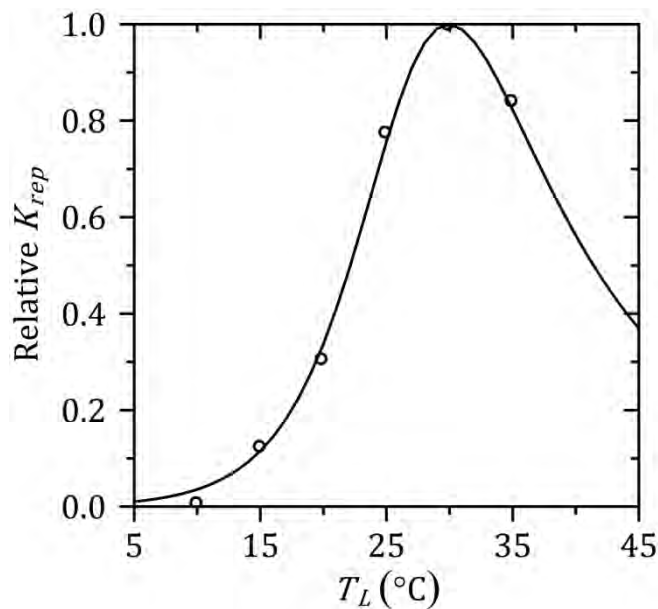


Figure 4.16: Measured (symbols) and predicted (line) values of k_{rep} . Measurements from Greer et al. (1986) for *Phaseolus vulgaris*. Predictions made with Equation 4.43 assuming $H_{a,krep} = 1.61 \times 10^5 \text{ J mol}^{-1}$, $S_{krep} = 780 \text{ J mol}^{-1} \text{ K}^{-1}$ and $H_{d,krep} = 2.33 \times 10^5 \text{ J mol}^{-1}$. $R^2 = 1.00$ and $\text{RMSE} = 1.93 \times 10^{-2}$.

where k_D (s⁻¹) is the rate constant of energy dissipation from excited chlorophyll pigments as heat in the antenna complexes associated with PSII, in the presence of qE (by definition $k_D > k_{D0}$, from Equation 4.23). Knowing that the maximum quantum yield of a functional PSII unit is defined as:

$$\phi_{IIa} = \frac{F_m - F_o}{F_m}, \quad (4.49)$$

where F_m and F_o were defined in Equations 4.23 and 4.24, and further knowing that the maximum quantum yield of a functional PSII unit in the presence of qE is:

$$\phi_{IIa} = \phi_{IIa} - \phi_{qE} = \frac{F'_{ma} - F'_{oa}}{F'_{ma}}, \quad (4.50)$$

the value of k_D can be calculated as:

$$k_D = \frac{k_p}{\phi_{IIa}} - k_f - k_p. \quad (4.51)$$

The maximum fluorescence yield of photoinhibited PSII units in the presence of qE and chloroplast movement is assumed to be:

$$F'_{md} = \alpha_r F_{md} \quad (4.52)$$

And the apparent maximum fluorescence yield of PSII at the leaf level in the presence of photoinhibition, qE and chloroplast movement is:

$$F'_m = (1 - f_{IIa})F'_{ma} + f_{IIa}F'_{md}. \quad (4.53)$$

Finally, the Stern-Volmer NPQ coefficient is defined as:

$$NPQ_{sv} = \frac{F_m}{F'_m} - 1 = \frac{1}{\alpha_r(k_f + k_{D0}) \left(\frac{1 - f_{IIa}}{k_f + k_D} + \frac{f_{IIa}}{k_f + k_{Dinh}} \right)} - 1 \quad (4.54)$$

This equation includes the dependency of NPQ_{sv} on three processes:

1. NPQ_{sv} increases as absorptance decreases, due to chloroplast movement.
2. Photoinhibition contributes positively to NPQ_{sv} due to up-regulation of heat dissipation in photoinhibited PSII units (if $k_{Dinh} > k_D$).
3. NPQ_{sv} increases as ϕ_{qE} increases.

Three additive components are used to quantify the effects of photoinhibition (qI), chloroplast movement (qM) and qE on NPQ_{sv} :

$$qI = \frac{F_m}{(1 - f_{IIa})F_m + f_{IIa}F_{md}} - 1, \quad (4.55)$$

$$qM = NPQ_{sv} - \left(\frac{F_m}{F'_{ma}}, \alpha_r - 1 \right), \quad (4.56)$$

$$qE = NPQ_{sv} - qI - qM. \quad (4.57)$$

qI represents the value of NPQ_{sv} in the absence of qE or chloroplast movement, qM is the additional NPQ_{sv} that is generated due to chloroplast movement (in the presence of photoinhibition and qE), and qE is calculated as the residual NPQ_{sv} in order to ensure that the terms are additive. It is important to emphasize that other indices could be proposed (e.g., qM could be calculated as NPQ_{sv} in the absence of photoinhibition and qE) but these indices do not influence the simulations of the model: they are functions of the outputs of a simulation that can be used to quantify the relative contribution of each process to NPQ_{sv} .

4.2.1.3 Triose phosphate utilisation

The rate of RuBP regeneration limited by triose phosphate utilisation is calculated as (Sharkey, 1985):

$$V_{R,TPU} = \frac{3TPU(2 + 1.5\phi)}{1 - \frac{\phi}{2}}, \quad (4.58)$$

where TPU ($\text{mol m}^{-2} \text{s}^{-1}$) is the maximum rate of triose phosphate utilisation which varies with leaf temperature (Figure 4.17). The sensitivity of TPU to temperature is calculated as proposed by Sharkey et al. (2007):

$$TPU = \frac{TPU_{25} e^{\left(\frac{(T_L - 298.15)H_{a,TPU}}{298.15RT_L}\right)} \left[1 + e^{\left(\frac{298.15S_{TPU} - H_{d,TPU}}{R298.15}\right)} \right]}{1 + e^{\left(\frac{T_L S_{TPU} - H_{d,TPU}}{RT_L}\right)}}, \quad (4.59)$$

where TPU_{25} is the value of TPU at 25 °C (298.15 K), $H_{a,TPU}$ (J mol^{-1}) is an apparent activation energy of TPU , S_{TPU} ($\text{J mol}^{-1} \text{K}^{-1}$) is the apparent entropy coefficient of TPU and $H_{d,TPU}$ (J mol^{-1}) is an apparent deactivation energy of TPU .

4.2.1.4 Enzyme activity in regeneration phase of Calvin cycle

The rate of RuBP synthesis limited by enzyme activity is calculated as:

$$V_{R,E} = \frac{f_R V_{rmax} PGA}{PGA + K_{m,PGA}}, \quad (4.60)$$

where f_R is the activation state of the limiting enzyme in the regeneration phase of the Calvin cycle, V_{rmax} ($\text{mol m}^{-2} \text{s}^{-1}$) is the maximum rate of PGA conversion into RuBP, PGA (mol m^{-2}) is the total amount of stromal PGA per unit of leaf, and $K_{m,PGA}$ is the apparent Michaelis-Menten constant for PGA at the leaf level (mol m^{-2}). In order to derive Equation 4.60, there is no need to assume which specific enzyme is limiting, as long as it is regulated, indirectly, by irradiance. Although experiments with mutants and transformants have revealed a high control coefficient for sedoheptulose-1,7-bisphosphatase (SBPase) in the steady state (Raines, 2003), studies on photosynthetic induction (Sassenrath-Cole and Pearcy, 1994b) have suggested that the limiting steps during light transients could be either fructose-1,6-bisphosphatase (FBPase) or phosphoribulokinase (PRK). Although activation of sedoheptulose-1,7-bisphosphatase is

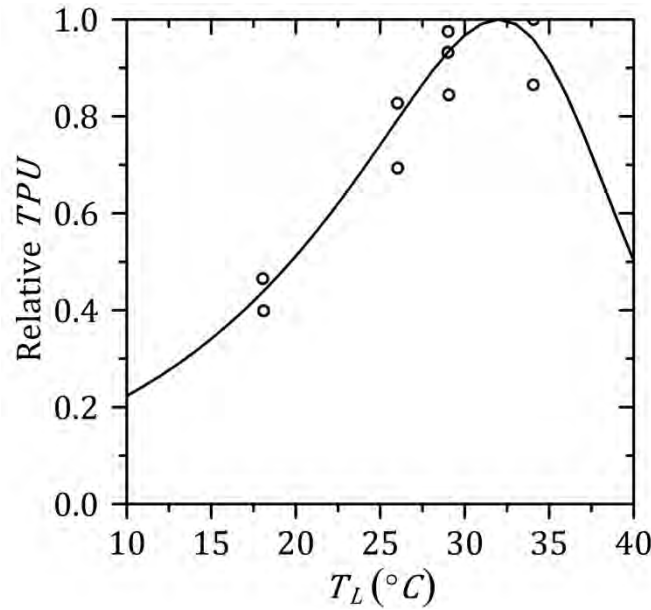


Figure 4.17: Measured (symbols) and predicted (line) values of TPU. Measurements from Harley *et al.* (1992b) for *Gossypium hirsutum*. Predictions made with Equation 4.59 assuming $H_{a,TPU} = 5.75 \times 10^4 \text{ J mol}^{-1}$, $S_{TPU} = 790 \text{ J mol}^{-1} \text{ K}^{-1}$, and $H_{d,TPU} = 2.47 \times 10^5 \text{ J mol}^{-1}$. $R^2 = 0.92$ and $RMSE = 0.06$.

another likely candidate (Percy *et al.*, 1996), no direct experimental evidence exists, as Sassenrath-Cole and Percy (1994b) only measured the activities of FBPase and PRK.

The activity of either of these two enzymes increases with irradiance (Figure 4.18) and the following relationship is assumed:

$$f_{Rss} = f_{R,0} + \frac{\alpha_{f_R} I_P + (1 - f_{R,0}) - \sqrt{(\alpha_{f_R} I_P + (1 - f_{R,0}))^2 - 4\alpha_{f_R} I_P \theta_{f_R} (1 - f_{R,0})}}{2\theta_{f_R}}, \quad (4.61)$$

where $f_{R,0}$ is the minimum fraction of the enzyme that is active in the darkness, α_{f_R} ($\text{mol}^{-1} \text{ m}^2 \text{ s}$) is initial slope of the response of enzyme activity to incident irradiance and θ_{f_R} is the curvature of this response.

The kinetics of changes in enzyme activity follow first-order kinetics, according to published observations (Figure 4.19):

$$\frac{df_R}{dt} = \begin{cases} (f_{Rss} - f_R)k_{iR} & \text{if } f_{Rss} > f_R \\ (f_{Rss} - f_R)k_{dR} & \text{if } f_{Rss} \leq f_R \end{cases}, \quad (4.62)$$

where k_{iR} (s^{-1}) and k_{dR} (s^{-1}) are the rate constants of enzyme activation and deactivation, respectively.

4.2.2 CO₂ diffusion

The $[\text{CO}_2]$ inside the chloroplast is computed assuming a two-compartment resistance-based approach that separates the cytosol (C_{cyt} , mol mol^{-1}) and chloroplast stroma (C_c , mol mol^{-1}). The equations, adapted from the model by Berghuijs *et al.* (2015) are:

$$\frac{dC_{cyt}}{dt} = \frac{[(C_i - C_{cyt})g_w + R_p + R_m - (C_{cyt} - C_c)g_c]T_L R}{V_r P}, \quad (4.63)$$

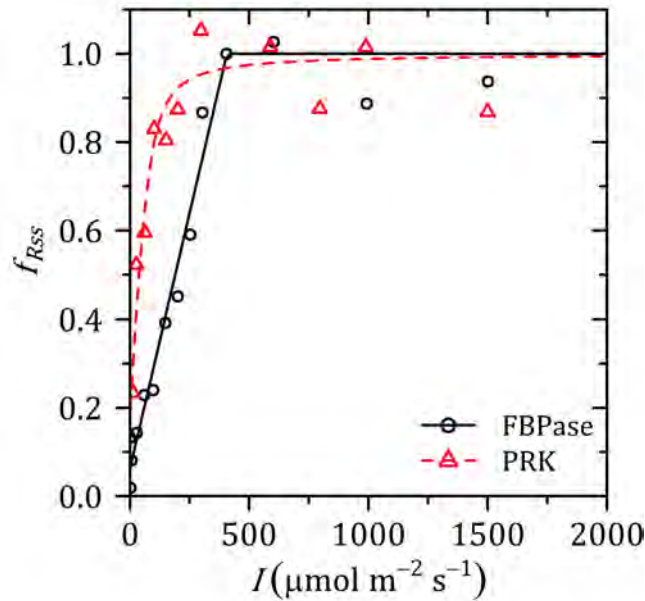


Figure 4.18: Measured (symbols) and predicted (lines) effect of irradiance on the fraction of active FBPase (black solid line, circles) and PRK (red dashed line, triangles). Measurements from Sassenrath-Cole et al. (1994) for Glycine max. Predictions made using Equation 4.61 assuming for FBPase, $\alpha_{f_R} = 2.31 \times 10^3 \text{ mol}^{-1} \text{ m}^2 \text{ s}$, $\theta_{f_R} = 1.00$ and $f_{R,0} = 0.06$, and for PRK, $\alpha_{f_R} = 8.64 \times 10^3 \text{ mol}^{-1} \text{ m}^2 \text{ s}$, $\theta_{f_R} = 0.85$ and $f_{R,0} = 0.20$. $R^2 = 0.97$ (FBPase) and 0.86 (PRK), and $RMSE = 0.07$ (FBPase) and $= 0.09$ (PRK).

$$\frac{dC_c}{dt} = \frac{[(C_{cyt} - C_c)g_c - V_c]T_L R}{V_r P}, \quad (4.64)$$

where g_w ($\text{mol m}^{-2} \text{ s}^{-1}$) and g_c ($\text{mol m}^{-2} \text{ s}^{-1}$) are the wall and chloroplast conductances to fluxes of CO_2 , respectively, R_m ($\text{mol m}^{-2} \text{ s}^{-1}$) and R_p ($\text{mol m}^{-2} \text{ s}^{-1}$) are the rates of CO_2 released from the mitochondria due to respiration and photorespiration, respectively, C_i and C_{cyt} (mol mol^{-1}) represent $[\text{CO}_2]$ in the intercellular spaces and cytosol, respectively, P is the pressure of the air ($1.01 \times 10^5 \text{ Pa}$), and V_r is the leaf volume per unit of surface (i.e., leaf thickness). The term g_w includes diffusion of CO_2 through the cell wall and membrane, and part of the cytosol diffusion pathway, whereas g_c includes the remainder of the cytosol diffusion pathway, the envelope of the chloroplast and diffusion through stroma into the catalytic sites of Rubisco (Berghuijs et al., 2015). R_m is assumed to increase with temperature (Figure 4.20) and the Arrhenius law is used

$$R_m = R_{m,25} e^{\left(\frac{(T_L - 298.15)H_{a,Rm}}{298.15RT_L}\right)}, \quad (4.65)$$

where $R_{m,25}$ ($\text{mol m}^{-2} \text{ s}^{-1}$) is the rate of mitochondrial respiration and $H_{a,Rm}$ (J mol^{-1}) is an apparent activation energy of R_m . Although experimental evidence indicates that mitochondrial respiration is partially inhibited in the light (Kromer, 1995; Yin et al., 2011), the absolute changes that have been estimated using various methods and C3 species are small ($< 1 \text{ } \mu\text{mol m}^{-2} \text{ s}^{-1}$) compared to typical rates of CO_2 assimilation in C3 species (Yin et al., 2011). Therefore, R_m was assumed to be independent of irradiance.

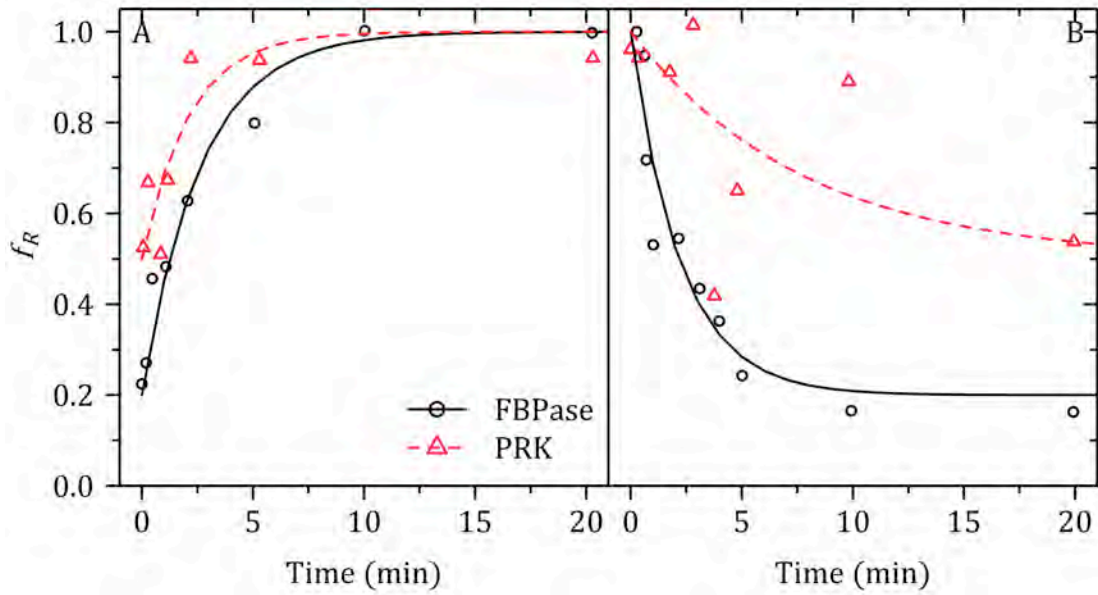


Figure 4.19: Measured (symbols) and predicted (lines) dynamics of the fraction of active FBPase (black solid line, circles) and PRK (red dashed line, triangles) after a stepwise increase in irradiance (A, $35 \mu\text{mol m}^{-2} \text{s}^{-1} - 1500 \mu\text{mol m}^{-2} \text{s}^{-1}$), and a stepwise decrease in irradiance (B, $1500 \mu\text{mol m}^{-2} \text{s}^{-1} - 35 \mu\text{mol m}^{-2} \text{s}^{-1}$). Measurements from Sassenrath-Cole and Percy (1994b) for Glycine max. Predictions made with Equation 4.62 assuming for FBPase $k_{iR} = 6.28 \times 10^{-3} \text{ s}^{-1}$ and $k_{dR} = 7.50 \times 10^{-3} \text{ s}^{-1}$, and for PRK $k_{iR} = 7.88 \times 10^{-3} \text{ s}^{-1}$ and $k_{dR} = 2.16 \times 10^{-3} \text{ s}^{-1}$. $R^2 = 0.96$ (FBPase, A), 0.91 (FBPase, B), 0.81 (PRK, A) and 0.35 (PRK, B), and RMSE = 0.06 (FBPase, A), 0.09 (FBPase, B), 0.09 (PRK, A) and 0.36 (PRK, B).

After a transition from light to darkness, the amounts of glycine in leaves decrease following first-order kinetics (Figure 4.21). Thus, the effect of photorespiration on dynamic CO₂ assimilation is modelled using a first-order approximation (Percy et al. (1997):

$$R_p = \frac{k_{PR}PR}{2}, \quad (4.66)$$

where PR (mol m^{-2}) represents the pool of photorespiration intermediates between phosphoglycolate and glycine, and k_{PR} (s^{-1}) is the apparent rate constant at which these photorespiration intermediates are consumed (dependent on the activity of glycine decarboxylase). A low value of k_{PR} introduces a delay between oxygenation of RuBP and the release of CO₂ from glycine decarboxylase. This delay will affect the net flux of CO₂ into the chloroplasts (Kaiser et al., 2015). Changes in PR are derived from mass balance as:

$$\frac{dPR}{dt} = V_C\phi - k_{PR}PR. \quad (4.67)$$

Changes in intercellular [CO₂] (C_i , mol mol^{-1}) are computed as:

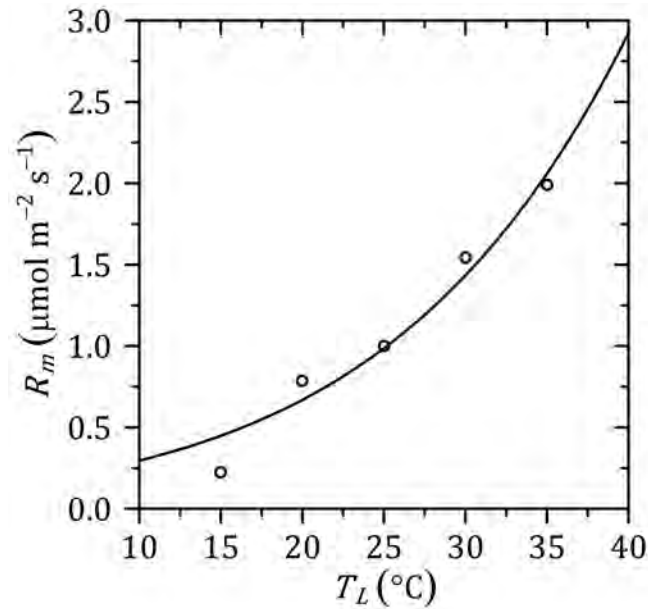


Figure 4.20: Measured (symbols) and predicted (lines) values of R_m . Measurements from Walker et al. (2013) for *Arabidopsis thaliana*. Predictions made with Equation 4.65 assuming $R_{m,25} = 9.9 \times 10^{-7} \text{ mol m}^{-2} \text{ s}^{-1}$ and $H_{a,Rm} = 5.62 \times 10^4 \text{ J mol}^{-1}$. $R^2 = 0.95$ and $RMSE = 1.4 \times 10^{-7} \text{ mol m}^{-2} \text{ s}^{-1}$.

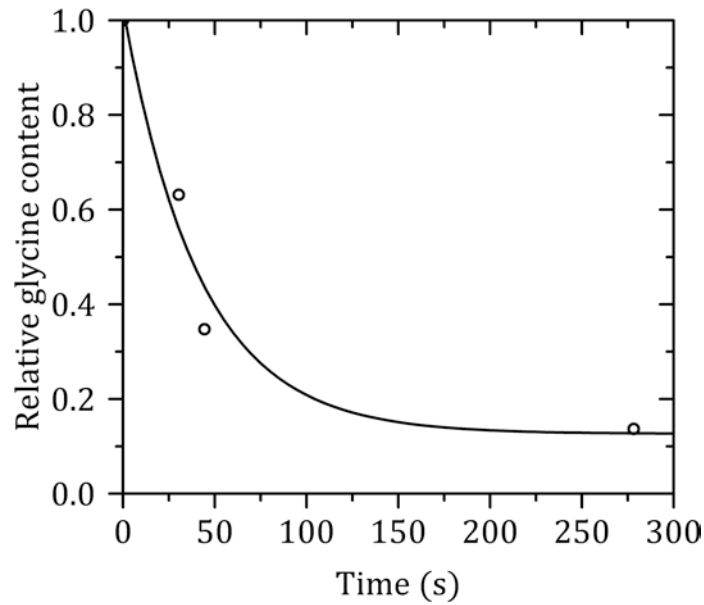


Figure 4.21: Measured (symbols) and predicted (line) relative leaf glycine content of a light-adapted leaf after a transition to darkness. Measurements from Rawsthorne and Hylton (1991) for *Moricandia moricandioides*. Prediction made with Equation 4.66 assuming $k_{PR} = 0.024 \text{ s}^{-1}$. $R^2 = 0.96$ and $RMSE = 6.73 \times 10^{-2}$.

$$\frac{dC_i}{dt} = \frac{\left[\frac{C_a - C_i}{\frac{1}{g_{sc}} + \frac{1}{g_{bc}}} - (C_i - C_{cyt})g_w \right] T_L R}{V_r P}, \quad (4.68)$$

where g_{sc} ($\text{mol m}^{-2} \text{ s}^{-1}$) and g_{bc} ($\text{mol m}^{-2} \text{ s}^{-1}$) are the stomatal and boundary layer conductances to fluxes of CO_2 , respectively, and C_a (mol mol^{-1}) represents air $[\text{CO}_2]$.

Finally, the net rate of CO₂ assimilation (A , mol m⁻² s⁻¹) is defined as the net flux of CO₂ that enters the leaf according to Ohm's law:

$$A = \frac{C_a - C_i}{\frac{1}{g_{sc}} + \frac{1}{g_{bc}}} \quad (4.69)$$

4.2.2.1 Boundary layer conductance

The boundary layer conductance for heat transfer (g_{bH} , m s⁻¹) is calculated as (Monteith and Unsworth, 2013):

$$g_{bH} = 2 \frac{Nu \cdot \kappa}{d}, \quad (4.70)$$

where Nu is the Nusselt number, κ is the thermal diffusivity of dry air (2.0×10^{-5} m² s⁻¹) and d (m) is the characteristic length of the surface, in this case, the shortest distance between opposite borders of a leaf (usually leaf width). The coefficient 2 is required, because heat transfer occurs through both sides of the leaf (Leuning et al., 1995). The value of Nu depends on whether the exchange of heat with the air occurs via forced or free convection (Monteith and Unsworth, 2013). Heat transfer due to forced convection occurs through a boundary layer in the presence of a moving fluid and the rate of transfer is dependent on the velocity of the fluid. Heat transfer under free convection depends on the upward movement of warm air in the atmosphere due to the temperature dependency of air density. Under forced convection conditions, Nu is calculated as (Monteith and Unsworth, 2013):

$$Nu_{forced} = A Re^n, \quad (4.71)$$

where $A = 0.60$ and $n = 0.5$ are empirical coefficients and Re is the Reynolds number. Re is calculated as

$$Re = \frac{\omega d}{\nu}, \quad (4.72)$$

where ω (m s⁻¹) is wind velocity and ν (1.5×10^{-5} m² s⁻¹) is the kinematic viscosity of the air. Under free convection conditions, Nu is calculated as (Monteith and Unsworth, 2013)

$$Nu_{free} = B Gr^m, \quad (4.73)$$

where $B = 0.5$ and $m = 0.25$ are empirical coefficients and Gr is the Grashof number, calculated as (Monteith and Unsworth, 2013):

$$Gr = C d^3 (T_L - T_a), \quad (4.74)$$

where $C = 1.57 \times 10^8$ K⁻¹ m⁻³ is an empirical coefficient and T_a (K) is the air temperature.

Both free and forced convection occur around a leaf and their relative importance depends on the wind velocity and the difference between leaf and air temperature. Under such conditions, the total value of Nu may be approximated as (Leuning et al., 1995):

$$Nu = Nu_{free} + Nu_{forced}. \quad (4.75)$$

Wind velocity has a larger effect on the boundary layer conductance than the temperature difference between leaf and air, but omitting free convection from the calculations could result in underestimations of g_{bH} for leaves in the bottom of the canopy exposed to sunflecks (Leuning et al., 1995). The boundary layer conductance to fluxes of CO₂ (g_{bc} , mol m⁻² s⁻¹) and H₂O (g_{bw} , m s⁻¹) are proportional to g_{bH} (Farquhar and Sharkey, 1982; Leuning et al., 1995):

$$g_{bw} = \frac{g_{bH}}{f_h 0.93}, \quad (4.76)$$

$$g_{bc} = \frac{g_{bw}}{f_h 1.37 V_m}, \quad (4.77)$$

where V_m (m³ mol⁻¹) is the volume per mol of air at ambient temperature, calculated as $V_m = RT_a/P$, and $f_h = 1$ for amphistomatous leaves (i.e., stomatal pores on both sides of the leaf), or $f_h = 2$ for hypostomatous leaves (i.e., stomatal pores only on one side of the leaf).

4.2.2.2 Stomatal conductance

Most published models of steady-state stomatal conductance are based on the work by Ball et al. (1987), who assumed that stomatal conductance was linearly proportional to CO₂ assimilation and the slope was modulated by environmental factors such as CO₂ or humidity. However, several experiments on genetically transformed plants showed that this correlation is not causal, as reductions of CO₂ assimilation by transforming the Calvin cycle did not affect stomatal conductance (Lawson et al., 2011) Furthermore, the exact nature of the metabolic regulation of stomatal conductance is still unclear (Lawson et al., 2014). Thus, an empirical approach that captures the response of stomatal conductance to environmental conditions is used. When exposed to a rapid change in irradiance, the temporal evolution of stomatal conductance follows a sigmoidal pattern (Figure 4.22). The empirical model of Vialet-Chabrand et al. (2013) was used to reproduce the dynamics of stomatal conductance to fluxes of water vapour (g_{sw} , mol m⁻² s⁻¹) when exposed to changes in environmental conditions:

$$\frac{dg_{sw}}{dt} = k_{gs}(g_{sw} - r_0 f_{VPDL}) \ln \left(\frac{g_{sw,ss} - r_0 f_{VPDL}}{g_{sw} - r_0 f_{VPDL}} \right), \quad (4.78)$$

where $g_{sw,ss}$ (mol m⁻² s⁻¹) is the steady-state value of g_{sw} calculated as a function of environmental variables, k_{gs} (s⁻¹), is a rate constant and r_0 (mol m⁻² s⁻¹) is an empirical parameter that affects the sigmoidicity of g_{sw} transients. Equation 4.78 predicts that, after a rapid change in irradiance, the initial rates of change of stomatal conductance are higher for higher initial values of g_{sw} , for both increases and decreases in irradiance. Equation 4.78 was modified with respect to the original to take into account the effect of VPD as r_0 should always be lower than $g_{sw,ss}$. Due to the differences between the diffusivities of CO₂ and water vapour through air (Farquhar and Sharkey, 1982), $g_{sc} = g_{sw}/1.6$. A multiplicative model that captures the effects of most relevant environmental conditions is used to calculate $g_{sw,ss}$:

$$g_{sw,ss} = g_{swm} f_I f_{VPDL}, \quad (4.79)$$

where g_{swm} ($\text{mol m}^{-2} \text{s}^{-1}$) is the maximum value of g_{sw} , and f_l and f_{VPD_L} are empirical factors that capture the relative effect of irradiance and leaf-to-air vapour pressure difference (VPD_L) on $g_{sw,ss}$, respectively. The effect of irradiance on $g_{sw,ss}$ can be described by a hyperbolic relationship (Figure 4.23A):

$$f_l = f_{l,0} + \frac{1 - f_{l,0} + \alpha_{f_l} I_P - \sqrt{(1 - f_{l,0} + \alpha_{f_l} I_P)^2 - 4\theta_{f_l} \alpha_{f_l} I_P (1 - f_{l,0})}}{2\theta_{f_l}}, \quad (4.80)$$

where $f_{l,0}$ is the minimum value of f_l , α_{f_l} ($\text{mol}^{-1} \text{m}^2 \text{s}$) is the initial slope, and θ_{f_l} is a parameter describing the curvature of the relationship.

The relative effect of VPD on $g_{sw,ss}$ can be described by a hyperbolic relationship (Figure 4.23), such as the one proposed by Lohammar et al. (1980):

$$f_{VPD_L} = \frac{1}{1 + VPD_L/D_0}, \quad (4.81)$$

where D_0 (Pa) is the value of VPD_L at which $f_{VPD_L} = 0.5$. VPD_L , defined as:

$$VPD_L = e_{s,L} - e_a, \quad (4.82)$$

where $e_{s,L}$ (Pa) is the saturating partial pressure of water vapour at the leaf temperature and e_a (Pa) is the partial pressure of water vapour in the air. The value of $e_{s,L}$ increases with leaf temperature as described by the following empirical expression (Murray, 1967)

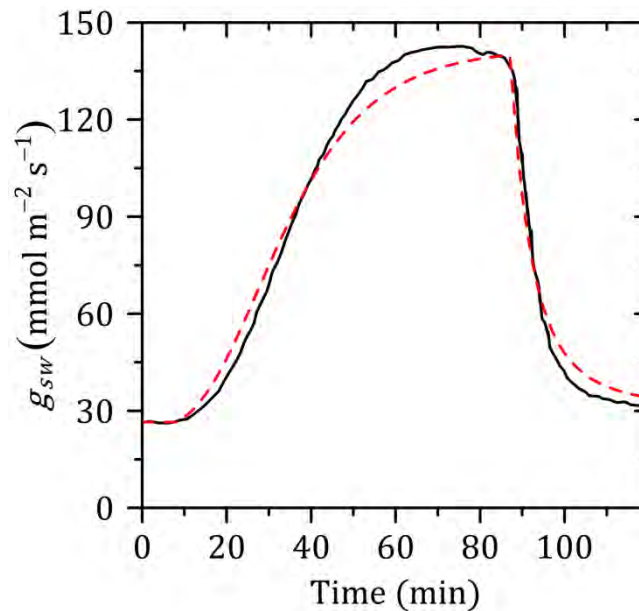


Figure 4.22: Measured (black, solid line) and predicted (red, dashed line) dynamics of stomatal conductance to fluxes of water vapour for a light transient from darkness to $130 \mu\text{mol m}^{-2} \text{s}^{-1}$ followed by a return to darkness. Measurements from De Angeli et al. (2013) for *Arabidopsis thaliana*. Predictions made with Equation 4.78 assuming $k_{gs} = 1.14 \cdot 10^{-3} \text{s}^{-1}$, $r_0 = 2.36 \cdot 10^{-2} \text{mol m}^{-2} \text{s}^{-1}$. Values for $g_{sw,ss}$ were calculated directly from the data. $R^2 = 0.97$ and $\text{RMSE} = 6.36 \text{mmol m}^{-2} \text{s}^{-1}$.

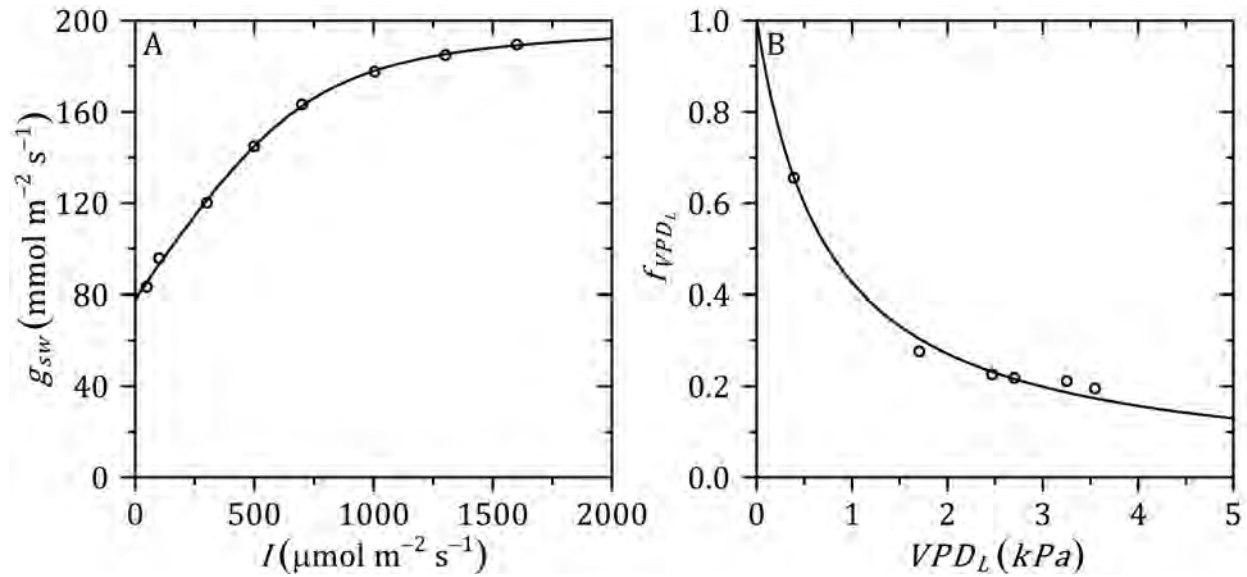


Figure 4.23: A. Measured (symbols) and predicted (line) steady-state stomatal conductance (g_{sw}) as a function of irradiance. Measurements from Matrosova et al. (2015) for *Arabidopsis thaliana* at a leaf-to-air vapour pressure deficit (VPD_L) of 1.0 kPa. Predictions made with Equations 4.79 and 4.80 assuming $g_{swm} = 0.48 \text{ mol m}^{-2} \text{ s}^{-1}$, $f_{l,0} = 0.39$, $\alpha_{f_1} = 7.67 \times 10^2 \text{ mol}^{-1} \text{ m}^2 \text{ s}$ and $\theta_{f_1} = 0.88$. $R^2 = 1.00$ and $RMSE = 1.41 \text{ mmol m}^{-2} \text{ s}^{-1}$. B. Measured (symbols) and predicted (line) relative, steady-state stomatal conductance as a function of VPD_L . Measurements from Dai et al. (1992) for *Nicotiana tabacum*. Predictions made with Equation 4.81 assuming $D_0 = 740 \text{ Pa}$. $R^2 = 0.99$ and $RMSE = 0.02$.

$$e_{s,L} = 0.61 e^{\frac{17.27(T_L - 273.15)}{237.15 + (T_L - 273.15)}} \quad (4.83)$$

4.2.2.3 Mesophyll conductance

In leaves of *A. thaliana*, chloroplast movements decrease the area of chloroplast surface per unit of leaf area that is exposed to intercellular spaces (S_c) which leads to a decrease in apparent mesophyll conductance (Tholen et al., 2008). Assuming that changes in S_c are proportional to changes in absorptance due to chloroplast movement, the following linear relationship between S_c and α_r is proposed:

$$S_c = S_{cm} f_{\alpha Sc} \alpha_r, \quad (4.84)$$

where S_{cm} is the value of S_c for dark-adapted leaves and $f_{\alpha Sc}$ is the proportionality coefficient between changes in α_r and S_c . Tholen et al. (2008) only measured S_c at two chloroplast positions, so only a linear relationship can be assumed. From the equations by Berghuijs et al. (2015) it can be deduced that changes in S_c result in proportional changes in g_c :

$$g_c = \frac{g_{cm} S_c}{S_m}, \quad (4.85)$$

where S_m is the area of mesophyll surface per unit of leaf area exposed to intercellular spaces and g_{cm} ($\text{mol m}^{-2} \text{ s}^{-1}$) is the maximum chloroplast conductance for $S_c/S_m = 1$. The apparent mesophyll conductance varies with leaf temperature (Figure 4.24), although there are important variations across species (von Caemmerer and Evans, 2015). The temperature dependency of the chloroplast and wall conductances depend

on the temperature dependency of CO₂ diffusion through the liquid phases of cytosol and stroma and across the cellular and chloroplast membranes. This would predict the existence of an optimal temperature (Evans and Von Caemmerer, 2013). The following equations suffice to reproduce the different observed patterns:

$$g_{cm} = \frac{g_{cm,25} e^{\left(\frac{(T_L - 298.15)H_{a,gc}}{298.15RT_L}\right)} \left[1 + e^{\left(\frac{298.15S_{gc} - H_{d,gc}}{298.15R}\right)} \right]}{1 + e^{\left(\frac{T_L S_{gc} - H_{d,gc}}{RT_L}\right)}}, \quad (4.86)$$

$$g_w = \frac{g_{w,25} e^{\left(\frac{(T_L - 298.15)H_{a,gw}}{298.15RT_L}\right)} \left[1 + e^{\left(\frac{298.15S_{gw} - H_{d,gw}}{298.15R}\right)} \right]}{1 + e^{\left(\frac{T_L S_{gw} - H_{d,gw}}{RT_L}\right)}}, \quad (4.87)$$

where $g_{cm,25}$ and $g_{w,25}$ are the values of g_{cm} and g_w at 25 °C (298.15 K), $H_{a,gc}$ and $H_{a,gw}$ (J mol⁻¹) are apparent activation energies of g_{cm} and g_w , S_{gc} and S_{gw} (J mol⁻¹ K⁻¹) are the apparent entropy coefficients of g_{cm} and g_w , and $H_{d,gc}$ and $H_{d,gw}$ (J mol⁻¹) are apparent deactivation energies of g_{cm} and g_w . For simplification, and due to the lack of available data, the same temperature dependency for g_{cm} and g_w is assumed.

4.2.3 Leaf energy balance

The temperature of a leaf is determined by the balance between net radiation absorbed by the leaf (R_n , W m⁻²), the exchange of energy with the environment as sensible heat (H , W m⁻²) and latent heat (L , W m⁻²), and the heat capacity of the leaf (σ_L , J m⁻² K⁻¹):

$$\frac{dT_L}{dt} = \frac{R_n - H - L}{\sigma_L}. \quad (4.88)$$

The net radiation absorbed by a leaf is calculated as (Monteith and Unsworth, 2013):

$$R_n = \alpha_u I_u + \frac{\alpha_b I_b}{E_b} + \frac{\alpha_g I_g}{E_g} + \frac{\alpha_r I_r}{E_r} + \alpha_n I_n + 2\epsilon\sigma_B(T_a^4 - T_L^4), \quad (4.89)$$

where α_u , α_b , α_g , α_r , and α_n are the fractions of irradiance absorbed by a leaf in the UV-A (320 – 400 nm), blue (400 – 500 nm), green (500 – 600 nm), red (600 – 700 nm) and near infrared (NIR, 700 – 2500 nm) wavebands, respectively. I_u (W m⁻²), I_b (mol m⁻² s⁻¹), I_g (mol m⁻² s⁻¹), I_r (mol m⁻² s⁻¹) and I_n (W m⁻²) are the irradiances in the UV-A, blue, green, red and NIR wavebands, respectively, E_b , E_g and E_r (J mol⁻¹) are the energies of a μmol of photons in the blue, green or red wavebands, respectively, $\epsilon = 0.95$ is the emissivity of a leaf for the thermal waveband (i.e. 3 – 10 μm), and $\sigma_B = 5.67 \times 10^{-8}$ W m⁻² K⁻⁴ is the Stefan-Boltzmann constant. The flux of sensible heat exchanged between leaf and environment is defined as (Monteith and Unsworth, 2013):

$$H = \rho_a c_p g_{bH} (T_L - T_a), \quad (4.90)$$

where ρ_a (1.2 × 10³ g m⁻³) is the air density and c_p (1.1 J g⁻¹ K⁻¹) is the specific heat capacity of the air. Latent heat refers to the energy lost from the leaf due to water evaporation via transpiration (Tr , mol m⁻² s⁻¹). It is proportional to the latent heat of vaporization ($\lambda = 4.4 \times 10^4$ J mol⁻¹):

$$L = \lambda Tr. \quad (4.91)$$

Transpiration is calculated as (Farquhar and Sharkey, 1982):

$$Tr = \frac{VPD_L}{\left(P - \frac{(e_{s,L} + e_a)}{2}\right) \left(\frac{1}{g_{sw}} + \frac{1}{g_{bw}}\right)}. \quad (4.92)$$

4.2.4 Irradiance and leaf optical properties

4.2.4.1 Spectral composition of solar radiation

The fractions of energy or photons associated to the different components depend on the light source. In solar irradiance, it also depends on the atmospheric conditions and whether it is direct or diffuse (Bird and Riordan, 1986). The absorptance of a leaf in each waveband (i.e. α_u , α_b , α_g , α_r and α_n) will depend on the spectral distribution of leaf absorptance and irradiance for each waveband. The simulations in this study emulate either solar irradiance or an artificial LED light source with 10% blue and 90% red (proportion of photons). Here, the fractions of irradiance in each waveband and for each light source are calculated.

A reference spectrum for direct and diffuse solar irradiance was generated with the model of Bird and Riordan (1986). The calculations were performed with the Excel implementation of the model (<http://rredc.nrel.gov/solar/models/spectral/>) for solar noon on June 21th in The Netherlands under clear-sky conditions (Figure 4.25). The separation between direct and diffuse irradiance is important, because Rayleigh scattering in the atmosphere is wavelength-dependent, so that diffuse irradiance has a higher fraction of blue and less of NIR. The normalized spectral photon distribution (NSPD) is different from the normalized spectral power distribution (not shown) because the energy per photon is also wavelength dependent as described by the Planck-Einstein relation.

By integrating over the NSPD, it was calculated that 56% of the direct solar irradiance (expressed as power per unit of area, $W m^{-2}$) is in the form NIR, but only 27% for diffuse solar irradiance (Table 4.1). Since diffuse solar irradiance accounted for 24% of total solar irradiance, this resulted in 50% of total solar irradiance being in the form of NIR, which is in agreement with experimental observations (Szeicz, 1974). The fraction of solar irradiance in the UV-A range was 5%, but differed strongly between direct and diffuse components (Table 4.1). Finally, 45% of the total solar irradiance was in the form of photosynthetically active radiation (PAR; 400–700 nm). Whereas the leaf energy balance requires irradiance to be expressed as power per unit of area (Equation 4.89), calculations of CO_2 assimilation require a flux of photons as input (Equation 4.19) and the conversion is performed using the Planck-Einstein relation. The energy per μmol of photons for each waveband was calculated taking into account the spectral distribution, resulting in similar values for direct and diffuse solar irradiance (Table 4.2).

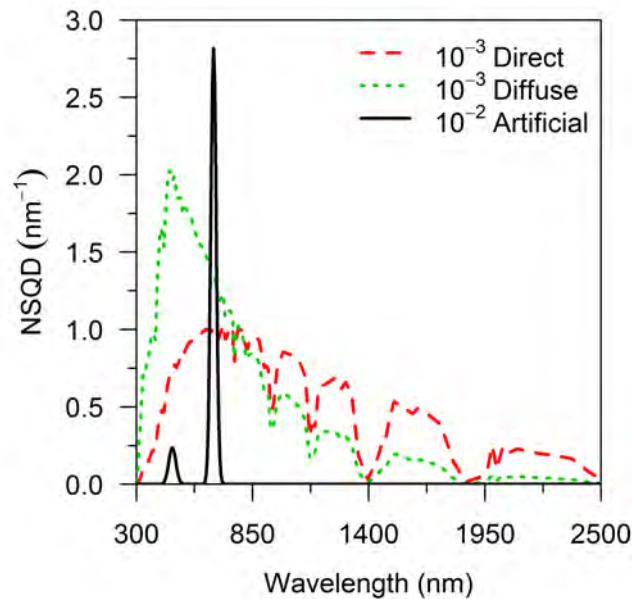


Figure 4.24: Normalized spectral quanta distribution (NSQD) of direct and diffuse solar irradiance generated with the model of Bird and Riordan (1986) and for an artificial LED light source with 10% blue and 90% red (proportion of photons). The distributions for solar radiation have been amplified by a factor of 1000 and the distribution for the artificial light source has been amplified by a factor of 100.

4.2.4.2 Optical properties of leaves

The fraction of irradiance absorbed by a leaf varies with wavelength and the spectrum depends on pigment content and composition as well as leaf water content. In a typical green leaf, chlorophyll pigments absorb mostly blue and red irradiance (and, to a small degree, also UV and infrared), carotenoids absorb blue and green irradiance, whereas phenolic compounds and extra-thylakoid carotenoids absorb from UV-B to green irradiance (Solovchenko, 2010). Absorbance of NIR is mostly due to leaf water content (Jacquemoud and Ustin, 2001). Using measurements of transmittance and reflectance in the PAR region for *A. thaliana* (de Wit et al., 2012), measurements of the same properties for poplar in the NIR region (Jacquemoud and Ustin, 2001) and for different leaves in UV-A region (McCree, 1972), a reference spectrum of optical properties for fresh green leaves (Figure 4.26) was constructed.

By integrating the spectral distribution of leaf optical properties weighted by the spectral distribution of solar radiation, the fractions of irradiance within each waveband that are reflected, transmitted and absorbed by the leaf were obtained (Table 4.3). Differences in transmittance, reflectance and absorbance for direct and diffuse irradiance were always below 0.5% for PAR and UV-A wavebands, and between 1% and 3.4% for NIR (results not shown). Differences between weighting absorbance by the spectral distribution of photons or power were below 0.5% except for NIR (but in that case, only the power spectrum is relevant). The absorbance of PAR was 81% in direct and diffuse solar irradiance and 85% for the artificial light source.

Across 22 species, McCree (1972) observed that the relative low-light quantum yield of CO₂ assimilation at different wavelengths, even when corrected for the absorbance spectra, was lower for the green and blue wavebands compared to red (Figure 4.27).

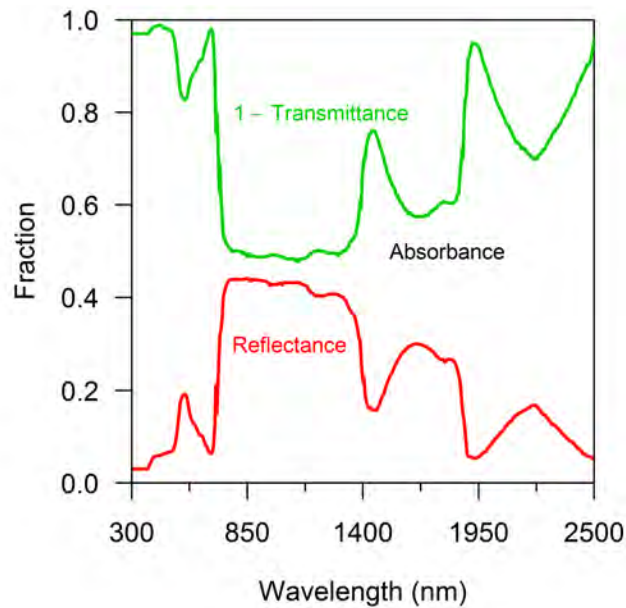


Figure 4.25: Optical properties of a typical green leaf. Reconstructed from several sources (see text for details). The area between the two curves represents the spectral distribution of absorbance.

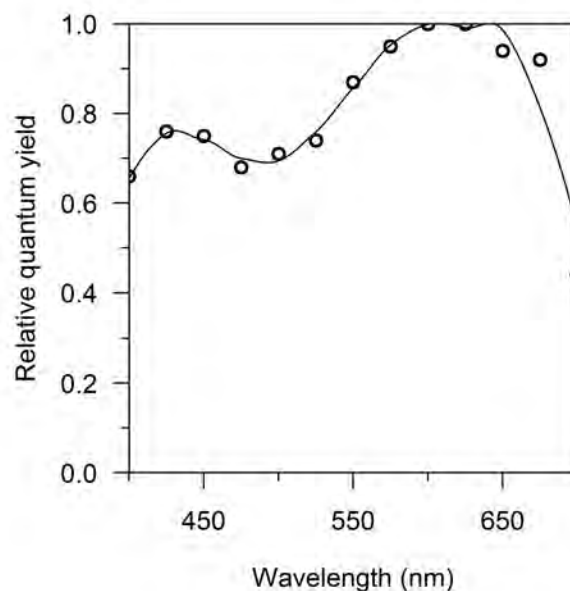


Figure 4.26: Average spectrum of the relative low-light quantum yield of photosynthesis from 22 species. The continuous line is the result of fitting a local polynomial regression to the measurements. Measurements from McCree (1972).

This decrease in efficiency can be caused by (i) absorbance from non-photosynthetic pigments, (ii) low efficiency of transfer from accessory carotenoids to chlorophylls, or (iii) imbalances in the excitation of PSII and PSI due to the different pigment composition of the associated antenna complexes (Terashima et al., 2009; Hogewoning et al., 2012; Laisk et al., 2014). Accounting for imbalances in the excitation of PSI and PSII is beyond the scope of this study, but the effects of non-photosynthetic pigments and limited efficiency in energy transfer from carotenoids can be incorporated by defining fractions of absorbed irradiance that become available for photosynthesis for each wavelength. To obtain these fractions, the relative quantum yield distribution

Table 4.1: Fraction of direct and diffuse solar irradiance and artificial light (10% blue, 90% red, proportion of photons) associated with each waveband. For direct and diffuse solar radiation, the values inside parentheses correspond to the integration of the normalized spectral photon distribution, whereas the main values correspond to integration of the normalized spectral power distribution. For the artificial light source, all values correspond to the normalized spectral photon distribution. UV-A = 320 – 400 nm, Blue = 400 – 500 nm, Green = 500 – 600 nm, Red = 600 – 700 nm, PAR = 400 – 700 nm, NIR = 700 nm – 2500 nm.

	Waveband					
	UV-A	Blue	Green	Red	PAR	NIR
Direct	0.03 (0.01)	0.12 (0.06)	0.16 (0.09)	0.13 (0.09)	0.40 (0.25)	0.56 (0.74)
Diffuse	0.13 (0.07)	0.25 (0.18)	0.22 (0.19)	0.13 (0.13)	0.60 (0.50)	0.27 (0.43)
Artificial	0.0	0.10	0.0	0.90	-	0.0

Table 4.2: Energy per μmol of photons ($\text{J } \mu\text{mol}^{-1}$) for different wavebands of direct and diffuse solar radiation and artificial light source with 10% blue and 90% red light. UV-A = 320 – 400 nm, Blue = 400 – 500 nm, Green = 500 – 600 nm, Red = 600 – 700 nm, PAR = 400 – 700 nm, NIR = 700 nm – 2500 nm.

	Waveband					
	UV-A	Blue	Green	Red	PAR	NIR
Direct	0.327	0.263	0.217	0.184	0.216	0.105
Diffuse	0.332	0.265	0.219	0.185	0.226	0.122
Artificial	0.000	0.256	0.000	0.180	0.187	0.000

Table 4.3: Optical properties of a leaf based on spectral distribution of transmittance, reflection and absorptance at different wavebands of the solar spectrum and for an artificial light with 10% blue and 90% red light (proportion of photons). Values are weighted by the normalized spectral power distribution of direct solar radiation and by the normalized spectral quanta distribution of artificial light. UV-A = 320 – 400 nm, Blue = 400 – 500 nm, Green = 500 – 600 nm, Red = 600 – 700 nm, PAR = 400 – 700 nm, NIR = 700 nm – 2500 nm.

	Solar spectrum						Artificial light
	UV-A	Blue	Green	Red	NIR	PAR	
Transmittance	0.03	0.02	0.13	0.07	0.45	0.08	0.04
Reflectance	0.03	0.06	0.15	0.09	0.37	0.11	0.07
Absorptance	0.94	0.92	0.72	0.83	0.18	0.81	0.89

Table 4.4: Fraction of absorbed and incident irradiance available for photosynthesis (see text for details) at different wavebands of the solar spectrum and for an artificial light source with 10% blue and 90% red light (proportion of photons). Values are weighted by the normalized spectral power distribution of direct solar irradiance and by the normalized spectral quanta distribution of artificial light, as well as the absorptance spectrum of the leaf. UV-A = 320 – 400 nm, Blue = 400 – 500 nm, Green = 500 – 600 nm, Red = 600 – 700 nm, PAR = 400 – 700 nm, NIR = 700 nm – 2500 nm.

	Solar spectrum						Artificial Light
	UV-A	Blue	Green	Red	PAR	NIR	
Reference							
Absorbed	0.0	0.72	0.85	0.95	0.86	0.0	0.91
Incident	0.0	0.66	0.60	0.80	0.73	0.0	0.80

(Figure 4.27) weighted by the spectrum of absorbed irradiance was integrated per waveband. These calculations indicated that 28% of the absorbed blue irradiance is not used for photosynthesis (Table 4.4), similar to the 30% estimated by Laisk et al. (2014), whereas losses for green and red irradiance amount to 12% and 5%, respectively. This means that the fraction of incident PAR that is available for photosynthesis is 73% and 72% for direct and diffuse irradiance, respectively, and becomes 80% for the artificial light source.

4.2.5 Open gas exchange systems

Measurements of CO₂ assimilation and stomatal conductance are often performed with open gas exchange systems (Farquhar and Sharkey, 1982). In an open gas exchange system, inflow of air with known properties is modified inside a leaf cuvette by exchange of gases and energy with the leaf surface. Because the cuvette has a non-negligible volume, changes in the properties of the outflow are delayed with respect to changes in fluxes of gas and energy through the leaf surface. This mixing time introduces artefacts into measurements of the dynamics of CO₂ assimilation and stomatal conductance.

In order to account for these artefacts, equations are included to simulate the mixing of the air inside the cuvette, based on Farquhar and Sharkey (1982). Given an air flow (F_L , mol s⁻¹) that enters the cuvette with a known [CO₂] (C_r , mol mol⁻¹), the [CO₂] of the air leaving the cuvette can be calculated from the expression:

$$\frac{dC_s}{dt} = \frac{-(F_L + s_L T_r)C_s + F_L C_r + s_L A}{V_{ch} P} RT_a, \quad (4.93)$$

where s_L (m²) is the leaf surface in the cuvette, T_r (mol m⁻² s⁻¹) is the transpiration flux and V_{ch} (m³) is the volume of the chamber where the air is mixed. V_{ch} is an effective volume that may include tubing and volume of IRGA chambers, and should be calculated or obtained from the manufacturer. Equation 4.93 relies on the assumption that the air within the system is well-mixed. Similarly, the water vapour mole fraction of the air leaving the cuvette (ω_s , mol mol⁻¹) depends on the same property for the air entering the cuvette (ω_r , mol mol⁻¹), according to the expression:

$$\frac{d\omega_s}{dt} = \frac{-(F_L + s_L T_r)\omega_s + F_L \omega_r + s_L T_r}{V_{ch} P} RT_a. \quad (4.94)$$

Given the true values of CO₂ assimilation and transpiration, the apparent CO₂ assimilation (A_{app} , mol m⁻² s⁻¹) and transpiration (Tr_{app} , mol m⁻² s⁻¹) are calculated from the simulated properties of inflow and outflow air, according to the expressions:

$$A_{app} = \frac{F_L C_r - (F_L + s_L T_r)C_s}{s_L} \quad (4.95)$$

and

$$Tr_{app} = \frac{F_L (\omega_s - \omega_r)}{s_L (1 - \omega_s)}. \quad (4.96)$$

Similarly, the apparent stomatal conductance to fluxes of water vapour ($g_{sw,app}$, mol m⁻² s⁻¹) is calculated as

$$g_{sw,app} = \frac{1}{\frac{e_{sL} - e_a}{Tr_{app} \left(P - \frac{e_{sL} + e_a}{2} \right)} - \frac{1}{g_{bw}}} \quad (4.97)$$

Equations 4.93 – 4.97 are only used when comparing simulations with measurements. They introduce two new state variables (C_s and ω_s) and two dynamic inputs (C_r and ω_r) to the model.

Table 4.5: State variables of the model.

Variable	Definition	Units	Equation
PGA	Amount of PGA per unit of leaf area	mol m ⁻²	4.2
$RuBP$	Amount of RuBP per unit of leaf area	mol m ⁻²	4.3
f_{RB}	Fraction of Rubisco catalytic sites that are carbamylated and not occupied by inhibitors		4.12
ϕ_{qE}	Loss of quantum yield of PSII due to qE		4.33
α_R	Relative change in absorptance of irradiance at the leaf level with respect to dark-adapted state due to chloroplast movement		4.38
f_{IId}	Fraction of photoinhibited PSII units		4.41
f_R	Activation state of limiting enzyme in the regeneration phase of the Calvin cycle		4.62
C_{cyt}	[CO ₂] in the cytosol	mol mol ⁻¹	4.63
C_c	[CO ₂] in the stroma	mol mol ⁻¹	4.64
C_i	[CO ₂] in the intercellular spaces	mol mol ⁻¹	4.68
PR	Amount of photorespiratory intermediates	mol m ⁻²	4.67
g_{sw}	Stomatal conductance to fluxes of water vapour	mol m ⁻² s ⁻¹	4.78
T_L	Leaf temperature	K	4.88
C_s	[CO ₂] of the air inside a cuvette	mol mol ⁻¹	4.93
ω_s	Water vapour mole fraction of the air inside a cuvette	mol mol ⁻¹	4.94

Table 4.6: Dynamic inputs of the model.

Variable	Definition	Units
I_u	Incident ultraviolet A irradiance (320 – 400 nm)	W m ⁻²
I_b	Incident blue irradiance (400 – 500 nm)	mol m ⁻² s ⁻¹
I_g	Incident green irradiance (500 – 600 nm)	mol m ⁻² s ⁻¹
I_r	Incident red irradiance (600 – 700 nm)	mol m ⁻² s ⁻¹
I_n	Incident near infrared irradiance (700 – 2500 nm)	W m ⁻²
C_a	[CO ₂] in the air	mol mol ⁻¹
T_a	Temperature of the air	K
e_a	Partial pressure of water vapour of the air	Pa
ω	Wind velocity	m s ⁻¹
C_r	[CO ₂] of the inflow air in a cuvette	mol mol ⁻¹
ω_r	Water vapour mole fraction of the of the inflow air in a cuvette	mol mol ⁻¹

Table 4.7: Parameter values of the model with sources from where they were estimated. Most parameters were obtained by fitting the model (or specific equations within the model) to published data. A few parameter values were taken from published data or calculated from other published parameter values. Details on the calculations and fitting procedures are given in the text.

Parameter	Value	Source
a_c	0.27	Fitted to data from von Caemmerer and Edmondson (1986)
$\alpha_{\alpha_r,25}$	$4.35 \times 10^{-3} \text{ mol}^{-1} \text{ m}^2 \text{ s}$	Fitted to data from Łabuz et al. (2015) and Davis and Hangarter (2012)
α_b	0.92	See Table 4.3
α_{bpp}	0.66	See Table 4.4
α_{fI}	$6.00 \times 10^3 \text{ mol}^{-1} \text{ m}^2 \text{ s}$	Fitted to data from Kaiser et al. (2016)
α_{fR}	$2.31 \times 10^3 \text{ mol}^{-1} \text{ m}^2 \text{ s}$	Fitted to data from Sassenrath-Cole and Pearcy (1994b)
α_g	0.72	See Table 4.3
α_{gp}	0.60	See Table 4.4
α_n	0.18	See Table 4.3
α_{rac}	0.05	Fitted to data from Łabuz et al. (2015) and Davis and Hangarter (2012)
α_{rav}	0.15	Fitted to data from Davis and Hangarter (2012)
α_r	0.83	See Table 4.3
α_{rp}	0.80	See Table 4.4
α_u	0.94	See Table 4.3
b_c	$1.4 \times 10^4 \text{ mol mol}^{-1}$	Fitted to data from von Caemmerer and Edmondson (1986)
d	$2 \times 10^{-2} \text{ m}$	Specifications of measurement instrument
D_0	695 Pa	Fitted to data from Dai et al. (1992)
$H_{a,\alpha ar}$	$-7.46 \times 10^4 \text{ J mol}^{-1}$	Fitted to data from Łabuz et al. (2015) and Davis and Hangarter (2012)
$H_{a,gc}$	$7.02 \times 10^4 \text{ J mol}^{-1}$	Fitted to data from Walker et al. (2013)
$H_{a,gw}$	$7.02 \times 10^4 \text{ J mol}^{-1}$	Fitted to data from Walker et al. (2013)
$H_{a,k\alpha}$	$9.05 \times 10^4 \text{ J mol}^{-1}$	Fitted to data from Brugnoli and Björkman (1992)
$H_{a,kc}$	$4.18 \times 10^4 \text{ J mol}^{-1}$	Fitted to data from Walker et al. (2013)
$H_{a,Kmc}$	$4.94 \times 10^4 \text{ J mol}^{-1}$	Fitted to data from Walker et al. (2013)
$H_{a,Kmo}$	$2.91 \times 10^4 \text{ J mol}^{-1}$	Fitted to data from Walker et al. (2013)
$H_{a,ko}$	$5.51 \times 10^4 \text{ J mol}^{-1}$	Fitted to data from Walker et al. (2013)
$H_{a,Jmax}$	$3.62 \times 10^4 \text{ J mol}^{-1}$	Fitted to data from Yamori et al. (2008)
$H_{a,krep}$	$1.60 \times 10^5 \text{ J mol}^{-1}$	Fitted to data from Greer et al. (1986)
$H_{a,Rca}$	$3.00 \times 10^4 \text{ J mol}^{-1}$	Fitted to data from Carmo-Silva and Salvucci (2013)
$H_{a,Rm}$	$5.62 \times 10^4 \text{ J mol}^{-1}$	Fitted to data from Walker et al. (2013)
$H_{a,TPU}$	$5.75 \times 10^4 \text{ J mol}^{-1}$	Fitted to data from Harley et al. (1992b)
S_{gc}	$320 \text{ J mol}^{-1} \text{ K}^{-1}$	Fitted to data from Walker et al. (2013)
S_{gw}	$320 \text{ J mol}^{-1} \text{ K}^{-1}$	Fitted to data from Walker et al. (2013)
S_{Jmax}	$690 \text{ J mol}^{-1} \text{ K}^{-1}$	Fitted to data from Bernacchi et al. (2003)
$S_{k\alpha}$	$108 \text{ J mol}^{-1} \text{ K}^{-1}$	Fitted to data from Brugnoli and Björkman (1992)
S_{krep}	$780 \text{ J mol}^{-1} \text{ K}^{-1}$	Fitted to data from Greer et al. (1986)

Parameter	Value	Source
S_{TPU}	$790 \text{ J mol}^{-1} \text{ K}^{-1}$	Fitted to data from Harley et al. (1992b)
$H_{d,gc}$	$9.40 \times 10^3 \text{ J mol}^{-1}$	Fitted to data from Walker et al. (2013)
$H_{d,gw}$	$9.40 \times 10^3 \text{ J mol}^{-1}$	Fitted to data from Walker et al. (2013)
$H_{d,jmax}$	$2.16 \times 10^5 \text{ J mol}^{-1}$	Fitted to data from Bernacchi et al. (2003)
$H_{d,k\alpha}$	$3.28 \times 10^5 \text{ J mol}^{-1}$	Fitted to data from Brugnoli and Björkman (1992)
$H_{d,krep}$	$2.33 \times 10^5 \text{ J mol}^{-1}$	Fitted to data from Greer et al. (1986)
$H_{d,Rca}$	$2.90 \times 10^5 \text{ J mol}^{-1}$	Fitted from Carmo-Silva and Salvucci (2013)
$H_{d,TPU}$	$2.47 \times 10^5 \text{ J mol}^{-1}$	Fitted to data from Harley et al. (1992b)
E_b	$2.6 \times 10^5 \text{ J mol}^{-1}$	Calculated from the Planck-Einstein relation
E_g	$2.2 \times 10^5 \text{ J mol}^{-1}$	Calculated from the Planck-Einstein relation
E_r	$1.8 \times 10^5 \text{ J mol}^{-1}$	Calculated from the Planck-Einstein relation
$f_{\alpha Sc}$	0.93	Calculated from data from Tholen et al. (2008)
f_{cyc}	0.05	Taken from Yin and Struik (2009)
$f_{I,0}$	0.37	Fitted to data from Kaiser et al. (2016)
f_{prot}	$0.51 \text{ m}^2 \text{ mol}^{-1}$	Fitted to data from Kaiser et al. (2016)
f_{pseudo}	0.13	Taken from Yin and Struik (2009)
$f_{R,0}$	0.06	Fitted to data from Sassenrath-Cole and Pearcy (1994b) assuming FBPase is limiting the regeneration of RuBP
f_{qE}	3.93×10^{-2}	Fitted to data from Kaiser et al. (2016)
$f_{RB,m}$	0.25	Fitted to data from Kaiser et al. (2016)
$g_{cm,25}$	$0.39 \text{ mol m}^{-2} \text{ s}^{-1}$	Calculated with data from Flexas et al. (2007b) and Tholen et al. (2012)
g_{swm}	$0.53 \text{ mol m}^{-2} \text{ s}^{-1}$	Fitted to data from Kaiser et al. (2016)
$g_{w,25}$	$0.75 \text{ mol m}^{-2} \text{ s}^{-1}$	Calculated with data from Flexas et al. (2007b) and Tholen et al. (2012)
I_{ac}	$1.60 \times 10^{-6} \text{ mol m}^{-2} \text{ s}^{-1}$	Fitted to data from Łabuz et al. (2015) and Davis and Hangarter (2012)
$J_{max,25}$	$1.21 \times 10^{-4} \text{ mol m}^{-2} \text{ s}^{-1}$	Fitted to data from Kaiser et al. (2016)
$K_{A,Rca}$	$1.02 \times 10^{-2} \text{ g m}^{-2}$	Fitted to data from Mott and Woodrow (2000)
$k_{c,25}$	4.16 s^{-1}	Fitted to data from Walker et al. (2013)
k_{D0}	$4.5 \times 10^8 \text{ s}^{-1}$	Taken from Loriaux et al. (2013)
k_{Dinh}	$5 \times 10^9 \text{ s}^{-1}$	Assumed
$k_{d\alpha,25}$	$3.84 \times 10^{-3} \text{ s}^{-1}$	Fitted to data from Łabuz et al. (2015) and Davis and Hangarter (2012)
k_{dR}	$7.5 \times 10^{-3} \text{ s}^{-1}$	Fitted to data from Sassenrath-Cole and Pearcy (1994b) assuming FBPase is limiting
k_{dqE}	$9.28 \times 10^{-3} \text{ s}^{-1}$	Fitted to data from Kaiser et al. (2016)
k_{dRB}	$6.80 \times 10^{-4} \text{ s}^{-1}$	Fitted to data from Sassenrath-Cole and Pearcy (1994b)
k_f	$6.9 \times 10^7 \text{ s}^{-1}$	Taken from Loriaux et al. (2013)
$k_{i\alpha,25}$	$2.50 \times 10^{-3} \text{ s}^{-1}$	Fitted to data from Łabuz et al. (2015) and Davis and Hangarter (2012)
$K_{I,PGA}$	0.84 mol m^{-3}	Taken from von Caemmerer (2000)
k_{iqE}	$2.34 \times 10^{-2} \text{ s}^{-1}$	Fitted to data from Kaiser et al. (2016)

Parameter	Value	Source
k_{iR}	$6.28 \times 10^{-3} \text{ s}^{-1}$	Fitted to data from Sassenrath-Cole and Pearcy (1994b) assuming that FBPase limits the regeneration of RuBP
k_{inh0}	$0.16 \text{ m}^2 \text{ mol}^{-1}$	Fitted to data from Kaiser et al. (2016)
k_{gs}	$7.99 \times 10^{-4} \text{ s}^{-1}$	Fitted to data from Kaiser et al. (2016)
$K_{mc,25}$	$2.62 \times 10^{-4} \text{ mol mol}^{-1}$	Fitted to data from Walker et al. (2013)
$K_{mo,25}$	$0.20 \text{ mol mol}^{-1}$	Fitted to data from Walker et al. (2013)
$K_{m,PGA}$	$5 \times 10^{-6} \text{ mol m}^{-2}$	Taken from Kirschbaum et al. (1998)
$K_{m,RuBP}$	$2.2 \times 10^{-2} \text{ mol m}^{-3}$	Taken from Farquhar (1979)
$k_{o,25}$	1.26 s^{-1}	Fitted to data from Walker et al. (2013)
k_p	$2.6 \times 10^9 \text{ s}^{-1}$	Taken from Loriaux et al. (2013)
k_{pR}	$6.79 \times 10^{-2} \text{ s}^{-1}$	Fitted to data from Kaiser et al. (2016)
k_{Rca}	$6.38 \times 10^{-2} \text{ m}^2 \text{ g}^{-1} \text{ s}^{-1}$	Fitted to data from Kaiser et al. (2016)
$k_{rep,25}$	$1.1 \times 10^{-4} \text{ s}^{-1}$	Fitted to data from Kasahara et al. (2002)
ϕ_{qEm}	0.21	Fitted to data from Kaiser et al. (2016)
r_0	$1.02 \times 10^{-2} \text{ mol m}^{-2} \text{ s}^{-1}$	Fitted to data from Kaiser et al. (2016)
RB	$1.4 \times 10^{-5} \text{ mol m}^{-2}$	Fitted to data from Kaiser et al. (2016)
Rca	0.12 g m^{-2}	Calculated with data from Mott and Woodrow (2000) and Carmo-Silva and Salvucci (2013)
$R_{m,25}$	$8.5 \times 10^{-7} \text{ mol m}^{-2} \text{ s}^{-1}$	Fitted to data from Flexas et al. (2007b)
S_{cm}	7.1	Taken from Tholen et al. (2008)
S_m	9.8	Taken from Tholen et al. (2008)
σ_L	$651 \text{ J m}^{-2} \text{ K}^{-1}$	Calculated with data from Goudriaan and van Laar (1994) and Weraduwege et al. (2015)
σ_2	0.5	Taken from Yin and Struik (2009)
s_L	$2 \times 10^{-4} \text{ m}^2$	Known
θ	0.7	Taken from Yin and Struik (2009)
θ_{α_r}	0.36	Fitted to data from Łabuz et al. (2015) and Davis and Hangarter (2012)
θ_{fI}	0.98	Fitted to data by Kaiser et al. (2016)
θ_{fR}	1.00	Fitted to data from Sassenrath-Cole and Pearcy (1994b) assuming FBPase is limiting
$T_{o,Rca}$	300.4 K	Fitted from Carmo-Silva and Salvucci (2013)
TPU_{25}	$7.82 \times 10^{-6} \text{ mol m}^{-2} \text{ s}^{-1}$	Fitted to data from Kaiser et al. (2016)
V_{st}	$7 \times 10^{-6} \text{ m}$	Calculated assuming $25 \mu\text{L mg}^{-1}$ and chlorophyll content of 280 mg m^{-2} (Walters et al., 1999; Mishra et al., 2012)
V_r	$1.5 \times 10^{-4} \text{ m}$	Calculated with data from Weraduwege et al. (2015)
V_{rmax}	$1.10 \times 10^{-4} \text{ mol m}^{-2} \text{ s}^{-1}$	Calculated assuming $2RBk_C$ based on Pearcy et al. (1997)

4.3 Model calibration with photosynthetic mutants

4.3.1 Experiment and calibration protocol

The model was fitted to dynamic measurements of gas exchange and fluorescence on *A. thaliana* Col-0 and four associated photosynthetic mutants (Kaiser et al., 2016). The fitting procedure entailed the estimation of 17 parameters using the method of maximum likelihood. The use of four mutants had a dual objective: (i) to enhance the estimation of some of the parameters that were not well identified by the existing literature and (ii) to test the assumptions of the model regarding the effect of different processes on dynamic CO₂ assimilation.

All experiments described below were performed with a light source composed of 10% blue and 90% red (proportions of photons). All measurements were repeated for five replicates per genotype, except for Col-0 for which 15 replicates were used. The data was aggregated to the genotype level by averaging across replicates (i.e., average time series for each combination of genotype and measurement protocol were created from the original data). The model was fitted to all data simultaneously, by minimising the weighted sum of squared relative deviations between the model predictions and the measurements. The weights were chosen to compensate for the fact that the number of data points were different for each measurement protocol.

The minimisation was done with the derivative-free algorithm BOBYQA (Powell, 2009) as implemented in the NLOpt library (Johnson, 2016). The algorithm was allowed to vary the 17 parameters being fitted, plus additional parameters that were specific to each mutant (i.e., mutants differed from the wildtype in one or more parameters). The optimization was constrained by minimum and maximum values imposed on each parameter to ensure that solutions were physiologically feasible.

The four photosynthesis mutants were:

1. The Rubisco activase mutant *rca-2* (Shan et al., 2011) was used to test how well the model captures the effect of Rubisco activase. This genotype contains a “leaky” mutation that allows some residual expression of Rubisco activase (Shan et al., 2011). Therefore, for practical purposes, it can be considered analogous to a Rubisco activase underexpressor. The only parameter that was modified in the model for this mutant was the amount of Rubisco activase (*Rca*, Table 4.8).

2. The PsbS mutant *npq4-1* (Li et al., 2000a) was used to test the ability of the model to simulate the different components of NPQ_{sv} correctly. This mutant is characterized by a strong reduction in qE and an increase in photoinhibition due to reduced photoprotection (Nilkens et al., 2010; Dall'Osto et al., 2014). The only parameter that was modified for this mutant was the coefficient f_{qE} (Table 4.8).

3. The mutant with low endogenous ABA levels, *aba2-1* (Léon-Kloosterziel et al., 1996), was used to test the effect of higher stomatal conductance. ABA is also required for chloroplast light avoidance movement (Rojas-Pierce et al., 2014), so this mechanism was turned off in the simulations for this genotype. Experiments with exogenous addition of ABA indicate that ABA also affects mesophyll conductance and other photosynthetic parameters (Flexas et al., 2008; Mizokami et al., 2014). Based on those results, $J_{max,25}$,

Table 4.8: Parameters of the model that were modified for each mutant when fitting the model to the data from Kaiser et al. (2016).

Genotype	Parameter	Value
<i>aba2-1</i>	$g_{cm,25}$	3.54 mol m ⁻² s ⁻¹
<i>aba2-1</i>	$g_{w,25}$	6.82 mol m ⁻² s ⁻¹
<i>aba2-1</i>	$J_{max,25}$	1.42×10 ⁻⁴ mol m ⁻² s ⁻¹
<i>aba2-1</i>	α_{rav}	0
<i>aba2-1</i>	TPU_{25}	1.13×10 ⁻⁵ mol m ⁻² s ⁻¹
<i>aba2-1</i>	$f_{I,0}$	0.52
<i>aba2-1</i>	g_{swm}	1.11 mol m ⁻² s ⁻¹
<i>aba2-1</i>	α_{fI}	3.94×10 ³ mol ⁻¹ m ² s
<i>aba2-1</i>	θ_{fI}	0.97
<i>rca-2</i>	Rca	2.35×10 ⁻² g m ⁻²
<i>npq4-1</i>	f_{qE}	9.37×10 ⁻³
<i>spsa1</i>	TPU_{25}	5.65×10 ⁻⁶ mol m ⁻² s ⁻¹

V_{rmax} , TPU_{25} , parameters associated to mesophyll conductance, and chloroplast movement were modified for this mutant (Table 4.8).

4. The mutant *spsa1* (Sun et al., 2011), with lower activities of sucrose phosphate synthase, was used to test the concept of triose phosphate utilisation as implemented by the model, thus only modifying the value of TPU_{25} (Table 4.8).

In the experiment, measurements were performed on leaves of 6 to 8-week-old *A. thaliana* plants using a LI-6400 system (Li-Cor Biosciences, Lincoln, Nebraska, USA). Below, a summary of the measurement protocols is given (for details, see Kaiser et al. 2016):

- Photosynthetic induction: irradiance was increased within two seconds from an initial irradiance 0 $\mu\text{mol m}^{-2} \text{s}^{-1}$, 70 $\mu\text{mol m}^{-2} \text{s}^{-1}$, or 130 $\mu\text{mol m}^{-2} \text{s}^{-1}$ to 1000 $\mu\text{mol m}^{-2} \text{s}^{-1}$, 800 $\mu\text{mol m}^{-2} \text{s}^{-1}$, or 600 $\mu\text{mol m}^{-2} \text{s}^{-1}$, respectively. Leaves had been previously adapted to the initial irradiance until gas exchange measurements reached a steady state (at least 40 minutes). Fluorescence measurements were taken throughout the 0 → 1000 $\mu\text{mol m}^{-2} \text{s}^{-1}$ light transient.

- Loss of induction: irradiance was decreased from an initial level of 800 $\mu\text{mol m}^{-2} \text{s}^{-1}$ or 600 $\mu\text{mol m}^{-2} \text{s}^{-1}$ to 130 $\mu\text{mol m}^{-2} \text{s}^{-1}$ or 200 $\mu\text{mol m}^{-2} \text{s}^{-1}$, respectively. Leaves were adapted to the initial irradiance until gas exchange measurements reached a steady-state.

- CO₂ response curves: steady-state measurements of CO₂ assimilation were performed at a saturating irradiance of 1000 $\mu\text{mol m}^{-2} \text{s}^{-1}$ and air [CO₂] between 50 $\mu\text{mol mol}^{-1}$ and 1500 $\mu\text{mol mol}^{-1}$.

4.3.2 Results of calibration

The model fitted the measurements of net CO₂ assimilation after light transients accurately (Figure 4.28) and explained 94% to 97% (depending on the genotype) of the variance in the data. The root mean square error (RMSE) of the fits was more variable, with the smallest value found for *rca-2* (0.28 $\mu\text{mol m}^{-2} \text{s}^{-1}$) and the largest value for

aba2-1 (0.88 $\mu\text{mol m}^{-2} \text{s}^{-1}$). In most cases, the predictions fell within the 95% confidence intervals calculated from the standard error of the measurements (Figure 4.28). The model reproduced the slower kinetics of induction in dark-adapted leaves compared to leaves adapted to low irradiance, as well as the reduction in these dynamics on the Rubisco activase mutant. It also captured the increase in CO₂ assimilation in *aba2-1*. The kinetics of CO₂ assimilation after a decrease in irradiance were also captured accurately, especially in Col-0 and *aba2-1* (Figure 4.28). In all cases there was a short “CO₂ burst” of 5 to 10 minutes after the decrease in irradiance. Measurements and simulations for the 70 → 800 $\mu\text{mol m}^{-2} \text{s}^{-1}$ and 130 → 600 $\mu\text{mol m}^{-2} \text{s}^{-1}$ transients were similar and only the former is shown on Figure 4.28. For the same reason, the 600 → 200 $\mu\text{mol m}^{-2} \text{s}^{-1}$ transient is not shown as it was similar to the 800 → 130 $\mu\text{mol m}^{-2} \text{s}^{-1}$ transient.

The model also fitted the steady-state CO₂ response curves satisfactorily, which were measured for the different mutants (Figure 4.29) and explained more than 98% of the variation in the measurements, with similar RMSE as in the transients (i.e. 0.50 – 0.89 $\mu\text{mol m}^{-2} \text{s}^{-1}$). The main features of the measurements and simulations were: (i) a decrease in the initial slope due a decrease in *Rca*, (ii) a reduction of the saturating value of CO₂ assimilation due to a reduction in SPS activity, and (iii) an increase in CO₂ assimilation at all [CO₂] for the ABA mutant. The model predicted a slightly higher CO₂ assimilation at high [CO₂] for the NPQ mutant compared to the wildtype, although the measurements suggested otherwise. It is possible that the maximum rates of electron transport were lower in *npq4-1* due to pleiotropic effects of the mutation or different acclimation to the same growth conditions.

However, another possible explanation for the mismatch is that the model may have overestimated the transient limitations by qE. That is, given that simulated qE decreased with [CO₂] and that the time between consecutive CO₂ levels was only 4 minutes, the simulations of potential rates of electron transport (and consequently CO₂ assimilation) at high CO₂ were reduced in the wildtype by around 6%. In the model, any transient excess in qE with respect to the steady-state may result in a decrease of CO₂ assimilation, regardless of whether the excess is caused by a decrease in irradiance or increase in CO₂. However, in reality, different mechanisms may be responsible for regulation of qE in response to changes in CO₂ or irradiance (Kramer et al., 2004a).

The dynamics of NPQ_{sv} during induction were simulated accurately by the model (Figure 4.30A), which explained 96% to 99% of the observed variance, with RMSE in the range 0.04 – 0.06. Measured and simulated NPQ_{sv} values for *spsa1* were similar to those of Col-0, with lower values (but similar dynamics) for *aba2-1*, higher values for *rca-2* and lower values (and slower rate of induction) for *npq4-1* (Figure 4.30A). The success in reproducing NPQ_{sv} for *rca-2* indicates that the model captures the effect of changes in the metabolism on NPQ_{sv} correctly.

The fitting procedure resulted in qE for *npq4-1* being 25% of that achieved in the wildtype, which is in agreement with the calculations performed by Nilkens et al. (2010) for the same genotypes based on time decomposition of NPQ_{sv} relaxation curves. This result is also in agreement with the hypothesis that PsbS contributes to qE, but is not compulsory for its formation (Johnson and Ruban, 2011).

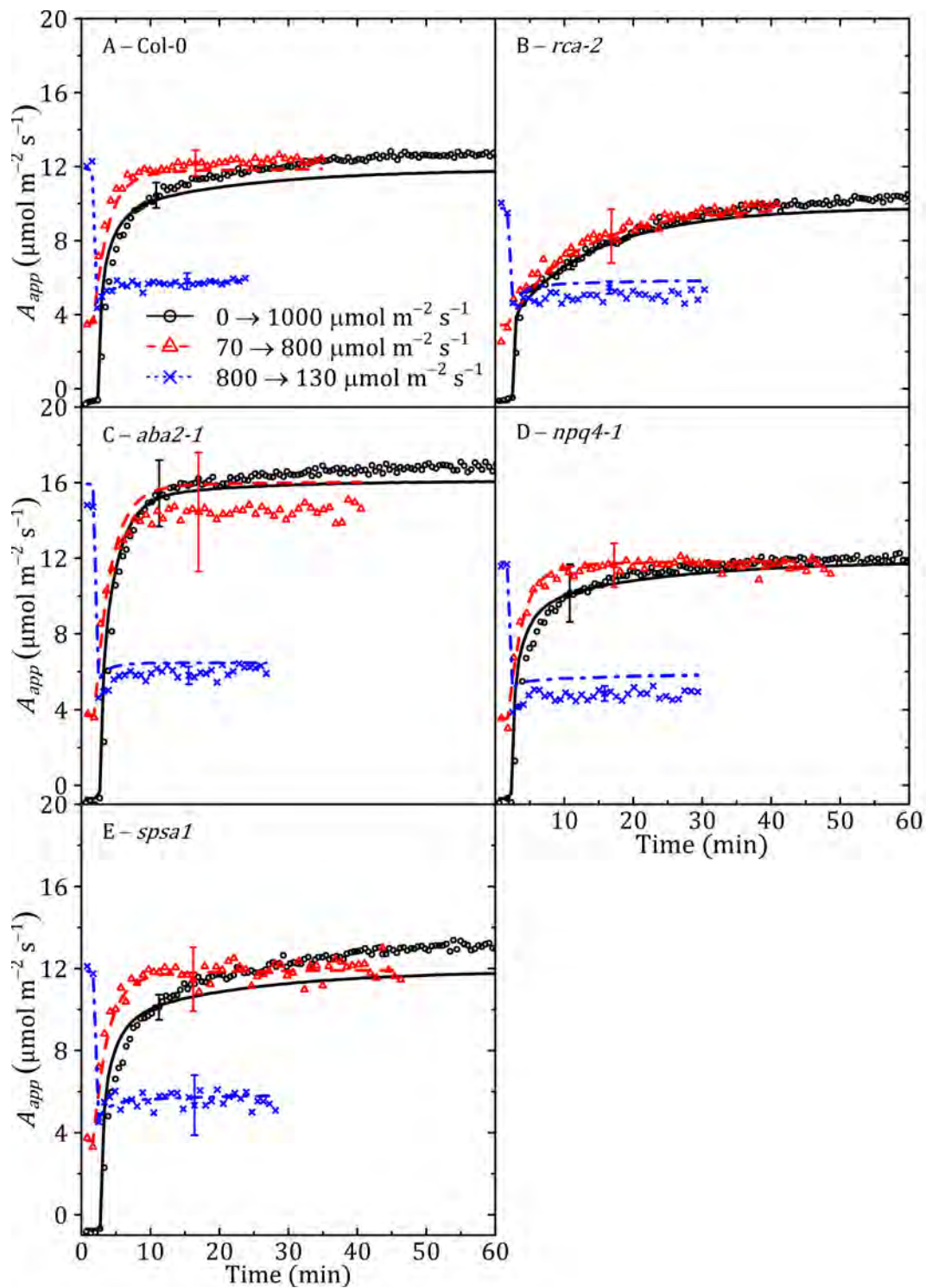


Figure 4.27: Measured (symbols) and simulated (lines) apparent CO₂ assimilation corrected for the time response of the measuring instrument (A_{app}) as a function of time after a rapid change in incident irradiance from 0 to 1000 $\mu\text{mol m}^{-2} \text{s}^{-1}$ (black circles and solid lines), from 70 to 800 $\mu\text{mol m}^{-2} \text{s}^{-1}$ (red triangles and dashed lines) and from 800 to 130 $\mu\text{mol m}^{-2} \text{s}^{-1}$ (blue crosses and dash-dotted lines) for Arabidopsis thaliana Col-0 (A) and associated photosynthetic mutants (B – E). Measurements from Kaiser et al. (2016). Error bars represent 95% confidence intervals of the mean across replicates. Parameters for wildtype (Col-0) as in Table 4.7. Mutants have the same parameter values as the wildtype except for the parameters indicated in Table 4.8.

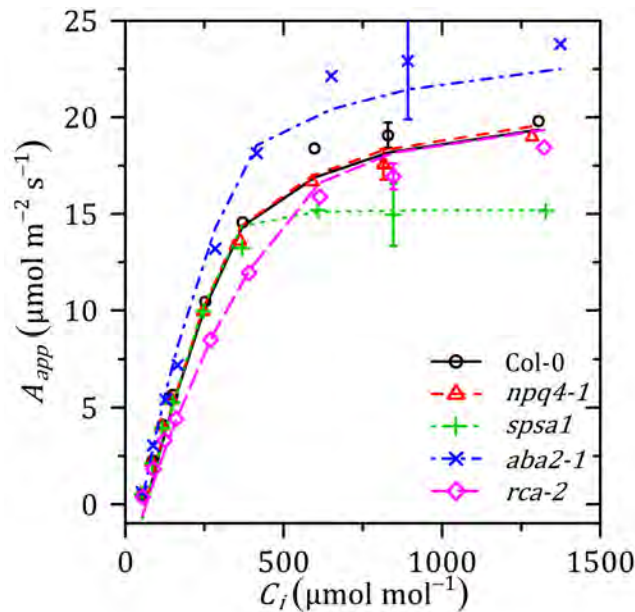


Figure 4.28: Measured (symbols) and simulated (lines) steady-state response of apparent CO₂ assimilation corrected for the time response of the measuring instrument (A_{app}) to intercellular [CO₂] (C_i). Error bars represent the 95% confidence interval of the mean across replicates. Measurements from Kaiser et al. (2016). Parameters for wildtype (Col-0) as in Table 4.7. Mutants have the same parameter values as the wildtype except for the parameters indicated in Table 4.8.

The pattern of variation of qE (Figure 4.30B) did not coincide with the pattern of variation of the loss of maximum PSII quantum yield due to qE (ϕ_{qE} , Figure 4.31) for all genotypes (e.g., *rca-2*). This mismatch is an artefact of the way the qE component is computed, to ensure that all NPQ_{sv} components are strictly additive (Equation 4.57). The values of ϕ_{qE} were always higher in the first minutes of the light transients than in the final steady-state. This behaviour is in agreement with patterns predicted from mechanistic models of qE (Zaks et al., 2012; Matuszyńska et al., 2016) and is associated with transiently lower lumen pH. However, the simulated patterns in Figure 4.30B are actually the result of the fact that Q_A is transiently more reduced during the first minutes of photosynthetic induction. Both variables (pH and Q_A) tend to vary simultaneously, which is the reason why the model is able to capture the temporal pattern correctly.

The assumption that ABA is required for chloroplast movement at high irradiance (Rojas-Pierce et al., 2014) explained most of the difference in NPQ_{sv} between the wildtype and *aba2-1* (Figure 4.30A). The component of NPQ_{sv} associated with chloroplast movement (qM) depends on ϕ_{qE} and f_{IId} (Equation 4.56), which explains the differences in qM for *npq4-1* and *rca-2* (Figure 4.30C). The index qM should be interpreted as the differences in NPQ_{sv} obtained if chloroplast movement was turned off (e.g., via genetic transformation or absence of blue irradiance). After 60 minutes in high irradiance, qM represented around 13% of NPQ_{sv} in the wildtype, whereas it increased to 18% in *npq4-1*. These ratios are comparable with the calculations reported by Dall'Osto et al. (2014) by comparing NPQ_{sv} induction in Col-0, *npq4-1* and *npq4phot2* (where the phototropin mutation, *phot2*, is required for chloroplast movement).

The amount of NPQ_{sv} due to heat dissipation induced by photoinhibition (qI) also varied across genotypes (Figure 4.30D) due to differences in the photoprotective effects of qE (for *rca-2* and *npq4-1*) and chloroplast movement (for *aba2-1*). In all cases, simulated qI increased linearly with time and was not saturated even after 60 minutes of exposure to

high irradiance. In the wildtype, simulated qI represented 9.2% of the total NPQ_{sv} at the end of the simulation, whereas this ratio increased to 36% in $npq4-1$. These values are similar to the ratios calculated by Dall'Osto et al. (2014) and Nilkens et al. (2010) for similar irradiances and the same length of exposure.

Finally, the equations describing the dynamics of stomatal conductance (g_{sw}) were fitted to the $0 \rightarrow 1000 \mu\text{mol m}^{-2} \text{s}^{-1}$ transient measured by Kaiser et al. (2016), resulting in a small RMSE ($10^{-3} - 6 \times 10^{-3} \text{ mol m}^{-2} \text{s}^{-1}$ across genotypes) and $> 95\%$ of the variance being explained by the model (Figure 4.32). Although g_{sw} was also measured for the other transients, the saturation of g_{sw} at low irradiance (Figure 4.32B) resulted in a high noise/signal ratio for all measurements except for the $0 \rightarrow 1000 \mu\text{mol m}^{-2} \text{s}^{-1}$ transient. Hence, only data from this transient was used to estimate the parameters associated to the kinetics of stomatal conductance. However, the initial and final steady-states of all transients were used to construct steady-state irradiance response curves, by averaging for 120 s in order to reduce the noise/signal ratio (Figure 4.32).

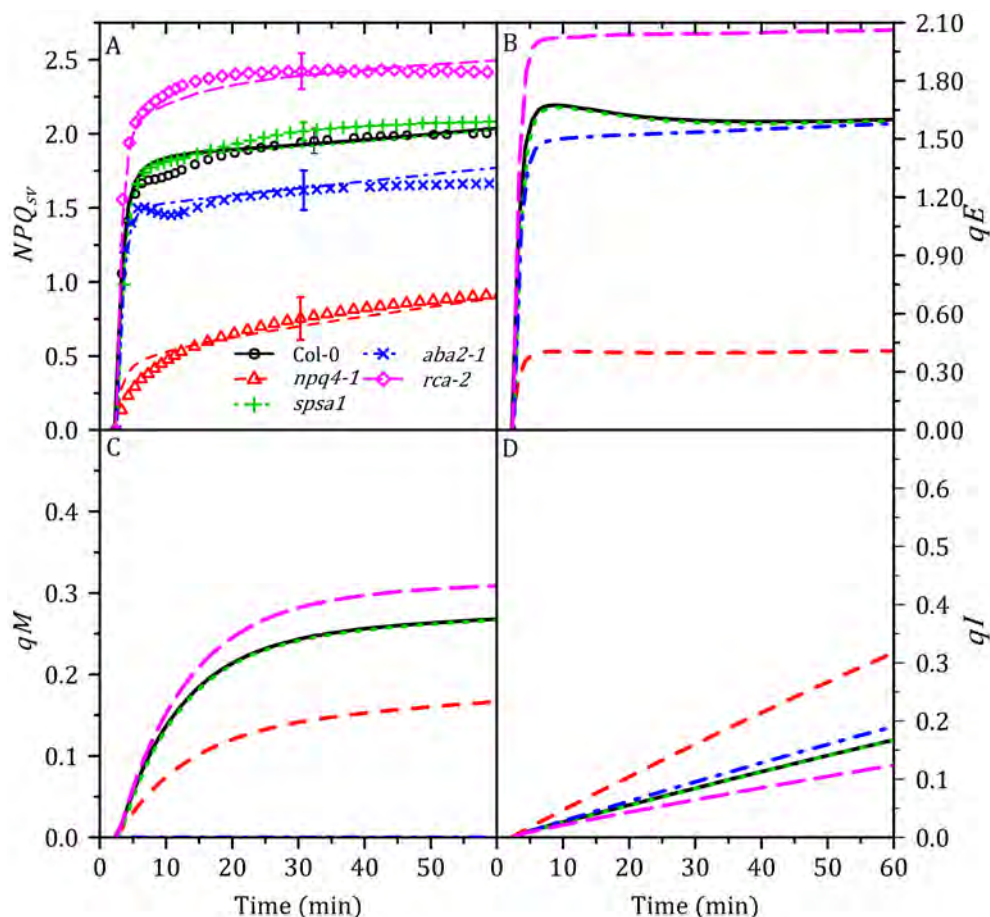


Figure 4.29: Measured (symbols) and simulated (lines) Stern-Volmer NPQ coefficient as a function of time after a rapid increase in irradiance from 0 to $1000 \mu\text{mol m}^{-2} \text{s}^{-1}$ (A) and simulated additive NPQ_{sv} components associated to qE (B), chloroplast movement (C) and photoinhibition (D) for Arabidopsis thaliana Col-0 and associated photosynthetic mutants. Measurements from Kaiser et al. (2016). Parameters for wildtype (Col-0) as in Table 4.7. Mutants have the same parameter values as the wildtype except for the parameters indicated in Table 4.8.

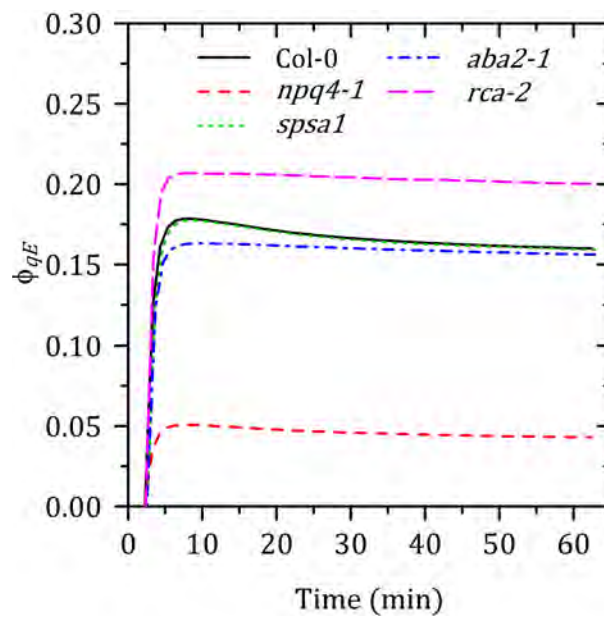


Figure 4.30: Simulated loss of maximum PSII quantum yield due to qE mechanism as a function of time after a rapid increase in irradiance from 0 to 1000 $\mu\text{mol m}^{-2} \text{s}^{-1}$. Parameters for wildtype (Col-0) as in Table 4.7. Mutants have the same parameter values as the wildtype except for the parameters indicated in Table 4.8.

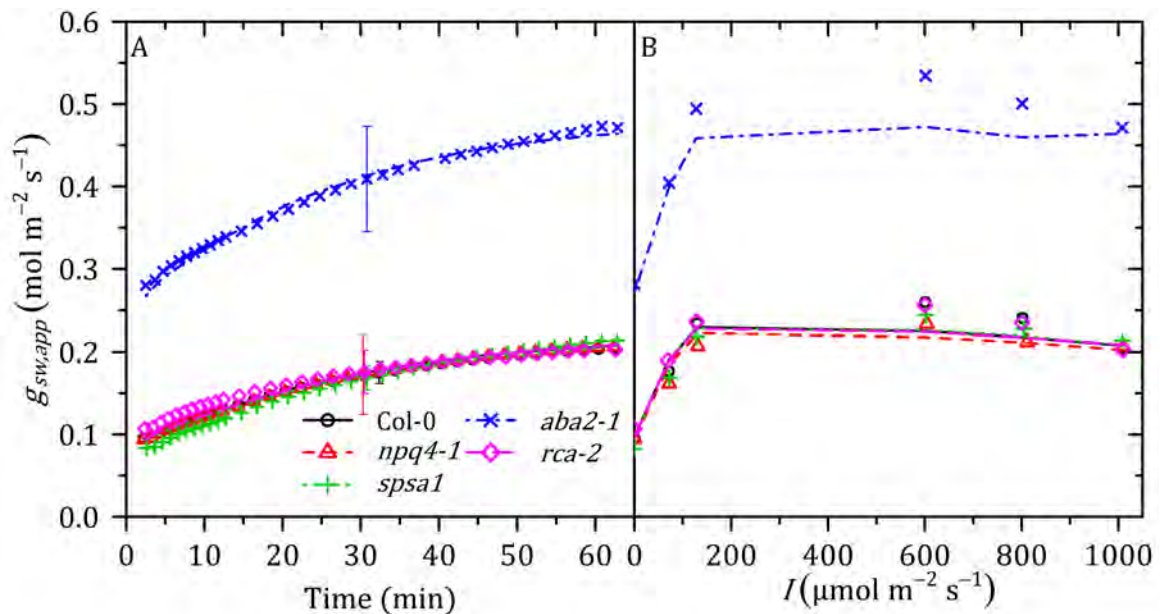


Figure 4.31: Measured (symbols) and simulated (lines) of apparent stomatal conductance to fluxes of water vapour corrected for the time response of the measurement instrument ($g_{\text{sw,app}}$) as a function of time after a rapid increase in irradiance from 0 to 1000 $\mu\text{mol m}^{-2} \text{s}^{-1}$ (A) and its steady-state value as a function of irradiance (B) for *Arabidopsis thaliana* Col-0 and associated photosynthetic mutants. Measurements from Kaiser et al. (2016). Parameters for wildtype (Col-0) as in Table 4.7. Mutants have the same parameter values as the wildtype except for the parameters indicated in Table 4.8.

4.4 Model validation

To test the predictive power of the model, measurements of CO₂ assimilation under fluctuating conditions (i.e., lightflecks) by Kaiser et al. (2016) were used. The measurements were performed on the same plants used for parameter estimation (Section 4.3), but were statistically independent and explored a different dynamic behaviour of the system. In these measurements, irradiance was varied as a square wave in order to produce symmetrical, periodical lightflecks (Figure 4.33). A square wave is a function of time that consists of a periodic repetition of cycles. Each cycle consists of two half-cycles of equal length. The total length of a cycle is called “period”. During each half-cycle, irradiance was kept constant. For each cycle, the irradiance of the first half-cycle was always higher than in the second half-cycle. The difference between the irradiance of the first and second half-cycle is called “amplitude”. The average of the irradiances of the first and second half-cycle was always 300 $\mu\text{mol m}^{-2} \text{s}^{-1}$, but three amplitudes of 100, 200 and 500 $\mu\text{mol m}^{-2} \text{s}^{-1}$ were used. Each amplitude was combined with three periods (120, 60 and 10 s). This resulted in nine amplitude \times period combinations that were used for measurements on biological replicates of each genotype (same replicates and genotypes as in Section 4.3). The measurements were averaged across replicates for each combination of genotype, period and amplitude, and compared to simulations with the model, choosing the inputs to emulate the measurement protocols.

There was good agreement between the predictions of the model and measurements of average CO₂ assimilation in the lightfleck experiment (Figure 4.34A). The fraction of variance explained by the model across genotypes varied between 96% and 99%, whereas the RMSE varied from 0.16 $\mu\text{mol m}^{-2} \text{s}^{-1}$ to 0.31 $\mu\text{mol m}^{-2} \text{s}^{-1}$. The linear regression between simulated and measured CO₂ assimilation did not have a significant intercept whereas the slope was 0.88 (Figure 4.34A). This indicates that the predictions of the model were, on average, not biased and that the model captured the general trend of variation across genotype, lightfleck period and amplitude.

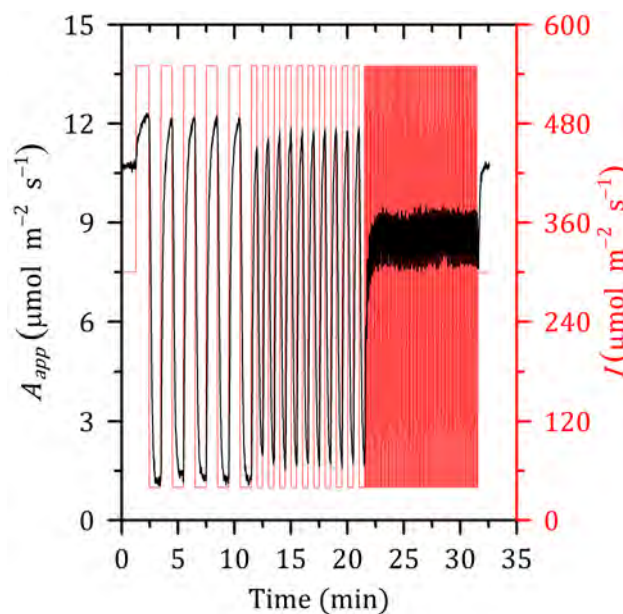


Figure 4.32: Example of measured time series of apparent CO₂ assimilation (A_{app} , black lines) and irradiance (I , red lines) in the lightfleck experiment by Kaiser et al. (2016).

However, predictions underestimated the measurements on Col-0 (on average, by 0.90 $\mu\text{mol m}^{-2} \text{s}^{-1}$) which explains the slope of 0.88. To identify the origin of this deviation, measurements and simulations were normalized by the steady-state values at the beginning of each lightfleck series (Figure 4.34B). The agreement between simulations and measurements increased slightly and, more importantly, there was no significant bias in the predictions with respect to each individual genotype. This indicates that the model captured accurately the relative effect of fluctuating irradiance on average CO₂ assimilation, but the absolute values may have varied due to factors not considered in the model, such as leaf age or time of the day at which the measurements took place.

To further test the model, an analysis of variance of the measurements that included all main effects and interactions among genotype, lightfleck period and amplitude was performed on the measurements and simulations. This analysis revealed that 65% of the variation in the experimental data was explained by the amplitude, 28% by the genotype, whereas the period only explained 2% of the variation (interactions among factors explained small fractions of the total variance). In the simulations, the amplitude, genotype and period explained 65%, 29% and 1.7% of the total variation. The similar results for both ANOVAs performed on the measurements and simulations provides further evidence that the model captured the influence of fluctuating irradiance on CO₂ assimilation correctly.

4.5 Factors limiting dynamic CO₂ assimilation at the leaf level

To gain insights into the role of the different physiological processes that may limit photosynthesis, a series of *in silico* experiments were performed, where virtual leaves adapted to low irradiance (50 $\mu\text{mol m}^{-2} \text{s}^{-1}$) were exposed to high irradiance (1000 $\mu\text{mol m}^{-2} \text{s}^{-1}$) for 40 minutes and then returned to 50 $\mu\text{mol m}^{-2} \text{s}^{-1}$ for 40 minutes. Other environmental conditions were: air temperature of 20 °C, air [CO₂] of 400 $\mu\text{mol mol}^{-1}$, vapour pressure of the air of 2×10^3 Pa and a wind velocity of 20.5 m s^{-1} (required for boundary layer conductance of 9.2 $\text{mol m}^{-2} \text{s}^{-1}$). Unlike in Sections 4.3 and 4.4, the simulations in this section did not include the corrections for the time response of the measurement instrument.

The virtual experiment was repeated for a series of virtual mutants in which each process was either knocked-out or assumed to respond instantaneously to changes in irradiance. These mutants were achieved by modifying the values of specific parameters (Table 4.9), and do not correspond to any real mutant and may not even be feasible to achieve due to physical and chemical constraints. Instead, they represent the (theoretical) situation where a process no longer limits CO₂ assimilation. The differences in predicted CO₂ assimilation with respect to the original parameterization was used to calculate the limitation imposed by the process being modified in each virtual mutant.

Several virtual mutants were constructed to quantify the limitations associated to CO₂ diffusion by assuming instantaneous changes in stomatal conductance, or non-limiting stomatal and/or mesophyll conductance (Figure 4.35A). The values for the parameters were chosen manually by increasing the rate constant of changes in stomatal conductance (k_{gs}) until changes in predicted assimilation were negligible (i.e., below 0.1%), which was achieved with a k_{gs} that was 10^4 higher than the original value (Tables 4.7 and 4.9). The same approach was used to ensure that stomatal and mesophyll

conductance were not limiting, resulting in values that were 10^6 higher than the original values (Tables 4.7 and 4.9).

The simulations indicated that the kinetics of stomatal opening reduced CO_2 assimilation throughout the first half of the experiment (i.e., increasing irradiance), and that the maximum level of limitation (more than 10% reduction) occurred during the first 10 minutes (Figure 4.35A). Assuming non-limiting stomatal conductance resulted in a similar pattern, although the maximum reduction was 25% and this maximum occurred at a later stage of induction. The effect of removing the limitation imposed by a finite mesophyll conductance differed significantly, as the limitation increased progressively during the induction up to a maximum of 25% (Figure 4.35A). Finally, when all the conductances were assumed to be non-limiting, the total diffusional limitation reached a maximum of 37%, its temporal evolution resembled that of stomatal limitation and its values were smaller than the sum of limitations imposed separately by stomatal and mesophyll conductances.

In the second half of the virtual experiment where irradiance was decreased, the kinetics of stomatal closure had a small positive effect on assimilation, though this was always below 2%, and the effect rapidly decreased towards the end of the transition (Figure 4.35A). The limitation due to a finite mesophyll conductance was also small (2%). The limitation due to a finite stomatal conductance was, however, larger (20%) and total diffusional limitation remained lower than in the first half of the experiment.

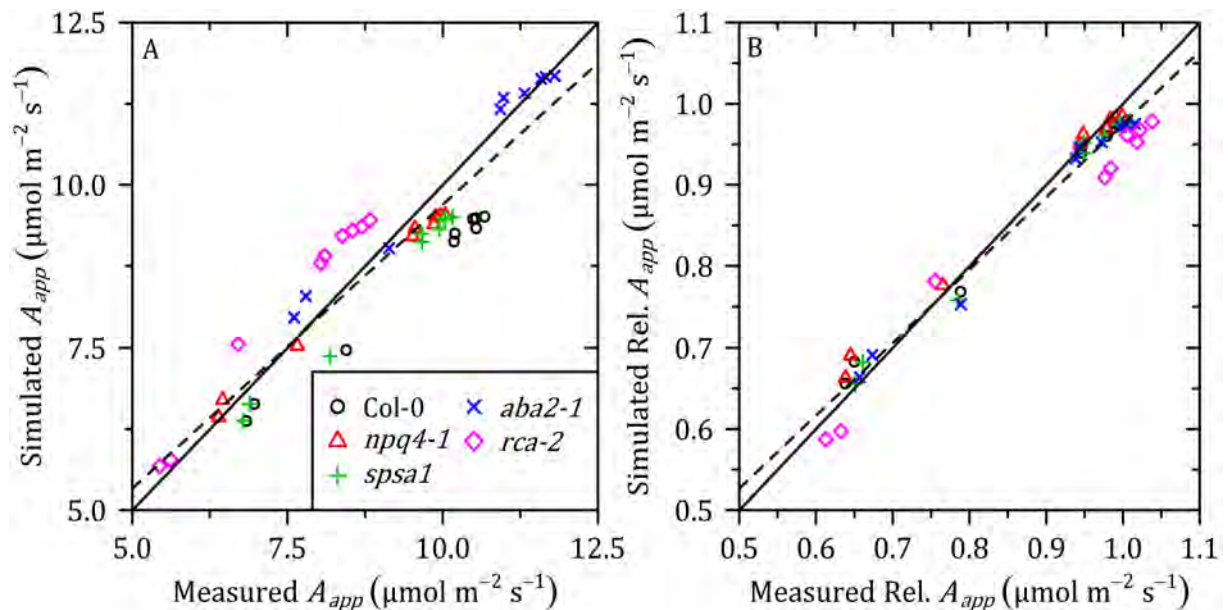


Figure 4.33: Simulated and measured average apparent CO_2 assimilation, corrected for the time response of the measurement instrument (A_{app}) during the lightfleck measurements (A) and the same values normalized by the simulated and measured steady-state values of A_{app} at the beginning of each lightfleck sequence (B). Each value corresponds to a combination of genotype, lightfleck period and amplitude. The solid line represents the 1:1 line in both panels whereas the dashed line represents the linear regression between simulated and measured A_{app} (A) and relative A_{app} (B). Measurements from Kaiser et al. (2016). Parameters for wildtype (Col-0) as in Table 4.7. Mutants have the same parameter values as the wildtype except for the parameters indicated in Table 4.8.

In order to quantify the limitations imposed by metabolism, three virtual mutants were constructed where CO₂ assimilation was not limited by (i) kinetics of Rubisco activation, (ii) kinetics of activation of enzymes in the regeneration phase of the Calvin cycle, and (iii) delays in CO₂ release from photorespiration. As with the previous virtual mutants, the values of the relevant parameters (Table 4.9) were increased until differences in simulated CO₂ assimilation for the virtual experiment were negligible. This was achieved in all cases by increasing the relevant rate constants by three orders of magnitude.

The limitation imposed by activation of enzymes in the regeneration phase of the Calvin cycle was small (< 10%, Figure 4.35B) and limited to the first minute after an increase in irradiance (no effect after a decrease in irradiance). A larger reduction by the kinetics of Rubisco activation was observed, with a maximum value of 60% at the start of the virtual experiment and a decrease to negligible values after 10 minutes of exposure to high irradiance. As the rate constant of Rubisco deactivation was not modified, no effect was observed after a decrease in irradiance for this mutant (Figure 4.35B). Finally, the delay in the release of CO₂ due to photorespiration had a positive effect on assimilation during the first 5 minutes of the virtual experiment, as well as the first two minutes after the decrease in irradiance (Figure 4.35B), though maximum relative changes were always lower than 5%. In addition, effects after increasing and decreasing irradiance compensated each other, such that time-integrated CO₂ assimilation was not affected.

To quantify effects of the regulation of the electron transport chain on CO₂ assimilation under fluctuating light conditions, six virtual mutants were created. The first three consisted of virtual mutants for which the rate constants of qE induction and relaxation, chloroplast movement, and the quantum yield of photoinhibition and rate constant of PSII repair were increased until they were no longer kinetically limiting (Table 4.9), while maintaining the steady-state values of qE, relative absorbance changes due to chloroplast movement and fraction of photoinhibited PSII reaction centres. The other three virtual mutants were constructed such that they lacked qE, photoinhibition or chloroplast movement, by setting the relevant parameter values to zero (Table 4.9).

Assuming instantaneous changes in qE did not affect CO₂ assimilation during the first half of the experiment, but it limited assimilation up to 40% after the decrease in irradiance (Figure 4.35C). However, this limitation only lasted for the first 5 minutes, given the high rate of qE relaxation. These predictions are in agreement with experimental results by Armbruster et al. (2014) and Kromdijk et al. (2016), where a faster qE relaxation resulted in increases of CO₂ assimilation.

The slow rate of chloroplast movement had a small positive effect during the first half of the experiment, which disappeared after 25 minutes of exposure to high irradiance. On the other hand, after the decrease in irradiance, the rate at which the chloroplasts returned to its original position resulted in a strong reduction in assimilation that lasted until the end of the simulation (Figure 4.35C). The larger effect of chloroplast movement at low irradiances can be explained by the fact that, at ambient temperature and [CO₂], CO₂ assimilation was proportional to absorbed irradiance below 100 $\mu\text{mol m}^{-2} \text{s}^{-1}$, but it was less sensitive at high irradiance. Instantaneous changes in the fractions of photoinhibited PSII reaction centres had a very small effect on CO₂ assimilation in the first half of the experiment and a small but sustained effect in CO₂ assimilation after the decrease in irradiance, due to the slow rate of PSII repair (Table 4.7).

Table 4.9: Virtual mutants designed to quantify limitations by different processes on dynamic CO₂ assimilation. Simulations for all virtual mutants were calculated with the parameter values in Table 4.7, except for those listed below.

Scenario	Modified parameters
Non-limiting stomatal kinetics	$k_{gs} = 10 \text{ s}^{-1}$
Non-limiting stomatal conductance	$g_{swm} = 10^6 \text{ mol m}^{-2} \text{ s}^{-1}$
Non-limiting mesophyll conductance	$g_{cm,25} = g_{w,25} = 10^6 \text{ mol m}^{-2} \text{ s}^{-1}$
Non-limiting stomatal and mesophyll conductance (no diffusional limitation)	$g_{swm} = g_{cm,25} = g_{w,25} = 10^6 \text{ mol m}^{-2} \text{ s}^{-1}$
No photoinhibition	$K_{inh0} = 0 \text{ m}^2 \text{ mol}^{-1}$
No limitation due to kinetics of photoinhibition	$k_{inh0} = 0.21 \times 10^6 \text{ m}^2 \text{ mol}^{-1}$ and $k_{rep,25} = 10^2 \text{ s}^{-1}$
No qE	$f_{qE} = 0$
No limitation due to kinetics of qE	$k_{iqE} = 2.53 \times 10^2 \text{ s}^{-1}$ and $k_{dqE} = 1.37 \times 10^2 \text{ s}^{-1}$
No chloroplast movement	$\alpha_{rac} = 0$ and $\alpha_{rav} = 0$
No limitation due to kinetics of chloroplast movement	$k_{i\alpha,25} = 1.49 \times 10^2 \text{ s}^{-1}$ and $k_{d\alpha,25} = 1.85 \times 10^2 \text{ s}^{-1}$
Non-limiting activation of enzyme responsible for regeneration of RuBP	$k_{iR} = 10 \text{ s}^{-1}$
Non-limiting kinetics of Rubisco activation	$k_{RCA} = 10 \text{ m}^2 \text{ mg}^{-2} \text{ s}^{-1}$
No delay in CO ₂ release by photorespiration	$k_{PR} = 10^2 \text{ s}^{-1}$

The analysis of the simulations with mutants that lacked qE, photoinhibition or chloroplast movement yielded similar results compared to the mutants that affected the kinetics of these processes. The lack of qE did not affect CO₂ assimilation in the first half of the experiment (Figure 4.35D) and it resulted in an increase of assimilation in the first minutes after a decrease in irradiance. However, it also resulted in a decrease in CO₂ assimilation for most of the second half of the experiment (Figure 4.35D), due to enhanced photoinhibition caused by the decrease in photoprotection.

The lack of chloroplast movement resulted in a small increase in CO₂ assimilation in the first half of the experiment, whereas, after a decrease in irradiance, there was a strong enhancement of CO₂ assimilation during the first 20 minutes and a decrease afterwards, as the steady-state absorptance at low irradiance is higher than at dark-adapted levels due to the chloroplast accumulation response. These results indicate that the reduction of photoinhibition due to chloroplast avoidance movement at high irradiance does not offset the direct effects on CO₂ assimilation by reduced absorptance. This may explain why sun-adapted leaves generally display very little (if any) changes in absorptance due to chloroplast movement (Davis et al., 2011), as the losses outweighs the benefits. Because the plants used to parameterize chloroplast movement were grown at continuous, low irradiance (Section 4.3.1), the movement of chloroplasts at high irradiance did not represent a limitation to their growth and it may be advantageous if leaves are exposed to short sunflecks on a low irradiance background.

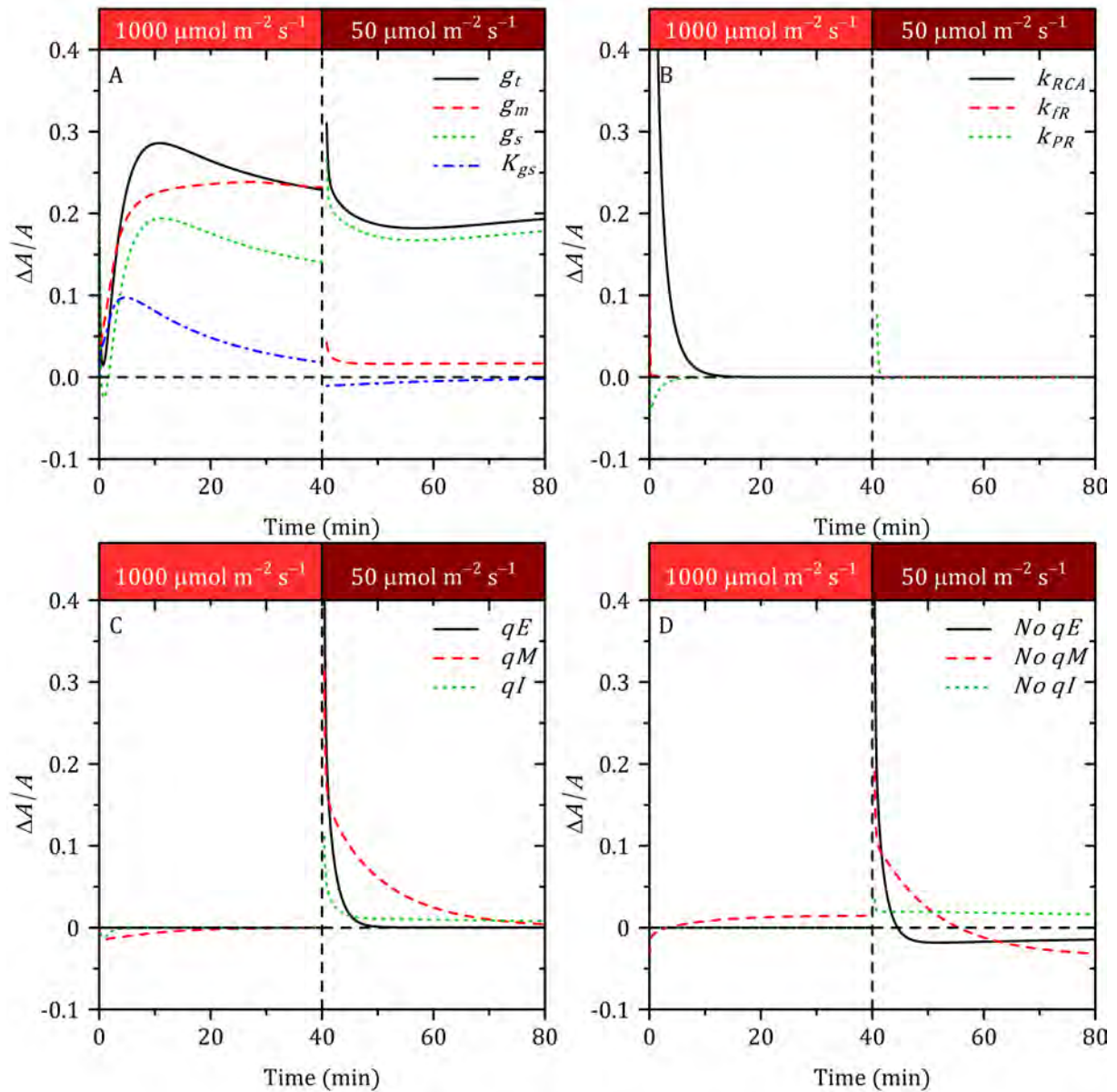


Figure 4.34: Simulated relative changes in CO₂ assimilation as a function of time after an increase in irradiance from $50 \mu\text{mol m}^{-2} \text{s}^{-1}$ to $1000 \mu\text{mol m}^{-2} \text{s}^{-1}$, followed by a second transient back to $50 \mu\text{mol m}^{-2} \text{s}^{-1}$, for different virtual mutants. The system was in steady-state at the beginning of the simulation. The dashed vertical line at Time = 40 min, indicates the transition between irradiances. Parameter values as in Table 4.7, with changes for each virtual mutant as described in Table 4.9. The mutant “ K_{gs} ” assumes stomatal conductance to be in quasi-steady state, whereas “ g_m ”, “ g_s ”, and “ g_t ” are mutants with non-limiting mesophyll conductance, non-limiting stomatal conductance and the combination of these two mutations, respectively. The mutants “ k_{RCA} ”, and “ k_{FR} ” are characterized by non-limiting kinetics of activation of Rubisco and enzymes that regenerate RuBP, respectively. The mutant “ k_{PR} ” assumes no delays in the release of CO₂ by photorespiration. The mutants “ qE ”, “ qI ”, and “ qM ” assume that qE , photoinhibition and chloroplast movement are in quasi-steady state. “No qI ” is a mutant without photoinhibition, “No qM ” lacks chloroplast movement, and “No qE ” does not have qE .

4.6 Factors limiting dynamic CO₂ assimilation at the canopy level

In the previous section, a detailed analysis of the limitations imposed by different processes on CO₂ assimilation after rapid changes in irradiance was performed. While this analysis provides valuable information at the leaf level and resembles experimental protocols used in dynamic photosynthesis research (Kaiser et al., 2015), it is necessary to scale these simulations to the canopy level in order to understand how they could affect plant production under natural environmental conditions, given the complex spatio-temporal distribution of irradiance within canopies. For this purpose, simulations of CO₂ assimilation at the canopy level (A_{can}) were performed for a theoretical canopy under different weather scenarios. A subset of the virtual mutants discussed above was then used to quantify the limitations imposed by different processes on A_{can} .

A 3D canopy, composed of squared leaves, each with an area of 100 cm², and randomly distributed within a canopy, was constructed. Although the model has been calibrated and validated with measurements on *A. thaliana*, the 3D canopy was constructed to resemble a typical commercial field crop (e.g., cereal) with high LAI and complete canopy closure. The canopy had a height of 0.8 m and a leaf area density of 3.75 m² m⁻³, which results in a leaf area index of 3. The distribution of leaf angles with respect to the North (i.e., azimuth angles) was assumed to be uniform, whereas the inclination angles of the leaves followed a spherical distribution (Campbell, 1986). The modelling platform GroIMP (Kniemeyer et al., 2007) was used to construct the canopy and to calculate the irradiance absorbed by each leaf using a built-in ray tracer algorithm. Calculations were performed for a column of the canopy of 1 m² base area that contained 300 leaves.

Two irradiance scenarios were simulated: a clear day and a cloudy day. For the clear day scenario, the diurnal variation in diffuse and direct solar radiation was calculated using the equations by Spitters et al. (1986), assuming an atmospheric transmissivity of 75%, a latitude of 52° N and day of year (DOY) 172. For the cloudy day scenario, measurements of diffuse and direct solar radiation with a time resolution of 1 min at the Veenkampen (The Netherlands) weather station (latitude of 51.98° N) on 18th June 2015 (DOY 169) were used (Figure 4.36A). In both scenarios, the spectra of diffuse and direct solar radiation were calculated with the model of Bird and Riordan (1986) at a resolution of 5 nm and then binned into the wavebands defined by the following ranges of wavelengths: 320 – 400 nm, 400 – 500 nm, 500 – 600 nm, 600 – 700 nm and 700 – 2500 nm. The optical properties of the leaves were calculated for the same wavebands (see Section 4.2.4.2 for details) and were varied during the day to account for effects of chloroplast movement. An explicit Euler integration method with a time step of 1 min was used to calculate changes in the optical properties of the leaves according to Equations 4.36 – 4.40. Using a smaller time step did not change the simulations of the optical properties significantly, which indicates that adequate numerical convergence was achieved.

For each of the irradiance scenarios, three temperature scenarios were chosen corresponding to diurnal average air temperatures of 15 °C, 25 °C and 35 °C (Figure 4.36B). In the clear day scenario, it was assumed that air temperature varied during the day following a sinusoidal function of time, with maximum temperature occurring 2 hours after solar noon and a temperature amplitude of 8 °C (Figure 4.36B). In the cloudy day scenario, measured air temperature (with an average of 15.2 °C and small variations

during the day) was used and two additional temperature scenarios were built by adding 10 °C and 20 °C to the original scenario (Figure 4.36B). Although some of the combinations of irradiance and temperature may not result in realistic weather scenarios, this approach allowed evaluating the relative effects of temperature on A_{can} without confounding the analysis by changes in the other environmental factors.

For all the scenarios, a wind speed of 5 m s⁻¹ at the top of the canopy was assumed, decreasing exponentially with height with an extinction coefficient of 0.5 (Leuning et al. (1995)). The vapour pressure of the air was assumed constant and was adjusted such that the relative humidity was 80% at the moment of minimum temperature in the clear day scenarios, resulting in values of 0.85 kPa, 1.3 kPa and 2.96 kPa for the 15 °C, 25 °C and 35 °C temperature scenarios, respectively. The same values of vapour pressure were used for the cloudy day scenarios.

For each of the scenarios, the irradiance absorbed by every leaf within the canopy was calculated at each of the wavebands and for every minute of the simulated days. The resulting time series of irradiance for each leaf was then used as an input for the dynamic model of CO₂ assimilation. All leaves were assumed to have the same values for all the parameters in the model, except for Rubisco content (RB), the maximum potential rate of electron transport at 25 °C ($J_{max,25}$), and the maximum stomatal conductance (g_{swm}) which were assumed to decline exponentially with height within the canopy assuming an extinction coefficient of 0.21 (Yin and Struik, 2015) and average values of $RB = 1.58 \times 10^{-5}$ mol m⁻², $J_{max,25} = 1.44 \times 10^{-4}$ mol m⁻² s⁻¹ and $g_{swm} = 0.55$ mol m⁻² s⁻¹. The time series of assimilation generated for the different leaves were then aggregated to the canopy level to generate the values of A_{can} .

A potential problem with the use of Monte Carlo ray-tracing is that the simulations are stochastic. This introduces variations in the time series of irradiance which, although they may not be large (e.g. < 1%), they could distort the results of the analysis. At the same time, there is a trade-off between the number of rays (N) used in the ray-tracer and the stochastic variance in the output: while the computational time of the simulation increases linearly with N , the variance of a Monte Carlo simulation decreases at a rate in the order of $N^{-1/2}$ (Caflisch, 1998). The simulations were performed with 5 million rays, which was observed to be sufficient for a reasonably low variance in simulations with the GPU-based ray tracer within GroIMP.

To test the effect of stochastic variance in the output, all results discussed below were re-calculated by smoothing the time series of absorbed irradiance using a local polynomial regression (Cleveland et al., 1992) with a span of 0.01. The residuals after smoothing the time series were normally distributed with a standard deviation that represented 6% of the mean irradiance across different wavebands. The results, calculated with the smoothed time series, did not differ from the ones using the original time series (i.e., relative differences < 0.1%). Thus, the stochastic error in the simulations of absorbed irradiance did not have a significant effect on the analysis below.

In the clear day scenarios, simulated A_{can} decreased with air temperature (Figure 4.37A) and the diurnal pattern became progressively more asymmetric, with a pronounced reduction in CO₂ assimilation after the solar noon in the scenario with an average air temperature of 35 °C. The decrease in A_{can} between the 15 °C and 25 °C scenarios was caused by a doubling in photorespiration, which offsets the small increase

(13%) in carboxylation (Table 4.10). The additional decrease between the 25 °C and 35 °C scenarios was a combination of a further increase in the ratio between photorespiration and carboxylation and a decrease in Rubisco activation state due to thermal downregulation of Rca activity (Table 4.10). In addition, the asymmetry in the diurnal trend of A_{can} in the 35 °C scenario was caused by a decrease in carboxylation due to a progressive reduction in the activation state of Rubisco (results not shown).

In the cloudy scenarios, A_{can} oscillated at a high frequency in response to the fluctuations in solar irradiance (Figure 4.37B) resulting in very different diurnal pattern

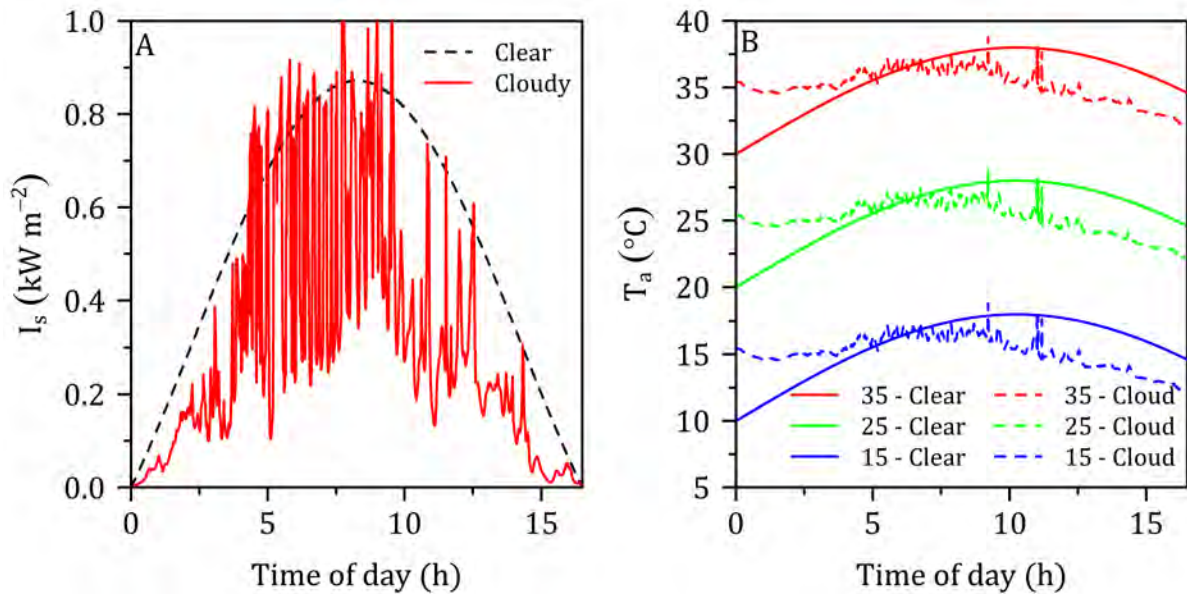


Figure 4.35: Simulated solar irradiance (I_s) for a clear day and measured solar irradiance on a cloudy day (A). Simulated air temperature (T_a) for a clear day with averages of 15 °C, 25 °C and 35 °C, measured air temperature in a cloudy day with average of 15.2 °C, plus two parallel temperature scenarios with averages of 25.2 °C and 35.2 °C (B).

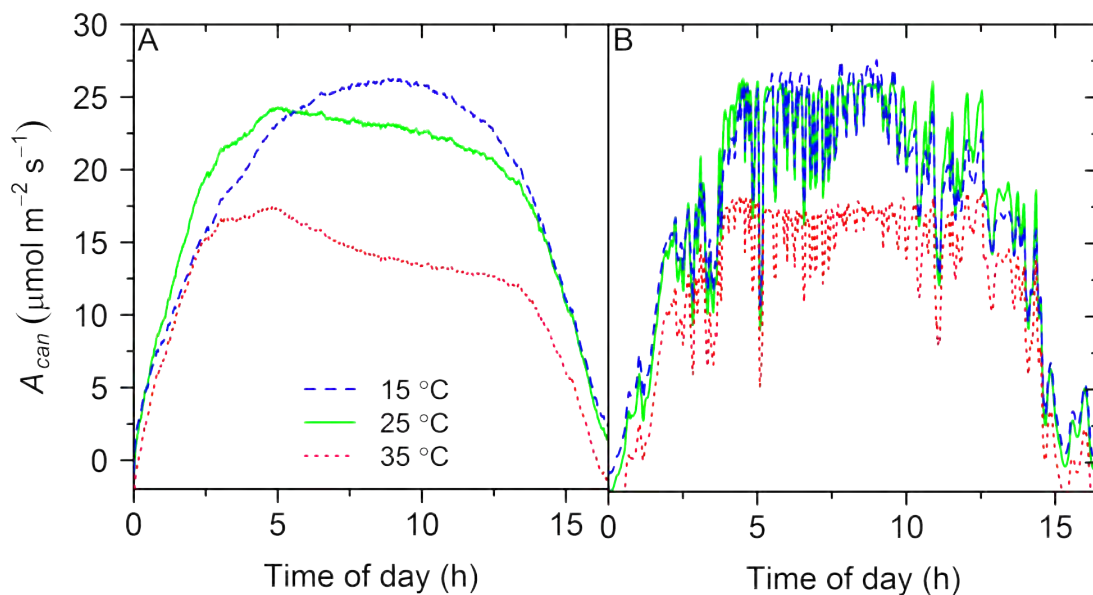


Figure 4.36: Simulated diurnal variation in canopy CO_2 assimilation (A_{can}) for the clear (A) and cloudy (B) weather scenarios at the different temperature scenarios.

compared to clear day scenarios. However, the relative effect of air temperature on total daily CO₂ assimilation was similar in both irradiance scenarios and could be explained by the same factors. The amount of photosynthetically irradiance absorbed by the canopy in the cloudy day scenario was 65% lower than in the clear day scenario, but CO₂ assimilation only decreased between 6% to 13% (Table 4.10) due to the increase in the efficiency at which the absorbed irradiance was used. Part of this increase is associated to the non-linear response of CO₂ assimilation to irradiance, but also due to a reduction in average leaf temperature of 1.2 °C (Table 4.10), as the result of the lower energy load on leaves, which resulted in lower ratios between photorespiration and carboxylation.

Using the values in Table 4.10 as a reference, the virtual mutants described in Table 4.9 were used to compute the limitation of the different processes on daily A_{can} . An additional mutant (“No Reg”) was used to quantify the total limitation on daily A_{can} imposed by regulation of enzymes in the Calvin cycle, the electron transport chain, and the kinetics of stomatal conductance.

Across the different irradiance and temperature scenarios, the total relative decrease on daily A_{can} for the “No Reg” mutant varied between 5.0% and 9.2% with larger limitations observed in the cloudy scenarios (Figure 4.38). When individual processes were analysed, the largest limitations were found for chloroplast movement (2.2% – 4.7%), photoinhibition (1.0% – 2.5%) and activation of Rubisco (1.0% – 2.8%). These processes also had a large effect on leaf-level A (Figure 4.35). However, these limitations were not as large as the total diffusional limitation imposed by stomatal and mesophyll conductances (2.55% – 26.10%), especially at intermediate and high temperature. These results indicate that, at the canopy level, limitations on dynamic assimilation after a decrease in irradiance are as important as after increases in irradiance.

Although there were clear limitations on CO₂ assimilation due to CO₂ diffusion, there was a small effect of the kinetics of stomatal conductance (g_{sw}). Furthermore, the assumption of quasi-steady state g_{sw} resulted in an increase of CO₂ assimilation (Figure 4.38). Further analysis of the simulations (results not shown) indicates that, in the clear day scenarios, g_{sw} was close to the quasi-steady state situation except for the first 2 hours of the simulated days (when g_{sw} was below the steady-state) and in the last hour of the simulated day (when g_{sw} was above the steady-state). Thus, for most of the day, the kinetics of changes in stomatal conductance hardly affected CO₂ assimilation. In addition, when the kinetics were relevant, the irradiance was low, thus having a smaller contribution to total daily CO₂ assimilation. In the cloudy day scenario, stomatal conductance was within 10% of the steady-state value throughout the simulated day (results not shown), such that changes in the kinetics did not have a major impact on simulated A . A possible explanation for g_{sw} being close to quasi-steady state for most of the limitations is that, given the parameters in Table 4.7, stomatal conductance saturated at relatively low irradiance (see Figure 4.32).

The large effect of Rubisco activation at high temperatures (Figure 4.38) can be expected given the decrease in Rca activity (Table 4.10), in agreement with the experimental results reported by Yamori et al. (2012) in *Oryza sativa*. Similarly, the larger effect of photoinhibition on daily A_{can} at low and high temperatures may be explained by the temperature dependency of the rate of repair of PSII reaction centres (Figure 4.16). The effect of chloroplast movement on CO₂ assimilation varied with temperature due to the thermal sensitivity of the kinetics and magnitude of chloroplast movement (Figure 4.13).

Limitations by the kinetics of enzyme activation in the regeneration phase of the Calvin cycle and by the delay in CO₂ released by photorespiration were negligible (Figure 4.38), which coincide with the small effects observed at the leaf level (Figure 4.35). It has previously been hypothesized that the fast deactivation of these enzymes would limit CO₂ assimilation under sunflecks (Pearcy et al., 1996). However, these analyses were performed at the leaf level, rather than at the canopy level, and, therefore, there is no reference to contrast the results in Figure 4.38. Nevertheless, some simplifications in the simulations may have influenced this result. Firstly, due to lack of adequate data, the kinetics of enzyme activation were not estimated from measurements on *A. thaliana*, but rather from published data on *Glycine max* (Sassenrath-Cole and Pearcy, 1994b), which may have caused inconsistencies among the parameter values. Secondly, due to technical limitations, the ray tracer calculated the distribution of irradiance at intervals of 30 s, whereas many sunflecks measured in the field last for less than 10 s (Way and Pearcy, 2012; Smith and Berry, 2013). Given that the rate of activation of these enzymes limits CO₂ assimilation during the first minute of photosynthetic induction (Pearcy et al., 1996), it would become more limiting for shorter sunflecks than the ones generated by the ray tracer.

The small limitation on daily A_{can} by the delay in CO₂ release due to photorespiration suggests a compensation of the positive and negative effects that this delay has on CO₂ assimilation after increasing and decreasing irradiance, respectively (Figure 4.35B). This may be the result of the specific regime of sunflecks and cloudflecks generated in the simulations and therefore these results cannot be generalized. Whether a more significant effect will be observed for different canopy structures or irradiance scenarios requires further research.

As expected from the simulations at the leaf level, assuming qE to be in quasi-steady state resulted in an increase in CO₂ assimilation, although very limited (less than 0.35%). Although the relative reductions in CO₂ assimilation observed at the leaf level were larger (Figure 4.35), these reductions occurred at low irradiances and thus low CO₂ assimilation, so the overall effect on canopy CO₂ assimilation is reduced. A similar reasoning explains a small effect of the kinetics of chloroplast movement and photoinhibition (Figure 4.38). In addition, the assumption of quasi-steady state for chloroplast movement and photoinhibition has a negative effect on CO₂ assimilation after increases in irradiance (Figure 4.35), which could compensate for the positive effects after decreases in irradiance.

Table 4.10: Canopy CO₂ assimilation integrated over the day (daily A_{can} , mol m⁻²), carboxylation ($V_{c,T}$, mol m⁻²) and photorespiration ($R_{p,T}$, mol m⁻²), diurnal average activation state of Rubisco ($\overline{f_{RB}}$) and Rubisco activase (\overline{RCA}) and diurnal average leaf temperature ($\overline{T_L}$, °C) for each combination of irradiance and temperature scenario. See text for details on the characteristics of each irradiance and temperature scenario.

Irradiance	Temperature	Daily A_{can}	$V_{c,T}$	$R_{p,T}$	$\overline{f_{RB}}$	\overline{RCA}	$\overline{T_L}$
Clear	15	1.13	1.40	0.19	0.59	0.71	16.4
	25	1.10	1.67	0.41	0.61	0.94	26.0
	35	0.71	1.53	0.50	0.43	0.44	35.8
Cloudy	15	0.98	1.17	0.13	0.53	0.68	15.3
	25	0.98	1.40	0.28	0.54	0.95	24.8
	35	0.67	1.32	0.36	0.39	0.54	34.6

The effect of removing qE was small, and always negative, indicating that decreases in CO₂ assimilation due to the reduction in photoprotection were slightly higher than the gains in CO₂ assimilation during the first minutes after each decrease in irradiance (as depicted in Figure 4.35D). This negative net effect agrees with reports of *A. thaliana* qE mutants having a lower biomass production and seed yield under natural environments relative to the wildtype (Külheim et al., 2002; Krah and Logan, 2010), although canopies of *A. thaliana* are not comparable with the canopy assumed in the simulations.

The stronger effects obtained when removing chloroplast movements or photoinhibition (Figure 4.38) contrasted with the results obtained when these processes were assumed to be in quasi-steady state. Even though removing chloroplast movements increased photoinhibition, the decreases in absorptance affected CO₂ assimilation at both high and low irradiance (Figure 4.35), which could explain why removing chloroplast movement had a strong positive effect on CO₂ assimilation at the canopy level. Even though at the leaf level (Figure 4.35), the removal of photoinhibition increased time-integrated CO₂ assimilation by 70% more than the mutant where photoinhibition was in quasi-steady state, the difference was much larger at the canopy level. This emphasizes the importance of proper scaling to the canopy level, as results from leaf-level experiments do not translate directly to canopies under field conditions.

In summary, the analysis at the canopy level indicates that limitations to CO₂ assimilation under fluctuating irradiance can be attributed to different processes that play different roles during sunflecks and cloudflecks. Additionally, the results observed at the leaf level cannot be extrapolated directly to the canopy level. Very little is known of the differences in dynamic photosynthesis across species. Therefore, the results obtained in these simulations should not be extrapolated to other situations. On the other hand, the different processes responsible for limiting CO₂ assimilation were similar across various temperatures and irradiance scenarios, suggesting that differences in the physical environment (in the absence of abiotic stress) may not be so relevant in determining the relative importance of each process.

The results obtained from canopy simulations imply that ignoring the regulation of enzymes in the Calvin cycle, regulation of the electron transport, and the dynamics of g_{sw} would result in an overestimation of 5.0% and 9.2% of daily A_{can} . These results question how accurate commonly used models of canopy photosynthesis (Wang and Jarvis, 1990; De Pury and Farquhar, 1997) and plant biomass production (Jones et al., 2003; Yin and Struik, 2010) are, and warrant further research to improve existing models.

4.7 Conclusions

The model accurately predicted the dynamics of CO₂ assimilation and NPQ_{sv} under a wide range of irradiances. It could capture the effect of several photosynthetic mutations on these dynamics, by modifying the values of the parameters that were expected to vary with the mutations, which strongly suggests that the assumptions of the model are sound and represent the underlying mechanisms correctly. In addition, the model was calibrated and validated successfully, employing mostly measurements of gas exchange and chlorophyll fluorescence, which facilitates future adaptation of the model to different species and growth conditions.

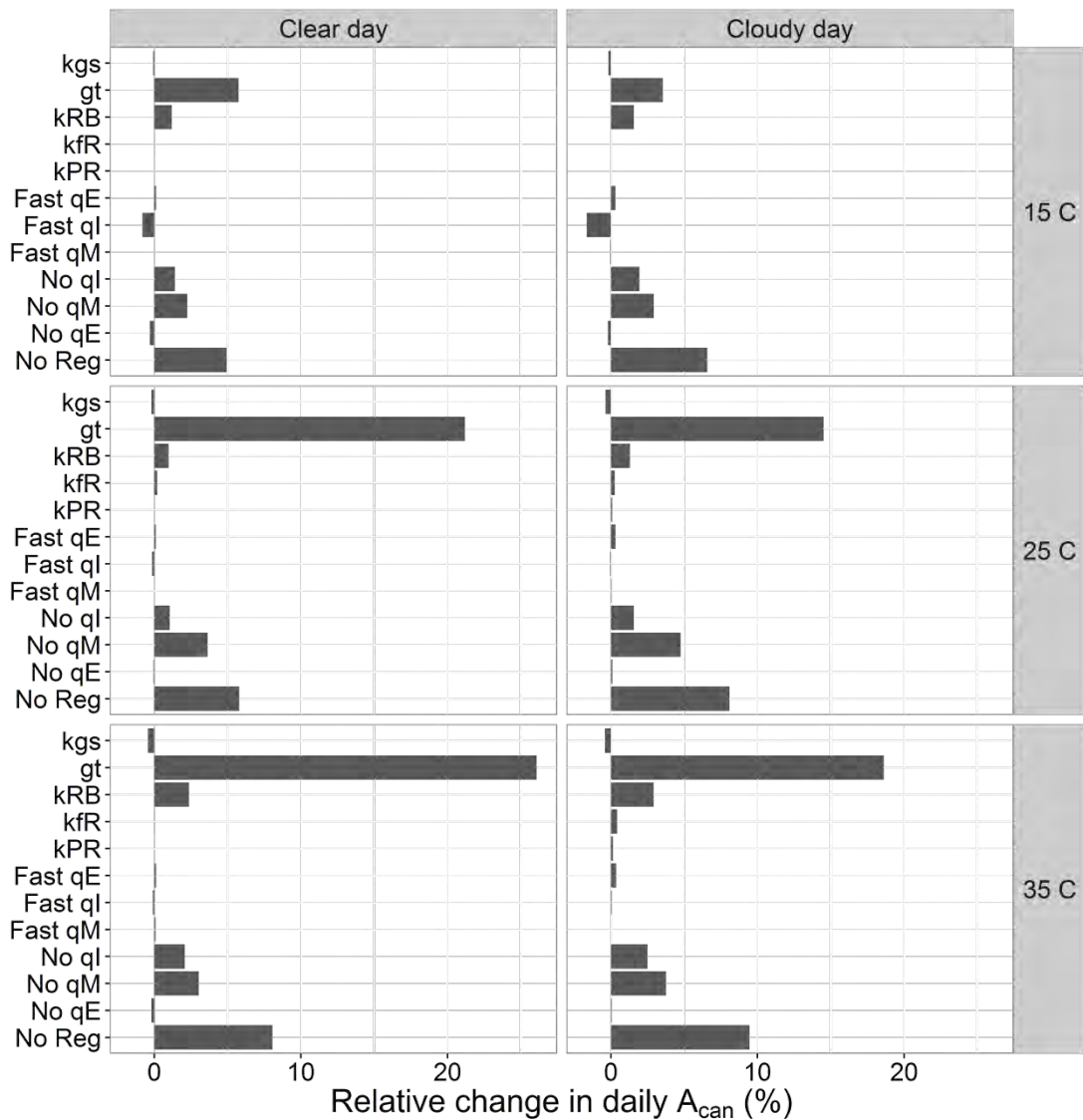


Figure 4.37: Simulated relative change in daily canopy CO₂ assimilation (A_{can}) for the different weather scenarios and the different virtual mutants. The mutant “kgs” assumes stomatal conductance to be in quasi-steady state, whereas “gt” is a mutant with non-limiting mesophyll and stomatal conductance (i.e., chloroplast [CO₂] equal to leaf surface [CO₂]). The mutants “kRB”, and “kfR” are characterized by non-limiting kinetics of activation of Rubisco and enzymes that regenerate RuBP, respectively. The mutant “kPR” assumes no delays in the release of CO₂ by photorespiration. The mutants “Fast qE”, “Fast qI”, and “Fast qM” assume that qE, photoinhibition and chloroplast movement are in quasi-steady state. “No qI” is a mutant without photoinhibition, “No qM” lacks chloroplast movement, and “No qE” does not have qE.

The analysis of limiting factors at the leaf and canopy levels indicated that the dynamics of CO₂ assimilation are limited by several mechanisms that play different roles depending on whether irradiance transiently increases or decreases. The most relevant mechanisms are activation of Rubisco, photoinhibition, qE, chloroplast movement and stomatal and mesophyll conductances. These processes decreased canopy photosynthesis by more than 5% across several scenarios, including clear sky conditions, a dense canopy and mild temperatures. The methodology presented in this study may be used to improve current predictions of canopy CO₂ assimilation in models of plant production.

4.8 Acknowledgements

This work was carried out within the IPOP programme on Systems Biology financed by Wageningen University. This research was also partly funded by the BioSolar Cells open innovation consortium, supported by the Dutch Ministry of Economic Affairs, Agriculture and Innovation. We thank Herman N. C. Berghuijs and Thomas D. Sharkey for their useful suggestions in the early phase of model development.

Chapter 5

An in silico* analysis of the metabolic regulation of the photosynthetic electron transport chain in C3 plants

* **Morales A**, Yin X, Harbinson J, Driever SM, Molenaar J, Struik PC, Kramer DM *An in silico* analysis of the metabolic regulation of the photosynthetic electron transport chain in C3 plants. *In preparation*

Abstract

A simulation model of the reactions in the photosynthetic electron transport chain of C3 species is presented. The model was parameterized with data from the literature, with a focus on measurements reported for *Arabidopsis thaliana*. A dataset was constructed from multiple sources including measurements of steady-state and dynamic gas exchange, chlorophyll fluorescence and absorbance spectroscopy on *A. thaliana* ecotype under different levels of irradiance and CO₂. The dataset was used to adjust some of the parameter values in the literature and test predictions of the model under the different experimental conditions. The simulations suggested that the cyclic electron flux around PSI was lower than the flux into alternative electron sinks. Furthermore, the model predicted that, under specific conditions, reduction of ferredoxin by plastoquinol is possible, especially during photosynthetic induction. The model analysis also revealed that the relationship between ATP synthesis and proton motive force was highly regulated by the concentrations of substrates for ATP synthesis, and this facilitated an increase in non-photochemical quenching under conditions of metabolic limitations such as low CO₂ or high irradiance. The generality of the model allows for further research on the regulation of photosynthetic electron transport.

Table of contents

5.1 Introduction	129
5.2 Model description and parameterization	132
5.2.1 Photosystem II	132
5.2.2 Cytochrome b ₆ f complex	145
5.2.3 Photosystem I	147
5.2.4 Electron transport pathways	151
5.2.5 ATP synthase	160
5.2.6 Proton motive force	164
5.2.7 Calvin cycle and CO ₂ diffusion	167
5.2.8 Regulation by thioredoxin	173
5.2.9 Concentrations and amounts	177
5.2.10 Model implementation	182
5.3 Model tests with experimental results	182
5.3.1 Net CO ₂ assimilation and Rubisco regulation	183
5.3.2 Chlorophyll fluorescence	184
5.3.3 Electrochromic shift	187
5.3.4 P ₇₀₀ reduction	190
5.4 In silico analysis of metabolic regulation of electron transport	192
5.4.1 Steady-state regulation	192
5.4.2 Effect of H ⁺ /ATP ratio	196
5.4.3 Dynamic regulation	200
5.5 Conclusions	205
5.6 Acknowledgements	205

Abbreviations

A_0 : Primary stable electron acceptor in the reaction centre of PSI, ADP: Adenosine diphosphate, A_n : Net CO₂ assimilation at the leaf level, ATP: Adenosine triphosphate, ATPase: ATP synthase, cyt b₆f: Cytochrome b₆f complex, ΔpH : Difference in pH between stroma and lumen, $\Delta\Psi$: Voltage of the electrical field across thylakoid membrane, ecs: Electrochromic shift, EPO: Zeaxanthin epoxidase, F_0 : Subunit of ATP synthase embedded inside the thylakoid membrane, F_1 : Subunit of ATP synthase exposed to the stroma, FBPase: Fructose-1,6-bisphosphatase, Fd: Ferredoxin, FNR: Ferredoxin-NADP⁺ reductase, FQR: Ferredoxin-plastoquinone reductase, FTR: Ferredoxin-thioredoxin reductase, g_H : ATP synthase conductance, I: Irradiance, ISP: Iron-sulfur protein, J : Rate of linear electron transport, J_{cyt} : Rate of electron transport through the cytochrome b₆f complex, J_{II} : Rate of electron transport through PSII, MAL: Malate, MDH: Malate dehydrogenase, MPR: Mehler peroxidase reaction, MT: Malate transporter, NH₄⁺: Ammonium, NO₂⁻: Nitrite, NO₃⁻: Nitrate, NADPH: Nicotinamide adenine dinucleotide phosphate, NDH: NADPH dehydrogenase, NiR: Nitrite reductase, NPQ: Non-photochemical quenching, OAA: Oxaloacetate, OEC: Oxygen evolving complex, P₆₈₀: Chlorophyll pigment in the reaction centre of PSII, P₇₀₀: Chlorophyll pigment in the reaction centre of PSI, Pc: Plastocyanin, ϕ_{II} : Quantum yield of PSII, PGA: Phosphoglycerate, Pi: Inorganic phosphate in the stroma, pmf: Proton motive force, PQ: Plastoquinone, PQH₂: Plastoquinol, PSI: Photosystem I, PSI_{ac}: Antenna complexes associated to PSI, PSII: Photosystem II, PSII_{ac}: Antenna complexes associated to PSII, Q_A: Quinone A in the reaction centre of PSII, Q_B: Quinone bound to Q_B site of PSII, qE: Energy-dependent non-photochemical quenching, Q_N: Plastoquinone binding site on the stromal side of cytochrome b₆f complex, Q_P: Plastoquinol binding site on the luminal side of cytochrome b₆f complex, Rca: Rubisco activase, RMSE: Root mean square error, Rubisco: Ribulose-1,5-bisphosphate carboxylase oxygenase, RuBP: Ribulose-1,5-bisphosphate, VDE: Violaxanthin de-epoxidase, v_H : Flux of H⁺ through the ATP synthase, WWC: Water-water cycle, Y_Z: Tyrosine residue of the oxygen evolving complex

5.1 Introduction

The environmental conditions faced by photosynthetic organs of plants are variable with diurnal fluctuations of irradiance, temperature, humidity, and CO₂ mole fraction ([CO₂]). In addition, absorbed irradiance can be in excess of the capacity of the system to assimilate CO₂. Under such conditions, photosynthesis faces two main challenges:

1. To dissipate the excess of energy that could otherwise result in the production of reactive oxygen species (Foyer and Shigeoka, 2011).
2. To couple the production and demand of ATP and NADPH in chloroplasts and maintain homeostasis in a fluctuating environment (Noctor and Foyer, 2000).

These two objectives must be met simultaneously, and several physiological mechanisms have been identified as contributing to these goals (Kramer et al., 2004a). These mechanisms include (Kramer et al., 2004a):

1. Non-photochemical quenching (NPQ) of excess energy absorbed by photosynthetic pigments;

2. Cyclic electron transport around Photosystem I (PSI) including NADPH dehydrogenase (NDH) and ferredoxin-plastoquinone reductase (FQR);
3. Consumption of electrons by alternative electron sinks including the water-water cycle (WWC), the malate valve (MDH), and NO_2^- reduction (NiR);
4. Regulation of the proton motive force (pmf) via changes in ATP synthase activity and transport of ions across the thylakoid membrane.

The study of NPQ in leaves makes use of modulated chlorophyll fluorescence which is a commonly applied technique for photosynthesis research. These studies rely on measurements of the decrease in maximum chlorophyll fluorescence (F'_m) associated to Photosystem II (PSII). However, the values of F'_m are affected by other processes, such as chloroplast movement (Dall'Osto et al., 2014), photoinhibition of PSII (Gilmore et al., 1996), and state transitions that redistribute excitations among the photosystems (Ruban and Johnson, 2009). Research on NPQ has also made use of measurements of chlorophyll fluorescence lifetimes (Renger et al., 1995; Gilmore et al., 1996; Matsubara and Chow, 2004), although this has often been done under *in vitro* conditions. Recently, Sylak-Glassman et al. (2016) obtained measurements of chlorophyll fluorescence lifetimes in leaves of *A. thaliana*, and these were correlated with changes in F'_m through time, under conditions of no chloroplast movement.

Under most circumstances, decreases in F'_m consist mostly of the so-called qE process, which is sensitive to the pH of the lumen of the thylakoid (Zaks et al., 2013), but absolute measurements of this pH are difficult to obtain *in vivo* and current estimates remain uncertain (Takizawa et al., 2007). In recent decades, molecular genetic methods, usually performed on *A. thaliana*, have been used to study NPQ (Horton, 2014). Screening of mutant collections allowed the identification of NPQ mutants (Niyogi et al., 1998; Li et al., 2000b), whereas manipulations in gene expression (Niyogi et al., 2005) and the creation of double and triple mutants (Dall'Osto et al., 2014) have further contributed to understanding NPQ *in vivo*.

There are also strong limitations to the experimental study of cyclic electron transport and alternative electron sinks. Although several techniques are available for targeting different mechanisms (Bloom et al., 2002; Munekage et al., 2002; Driever and Baker, 2011; Walker et al., 2014; Strand et al., 2016a), these techniques do not provide a complete quantification of the different fluxes of electrons and their regulation in response to environmental conditions and rely on assumptions that are difficult to verify experimentally (Driever and Baker, 2011; Johnson, 2011; Walker et al., 2014; Fan et al., 2016).

Research into the regulation of the pmf is also hindered by difficulties in obtaining absolute measurements of pmf, lumen pH, and the electrical field across the thylakoid membrane *in vivo*. Recent technological developments (Sacksteder and Kramer, 2000; Sacksteder et al., 2001) have led to a better understanding of the regulation of ATP synthase (Kanazawa and Kramer, 2002), the partitioning of pmf into an electrical and pH component (Cruz et al., 2001; Takizawa et al., 2007) and the range of pH for the lumen of the thylakoid that is physiologically feasible (Kramer et al., 1999). However, the multiple, complex interactions that determine the transport of H^+ across the thylakoid membrane and their effect on the regulation of electron transport have not yet been fully elucidated (Strand and Kramer, 2014).

Given the limitations of current experimental technology and the complex interactions among the different mechanisms, simulation models are an attractive, complementary research tool (Kitano, 2002). Indeed, several models of the photosynthetic electron transport chain in C3 plants have been published in recent years (Laisk et al., 2009a; Riznichenko et al., 2009; Ebenhöh et al., 2011; Zaks et al., 2012; Zhu et al., 2013; Tikhonov and Vershubskii, 2014; Matuszyńska et al., 2016). However, most of these models were developed to study specific processes, which resulted in simplifications of the rest of the biological processes that were not considered to be critical for the simulations. For example, several models developed to study qE (Ebenhöh et al., 2011; Zaks et al., 2012; Matuszyńska et al., 2016) simplify the transport of electrons from PSII to NADPH and do not include any equations describing the Calvin cycle and associated pathways. While such simplifications may be justified for specific situations, they prevent studying the complex interactions that characterize the behaviour of the system under natural conditions, where the electron transport chain is coupled to the Calvin cycle.

A more detailed model can aid in identifying molecular targets for genetic improvement of crops, as demonstrated by previous use of models of photosynthesis (Zhu et al., 2007; Ort et al., 2011). Although detailed models of the electron transport chain have been published recently (Laisk et al., 2009a; Zhu et al., 2013), they do not include some of the mechanisms of interest in the regulation of electron transport chain, such as NiR (Bloom et al., 2002) or NDH (Strand et al., 2016b). Furthermore, the testing of these models with experimental data has been limited to a narrow range of experimental conditions and measurement techniques, and thus it is not known to what extent their simulations realistically reproduce the conditions *in vivo*. Therefore, a new model is required, developed with the aim of analysing complex interactions among the mechanisms involved in the regulation of the electron transport.

In this study, a mechanistic model of the electron transport chain is presented with the aim of analysing, *in silico*, the role of the different mechanisms involved in the regulation of photosynthesis under steady-state and fluctuating environmental conditions. Special emphasis is placed on qE (i.e., rapidly-reversible form of NPQ), cyclic electron transport, alternative electron sinks, linear electron transport, and ATP synthase. Still, all relevant process at the chloroplast and leaf level are included in order to ensure physiologically reasonable conditions. This includes a simplified, yet realistic description of the stromal metabolism. This allows accurate simulations of the demand of ATP and NADPH under different environmental conditions.

In order to ensure transparency and facilitate future usage and adaptations of the model, a complete and detailed description of all equations in the model, including the assumptions behind their derivation and their parameterization from the literature, is included in Section 4.2. The model was tested with published experimental data gathered on *Arabidopsis thaliana*, including steady-state and dynamic measurements of gas exchange, modulated chlorophyll fluorescence, and absorbance changes at different wavelengths that probed the activities of PSI and ATP synthase, as well as pmf and its components. These tests are discussed in Section 5.3. After testing the model, additional simulations were performed and analysed in order to gain insight into the metabolic regulation of the electron transport chain under different steady-state and dynamic environmental conditions. Finally, the simulations include a sensitivity analysis to discuss the effect of the assumed H^+ /ATP stoichiometry of ATP synthase on the system. These simulations are discussed in Section 5.4.

5.2 Model description and parameterization

In this section, the equations of the model are presented and discussed, along with the assumptions behind them and how such assumptions affect the interpretation of the simulations of the model and limit its range of applicability. The values of all parameters are given in tables and discussed in the text, with references to the sources from which they were obtained. This section is structured according to the different modules of the model (Figure 5.1):

- Photosystem II (Section 5.2.1)
- Cytochrome b_6f (Section 5.2.2)
- Photosystem I (Section 5.2.3)
- Electron transport pathways (Section 5.2.4)
- ATP synthase (Section 5.2.5)
- Proton motive force (Section 5.2.6)
- Calvin cycle and CO_2 diffusion (Section 5.2.7)
- Regulation by thioredoxin (Section 5.2.8)

In addition, in Section 5.2.9 a set of possible parameter values for the amounts of protein complexes, electron carriers, metabolites in the stroma and maximum enzymatic activities are presented and discussed. The reason for a dedicated section is that although the kinetic properties of the different enzymes and protein complexes are expected to be conserved or to vary in a narrow range within the different taxa of C_3 plants, the concentrations and maximum activities discussed in Section 5.2.9 vary with species (Albertsson et al., 1991; Chow et al., 1991; Wullschleger, 1993; Burkey et al., 1996) and growth conditions (Schöttler and Tóth, 2014). Given that no publication exists reporting all such values, it is especially important to have a consistent set of values. Whenever possible, values for *A. thaliana* (or other C_3 species) grown at low irradiance were used as a reference, as this species and growth conditions have been used in many of the experiments on the regulation of the electron transport chain in recent years. Since photosynthesis in plants acclimates to growth conditions (Bailey et al., 2001), and there is an important inter- and intraspecific genetic variation in photosynthesis (Flood et al., 2011), conclusions of this study may not apply to other species or growth conditions. Some parameters were further adjusted to obtain better fits to specific datasets that were used to test the model, as discussed in Section 5.3.

Technical details pertaining to the implementation of the model and algorithms required for its solution are discussed in Section 5.2.10 with the aim of aiding potential users interested in using or adapting the model.

5.2.1 Photosystem II

PSII is a protein complex in the thylakoid membrane that catalyses the reduction of plastoquinone (PQ) into plastoquinol (PQH_2) and extraction the electrons from H_2O via the oxygen evolving complex (OEC). The energy required for these reactions is absorbed by the pigments in the antenna complexes associated to PSII (PSII_{ac}) and transferred to

the reaction centre. This results in the oxidation of a chlorophyll pigment in the reaction centre (P_{680}) and reduction of Pheophytin (Pheo). The charge is further transported to a quinone permanently bound to PSII (Q_A) and finally to PQ bound at the Q_B site (Figure 5.2). P_{680}^+ drives the oxidation of H_2O into O_2 catalysed by the OEC, through a Tyrosine residue (Y_Z) that acts as intermediate. A complete cycle of the OEC produces four electrons and releases four H^+ into the lumen, that contributes to the formation of a H^+ gradient across the thylakoid membrane that is used for ATP synthesis. In this section, the equations describing these reactions are presented and discussed. First, we describe the calculations of light harvesting and energy balance in $PSII_{ac}$, followed by an empirical model of chloroplast movement and their effect on absorptance of irradiance by the leaf, ending with a comprehensive model of the reactions of electron transport within the reaction centre. The kinetics of these reactions are modelled according to the following master equation:

$$\frac{d\mathbf{PSII}}{dt} = \mathbf{A} \cdot \mathbf{PSII}, \quad (5.1)$$

where \mathbf{PSII} is the set of all possible states of PSII, which is determined by the combination of the states of the components of PSII and \mathbf{A} is a matrix of rate constants of the different transitions among states of PSII. These transitions are not related to the “state transitions” involving redistribution of excitations between PSII and PSI (Ruban and Johnson, 2009). In this model, the state of PSII is determined by the states of Y_Z , P_{680} , Pheo, Q_A , Q_B and $PSII_{ac}$. Y_Z may be in its basal state or oxidised (Y_Z and Y_Z^+), P_{680} may be in its basal state (P_{680}), excited (P_{680}^*) or oxidised (P_{680}^+).

Pheo is assumed to be either in its basal state ($Pheo$) or reduced ($Pheo^-$). Q_A is also assumed to be either in its basal state (Q_A) or singly reduced (Q_A^-). The Q_B site may be empty (Q_B^e), occupied by a quinone (Q_B), a semiquinone (Q_B^-) or a quinol (Q_B^{2-}). $PSII_{ac}$ may contain no excitations (L^0) or one excitation (L^1).

Several models of PSII kinetics have been published in recent years (Lebedeva et al., 2002; Lazár, 2003; Zhu et al., 2005; Belyaeva et al., 2008; Laisk et al., 2009b; Zaks et al., 2012; Loriaux et al., 2013; Xin et al., 2013; Zhu et al., 2013). These models differ in their degree of detail, with the most comprehensive description achieved by the model by Xin et al. (2013), who use a Monte Carlo kinetic approach to integrate the master equation.

Many of these models have been used to analyse chlorophyll fluorescence induction at scales of microseconds to seconds (Stirbet and Govindjee, 2011). However, the goal in this study is to investigate the regulation of the electron transport chain at the scale of seconds to minutes, such that much of the molecular detail about PSII can be simplified, by assuming rapid equilibrium among internal components and using proper parameterizations.

The combination of states of all the components results in 192 different possible states in which PSII can be. This means that \mathbf{A} is a matrix with 36864 elements. Fortunately, most of those elements are null as many of the transitions have a negligible probability of occurring or are physically impossible due to conservation of energy and matter. Each element a_{ij} of \mathbf{A} corresponds to a transition from state i to state j and the value of a_{ij} is the rate constant (or expression that evaluates to a relative rate of change) of such a transition. In order for Equation. 5.1 to be valid, rows and columns of \mathbf{A} have to be in the

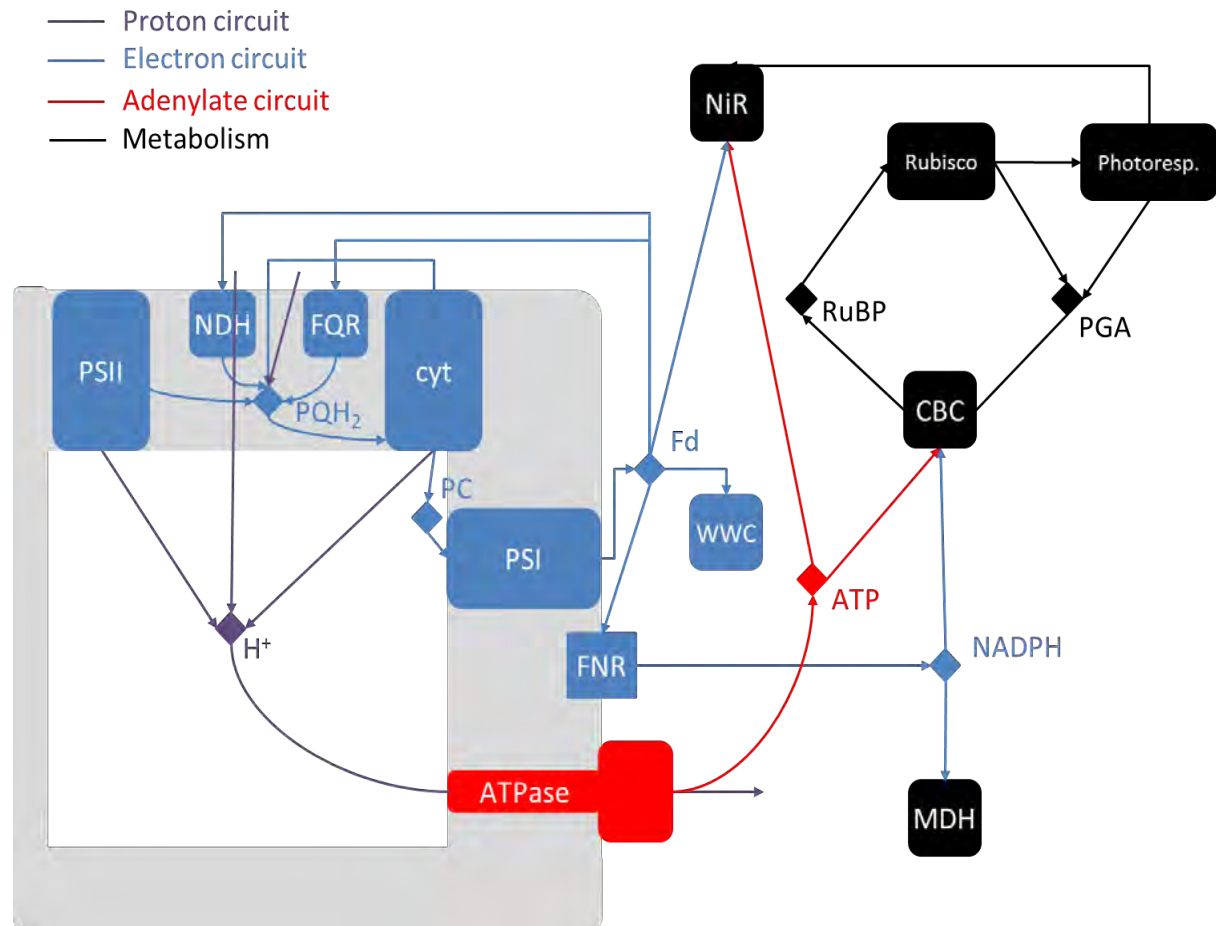


Figure 5.1: Schematic diagram of the model of photosynthetic electron transport chain coupled to the stromal metabolism. PSI and PSII stand for Photosystem I and II. NDH and FQR are the cyclic pathways involving NDH and PGRL1. *cyt* stands for the cytochrome *b₆f* complex, whereas ATPase is the ATP synthase. FNR represents the Fd-NADP⁺ reductase enzymes and WWC stands for the water-water cycle. MDH represents malate dehydrogenase and export of malate via the malate shuttle. NiR represents all reactions within the chloroplast responsible for reduction of NO₂⁻ and assimilation of NH₄⁺. CBC stands for the reactions involved in conversion of PGA into RuBP and Photoresp. represents the reactions involved in the conversion of phosphoglycolate into PGA coupled to release of CO₂ and NH₄⁺ from the mitochondria.

same order as **PSII**. Given that most elements of **A** are null it is only necessary to document the transitions that have non-null values. In addition, many of the transitions are characterized by the same kinetics and are thus lumped together.

To facilitate the documentation of the large number of transitions included in the model, a novel notation is used. This notation introduces the concept of “transition rule”. A transition rule is a notation that identifies all transitions in the master equation where the components of the system that are modified by the transition or affect the transition are the same. The assumption is that the kinetics (i.e., a rate constant or expression that evaluates to a rate constant) associated with a transition rule apply equally to the set of transitions identified by the transition rule. For example, the transition rule $Y_Z^+ \rightarrow Y_Z$ (Table 5.1) denotes the reduction of an oxidised Y_Z by OEC. There are 96 transitions where Y_Z^+ evolves into Y_Z , each associated with different states of P_{680} , Pheo, Q_A , Q_B and PSII_{ac}, which are all left unspecified by the rule.

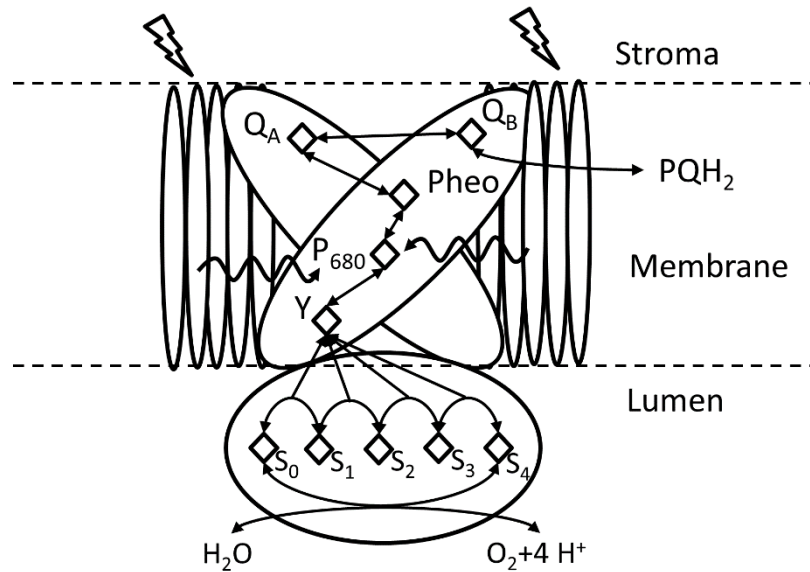


Figure 5.2: Schematic diagram of electron transport within Photosystem II.

This means that the 96 locations in matrix **A** that correspond to this transition will all have the same value which will be either a rate constant or an expression that evaluates to a relative rate of change. In most cases, transition rules will affect more than one component and the different components are separated by a “.” symbol. The order in which different components appear in a transition rule is irrelevant. Each transition rule has an associated rate vector that contains the rates of all the transitions identified by a transition rule. Each rate vector is calculated as the product of the starting state vector of the transition times the expression that characterizes the kinetics of the transition rule. The electron transport through PSII is simulated by 744 transitions identified by 21 transition rules (Table 5.1).

5.2.1.1 Light harvesting and energy transfer

5.2.1.1.1 Light harvesting

The fraction of incident irradiance (I , $\mu\text{mol m}^{-2} \text{s}^{-1}$) absorbed by a leaf (α), in the absence of chloroplast movement, is calculated from the total chlorophyll content of the leaf (C_t , mol m^{-2}) using the empirical relationship described by Evans (1993):

$$\alpha = \frac{C_t}{C_t + K_{chl}}, \quad (5.2)$$

where K_{chl} (mol m^{-2}) is an apparent half-saturation constant assumed to have a value of $7.6 \times 10^{-5} \text{ mol m}^{-2}$ (Evans, 1993), originally determined for *Medicago sativa*. Similar relationships were found for other species (Lin and Ehleringer, 1982; Kirchhoff et al., 1989; Evans and Poorter, 2001).

Because K_{chl} was estimated from measurements at the leaf level, it includes absorption by non-photosynthetic pigments (e.g., phenolic compounds and non-photosynthetic carotenoids) as well as auxiliary photosynthetic pigments (carotenoids) that transfer energy to chlorophyll pigments of PSII_{ac} and the antenna complexes associated to PSI (Solovchenko, 2010). A detailed simulation of the optical properties of a leaf is beyond the

Table 5.1: Transition rules and associated kinetics that describe the electron transport within Photosystem II (see text for details on how transition rules are used to construct the master equation). Each rate-vector is calculated as the initial state times the kinetic expression and the number of elements of each vector is indicated with parentheses.

Transition rule	Kinetics expression	Rate vector
$Y_Z^+ \rightarrow Y_Z$	$k_{oec}/(1 + 10^{n_{oec}(pK_{oec}-pH_L)})$	\mathbf{v}_{oec} (96)
$Y_Z \cdot P_{680}^+ \rightarrow Y_Z^+ \cdot P_{680}$	k_{tp}	\mathbf{v}_{tp} (24)
$Y_Z^+ \cdot P_{680} \rightarrow Y_Z \cdot P_{680}^+$	$k_{tp}/\exp[(-\Delta G_{tp} - \Delta\Psi f_{tp}F)/RT]$	\mathbf{v}_{pt} (24)
$L^0 \rightarrow L^1$	$I\alpha_p\alpha_r\sigma_2/\Sigma\text{PSII} + f_{II}^{ex}k_{UU}$	\mathbf{v}_{e2} (96)
$L^1 \rightarrow L^0$	$k_{f2} + k_{D2} + Qk_{qE} + k_{UU}$	\mathbf{v}_{q2} (96)
$L^1P_{680} \rightarrow L^0P_{680}^*$	k_{ac}	\mathbf{v}_{ac} (48)
$L^0P_{680}^* \rightarrow L^1P_{680}$	k_{ca}	\mathbf{v}_{ca} (48)
$P_{680}^* \cdot Pheo \cdot Q_A \rightarrow P_{680}^+ \cdot Pheo^- \cdot Q_A$	k_{cso}	\mathbf{v}_{cso} (12)
$P_{680}^* \cdot Pheo \cdot Q_A^- \rightarrow P_{680}^+ \cdot Pheo^- \cdot Q_A^-$	k_{csc}	\mathbf{v}_{csc} (12)
$P_{680}^+ \cdot Pheo^- \cdot Q_A \rightarrow P_{680}^* \cdot Pheo \cdot Q_A$	$k_{cso}/\exp[(-\Delta G_{cso} - \Delta\Psi f_{cs}F)/(RT)]$	\mathbf{v}_{cro} (12)
$P_{680}^+ \cdot Pheo^- \cdot Q_A^- \rightarrow P_{680}^* \cdot Pheo \cdot Q_A^-$	$k_{csc}/\exp[(-\Delta G_{csc} - \Delta\Psi f_{cs}F)/(RT)]$	\mathbf{v}_{crc} (12)
$Pheo^- \cdot Q_A \rightarrow Pheo \cdot Q_A^-$	k_{pa}	\mathbf{v}_{pa} (48)
$Pheo \cdot Q_A^- \rightarrow Pheo^- \cdot Q_A$	$k_{pa}/\exp[(E_{m,Q_A} - E_{m,Pheo} - \Delta\Psi f_{pa}F)/(RT)]$	\mathbf{v}_{ap} (48)
$Q_A^- Q_B \rightarrow Q_A Q_B^-$	k_{ab1}	\mathbf{v}_{ab1} (24)
$Q_A Q_B^- \rightarrow Q_A^- Q_B$	$k_{ab1}/\exp[(E_{m,Q_A} - E_{m,Q_B/Q_B^-} - \Delta\Psi f_{ab}F)/(RT)]$	\mathbf{v}_{ba1} (24)
$Q_A^- Q_B^- \rightarrow Q_A Q_B^{2-}$	k_{ab2}	\mathbf{v}_{ab2} (12)
$Q_A Q_B^{2-} \rightarrow Q_A^- Q_B^-$	$k_{ab2}/\exp[(E_{m,Q_A} - E_{m,Q_B^-/Q_B^{2-}} - \Delta\Psi f_{ab}F)/(RT)]$	\mathbf{v}_{ba2} (12)
$Q_B^e \rightarrow Q_B^{2-}$	$k_{bPQH2b} PQH_2/(PQH_2 + PQ)$	\mathbf{v}_{bPQH2b} (24)
$Q_B^{2-} \rightarrow Q_B^e$	k_{bPQH2r}	\mathbf{v}_{bPQH2r} (24)
$Q_B^e \rightarrow Q_B$	$k_{bPQb} PQ/(PQH_2 + PQ)$	\mathbf{v}_{bPQb} (24)
$Q_B \rightarrow Q_B^e$	k_{bPQr}	\mathbf{v}_{bPQr} (24)

scope of this model, but the effects can be incorporated by defining correction factors derived from the spectral distribution of low-light quantum yield of CO₂ uptake. The average spectrum from 22 species determined by McCree (1972) was used to calculate these correction factors, assuming a normalized correction factor of 1 for the red waveband. Thus, the fraction of I used for photochemistry (α_p) is calculated as

$$\alpha_p = \alpha(f_b c_{fb} + f_g c_{fg} + f_r), \quad (5.3)$$

where f_b , f_g and f_r are the fractions of I in the blue (400 – 500 nm), green (500 – 600 nm) and red (600 – 700 nm) wavebands respectively and c_{fb} and c_{fg} are the correction factors

for blue and green wavebands with values of 0.76 and 0.89 calculated from the curve published by McCree (1972). By default, an uniform distribution of I across the three wavebands is assumed. C_t is calculated from the amounts of PSII and PSI and the number of chlorophyll molecules per reaction centre (a_{II} and a_I) as

$$C_t = a_{II}\Sigma\text{PSII} + a_I\Sigma\text{PSI}. \quad (5.4)$$

The values of a_I and a_{II} may change in the short term (minutes) due to state transitions, a mechanism that balances the distribution of energy to the two types of photosystems affecting a small fraction of the PSII_{ac} pool (Dietzel et al., 2008). State-transitions are restricted to low light as they are inhibited by reduction of thioredoxin (Rintamäki et al., 2000; Breitholtz et al., 2005; Nikkanen and Rintamäki, 2014). Recent evidence indicates that the magnitude of state transitions *in vivo* when exposed to changes in irradiance levels is small (Mekala et al., 2015), as opposed to changes in the spectrum to favour excitation of PSI or PSII (Hogewoning et al., 2012). Also, when measured under white light, the state transition mutant *stn7* of *A. thaliana* shows similar chlorophyll fluorescence parameters compared to the wildtype (Nilkens et al., 2010; Dall'Osto et al., 2014). Therefore, state transitions may play a more important role in response to changes in the spectrum of incoming irradiance, like a reduction in the red:far-red ratio by shading (McTavish, 1988), than in response to changes of irradiance levels. Such changes in the spectrum are beyond the scope of this model and the effect of state transitions are therefore not taken into account. The values of a_I and a_{II} may also change with acclimation to irradiance, as certain components of PSII_{ac} (e.g., LHCII) bind PSI_{ac} (Wientjes et al., 2013).

In order to reproduce correctly the measurements of PSII and PSI quantum yield discussed in Section 5.3, the ratio $\sigma_2 = a_{II}\Sigma\text{PSII}/C_t$ was set to 0.55. In addition, Walters and Horton (1995) measured a PSII: C_t ratio of 2.01×10^{-3} at low irradiance. Assuming a PSI:PSII ratio of 0.8 (see Section 5.2.9), the values of a_I and a_{II} were deduced to be 196 and 200 (Table 5.2), respectively. With a PSII content of 0.80×10^{-6} mol m⁻² (see Section 5.2.9), this resulted in C_t being 285×10^{-6} mol m⁻² and an absorptance of 0.79.

The chloroplast light avoidance movement is a mechanism by which the positions of chloroplasts within a mesophyll cell are modulated by blue irradiance (I_b). At high I_b , chloroplasts migrate towards the anticlinal walls (avoidance movement), reducing α , whereas at low I_b , they migrate towards the periclinal walls (accumulation movement) increasing α (Haupt and Scheuerlein, 1990; Davis and Hangarter, 2012). To the knowledge of the author, no simulation model of chloroplast movement and its effect on the optical properties of leaves exists. Based on published measurements on *A. thaliana* (Kasahara et al., 2002; Davis and Hangarter, 2012; Łabuz et al., 2015), the following expressions were derived:

$$\alpha_{r_{SS}} = \begin{cases} 1 + \frac{I_b}{I_{ac}} \alpha_{rac} & \text{if } I_b \leq I_{ac} \\ 1 + \alpha_{rac} - \frac{\alpha_{ar} I_b + \alpha_{rav} - \sqrt{(\alpha_{ar} I_b + \alpha_{rav})^2 - 4\alpha_{ar} I_b \theta_{ar} \alpha_{rav}}}{2\theta_{ar}} & \text{if } I_b > I_{ac} \end{cases}, \quad (5.5)$$

and

$$\frac{d\alpha_r}{dt} = \begin{cases} (\alpha_{r_{SS}} - \alpha_r) k_{ia} & \text{if } \alpha_{r_{SS}} > \alpha_r \\ (\alpha_{r_{SS}} - \alpha_r) k_{da} & \text{if } \alpha_{r_{SS}} \leq \alpha_r \end{cases}, \quad (5.6)$$

where $\alpha_{r_{ss}}$ is the steady-state relative α (i.e., with respect to dark-adapted state), I_{ac} is the value of I_b at which the accumulation response is maximised, α_{rac} and α_{rav} are the maximum relative increase and decrease in α due to chloroplast movement, α_{ar} and θ_{ar} are the apparent initial slope and curvature of changes in $\alpha_{r_{ss}}$ with I_b , and $k_{i\alpha}$ and $k_{d\alpha}$ are the apparent rate constants at which relative α increases and decreases. In some species and/or growth conditions, changes in absorbance due to chloroplast movement are negligible (Davis et al., 2011; Higa and Wada, 2016). For such species, α_{rac} and α_{ar} can be set to zero to remove any effects of chloroplast movement. Details on the calibration of Equations 5.5 and 5.6 are given in Chapter 4 of this dissertation.

5.2.1.1.2 Energy balance in the antenna complexes of Photosystem II

Assuming 200 chl per PSI or PSII reaction centre and a total PSI + PSII content of $2 \mu\text{mol m}^{-2}$, the average time between two consecutive excitations per chl pigment in the antenna complexes is at least 25 ms (for an absorbed irradiance $\leq 10^4 \mu\text{mol m}^{-2} \text{s}^{-1}$). Given that the lifetime of an excitation in PSII_{ac} is in the order of nanoseconds or lower, the probability that two excitations coexist in one antenna complex is negligible. This allows defining, in the model, a binary component per PSII unit that determines whether the PSII_{ac} contains an excitation (L^0 and L^1 , see Table 5.1). Excitations are formed by absorbed irradiance (as calculated in the previous section) and excitations can be exchanged among PSII_{ac} (\mathbf{v}_{e2} in Table 5.1).

The method followed to simulate migration of excitations among PSII_{ac} is similar to that proposed by Lavergne and Trissl (1995). A rate constant k_{UU} of excitation migration among PSII_{ac} is assumed. For a given non-excited PSII_{ac}, the rate constant of excitation due to immigration of excitations is $f_{II}^{ex} k_{UU}$, where f_{II}^{ex} is the fraction of PSII_{ac} that is excited. For an excited PSII_{ac}, the rate constant of excitation emigration is k_{UU} . This approach results in a net transfer of energy from PSII units where excitations have a longer lifetime due to lack of photochemistry (i.e., closed reaction centres) to those where it is lower (i.e., open reaction centres). The main difference with the approach by Lavergne and Trissl (1995) is that they used the fraction of reaction centres that are closed as opposed to f_{II}^{ex} . Still, the most important factor in determining the lifetime of an excitation in PSII_{ac} is whether the reaction centre can perform photochemistry or not (based on the relative values of the different rate constants, see Table 5.3), so both modelling approaches will generate similar results. A value of $5 \times 10^9 \text{ s}^{-1}$ was assumed for k_{UU} as this gave an intermediate behaviour between the theoretical extremes of complete and absence of connection (i.e., the so-called lake and puddle models). Apart from migration towards other PSII_{ac}, excitations may also be transferred to the reaction centre, reversibly, or quenched as fluorescence or heat. Two forms of heat dissipation are considered: (i) a non-regulated form that is present in dark-adapted thylakoids and assumed constant, and (ii) a regulated form that increases with acidification of the lumen (qE).

The transfer of excitations from PSII_{ac} to P_{680} is assumed to be reversible with rate constants of $1.5 \times 10^{10} \text{ s}^{-1}$ (to the reaction centre) and $3.0 \times 10^{10} \text{ s}^{-1}$ (to the antennae) as determined by Holzwarth et al. (2006). Previous models of PSII have used values of the rate constant of fluorescence emission (k_{f2}) between $5.6 \times 10^7 \text{ s}^{-1}$ and $6.7 \times 10^7 \text{ s}^{-1}$ (Lavergne and Trissl, 1995; Xin et al., 2013; Zaks et al., 2013). The values of the basal rate constant of heat dissipation (k_{D2}) in those models varied between $2.45 \times 10^8 \text{ s}^{-1}$ and $5.5 \times 10^8 \text{ s}^{-1}$ (Lavergne and Trissl, 1995; Xin et al., 2013; Zaks et al., 2013), which agree

with maximum chlorophyll fluorescence lifetimes of 2 ns for PSII_{ac} in intact thylakoids (Belgio et al., 2012). Values of $6.7 \times 10^7 \text{ s}^{-1}$ and $5.0 \times 10^8 \text{ s}^{-1}$ were chosen for k_{f2} and k_{D2} , respectively (Table 5.2).

The magnitude of the rate constant associated to qE-dependent heat dissipation increases as the pH of the lumen decreases, due to changes in the concentration of zeaxanthin and protonation of the PsbS protein, although other xanthophylls may also play a role (Zaks et al., 2013). These effects are quantified in the model by a factor Q that varies between 0 and 1 and a maximum rate constant of qE-dependent heat dissipation (Table 5.2) of $1.9 \times 10^9 \text{ s}^{-1}$, which was necessary to obtain good agreement with measurements of NPQ (see Section 5.3 for details). The value of Q is calculated from the concentration of zeaxanthin and protonation of the PsbS protein as described below. The exact mechanism associated with qE is still under debate and current mathematical models therefore resort to phenomenological approaches (Zaks et al., 2012; Zhu et al., 2013; Matuszyńska et al., 2016). An adaptation of the “4-state” model described by Matuszyńska et al. (2016) was used in the current study, as it reproduces the kinetics of qE induction and relaxation best.

The factor Q is calculated as

$$Q = \gamma_1(1 - f_{ZX})f_{PsbSp} + \gamma_2 f_{ZX}f_{PsbSp} + \gamma_3 f_{ZX}(1 - f_{PsbSp}), \quad (5.7)$$

where f_{ZX} is the fraction of the xanthophyll pool in the form of zeaxanthin, f_{PsbSp} is the fraction of PsbS protein that is protonated and γ_1 (0.3), γ_2 (0.6) and γ_3 (0.1) are empirical parameters that add up to 1 and represent the contribution to qE of each combination of f_{ZX} and f_{PsbSp} . The fourth state (dark-adapted PSII) is already captured by k_{D2} . The values of the parameters are empirical and were estimated to ensure reasonable simulations of qE kinetics during induction and relaxation (see Section 5.3 for details). Changes in f_{PsbSp} are assumed to follow first-order kinetics as described by the expression

$$\frac{df_{PsbSp}}{dt} = \begin{cases} (f_{PsbSp,ss} - f_{PsbSp})k_{PsbSi} & f_{PsbSp,ss} \geq f_{PsbSp} \\ (f_{PsbSp,ss} - f_{PsbSp})k_{PsbSd} & f_{PsbSp,ss} < f_{PsbSp} \end{cases}, \quad (5.8)$$

where $f_{PsbSp,ss}$ is the steady-state fraction of PsbS that is protonated and k_{PsbSi} (s^{-1}) and k_{PsbSd} (s^{-1}) are the rate constants at which f_{PsbSp} increases and decreases, respectively. These rate constants do not necessarily represent the rate constants of protonation or deprotonation of PsbS, but rather quantify the time it takes for a protonation (or deprotonation) event to affect the quenching properties of PSII_{ac}. Using this approach, one is not required to make explicit assumptions about the mechanism by which such effect would take place. It is further assumed that changes in PsbS protonation are responsible for the initial rapid changes in maximum chlorophyll fluorescence yields during a light transient. With the data reported by Nilkens et al. (2010) on *A. thaliana*, k_{PsbSi} and k_{PsbSd} were estimated to be $1.7 \times 10^{-2} \text{ s}^{-1}$ and $3.0 \times 10^{-2} \text{ s}^{-1}$, respectively. Similar values could be deduced from the data by Dall'Osto et al. (2014).

The protonation of PsbS is assumed to follow a Hill equation with respect to the concentration of free protons. When expressed as a function of pH, such relationship adopts the following form (Takizawa et al., 2007):

$$f_{pH,PsbS} = \frac{1}{1 + 10^{n_p(pH_l - pK_p)}}, \quad (5.9)$$

Table 5.2: Parameters associated to light harvesting, chloroplast movement and non-photochemical quenching of excited chl states. See bottom of the table for sources.

Symbol	Description	Value	Source
K_{chl}	Apparent half-saturation constant of leaf-level absorptance with respect to chlorophyll content	$76 \times 10^{-6} \text{ mol m}^{-2} \text{ s}^{-1}$	1
a_I	Average number of chlorophyll molecules per PSI reaction centre	200	2
a_{II}	Average number of chlorophyll molecules per PSII reaction centre	196	2
I_{ac}	Blue light intensity at which the accumulation response is maximised	$1.6 \times 10^{-6} \text{ mol m}^{-2} \text{ s}^{-1}$	3
α_{rac}	Maximum relative increase in absorptance due to the chloroplast accumulation movement	0.05	3
α_{ar}	Apparent initial slope of the dependency of chloroplast avoidance movement on blue light	$6.55 \times 10^3 \text{ mol}^{-1} \text{ m}^2 \text{ s}$	3
α_{rav}	Maximum relative decrease in absorptance due to chloroplast avoidance movement	0.16	3
θ_{ar}	Curvature of the dependency of chloroplast avoidance movement on blue light	0.36	3
$k_{i\alpha}$	Apparent rate constant at which absorptance increases due to chloroplast movement	$2.50 \times 10^{-3} \text{ s}^{-1}$	3
$k_{d\alpha}$	Apparent rate constants at which absorptance decreases due to chloroplast movement	$3.84 \times 10^{-3} \text{ s}^{-1}$	3
c_{fb}	Correction factor for blue light due to absorption by non-photosynthetic and auxiliary pigments	0.76	4
c_{fg}	Correction factor for green light due to absorption by non-photosynthetic and auxiliary pigments	0.89	4
k_{f2}	Rate constant of excitation quenching as fluorescence in the antenna complexes of PSII	$6.67 \times 10^7 \text{ s}^{-1}$	5
k_{D2}	Basal (non-regulated) rate constant of excitation quenching as heat in the antenna complexes of PSII	$2.33 \times 10^8 \text{ s}^{-1}$	5
γ_1	Relative contribution of protonated PsbS to qE in the absence of zeaxanthin	0.3	6
γ_2	Relative contribution of protonated PsbS and zeaxanthin to qE	0.6	6
γ_3	Relative contribution of zeaxanthin to qE in the absence of protonated PsbS	0.1	6
k_{PsbSi}	Rate constant of qE increase due to protonation of PsbS	$1.7 \times 10^{-2} \text{ s}^{-1}$	7

Symbol	Description	Value	Source
k_{PsbSd}	Rate constant of qE decrease due to deprotonation of PsbS	$3.0 \times 10^{-2} \text{ s}^{-1}$	7
pK_p	pK of PsbS protonation	6.3	6
n_p	Hill coefficient of PsbS protonation	1	8
k_{VDE1}	Maximum rate constant of violaxanthin conversion into antheraxanthin	$2.33 \times 10^{-3} \text{ s}^{-1}$	9
k_{epo1}	Maximum rate constant of antheraxanthin conversion into violaxanthin	$1.83 \times 10^{-4} \text{ s}^{-1}$	10
k_{VDE2}	Maximum rate constant of antheraxanthin conversion into zeaxanthin	$8.33 \times 10^{-3} \text{ s}^{-1}$	9
k_{epo2}	Maximum rate constant of zeaxanthin conversion into antheraxanthin	$4.83 \times 10^{-4} \text{ s}^{-1}$	10
pK_v	pK of violaxanthin de-epoxidase activity with respect to pH of the lumen	6.4	8
n_v	Hill coefficient of violaxanthin de-epoxidase activity with respect to lumen pH	3	8
k_{qE}	Maximum rate constant of excitation quenching by qE in the antenna complexes of Photosystem II	$1.9 \times 10^9 \text{ s}^{-1}$	6

1. (Evans, 1993).
2. Calculated from data by Walters et al., (1999) and Walters and Horton (1995).
3. Calculated from multiple sources in Chapter 4 (Brugnoli and Björkman, 1992; Davis and Hangarter, 2012; Łabuz et al., 2015).
4. Calculated from McCree (1972)
5. (Xin et al., 2013).
6. Estimated from data in Section 5.4.
7. (Nilkens et al., 2010).
8. (Takizawa et al., 2007).
9. (Frommolt et al., 2001).
10. (Härtel et al., 1996).

where n_p and pK_p are the Hill coefficient and pK of the reaction of PsbS protonation, respectively. Takizawa et al. (2007) calculated from *in vivo* measurements values for n_p and pK_p of 1 and 6.8, though there was high uncertainty in the exact value of the latter given that the absolute measurements of lumen pH were not available. Zaks et al. (2012) estimated values for n_p and pK_p of 3 and 6.4, by fitting their model to time series of chlorophyll fluorescence, whereas Matuszyńska et al. (2016) assumed values for n_p and pK_p of 3 and 5.9 also by fitting their model to data. A good agreement between simulations and measurements (see Section 5.3 for details) was obtained assuming values of 1 and 6.3 for n_p and pK_p (Table 5.2).

Interconversions among the different pigments in the xanthophyll pool are catalysed by violaxanthin de-epoxidase (VDE) and zeaxanthin epoxidase (EPO). VDE is mostly located in the lumen and its activity is strongly dependent on lumen pH, whereas EPO is located in the stroma where the pH is highly buffered. Assuming first-order kinetics (Zaks et al., 2012; Zhu et al., 2013), the dynamics of the different components of the xanthophyll pool are described by the following system of equations:

$$\begin{aligned}
\frac{df_{VX}}{dt} &= -k_{VDE1}f_{pH}f_{VX} + k_{epo1}f_{AX}, \\
\frac{df_{AX}}{dt} &= k_{VDE1}f_{pH}f_{VX} - k_{epo1}f_{AX} - k_{VDE2}f_{pH}f_{AX} + k_{epo2}f_{ZX}, \\
\frac{df_{ZX}}{dt} &= k_{VDE2}f_{pH}f_{AX} - k_{epo2}f_{ZX},
\end{aligned} \tag{5.10}$$

where f_{VX} , f_{AX} and f_{ZX} are the fractions of the xanthophyll pool in the form of violaxanthin, antheraxanthin, and zeaxanthin, respectively; k_{VDE1} (s^{-1}) and k_{VDE2} (s^{-1}) are the rate constants of de-epoxidation, k_{epo1} (s^{-1}) and k_{epo2} (s^{-1}) are the rate constants of epoxidation, and f_{pH} is the relative effect of lumen pH of the activity of VDE. Frommolt et al. (2001) measured k_{VDE1} and k_{VDE2} in *Spinacia oleracea* at a pH of 5 ($f_{pH} = 1$) resulting in values of $2.33 \times 10^{-3} s^{-1}$ and $8.33 \times 10^{-3} s^{-1}$, respectively. Härtel et al. (1996) calculated k_{VDE1} and k_{VDE2} at high light (where VDE activity may not be maximized) for leaves of *Hordeum vulgare* and obtained similar values of $2.0 \times 10^{-3} s^{-1}$ and $9.17 \times 10^{-3} s^{-1}$, respectively. For the same species, Härtel et al. (1996) calculated k_{epo1} and k_{epo2} to be $1.83 \times 10^{-4} s^{-1}$ and $4.83 \times 10^{-4} s^{-1}$, respectively. The values of k_{VDE1} and k_{VDE2} by Frommolt et al. (2001) were used, as they represent true maximum rates, whereas the values of k_{epo1} and k_{epo2} were taken from Härtel et al. (1996). The same type of Hill equation as for PsbS protonation was used to calculate the coefficient f_{pH} as:

$$f_{pH} = \frac{1}{1 + 10^{n_v(pH_L - pK_v)}}, \tag{5.11}$$

where n_v and pK_v are the Hill coefficient and pK of VDE, respectively. Takizawa et al. (2007) calculated the apparent Hill coefficient and pK of de-epoxidation *in vivo* to be 4 and 6.8, respectively. These values are related to n_v and pK_v , but the relationship depends on the rate constants of epoxidation and de-epoxidation. In order to achieve the relationship reported by Takizawa et al. (2007) and given the rate constants assumed above, it is required to set $pK_v = 6.4$ and $n_v = 3$. This is in agreement with measurements of pK_v *in vitro* that range from 6.0 (Pfundel and Dilley, 1993) to 6.7 (Bratt et al., 1995). However, other models of qE, assumed a pK_v of 6.0 (Zaks et al., 2012), or 5.8 (Matuszyńska et al., 2016), which are at the limit or below *in vitro* values.

5.2.1.2 Electron transport within Photosystem II

Due to effects of the local electrical field, the rate constants of charge separation are considered different for reaction centres with oxidised and reduced Q_A , with values of $3 \times 10^9 s^{-1}$ and $4.7 \times 10^8 s^{-1}$, respectively (Roelofs et al., 1992). Charge separation is reversible and the apparent Gibbs free energy is also affected by the redox state of Q_A , with values of $-5.7 \cdot 10^3 J mol^{-1}$ and $-0.8 \cdot 10^3 J mol^{-1}$ (Table 5.3) for oxidised and reduced Q_A , respectively (Roelofs et al., 1992). Because charge separation results in the transport of a charge orthogonal to the thylakoid membrane surface, the free energy of this reaction is affected by the existence of an electrical field ($\Delta\Psi$) across the thylakoid membrane (Lebedeva et al., 2002). The effect is calculated based on the electrogenicity of the reaction using coefficients calculated by Belyaeva et al. (2008). Pheo reduces Q_A in a reversible reaction which is also affected by the electrical field across the thylakoid membrane. The midpoint redox potentials of Q_A and Pheo were assumed to be $-0.145 V$ (Krieger et al., 1995) and $-0.640 V$ (Rappaport et al., 2002), whereas the forward rate constant was set to $2.3 \times 10^9 s^{-1}$ (Roelofs et al., 1992).

The OEC contains a cluster with four atoms of manganese (Mn) that donates four electrons to Y_z^+ , leading to five states of the OEC (Figure 5.2), although the lifetime of the fifth state is negligible compared to the other states (Razeghifard et al., 1997). Although the different transitions are characterized by different kinetics (Dekker et al., 1984; van Leeuwen et al., 1993; Razeghifard et al., 1997), simulations with a full representation of the OEC indicated that the steady-state value of Y_z^+ was linearly related to the rate constant of Y_z oxidation (results not shown). This allowed to simplify the system and assume a single rate constant (k_{oec}) of Y_z^+ reduction. In addition, the relative distributions of OEC states barely changed with the rate constant of Y_z oxidation. This simplification relies on two assumptions: (i) the system is in quasi-steady state at the timescale of interest, and (ii) the oxidation of Y_z follows first-order kinetics and is kinetically limited by charge separation. From the measurements by Razeghifard et al. (1997) at 282 K, and correcting for the temperature dependency of the OEC (Reinman and Mathis, 1981) a value of $k_{oec} = 1.09 \times 10^4 \text{ s}^{-1}$ was calculated (the rate constants for the individual transitions were $k_{0 \rightarrow 1} = 5.7 \times 10^4 \text{ s}^{-1}$, $k_{1 \rightarrow 2} = 3.4 \times 10^4 \text{ s}^{-1}$, $k_{2 \rightarrow 3} = 5.7 \times 10^4 \text{ s}^{-1}$ and $k_{3 \rightarrow 0} = 3.7 \times 10^3 \text{ s}^{-1}$). The same calculation with data from other experiments (Dekker et al., 1984; van Leeuwen et al., 1993) yielded similar results for k_{oec} .

Y_z reduces P_{680}^+ in a reversible reaction which is also affected by the electrical field across the thylakoid membrane (Lebedeva et al., 2002). Brettel et al. (1984) observed that the rate constant of P_{680}^+ reduction by Y_z (k_{tp}) and the free energy of the reaction (ΔG_{tp}) were dependent on the state of the OEC. Thus, an average was calculated weighting by the probabilities of each state as in the previous calculation, yielding values for k_{tp} and ΔG_{tp} of $6.3 \times 10^6 \text{ s}^{-1}$ and $-2.81 \times 10^3 \text{ J mol}^{-1}$, respectively. The activity of the OEC decreases with acidification of the lumen (Reinman and Mathis, 1981; Ono and Inoue, 1988), which has been linked to the loss of Ca^{2+} from the Mn cluster (Ono and Inoue, 1988). A Hill equation was assumed (Table 5.1) and fitted to the data reported by Ono and Inoue (1988), resulting in a pK of 5.3 and a Hill coefficient (n_{oec}) of 1.

The reduction of Q_B follows the two-electron gate model (Crofts and Wraight, 1983). The intermediate state (Q_B^-) is bound very tightly to the site (Crofts and Wraight, 1983), such that only Q_B and Q_B^{2-} are exchanged with the free pool of PQ and PQH_2 . The reductions of Q_B and Q_B^- are reversible and also affected by the existence of an electrical field across the thylakoid membrane (Belyaeva et al., 2008). The rate constants of Q_B and Q_B^- reduction were set to $5.0 \times 10^3 \text{ s}^{-1}$ and $2.0 \times 10^3 \text{ s}^{-1}$, based on measurements by de Wijn and van Gorkom (2001), and are within the range of values reported in the literature for these parameters ($2.5 \times 10^3 - 5.0 \times 10^3 \text{ s}^{-1}$ and $1.2 \times 10^3 - 3.3 \times 10^3 \text{ s}^{-1}$, respectively (Lazár, 1999)). For the reduction of Q_B , an equilibrium coefficient of 20 was assumed (Diner, 1977; Crofts and Wraight, 1983) which implies a midpoint redox potential of $E_{mQ_B/Q_B^-} = -0.065 \text{ V}$.

The equilibrium coefficient for Q_B^- reduction is uncertain (Crofts and Wraight, 1983), although a value of 50 is often assumed (Joliot et al., 1992; Cleland, 1998; Lazár, 1999). However, predictions from these coefficients result in QA being more oxidised than observed in experiments (Joliot et al., 1992; Cleland, 1998). On the other hand, the equilibrium coefficient between bound Q_B^-/Q_B^{2-} and the free pool of PQ/ PQH_2 is 1 (Crofts and Wraight, 1983), which means that $E_{mQ_B/Q_B^{2-}} = E_{mPQ/PQH_2} = 0.08 \text{ V}$ (Strand et al., 2016b). Therefore, instead of using an equilibrium coefficient of 50, $E_{mQ_B^-/Q_B^{2-}}$ was derived from $E_{mQ_B/Q_B^{2-}}$ and E_{mQ_B/Q_B^-} , resulting in a value of 0.225 V. The exchange with

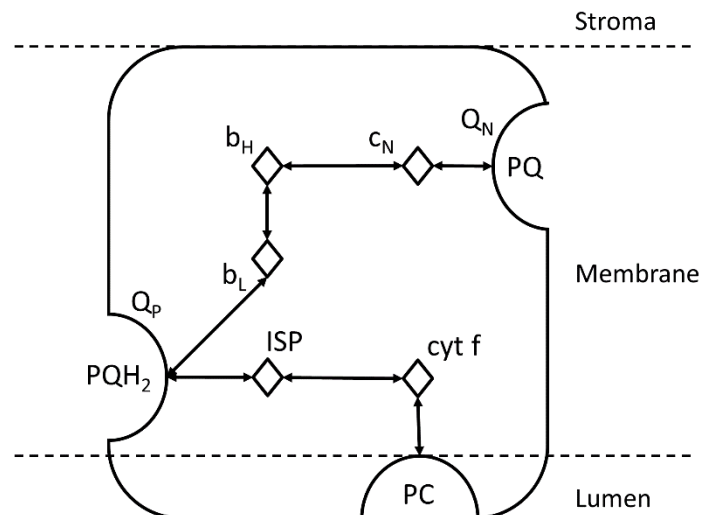


Figure 5.3: Schematic diagram of electron transport within the cytochrome *b₆f* complex and the binding sites of plastoquinone/ol and plastocyanin.

Table 5.3: Parameters associated with electron transport within PSII. See text for details on the source of each parameter value

Symbol	Description	Value	Source
f_{tp}	Fraction of $\Delta\Psi$ across the thylakoid that affects the equilibrium coefficient of P_{680}^+ reduction by Y_Z	0.1	1
k_{oec}	Average rate constant of Y_Z^+ by OEC	$1.09 \times 10^4 \text{ s}^{-1}$	2
n_{oec}	Hill coefficient of OEC activity with respect to pH	1	3
pK_{oec}	pK of OEC activity	5.28	3
k_{tp}	Rate constant of P_{680}^+ reduction by Y_Z	$6.3 \times 10^6 \text{ s}^{-1}$	4
ΔG_{tp}	Gibbs free energy of P_{680}^+ reduction by Y_Z in the absence of a $\Delta\Psi$ across the thylakoid	$-2.8 \times 10^3 \text{ J mol}^{-1}$	4
k_{ac}	Rate constant of energy transfer from PSII _{ac} to PSII reaction centre	$1.5 \times 10^{10} \text{ s}^{-1}$	5
k_{ca}	Rate constant of energy transfer from PSII reaction centre to PSII _{ac}	$3.0 \times 10^{10} \text{ s}^{-1}$	5
k_{cso}	Rate constant of charge separation in open reaction centres	$3 \times 10^9 \text{ s}^{-1}$	6
k_{csc}	Rate constant of charge separation in closed reaction centres	$4.7 \times 10^8 \text{ s}^{-1}$	6
f_{cs}	Fraction of $\Delta\Psi$ across the thylakoid that affects the equilibrium coefficient of charge separation	0.4	1
ΔG_{cso}	Gibbs free energy of charge separation in open reaction centres in the absence of a $\Delta\Psi$ across the thylakoid	$-5.7 \times 10^3 \text{ J mol}^{-1}$	6
ΔG_{csc}	Gibbs free energy of charge separation in closed reaction centres in the absence of a $\Delta\Psi$ across the thylakoid	$-0.8 \times 10^3 \text{ J mol}^{-1}$	6
k_{pa}	Rate constant of Q_A reduction by Ph	$2.3 \times 10^9 \text{ s}^{-1}$	6
f_{pa}	Fraction of $\Delta\Psi$ across the thylakoid that affects the equilibrium coefficient of Q_A reduction by Ph	0.4	1
$E_{m,QA}$	Midpoint redox potential of Q_A at a pH of 7	$-145 \times 10^{-3} \text{ V}$	7
$E_{m,Pheo}$	Midpoint redox potential of Q_A at a pH of 7	$-640 \times 10^{-3} \text{ V}$	8

k_{ab1}	Rate constant of Q_B by Q_A^-	$5 \times 10^3 \text{ s}^{-1}$	9
f_{ab}	Fraction of $\Delta\Psi$ across the thylakoid that affects the equilibrium coefficient of Q_B reduction by Q_A^-	0.1	1
E_{mQ_B/Q_B^-}	Midpoint redox potential of the Q/Q^- pair bound at the Q_B site	$-65 \times 10^{-3} \text{ V}$	10
k_{ab2}	Rate constant of Q_B^- reduction by Q_A^-	$2 \times 10^3 \text{ s}^{-1}$	9
$E_{mQ_B^-/Q_B^{2-}}$	Midpoint redox potential of the Q^-/Q^{2-} pair bound at the Q_B site	$225 \times 10^{-3} \text{ V}$	10
k_{bPQH_2b}	Rate constant of PQH_2 binding to the Q_B site	500 s^{-1}	9, 10
k_{bPQH_2r}	Rate constant of PQH_2 release from the Q_B site	500 s^{-1}	9, 10
k_{bPQb}	Rate constant of PQ binding to the Q_B site	500 s^{-1}	9, 10
k_{bPQr}	Rate constant of PQ release from the Q_B site	500 s^{-1}	9, 10

1. (Belyaeva et al., 2008).
2. Calculated from data by Razeghifard et al. (1997).
3. Calculated from data by Ono and Inoue (1988)
4. Calculated from data by Brettel et al. (1984).
5. (Holzwarth et al., 2006).
6. (Roelofs et al., 1992).
7. (Krieger et al., 1995).
8. (Rappaport et al., 2002).
9. (de Wijn and van Gorkom, 2001).
10. Calculated from data by Crofts and Wraight (1983).

the free pool of PQ and PQH_2 is assumed to follow the law of mass action (Table 5.1) with equal rate constants of binding and release for each species (Crofts and Wraight, 1983; Lazár, 1999). A rate constant of 500 s^{-1} was assumed based on measurements by de Wijn and van Gorkom (2001). Similar values ($120 - 1000 \text{ s}^{-1}$) have been reported in other studies, reviewed by Lazár (1999)

5.2.2 Cytochrome b_6f complex

The cytochrome b_6f complex (cyt b_6f) is a protein complex that catalyses the reduction of plastocyanin (Pc) by plastoquinol (PQH_2), coupled to the release of H^+ into the lumen, while the protonation of Q^{2-} occurs in the stroma. Cyt b_6f consists of multiple proteins and three binding sites that form two electron transport chains (Figure 5.3). The PQH_2 bound to the Q_P site first reduces the ‘‘Rieske’’ iron-sulfur protein (ISP), releasing $2 H^+$ into the lumen and producing a semiquinone anion (Q^-), which reduces heme b_L (Figure 5.3). A series of electron transfer reactions (known as the ‘‘high potential chain’’) follows the reduction of ISP and ends in the reduction of a bound Pc . The ‘‘low potential chain’’ transfers an electron in the reduced heme b_L to a Q or Q^- bound at the Q_N site (Figure 5.3). The consecutive oxidation of two PQH_2 at the Q_P site will reduce one Q bound at the Q_N site in what is called the ‘‘Q cycle’’. This Q cycle appears to be active under physiologically relevant conditions (Sacksteder et al., 2000).

The kinetics of electron transport within the cytochrome b_6f complex are described by the following master equation:

$$\frac{d\mathbf{cyt}}{dt} = \mathbf{B} \cdot \mathbf{cyt}, \quad (5.12)$$

where \mathbf{cyt} is the set of all possible states of the cytochrome b_6f complex, which is determined by the combination of the redox states of the components of cyt b_6f and \mathbf{B} is a

matrix of rate constants of the different transitions between states of cyt b₆f. The state of cyt b₆f is determined by the combinations of states of Q_P and Q_N and Pc-binding site. In the model, the Q_P site can be empty, occupied by Q or QH₂ (i.e., Q_P^e, Q_P, or Q_PH₂). The Q_N site can be empty or occupied by Q, Q⁻, or Q²⁻ (i.e., Q_N^e, Q_N⁻, Q_N²⁻, or Q_N²⁻). The Pc-binding site may be empty, occupied by an oxidised Pc, or a reduced Pc (i.e., Pc^e, Pc⁺, or Pc). The matrix **B** is documented in the rest of this section by means of transition rules (Table 5.4) and associated kinetics (see beginning of Section 5.2.1 for details on the notation used to describe transition rules). The electron transport through the cytochrome b₆f is simulated with 36 states and 142 transitions, identified by 16 transitions rules (Table 5.4).

It is assumed that the lifetime of Q⁻ bound to the Q_P site is negligible which prevents bypassing the Q cycle. Based on this assumption, the oxidation of PQH₂ bound to the Q_P site is modelled as a bifurcated reaction (Table 5.4), which is kinetically limited by reduction of ISP with a maximum rate constant k_{cyt} of 500 s⁻¹ (Zhu et al., 2013). This rate constant decreases with the pH of the lumen and the same mathematical expression as for VDE and PsbS (i.e., Equations 5.9 and 5.11) is used to describe this effect. A Hill coefficient of 1.5 was assumed (Table 5.5), based on the estimations by Takizawa et al. (2007), though good fits to measurements *in vitro* have been obtained with a Hill coefficient of 1 (Hope et al., 1994). The pK was assumed to be 6.1, lower than the original one by Takizawa et al. (2007) but closer to *in vitro* measurements (Nishio and Whitmarsh, 1993; Hope et al., 1994).

For simplicity and given that the internal electron transport within cyt b₆f can be assumed to be in quasi-steady state at the scale of milliseconds (Berry and Rumberg, 2001), the bifurcated reaction is modelled as a pseudo-reaction that reduces directly Q (or Q⁻) bound to the Q_N site, as well as bound Pc⁺ (Kramer and Crofts, 1993). That is, both electron transport chains within cyt b₆f are simulated in a single step. These electron acceptors are used to calculate the apparent equilibrium coefficient from differences in midpoint redox potentials. $E_{m,Pc}$ has a value of 0.36 V (Drepper et al., 1996). It is further assumed that $E_{m,Q_P/Q_P H_2} = E_{m,PQ/PQ H_2} = 0.08$ V (Strand et al., 2016b). The values of $E_{m,Q_N/Q_N^-}$ and $E_{m,Q_N^-/Q_N^{2-}}$ depend on the stability of the Q⁻ bound to the Q_N site (Osyczka et al., 2005). Assuming a stability constant of 10⁻⁵ (Hauska et al., 1996), and $E_{m,Q_N/Q_N^{2-}} = 0.08$ V, it is deduced that $E_{m,Q_N/Q_N^-} = -0.07$ V and $E_{m,Q_N^-/Q_N^{2-}} = 0.23$ V. The resulting equilibrium coefficients for the bifurcated reaction when Q is bound at the Q_N site is 212, whereas the reaction becomes practically irreversible when Q⁻ is bound at the Q_N site (> 10⁷).

Note that this equilibrium coefficients do not correspond to the concerted reduction of cyt f and cyt b_H, which has a lower value of 10 (Kramer and Crofts, 1993). Whereas $E_{m,Pc}$ is similar to the midpoint redox potential of cyt f, cyt b_H has a midpoint redox potential of -0.05 V, hence the differences in the calculations. Also, Kramer and Crofts (1993) assumed $E_{m,Q_P/Q_P H_2}$ to be 0.120 V. If a value of 0.08 V had been used, the equilibrium coefficient would have been 234, similar to the situation where Q is bound to the Q_N site.

The exchange of PQ, PQH₂ and Pc is simulated between the binding sites of cyt b₆f and the medium is assumed to follow the law of mass action (Table 5.4). The rate constants estimated *in vitro* by Schumaker and Kramer (2011) were used, except for Pc as they were not reported in the original study. Several experiments have measured a second order rate constant of Pc reduction by cyt b₆f, with values in the order of 10⁷ M⁻¹ s⁻¹ (Cruz-

Gallardo et al., 2012; Ueda et al., 2012). Given that the concentration of Pc in the thylakoid lumen is in the order of 10^{-3} M (see Section 5.2.9), the pseudo-first order rate constants of Pc reduction would be in the order of 10^5 s⁻¹. It is further assumed that the equilibrium coefficient between bound and free Pc is one.

5.2.3 Photosystem I

PSI is a protein complex in the thylakoid membrane that catalyses the reduction of ferredoxin (Fd) employing energy absorbed by chlorophyll pigments and extracting the electrons from Pc (Figure 5.4). The energy is absorbed by the pigments in the antennae complexes and transferred to a chlorophyll pigment in the reaction centre (P₇₀₀). This energy oxidises P₇₀₀ (P₇₀₀⁺), an electron is transferred to the first electron acceptor (A₀), followed by a chain of intermediates that at the end reduces bound Fd (Figure 5.4), whereas P₇₀₀⁺ is reduced by bound Pc in a reversible reaction. Structural data on the reaction centre of PSI indicates that there is one binding site for Pc and one binding site for Fd (Busch and Hippler, 2011; Ueda et al., 2012). The structure of PSI reveals two parallel electron transport chains (Rutherford et al., 2012). As for PSII and cyt b₆f, the nature of electron transport through PSI is such that it is most adequately described by the master equation formalism. That is, the kinetics of electron transport within PSI are modelled according to the master equation:

$$\frac{d\mathbf{PSI}}{dt} = \mathbf{C} \cdot \mathbf{PSI}, \quad (5.13)$$

where **PSI** is the set of all possible states of PSI, determined by the combination of states of the components of PSI and **C** is a matrix of rate constants of the different transitions between states of PSI. The state of PSI is determined by the redox states of bound Pc, the redox state of bound Fd, the state of the chlorophyll P₇₀₀ and the electron acceptor A₀. The binding site of Pc may be empty or occupied by a reduced or oxidised Pc (i.e., Pc^e , Pc , or Pc^+) and analogous states exist for Fd (i.e., Fd^e , Fd_o , or Fd_r). P₇₀₀ is assumed to be in its basal state, excited or oxidised (i.e. P_{700} , P_{700}^* , or P_{700}^+). Finally, A₀ may be in its basal state or reduced (i.e., A_0 , or A_0^-). The matrix **C** is documented in this section by means of transition rules (Table 5.6) and associated kinetics (see beginning of Section 5.2.1 for details on the notation used to describe transition rules). The electron transport through PSI is simulated with 54 states and 210 transitions identified by 15 transitions rules (Table 5.6).

The reduction of bound oxidised Fd occurs in the timescale of microseconds (Brettel, 1997). Thus, only two components (A₀ and Fd) are considered in the acceptor side and the intermediates are assumed to be in quasi-steady state. The rate constant of bound oxidised Fd reduction by A₀⁻ is thus assumed to be 10^6 s⁻¹ (Table 5.7) and the equilibrium coefficient is calculated from the midpoint redox potentials of A₀, $E_{m,A_0} = -1.1$ V (Brettel, 1997) and Fd, $E_{m,Fd} = E_{7m,Fd} - 59 \times 10^{-3} (pH_s - 7)$, where $E_{7m,Fd} = -0.42$ V (Schurmann, 2003), though there is some variation across species, from -0.39 V to -0.43 V (Cammack et al., 1977). On the donor side, the rate constant of P₇₀₀⁺ reduction by Pc was assumed to be 5.8×10^4 s⁻¹ and a rate constant of 4.5×10^3 s⁻¹ for the reverse reaction, as calculated by Drepper et al. (1996).

The antenna complexes of PSI (PSI_{ac}) can transfer excitations to the reaction centre with an efficiency close to 1 (Croce and van Amerongen, 2013). Although the quantum yield of energy transfer to the reaction centre (ϕ_I) is not exactly 1 since PSI_{ac} emit a small amount

of fluorescence at ambient temperature (Pfündel et al., 2013), energy losses at PSI_{ac} are generally not considered an important component in energy balance of PSI, especially given the strong quenching by P_{700}^+ which has a longer lifetime than P_{680}^+ at PSII. It is further assumed that all excitations transferred to a reaction centre containing P_{700}^+ are quenched as heat and that the PSI_{ac} are highly interconnected (Lavergne and Trissl, 1995). This means that, in the absence of kinetic limitation on the acceptor side of PSI and charge recombination, the quantum yield PSI is determined by the fraction of reaction centres that contain P_{700}^+ .

The rate constant of charge separation within PSI (k_{cs1}) cannot be measured directly, but it is estimated to be between 3×10^{11} and $2 \times 10^{12} \text{ s}^{-1}$ (Savikhin, 2006), so a value of $k_{\text{cs1}} = 10^{12} \text{ s}^{-1}$ was assumed. Shinkarev et al. (2002) estimated a rate constant of charge recombination between A_0 and P_{700}^+ of $3 \times 10^7 \text{ s}^{-1}$. However, this rate constant leads to large rates of charge recombination, since the reduction of P_{700}^+ by bound Pc^+ is three orders of

Table 5.4: Transition rules and associated kinetics that describe the electron transport within cytochrome *b_f* (see text for details on how transition rules are used to construct the master equation). Each rate-vector is calculated as the initial state times the kinetic expression and the number of elements of each vector is indicated within parentheses.

Transition rule	Kinetic expression	Rate vector
$Q_P H_2 \cdot Q_N \cdot \text{Pc}^+ \rightarrow Q_P \cdot Q_N^- \cdot \text{Pc}$	$k_{\text{cyt}} / (1 + 10^{n_c(pK_c - pH_L)})$	$\mathbf{v}_{\text{cyt}f1}$ (1)
$Q_P \cdot Q_N^- \cdot \text{Pc} \rightarrow Q_P H_2 \cdot Q_N \cdot \text{Pc}^+$	$\frac{k_{\text{cyt}}}{\exp\left[\frac{(E_{m,Q_N/Q_N^-} + E_{m,\text{Pc}} - 2E_{m,Q_P/Q_P H_2})F}{RT}\right]}$	$\mathbf{v}_{\text{cyt}b1}$ (1)
$Q_P H_2 \cdot Q_N^- \cdot \text{Pc}^+ \rightarrow Q_P \cdot Q_N^{2-} \cdot \text{Pc}$	$k_{\text{cyt}} / (1 + 10^{n_c(pK_c - pH_L)})$	$\mathbf{v}_{\text{cyt}f2}$ (1)
$Q_P \cdot Q_N^{2-} \cdot \text{Pc} \rightarrow Q_P H_2 \cdot Q_N^- \cdot \text{Pc}^+$	$\frac{k_{\text{cyt}}}{\exp\left[\frac{(E_{m,Q_N^-/Q_N^{2-}} + E_{m,\text{Pc}} - 2E_{m,Q_P/Q_P H_2})F}{RT}\right]}$	$\mathbf{v}_{\text{cyt}b2}$ (1)
$Q_P^e \rightarrow Q_P H_2$	$k_{pPQH2b} PQH_2 / (PQH_2 + PQ)$	\mathbf{V}_{pPQH2b} (12)
$Q_P H_2 \rightarrow Q_P^e$	k_{pPQH2r}	\mathbf{V}_{pPQH2r} (12)
$Q_P^e \rightarrow Q_P$	$k_{pPQb} PQ / (PQH_2 + PQ)$	\mathbf{V}_{pPQb} (12)
$Q_P \rightarrow Q_P^e$	k_{pPQr}	\mathbf{V}_{pPQr} (12)
$Q_N^e \rightarrow Q_N^{2-}$	$k_{nPQH2b} PQH_2 / (PQH_2 + PQ)$	\mathbf{V}_{nPQH2b} (12)
$Q_N^{2-} \rightarrow Q_N^e$	k_{nPQH2r}	\mathbf{V}_{nPQH2r} (12)
$Q_N^e \rightarrow Q_N$	$k_{nPQb} PQ / (PQH_2 + PQ)$	\mathbf{V}_{nPQb} (9)
$Q_N \rightarrow Q_N^e$	k_{nPQr}	\mathbf{V}_{nPQr} (9)
$\text{Pc}^e \rightarrow \text{Pc}^+$	$k_{cPcob} \text{Pc}^+ / (\text{Pc}^+ + \text{Pc})$	\mathbf{V}_{Pcob} (12)
$\text{Pc}^+ \rightarrow \text{Pc}^e$	k_{cPcor}	\mathbf{V}_{Pcor} (12)
$\text{Pc}^e \rightarrow \text{Pc}$	$k_{cPcrb} \text{Pc} / (\text{Pc}^+ + \text{Pc})$	\mathbf{V}_{Pcrb} (12)
$\text{Pc} \rightarrow \text{Pc}^e$	k_{cPcrr}	\mathbf{V}_{Pcrr} (12)

Table 5.5: Parameters associated with electron transport within *cyt b₆f*. See bottom of the table for sources.

Symbol	Description	Value	Source
k_{cyt}	Rate constant of PQH ₂ oxidation at the Q _P site of the <i>cyt b₆f</i>	500 s ⁻¹	1
n_c	Hill coefficient of the rate constant of PQH ₂ oxidation with respect to lumen pH	1.53	2
pK_c	pK of the rate constant of PQH ₂ oxidation with respect to lumen pH	6.1	3
$E_{m,PC}$	Midpoint redox potential of Pc	365×10 ⁻³ V	4
$E_{m,PQ/PQH_2}$	Midpoint redox potential of the PQ/PQH ₂ pair	80×10 ⁻³ V	5
$E_{m,Q_N/Q_N^-}$	Midpoint redox potential of the Q/Q ⁻ pair bound to the Q _N site	-67.5×10 ⁻³ V	5,6
$E_{m,Q_N^-/Q_N^{2-}}$	Midpoint redox potential of the Q ⁻ /Q ²⁻ pair bound to the Q _N site	227.5×10 ⁻³ V	5,6
k_{pPQH_2b}	Rate constant of PQH ₂ binding to the Q _P site	9.0×10 ⁴ s ⁻¹	7
k_{pPQH_2r}	Rate constant of PQH ₂ release from the Q _P site	3.4×10 ³ s ⁻¹	7
k_{pPQb}	Rate constant of PQ binding to the Q _P site	3.1×10 ⁴ s ⁻¹	7
k_{pPQr}	Rate constant of PQ release from the Q _P site	1.6×10 ³ s ⁻¹	7
k_{nPQH_2b}	Rate constant of PQH ₂ binding to the Q _N site	2.5×10 ³ s ⁻¹	7
k_{nPQH_2r}	Rate constant of PQH ₂ release from the Q _N site	2.2×10 ³ s ⁻¹	7
k_{nPQb}	Rate constant of PQ binding to the Q _N site	2.8×10 ⁵ s ⁻¹	7
k_{nPQr}	Rate constant of PQ release from the Q _N site	2.6 s ⁻¹	7
k_{cPcrb}	Rate constant of Pc binding to <i>cyt b₆f</i>	10 ⁵ s ⁻¹	8
k_{cPcrr}	Rate constant of Pc release from <i>cyt b₆f</i>	10 ⁵ s ⁻¹	8
k_{cPcob}	Rate constant of Pc ⁺ binding to <i>cyt b₆f</i>	10 ⁵ s ⁻¹	8
k_{cPcor}	Rate constant of Pc ⁺ release from <i>cyt b₆f</i>	10 ⁵ s ⁻¹	8

1. (Zhu et al., 2013).
2. (Takizawa et al., 2007).
3. (Hope et al., 1994).
4. (Drepper et al., 1996).
5. (Strand et al., 2016b).
6. (Hauska et al., 1996).
7. (Schumaker and Kramer, 2011).
8. Estimated (see text for details).

magnitude slower (Drepper et al., 1996), unless most A₀ is kept oxidised by the forward reactions (Rutherford et al., 2012). However, the model would not reproduce this phenomenon as it assumes a simplified structure for PSI. Therefore, in order to avoid excessive rate of charge recombination, a value of 200 s⁻¹ was used instead. This value was estimated from simulations to ensure that recombination within PSI did not limit the rate of electron transport under conditions where the acceptor-side of PSI was not kinetically limiting.

As with other protein complexes, binding and release of Pc and Fd is simulated by applying the law of mass action. The rate constants of binding and release of Pc were taken from Drepper et al. (1996) and different values were assumed depending on the redox state of Pc but not the redox state of P₇₀₀. The rate constants for Fd are not known, although Sétif (2001) estimated a second-order rate of Fd reduction by PSI in the order of 10⁸ M⁻¹

s⁻¹. Assuming an Fd concentration in the order of 10⁻⁴ M (see Section 5.2.9), this leads to a pseudo-first order rate constant in the order of 10⁴ s⁻¹. It is further assumed that an equilibrium coefficient between free and bound Fd of one.

Table 5.6: Transition rules and associated kinetics that describe the electron transport with Photosystem I (see text for details on how transition rules are used to construct the master equation). Each rate-vector is calculated as the initial state times the kinetic expression and the number of elements of each vector is indicated in parenthesis.

Transition rule	Kinetics expression	Rate vector
$P_{700} \rightarrow P_{700}^*$	$I\alpha\sigma_2\phi_1/\Sigma\text{PSI}$	\mathbf{v}_{e1} (18)
$P_{700}^* \cdot A_0 \rightarrow P_{700}^+ \cdot A_0^-$	k_{cs1}	\mathbf{v}_{cs1} (9)
$P_{700}^+ \cdot A_0^- \rightarrow P_{700} \cdot A_0$	k_{cr1}	\mathbf{v}_{cr1} (9)
$A_0^- \cdot Fd_o \rightarrow A_0 \cdot Fd_r$	k_{Fdr}	\mathbf{v}_{Fdr} (9)
$A_0 \cdot Fd_r \rightarrow A_0^- \cdot Fd_o$	$k_{Fdr}/\exp[F(E_{m,Fd} - E_{m,A0})/(RT)]$	\mathbf{v}_{Fdo} (9)
$Pc \cdot P_{700}^+ \rightarrow Pc^+ \cdot P_{700}$	k_{p700r}	\mathbf{v}_{p700r} (6)
$Pc^+ \cdot P_{700} \rightarrow Pc \cdot P_{700}^+$	k_{pcr}	\mathbf{v}_{pcr} (6)
$Pc^e \rightarrow Pc$	$k_{pPcrb} Pc/(Pc^+ + Pc)$	\mathbf{v}_{pCrb} (18)
$Pc^e \rightarrow Pc^+$	$k_{pPcob} Pc^+/(Pc^+ + Pc)$	\mathbf{v}_{pCob} (18)
$Pc^+ \rightarrow Pc^e$	k_{pPcor}	\mathbf{v}_{pCor} (18)
$Pc \rightarrow Pc^e$	k_{pPcrr}	\mathbf{v}_{pCrr} (18)
$Fd^e \rightarrow Fd_o$	$k_{Fdob} Fd_o/(Fd_r + Fd_o)$	\mathbf{v}_{Fdob} (18)
$Fd^e \rightarrow Fd_r$	$k_{Fdrb} Fd_r/(Fd_r + Fd_o)$	\mathbf{v}_{Fdrb} (18)
$Fd_o \rightarrow Fd^e$	k_{Fdor}	\mathbf{v}_{Fdor} (18)
$Fd_r \rightarrow Fd^e$	k_{Fdr}	\mathbf{v}_{Fdr} (18)

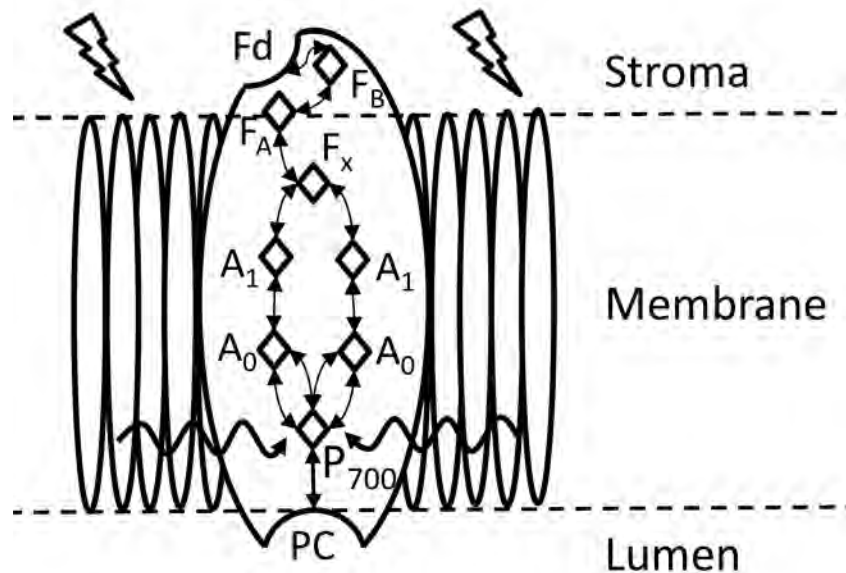


Figure 5.4: Schematic diagram of electron transport within Photosystem I.

Table 5.7: Parameters associated with electron transport within PSI and synthesis of NADPH. See bottom of the table for sources.

Symbol	Description	Value	Source
ϕ_I	Quantum yield of energy transfer to the reaction centre of PSI	1	1
k_{cs1}	Rate constant of charge separation in the reaction centre of PSI	10^{12} s^{-1}	2
k_{cr1}	Rate constant of charge recombination in the reaction centre of PSI	10^2 s^{-1}	3
k_{Fdr}	Rate constant of Fd reduction by A_0	10^6 s^{-1}	3
E_{m,A_0}	Midpoint redox potential of A_0	-1.1 V	4
$E_{m7,Fd}$	Midpoint redox potential of Fd at a pH of 7	$-420 \times 10^{-3} \text{ V}$	5
k_{P700r}	Rate constant of P_{700}^+ reduction by Pc^+	$5.8 \times 10^4 \text{ s}^{-1}$	6
k_{Pcr}	Rate constant of Pc^+ reduction by P_{700}	$4.5 \times 10^3 \text{ s}^{-1}$	6
k_{pPcrb}	Rate constant of Pc binding to PSI	$2.3 \times 10^5 \text{ s}^{-1}$	6
k_{pPcob}	Rate constant of Pc^+ binding to PSI	$1.1 \times 10^5 \text{ s}^{-1}$	6
k_{pPcrr}	Rate constant of Pc release from PSI	$2.8 \times 10^3 \text{ s}^{-1}$	6
k_{pPcor}	Rate constant of Pc^+ release from PSI	$7.3 \times 10^3 \text{ s}^{-1}$	6
k_{Fdrb}	Rate constant of Fd_r binding to PSI	10^4 s^{-1}	3
k_{Fdob}	Rate constant of Fd_o binding to PSI	10^4 s^{-1}	3
k_{Fdr}	Rate constant of Fd_r release from PSI	10^4 s^{-1}	3
k_{Fdor}	Rate constant of Fd_o release from PSI	10^4 s^{-1}	3

1. (Croce and van Amerongen, 2013).
2. (Savikhin, 2006).
3. Estimated (see text for details).
4. (Brettel, 1997).
5. (Schurmann, 2003).
6. (Drepper et al., 1996).

5.2.4 Electron transport pathways

In this section, the different pathways responsible for transporting electrons in the thylakoid are discussed. These include the different forms of cyclic electron transport around PSI, activity of alternative electron sinks on the acceptor side of PSI as well as the linear electron transport pathway that results from the interactions of PSII, $cyt\ b_6/f$, PSI, the electron carriers and production of NADPH by Ferredoxin-NADP⁺ reductase (FNR). In the following sub-sections, the equations used to simulate the different electron transport pathways are discussed, along with their parameterization.

5.2.4.1 Dynamic balance of electron carriers

The molecules of Fd_r produced by PSI are used to produce NADPH from NADP⁺ via ferredoxin-NADP⁺ reductase (FNR). Although the reaction mechanism of FNR is known (Batie and Kamin, 1984), some of the relevant kinetic constants are still unknown (Carrillo and Ceccarelli, 2003). Thus, the rate of NADPH synthesis (v_{FNR} , $\text{mol m}^{-2} \text{ s}^{-1}$) is calculated assuming hyperbolic kinetics:

$$v_{FNR} = \frac{v_{\max,FNR} Fd_r NADP^+}{(Fd_r + K_{FNR,Fdr})(NADP^+ + K_{FNR,NADP})} - \frac{v_{\max,FNR} Fd_o NADPH}{K_{FNR}(Fd_o + K_{FNR,Fdo})(NADPH + K_{FNR,NADPH})}, \quad (5.14)$$

where $v_{\max,FNR}$ is the maximum rate constant of NADPH production, K_{FNR} is the equilibrium coefficient of the reaction and $K_{FNR,Fdr}$, $K_{FNR,Fdo}$, $K_{FNR,NADP}$, and $K_{FNR,NADPH}$ are half-saturation constants with respect to Fd_r , Fd_o , $NADP^+$, and $NADPH$. $v_{\max,FNR}$, $K_{FNR,NADP}$, and $K_{FNR,NADPH}$ were assigned values of $1.6 \times 10^{-3} \text{ mol m}^{-2} \text{ s}^{-1}$, $5.0 \times 10^{-2} \text{ mol m}^{-3}$ and $3.5 \times 10^{-2} \text{ mol m}^{-3}$, taken from Fridlyand and Scheibe (1999a). $K_{FNR,Fdr}$ and $K_{FNR,Fdo}$ were assigned values of $10^{-2} \text{ mol m}^{-3}$ and $10^{-3} \text{ mol m}^{-3}$, taken from Carrillo and Ceccarelli (2003). K_{FNR} is calculated as:

$$K_{FNR} = \exp \left[\frac{2F(E_{m,NADPH} - E_{m,Fd})}{RT} \right], \quad (5.15)$$

where $E_{m,NADPH}$ (V) is the midpoint redox potential of NADPH at the pH of the stroma (pH_s), calculated as $E_{m,NADPH} = E_{7m,NADPH} - 59 \times 10^{-3} (pH_s - 7)$, where $E_{7m,NADPH} = -0.335 \text{ V}$ (Strand et al., 2016b).

In order to have a complete simulation of the electron transport chain, the mass balance of the different pools of electron carriers need to be calculated. In the equations below, bold font denotes vectors. Each vector corresponds to all the transitions associated to a transition rule (described in Tables 5.1, 5.4, and 5.6). The \sum symbol represents the sum over all components of a vector. The mass balances for PQH_2 and PQ are calculated as

$$\frac{dPQH_2}{dt} = - \sum \mathbf{v}_{bPQH2b} + \sum \mathbf{v}_{bPQH2r} - \sum \mathbf{v}_{pPQH2b} + \sum \mathbf{v}_{pPQH2r} - \sum \mathbf{v}_{nPQH2b} + \sum \mathbf{v}_{nPQH2r} + v_{NDH} + v_{FQR}, \quad (5.16)$$

and

$$\frac{dPQ}{dt} = - \sum \mathbf{v}_{bPQb} + \sum \mathbf{v}_{bPQr} - \sum \mathbf{v}_{pPQb} + \sum \mathbf{v}_{pPQr} - \sum \mathbf{v}_{nPQb} + \sum \mathbf{v}_{nPQr} - v_{NDH} - v_{FQR}, \quad (5.17)$$

The mass balances of reduced and oxidised Pc are calculated as

$$\frac{dPc}{dt} = - \sum \mathbf{v}_{PCrb} + \sum \mathbf{v}_{PCrr} - \sum \mathbf{v}_{PCrb} + \sum \mathbf{v}_{PCrr}, \quad (5.18)$$

and

$$\frac{dPc^+}{dt} = - \sum \mathbf{v}_{PCob} + \sum \mathbf{v}_{PCor} - \sum \mathbf{v}_{PCob} + \sum \mathbf{v}_{PCor}, \quad (5.19)$$

The mass balances of reduced and oxidised Fd are calculated as

$$\frac{dFd_r}{dt} = - \sum \mathbf{v}_{Fdrb} + \sum \mathbf{v}_{Fdr} - 2V_S C_t (v_{FNR} + v_{FTR}) - \frac{2v_{NDH} - 2v_{FQR} - v_{WWC} - 8v_{NR}}{2v_{NDH} - 2v_{FQR} - v_{WWC} - 8v_{NR}} \quad (5.20)$$

and

$$\frac{dFd_o}{dt} = - \sum \mathbf{v}_{Fdob} + \sum \mathbf{v}_{Fdor} + 2V_S C_t (v_{FNR} + v_{FTR}) + \frac{2v_{NDH} + 2v_{FQR} + v_{WWC} + 8v_{NR}}{2v_{NDH} + 2v_{FQR} + v_{WWC} + 8v_{NR}} \quad (5.21)$$

respectively. V_S ($\text{dm}^3 \text{mol}^{-1}$) is the volume of the stroma per amount of chlorophyll. The value of V_S is discussed in Section 5.2.6.

5.2.4.2 Cyclic electron transport

Two main protein complexes are responsible for cyclic electron transport around PSI in plants (Strand and Kramer, 2014): NADPH dehydrogenase (NDH) and ferredoxin-quinone reductase (FQR). Although the molecular identity of FQR is still unclear (Strand and Kramer, 2014), some of its properties are known (Strand et al., 2016a). However, the kinetics of cyclic electron transport *in vivo* are not completely understood (Eberhard et al., 2008), which means that most of the parameters in this section have been estimated and rely on assumptions that await experimental confirmation.

5.2.4.2.1 NDH

NDH is functionally similar to the respiratory NADH:quinone reductase type I (NDH-I), but it most likely uses ferredoxin as electron donor (Kramer et al., 2004a; Yamamoto and Shikanai, 2013; Shikanai, 2016; Strand et al., 2016b). It is assumed that the reaction catalysed by NDH is reversible and that it follows hyperbolic kinetics, resulting in the following expression:

$$v_{NDH} = \frac{NDH \cdot k_{NDH} \cdot Fd_r PQ}{(K_{NDH,Fdr} + Fd_r)(K_{NDH,PQ} + PQ)} - \frac{NDH \cdot k_{NDH} \cdot Fd_o PQH_2}{K_{NDH}(K_{NDH,Fdo} + Fd_o)(K_{NDH,PQH_2} + PQH_2)}, \quad (5.22)$$

where NDH (mol m^{-2}) is the amount of NDH per unit of leaf surface, k_{NDH} (s^{-1}) is the maximum rate of PQ reduction per unit of NDH, $K_{M,NDH,Fdr}$ (mol m^{-2}), $K_{M,NDH,Fdo}$ (mol m^{-2}), $K_{M,NDH,PQ}$ (mol m^{-2}), and K_{M,NDH,PQH_2} (mol m^{-2}) are the half-saturation constants with respect to Fd_r , Fd_o , PQ, and PQH_2 , respectively, and K_{NDH} (mol m^{-2}) is the equilibrium coefficient of the reaction. k_{NDH} is estimated to be 200 s^{-1} in analogy to NDH-I (Fato et al., 1996; Hirst, 2013; Hu et al., 2013). Yamamoto and Shikanai (2013) measured *in vitro*, using post-illumination chlorophyll fluorescence rise (PIFR), the sensitivity of NDH to Fd_r via Q_A reduction in the presence of antimycin and observed that 90% of maximum reduction was achieved with a Fd_r concentration of $3 \mu\text{M}$. However, this very high affinity result in unrealistic simulations with Equation 5.22. NDH *in vivo* may be generally associated with PSI, which may result in substrate channelling (Shikanai, 2016) and thus different kinetics properties with respect to *in vitro* experiments that add exogenous Fd. To obtain reasonable results, a higher value (one third of maximum possible Fd_r in the model) was assumed for $K_{M,NDH,Fdr}$. The same assumption was used to estimate the values of $K_{M,NDH,Fdo}$, $K_{M,NDH,PQ}$, and K_{M,NDH,PQH_2} , using as reference the corresponding pools of metabolites. These values ensure that the concentrations of substrates are

effective regulators of NDH activities, allowing for changes with irradiance and CO₂. The estimation of the amount of NDH in the leaf is discussed in Section 5.2.9.

Like NDH-I, two H⁺ are translocated across the thylakoid membrane per electron transported (Strand et al., 2016b). This coupled proton translocation activity will affect the thermodynamics of the reaction (Strand et al., 2016b). Thus, the equilibrium coefficient is calculated as:

$$K_{NDH} = \exp\left(\frac{2F(E_{m,PQ} - E_{m,Fd}) - 4F \cdot pmf}{RT}\right), \quad (5.23)$$

where pmf (V) is the proton motive force across the thylakoid membrane. NDH activity is also regulated by H₂O₂ (Strand et al., 2015). H₂O₂ levels increase with irradiance (Wen et al., 2008; Mubarakshina et al., 2010), although the distribution across subcellular compartments *in vivo* is not well known. These results suggest the possibility that the activity of NDH may be regulated as a function of irradiance under normal physiological conditions, but given the uncertainties in the modelling of H₂O₂ metabolism, regulation of NDH activity by H₂O₂ is not included in the model.

5.2.4.2.2 FQR

FQR has been associated to the PGR5 and PGRL1 thylakoid proteins (Kramer et al., 2004a; Strand et al., 2016a), but its kinetic properties are still unknown. Experimental evidence indicates that the activity of this reaction is regulated by thiol reduction in a reversible and rapid manner (Strand et al., 2016a) which would imply up-regulation by thioredoxin *in vivo*. This is in contradiction with evidence obtained from mutants that suggest thioredoxin suppresses FQR activity *in vivo* (Courteille et al., 2013), though the exact mechanism of such suppression was unclear. Assuming hyperbolic kinetics, the rate of PQ reduction by FQR is calculated as

$$v_{FQR} = \frac{FQR_r \cdot k_{FQR} \cdot Fd_r PQ}{(K_{FQR,Fdr} + Fd_r)(K_{FQR,PQ} + PQ)} - \frac{FQR \cdot k_{FQR} \cdot Fd_o PQH_2}{K_{FQR}(K_{FQR,Fdo} + Fd_o)(K_{FQR,PQH_2} + PQH_2)}, \quad (5.24)$$

where FQR_r (mol m⁻²) is the amount of FQR that has been reduced by thioredoxin, k_{FQR} (s⁻¹) is the maximum rate of PQ reduction per unit of FQR, $K_{FQR,Fdr}$ (mol m⁻²), $K_{FQR,PQ}$ (mol m⁻²), $K_{FQR,Fdo}$ (mol m⁻²) and K_{FQR,PQH_2} (mol m⁻²) are the half-saturation constants with respect to Fd_r, PQ, Fd_o, and PQH₂, and K_{FQR} is the equilibrium coefficient of the reaction, calculated as

$$K_{FQR} = \exp\left[\frac{2F(E_{m,PQ/PQH_2} - E_{m,Fd})}{RT}\right]. \quad (5.25)$$

No values were found in the literature for any of the parameters in Equation 5.24 except for the amount of FQR, which is discussed in Section 5.2.9. Strand et al. (2016b) reported that blocking FQR via antimycin reduced PIFR by 60% in *S. oleracea* and *A. thaliana*, which would indicate that the rate of PQ reduction via FQR is at least 50% higher than via NDH. However, the accuracy of PIFR as a measure of cyclic electron transport is under debate due to other possible sources of Q_A reduction (Fisher and Kramer, 2014). In the light of

these uncertainties, it is assumed that the maximum flux of electrons through FQR is twice as large as for NDH. Assuming that the half-saturation constants are the same as for NDH (Table 5.8) and knowing that the ratio NDH:FQR is 0.1 (see Section 5.2.9 for details), k_{FQR} is calculated to be 40 s^{-1} .

5.2.4.3 Alternative electron sinks

5.2.4.3.1 Water-water cycle

The Mehler peroxidase reaction (MPR) is started by the reduction of O_2 into O_2^- via electron transfer at the stromal side of PSI (Asada, 2000). As O_2^- is reactive and can damage the electron transport chain and membrane lipids (Mishra and Singhal, 1992; Krieger-Liszkay et al., 2011), a series of enzymes scavenge it and convert it via hydrogen peroxide into water, which consumes additional electrons via NADPH (Asada, 1999). Given that the electrons ultimately come from water oxidation by the OEC, the combination of electron transport, O_2^- production, and its conversion back to water is known as the “water-water cycle” (WWC), which consumes the 4 electrons per O_2 produced by the OEC. Although frequently assumed to be an ATP/NADPH balancing or a photoprotective mechanism, the rate of light-induced O_2^- formation is relatively low in the steady-state, meaning that the capacity of the WWC as an alternative electron sink is low (Driever and Baker, 2011).

The molecular identity of the reductant responsible for O_2^- production is still unknown, and there may be several (Robinson, 1988), so an unknown “stromal factor” has been hypothesized (Asada, 1999). Indeed, isolated thylakoids (as opposed to isolated chloroplasts) are not capable of significant rates of O_2^- production (Asada, 2000). Based on this evidence, the following expression is proposed to calculate the rate of Fd_r oxidation by WWC:

$$v_{WWC} = \frac{Fd_r O_2 v_{max,WWC}}{(Fd_r + K_{WWC,Fd_r})(O_2 + K_{WWC,O_2})}, \quad (5.26)$$

where $v_{max,WWC}$ ($\text{mol m}^{-2} \text{ s}^{-1}$) is the maximum rate of O_2^- production by MPR and K_{WWC,Fd_r} (mol m^{-2}) and K_{WWC,O_2} (mol mol^{-1}) are the half-saturation constants with respect to Fd_r and O_2 . K_{WWC,O_2} was set to be $7.9 \times 10^{-3} \text{ mol mol}^{-1}$ (Asada, 2000). Furbank and Badger (1983) measured O_2 uptake of chloroplasts in the absence of NADP^+ , from which a half-saturation constant of $70 \text{ }\mu\text{M}$ can be derived. At the leaf level and with the assumed chloroplast volume (see Section 5.2.6), this results in $K_{WWC,Fd_r} = 7.3 \times 10^{-7} \text{ mol m}^{-2}$. This corresponds to 40% of the total leaf Fd content assumed in the model (see Section 5.2.9), which ensures that the production of O_2^- is regulated by physiological concentrations of reduced Fd, as expected from the observations by Driever and Baker (2011). Based on steady-state measurements of $^{18}\text{O}_2$ uptake and evolution, the ratio between $v_{max,WWC}$ and maximum rate of linear electron transport was estimated to be 4.5% in *Phaseolus vulgaris* (Driever and Baker, 2011) and 5.9% in *Nicotiana tabacum* (Ruuska et al., 2000). The amounts of protein complexes assumed for the thylakoid membrane (Section 5.2.9) resulted in a maximum rate of linear electron transport at ambient $[\text{CO}_2]$ of $110 \text{ }\mu\text{mol m}^{-2} \text{ s}^{-1}$, which results in a value of $v_{max,WWC}$ of $5 \text{ }\mu\text{mol m}^{-2} \text{ s}^{-1}$.

5.2.4.3.2 Malate valve

The malate valve is a pathway composed of two reactions: chloroplast malate dehydrogenase (MDH) that converts oxaloacetate (OAA) into malate (MAL) by

consumption of NADPH, and the malate shuttle (MT) that exports MAL to the cytosol in exchange of OAA (Heineke et al., 1991; Fridlyand et al., 1998). The exported MAL in the cytosol may be transported into the vacuole (Gerhardt and Heldt, 1984), mitochondria (Noctor and Foyer, 1998), or peroxisomes (Cousins et al., 2008). It may also be oxidised into OAA, releasing NADH which can be used for redox metabolism in the cytosol, e.g., nitrate assimilation (Noctor and Foyer, 1998). Gerhardt and Heldt (1984) observed strong increases in MAL content of vacuoles in leaves of *S. oleracea* during the day, but little change in other sub-cellular compartments, suggesting that concentrations in the cytosol are buffered by exchange with the vacuole. Thus, the model assumes that the concentration of MAL and OAA in the cytosol remain constant and in equilibrium due to high activity of cytosolic MDH (Heineke et al., 1991).

We used the equations proposed by Fridlyand et al. (1998) to describe the kinetics of MDH and MT. The original equations were modified to include regulation of MDH activity by thioredoxin (Carr et al., 1999). Also, the effect of NADPH on MDH activity was smoothed with respect to the original piecewise linear function (without significant changes in the results) to avoid numerical instabilities. The rate of MAL production in the chloroplast is thus calculated as

$$v_{MDH} = \frac{V_{mMDH} \cdot OAA_s \cdot NADPH}{K_{MDH,OAA} K_{MDH,NADPH} D_{MDH}} - \frac{V_{mMDH} \cdot MAL_s \cdot NADP^+}{K_{MDH} K_{MDH,MAL} K_{MDH,NADP^+} D_{MDH}}, \quad (5.27)$$

where

$$D_{MDH} = 1 + \frac{OAA_s}{K_{MDH,OAA}} + \frac{NADPH}{K_{MDH,NADPH}} + \frac{MAL_s}{K_{MDH,MAL}} + \frac{NADP^+}{K_{MDH,NADP^+}} + \frac{OAA_s NADPH}{K_{MDH,OAA} K_{MDH,NADPH}} + \frac{MAL_s NADP^+}{K_{MDH,MAL} K_{MDH,NADP^+}} \quad (5.28)$$

and

$$V_{mMDH} = f_{MDHr} V_{MDH,max} \frac{\left(\frac{NADPH}{NADPH + NADP^+}\right)^{nM}}{\left(\frac{NADPH}{NADPH + NADP^+}\right)^{nM} + pN^{nM}}. \quad (5.29)$$

$K_{MDH,OAA}$, $K_{MDH,MAL}$, $K_{MDH,NADPH}$ and $K_{MDH,NADP^+}$ are the half-saturation constants with respect to OAA, MAL, NADPH and $NADP^+$ with values of $4.8 \times 10^{-2} \text{ mol m}^{-3}$, 14.5 mol m^{-3} , $3.9 \times 10^{-2} \text{ mol m}^{-3}$ and $6.3 \times 10^{-2} \text{ mol m}^{-3}$, respectively, taken from Fridlyand et al. (1998). $V_{MDH,max}$ is the maximum rate of MAL production, with a value of $1.2 \text{ mol m}^{-3} \text{ s}^{-1}$ taken from Foyer et al. (1992), which is lower than the value of $2.9 \text{ mol m}^{-3} \text{ s}^{-1}$ assumed by Fridlyand et al. (1998). nM and pN are the Hill coefficient and half-saturation constant for the effect NADPH on MDH activity, which were fitted to the original data by Fridlyand et al. (1998), resulting in $nM = 8$ and $pN = 0.52$.

The exchange of MAL for OAA in the cytosol is calculated according to the expression developed by Giersch (1982):

$$V_{MT} = \frac{v_{MT,max} (MAL'_s S_2 - MAL'_c S_1)}{S_1 + S_2 + 0.5(S_1 S_4 + S_2 S_3)}, \quad (5.30)$$

where

$$S_1 = v_{MT,max}(OAA'_s + MAL'_s), \quad (5.31)$$

$$S_2 = v_{MT,max}(OAA'_c + MAL'_c), \quad (5.32)$$

$$S_3 = OAA'_s + MAL'_s, \quad (5.33)$$

and

$$S_4 = OAA'_c + MAL'_c, \quad (5.34)$$

where

$$OAA'_s = \frac{OAA_s}{K_{MT,OAA}}, \quad (5.35)$$

$$MAL'_s = \frac{MAL_s}{K_{MT,MAL}}, \quad (5.36)$$

$$OAA'_c = \frac{OAA_c}{K_{MT,OAA}}, \quad (5.37)$$

and

$$MAL'_c = \frac{MAL_c}{K_{MT,MAL}}, \quad (5.38)$$

where $V_{MT,max}$ is the maximum rate of malate export, $K_{MT,OAA}$ and $K_{MT,MAL}$ are the half-saturation constants with respect to OAA and MAL with values of 0.17 mol m^{-3} and 2.7 mol m^{-3} , respectively. The value of $V_{MT,max}$ was calculated assuming a constant $V_{MT,max}/V_{MDH,max}$ from Fridlyand et al. (1998) and the value of $V_{MDH,max}$ reported by Foyer et al. (1992), resulting in $V_{MT,max} = 2.0 \text{ mol m}^{-3} \text{ s}^{-1}$. OAA_c and MAL_c are the concentrations of OAA and MAL in the cytosol, assumed to be 0.098 mol m^{-3} and 1 mol m^{-3} , respectively (Heineke et al., 1991).

Finally, the mass balance of MAL and OAA results in the following differential equations:

$$\frac{dMAL}{dt} = v_{MDH} - v_{MT}, \quad (5.39)$$

and

$$\frac{dOAA}{dt} = -\frac{dMAL}{dt}, \quad (5.40)$$

5.2.4.3.3 Nitrite reduction

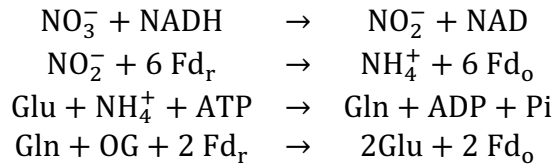
Experimental evidence shows an increase in O_2 evolution with respect to CO_2 uptake when NO_3^- (Reed et al., 1983; Bloom et al., 1989; de la Torre et al., 1991) is used as the source of nitrogen assimilation in plants. These results can be interpreted as a role of nitrogen assimilation as an alternative electron sink. The pathway of NO_3^- assimilation into glutamate in a mesophyll cell of a leaf (Noctor and Foyer, 1998) is composed of the following reactions:

Table 5.8: Parameters associated to the different electron pathways. See bottom of the table for sources.

Symbol	Description	Value	Source
k_{NDH}	Maximum rate of PQ reduction per unit of NDH	200 s^{-1}	1
$K_{NDH,Fdr}$	Half-saturation constant of NDH with respect to Fd_r	$5.0 \times 10^{-7} \text{ mol m}^{-2}$	2
$K_{NDH,Fdo}$	Half-saturation constant of NDH with respect to Fd_o	$5.0 \times 10^{-7} \text{ mol m}^{-2}$	2
$K_{NDH,PQ}$	Half-saturation constant of NDH with respect to PQ	$2.0 \times 10^{-6} \text{ mol m}^{-2}$	2
K_{NDH,PQH_2}	Half-saturation constant of NDH with respect to PQH_2	$2.0 \times 10^{-6} \text{ mol m}^{-2}$	2
k_{FQR}	Maximum rate of PQ reduction per unit of FQR	40 s^{-1}	2
$K_{FQR,Fdr}$	Half-saturation constant of FQR with respect to Fd_r	$5.0 \times 10^{-7} \text{ mol m}^{-2}$	2
$K_{FQR,PQ}$	Half-saturation constant of FQR with respect to PQ	$2.0 \times 10^{-6} \text{ mol m}^{-2}$	2
$K_{FQR,Fdo}$	Half-saturation constant of FQR with respect to Fd_o	$5.0 \times 10^{-7} \text{ mol m}^{-2}$	2
K_{FQR,PQH_2}	Half-saturation constant of FQR with respect to PQH_2	$2.0 \times 10^{-6} \text{ mol m}^{-2}$	2
K_{WWC,O_2}	Half-saturation constant of Mehler reaction with respect to O_2	$7.9 \times 10^{-3} \text{ mol mol}^{-1}$	3
$v_{max,WWC}$	Maximum rate of electron consumption by the water-water cycle	$5 \times 10^{-6} \text{ mol m}^{-2} \text{ s}^{-1}$	4
$K_{WWC,Fdr}$	Half-saturation of the water-water cycle with respect to Fd_r	$7.3 \times 10^{-7} \text{ mol m}^{-2}$	5
$K_{MDH,MAL}$	Half-saturation constant of malate dehydrogenase with respect to malate	14.5 mol m^{-3}	6
$K_{MDH,NADP^+}$	Half-saturation constant of malate dehydrogenase with respect to $NADP^+$	$6.3 \times 10^{-2} \text{ mol m}^{-3}$	6
$K_{MDH,NADPH}$	Half-saturation constant of malate dehydrogenase with respect to $NADPH$	$3.9 \times 10^{-2} \text{ mol m}^{-3}$	6
$K_{MDH,OAA}$	Half-saturation constant of malate dehydrogenase with respect to oxaloacetate	$4.8 \times 10^{-2} \text{ mol m}^{-3}$	6
$K_{MT,MAL}$	Half-saturation of the malate-oxaloacetate transporter with respect to malate	2.7 mol m^{-3}	6
$K_{MT,OAA}$	Half-saturation of the malate-oxaloacetate transporter with respect to oxaloacetate	0.2 mol m^{-3}	6
OAA_C	Concentration of oxaloacetate in the cytosol	$9.8 \times 10^{-2} \text{ mol m}^{-3}$	7
MAL_C	Concentration of malate in the cytosol	1 mol m^{-3}	7
$V_{MDH,max}$	Maximum rate of malate dehydrogenase	$1.2 \text{ mol m}^{-3} \text{ s}^{-1}$	8

$V_{MT,max}$	Maximum rate of the malate-oxaloacetate transporter	$2 \text{ mol m}^{-3} \text{ s}^{-1}$	6,8
nM	Hill coefficient in the relationship between malate dehydrogenase activity and NADPH	8	6
pN	Half-saturation constant of malate dehydrogenase activity with respect to NADPH	0.52	6
$K_{NiR,ATP}$	Half-saturation constant of nitrogen assimilation with respect to ATP	$10^{-2} \text{ mol m}^{-3}$	2
$K_{NiR,Fd}$	Half-saturation constant of nitrogen assimilation with respect to Fd	$1.7 \times 10^{-7} \text{ mol m}^{-2}$	9
K_{NiR,NO_2}	Half-saturation constant of nitrogen assimilation with respect to NO_2^-	$2.37 \times 10^{-2} \text{ mol m}^{-3}$	10
k_{NiR}	Maximum rate of NO_2^- reduction	$3 \times 10^{-6} \text{ mol m}^{-2} \text{ s}^{-1}$	11
NO_2^-	Concentration of NO_2^- in the stroma of the chloroplast	$2.5 \times 10^{-2} \text{ mol m}^{-3}$	2
$K_{FNR,NADP}$	Half-saturation constant of NADPH synthesis by Fd-NADP ⁺ reductase with respect to NADP ⁺	$5.0 \times 10^{-2} \text{ mol m}^{-3}$	9
$K_{FNR,NADPH}$	Half-saturation constant of NADPH synthesis by Fd-NADP ⁺ reductase with respect to NADPH	$3.5 \times 10^{-2} \text{ mol m}^{-3}$	9
K_{FNR,Fd_o}	Half-saturation constant of NADPH synthesis by Fd-NADP ⁺ reductase with respect to Fd _o	$10^{-3} \text{ mol m}^{-3}$	12
K_{FNR,Fd_r}	Half-saturation constant of NADPH synthesis by Fd-NADP ⁺ reductase with respect to Fd _r	$10^{-2} \text{ mol m}^{-3}$	12
$v_{max,FNR}$	Maximum rate of NADPH synthesis by Fd-NADP ⁺ reductase	$1.6 \times 10^{-3} \text{ mol m}^{-2} \text{ s}^{-1}$	9
$E_{m,NADPH}$	Midpoint redox potential of NADPH	-0.3 V	13

1. (Fato et al., 1996; Hirst, 2013; Hu et al., 2013).
2. Estimated (see text for details).
3. (Asada, 2000).
4. (Ruuska et al., 2000; Driever and Baker, 2011).
5. (Furbank and Badger, 1983).
6. (Fridlyand et al., 1998).
7. (Heineke et al., 1991).
8. (Foyer et al., 1992).
9. (Fridlyand and Scheibe, 1999b).
10. (Hirasawa et al., 2009).
11. (Bloom et al., 2002).
12. (Carrillo and Ceccarelli, 2003).
13. (Strand et al., 2016b).



where Glu and OG stand for glutamate and 2-oxoglutarate, respectively. If one assumes that the source of NADH required for NO_3^- reductase in the cytosol proceeds from mitochondrial respiration or the malate valve, this results in 8 Fd_r and one ATP consumed within the chloroplast, for each molecule of NO_3^- assimilated into Glu.

The *in vivo* kinetics of the different reactions described in the above are still poorly understood (Fridlyand and Scheibe, 1999a). Due to the lack of NO_2^- or NH_4^+ accumulation in leaves, studies have suggested that the rate limiting step is NO_3^- reduction in the cytosol (Imssande and Touraine, 1994). However, the activity of NO_3^- reductase is regulated *in vivo* and responds to changes irradiance and CO_2 (Kaiser et al., 2002) and this regulation may be responsible for preventing levels of NO_2^- and NH_3 from accumulating. A single pseudo-reaction is used to calculate the rate of NO_2^- reduction (v_{NiR}):

$$v_{\text{NiR}} = \frac{k_{\text{NiR}} \cdot \text{Fd}_r \cdot \text{ATP} \cdot \text{NO}_2^-}{(\text{Fd}_r + K_{\text{NiR},\text{Fd}})(\text{ATP} + K_{\text{NiR},\text{ATP}})(\text{NO}_2^- + K_{\text{NiR},\text{NO}_2})}, \quad (5.41)$$

where k_{NiR} ($\text{mol m}^{-2} \text{s}^{-1}$) is the maximum rate of NO_2^- reduction (NiR), $K_{\text{NiR},\text{Fd}}$ (mol m^{-3}) and $K_{\text{NiR},\text{ATP}}$ (mol m^{-3}) are the half-saturation constants of the pseudo-reaction with respect to Fd_r and ATP. $K_{\text{NiR},\text{Fd}}$ was set to $2.37 \times 10^{-2} \text{ mol m}^{-3}$ (Fridlyand and Scheibe, 1999a) and a value of $10^{-2} \text{ mol m}^{-3}$ (Hirasawa et al., 2009) was assumed for $K_{\text{NiR},\text{NO}_2}$. No values were found for $K_{\text{NiR},\text{ATP}}$, so it was assumed to be $10^{-2} \text{ mol m}^{-3}$ which results in the reaction being saturated with respect to ATP under typical *in vivo* conditions.

Bloom et al. (2002) estimated a maximum rate of NiR of $0.3 \mu\text{mol m}^{-2} \text{s}^{-1}$ (equivalent to $2.4 \mu\text{mol e}^- \text{m}^{-2} \text{s}^{-1}$) in leaves of *Triticum aestivum* for an O_2 evolution rate of $12 \mu\text{mol m}^{-2} \text{s}^{-1}$ (i.e., NiR consumed 5% of the electrons generated by PSII) at ambient $[\text{CO}_2]$ and an irradiance of $1200 \mu\text{mol m}^{-2} \text{s}^{-1}$. This value was calculated as the difference in O_2 evolution for plants fed with NH_4^+ and NO_3^- , but these conditions do not guarantee maximum rates if the substrates are not saturating. Assuming that the levels of Fd_r and NO_2^- were around their corresponding half-saturation constants, the maximum rate of NiR would be four times higher than the reported value. For the current parameterization of this model, this results in $3 \times 10^{-3} \text{ mol m}^{-2} \text{s}^{-1}$ ($120 \times 10^{-3} \text{ mol e}^- \text{m}^{-2} \text{s}^{-1} \times 0.20 \times 1 \text{ mol NO}_3^- / 8 \text{ mol e}^-$).

5.2.5 ATP synthase

The ATPase complex is composed of two components named F_0 and F_1 . The F_1 component is exposed to the stroma and it contains three catalytic sites where ATP synthesis and hydrolysis take place. The F_0 component is embedded in the thylakoid membrane and its structure is organized in the form of a rotor. Regarding the mechanism of ATP synthesis, the currently dominant paradigm is the cooperative binding theory (Boyer, 1993) which explains ATP synthesis in terms of rotations of the components and changes in affinity of the catalytic sites on the F_1 component (Figure 5.5). The rotations of F_0 are coupled to transport of H^+ from the lumen to the stroma via the c subunits. According to the cooperating binding theory, the number of H^+ required for a full rotation (HPR) is equal to the number of c subunits. The energy transferred by a H^+ transported through ATPase

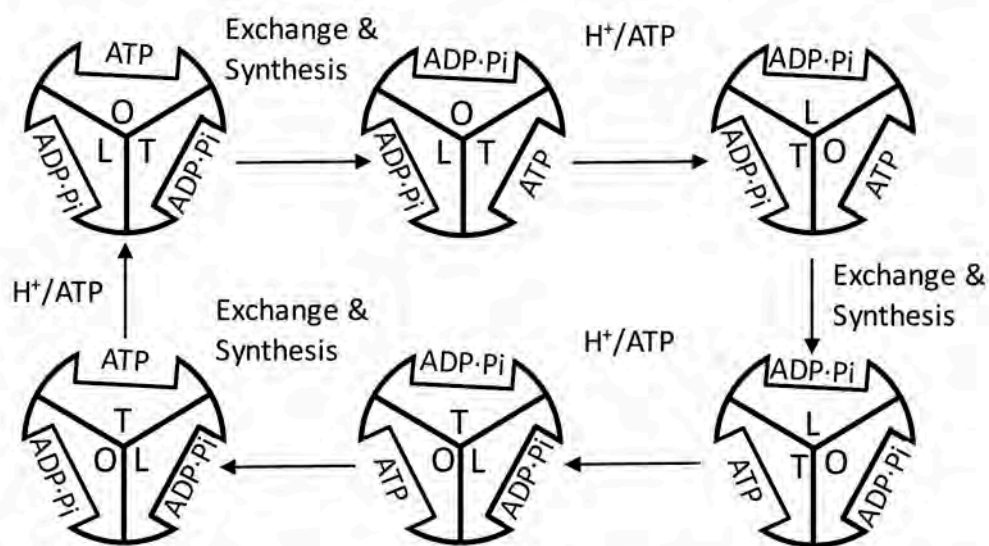


Figure 5.5: Scheme describing the different states of catalytic sites in the F_1 subunit of ATPase according to the cooperative binding theory. Three types of transitions exist: (i) exchange of metabolites between open catalytic sites and the medium, (ii) synthesis of ATP from ADP and Pi inside a tight catalytic site and (iii) conformational change of the F_1 subunit coupled to H^+ transport (H^+/ATP in the figure) that advances the states of all catalytic sites in a coordinated manner. For simplification, we depict the exchange of metabolism and ATP synthesis in a single step. L, T and O stand for loose, tight and open catalytic site.

is equivalent to the electrochemical gradient of H^+ across the thylakoid membrane, also known as proton motive force (pmf).

Across different species of bacteria, plants, and animals, the number of c subunits varies from 8 to 15 (Pogoryelov et al., 2012) which would yield H^+/ATP ratios from 8/3 to 5. Seelert et al. (2000) observed 14 c subunits for ATPase of *S. oleracea* using atom force microscopy. This number was confirmed by Varco-Merth et al. (2008) and Vollmar et al. (2009) using X-ray crystallography. A non-integer H^+/ATP ratio can be explained by an elastic torque transmission from F_0 to F_1 , thus allowing for a transient accumulation of energy during the rotation (Pänke and Rumberg, 1999; Junge, 2013).

However, Turina et al. (2003), Petersen et al. (2012) and Steigmiller et al. (2008) determined the H^+/ATP ratio for ATPase of *S. oleracea* using biochemical equilibrium approaches and obtained a value of 4 in all experiments, suggesting a mismatch between the structure-based and biochemistry-based ratios. A similar mismatch between the predictions based on structural and biochemistry methods was observed for *Escherichia coli* (Steigmiller et al., 2008) and *Saccharomyces cerevisiae* (Petersen et al., 2012). The H^+/ATP ratio for ATPase of *S. oleracea* was also calculated using a biochemical kinetic approach by Berry and Rumberg (1996) also resulting in a value of 4. The reasons for the discrepancy between biochemical and structural estimations of the H^+/ATP ratio are yet unknown.

Another important aspect of ATPase is its redox regulation. ATP synthesis responds to pmf in a sigmoidal manner and the shape of the response depends on the redox state of two thiol groups in the γ subunit of the F_1 component, which are reduced by thioredoxin *in vivo* (Schwarz et al., 1997). From a mathematical perspective, the effect of thiol reduction on ATPase activity is a “displacement” of the response of ATP synthesis to pmf.

Pänke and Rumberg (1996) developed a mechanistic model of ATPase that describes accurately the kinetics of ATP synthesis *in vitro*. The original experiment used to develop and calibrate the model was performed under conditions of no voltage across the thylakoid membrane, which is not representative of conditions *in vivo* (Kramer et al., 1999). The equations were thus extended to take into account both components of pmf (Cruz et al., 2001), under the assumption that they are kinetically equivalent (Junesch and Gräber, 1991). In addition, all ATPase used in the experiment by Pänke and Rumberg (1996) were fully reduced, so additional modifications were required to simulate the situation of intermediate reduction levels of the pool of ATPase. Finally, the model was recalibrated under the assumption that H^+/ATP was 14/3 and not 4 as assumed by the original authors.

The equations calculating ATP synthesis are described in detail below. To simplify the mathematical expressions, F will be used when referring to ATPase in equations and diagrams (Figure 5.6). A catalytic site of ATPase bound to ADP is denoted as F_D , F_P when bound to inorganic phosphate (Pi), F_{DP} when bound to both ADP and Pi and F_T when bound to ATP. An empty catalytic site is denoted as F . A transition between two states of the catalytic site is denoted as v with suffixes that determine the initial and final state of the transition. For example, the transition from F to F_D is $v_{F,FD}$ (Figure 5.6). The binding and release of Pi, ADP and ATP are simulated according to the law of mass action. Based on the schema described in Figure 5.6 the rate of Pi binding to an empty catalytic site is calculated as

$$v_{F,FP} = k_{FPf}Pi \cdot F - k_{FPr}F_P, \quad (5.42)$$

where k_{FPf} ($m^3 \text{ mol}^{-1} \text{ s}^{-1}$) and k_{FPr} (s^{-1}) are rate constants with values $8.1 \times 10^2 \text{ m}^3 \text{ mol}^{-1} \text{ s}^{-1}$ and $2 \times 10^3 \text{ s}^{-1}$ (Table 5.9), respectively (Pänke and Rumberg, 1996). The rate of ADP binding to an empty catalytic site is calculated as

$$v_{F,FD} = k_{FDf}ADP \cdot F - k_{FDr}F_D, \quad (5.43)$$

where k_{FDf} ($m^3 \text{ mol}^{-1} \text{ s}^{-1}$) and k_{FDr} (s^{-1}) are rate constants with values $1.24 \times 10^4 \text{ m}^3 \text{ mol}^{-1} \text{ s}^{-1}$ and $3.7 \times 10^2 \text{ s}^{-1}$, respectively (Pänke and Rumberg, 1996, 1999). It is assumed that the presence of a reactant already bound to the site does not affect the rate of binding of the other reactant. Thus, the binding of ADP when Pi is already bound proceeds as

$$v_{FP,FDP} = k_{FDf}ADP \cdot F_P - k_{FDr}F_{DP}, \quad (5.44)$$

and Pi binding when ADP is already bound is calculated as

$$v_{FD,FDP} = k_{FPf}Pi \cdot F_D - k_{FPr}F_{DP}. \quad (5.45)$$

The binding of ATP follows analogous kinetics to the other reactants, with the exception that ATP may only bind to an empty catalytic site:

$$v_{F,FT} = k_{FTf}ATP \cdot F - k_{FTr}F_T, \quad (5.46)$$

where k_{FTf} ($m^3 \text{ mol}^{-1} \text{ s}^{-1}$) and k_{FTr} (s^{-1}) are rate constants with values $2.14 \times 10^3 \text{ m}^3 \text{ mol}^{-1} \text{ s}^{-1}$ and $2.2 \times 10^2 \text{ s}^{-1}$, respectively (Pänke and Rumberg, 1996, 1999). All the conformational changes of a catalytic site are included in a single step assumed to follow first-order

kinetics (Pänke and Rumberg, 1996) and takes into account the effects of pmf on the kinetics and thermodynamics of the conformational changes:

$$v_{FDP,FT} = F_{DP}k_{F1} - F_Tk_{F2}, \quad (5.47)$$

where k_{F1} (s^{-1}) and k_{F2} (s^{-1}) are the apparent rate constants for the conformational changes in the directions of synthesis and hydrolysis of ATP. The rate constants are assumed proportional to the probability that a transition in one direction occurs, that is

$$k_{F1} = k_{F10}p_1 \quad (5.48)$$

and

$$k_{F2} = k_{F20}p_2, \quad (5.49)$$

where k_{F10} (s^{-1}) and k_{F20} (s^{-1}) are kinetic parameters with values of $5.2 \times 10^3 s^{-1}$ and $2.2 \times 10^3 s^{-1}$, respectively (Pänke and Rumberg, 1996) and p_1 and p_2 are the probabilities that a transition in the direction of ATP synthesis or hydrolysis occurs, respectively. The probability of ATP synthesis is calculated as

$$p_1 = \frac{K_{FC}x^4}{(1 + K_{FC})D} \quad (5.50)$$

and for ATP hydrolysis it is

$$p_2 = \frac{1}{(1 + K_{FC})D}, \quad (5.51)$$

where D and x are computed as

$$D = 1 + x + x^2 + x^3 + x^4 \quad (5.52)$$

and

$$x = \frac{1}{K_F} (f_{Fr} 10^{pmf/V_{pH}} + f_{Fo} 10^{(pmf - pmf_d)/V_{pH}}), \quad (5.53)$$

where pmf_d (V) is the displacement in the sensitivity of ATP synthesis to proton motive force due to thiol reduction, f_{Fr} and f_{Fo} are the fractions of ATPase that contain reduced and oxidised regulatory γ subunit, respectively. pmf_d was estimated to be 0.06 V from the measurements by Junesch and Gräber (1987). K_{FC} is the equilibrium coefficient of the conversion of substrates into products within a tight catalytic site and K_F is the equilibrium coefficient of each conformational change of F. The original values for K_{FC} and K_F were 2.5 and 220, but assuming an H^+/ATP ratio of 14/3, they become 3.1 and 110. The new values were estimated by recalculating the rates of ATP synthesis and pH from their original data (both variables were calculated by the authors using experimental calibrations that assumed $H^+/ATP = 4$) assuming an $H^+/ATP = 14/3$ and fitting the model to the new data. The new calibration also affected the values of k_{FDr} and k_{FTr} and the values reported in the above and in Table 5.9 refer to the new values estimated assuming $H^+/ATP = 14/3$. The original values of k_{FDr} and k_{FTr} for $H^+/ATP = 4$ were $490 s^{-1}$ and $270 s^{-1}$, respectively. Applying mass balance to the different forms of ATPase leads to the following differential equations:

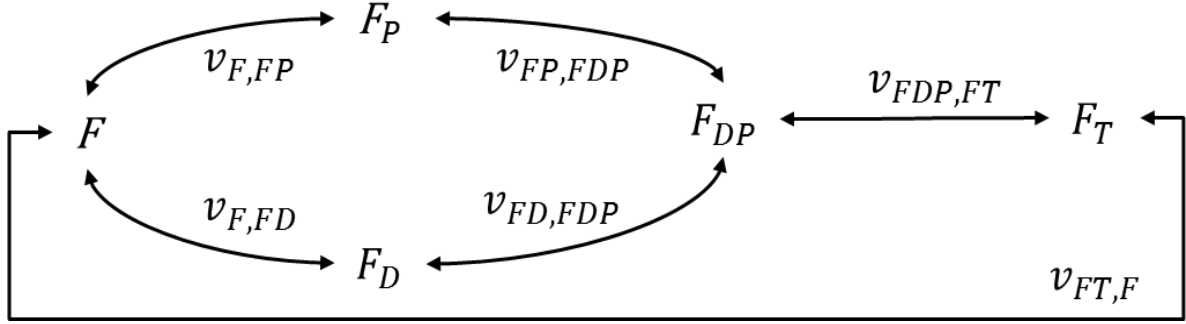


Figure 5.6: Reaction network associated to the mathematical model of ATP synthesis based on the model by Pänke and Rumberg (1996). Each node represents an open catalytic site of the ATP synthase (denoted by F), where subscripts refer to the different reactants of the reaction. The transitions through the loose bound and tight bound states are implicit in $v_{FDP,FT}$, whereas the rest of transitions describe exchange of metabolites between open sites and the stroma. F stands for an ATPase catalytic site and the subscripts indicate bound substrates: P is phosphate, D is ADP and T is ATP.

$$\frac{dF}{dt} = -v_{F,FP} - v_{F,FD} - v_{F,FT}, \quad (5.54)$$

$$\frac{dF_D}{dt} = v_{F,FD} - v_{FD,FDP}, \quad (5.55)$$

$$\frac{dF_P}{dt} = v_{F,FP} - v_{FP,FDP}, \quad (5.56)$$

$$\frac{dF_{DP}}{dt} = v_{FP,FDP} + v_{FD,FDP} - v_{FDP,FT} \text{ and} \quad (5.57)$$

$$\frac{dF_T}{dt} = v_{F,FT} + v_{FDP,FT}. \quad (5.58)$$

5.2.6 Proton motive force

The pH of the lumen of the thylakoid and stroma are determined by the balance of inbound and outbound H^+ fluxes and the buffering capacity of each compartment. In the equations below, bold font denotes vectors. Each vector corresponds to all the transitions associated to a transition rule (described in Tables 5.1, 5.4, and 5.6). The \sum symbol represents the sum over

all components of a vector. Several buffering species exist with different pK but their overall effect results in changes of pH being proportional to changes in total H^+ (Junge et al., 1979). Therefore, changes in pH in the lumen are computed as

$$\frac{d(pH_L)}{dt} = -\frac{\beta_L}{V_L C_t} \left[\sum \mathbf{v}_{OEC} + 2 \left(\sum \mathbf{v}_{cytf1} + \sum \mathbf{v}_{cytf2} - \sum \mathbf{v}_{cytb1} - \sum \mathbf{v}_{cytb2} \right) \right] - \frac{\beta_L}{V_L C_t} \left(4v_{NDH} - \frac{v_{FDP,FT} HPR}{3} \right), \quad (5.59)$$

whereas, for the stroma, the changes are described by the expression

$$\frac{d(pH_S)}{dt} = \frac{\beta_S}{V_S C_t} \left[v_{FDP,FT} HPR - 2 \left(\sum \mathbf{v}_{pPQH2r} - \sum \mathbf{v}_{pPQH2b} + \sum \mathbf{v}_{nPQH2r} - \sum \mathbf{v}_{nPQH2b} \right) \right] - \frac{\beta_S}{V_S C_t} (6v_{NDH} + v_{FNR} + 2v_{FQR} + 2v_{FTR} + v_{wvc} + 8v_{NR}) - \beta_S \left(\frac{2 + 2\phi}{2 + 1.5\phi} v_r + v_{MDH} \right), \quad (5.60)$$

Table 5.9: Parameters associated to ATP synthase. See bottom of the table for sources.

Symbol	Description	Value	Source
k_{FPf}	Rate constant of phosphate binding to ATP synthase	$8.1 \times 10^2 \text{ m}^3 \text{ mol}^{-1} \text{ s}^{-1}$	1
k_{FDf}	Rate constant of ADP binding to ATP synthase	$1.2 \cdot 10^4 \text{ m}^3 \text{ mol}^{-1} \text{ s}^{-1}$	1
k_{FPr}	Rate constant of phosphate release from ATP synthase	$2 \times 10^3 \text{ s}^{-1}$	1
k_{FDr}	Rate constant of ADP release from ATPase	$3.7 \times 10^2 \text{ s}^{-1}$	1
k_{FTf}	Rate constant of ATP binding to ATP synthase	$2.1 \times 10^3 \text{ m}^3 \text{ mol}^{-1} \text{ s}^{-1}$	1
k_{FTr}	Rate constant of ATP release from ATP synthase	$2.2 \times 10^2 \text{ s}^{-1}$	1
k_{F10}	Maximum rate constant of ATP synthesis inside a tight catalytic site	$5.1 \times 10^3 \text{ s}^{-1}$	1
k_{F20}	Maximum rate constant of ATP hydrolysis inside a tight catalytic site	$2.2 \times 10^3 \text{ s}^{-1}$	1
K_{FC}	Equilibrium coefficient of ATP synthesis inside a tight catalytic site	3.1	1
K_F	Equilibrium coefficient of conformational changes of ATP synthase	110	1
pmf_d	Displacement in the sensitivity of ATP synthesis to proton motive force due to reduction of the γ subunit	$6 \times 10^{-2} \text{ V}$	2
HPR	Amount of H^+ transported per rotation of the ATPase	14	3

1. (Pänke and Rumberg, 1996).

2. (Junesch and Gräber, 1987).

3 (Seelert et al., 2000; Varco-Merth et al., 2008; Vollmar et al., 2009).

where β_L ($\text{m}^3 \text{ mol}^{-1}$) and β_S ($\text{m}^3 \text{ mol}^{-1}$) are the total buffering capacities of the lumen and stroma (i.e. the ratio $\Delta\text{pH}/\Delta\text{H}^+$), and V_L ($\text{m}^3 \text{ mol}^{-1}$) and V_S ($\text{m}^3 \text{ mol}^{-1}$) are the volumes of the lumen and stroma per amount of chlorophyll. An often assumed value for V_S is $25 \mu\text{L mg}^{-1}$, which has been confirmed experimentally for *S. oleracea* using osmotic methods by Robinson (1985) and Lunn and Douce (1993). However, using electron micrographs, Winter et al. (1994) estimated the volume of the stroma per amount of chlorophyll to be $65 \mu\text{L mg}^{-1}$ in *S. oleracea* and $35 \mu\text{L mg}^{-1}$ in *H. vulgare*, which indicates variability across species and experimental methods. As default and in line with most studies, the value of $25 \mu\text{L mg}^{-1}$, (equivalent to $2.2 \times 10^{-2} \text{ m}^3 \text{ mol}^{-1}$, Table 5.10) was assumed for V_S . Different ratios between the V_S and V_L have been reported, including values of 2 (Winter et al., 1993), 8 (Laisk et al., 2009a; Oja et al., 2011) and 14 (Lawlor, 2001). An intermediate value of 8 is assumed, leading to V_L being $2.8 \times 10^{-3} \text{ m}^3 \text{ mol}^{-1}$.

The pmf is of made of two components: the difference in pH across the thylakoid membrane (ΔpH) and the electrical field across the thylakoid membrane ($\Delta\Psi$, V):

$$pmf = \Delta\Psi + \frac{2.3RT_L}{F} (\Delta\text{pH}), \quad (5.61)$$

where $\Delta pH = pH_S - pH_L$, R is the ideal gas constant ($8.31 \text{ J mol}^{-1} \text{ K}^{-1}$), and F is the Faraday constant (96485 C mol^{-1}). Ions are transported across the thylakoid membrane, which affects the value of $\Delta\Psi$. The rate of change of $\Delta\Psi$ is calculated as

$$\frac{d\Delta\Psi}{dt} = \frac{[(v_{Hin} - v_{Hout})/(S_{th}C_t) + F_i]F}{C_{mem}}, \quad (5.62)$$

where C_{mem} is the electrical capacitance of the thylakoid membrane assumed to be $0.6 \times 10^{-2} \text{ F m}^{-2}$ (Cruz et al., 2001), F_i ($\text{mol m}^{-2} \text{ s}^{-1}$) is the flux of ions across the thylakoid membrane and S_{th} ($\text{m}^2 \text{ mol}^{-1}$) is the surface of the thylakoid membrane per amount of chlorophyll, assumed to be $5.3 \times 10^5 \text{ m}^2 \text{ mol}^{-1}$ (Lawlor, 2001).

Existing models of ion transport across the thylakoid membrane include the use of the Goldman–Hodgkin–Katz flux equation (Vredenberg and Tonk, 1975; van Kooten et al., 1986) or a linear Ohmic model where the flux of an ion is proportional to its ionic proton motive force (Cruz et al., 2001; Zaks et al., 2012). In preliminary simulations with these models, it was observed that both approaches led to an increase in the ratio $\Delta\Psi/\text{pmf}$ as pmf increased. However, estimations of these components *in vivo* from measurements of electrochromic shift (ecs) and for different $[\text{CO}_2]$ and light intensities (Avenson et al., 2004; Takizawa et al., 2007) indicate that the ratio $\Delta\Psi/\text{pmf}$ decreases as pmf increases.

From a mechanistic point of view, such behaviour could be achieved by regulating the activities of channels that facilitate transport of ions, additional ion transport across the chloroplast envelope, and H^+/K^+ counterion transport across the thylakoid membrane (Finazzi et al., 2015; Pottosin and Shabala, 2016). Recent experimental evidence indicates that the partitioning of pmf into its pH and electrical components is regulated by the activities of such channels (Armbruster et al., 2014; Kunz et al., 2014; Herdean et al., 2016). However,

quantitative information of the kinetics and regulation of these channels is still lacking which prevents the development of a mechanistic model. Instead, an empirical approach is proposed based on (i) observed relationship between $\Delta\Psi$, $pH_S - pH_L$, and pmf and (ii) first-order kinetics to describe dynamical changes. From measurements of electrochromic shift, Takizawa et al. (2007) observed a linear relationship between light-induced ΔpH and pmf, with a positive intercept. Given that their measurements were all performed at pmf higher than the pmf in the darkness, a second linear expression was added (only limiting for $\Delta pH < 0.04$ such that it has no effect on the relationship in the light) to avoid negative ΔpH values in the simulations. The resulting relationship is

$$pmf_{ss} = \min \left[a_{pmf} + b_{pmf} \frac{2.3RT}{F} \Delta pH, (a_{pmf} + b_{pmf}) \frac{2.3RT}{F} \Delta pH \right], \quad (5.63)$$

where a_{pmf} (V) and b_{pmf} are empirical parameters. From the measurements of Takizawa et al. (2007) the values of $a_{pmf} = 0.03 \text{ V}$ and $b_{pmf} = 1.87$ were derived, assuming that 90% of the pmf in the darkness was in the form of $\Delta\Psi$, by extrapolating from the values in the light. From pmf_{ss} , the steady-state value of $\Delta\Psi$ ($\Delta\Psi_{ss}$) is calculated as

$$\Delta\Psi_{ss} = pmf_{ss} - \frac{2.3RT}{F} \Delta pH. \quad (5.64)$$

Assuming first-order kinetics, the flow of ions (F_i) required to achieve $\Delta\Psi_{ss}$ is calculated as

Table 5.10: Parameters associated with regulation of the pH in the lumen and stroma, proton motive force, and electrical field across the thylakoid membrane. See bottom of the table for sources.

Symbol	Description	Value	Source
β_L	Buffering capacity of the lumen of the thylakoid	$3.3 \times 10^{-2} \text{ m}^3 \text{ mol}^{-1}$	1
β_S	Buffering capacity of the stroma	$3.3 \times 10^{-2} \text{ m}^3 \text{ mol}^{-1}$	1
C_{mem}	Electrical capacitance of the thylakoid membrane	$0.6 \times 10^{-2} \text{ F m}^{-2}$	1
V_s	Volume of the stroma per unit of chlorophyll	$2.2 \times 10^{-2} \text{ m}^3 \text{ mol}^{-1}$	2
V_L	Volume of the lumen of the thylakoid per unit of chlorophyll	$2.8 \times 10^{-3} \text{ m}^3 \text{ mol}^{-1}$	2,3
S_{th}	Surface of the thylakoid membrane per unit of chlorophyll	$5.3 \times 10^5 \text{ m}^2 \text{ mol}^{-1}$	
a_{pmf}	Intercept of the relationship between proton motive force and $\Delta pH 2.3RT/F$ observed in leaves	$3 \times 10^{-2} \text{ V}$	4
b_{pmf}	Slope of the relationship between proton motive force and $\Delta pH 2.3RT/F$ observed in leaves	1.87	4
k_ψ	Rate constant of changes in the electrical field across the thylakoid membrane due counterion movement	10 s^{-1}	5

1. (Lunn and Douce, 1993; Cruz et al., 2001).
2. (Winter et al., 1994).
3. (Laisk et al., 2009a; Oja et al., 2011).
4. (Takizawa et al., 2007).
5. Estimated (see text for details).

$$F_i = \frac{(\Delta\Psi_{ss} - \Delta\Psi)k_\psi C_{mem}}{F}, \quad (5.65)$$

where k_ψ (s^{-1}) is an empirical rate constant representing the kinetics of changes in $\Delta\Psi$ and it can be estimated from ecs measurements. In order to reproduce observed time series of ecs (van Kooten et al., 1986; Cruz et al., 2001), a value of $k_\psi = 10 \text{ s}^{-1}$ was assumed.

5.2.7 Calvin cycle and CO₂ diffusion

A detailed model of the metabolism of the stroma is beyond the scope of this model, but realistic rates of ATP and NADPH consumption are required in order to define proper boundary conditions for the electron transport chain. This is especially important as the physiological roles of the different forms of alternative electron transport and NPQ are to regulate the total production of ATP and NADPH as well as their ratio. Since it is not among the objectives of this model to study the Calvin cycle and related metabolic pathways in detail, a simpler approach is used. The kinetics of Rubisco are described in detail, following the approach by Farquhar (1979), and the regulation of Rubisco activity is modelled based on empirical observations on the interaction between Rubisco activase (Rca) and Rubisco. Assuming that Rubisco limits the flow of carbon through the Calvin cycle, the rest of the cycle is simplified into a single step, catalysed by a light-regulated pseudo-enzyme (as many of the enzymes in the Calvin cycle increase their activities with

irradiance) that takes into account the stoichiometry of ATP and NADPH consumption of the Calvin cycle and photorespiration. Finally, in order to reproduce correctly the steady-state and dynamic conditions in leaves, an empirical, dynamical model of CO₂ diffusion is included. All parameters for this module can be found in Table 5.11.

5.2.7.1 Rubisco kinetics and regulation

Rubisco is the enzyme responsible for assimilation of CO₂ in the Calvin cycle, which drives most of the consumption of ATP and NADPH in the stroma. Modifying the equations by Farquhar (1979), in order to include the effect of partially active Rubisco, the rate of carboxylation (v_C) and oxygenation (v_O) can be calculated as

$$v_C = \frac{f_{RB} f_{RuBP} k_C C_C RB}{C_C + K_C \left(1 + \frac{O_2}{K_O}\right)} \quad (5.66)$$

and

$$v_O = \frac{f_{RB} f_{RuBP} k_O O_2 RB}{O_2 + K_O \left(1 + \frac{C_C}{K_C}\right)}, \quad (5.67)$$

where C_C (mol mol⁻¹) is the [CO₂] in the chloroplast, f_{RB} is fraction of Rubisco catalytic sites that are active (i.e., carbamylated and not bound to tight inhibitors), f_{RuBP} is the effect of RuBP concentration of Rubisco kinetics, k_C (s⁻¹) is the rate constant of carboxylation, RB (mM) is the concentration of Rubisco catalytic sites, K_C (mol mol⁻¹) is the half-saturation constant of RuBP carboxylation with respect to CO₂, K_O (mol mol⁻¹) is the half-saturation constant of RuBP oxygenation with respect to O₂, and k_O (s⁻¹) is the rate constant of oxygenation. The values of k_C , k_O , K_C , and K_O were assumed to be 4.16 s⁻¹, 1.0 s⁻¹, 3.1×10⁻⁴ mol mol⁻¹, and 0.18 mol mol⁻¹, respectively, based on measurements on *A. thaliana* by Walker et al. (2013). The value of f_{RuBP} is calculated as proposed by Farquhar (1979):

$$f_{RuBP} = \frac{RB + K'_{RuBP} + RuBP - \sqrt{(RB + K'_{RuBP} + RuBP)^2 - 4RB RuBP}}{2RB}, \quad (5.68)$$

where K'_{RuBP} (mol m⁻³) is the apparent half-saturation constant with respect to RuBP, which increases in the presence of PGA due to competitive inhibition (von Caemmerer, 2000):

$$K'_{RuBP} = K_{RuBP} \left(1 - \frac{PGA}{K_{I,PGA}}\right), \quad (5.69)$$

where K_{RuBP} (mol m⁻³) is the value of K'_{RuBP} in the absence of PGA and $K_{I,PGA}$ (mol m⁻³) is the inhibition constant with respect to PGA. The values of K_{RuBP} and $K_{I,PGA}$ were assumed to be 2.2×10⁻² mol m⁻³ and 0.84 mol m⁻³, respectively (von Caemmerer, 2000).

The activity of Rubisco changes with irradiance and [CO₂] due to changes in the concentration of Rubisco inhibitors and regulation of Rubisco activase activity (Zhang and Portis, 1999; Parry et al., 2013). The activity of Rubisco activase (f_{Rca}) decreases with the ratio of ADP over ATP (ADP/ATP) and the sensitivity to this ratio depends on reduction of the larger isoform of Rca (Zhang and Portis, 1999; Carmo-Silva and Salvucci, 2013), at

least in species that contain two isoforms of Rca. The following empirical expression captures the sensitivity of a population of Rca to ADP/ATP:

$$f_{Rca} = f_{Rca,m} + (1 - f_{Rca,m}) \left(f_{Rca,r} \exp\left(-\frac{f_{Rca,s}^r ADP}{ATP}\right) + f_{Rca,o} \exp\left(-\frac{f_{Rca,s}^o ADP}{ATP}\right) \right), \quad (5.70)$$

where $f_{Rca,r}$ and $f_{Rca,o}$ are the fractions of the Rca pool that are reduced and oxidised, respectively and $f_{Rca,m}$, $f_{Rca,s}^r$, and $f_{Rca,s}^o$ are empirical parameters with values equal to 0.04, 2.0, and 10.8 based on the measurements reported by Zhang and Portis (1999) for *A. thaliana*.

The activity of Rca affects both steady-state activation state of Rubisco ($f_{RB,ss}$) as well as the rate of activation of Rubisco. Based on the conceptual model of Mate et al. (1996) and measurements reported by Mott and Woodrow (2000), the relationship between $f_{RB,ss}$ and Rca is assumed to be hyperbolic:

$$f_{RB,ss} = \frac{f_{Rca} Rca}{f_{Rca} Rca + K_{A,Rca}}, \quad (5.71)$$

where $K_{A,Rca}$ is an apparent half-saturation constant with a value of 0.1 mol m^{-3} estimated from measurements reported by Mott and Woodrow (2000). Knowing a maximum value of $f_{RB,ss}$ *in vivo* of 0.92 for *A. thaliana* (Carmo-Silva and Salvucci, 2013), the concentration of Rca was estimated to be 1.23 mol m^{-3} .

Changes in Rubisco activity follow first-order kinetics (Sassenrath-Cole et al., 1994; Percy et al., 1997; Mott and Woodrow, 2000) and the rate constant of Rubisco activation is proportional to the concentration of reduced Rca:

$$\frac{df_{RB}}{dt} = \begin{cases} k_{Rbi} f_{Rca} Rca (f_{RB,ss} - f_{RB}) & \text{if } f_{RB,ss} > f_{RB} \\ k_{RBd} (f_{RB,ss} - f_{RB}) & \text{if } f_{RB,ss} \leq f_{RB} \end{cases}, \quad (5.72)$$

where k_{Rbi} (s^{-1}) is the maximum rate constant of Rubisco activation with fully active Rca, and k_{RBd} (s^{-1}) is the rate constant of Rubisco inhibition. The values reported in the literature for k_{RBd} vary between $4.2 \times 10^{-4} \text{ s}^{-1}$ (Gross et al., 1991) to $1.6 \times 10^{-3} \text{ s}^{-1}$ (Hammond et al., 1998) and we chose a value of $4.2 \times 10^{-4} \text{ s}^{-1}$. In order to reproduce the rates of photosynthetic induction measured by Kaiser et al. (2016), as discussed in Section 5.3.1, it was assumed that $k_{Rbi} = 4.5 \text{ m}^3 \text{ mol}^{-1} \text{ s}^{-1}$.

5.2.7.2 Regeneration of RuBP

In order to minimize the number of parameters required to calculate RuBP regeneration but still produce realistic rates of ATP and NADPH consumption, we simplified the regeneration phase of the Calvin cycle into a single pseudo-reaction. This simplified approach is similar to previous simplified models of the Calvin cycle (Percy et al., 1997; Kirschbaum et al., 1998). The following known features are represented in the model:

1. Part of the carbon stored in the PGA pool will not be converted to RuBP but used for sucrose and starch synthesis.

2. The consumption of ATP and NADPH is coupled with a stoichiometric ratio that depends on the ratio of oxygenation to carboxylation.

3. Several enzymes of the Calvin cycle are regulated by thiol reduction as well as other allosteric regulators which results in an increase of their activities with irradiance.

In addition, the following assumptions are made:

1. The total amounts of carbon and phosphate stored as intermediates of the Calvin cycle are conserved.

2. The photorespiration pathway returns one PGA to the Calvin cycle for every two phosphoglycolates generated by oxygenation.

3. The NH_4^+ released by glycine decarboxylase is re-assimilated in the stroma using ATP and NADPH produced by the photosynthetic electron transport chain.

From these features and assumptions, the following expression is deduced to calculate the rate of PGA conversion into RuBP (v_r , $\text{mol m}^{-2} \text{s}^{-1}$)

$$v_r = \frac{\text{PGA ATP NADPH } f_R V_{rmax}}{(\text{PGA} + K_{PGA})(\text{ATP} + K_{R,ATP})(\text{NADPH} + K_{R,NADPH})}, \quad (5.73)$$

where f_R is the activation state of the pseudo-enzyme in the regeneration phase of the Calvin cycle, V_{rmax} ($\text{mol m}^{-2} \text{s}^{-1}$) is the maximum rate of PGA conversion into RuBP, K_{PGA} (mol m^{-3}), $K_{R,ATP}$ (mol m^{-3}) and $K_{R,NADPH}$ (mol m^{-3}) are the half saturation constants with respect to PGA, ATP and NADPH, respectively. Pearcy et al. (1997) and Kirschbaum et al. (1998) assumed values for K_{PGA} of $25 \mu\text{mol m}^{-2}$ and $5 \mu\text{mol m}^{-2}$ (expressed as amount per unit of leaf area). Given the volume of stroma assumed in this study, these values correspond to 2.5 mol m^{-3} and 0.5 mol m^{-3} , respectively, and a value of 0.5 mol m^{-3} was chosen for the model. In the Calvin cycle, NADPH is only consumed by glyceraldehyde 3-phosphate dehydrogenase, with a half-saturation constant of $2.3 \times 10^{-2} \text{ mol m}^{-3}$ (Fridlyand, 1992). ATP is consumed by different reactions, catalysed by phosphoglycerate kinase (PGK) and ribulose-5-phosphate kinase (PRK). Reported values for the Michaelis-Menten constant of PGK vary between 0.24 and 0.70 mol m^{-3} (Köpke-Secundo et al., 1990; Fridlyand, 1992), whereas for PRK it varies between 0.03 and 0.065 mol m^{-3} (Laing et al., 1981; Gardemann et al., 1982). A value of 0.24 mol m^{-3} , corresponding to PGK, was assumed for $K_{R,ATP}$, as it is more limiting than the value for PRK.

Based on measurements of the steady-state activity of PRK and fructose-1,6-bisphosphate (FBPase) as a function of irradiance (Sassenrath-Cole and Pearcy, 1994b) a non-rectangular hyperbola was chosen to calculate the steady-state value of f_R (f_{Rss}) as a function of irradiance:

$$f_{Rss} = f_{R,0} + \frac{\alpha_{f_R} I_P + (1 - f_{R,0}) - \sqrt{(\alpha_{f_R} I_P + (1 - f_{R,0}))^2 - 4\alpha_{f_R} I_P \theta_{f_R} (1 - f_{R,0})}}{2\theta_{f_R}}, \quad (5.74)$$

where $f_{R,0}$ is the minimum value of f_R (in the darkness), α_{f_R} ($\text{mol}^{-1} \text{m}^2 \text{s}$) is the initial slope of the hyperbola and θ_{f_R} determines the curvature of the hyperbola. From the data of Sassenrath-Cole et al. (1994), the values for $f_{R,0}$, α_{f_R} and θ_{f_R} were estimated to be 0.04, $2.5 \times 10^3 \text{ mol}^{-1} \text{m}^2 \text{s}$ and 0.96, respectively. These values correspond to FBPase, but similar values could be derived for PRK from the same source. Changes in the activity of enzymes

like PRK and FBPase follow first-order kinetics (Sassenrath-Cole et al., 1994) with different rate constants for increases and decreases:

$$\frac{df_R}{dt} = \begin{cases} (f_{R_{SS}} - f_R)k_{iR} & \text{if } f_{R_{SS}} > f_R \\ (f_{R_{SS}} - f_R)k_{dR} & \text{if } f_{R_{SS}} \leq f_R \end{cases} \quad (5.75)$$

where k_{iR} (s^{-1}) and k_{dR} (s^{-1}) are the rate constants for increase and decreases in the activities of the regulated enzymes. From the data by Sassenrath-Cole et al. (1994), k_{iR} and k_{dR} were estimated to be 6.3×10^{-3} and $7.5 \times 10^{-3} s^{-1}$, respectively, for FBPase. From the same source, similar values could be derived for PRK.

5.2.7.3 Dynamic balance of metabolites

In order to complete the Calvin cycle, dynamic changes in the concentrations of metabolites and CO_2 are computed from the rates given. Changes in PGA are determined by the two reactions involved in its production and consumption:

$$\frac{dPGA}{dt} = (2 + 1.5\phi)v_c - v_r, \quad (5.76)$$

and similarly for RuBP

$$\frac{dRuBP}{dt} = \frac{1 + \phi}{2 + 1.5\phi} v_r - (1 + \phi)v_c. \quad (5.77)$$

where ϕ is defined as:

$$\phi = \frac{v_o}{v_c}. \quad (5.78)$$

The coefficient $(1 + \phi)/(2 + 1.5\phi)$ takes into account the different carbon compositions of PGA (3C) and RuBP (5C) as well as the consumption of intermediates for sucrose and starch synthesis, which is assumed to proceed in such a way that the total carbon and phosphate in the Calvin cycle are conserved. That is, as ϕ increases, the fraction of PGA that is converted into RuBP increases, the fraction allocated to starch and sucrose synthesis decreases.

The dynamics of ATP and ADP are driven by the balance of their synthesis and consumption by ATPase, regeneration of RuBP, photorespiration, and nitrate assimilation. The differential equation for ATP is:

$$\frac{dATP}{dt} = -v_{F,FT} - v_{NR} - \frac{3 + 3.5\phi}{2 + 1.5\phi} v_r, \quad (5.79)$$

and for ADP it is:

$$\frac{dADP}{dt} = -v_{F,FD} - v_{FP,FDP} + v_{NR} + \frac{3 + 3.5\phi}{2 + 1.5\phi} v_r. \quad (5.80)$$

The free inorganic phosphate can be derived from the total phosphate in the system (Pi_T , mol m^{-3}) and phosphate bound in different forms as:

$$Pi = Pi_T - 3ATP - 2ADP - 2RuBP - PGA. \quad (5.81)$$

The balance of NADPH is calculated from its production by FNR, consumption by the Calvin cycle (considering the extra consumption by photorespiration) and consumption by the malate shuttle as:

$$\frac{dNADPH}{dt} = v_{FNR} - \frac{2 + 2\phi}{2 + 1.5\phi} v_r - v_{MDH}, \quad (5.82)$$

whereas the dynamics of NADP⁺ is simply given by:

$$\frac{dNADP^+}{dt} = -\frac{dNADPH}{dt}. \quad (5.83)$$

In order to capture the effect of fluctuating irradiance on the value of C_c , empirical equations for CO₂ diffusion are included. The path between the air and the stroma of the chloroplast is separated into three components: a component associated with the stomatal pores (g_s , mol m⁻² s⁻¹), a component associated with the wall of mesophyll cells, the cellular membrane and part of the cytosol (g_w , mol m⁻² s⁻¹) and a component associated with the rest of the cytosol, the chloroplast envelope, and the stroma of the chloroplast (g_c , mol m⁻² s⁻¹).

Thus, changes in [CO₂] in the stroma (C_c), in the cytosol of mesophyll cells (C_{cyt}), and in the intercellular spaces (C_i) can be simulated with the following differential equations:

$$\frac{dC_c}{dt} = \left((C_{cyt} - C_c)g_c - V_c \right) \frac{RT}{PV_r}, \quad (5.84)$$

$$\frac{dC_{cyt}}{dt} = \left((C_i - C_{cyt})g_w + R_d + \frac{1}{2}k_{PR}PR - (C_{cyt} - C_c)g_c \right) \frac{RT}{PV_r} \quad (5.85)$$

$$\frac{dC_i}{dt} = \left((C_a - C_i)g_s - (C_i - C_{cyt})g_w \right) \frac{RT}{PV_r} \quad (5.86)$$

where R_d is the rate of mitochondrial respiration assumed to be 0.65×10^{-6} mol m⁻² s⁻¹ based on the measurements by Kaiser et al. (2016). Changes in g_s were modelled as proposed by Vialet-Chabrand et al. (2013):

$$\frac{dg_s}{dt} = k_{g_s} \ln \left(\frac{G - r_0}{g_s - r_0} \right) (g_s - r_0), \quad (5.87)$$

where G (mol m⁻² s⁻¹) is the steady-state value of g_s , k_{g_s} (s⁻¹) is a rate constant, and r_0 (mol m⁻² s⁻¹) is an empirical parameter that determines the initial time lag in changes in stomatal conductance after a rapid change in irradiance. We estimated k_{g_s} and r_0 from measurements on *A. thaliana* by Kaiser et al. (2016) resulting in values of 7.0×10^{-4} s⁻¹ and 1.0×10^{-2} mol m⁻² s⁻¹, respectively. G increases with irradiance according to the following expression (Kirschbaum et al., 1988):

$$G = g_{sm} \left(f_{l,0} + \frac{1 - f_{l,0} + \alpha_{f_l} I - \sqrt{(1 - f_{l,0} + \alpha_{f_l} I)^2 - 4\theta_{f_l} \alpha_{f_l} I (1 - f_{l,0})}}{2\theta_{f_l}} \right), \quad (5.88)$$

where g_{sm} ($\text{mol m}^{-2} \text{s}^{-1}$) is the maximum stomatal conductance to fluxes of CO_2 , $f_{l,0}$ is the ratio between minimum and maximum stomatal conductance, α_G ($\text{mol}^{-1} \text{m}^2 \text{s}$) and θ_{f_I} are the initial slope and curvature of the response of steady-state stomatal conductance to irradiance. The values of g_{sm} , $f_{l,0}$, θ_{f_I} , and α_{f_I} were estimated from measurements by Kaiser et al. (2016), resulting in values of $0.16 \text{ mol m}^{-2} \text{ s}^{-1}$, 0.36 , 0.97 , and $5.6 \times 10^3 \text{ mol}^{-1} \text{ m}^2 \text{ s}$, respectively. Finally, the net rate of CO_2 assimilation is calculated as:

$$A = (C_a - C_i)g_s, \quad (5.89)$$

5.2.8 Regulation by thioredoxin

The kinetic properties of several protein complexes and enzymes in the stroma and thylakoid membrane are regulated by reduction of disulfide bonds by thioredoxin to form thiol residues. Although different forms of thioredoxin exist and two (thioredoxin m and f) are most important in the redox regulation of photosynthesis, their midpoint redox potentials are similar (Schürmann and Buchanan, 2008) and thus the thioredoxin system can be well approximated by assuming a single pool of thioredoxin. A further simplification is that only reduction of thioredoxin by ferredoxin is considered, although recent experimental evidence indicates that NADPH may also contribute to thioredoxin reduction in chloroplasts via NADPH-dependent thioredoxin reductase C (NTRC). NTRC is involved in the regulation of ATP synthase at low irradiance (Carrillo et al., 2016), among other physiological functions (Schürmann and Buchanan, 2008). The model does not include NTRC due to lack of adequate kinetic data and details on its mechanism of action and this may affect simulations of ATP synthase activity at low irradiance. Given the simplifications assumed for the metabolism of the stroma, this model does not include regulation of enzymes in the Calvin cycle. Thus, the four enzymes and protein complexes considered for thioredoxin regulation in the model are Rca (Sections 5.2.7.1), ATPase (Section 5.2.5), MDH (Section 5.2.4.3.2), and FQR (Section 5.2.4.2.2).

The reduction of thioredoxin by ferredoxin is catalysed by ferredoxin:thioredoxin reductase (FTR). The activity of FTR cannot be measured directly, so a second reaction that is sensitive to thioredoxin needs to be included in the assay (Schürmann, 2002). However, these assays are only useful to determine the kinetics of the reaction in the forward direction (i.e., thioredoxin reduction by ferredoxin), so assumptions were made regarding the kinetics of the reverse reaction. It is assumed that the reaction follows hyperbolic kinetics, so the following expression is used:

$$v_{FTR} = \frac{v_{max,FTR}F_d_rTh_o}{(F_d_r + K_{FTR,Fdr})(Th_o + K_{FTR,Tho})} - \frac{v_{max,FTR}F_d_oTh_r}{K_{FTR}(F_d_o + K_{FTR,Fdo})(Th_r + K_{FTR,Thr})}, \quad (5.90)$$

where $v_{max,FTR}$ ($\text{mol m}^3 \text{ s}^{-1}$) is the maximum activity of FTR, K_{FTR} is the equilibrium coefficient of the reaction, and $K_{FTR,Fdr}$ (mol m^{-3}), $K_{FTR,Fdo}$ (mol m^{-3}), $K_{FTR,Tho}$ (mol m^{-3}) and $K_{FTR,Thr}$ (mol m^{-3}) are half-saturation constants with respect to F_d_r , F_d_o , Th_o , and Th_r , respectively. The value of $K_{FTR,Tho}$ has been estimated to be $3 \times 10^{-3} \text{ mol m}^{-3}$ (Navarro et al., 1991) and $K_{FTR,Thr}$ was assumed to have the same value. Values reported for $K_{FTR,Fdo}$ vary from $1.7 \times 10^{-3} \text{ mol m}^3$ (Hirasawa et al., 1988) to $2 \times 10^{-2} \text{ mol m}^3$ (Glauser et al., 2004). A value of $2 \times 10^{-2} \text{ mol m}^3$ was chosen for both $K_{FTR,Fdr}$ and $K_{FTR,Fdo}$ (Table 5.12). The equilibrium coefficient is calculated as:

Table 5.11: Parameters associated to Calvin cycle and CO₂ diffusion. See bottom of the table for sources.

Symbol	Description	Value	Source
K_C	Half saturation constant of RuBP carboxylation with respect to CO ₂	$3.1 \times 10^{-4} \text{ mol mol}^{-1}$	1
K_O	Half saturation constant of RuBP oxygenation with respect to O ₂	$1.8 \times 10^{-1} \text{ mol mol}^{-1}$	1
k_C	Catalytic constant of RuBP carboxylation by Rubisco	4.16 s^{-1}	1
k_O	Catalytic constant of RuBP oxygenation by Rubisco	1.0 s^{-1}	1
$K_{I,PGA}$	Inhibition constant of PGA with respect to RuBP binding to Rubisco	$8.4 \times 10^{-1} \text{ mol m}^{-3}$	2
K_{RuBP}	Half saturation constant of RuBP oxygenation or carboxylation with respect to RuBP	$2.2 \times 10^{-2} \text{ mol m}^{-3}$	2
$f_{Rca,m}$	Minimum fraction of Rca at saturating values of ADP/ATP	0.04	3
$f_{Rca,s}^r$	Sensitivity to ADP/ATP when all redox-sensitive Rubisco activase isoforms are reduced	2.0	3
$f_{Rca,s}^o$	Sensitivity to ADP/ATP when all redox-sensitive Rubisco activase isoforms are oxidised	10.8	3
$K_{A,Rca}$	Apparent half-saturation constant of steady-state Rubisco activity with respect to Rubisco activase	0.1 mol m^{-3}	4
k_{Rbd}	Rate constant of Rubisco inhibition	$4.2 \times 10^{-4} \text{ s}^{-1}$	5
k_{Rbi}	Second order rate constant of Rubisco activation in the presence of fully active Rubisco activase	$4.5 \times 10^{-3} \text{ m}^3 \text{ mol}^{-1} \text{ s}^{-1}$	6
$K_{R,ATP}$	Half saturation constant of PGA reduction into RuBP with respect to ATP	$2.4 \times 10^{-1} \text{ mol m}^{-3}$	7
$K_{R,NADPH}$	Half saturation constant of PGA reduction into RuBP with respect to NADPH	$2.3 \times 10^{-2} \text{ mol m}^{-3}$	8
K_{PGA}	Half saturation constant of PGA reduction into RuBP with respect to PGA	0.5 mol m^{-3}	9
V_{rmax}	Maximum rate of PGA reduction into RuBP	$17.0 \text{ mol m}^{-3} \text{ s}^{-1}$	6
$f_{R,0}$	Minimum activation state of the pseudo-enzyme that converts PGA into RuBP	4.0×10^{-2}	10
α_{f_R}	Initial slope of the response of the activity of the pseudo-enzyme that converts PGA into RuBP with respect to irradiance	$2.5 \times 10^3 \text{ mol}^{-1} \text{ m}^2 \text{ s}$	10
θ_{f_R}	Curvature of the response of the activity of the pseudo-enzyme that converts PGA into RuBP with respect to irradiance	0.96	10

k_{dR}	Rate constant of decreases in the activity of the pseudo-enzyme that converts PGA into RuBP	$7.5 \times 10^{-3} \text{ s}^{-1}$	10
k_{iR}	Rate constant of increases in the activity of the pseudo-enzyme that converts PGA into RuBP	$6.3 \times 10^{-3} \text{ s}^{-1}$	10
Pi_T	Total concentration of phosphate in the stroma	30 mol m^{-3}	11
g_w	Conductance of the cell wall to fluxes of CO_2	$0.6 \text{ mol m}^{-2} \text{ s}^{-1}$	12
g_c	Conductance of the chloroplast fluxes of CO_2	$0.3 \text{ mol m}^{-2} \text{ s}^{-1}$	12
k_{g_s}	Rate constant at which stomatal conductance changes after a change in irradiance	$7 \times 10^{-4} \text{ s}^{-1}$	13
r_0	Empirical parameter that determines the initial time lag in changes in stomatal conductance after a rapid change in irradiance	$1.0 \times 10^{-2} \text{ mol m}^{-2} \text{ s}^{-1}$	13
g_{sm}	Maximum stomatal conductance to fluxes of CO_2	$0.16 \text{ mol m}^{-2} \text{ s}^{-1}$	13
$f_{l,0}$	Ratio between minimum and maximum stomatal conductance	0.361	13
θ_{f_l}	Curvature of the response of steady-state stomatal conductance to irradiance	0.97	13
α_{f_l}	Initial slope of the response of steady-state stomatal conductance to irradiance	$5.6 \times 10^3 \text{ mol}^{-1} \text{ m}^2 \text{ s}$	13
R_d	Rate of mitochondrial respiration	$0.6 \times 10^{-6} \text{ mol m}^{-2} \text{ s}^{-1}$	6

1. (Walker et al., 2013).
2. (von Caemmerer, 2000).
3. (Zhang and Portis, 1999).
4. (Mott and Woodrow, 2000; Carmo-Silva and Salvucci, 2013).
5. (Gross et al., 1991).
6. Estimated from data in Section 5.3.
7. (Köpke-Secundo et al., 1990; Fridlyand, 1992).
8. (Fridlyand, 1992).
9. (Kirschbaum et al., 1998).
10. (Sassenrath-Cole et al., 1994).
11. (Dietz and Heber, 1984; Schimkat et al., 1990).
12. Calculated in Chapter 4 with data from Flexas et al. (2007b) and Tholen et al. (2012).
13. Calculated in Chapter 4 with data from Chapter 3.

$$K_{FTR} = \exp \left[\frac{2F(E_{m,Th} - E_{m,Fd})}{RT} \right], \quad (5.91)$$

where $E_{m,Th}$ (V) is the midpoint redox potential of thioredoxin at the pH of the stroma, calculated from a midpoint redox potential at a pH of 7 of -0.3 V and taking into account a sensitivity of 0.059 V per pH unit (Schürmann and Buchanan, 2008). The reduction of redox-sensitive enzymes by thioredoxin are assumed to follow the law of mass action with the following general expression:

$$v_{DA} = k_{DA} \left\{ Th_r E_o - \frac{Th_r E_r}{\exp \left[\frac{2F(E_{m,E} - E_{m,Th})}{RT} \right]} \right\}, \quad (5.92)$$

where k_{DA} ($\text{m}^3 \text{mol}^{-1} \text{s}^{-1}$) is a second-order rate constant of electron transfer from thioredoxin to the enzyme, E_o (mol m^{-3}) and E_r (mol m^{-3}) are the concentrations of oxidised and reduced forms of the enzyme and $E_{m,E}$ (V) is the midpoint redox potential of the enzyme at the pH of the stroma. To calculate the redox state at the pH of the stroma from the value normalized at a pH of 7 the linear conversion $E_m = E_{m7} - 5.9 \times 10^{-2} (pH_S - 7)$ should be used. Also, for this general equation to be dimensionally correct, all concentrations must be expressed in units of mol m^{-3} . For FQR and ATPase, which are quantified as amounts per unit of surface in the model, they are divided by the term $V_S C_t$. Equation 5.92 is applied in the model to calculate the rates of MDH reduction (v_{MDHr}), ATPase reduction (v_{F_r}), reduction of the larger, redox-sensitive isoform of Rca (v_{Rcar}) and reduction of FQR (v_{FQRr}). In the case of Rca reduction, it is important to realize that, in some species like *N. tabacum*, only the smaller (redox-insensitive) Rca isoform is present. Such species could be simulated by setting $k_{Rcar} = 0$ such that the reduced form is never formed. However, the parameters regarding sensitivity to the ADP/ATP ratio should also be adjusted (Carmo-Silva and Salvucci, 2013).

The midpoint redox potentials of MDH, ATPase, Rca, and FQR at a pH of 7 were assumed to be -0.33 V (Schürmann and Buchanan, 2008), -0.28 V (Schürmann and Buchanan, 2008), -0.29 V (Schürmann and Buchanan, 2008), and -0.28 V (Strand et al., 2016a), respectively. The value for ATPase was confirmed *in vivo* by Wu et al. (2007) with ecs measurements, obtaining an E_{m7} of -0.284 V on *A. thaliana* ecotype Columbia (Col-0), though Kohzuma et al. (2012) estimated, for the same genotype and also using ecs measurements *in vivo*, an E_{m7} of -0.326 V. The reasons for such differences is not clear, but they could have a significant impact on the regulation of ATPase.

The rate constant of reduction by thioredoxin was assumed to be $10^2 \text{m}^3 \text{mol}^{-1} \text{s}^{-1}$ for all the enzymes (Table 5.12). When combined with the kinetics assumed for FTR, it yielded results that are in agreement with measured rates of ATPase reduction (Strelow and Rumberg, 1993), MDH reduction (Carr et al., 1999) and Rca reduction (Zhang and Portis, 1999). No kinetic data was found for the rate of FQR reduction, although they were characterized to be “rapid” by Strand et al. (2016a).

The rates of change of the reduced forms of the redox-regulated enzymes are calculated from the rates of reduction as:

$$\frac{dT h_r}{dt} = v_{FTR} - v_{MDHr} - v_{FQRr} - v_{Fr}, \quad (5.93)$$

$$\frac{dFQR_r}{dt} = v_{FQRr}, \quad (5.94)$$

$$\frac{dMDHr}{dt} = v_{MDHr}, \quad (5.95)$$

$$\frac{dRCAr}{dt} = v_{RCAr} \text{ and} \quad (5.96)$$

$$\frac{dFr}{dt} = v_{Fr}. \quad (5.97)$$

The rate of change of the concentrations of the oxidised forms are calculated from the negative of the rate of change of the reduced form (e.g. $dTh_o/dt = -dTh_r/dt$).

5.2.9 Concentrations and amounts

In this section, the concentrations of the different protein complexes, electron carriers and metabolites are discussed, along with the maximum rates of catalysed reactions. All values are taken from different sources in the literature and emphasis is placed on the relative amounts of the different components of the system, to ensure a realistic parameterization. The values are also adjusted to obtain reasonable fits to some of the measurements discussed in Section 5.3. Whenever possible, values corresponding to *A. thaliana* grown at low light ($< 300 \mu\text{mol m}^{-2} \text{s}^{-1}$) are chosen (if such data was not available, data from other appropriate C3 species were used). First, the concentration of protein complexes and electron carriers in the thylakoid membrane (including alternative electron sinks) is calculated. Then, the amount of Rubisco and maximum rate of RuBP regeneration is estimated. Finally, typical values for the concentrations of metabolites in the stroma are taken from the literature and assigned to the relevant parameters and state variables (Table 5.13).

For a given species, the contents of PSII, PSI and cyt b_6f increase with growth irradiance, in parallel with increases in leaf nitrogen content (Evans, 1987; Makino et al., 1997). For example, the PSII content of leaves varied between 0.3×10^{-6} and $1.3 \times 10^{-6} \text{ mol m}^{-2}$ across different species and different growth irradiances (Osmond et al., 1980; Chow et al., 1988; Chow et al., 1991; Schöttler and Tóth, 2014). In addition, acclimation of photosynthesis to irradiance results in changes of the ratios between PSI and PSII content (PSI:PSII ratio), and between cyt b_6f and PSII content (cyt b_6f :PSII ratio) with important differences across species (Figure 5.7). The Pc:PSII ratio also increases with irradiance, although values reported only varied between 1.9 and 3.1 (Graan and Ort, 1984; Burkey, 1993; Schöttler and Tóth, 2014) and in most cases were close to 2.0. Because of these variations, it is important that the stoichiometry of the electron transport chain is determined for the species and growth conditions used as reference (in this study, *A. thaliana* grown at low irradiance).

Walters et al. (1999) measured a PSII content of $0.80 \times 10^{-6} \text{ mol m}^{-2}$ for *A. thaliana* grown at $100 \mu\text{mol m}^{-2} \text{s}^{-1}$ of irradiance. For the same growth conditions and species, Walters and Horton (1995) observed a PSI:PSII ratio of 0.8, which results in a PSI content of $0.64 \times 10^{-6} \text{ mol m}^{-2}$. No values were found for the cyt b_6f :PSII ratio for *A. thaliana*, so a value was estimated from those reported for other species. In Figure 5.7, and excluding

Table 5.12: Parameters associated with regulation by thioredoxin of enzymes and protein complexes. See bottom of the table for sources.

Symbol	Description	Value	Source
$v_{max,FTR}$	Maximum rate of ferredoxin–thioredoxin reductase	$0.1 \text{ mol m}^{-3} \text{ s}^{-1}$	1
$K_{FTR,Fdr}$	Half saturation of ferredoxin–thioredoxin reductase with respect to reduced Fd	$2 \times 10^{-2} \text{ mol m}^{-3} \text{ s}^{-1}$	1
$K_{FTR,Fdo}$	Half saturation of ferredoxin–thioredoxin reductase with respect to oxidised Fd	$2 \times 10^{-2} \text{ mol m}^{-3} \text{ s}^{-1}$	2
$K_{FTR,Tho}$	Half saturation of ferredoxin–thioredoxin reductase with respect to reduced Th	$3 \times 10^{-3} \text{ mol m}^{-3}$	3
$K_{FTR,Thr}$	Half saturation of ferredoxin–thioredoxin reductase with respect to oxidised Th	$3 \times 10^{-3} \text{ mol m}^{-3}$	1
$E_{m7,Th}$	Midpoint redox potential of thioredoxin at a pH of 7	-0.29 V	4
k_{Fr}	Rate constant of thiol reduction of the γ subunit of ATP synthase	$10^2 \text{ m}^3 \text{ mol}^{-1} \text{ s}^{-1}$	1
$E_{m7,ATPase}$	Midpoint redox potential of the γ subunit of ATP synthase at a pH of 7	-0.29 V	4
k_{FQRr}	Rate constant of ferredoxin–plastoquinone reductase reduction by thioredoxin	$10^2 \text{ m}^3 \text{ mol}^{-1} \text{ s}^{-1}$	1
$E_{m7,FQR}$	Midpoint redox potential of ferredoxin–plastoquinone reductase at pH of 7	-0.28 V	5
k_{MDHr}	Rate constant of malate dehydrogenase reduction by thioredoxin	$10^2 \text{ m}^3 \text{ mol}^{-1} \text{ s}^{-1}$	1
$E_{m7,MDH}$	Midpoint redox potential of malate dehydrogenase at a pH of 7	-0.33 V	4
k_{RCAr}	Rate constant of Rubisco activase reduction by thioredoxin	$10^2 \text{ m}^3 \text{ mol}^{-1} \text{ s}^{-1}$	1
$E_{m7,RCA}$	Midpoint redox potential of Rubisco activase at a pH of 7	-0.29 V	4

1. Estimated.
2. (Glauser et al., 2004).
3. (Navarro et al., 1991).
4. (Schürmann and Buchanan, 2008).
5. (Strand et al., 2016a).

the measurements by Osmond et al. (1980) on *Atriplex triangularis*, the cyt b_6f :PSII at low irradiance varied from 0.25 to 0.75, and a value of 0.70 (which corresponded to most species in Figure 5.7A) was chosen, resulting in a cyt b_6f content of $0.56 \times 10^{-6} \text{ mol m}^{-2}$.

Assuming a Pc:PSII ratio of 2, the Pc content of the leaves becomes $1.60 \times 10^{-6} \text{ mol m}^{-2}$. Assuming a PQ/PSII ratio of 6 (Lavergne et al., 1992), the total plastoquinone pool content becomes $4.80 \times 10^{-6} \text{ mol m}^{-2}$. Cruz et al. (2001) calculated an ATPase:PSII of 0.5, from which the ATPase content is derived to be $0.40 \times 10^{-6} \text{ mol m}^{-2}$.

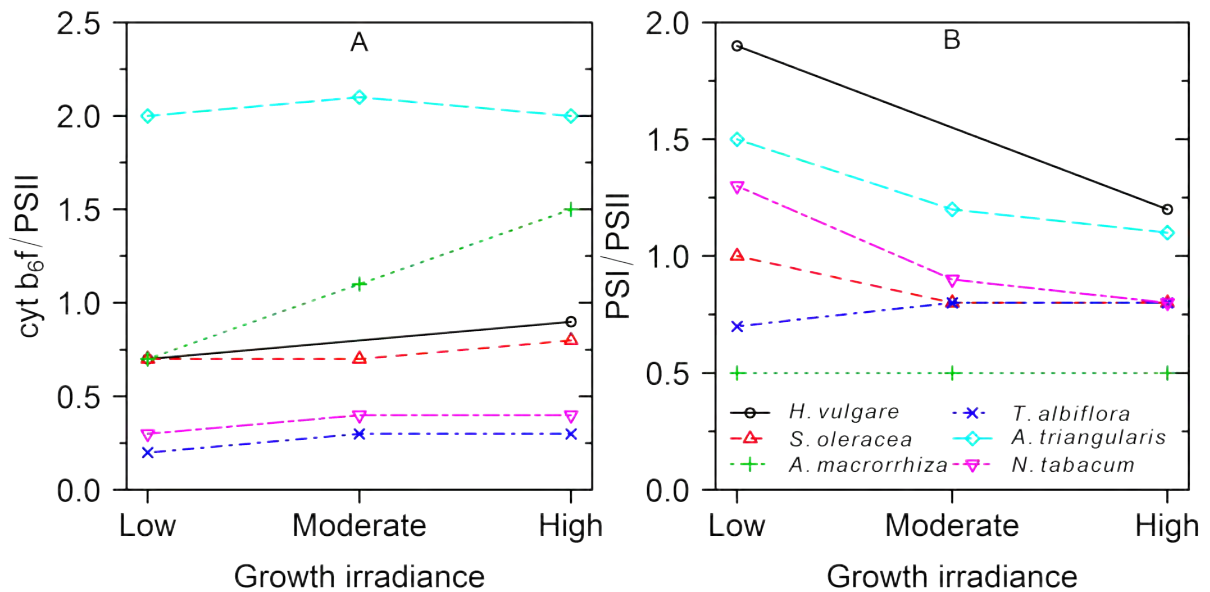


Figure 5.7: Measured ratios between leaf contents of cyt b_6f and PSII (A) and PSI and PSII (B) for different growth irradiances. Data for *Hordeum vulgare* from Burkey (1993), for *Spinacia oleracea* from Chow and Hope (1987), for *Alocasia macrorrhiza* from Chow et al. (1988), for *Tradescantia albiflora* from Chow et al. (1991), for *Atriplex triangularis* from Osmond et al. (1980), and for *Nicotiana tabacum* from Schöttler and Tóth (2014). The values of irradiance that correspond to low, moderate, or high irradiance vary across species, and the criteria of the original authors of each source was used.

Haslett et al. (1973) reported a ratio between total chlorophyll and Fd of 330 in *Phaseolus vulgaris*, measured with electron paramagnetic resonance. This is similar to the value of 400 in *S. oleracea* estimated by Tagawa and Arnon (1962). For the same species, and using antibodies to measure Fd, Böhme (1977) reported 475 Chl/Fd (2 Fd/ P_{700}) and Bohme (1978) reported a ratio of 250 Chl/Fd (3 Fd/PSI). However, Matson and Kimura (1975) reported a ratio of only 33 Chl/Fd in *S. oleracea* and 11 Chl/Fd in *Petroselinum crispum*, also using antibodies to measure Fd. It is unclear why the experiment by Matson and Kimura (1975) resulted in an order of magnitude difference with respect to the other experiments. Assuming 2 Fd/ P_{700} (which would result in 222 Chl/Fd with our parameter set), this leads to an Fd content of $1.28 \times 10^{-6} \text{ mol m}^{-2}$.

Scheibe (1981) measured concentrations of thioredoxin between 0.1 and 0.16 mol m^{-3} , so a concentration of 0.1 mol m^{-3} was used. Published measurements of NDH content in leaves include 0.09 mmol mol^{-1} of chlorophyll (Hertle et al., 2013), 0.015 mol mol^{-1} of PSII (Burrows et al., 1998) and 0.02 mol mol^{-1} of PSI (Peng et al., 2008). When combined with the values of C_t , PSII and PSI, it leads to $2.5 \times 10^{-8} \text{ mol m}^{-2}$, $1.2 \times 10^{-8} \text{ mol m}^{-2}$, and $1.3 \times 10^{-8} \text{ mol m}^{-2}$, respectively. An intermediate value of $2 \times 10^{-8} \text{ mol m}^{-2}$ was chosen. Hertle et al. (2013) measured an amount of FQR per unit of chlorophyll of $7 \times 10^{-4} \text{ mol mol}^{-1}$, which leads to $2.0 \times 10^{-7} \text{ mol m}^{-2}$. The concentration of MDH was estimated to be $5 \times 10^{-3} \text{ mol m}^{-3}$ based on a catalytic constant of 233 s^{-1} (Lemaire et al., 1996) and the maximum rate $V_{MDH,max} = 1.2 \text{ mol m}^{-3} \text{ s}^{-1}$ assumed in Section 5.2.4.3.2.

The amount of Rubisco was estimated from steady-state measurements of net CO_2 assimilation by Kaiser et al. (2016), resulting in a value of $\text{RB} = 2.30 \text{ mol m}^{-3}$. Assuming a ratio between the maximum rate of RuBP regeneration and the maximum rate of carboxylation of 2 (Percy et al., 1997), V_{rmax} was set to $17.0 \text{ mol m}^{-3} \text{ s}^{-1}$. Reported

Table 5.13: State variables of the model and their initial values. For PSII, cyt b_6f , and PSI only the total content is provided. As initial values for these protein complexes it is assumed that the binding sites are empty and internal components are in their basal states. See bottom of the table for sources.

Variable	Description	Initial value	Source
α_r	Relative leaf-level light absorptance due to chloroplast movement	1	1
$\sum \text{PSII}$	Amount of Photosystem II per unit of leaf area	$0.8 \times 10^{-6} \text{ mol m}^{-2}$	2
$\sum \text{cyt}$	Amount of cytochrome b_6f complex per unit of leaf area	$0.56 \times 10^{-6} \text{ mol m}^{-2}$	3
$\sum \text{PSI}$	Amount of Photosystem I per unit of leaf area	$0.64 \times 10^{-6} \text{ mol m}^{-2}$	4
PQ	Amount of plastoquinone per unit of leaf area	$4.80 \times 10^{-6} \text{ mol m}^{-2}$	5
PQH_2	Amount of plastoquinol per unit of leaf area	0.00 mol m^{-2}	5
P_c	Amount of reduced plastocyanin per unit of leaf area	0.00 mol m^{-2}	6
P_c^+	Amount of oxidised plastocyanin per unit of leaf area	$1.60 \times 10^{-6} \text{ mol m}^{-2}$	6
Fd_r	Amount of reduced ferredoxin per unit of leaf area	0.00 mol m^{-2}	7
Fd_o	Amount of oxidised ferredoxin per unit of leaf area	$1.28 \times 10^{-6} \text{ mol m}^{-2}$	7
$NADP^+$	Concentration of $NADP^+$ in the stroma	0.45 mol m^{-3}	8
$NADPH$	Concentration of $NADPH$ in the stroma	0.45 mol m^{-3}	8
f_{FR}	Fraction of ATP synthase reduced	0	13
Th_r	Concentration of reduced thioredoxin	0 mol m^{-3}	9
Th_o	Concentration of oxidised thioredoxin	0.10 mol m^{-3}	9
NDH	Amount of NDH per unit of leaf area	$2.0 \times 10^{-8} \text{ mol m}^{-2}$	10
FQR_r	Amount of reduced FQR per unit of leaf area	0 mol m^{-2}	11
FQR_o	Amount of oxidised FQR per unit of leaf area	$0.20 \times 10^{-6} \text{ mol m}^{-2}$	11
MDH_r	Concentration of reduced MDH in the stroma	0 mol m^{-3}	12
MDH_o	Concentration of oxidised MDH in the stroma	$1.9 \times 10^{-2} \text{ mol m}^{-3}$	12
f_{PsbSp}	Fraction of PsbS that is protonated	0.00	13
pH_L	pH of the lumen	7.80	1
pH_S	pH of the stroma	7.80	1
$\Delta\Psi$	Electrical field across the thylakoid	0 V	13
C_2^*	Amount of excitations in the antennae of PSII	0 mol m^{-2}	13
f_{AX}	Fraction of the xanthophyll pool in the form of antheraxanthin	0	13
f_{VX}	Fraction of the xanthophyll pool in the form of violaxanthin	1	13

f_{ZX}	Fraction of the xanthophyll pool in the form of zeaxanthin	0	13
F	Amount of ATP synthase per unit of leaf area	$0.40 \times 10^{-6} \text{ mol m}^{-2}$	14
F_T	Amount of ATP synthase bound to ATP per unit of leaf area	0 mol m^{-2}	14
F_D	Amount of ATP synthase bound to ADP per unit of leaf area	0 mol m^{-2}	14
F_P	Amount of ATP synthase bound to phosphate per unit of leaf area	0 mol m^{-2}	14
F_{DP}	Amount of ATP synthase bound to ADP and phosphate per unit of leaf area	0 mol m^{-2}	14
ADP	Concentration of ADP in the stroma	0.5 mol m^{-3}	15
ATP	Concentration of ATP in the stroma	0.5 mol m^{-3}	15
RB	Concentration of Rubisco catalytic sites	2.30 mol m^{-3}	16
RCA_r	Concentration of reduced Rubisco activase	0 mol m^{-3}	17
RCA_o	Concentration of oxidised Rubisco activase	1.23 mol m^{-3}	17
MAL	Concentration of malate in the stroma	3 mol m^{-3}	18
OAA	Concentration of oxaloacetate in the stroma	0.025 mol m^{-3}	18
PGA	Concentration of PGA in the stroma	16.0 mol m^{-3}	19
$RuBP$	Concentration of RuBP in the stroma	4.0 mol m^{-3}	19
f_{RB}	Fraction of Rubisco that is active	0.4	13
f_R	Relative activity of pseudo-enzyme for RuBP regeneration	0.04	13
C_C	$[\text{CO}_2]$ in the stroma	$4 \times 10^{-4} \text{ mol mol}^{-1}$	13
C_{cyt}	$[\text{CO}_2]$ in the cytosol	$4 \times 10^{-4} \text{ mol mol}^{-1}$	13
C_i	$[\text{CO}_2]$ in the intercellular spaces	$4 \times 10^{-4} \text{ mol mol}^{-1}$	13
g_s	Stomatal conductance to fluxes of CO_2	$0.1 \text{ mol m}^{-2} \text{ s}^{-1}$	13

1. Assumed.

2. (Walters et al., 1999).

3. (Chow and Hope, 1987; Chow et al., 1988; Chow et al., 1991; Burkey, 1993; Schöttler and Tóth, 2014).

4. (Walters and Horton, 1995).

5. (Lavergne et al., 1992).

6. (Graan and Ort, 1984; Burkey, 1993; Schöttler and Tóth, 2014).

7. (Böhme, 1977).

8. (Takahama et al., 1981; Heineke et al., 1991).

9. (Scheibe, 1981).

10. (Hertle et al., 2013) (Burrows et al., 1998) (Peng et al., 2008).

11. (Hertle et al., 2013).

12. (Foyer et al., 1992; Lemaire et al., 1996).

13. Arbitrary value as initial condition.

14. (Cruz et al., 2001).

15. (Stitt et al., 1980; Giersch and Robinson, 1987; Heineke et al., 1991; Igamberdiev et al., 2001).

16. (Kaiser et al., 2016).

17. (Mott and Woodrow, 2000; Carmo-Silva and Salvucci, 2013).

18. (Heineke et al., 1991).

19. Calculated from RB and $(RuBP + PGA)/RB$ by von Caemmerer and Edmondson (1986).

measurements of concentration of adenylates in the stroma of the chloroplast range from 0.26 mol m^{-3} to 2.6 mol m^{-3} (Stitt et al., 1980; Giersch and Robinson, 1987; Heineke et al., 1991; Igamberdiev et al., 2001). Values used in previous models of the Calvin cycle range from 0.5 mol m^{-3} to 1.5 mol m^{-3} (Poolman et al., 2000; Laisk et al., 2006; Zhu et al., 2013).

Resolving these discrepancies is beyond the scope of this study and, as a compromise solution, a value of 1 mol m^{-3} was chosen for the simulations. Total measured concentrations of NADPH and NADP^+ in the stroma vary from 0.5 to 0.9 mol m^{-3} (Takahama et al., 1981; Heineke et al., 1991) from where the value of 0.9 mol m^{-3} was chosen. von Caemmerer and Edmondson (1986) measured a total amount of PGA and RuBP of $2.6 \times 10^{-4} \text{ mol m}^{-2}$ from leaves with a Rubisco content of $2.15 \times 10^{-5} \text{ mol m}^{-2}$. Assuming a conserved $(\text{RuBP} + \text{PGA})/\text{RB}$ ratio, this would lead to $\text{PGA} + \text{RuBP} = 20 \text{ mol m}^{-3}$. Given these values and knowing that P_i varies *in vivo* between 3 and 8 mol m^{-3} (Dietz and Heber, 1984; Schimkat et al., 1990), P_{i_T} was assumed to be 30 mol m^{-3} .

5.2.10 Model implementation

The model described in the above was implemented as a system of ordinary differential equations (ODE) according to the state-space formalism. This mathematical formalism may be defined as the following system of equations:

$$\begin{aligned} \frac{d\mathbf{S}(t)}{dt} &= f(\mathbf{S}(t), \mathbf{P}, \mathbf{I}(t)), \\ \mathbf{O}(t) &= g(\mathbf{S}(t), \mathbf{P}, \mathbf{I}(t)) \end{aligned} \quad (5.98)$$

where \mathbf{S} is the vector of state variables, \mathbf{O} is a vector of observed variables, \mathbf{P} is a vector of parameters that remain constant throughout a simulation and \mathbf{I} are dynamic inputs that will change during a simulation (in this model, only CO_2 and irradiance). The functions f and g are the system of equations described in the previous section. An implementation of the model requires to translate f and g to the programming language of choice.

The system described by Equation 5.98 represents the “initial value problem” (Soetaert et al., 2012) which consists of calculating the sequences of values for every state variable along a temporal axis, provided the initial values are known. This problem is solved with time-stepping algorithms commonly known as ODE solvers. Numerous ODE solvers exist and a review of these algorithms is beyond the scope of this document. Most implementations of ODE solvers in programming languages commonly used for scientific research (e.g., Fortran, C/C++, Matlab, R, Python, or Julia) expect a user-defined procedure that returns the results of evaluating functions f and g given their inputs. A special property of the model in this study is that it integrates multiple time scales (i.e., it is a stiff ODE) and therefore, ODE solvers capable of integrating stiff ODE must be used. Such ODE solvers are commonly available in scientific programming environments. To perform the simulations required for this study, f and g were implemented in C++, according to the interface defined by the R package RcppSundials (source code available upon request) which interfaces the numerical library Sundials (Hindmarsh et al., 2005).

5.3 Model tests with experimental results

It is important to test how well the model can reproduce experimental observations. Successfully passing these tests does not prove that the combination of equations and parameters are “true” as (i) models are simplifications of reality and (ii) multiple

combinations of equations and parameter values may yield similar results. As indicated in the previous sections, for some parameters, the literature provides a range of values. In those cases, the values chosen were tuned manually to yield reasonable results in the tests below, but in all cases the parameter values were taken within the ranges derived from literature. Given that *A. thaliana* was used as model organism for the development of the model and its parameterization, only measurements on this species are used below.

Ideally, all measurements would be obtained from a single experiment using the same batch of plants, but all experiments described in the literature were missing several of the relevant measurements discussed below. Therefore, a dataset was assembled from different sources that reported measurements of *A. thaliana* Col-0, grown in climate chambers at similar growth conditions (20 – 23 °C, 100 – 170 $\mu\text{mol m}^{-1} \text{s}^{-1}$, 60 – 75% relative humidity). The following types of measurements were used to test the model's predictions:

1. Net CO₂ assimilation (A_n) as obtained from gas exchange systems. These measurements are indicative of CO₂ fixation and associated photorespiration and therefore test the ability of the model to correctly approximate the metabolism of the stroma and its coupling to the electron transport chain. These tests are described in Section 5.3.1.

2. Pulse amplitude modulated chlorophyll fluorescence at ambient temperature. These measurements test the ability of the model to simulate the quantum yield of PSII (also known as “operational efficiency” of PSII) and the Stern-Volmer NPQ coefficient (NPQ_{SV}). These tests are described in Section 5.3.2.

3. Electrochromic shift of pigment absorbance which is detected as changes in leaf absorbance at 515 nm and assumed proportional to the electrical field across the thylakoid membrane (Cruz et al., 2001). These measurements are used to test the ability of the model to simulate the regulation of pmf and its components. These tests are described in Section 5.3.3.

4. Redox state of P₇₀₀ measured as changes in absorbance at 820 nm. These measurements are indicative of the presence or absence of acceptor-side kinetic limitations for PSI activity, the quantum yield of PSI (Harbinson et al., 1989; Harbinson and Hedley, 1989a) and electron transport activity between PSII and PSI (Harbinson and Hedley, 1989a). These tests are described in Section 5.3.4.

5.3.1 Net CO₂ assimilation and Rubisco regulation

Simulations of steady-state and dynamic net CO₂ assimilation (A_n) were validated with measurements reported by Kaiser et al. (2016) and Flexas et al. (2007b) on *A. thaliana* Col-0. The following types of measurements were used:

1. Steady-state response of A_n to irradiance.
2. Steady-state response of A_n to C_i .
3. Dynamics of A_n after rapid increases or decreases in irradiance.

The irradiance response was simulated by taking 15 irradiance steps of 2000 s each, such that irradiance varies from darkness to 2000 $\mu\text{mol m}^{-2} \text{s}^{-1}$. A measured irradiance response curve was reconstructed from data by Kaiser et al. (2016) consisting of light

transients that were at least 2000 s long each. The light source in the simulations was adjusted to 10% blue and 90% red as in the experiment and CO₂ and O₂ mole fractions were set to ambient levels (400 μmol mol⁻¹ and 210 mmol mol⁻¹, respectively). The simulations reproduced accurately the measured irradiance response curve (Figure 5.8A), with saturation reached at 600 μmol m⁻² s⁻¹, a light compensation point of 9.5 μmol m⁻² s⁻¹ and a low light quantum yield of 5.1%.

Two measured CO₂ response curves were used for testing the model, one by Kaiser et al. (2016) with a constant irradiance level of 1000 μmol m⁻² s⁻¹ and another by Flexas et al. (2007b) with a constant irradiance level of 1500 μmol m⁻² s⁻¹. In both cases, ambient CO₂ and O₂ mole fractions were used, and the light source contained 10% blue and 90% red. The simulation settings were set to these experimental conditions and CO₂ steps were taken following the experimental protocols, that is, starting at 400 μmol mol⁻¹, decreasing towards zero, returning to 400 μmol mol⁻¹ and then increasing towards saturation. The simulations reproduced the measurements accurately (Figure 5.8B).

To test the modelling of dynamic changes in A_n , the light transients measured by Kaiser et al. (2016) were simulated using the model. In the simulations, the *in silico* system was always in steady-state at the beginning of the simulation, although for the measurements this was only confirmed for A_n and g_s . Given that steady-state levels of A_n have already been tested (see above), the emphasis in this test was on the relative rate at which A_n changes after a change in irradiance. Thus, all measurements and simulations were normalized by the initial and final values of A_n . The model predicted accurately the relative changes in A_n (Figure 5.9), both for increases and decreases in irradiance. In both measurements and simulations, the dynamics after a decrease in irradiance were similar for different irradiance levels, whereas the relative rate of increase of A_n was higher as the initial irradiance increased (Figure 5.9). In the model, the dynamics of A_n after an increase in irradiance were determined by stomatal opening and Rubisco activation, in agreement with the literature (Percy et al., 1996; Mott and Woodrow, 2000; Kaiser et al., 2015), whereas the dynamics of A_n after a decrease in irradiance were determined by NPQ relaxation and the delay in CO₂ release by photorespiration, also in agreement with the literature (Percy et al., 1996; Armbruster et al., 2014; Kaiser et al., 2015; Kromdijk et al., 2016).

5.3.2 Chlorophyll fluorescence

Simulations of steady-state and dynamic PSII quantum yield (ϕ_{II}) and Stern-Volmer NPQ coefficient (NPQ_{SV}) were used to test simulations of PSII activity with published measurements on *A. thaliana* Col-0. The following types of measurements were used:

1. Steady-state response of ϕ_{II} to irradiance.
2. Steady-state response of ϕ_{II} to C_i .
3. Dynamic changes in ϕ_{II} after an increase in irradiance.
4. Dynamic changes in NPQ_{SV} after an increase in irradiance.

Simulations of steady-state PSII quantum yield (ϕ_{II}) as a function of irradiance were compared to measurements by van Rooijen et al. (2015) at ambient CO₂ and Hald et al. (2008) at a CO₂ mole fraction of 2000 μmol mol⁻¹. Simulations of the steady-state response of ϕ_{II} to C_i were tested with measurements by Hald et al. (2008) at a constant

irradiance of $1500 \mu\text{mol m}^{-2} \text{s}^{-1}$ and from Kaiser et al. (2016) at a constant irradiance of $1000 \mu\text{mol m}^{-2} \text{s}^{-1}$. In all cases, ambient O_2 was used for the measurements. The simulations were performed with simulation protocols analogous to the ones described in the previous section, with the exception that rectangular flashes, with intensities taken from the descriptions of experiments (always between $6500 \mu\text{mol m}^{-2} \text{s}^{-1}$ and $8000 \mu\text{mol m}^{-2} \text{s}^{-1}$) were added at the end of each CO_2 and irradiance step to calculate ϕ_{II} and NPQ_{SV} .

An apparent, simulated chlorophyll fluorescence yield of the virtual leaf was calculated as the rate of fluorescence emission of the chlorophyll molecules associated to PSII_{ac}, divided by the irradiance incident on the leaf. ϕ_{II} was computed as $(F'_m - F')/F'_m$, where F' was the chlorophyll fluorescence yield before applying a flash and F'_m was the maximum chlorophyll fluorescence yield achieved during the flash. The model predicted accurately the effects of CO_2 and irradiance on ϕ_{II} (Figure 5.10), although in most cases, simulated ϕ_{II} was higher than those of measurements. No information on measurement errors was available, so it is not clear whether the differences between the simulations and measurements are significant.

The model is expected to underestimate measurements NPQ_{SV} as neither photoinhibition nor state transitions are being simulated and these processes contribute to NPQ_{SV} in *A. thaliana* (Kasahara et al., 2002; Nilkens et al., 2010; Dall'Osto et al., 2014). Given the large uncertainty in NPQ_{SV} values from different sources and the fact that the model does not take into account the effect of photoinhibition, NPQ_{SV} simulations were tested only with measurements by Kaiser et al. (2016) and Herdean et al. (2016) for the first 10 minutes after an increase in irradiance from a dark adapted state, assuming that, under such conditions, NPQ_{SV} is mostly determined by the qE mechanism and chloroplast movement. The same experiments were also used to test dynamic simulations of ϕ_{II} .

Steady-state responses of NPQ_{SV} were not used for testing the model, as the results obtained from different sources (Hald et al., 2008; van Rooijen et al., 2015; Kaiser et al., 2016) were not consistent. Possible factors explaining the lack of consistency across experiments would be the light history of the plants being measured, the rates of photoinhibition achieved during the measurements, the spectral distribution of the source of irradiance, and $[\text{CO}_2]$.

From the data reported by Herdean et al. (2016) and Kaiser et al. (2016), three photosynthetic induction curves from darkness to $70 \mu\text{mol m}^{-2} \text{s}^{-1}$, $600 \mu\text{mol m}^{-2} \text{s}^{-1}$ and $1000 \mu\text{mol m}^{-2} \text{s}^{-1}$ were chosen, all measured at ambient CO_2 , and O_2 . The simulation protocol was adapted to the experimental conditions and flashes were simulated at the same timepoints as in the experiments and with the same flash intensities. In all cases, ϕ_{II} decreased rapidly after the increase in irradiance followed by a slow recovery (Figure 5.11A). The simulations reproduced this behaviour qualitatively, and the agreement was best for the measurements by Kaiser et al. (2016), with a slight overestimation as expected from Figure 5.10.

The increase in NPQ_{SV} during the first 10 minutes of induction was also reproduced by the model in the case of the measurements by Kaiser et al. (2016). However, the agreement with some of the measurements was poorer, although the model still reproduced the dynamic patterns qualitatively. In the induction curve using $70 \mu\text{mol m}^{-2} \text{s}^{-1}$ as irradiance, measured NPQ_{SV} displayed a clear overshoot during the first three minutes. The model capture this correctly, although it underestimated the magnitude and extension of the overshoot. In the case of the induction curve at $650 \mu\text{mol m}^{-2} \text{s}^{-1}$ of

irradiance, the model predicted an increase in steady-state ϕ_{II} (to be expected based on Figure 5.10) which was not apparent in the measurements (despite the decrease in measured NPQ_{SV}). Herdean et al. (2016) did not report measurements of A_n or g_s and thus it is not possible to assess whether the simulations correctly reproduced metabolic demand, which would have an effect of NPQ_{SV} and ϕ_{II} during induction.

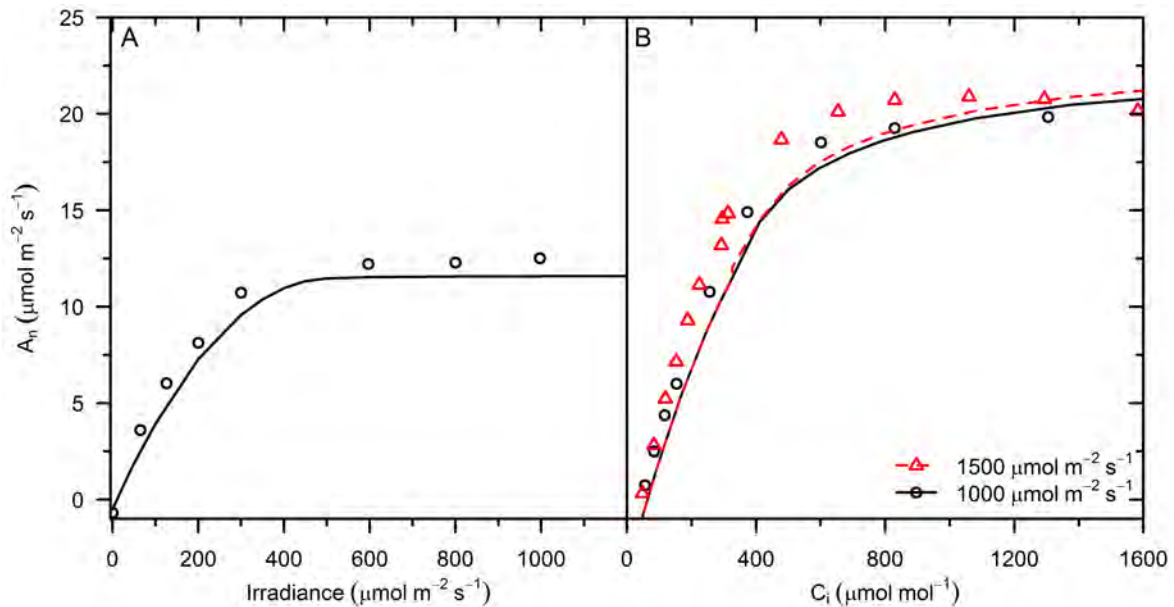


Figure 5.8: Measured (symbols) and simulated (lines) steady-state net CO₂ assimilation as a function of irradiance (A) and CO₂ mole fraction (B). The CO₂ response was measured with irradiances of 1000 $\mu\text{mol m}^{-2} \text{s}^{-1}$ by Kaiser et al. (2016) and 1500 $\mu\text{mol m}^{-2} \text{s}^{-1}$ by Flexas et al. (2007b). The irradiance response was measured at a CO₂ mole fraction of 400 $\mu\text{mol mol}^{-1}$ by Kaiser et al. (2016).

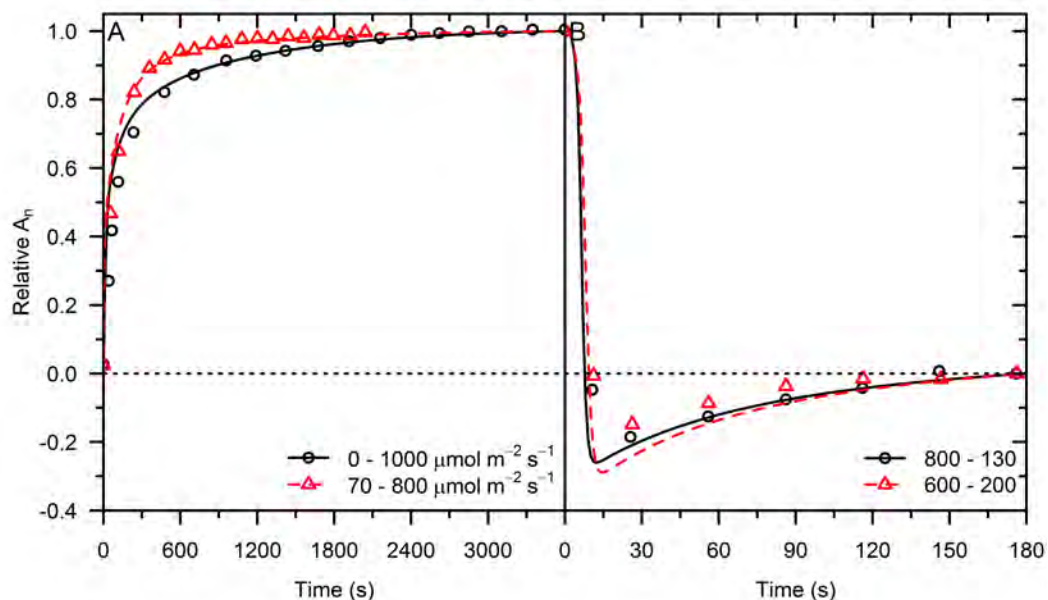


Figure 5.9: Measured (symbols) and simulated (lines) relative net CO₂ assimilation (A_n) as a function of time after an increase in irradiance level, from 0 $\mu\text{mol m}^{-2} \text{s}^{-1}$ to 1000 $\mu\text{mol m}^{-2} \text{s}^{-1}$ (black line and circles in panel A) and 70 $\mu\text{mol m}^{-2} \text{s}^{-1}$ to 800 $\mu\text{mol m}^{-2} \text{s}^{-1}$ (red line and triangles in panel A) and after a decrease in irradiance level from 800 $\mu\text{mol m}^{-2} \text{s}^{-1}$ to 130 $\mu\text{mol m}^{-2} \text{s}^{-1}$ (black line and circles in panel B) and from 600 $\mu\text{mol m}^{-2} \text{s}^{-1}$ to 200 $\mu\text{mol m}^{-2} \text{s}^{-1}$ (red line and triangles in panel B). Relative A_n was calculated by subtracting A_n at time = 0 and dividing by the difference between maximum and minimum A_n reached during the simulation or measurement.

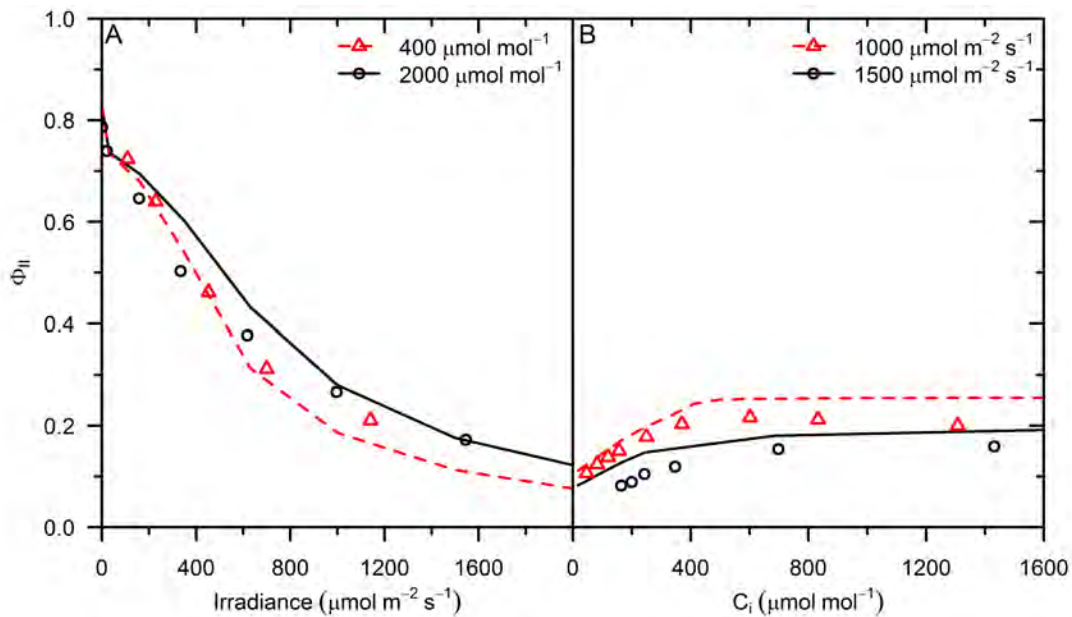


Figure 5.10: Measured (symbols) and simulated (lines) steady-state quantum yield of PSII (Φ_{II}) as a function of irradiance (a) and CO_2 mole fraction (b). The response to irradiance was measured and simulated for different CO_2 mole fraction (see legend). The response to CO_2 mole fraction was measured at two irradiances (see legend). The response to irradiance at an air CO_2 mole fraction of $2000 \mu\text{mol mol}^{-1}$ and the CO_2 response at an irradiance of $1500 \mu\text{mol m}^{-2} \text{s}^{-1}$ were taken from Hald et al. (2008). The irradiance response at $400 \mu\text{mol m}^{-2} \text{s}^{-1}$ was taken from van Rooijen et al. (2015). The CO_2 response at $1000 \mu\text{mol m}^{-2} \text{s}^{-1}$ was taken from Kaiser et al. (2016).

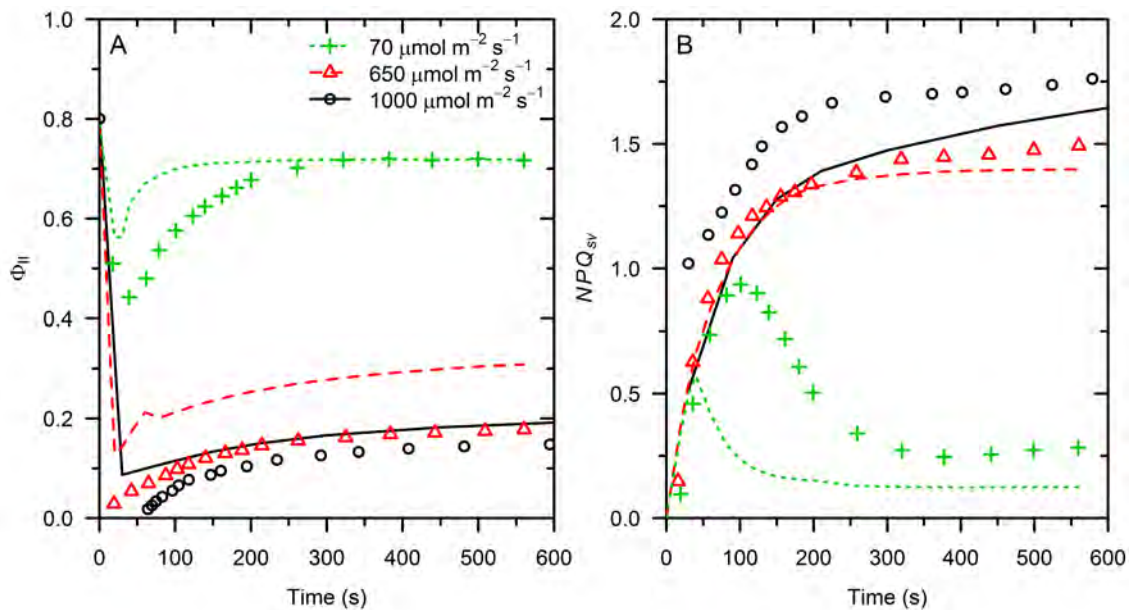


Figure 5.11: Measured (symbols) and simulated (lines) quantum yield of PSII (A) and NPQ_{sv} (B) as a function of time after an increase in irradiance from 0 to $1000 \mu\text{mol m}^{-2} \text{s}^{-1}$ (Kaiser et al., 2016), $650 \mu\text{mol m}^{-2} \text{s}^{-1}$ (Herdean et al., 2016) and $70 \mu\text{mol m}^{-2} \text{s}^{-1}$ (Herdean et al., 2016).

The mismatch may also be explained by an overestimation of the kinetics of the component of NPQ_{sv} associated with protonation of the PsbS protein, although this would not explain the low measured ϕ_{II} in the 0 – $650 \mu\text{mol m}^{-2} \text{s}^{-1}$ transient.

5.3.3 Electrochromic shift

Simulations of the electrochromic shift (ecs) were tested with experimental results reported on *A. thaliana*. The following types of steady-state measurements were used:

1. Total ecs (ecs_t) as a function of irradiance and CO_2 .
2. Inverse ecs (ecs_i) as a function of irradiance and CO_2 .
3. ATPase conductance (g_H) as a function of irradiance and CO_2 .

Throughout the simulations, it was assumed that ecs is proportional to $\Delta\Psi$. However, the relationship is leaf-specific and therefore ecs_t and ecs_i are expressed in arbitrary units (Cruz et al., 2001). This means that neither ecs_t nor ecs_i provide absolute estimations of pmf and its components, but they can capture the relative changes with irradiance and CO_2 . ecs_t is calculated as the difference between ecs in the light and the minimum ecs achieved in the darkness, whereas ecs_i is calculated as the difference between the steady-state level in the darkness and the minimum in the darkness (Figure 5.12). Minimum ecs was achieved around 200 – 300 ms after the transition to darkness and a steady-state value in the darkness was reached at around 10 s after the transition.

Simulations of steady-state values of ecs_t and ecs_i as a function of irradiance and for air [CO_2] of $372 \mu\text{mol mol}^{-1}$ and $50 \mu\text{mol mol}^{-1}$ were compared to measurements by Takizawa et al. (2007). A scaling factor of 11.76 V^{-1} was used to compare the simulations of $\Delta\Psi$ with measurements of ecs_t and ecs_i . The model predicted correctly the increase of ecs_t and ecs_i with irradiance and decrease with CO_2 (Figure 5.13). Under low C_i , both ecs_t and ecs_i saturated at low irradiance in the measurements and simulations, indicative of limitations due to lower metabolic capacity that increased pmf. Analysis of the simulations in Figure 5.13 indicated that pmf and ecs_t were linearly correlated, as well as ecs_i and ΔpH (Figure 5.14, in both cases $R^2 > 0.99$), in agreement with the model used by Cruz et al. (2001) to interpret ecs_t and ecs_i measurements.

An Ohmic model of ATP synthesis has been proposed (Cruz et al., 2001), whereby the flux of H^+ through the ATPase (v_H) is assumed proportional to the pmf. This allows defining a conductivity to H^+ , which is simply the ratio v_H/pmf . That model predicts that the initial relative rate of decrease of $\Delta\Psi$ (denote as g_H) during a dark interval (Figure 5.12) is proportional to v_H/pmf (Kanazawa and Kramer, 2002; Avenson et al., 2005). Simulations of g_H with our model for different irradiances and CO_2 were compared (Figure 5.15A) with the measurements reported by Avenson et al. (2005). There was poor agreement between the simulations and the measurements. In particular, the absolute values obtained from the simulations at low irradiance were an order of magnitude lower than the measured values. Although similar values were obtained for irradiance $> 200 \mu\text{mol m}^{-2} \text{ s}^{-1}$, the experiment by Avenson et al. (2005) did not include such conditions. Prior measurements in other species (Kanazawa and Kramer, 2002) suggest that the values of g_H would not change much for irradiances between $100 \mu\text{mol m}^{-2} \text{ s}^{-1}$ and $2000 \mu\text{mol m}^{-2} \text{ s}^{-1}$, whereas the model predicted an increase with irradiance, especially under ambient CO_2 conditions. Furthermore, the simulations indicated that g_H and v_H/pmf were not proportional to each other across different irradiances (Figure 5.15B), except at low irradiances. Although the dynamics of $\Delta\Psi$ were simulated correctly at the scale of seconds (Figure 5.12), the assumption of first-order kinetics for counter-ion transport may result in incorrect simulations of $\Delta\Psi$ at the scale of milliseconds, and this would affect calculations of g_H from simulated data.

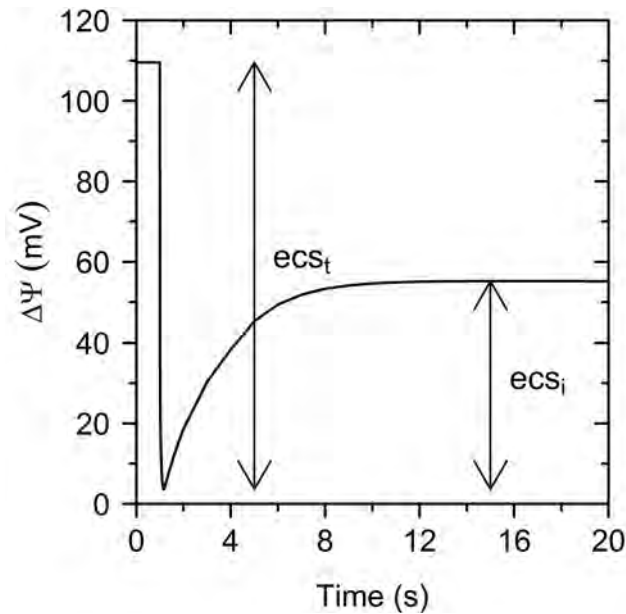


Figure 5.12: Simulation of the electrical field across the thylakoid membrane ($\Delta\Psi$) as function of time for a light-adapted virtual leaf that is exposed to darkness at time = 1 s. Arrows indicate the changes in $\Delta\Psi$ that are proportional to total electrochromic shift (ecs_t) and inverse electrochromic shift (ecs_i).

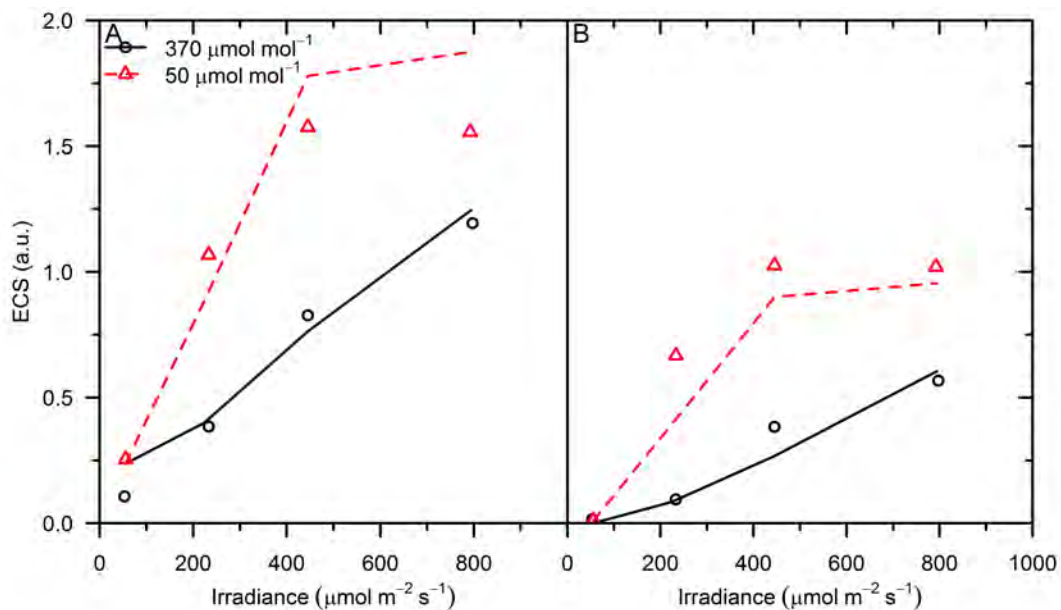


Figure 5.13: Simulated (lines) and measured (symbols) total electrochromic shift (A) and inverse electrochromic shift (B). Simulations were scaled by dividing changes in $\Delta\Psi$ by 0.085 V in order to obtain a similar scale to the measurements. Measurements from Takizawa et al. (2007).

If scaled values of v_H/pmf are compared with measurements of g_H , the observed patterns are still not captured by the model (Figure 5.15A), as v_H/pmf increased with irradiance, especially at ambient $[\text{CO}_2]$. If the concentrations of substrates for ATP synthesis are kept constant, v_H increases in a sigmoidal fashion with pmf (Figure 5.16A), which means that, in the pmf range 100–200 mV, v_H/pmf would vary with pmf (Figure 5.16B).

If g_H is proportional to v_H/pmf *in vivo*, a lack of g_H increase with irradiance would require regulation of ATPase activity (Kanazawa and Kramer, 2002). The model suggested that a decrease in the concentration of ADP (and/or an increase in ATP) would decrease

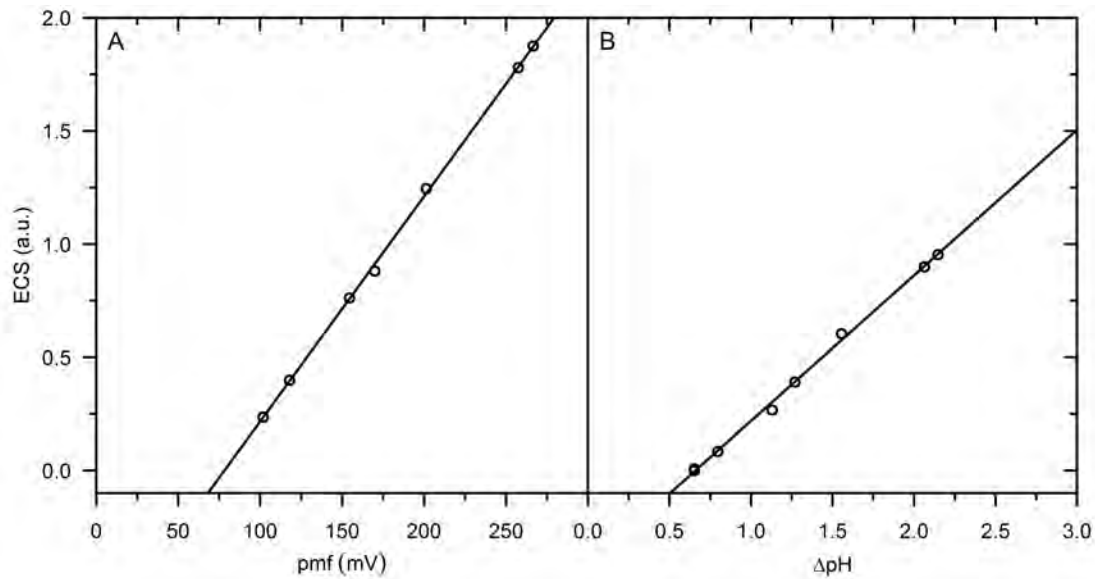


Figure 5.14: Comparison between simulated total electrochromic shift and pmf (A), and between simulated inverse electrochromic shift and ΔpH (B). Symbols correspond to simulations for the conditions of the experiment by Takizawa et al. (2007) as shown in Figure 5.13. Lines represent fitted linear models.

v_H/pmf , in accordance with the experimental results by Pänke and Rumberg (1996). Indeed, the small decrease in simulated v_H/pmf at $[\text{CO}_2] = 50 \mu\text{mol mol}^{-1}$ and irradiance $> 100 \mu\text{mol m}^{-2} \text{s}^{-1}$, which paralleled changes in measured g_H (Figure 5.15A), was possible because simulated ADP concentrations were as low as 0.1 mol m^{-3} ($\text{ADP}/\text{ATP} = 0.1$, $\text{ATP}/\text{ADP}/\text{Pi} = 3900 \text{ M}^{-1}$), whereas at ambient CO_2 , ADP remained higher than 0.2 mol m^{-3} ($\text{ADP}/\text{ATP} > 0.35$, $\text{ATP}/\text{ADP}/\text{Pi} < 500 \text{ M}^{-1}$).

Reported values of ADP/ATP in chloroplasts, across different irradiance and $[\text{CO}_2]$ levels are always higher than 0.35 (Hampp et al., 1982; Dietz and Heber, 1984; Prinsley et al., 1986a; Siebke et al., 1990; Heineke et al., 1991), whereas $\text{ATP}/\text{ADP}/\text{Pi}$ remained lower than 1000 M^{-1} (Giersch et al., 1980; Siebke et al., 1990), so regulation of ATPase activity by low ADP concentrations may not occur *in vivo* (Kanazawa and Kramer, 2002). The underestimation of ADP/ATP by the model may be the result of the parameter values chosen for regulation of Rubisco activase (Section 5.2.7.1) or consumption by the Calvin cycle in the regeneration of RuBP (Section 5.2.7.2).

Experimental evidence shows that reduction in Pi downregulates ATPase activity *in vivo* (Takizawa et al., 2008). In the simulations used for Figure 5.15, Pi decreased with irradiance in the range $7.3 - 5.3 \text{ mol m}^{-3}$ ($[\text{CO}_2] = 372 \mu\text{mol mol}^{-1}$) and $7.3 - 2.5 \text{ mol m}^{-3}$ ($[\text{CO}_2] = 50 \mu\text{mol mol}^{-1}$). These values are in agreement with some estimations of free Pi in the stroma (Hampp et al., 1982; Sharkey and Vanderveer, 1989; Siebke et al., 1990), although other estimations result in values an order of magnitude higher (Dietz and Heber, 1984; Prinsley et al., 1986a).

5.3.4 P_{700} reduction

In the absence of kinetic limitations on the acceptor side of P_{700} , its redox state is a measure of the quantum yield of PSI (Harbinson et al., 1989), due to the high quantum yield of PSI_{ac} and the strong quenching by long-lived P_{700}^+ (see Section 5.2.3 for details). The rate constant of P_{700}^+ reduction after a rapid transition to darkness is associated with

the kinetics of PQH₂ oxidation by the cytochrome b₆f complex (Harbinson and Hedley, 1989a) and thus gives an indication of electron transport regulation *in vivo*.

To test the model, measurements of steady-state P₇₀₀⁺ and the rate constant of P₇₀₀⁺ reduction (k_{P700}) by Hald et al. (2008) were used. Whereas the redox state of P₇₀₀ is an output of the model, the rate constant of P₇₀₀⁺ reduction was fitted to simulations of P₇₀₀ after rapid transition to darkness following the experimental protocol described by Hald et al. (2008). The measurements by Hald et al. (2008) consisted of an irradiance response curve at an air [CO₂] of 2000 μmol mol⁻¹, ambient O₂ and a CO₂ response curve at an irradiance of 1500 μmol m⁻² s⁻¹ and ambient O₂.

The model reproduced the measurements accurately (Figure 5.17), with a small overestimation of the rate constant of P₇₀₀⁺ reduction at high irradiance and [CO₂]. The response of the rate constant of P₇₀₀⁺ reduction to irradiance and CO₂ was dependent on the amount of PQH₂ before the transition to darkness and the rate constant of PQH₂ oxidation by cytochrome b₆f. Indeed, the relationship between the simulated variables could be well described as $k_{P700} = (k_{cyt}/2) PQH_2 / (PQ + PQH_2)$, where k_{cyt} is the rate constant of PQH₂ oxidation by the cytochrome b₆f complex. In the steady-state response to irradiance (Figure 5.17C), the changes in k_{P700} were dominated by changes in PQH₂ as k_{cyt} remained relatively constant due to moderate pH in the lumen (pH > 6.9). However, in the CO₂ response curve (Figure 5.17D), the changes in k_{P700} were dominated by changes k_{cyt} due to increasing acidification of the lumen at low [CO₂].

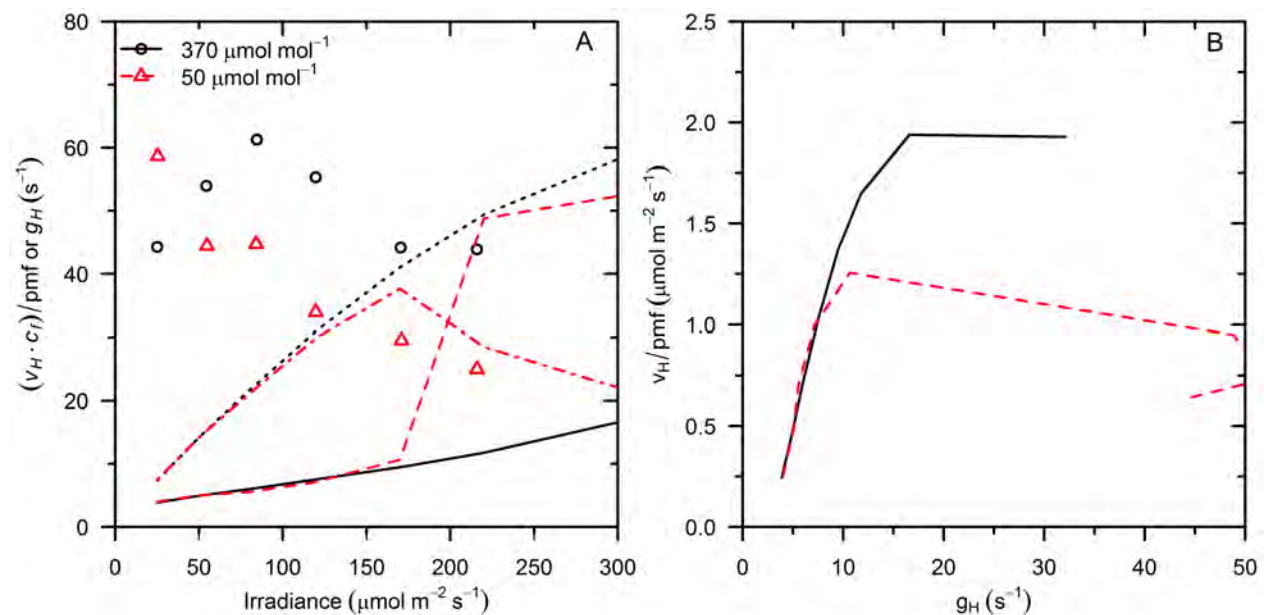


Figure 5.15: Panel A: Simulated (lines) and measured (symbols) steady-state response of ATPase conductance (g_H) as a function of irradiance at air [CO₂] of 372 μmol mol⁻¹ (black solid line and circles) and 50 μmol mol⁻¹ (red dashed line and triangles). In addition, simulated flux of H⁺ (v_H) over pmf multiplied by a conversion factor (c_j) of 30 μmol⁻¹ m² mV at [CO₂] of 372 μmol mol⁻¹ (dotted line) and 50 μmol mol⁻¹ (red, dash-dotted line). Measurements from Avenson et al. (2005). Panel B: Relationship between simulated $v_H/pm f$ and simulated g_H for the same conditions as in Panel A.

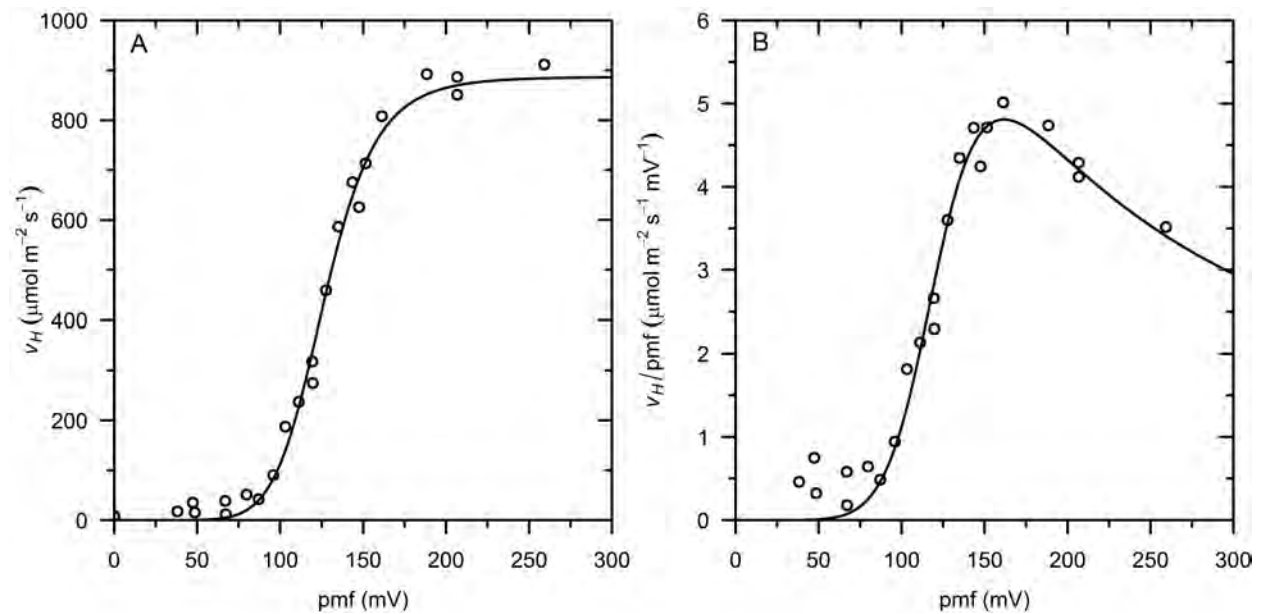


Figure 5.16: Relationship between the flux of H^+ through the ATPase (v_H) and the proton motive force (pmf) based on measurements of ATPase activity by Junesch and Gräber (1987), scaled assuming $0.5 \mu\text{mol m}^{-2}$ of ATP synthase and 14H^+ per rotation (symbols in Panel A), and the ratio between v_H and pmf as a function of pmf (symbols in Panel B). A Hill equation was fitted to the measurements of v_H (line in Panel A), and v_H/pmf derived from it (line in Panel B).

5.4 *In silico* analysis of metabolic regulation of electron transport

After testing that the model produced reasonable predictions of measurable steady-state and dynamic variables associated with photosynthesis (with poorer agreement with g_H at low irradiances), further simulations are analysed to gain insight into the regulation of the photosynthetic electron transport chain in C3 plants across a wide range of irradiance and CO_2 levels. Of course, the tests performed in the previous section do not guarantee that the model will make correct predictions regarding non-measurable variables such as cyclic electron transport or alternative electron sinks. On the other hand, the tests ensure that the simulations discussed below are physiologically reasonable, at least for *A. thaliana*.

In Section 5.4.1, the steady-state response of different variables to irradiance (at ambient CO_2 and O_2) and CO_2 (at an irradiance level of $1000 \mu\text{mol m}^{-2} \text{s}^{-1}$ and ambient O_2) are analysed. A major source of uncertainty in any analysis of the regulation of the electron transport chain is the H^+/ATP ratio of the ATP synthase. As discussed in Section 5.2.5, two values have been proposed (4.67 and 4) which are both supported by experimental evidence. Thus, a sensitivity analysis is performed in Section 0 that compares the irradiance and CO_2 responses performed in Section 5.2.5 (with $\text{H}^+/\text{ATP} = 4.67$) with the same simulations employing $\text{H}^+/\text{ATP} = 4$. In Section 5.4.3, two photosynthetic induction curves (at different $[\text{CO}_2]$) are analysed, in order to further understand the regulation of the electron transport chain under fluctuating light conditions.

5.4.1 Steady-state regulation

The flux of electrons required to sustain the Calvin cycle and photorespiration (J) increased with irradiance and CO_2 (insets within Figure 5.18), in a similar fashion to the evolution of net CO_2 assimilation (A_n , see Figure 5.8). The ratio of oxygenation over

carboxylation (ϕ) did not change much with irradiance as C_i varied within a small range (330 – 410 $\mu\text{mol mol}^{-1}$) and thus the relationship between J and A_n was approximately linear. In the CO_2 response curve, ϕ changed more strongly, as C_i varied in a larger range (15 – 1870 $\mu\text{mol mol}^{-1}$) and thus J and A_n were not linearly related. In particular, at sub-ambient $[\text{CO}_2]$, a higher J was required to maintain a given A_n , relative to the irradiance response curve. Thus, below the CO_2 compensation there was still a significant electron flux through the electron transport chain of almost 40 $\mu\text{mol m}^{-2} \text{s}^{-1}$.

The model predicted a significant difference between the flux of electrons generated by PSII (J_{II}) and J , due to consumption of electrons by alternative electron sinks. The differences between J_{II} and the flux of electrons through the cytochrome b_6f complex (J_{cyt}) was smaller due to low cyclic electron transport. The overall fraction of electrons allocated to all alternative electron sinks did not vary much with irradiance (15.5% – 17.0%). The water-water cycle consumed a small fraction of these electrons and most were allocated to NO_2^- reduction and the malate valve (Figure 5.18). At low irradiance, most of the electrons were allocated to MDH, whereas the other sinks were allocated less than 2% of the electrons. The reason for the higher importance of MDH at low irradiance is the ability of the system to keep 40% of the $\text{NADP}^+/\text{NADPH}$ reduced, whereas more than 95% of the ferredoxin (used by the other alternative electron sinks) was oxidised at low irradiance (Figure 5.19).

The fraction of J_{cyt} allocated to cyclic electron transport around PSI was small (always $\leq 4\%$) and increased with irradiance. The low rates can be explained by lower maximum rates of cyclic electron transport relative to alternative electron sinks (see Section 5.2.4 for details) and a more reduced state of the PQ/PQH₂ pair relative to ferredoxin at all irradiances (Figure 5.19). In the parameterization of NDH and FQR, and given the lack of adequate experimental data, it was assumed that all kinetic constants for both FQR and NDH were the same, except for the following differences: (i) the maximum electron flux through FQR was twice larger than for NDH, (ii) the reaction catalysed by NDH is sensitive to the proton motive force and (iii) FQR activity is redox sensitive. In the simulated irradiance response curve, the electron flux through FQR was always twice larger than through NDH as (i) FQR was fully reduced at low irradiance due to its relatively high midpoint redox potential and (ii) the effect of steady-state pmf on NDH activity was negligible despite its increase with irradiance (Figure 5.20).

In the CO_2 response curve, the fractions of J_{cyt} allocated to the MDH and NiR decreased with C_i and were relatively constant at $[\text{CO}_2]$ above ambient (Figure 5.18). WWC was a small sink at all C_i (between 1.3% and 2.3% of J_{cyt}). The total fraction of electrons allocated to alternative electron sinks decreased with C_i from 28.3% to 13.4%. Increases in C_i decrease the ratio between oxygenation and carboxylation of RuBP (ϕ) due to competitive inhibition of CO_2 on the oxygenation reaction. As the reactions in the photorespiration pathway that follow oxygenation have additional requirements for ATP and NADPH relative to the Calvin cycle, the ratio of the demand of ATP and NADPH decreases as ϕ decreases. Thus, changes in the fluxes of ATP and NADPH required to run the Calvin cycle and photorespiration drove the decrease in allocation of electrons to the alternative electron sinks with C_i . In the case of NiR, these changes in the fractions did not compensate the increase in linear electron transport (both J_{II} and J_{cyt} , inset in Figure 5.18B) such that the absolute flux of electrons consumed by NiR increased with C_i .

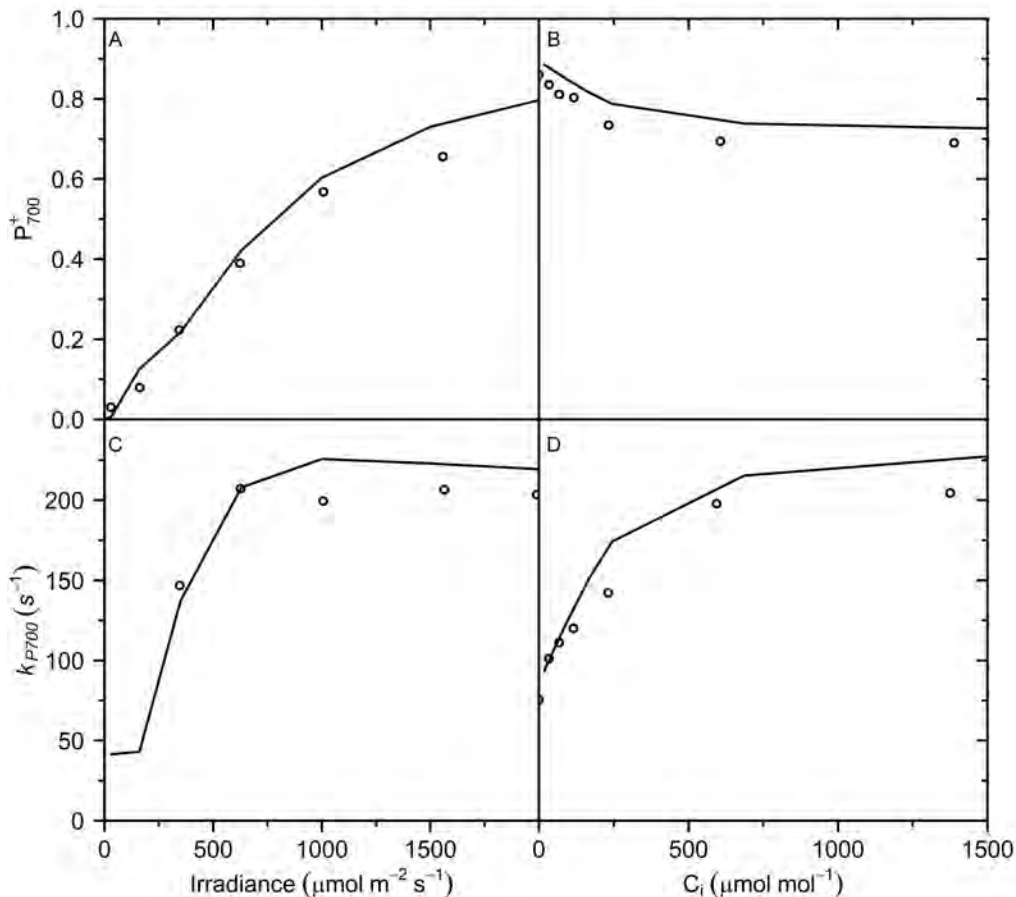


Figure 5.17: Simulated (lines) and measured (symbols) steady-state redox state of P_{700}^+ as a function of irradiance (A) and intercellular CO_2 mole fraction (B) and the rate constant of P_{700}^+ reduction after a rapid transition to darkness as a function of irradiance (C) and intercellular CO_2 mole fraction (D). Measurements from Hald et al. (2008).

As in the irradiance response curve, FQR and NDH were quantitatively less important than the alternative electron sinks. However, the larger values of pmf at low C_i did have a strong effect on NDH activity, to the point that, at the lowest C_i , NDH catalysed a reduction of oxidised F_d by PQH_2 coupled to the transport of H^+ ions from the lumen to the stroma. This reverse reaction only occurs at high pmf (in this case 270 mV), but the threshold for reversibility also depends on the redox states of the PQ/PQH_2 pair and F_d (see Section 5.2.4.2.1 for details). The additional electron flux into the F_d pool must be allocated to alternative electron sinks, (otherwise the F_d pool would become reduced), thus the strong increase in the flux towards NiR and the MDH at the lowest C_i (Figure 5.18).

The number of H^+ transported into or generated in the lumen per electron transported through cytochrome b_6f depends on the pathway for electron transport. As the model assumes that the Q cycle is always engaged, the stoichiometry for alternative electron sinks is 3 H^+ per electron. For cyclic electron transport mediated by FQR it is only 2 H^+ per electron, whereas for NDH it is 4 H^+ per electron (taking into account the H^+ pumping activity of NDH). When this stoichiometry is considered, the fraction of total H^+ flux into the lumen due to each type of electron transport can be calculated (Figure 5.21). The results are the same as in Figure 5.18 except for a higher fraction associated to NDH and a lower fraction associated to FQR, such that their contribution to H^+ fluxes was equal for both forms of cyclic electron transport, except at low C_i , when the reaction catalysed by NDH was reversed.

The proton motive force increased with irradiance and decreased with $[\text{CO}_2]$ (Figure 5.20). The fraction of pmf that was stored as $\Delta\Psi$ decreased with irradiance from 63% to 54%, whereas it increased with CO_2 from 52% to 56%. The pH of the stroma varied between 7.8 and 8.0 due to the high buffering capacity and a larger volume than the lumen of the thylakoid. This resulted in a decrease of lumen pH from 7.8 (in darkness) to 6.4 at high irradiance and ambient CO_2 , whereas, as CO_2 decreased below ambient levels, the pH of the lumen decreased down to a value of 5.8 (results not shown). These changes in lumen pH were responsible for the increase of NPQ_{SV} at high irradiances (Figure 5.22A) and low $[\text{CO}_2]$ (Figure 5.22B), through changes in PsbS protonation state and concentration of zeaxanthin (Figure 5.22). The effective pK of zeaxanthin formation was 6.8, compared to a pK of 6.3 assumed for protonation of PsbS. However, the Hill coefficient of violaxanthin de-epoxidase was 3, compared to a value of 1 for PsbS protonation. Thus, the contribution of PsbS to NPQ_{SV} at moderate lumen pH (pH > 6.8) was more important than the contribution of zeaxanthin, while the opposite became true at lower values (pH < 6.8). This is of importance for the dynamics of NPQ_{SV} , as changes in NPQ_{SV} due to changes in PsbS protonation occur an order of magnitude faster than synthesis of zeaxanthin (see Section 5.2.1.1.2 for details). Thus, NPQ_{SV} induction at low irradiance is expected to have faster kinetics and track variations in lumen pH (i.e., displaying an “overshoot” behaviour as in Figure 5.11B).

The changes in pmf with irradiance and CO_2 were not linear but rather presented a higher sensitivity to irradiance and ambient or sub-ambient $[\text{CO}_2]$ (Figure 5.20) with a similar pattern for NPQ_{SV} (Figure 5.22). These changes in the response of pmf coincided with a decrease in the flux of H^+ through ATPase per pmf unit (v_H/pmf , Figure 5.20). This is determined by the relationship between v_H and pmf (solid lines in Figure 5.23). When irradiance was increased, v_H changed in a sigmoidal fashion with respect to pmf, thus achieving a maximum ratio at intermediate pmf values, and decreasing above such level. When the source of variation was $[\text{CO}_2]$, the response was opposite, as v_H decreased with an increase in pmf. Both patterns are to be expected from the relationship between ATP consumption by the Calvin cycle and pmf in the irradiance and $[\text{CO}_2]$ response curve (see Figures 5.18 and Figure 5.20). In the simulations, ATPase was always fully reduced, except in darkness, due to its relatively high midpoint redox potential, implying that changes in v_H/pmf were caused entirely by changes in the concentrations of metabolites (Figure 5.24). In particular, the model predicted that, as the concentrations of ADP and ATP decreased and increased, respectively (Figure 5.24), the pmf required to sustain a given rate of ATP synthesis increase, in agreement with the experimental observations by Pänke and Rumberg (1996). In both irradiance and $[\text{CO}_2]$ response curves, an ADP concentration of 0.2 mol m^{-3} represented the critical point that triggered decreases in v_H/pmf . This relationship suggests that the failure of the model to predict correctly v_H/pmf at low irradiances as measured by Avenson et al. (2005), may be caused by an overestimation of the ADP/ATP ratio at such low irradiances, in addition to potential mismatches between simulated and real absolute values of pmf.

The changes in ATP and ADP concentration with irradiance and CO_2 were such that NPQ_{SV} was lowest under conditions where stromal metabolic activity was not limiting (i.e., low irradiance and/or high CO_2) and increased as excess energy increased (i.e., as CO_2 decreased and/or irradiance increased). Furthermore, these changes in the ATP/ADP ratio ensured that Rubisco activase (and hence Rubisco) were partly deactivated at low irradiance and high $[\text{CO}_2]$ (Figure 5.24), as observed in previous experiments (von Caemmerer and Edmondson, 1986). Thus, RuBP concentration remained saturating

throughout the simulation, except at irradiances below $200 \mu\text{mol m}^{-2} \text{s}^{-1}$. Due to the simplifications in the equations describing the metabolism in the stroma, these simulations do not offer insight into the physiological advantage of keeping RuBP levels at saturating level, which perhaps is related to regulating the concentration of Pi in the stroma (Sharkey, 1989).

5.4.2 Effect of H^+/ATP ratio

The simulations in the previous section were performed assuming a H^+/ATP ratio of 4.67, which has been proposed from measurements of the structure of the photosynthetic ATP synthase in *S. oleracea* (see Section 5.2.5 for details). However, a H^+/ATP ratio of 4 has also been proposed by different authors based on *in vitro* biochemical assays (see Section 5.2.5 for details). In order to evaluate the effect that this ratio has on the regulation of electron transport, irradiance and $[\text{CO}_2]$ response curves were simulated assuming $\text{H}^+/\text{ATP} = 4$ (other model inputs were kept as in the previous section).

A reduction of the H^+/ATP ratio by 14% would imply a reduction in the H^+ flux of 14% for the same environmental conditions and metabolic demand of ATP and NADPH. However, the thermodynamics of ATPase indicate that a reduction in the H^+/ATP ratio would require an increase in pmf to achieve the same ATP production given the same concentrations of substrates and products. Indeed, decreasing H^+/ATP resulted in a displacement of the relationship between H^+ flux and pmf towards higher pmf values (Figure 5.23).

Since the partitioning of pmf between ΔpH and $\Delta\Psi$ remained the same, this change resulted in a decrease in the pH of the lumen achieved at a particular irradiance and $[\text{CO}_2]$ (Figure 5.25). The decrease in lumen pH led to a reduction in J_{cyt} due to downregulation of PQH₂ oxidation (Figure 5.26) and an increase in NPQ_{SV} (results not shown).

In addition to a reduction in J_{cyt} , the fraction of J_{cyt} that was allocated to alternative electron sinks for $\text{H}^+/\text{ATP} = 4$ was on average, and for the irradiance response curve, 3.7% (versus 16.0% for $\text{H}^+/\text{ATP} = 4.67$), with negligible electron fluxes through FQR and NDH (Figure 5.26). The reduction in the fraction of electron flux allocated to alternative electron sinks resulted in an increase in J (Figure 5.26), despite the decrease in J_{cyt} . That is, the higher allocation of electrons to alternative electron sinks for $\text{H}^+/\text{ATP} = 4.67$ had resulted in a competition with the Calvin cycle and thus a decrease in the rate of CO_2 assimilation.

Having a higher H^+/ATP ratio allows the system to sustain high fluxes of ATP production with low pmf and moderate lumen pH, but this occurs at the expense of a decrease in the overall efficiency of the system due to the need for high rates of electron flux that do not contribute directly to CO_2 assimilation. Although these simulations cannot resolve the controversy regarding the true value of the H^+/ATP ratio, it provides important insights into the effect of the H^+/ATP ratio on different aspects of the system. These results would suggest that lower H^+/ATP ratios are favourable in terms of optimization of CO_2 assimilation. Given the large range of H^+/ATP ratios from ATP synthases across different taxa (Pogoryelov et al., 2012), reducing the H^+/ATP ratio may be a possible target for improvement of C3 plant photosynthesis. On the other hand, alternative electron sinks may actually be essential in order to sustain sufficient rates of nitrogen assimilation or to provide the cytosol with sufficient redox power to drive photosynthesis-dependent

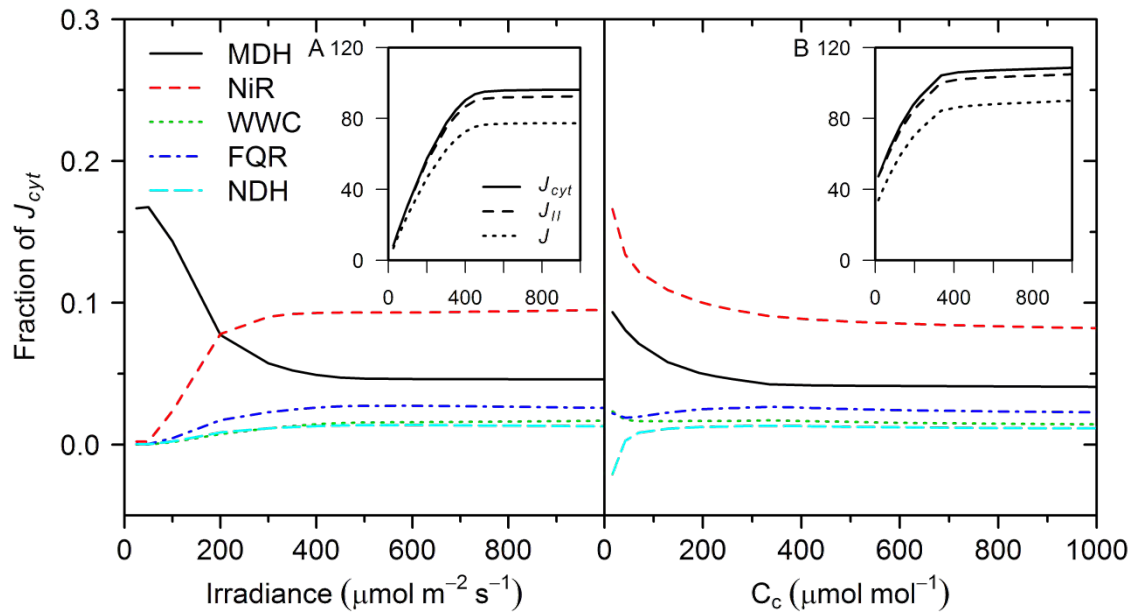


Figure 5.18: Simulated steady-state fraction of electron flux through cytochrome b_6 complex allocated to malate valve (MDH), NO_2^- reduction (NiR), water-water cycle (WWC), ferredoxin-quinone reductase (FQR) and NAD(P)H dehydrogenase (NDH) as a function of irradiance (A) and chloroplast CO_2 mole fraction (B). Insets describe the steady-state electron transport flux through cytochrome b_6 (J_{cyt} , $\mu\text{mol m}^{-2} \text{s}^{-1}$), PSII (J_{II} , $\mu\text{mol m}^{-2} \text{s}^{-1}$) and electron flux required to produce the NADPH consumed by the Calvin-Benson cycle and photorespiration (J , $\mu\text{mol m}^{-2} \text{s}^{-1}$) as a function of irradiance (inset in A) and chloroplast CO_2 mole fraction (inset in B).

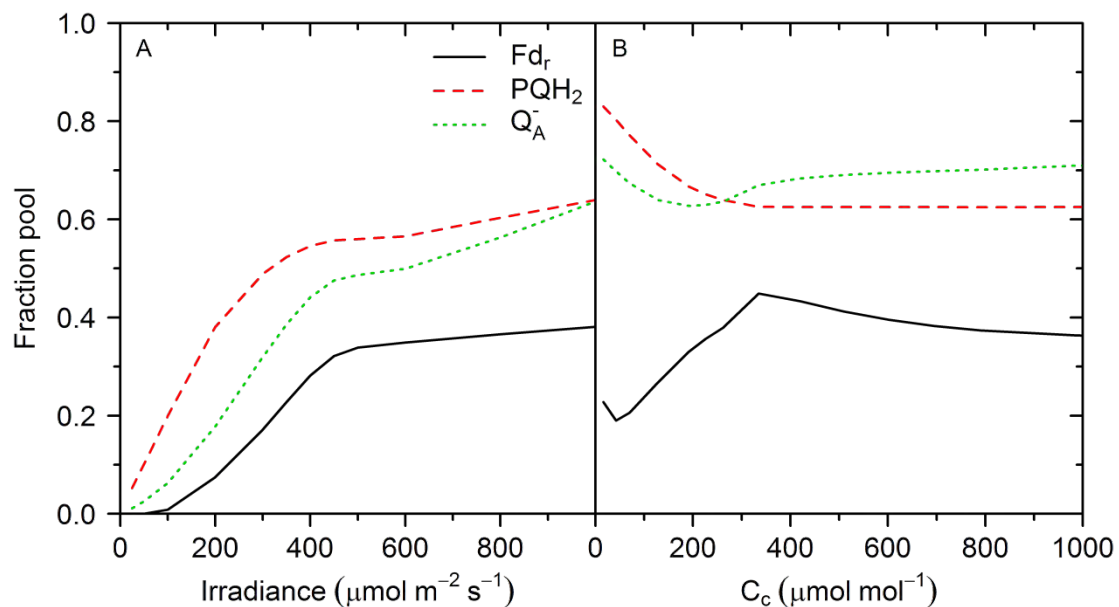


Figure 5.19: Simulated steady-state fraction of the pool of ferredoxin that is reduced (Fd_r), fraction of the free pool of PQ/ PQH_2 pair in PQH_2 form and fraction of PSII reaction centres that contain a reduced quinone A (Q_A^-) as a function of irradiance (A) and chloroplast CO_2 mole fraction (B).

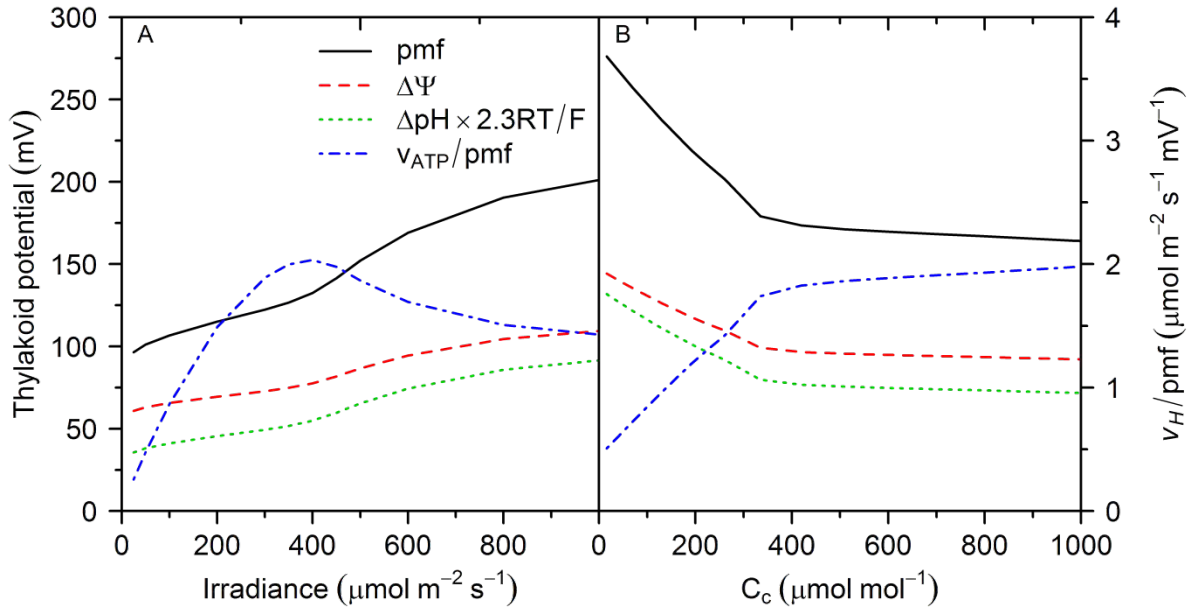


Figure 5.20: Simulated steady-state thylakoid proton motive force (pmf, mV), electrical field across the thylakoid membrane ($\Delta\Psi$, mV), potential associated with the difference in pH between stroma and lumen ($\Delta\text{pH} \times 2.3RT/F$, mV) and the ratio between the flux of H^+ through the ATPase and the proton motive force (v_H/pmf , $\mu\text{mol m}^{-2} \text{s}^{-1} \text{mV}^{-1}$) as a function of irradiance (A) and chloroplast CO_2 mole fraction (B).

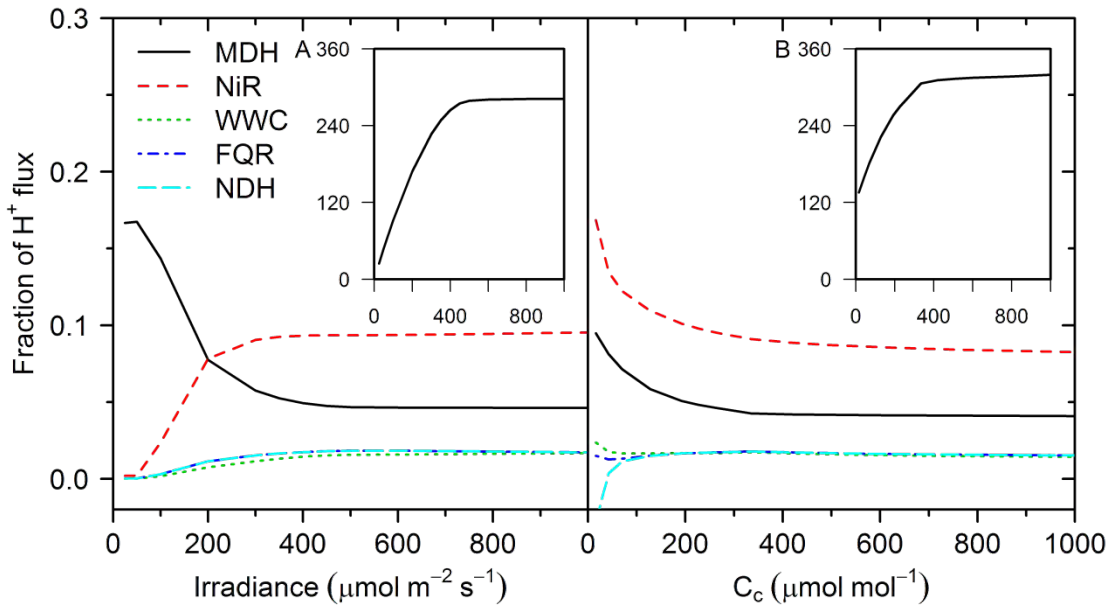


Figure 5.21: Simulated steady-state fraction of H^+ flux into the lumen due to electron flux associated to malate valve (MDH), nitrite reduction (NiR), water-water cycle (WWC), ferredoxin-quinone reductase (FQR) and NAD(P)H dehydrogenase (NDH) as a function of irradiance (A) and chloroplast CO_2 mole fraction (B). A negative fraction for NDH means reduction of Fd by PQH_2 . Insets represents the total steady-state H^+ flux into the lumen ($\mu\text{mol m}^{-2} \text{s}^{-1}$) as a function of irradiance (A) and chloroplast CO_2 mole fraction (B).

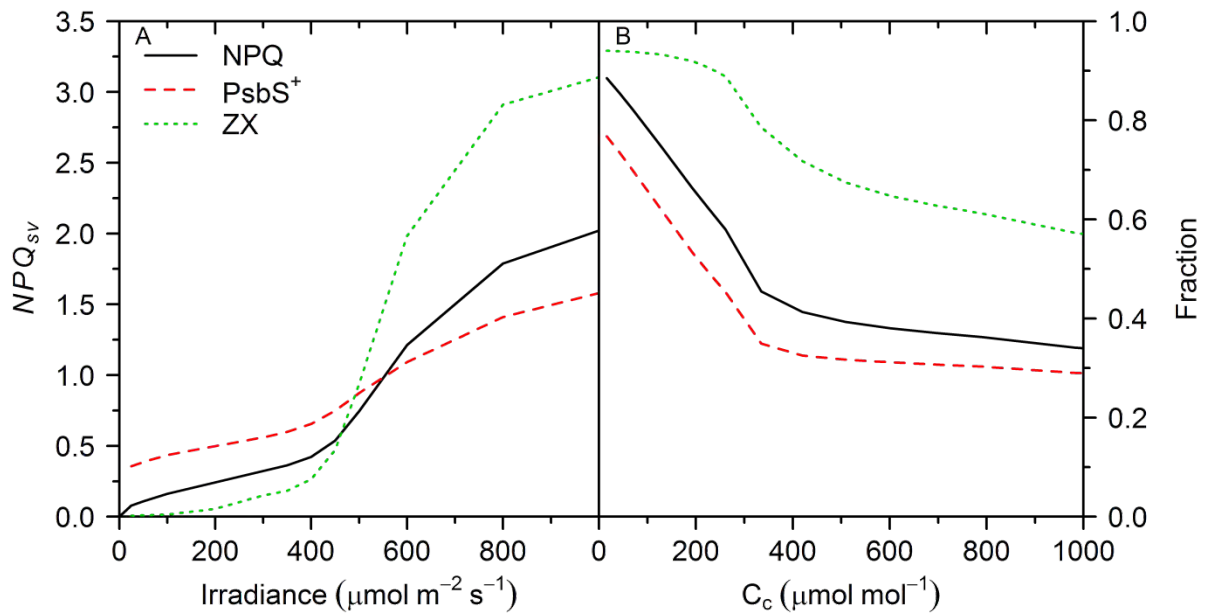


Figure 5.22: Simulated steady-state Stern-Volmer non-photochemical quenching coefficient (NPQ_{sv}), fraction of the PsbS protein that is protonated (PsbS^+) and fraction of the xanthophyll pool in the form of zeaxanthin (ZX) as a function of irradiance (A) and chloroplast CO_2 mole fraction (B).

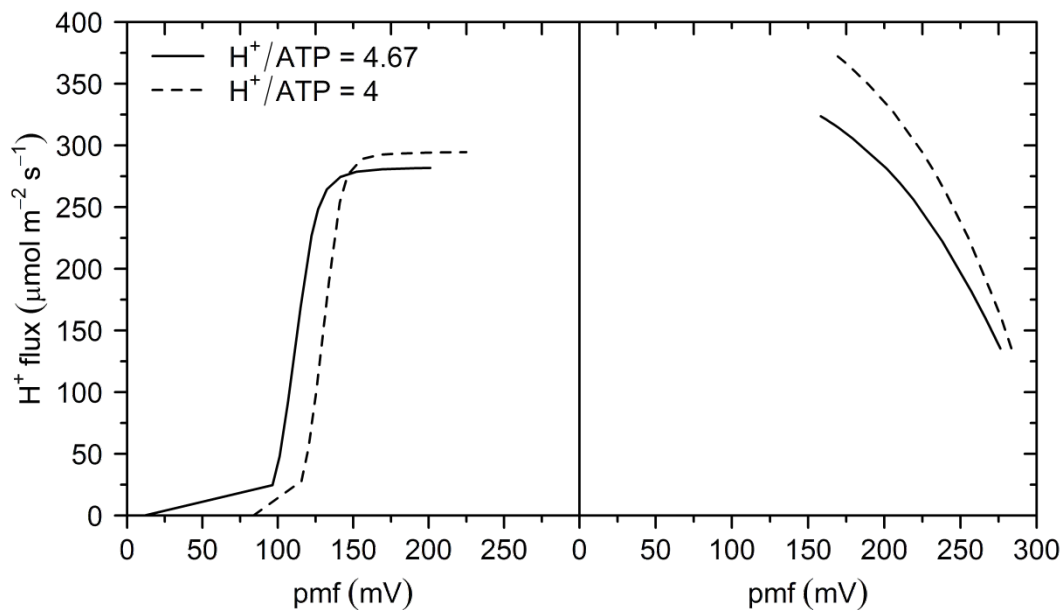


Figure 5.23: Simulated steady-state relationship between the flux of H^+ through ATP synthase and proton motive force as a function of irradiance (A) and CO_2 mole fraction (B) for two H^+/ATP ratios. The relevant parameters of ATP synthase were adjusted according to the H^+/ATP ratio as discussed in Section 5.2.5.

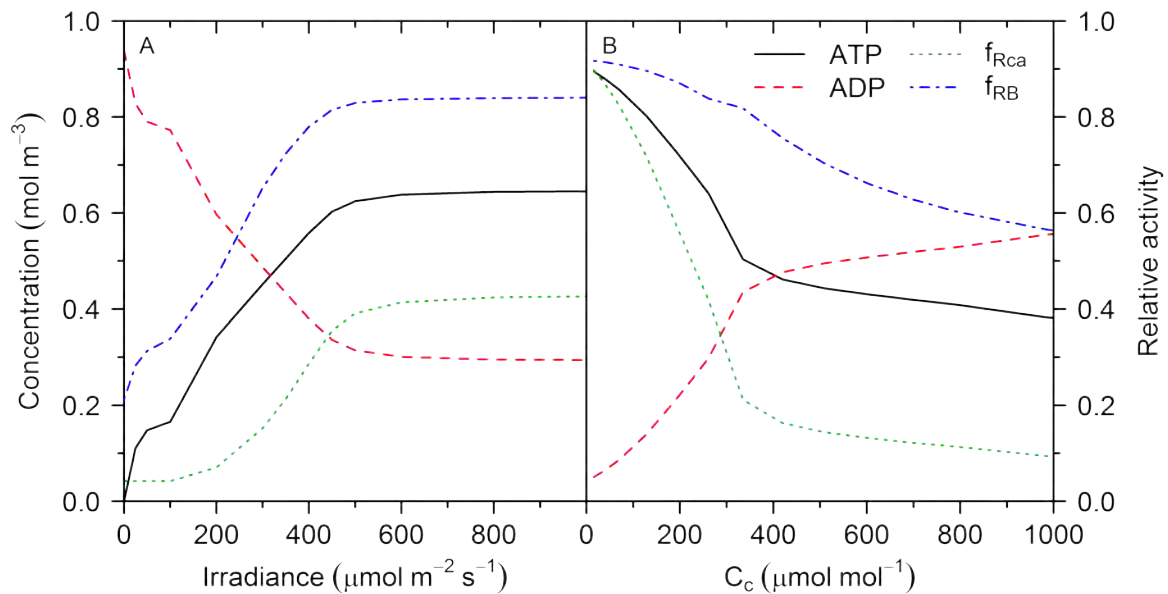


Figure 5.24: Simulated steady-state concentrations of ATP and ADP and relative activity of Rubisco activase (f_{Rca}) and Rubisco (f_{RB}) as a function of irradiance (A) and CO₂ mole fraction (B).

metabolism. Further research is needed to understand the trade-offs of a potential optimization of the H⁺/ATP ratio of ATPase.

5.4.3 Dynamic regulation

J increased with time after a rapid increase in irradiance from 50 μmol m⁻² s⁻¹ to 1000 μmol m⁻² s⁻¹ at both ambient and low [CO₂] (insets inside Figure 5.27). The rate of increase of J was faster in the first seconds of induction until the maximum flux sustained by stroma metabolism was reached, leading to a highly reduced PQ/PQH₂ pair and most PSII reaction centres closed (Figure 5.28). The high activity of alternative electron sinks, especially MDH and NiR ensured that Fd remained much more oxidised than the PQ/PQH₂ pair, which largely suppressed the cyclic flux of electrons around PSI (Figure 5.27). As Rubisco became more active (Figure 5.29), all electron fluxes increased and PSII reaction centres progressively opened. At the beginning of the induction curve, the ATP/ADP ratio was high, leading to low ATPase conductance, high pmf (Figure 5.30) and a rapid increase in NPQ_{SV} (Figure 5.31). The high pmf allowed Fd reduction by PQH₂ via NDH (Figure 5.27), which was most notable under low [CO₂].

Even though the activity of Rca decreased during induction (after a rapid increase to maximum activity in the first seconds), the simulated time series of Rubisco activity could be well described by an exponential function of time (Figure 5.29). The apparent rate constants of Rubisco activation were similar for ambient and low [CO₂] with values of $5.11 \times 10^{-3} \text{ s}^{-1}$ and $5.37 \times 10^{-3} \text{ s}^{-1}$, respectively (see Figure 5.29). This also implies that uncertainties in the calculation of Rca activity have a limited impact in the simulations of Rubisco activation. A limitation of these simulations is that they do not take into account the effect of CO₂ on stomatal conductance. Thus, in real leaves, [CO₂] may have a strong effect on the kinetics of induction (see Chapter 2 of this dissertation) and further research is needed to incorporate this behaviour into the model.

The dynamics of NPQ_{SV} induction is biphasic (Figure 5.31), in accordance with experimental results for induction at high irradiance (see Figure 5.11 as well as

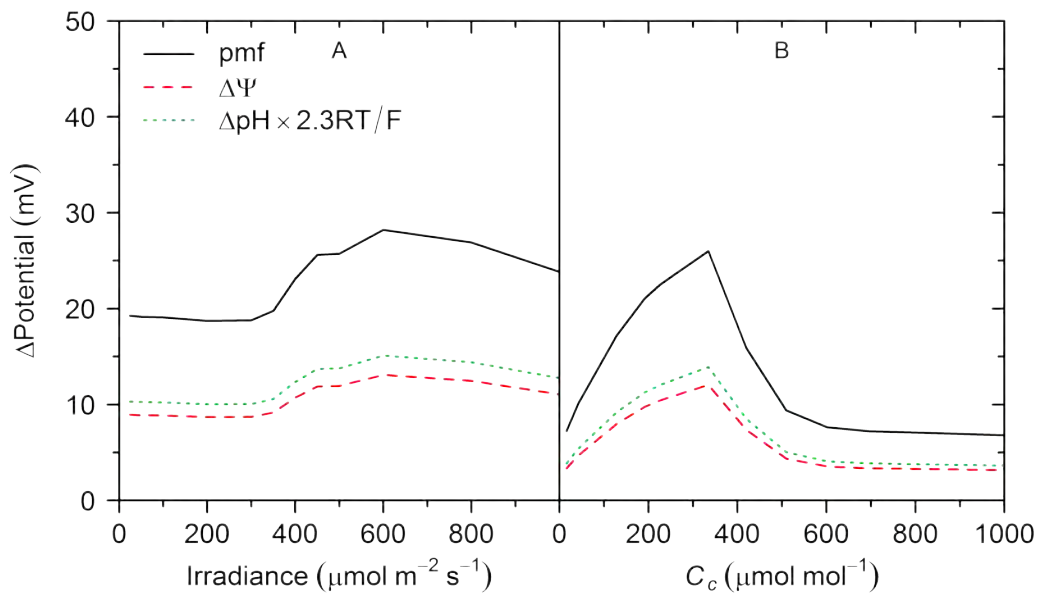


Figure 5.25: Difference in steady-state thylakoid proton motive force (pmf), electrical field across the thylakoid membrane ($\Delta\Psi$) and potential associated to the difference in pH between stroma and lumen ($\Delta pH \times 2.3RT/F$), between simulations with $H^+/ATP = 4.67$ and $H^+/ATP = 4$, as a function of irradiance (A) and chloroplast CO_2 mole fraction (B). The relevant parameters of ATP synthase were adjusted according to the H^+/ATP ratio as described in Section 5.2.5.

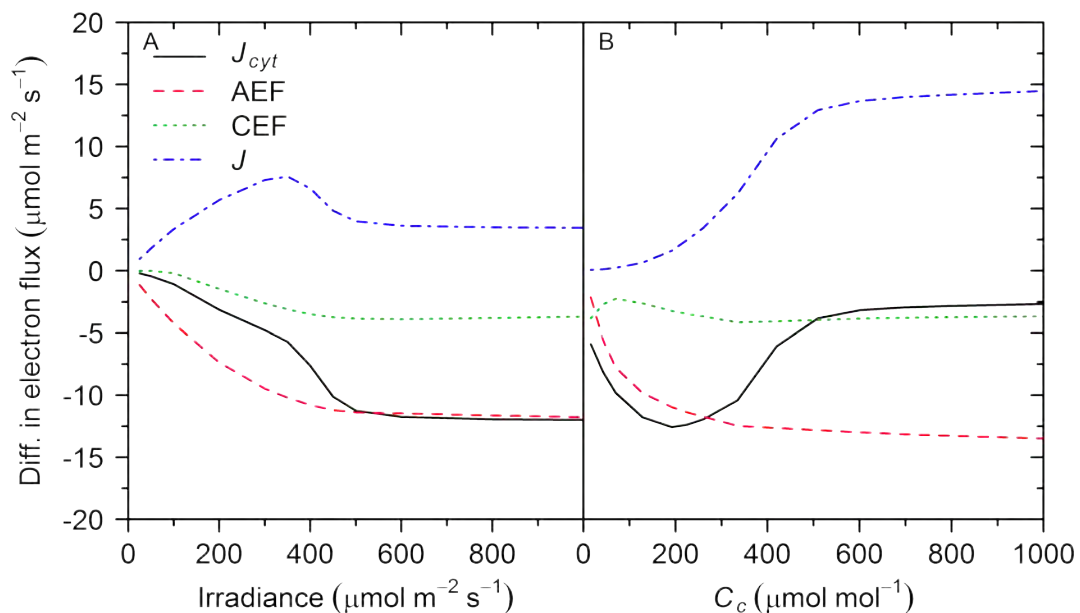


Figure 5.26: Difference in steady-state linear electron flux through cytochrome b_6f complex (J_{cyt}), alternative electron flux (AEF, sum of electron fluxes allocated to malate valve, nitrite reduction and water-water cycle) and cyclic electron flux around PSI (CEF, sum of electron fluxes allocated to ferredoxin-quinone reductase and NADPH dehydrogenase), between simulations with $H^+/ATP = 4.67$ and $H^+/ATP = 4$, as a function of irradiance (A) and CO_2 mole fraction (B). The relevant parameters of ATP synthase were adjusted according to the H^+/ATP ratio as described in Section 5.2.5.

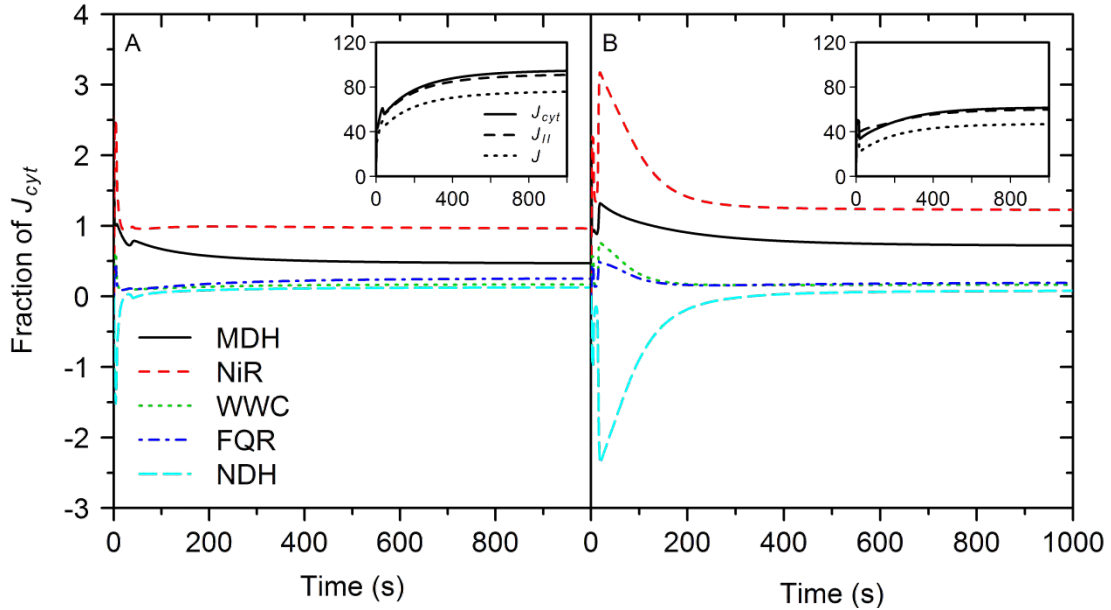


Figure 5.27: Simulated fraction of linear electron transport through the cytochrome b_6 complex allocated to malate valve (MDH), nitrite reduction (NiR), water-water cycle (WWC), ferredoxin-quinone reductase (FQR) and NAD(P)H dehydrogenase (NDH) as a function of time after a rapid increase of irradiance from $50 \mu\text{mol m}^{-2} \text{s}^{-1}$ to $1000 \mu\text{mol m}^{-2} \text{s}^{-1}$ and at air CO_2 mole fractions of $400 \mu\text{mol mol}^{-1}$ (A) and $100 \mu\text{mol mol}^{-1}$ (B). All the variables of the system were in steady-state at the beginning of the simulation. Insets describe the electron transport flux through cytochrome b_6 (J_{cyt} , $\mu\text{mol m}^{-2} \text{s}^{-1}$) and PSII (J_{II} , $\mu\text{mol m}^{-2} \text{s}^{-1}$) and electron flux required to produce the NADPH consumed by the Calvin-Benson cycle and photorespiration (J , $\mu\text{mol m}^{-2} \text{s}^{-1}$) as a function of time from the same simulations as the panels they belong to.

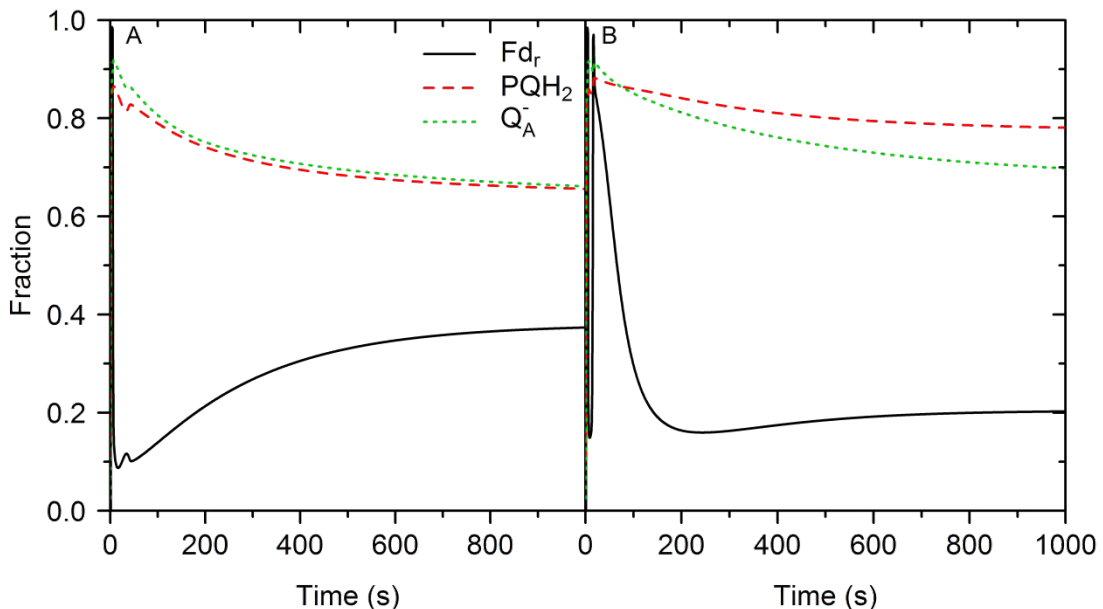


Figure 5.28: Simulated fraction of the pool of ferredoxin that is reduced (Fd_r), of the free pool of PQ/PQH₂ in PQH₂ form and of PSII reaction centres that contain a reduced quinone A (Q_A^-) as a function of time after a rapid increase of irradiance from $50 \mu\text{mol m}^{-2} \text{s}^{-1}$ to $1000 \mu\text{mol m}^{-2} \text{s}^{-1}$ and at an air CO_2 mole fraction of $400 \mu\text{mol mol}^{-1}$ (A) and $100 \mu\text{mol mol}^{-1}$ (B).

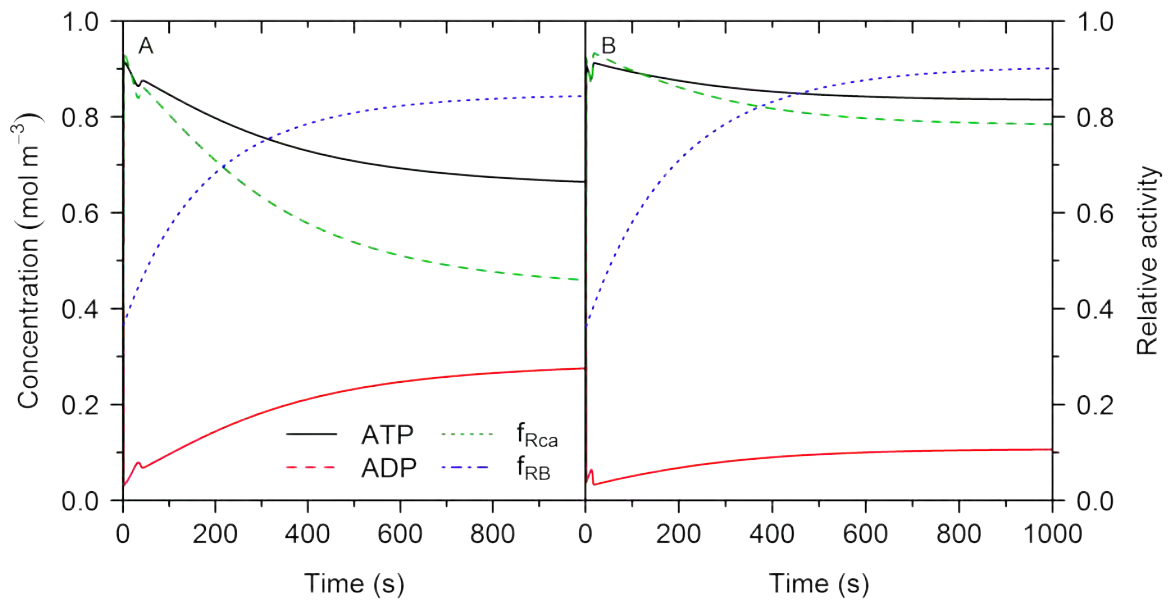


Figure 5.29: Simulated concentrations of ATP and ADP and relative activity of Rubisco activase (f_{Rca}) and Rubisco (f_{RB}) as a function of time after a rapid increase of irradiance from $50 \mu\text{mol m}^{-2} \text{s}^{-1}$ to $1000 \mu\text{mol m}^{-2} \text{s}^{-1}$ and at an air CO_2 mole fraction of $400 \mu\text{mol mol}^{-1}$ (A) and $100 \mu\text{mol mol}^{-1}$ (B).

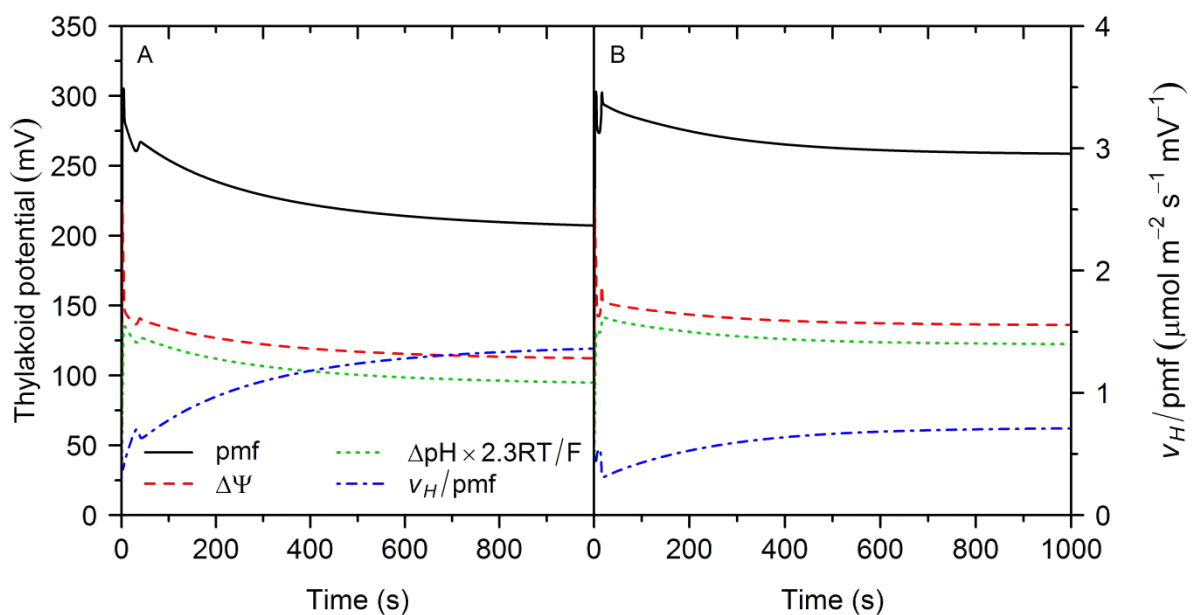


Figure 5.30: Simulated thylakoid proton motive force (pmf, mV), electrical field across the thylakoid membrane ($\Delta\Psi$, mV), potential associated to the difference in pH between stroma and lumen ($\Delta\text{pH} \times 2.3RT/F$, mV) and the ratio between the amount of ATP produced per unit of leaf area and the proton motive force (v_{ATP}/pmf , $\mu\text{mol m}^{-2} \text{s}^{-1}$) as a function of time after a rapid increase of irradiance from $50 \mu\text{mol m}^{-2} \text{s}^{-1}$ to $1000 \mu\text{mol m}^{-2} \text{s}^{-1}$ and at an air CO_2 mole fractions of $400 \mu\text{mol mol}^{-1}$ (A) and $100 \mu\text{mol mol}^{-1}$ (B).

measurements by Nilkens et al. (2010) or Dall'Osto et al. (2014)). According to the model, the fast increase in NPQ_{SV} during the first minutes was driven by PsbS protonation (Figure 5.31). Given that PsbS also deprotonates fast, this mechanism can be of great importance under fluctuating light conditions such as short sunflecks. The slow phase of NPQ_{SV} is more complex as it is affected by three simultaneous processes: (i) deprotonation of PsbS as the pH of the lumen increases, (ii) synthesis of zeaxanthin, and (iii) chloroplast light avoidance movement. The latter is not a true NPQ mechanism, but it would affect measurements of NPQ_{SV} and it aids in the dissipation of excess energy by reducing the amount of irradiance that reaches PSII_{ac}. In the simulations shown in Figure 5.31, the balance of the three processes is positive and NPQ_{SV} increases with time. However, at low irradiances, the contribution of zeaxanthin and chloroplast movement decreases (see Section 5.2.1.1 for details) and NPQ_{SV} may display an “overshoot” behaviour as shown in Figure 5.11.

The high pmf in the first minutes of induction allowed for an extended period of reversed NDH operation, which was compensated by an increase in electrons consumed by MDH and NiR (Figure 5.27). This behaviour was especially strong at low CO₂. This increase in the flux of electrons consumed by NiR and MDH led to an increase in the redox state of the ferredoxin pool (Figure 5.28), which affected FQR and WWC electron fluxes (Figure 5.27). Effectively, in the simulations, NDH behaved like a “safety valve”, dissipating excess energy during induction under strong metabolic restrictions. The simulation of photosynthetic induction at low [CO₂] were repeated for a leaf without NDH (results not shown). The new simulations yielded the same rates of CO₂ assimilations and J , but Q_A was up to 3% more reduced during the first three minutes of induction. Under conditions of fluctuating light, such as short sunflecks with a low irradiance background, this increase in Q_A reduction could lead to enhanced production of reactive oxygen species and photoinhibition of PSII. Thus, the ability of NDH to dissipate energy via Fd reduction may be considered a photoprotective mechanism under repeated short sunflecks. Evaluating the relevance of this mechanism under such conditions requires further research.

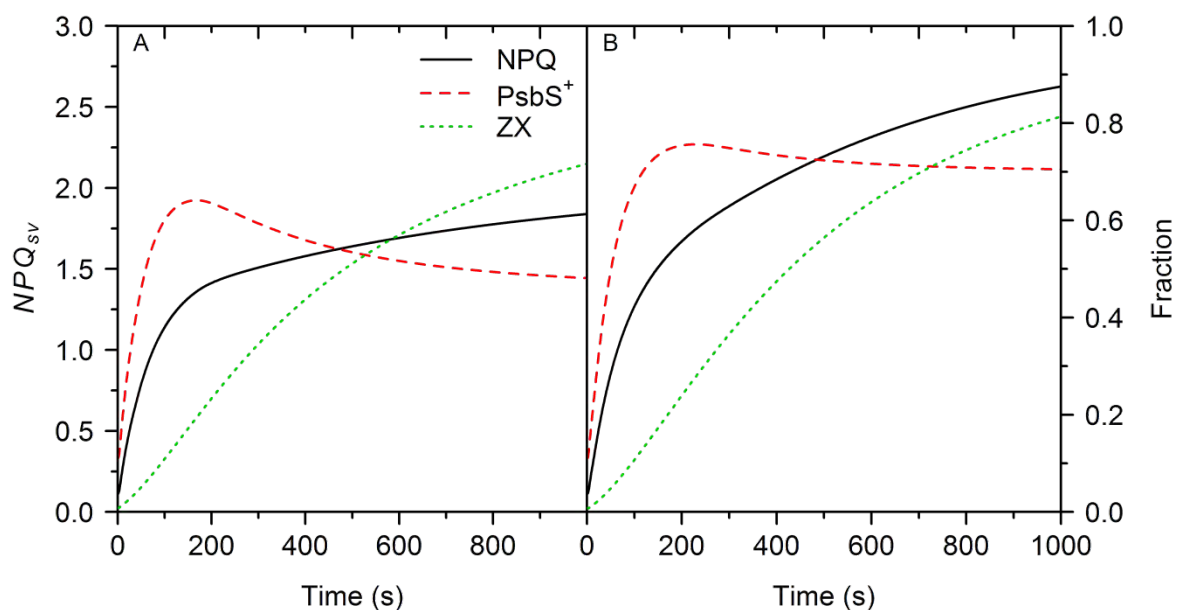


Figure 5.31: Simulated Stern-Volmer non-photochemical quenching coefficient (NPQ_{SV}), fraction of the PsbS protein that is protonated ($PsbS^+$) and fraction of the xanthophyll pool in the form of zeaxanthin (ZX) as a function of time after a rapid increase of irradiance from $50 \mu\text{mol m}^{-2} \text{s}^{-1}$ to $1000 \mu\text{mol m}^{-2} \text{s}^{-1}$ and at an air CO₂ mole fractions of $400 \mu\text{mol mol}^{-1}$ (A) and $100 \mu\text{mol mol}^{-1}$ (B).

5.5 Conclusions

The model can reproduce satisfactorily different aspects of steady-state and dynamic photosynthesis *in vivo* across a wide range of [CO₂] and irradiances, which ensures that the simulations of the model are physiologically reasonable.

The model predicts that electron fluxes that cycle around PSI are lower than those consumed by alternative electron sinks. The model simulations also show that, under certain conditions, reduction of Fd by PQH₂ is possible via NDH and this electron flux can have a photoprotective effect under fluctuating light conditions. The *in silico* analysis also shows that metabolic regulation of ATP synthase via changes in concentrations of substrates for ATP synthesis plays an important role in regulating NPQ, especially at low [CO₂] and high irradiance and that these changes are coordinated with changes in Rubisco activity via Rubisco activase.

Finally, a sensitivity analysis on the H⁺/ATP ratio of ATPase indicates that lowering this ratio increases net CO₂ assimilation, despite a decrease in linear electron flux and lower lumen pH, because of the strong reduction in fluxes consumed by alternative electron sinks.

5.6 Acknowledgements

This work was carried out within the IPOPOP programme on Systems Biology financed by Wageningen University. This research was also partly funded by the BioSolar Cells open innovation consortium, supported by the Dutch Ministry of Economic Affairs, Agriculture and Innovation. We thank Jeffrey A. Cruz for his useful suggestions in the development of the model.

Chapter 6

General discussion

“Remember that all models are wrong; the practical question is how wrong do they have to be to not be useful”

George E. P. Box, 1987

In this dissertation, I have investigated the dynamics of leaf photosynthesis in C3 plants under fluctuating irradiance. This had been achieved by reviewing the existing literature in a qualitative (Chapter 2) and quantitative manner (Chapters 4 and 5), analysing the results of a comprehensive experiment that used several photosynthetic mutants of *Arabidopsis thaliana* (Chapter 3), and developing two dynamic models of photosynthesis to analyse *in silico* (i) how different processes limit CO₂ assimilation under fluctuating irradiance, i.e., dynamic CO₂ assimilation (Chapter 4), and (ii) the dynamic regulation of the photosynthetic electron transport chain under constant and fluctuating irradiance (Chapter 5). The main findings of this dissertation include: (i) CO₂ mole fraction ([CO₂]), air temperature and initial irradiance affect the dynamics of CO₂ assimilation when a leaf is exposed to a rapid change in irradiance, (ii) these dynamics can be explained by changes in the activities of enzymes in the Calvin cycle, kinetics of stomatal conductance, and regulation of electron transport and light harvesting, (iii) these processes significantly decrease CO₂ assimilation at the canopy level, and (iv) the regulation of electron transport can be explained by the interactions among alternative forms of electron transport and ATP synthesis.

The aim of this chapter is to answer the specific research questions that motivated this dissertation, to discuss the limitations of the methodology employed and future research to overcome them, and to discuss potential applications of the models presented in this dissertation.

6.1 Addressing research questions

As discussed in Chapter 1, this dissertation was motivated by the need to answer four specific research questions. The knowledge presented in Chapters 2 – 5 is applied in the sections below to address these questions.

6.1.1 How does CO₂ assimilation respond to fluctuating irradiance, under different temperature, [CO₂] and air humidity?

In a review of the literature on dynamic photosynthesis, Chapter 2 revealed that major gaps exist in our knowledge of how the environment affects the dynamic responses of CO₂ assimilation to changes in irradiance. Most studies in the literature have focused on the effects of [CO₂] and temperature on photosynthetic induction (Table 2.1), and, to a lesser extent, the effect of vapour pressure deficit (VPD). Little or no information is available on how temperature and VPD affect CO₂ assimilation after a decrease in irradiance. This scarcity of knowledge contrasts with the more comprehensive understanding of the effect of the environment on steady-state photosynthesis, including both short-term (Farquhar et al., 1980; Sage and Kubien, 2007; Lawson et al., 2011), and long-term effects (Medlyn et al., 1999; Hikosaka et al., 2006). For example, only three publications (on four species) contained data suitable for the analysis of the effect of CO₂ on the rate of photosynthetic induction (Figure 2.3), whereas more than two decades ago, Wullschleger (1993) reviewed the effect of CO₂ on steady-state CO₂ assimilation for 109 species. Given the few data sources available and the different measurement protocols followed in the reviewed experiments, no formal statistical analysis was performed in Chapter 2. Thus, the

emphasis was on general trends in the data rather than on the magnitude of the effects and their significance (Table 2.1).

It was found that photosynthetic induction was faster with increasing $[\text{CO}_2]$. This resulted in a decrease in the time required to reach 90% of the final steady-state CO_2 assimilation (t_{90}), but no clear effect on the time required to reach 50% of the final steady-state (t_{50}). Published studies (Pearcy et al., 1996; Allen and Pearcy, 2000a) and the results of Chapter 5 suggest that the different effects of $[\text{CO}_2]$ on t_{90} and t_{50} can be interpreted as a weak effect of $[\text{CO}_2]$ on activation of Rubisco and other enzymes in the Calvin cycle, but a strong effect on stomatal opening. It was not possible to determine a clear effect of $[\text{CO}_2]$ on the kinetics of stomatal conductance (g_s) because (i) some of the articles used to analyse the effect on photosynthetic induction did not report measurements of g_s , and (ii) the trends in the articles that did report it were contradictory. Furthermore, the lack of standardized measurement protocols, and the complex interactions among the different environmental factors that affect g_s may result in apparent contradictions (Merilo et al., 2014). A further complication in the interpretation of the data is that $[\text{CO}_2]$ affects mesophyll conductance (Flexas et al., 2007a), although some of these effects may be the result of methodological artefacts (Tholen et al., 2012; Gu and Sun, 2014).

Woodrow et al. (1996) observed that $[\text{CO}_2]$ could sometimes affect the apparent rate constant of Rubisco activation through carbamylation, but only when the difference between initial and final irradiance was small. However, as sunflecks and cloudflecks are characterized by large changes in irradiance (Knapp and Smith, 1988; Smith and Berry, 2013), this observation may not be so relevant for the study of photosynthesis under naturally fluctuating irradiance. The other mechanism by which $[\text{CO}_2]$ could affect Rubisco activation is through changes in the activity of Rubisco activase (Rca). However, in Chapter 5, it was shown that, although changes in $[\text{CO}_2]$ lead to changes in ATP/ADP and therefore Rca activity, these changes were not large enough to affect the kinetics of Rubisco activation significantly (Figure 5.29).

The analysis of the effect of temperature on photosynthetic induction suggested the existence of an optimum temperature for t_{50} and t_{90} , albeit with strong scatter ($R^2 < 0.34$) and without clear trends for some of the individual experiments. A possible explanation for the existence of an optimum is the temperature sensitivity of Rca (Carmo-Silva and Salvucci, 2011), which would result in proportional changes in the rate constant of Rubisco activation. Indeed, experiments have shown that Rca downregulation at high temperature slows down significantly the induction of photosynthesis (Yamori et al., 2012). The simulations in Chapter 4 confirm that this could significantly reduce canopy-level CO_2 assimilation at high temperature (Figure 4.38). These simulations also indicated that enhanced photoinhibition at low and high temperature resulted in higher limitations to CO_2 assimilation. However, there is no experimental evidence for this, and only one modelling study addressed this issue (Zhu et al., 2004).

In summary, much is still unknown about the effects of environmental conditions on CO_2 assimilation under fluctuating irradiance, and this limits the possibility to model them. If new relationships are identified through careful experimentation, the models in this dissertation could be extended, providing a more complete description of how leaf and canopy CO_2 assimilation respond to the fluctuations in the microclimate throughout the day.

6.1.2 What is the importance of different photosynthetic processes in limiting dynamic CO₂ assimilation at the leaf and canopy level?

From the review of the literature in Chapter 2, it was concluded that several processes have been proposed to affect dynamic CO₂ assimilation. These processes are: (i) the slow (Zhu et al., 2004) and fast (Hubbart et al., 2012; Armbruster et al., 2014; Kromdijk et al., 2016) components of non-photochemical quenching, (ii) activation of enzymes in the Calvin cycle (Sassenrath-Cole et al., 1994; Mott and Woodrow, 2000), (iii) opening of stomata (Allen and Pearcy, 2000a), (iv) delays in CO₂ release by photorespiration (Vines et al., 1983), and (v) consumption of Calvin cycle metabolites after decreases in irradiance (Sharkey et al., 1986b). These observations were confirmed by the experiment described in Chapter 3 and the *in silico* analysis in Chapter 4. In addition, the simulations in Chapter 4 identified chloroplast movements as another factor that could limit dynamic CO₂ assimilation. Experiments at the leaf level generally apply single-step changes in irradiance (decreasing or increasing) after photosynthesis has reached a steady-state. The limitations on transient CO₂ assimilation by these processes depend on whether irradiance has been increased or decreased (Figure 4.35), and on the initial level irradiance (Figures 3.5 and 3.6). Below, the limitations imposed by each process are discussed.

Limitations after increases in irradiance

Stomatal (g_s) and mesophyll conductance limit CO₂ assimilation by lowering [CO₂] at the carboxylation site with respect to the air [CO₂]. That is, a hypothetical leaf with infinite mesophyll and stomatal conductance would result in a constant chloroplast [CO₂] equal to the air [CO₂]. However, in addition to these limitations, the kinetics of stomatal opening may impose an additional limitation on CO₂ assimilation by transiently lowering [CO₂] below the final steady-state value. By analysing the induction curves from different genotypes in Chapter 3, it was shown that the magnitude of this excess limitation depends on the value of g_s at the beginning of induction (Figure 3.6). Therefore, slowly closing stomata are advantageous to CO₂ assimilation under fluctuating irradiance, as this will allow more efficient use of sunflecks, by keeping higher g_s at the beginning of the sunflecks. Furthermore, the simulations in Chapter 4 also revealed that the slow kinetics of g_s had an additional positive effect after decreases in irradiance (Figure 4.35), by keeping chloroplast [CO₂] above steady-state levels. Therefore, depending on the spatio-temporal distribution of irradiance within a canopy, the irradiance at which g_s saturates, and the relative contribution of each leaf to canopy CO₂ assimilation, faster stomatal kinetics may have a net negative effect on total daily CO₂ assimilation (Figure 4.38).

The activity of Rubisco activase after an increase in irradiance is known to limit the rate of photosynthetic induction (Mott and Woodrow, 2000). This was confirmed in the experiment in Chapter 3 by using a genetic transformant where Rca was not redox regulated (*rwt43*) and a mutant with lower amount of Rca (*rca-2*). In addition, previous studies suggested that the maximum activation state was also dependent on Rca content (Mate et al., 1996; Mott and Woodrow, 2000). These assumptions were confirmed by measurements (Chapter 3) and simulations (Chapter 4) of the mutant *rca-2*. The model was also capable of reproducing the upregulation of NPQ in *rca-2*, due to the higher excess of energy in which the system incurred. The simulations confirmed that Rubisco activation also limited CO₂ assimilation at the canopy level, especially at high temperature, when Rca becomes partially deactivated.

Limitations on CO₂ assimilation after an increase in irradiance by activation of enzymes besides Rubisco have been associated with the fast component of photosynthetic induction (Pearcy et al., 1996), which lasts for less than 2 minutes. The measurements in Chapter 2 indicated that this fast component was only evident for dark-adapted leaves (especially on *rca-2*, see Figure 3.2), but not so clear when leaves were adapted to low irradiance (Figure 3.S2). Indeed, the simulations with the model in Chapter 4 confirmed that activation of such enzymes had a very small impact on dynamic CO₂ assimilation when leaves were adapted to low irradiance (Figure 4.35). It has been postulated (Pearcy et al., 1996) that the rapid deactivation of these enzymes could result in a strong limitation on CO₂ assimilation of a leaf exposed to sunflecks, but the simulations in Chapter 4 indicated that the kinetics of activation of these enzymes did not have a significant effect on canopy CO₂ assimilation (Figure 4.38). However, since these kinetics vary across species (Pearcy et al., 1996), the results from these simulations should not be generalized. In addition, whereas the model was validated with measurements of *A. thaliana* grown under constant environmental conditions, the simulations assumed a dense canopy with randomly distributed leaves under field conditions. It is possible that, if the model had been calibrated and validated with leaves acclimated to the microclimate of such a canopy (e.g., a cereal crop), the results could have been different.

Limitations after decreases in irradiance

The processes discussed above mostly limit the rate at which CO₂ assimilation changes after an increase in irradiance, but other processes become more relevant after a decrease in irradiance. As expected from the literature (Chapter 2), the temporal evolution of measured and simulated CO₂ assimilation after a decrease in irradiance can be decomposed into three parts (Figure 2.1): (i) CO₂ assimilation is higher than in the final steady-state for a period < 30 s (post-illumination CO₂ fixation or PICF), followed by (ii) CO₂ assimilation becoming transiently lower than in the final steady-state for a period < 2 min (post-illumination CO₂ burst or PICB), and finally, (iii) CO₂ assimilation approaches asymptotically the final steady-state. However the time response of the open gas exchange system distorted the measurements during the first minute after a decrease in irradiance (Figure 6.1). Thus, whereas the apparent PICF lasted for ca. 20 s, the real PICF (once the distortion was removed) only lasted for 10 s (Figure 6.1). In addition, the distortion resulted in a strong underestimation of PICB during the first 30s.

For the gas exchange system used in Chapter 2, the time constant of the response of the instrument was estimated to be 6.53 s, based on the specifications from the manufacturer. Although faster gas exchange systems have been used in the past (Laisk et al., 1984; Kirschbaum et al., 1988), such systems were not available during the experiment. In addition, it is important to consider that leaves of *A. thaliana* are small (ca. 2 cm²) and the measured rates of CO₂ assimilation were relatively low. A high flow rate (required for rapid responses of the system), low photosynthetic surface and low CO₂ assimilation would result in small differences in [CO₂] between the air entering and leaving the leaf cuvette of the gas exchange system (see Section 4.2.5), which would result in a high noise/signal ratio in the measurements.

These methodological artefacts imply that conclusions regarding PICF and PICB from measurements (Chapter 3) should be taken with caution. This may explain why no significant effects on PICF or PICB were observed for *npq4-1* or *npq1-2*. In addition, the

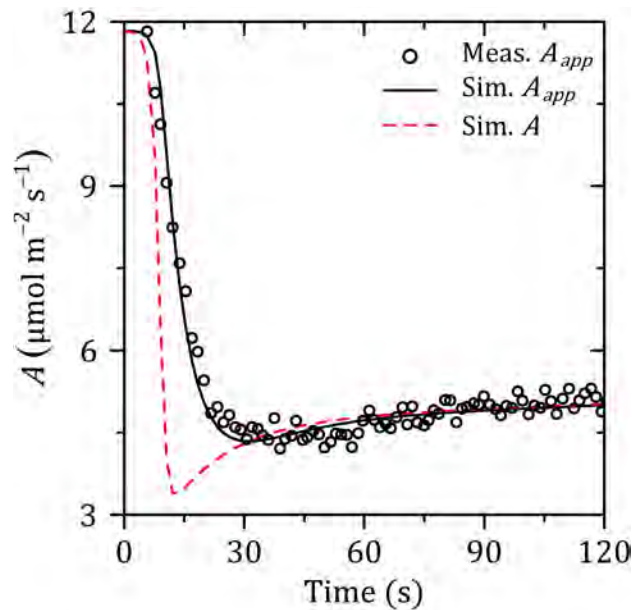


Figure 6.1: Measured apparent CO_2 assimilation ($\text{Meas. } A_{app}$), simulated apparent CO_2 assimilation as affected by the time response of the gas exchange system ($\text{Sim. } A_{app}$), and simulated CO_2 assimilation without the effect of the time response of the gas exchange system ($\text{Sim. } A$). Measurements and simulations from Chapters 3 and 4, respectively, for *Arabidopsis thaliana Col-0*, after a decrease of irradiance from $800 \mu\text{mol m}^{-2} \text{s}^{-1}$ to $130 \mu\text{mol m}^{-2} \text{s}^{-1}$.

PICF and PICB are also affected by the delays in CO_2 release by photorespiration, which can mask the differences due to downregulation of qE. However, the model in Chapter 4 suggested that limitations by qE were larger than the effect of delayed photorespiration. In addition, as delayed photorespiration also increased CO_2 assimilation after increases in irradiance, the time-integrated budget of CO_2 assimilation was not affected (Figures 4.35 and 4.38).

The model predicted that a faster relaxation of qE or the absence of qE increased CO_2 assimilation after a decrease in irradiance (Figure 4.35), in agreement with published experimental results (Hubbart et al., 2012; Armbruster et al., 2014; Kromdijk et al., 2016). However, qE also protects from photoinhibition, which can limit CO_2 assimilation for an extended period due to the low rates of Photosystem II (PSII) repair. Indeed, although not statistically significant, the values of CO_2 assimilation for *npq4-1* were always lower than in the wildtype after a decrease in irradiance (Figure 3.S6). The scaling to the canopy suggests that whether removing qE has a positive or negative effect depends on whether environmental conditions favour photoinhibition. On the other hand, a faster qE relaxation always resulted in an increase in CO_2 assimilation.

Photoinhibition had a strong effect on canopy CO_2 assimilation (A_{can}) and increased at high and low temperature (Figure 4.38), as expected from the temperature sensitivity of PSII repair. Zhu et al. (2004) estimated the effect of photoinhibition on A_{can} using a ray tracer and a steady-state irradiance response curve, coupled to an empirical model that assumed photoinhibition to be proportional to cumulative absorbed irradiance. They observed much larger relative decreases in daily A_{can} (17% – 32%) than obtained in Chapter 4. Werner et al. (2001) used a 3D turbid medium model in combination with the FvCB model and a similar model of photoinhibition to that used by Zhu et al. (2004), and observed a reduction of 6% on daily A_{can} . The predictions in Chapter 4 are much lower than both published estimations and it is unclear whether such differences are due to the use of a dynamic model of CO_2 assimilation, the differences in the simulated canopies, or

the weather scenarios selected. Regardless of these discrepancies, the overall conclusion is that photoinhibition can limit A_{can} under field conditions.

Finally, the model in Chapter 4 tested the effects of chloroplast movement, which was not included in Chapter 3 and, to my knowledge, has never been linked explicitly to dynamic CO_2 assimilation. Chloroplast movement may affect CO_2 assimilation in three ways: (i) by reducing the irradiance absorbed by the leaf, (ii) by decreasing the rates of photoinhibition, and (iii) by increasing or decreasing mesophyll conductance, depending on the anatomy of the leaf. In *A. thaliana*, chloroplast movements at high blue irradiance result in decreases of apparent mesophyll conductance (Tholen et al., 2008). Therefore, for this species, only the photoprotective role of chloroplast movements contributes positively to CO_2 assimilation. In the simulations, the overall effect of chloroplast movements at the canopy level was negative and exerted a stronger limitation than any other process. However, it is important to remember that strong chloroplast movement is associated with acclimation to low irradiance (Higa and Wada, 2016) and is rather unimportant in many species of agronomic interest (Davis et al., 2011).

6.1.3 How is the electron transport chain, coupled to the Calvin cycle, regulated under steady-state and fluctuating irradiance?

The simulations in Chapter 5 suggest that adenylates play a major role in the regulation of the electron transport chain by (i) adjusting the relationship between ATP synthesis and H^+ motive force (pmf), and (ii) regulating the activity of Rubisco through Rca and hence the potential demand of NADPH and ATP at different levels of irradiance and $[\text{CO}_2]$.

If irradiance increases, the rate of ATP synthesis and the pmf will increase, but if $[\text{CO}_2]$ decreases, the rate of ATP synthesis decreases with an increase in pmf (Kanazawa and Kramer, 2002; Takizawa et al., 2007). The model indicates that these two patterns can be explained by changes in the relationship between ATP synthesis and pmf (Figure 5.23). Simulations in Chapter 5 showed that, when irradiance is the source of variation, the H^+ flux increases proportionally with pmf for a wide range of pmf values, with a lower bound and a saturation level. This coincides with results from experiments in which irradiance was varied (Junesch and Gräber, 1985; Pänke and Rumberg, 1996). This has led to the idea that ATP synthesis can be modelled as proportional to pmf (Cruz et al., 2001; Zaks et al., 2012) but this does not hold for changes in $[\text{CO}_2]$ (Figure 5.23). This different pattern was caused by a decrease in the ADP/ATP ratio that decreases the ratio between ATP synthesis and pmf, which allows achieving lower rates of ATP synthesis at low $[\text{CO}_2]$, but at the same time, upregulating NPQ by increasing pmf. This pattern has also been observed experimentally (Kanazawa and Kramer, 2002; Avenson et al., 2004). ADP and ATP can have a strong effect on the regulation of ATP synthase (ATPase) because (i) the affinity of ATPase for ADP depends on pmf and (ii) ATP competes with ADP for the same catalytic site (Pänke and Rumberg, 1996).

The ratio ATP/ADP also played a major role in the regulation of Rubisco activity through Rca activity. Although no measurements were available on the steady-state and dynamic responses of Rubisco activity for *A. thaliana*, the simulated patterns presented in Figure 5.24 agree with experimental results for other species (von Caemmerer and Edmondson, 1986; Sassenrath-Cole et al., 1994). This indicates that, although the exact mechanisms for regulation of Rca are still unknown (Hazra et al., 2015), a simple phenomenological relationship between Rca activity and ATP/ADP appears to be sufficient to generate accurate predictions of *in vivo* Rubisco activity.

Simulations predicted that, on average, 16.2% of electrons that circulated through cyt b_6/f or Photosystem I (PSI) were used by alternative electron sinks (water-water cycle, nitrogen assimilation, and malate shuttle), whereas only 2.1% of those electrons were cycled around PSI by FQR or NDH. The maximum capacities of the different forms of alternative electron transport were taken from the literature or calculated from different sources, except for the case of FQR that had to be estimated. Thus, the value assumed for FQR maximum capacity influences these fractions. Unfortunately, these numbers are difficult to validate experimentally, given the difficulties in obtaining accurate, absolute measurements of cyclic electron fluxes *in vivo* (Fan et al., 2016).

Very little is known about the affinity of FQR and NDH with respect to their substrates and products. These were assumed, for simplicity, to be the same for FQR and NDH, and to be in the same order of magnitude as typical amounts of plastoquinone (PQ) and ferredoxin (Fd) in a leaf. However, this resulted in simulations where, on average, FQR and NDH were only operating at 15% of their maximum capacity. On the other hand, the water-water cycle, nitrogen assimilation and malate shuttle operated, on average, at 30%, 37% and 18% of their maximum capacity, respectively. Therefore, it is not sufficient to know the maximum fluxes of electrons that may circulate through each alternative path, but also how these fluxes respond to the redox states of the pools of electron donors and acceptors. In addition, additional forms of regulation of these reactions also needs to be considered. The simulations included the regulation of MDH and FQR by thioredoxin, but other forms of regulation, like the effect of H_2O_2 on NDH (Strand et al., 2015), could also have an impact on the simulations.

In the simulations, the malate shuttle was the most important alternative path at low irradiance, as Fd was mostly oxidised but half of the pool of NADPH was reduced. As irradiance increased, the relative flux through the malate shuttle decreased, but the relative fluxes into the other paths increased. The model also predicted a significant increase in alternative electron sinks at low $[CO_2]$, which contributed to the build-up of NPQ by acidifying the lumen, as well as increasing the ATP/NADPH ratio due to increasing levels of photorespiration. The model also predicted a higher fraction of alternative electron sinks at the beginning of photosynthetic induction, which also contributed to transient acidification of the lumen and adjustment of ATP/NADPH ratio at the lower transient chloroplast $[CO_2]$.

The most novel insight derived from the simulations is the verification that NDH may operate as a PQH_2 oxidase under conditions of high pmf. These conditions may be achieved at very low chloroplast $[CO_2]$ (Figure 5.18) or at the beginning of photosynthetic induction (Figure 5.27). This reversal of NDH catalysis relies on the hypothesis that pmf affects the thermodynamics of NDH because of its proton pumping activity. Thus, when pmf is sufficiently high and the ratio of PQH_2 to oxidised Fd is relatively low, NDH will reduce Fd using electrons donated by PQH_2 and transporting H^+ out of the lumen. This type of electron flux may be called “pseudolinear” as it results in reduction of Fd, but does not utilise the energy absorbed by PSI. The model further suggests that in order to keep Fd sufficiently oxidised, a significant alternative electron flux is required. A simulation without NDH indicated that reversibility of NDH did not have a significant effect on CO_2 assimilation, but it reduced the redox state of Q_A during the first minutes of induction, thus behaving as a rapid “safety” valve to release excess of energy.

6.1.4 What are potential targets for improvement of photosynthesis under fluctuating irradiance?

One of the roles of photosynthesis research is to propose potential targets for improvement of plant biomass production. Models are a useful tool for identifying these targets (Zhu et al., 2007; von Caemmerer, 2013). Based on studies of steady-state models of photosynthesis, as well as experimental work, several targets for improvement of photosynthesis have been postulated, including the introduction of CO₂ concentrating mechanisms in C3 plants (von Caemmerer et al., 2012), increasing concentrations of SBPase (Zhu et al., 2007; Rosenthal et al., 2011) or Rubisco (Quick et al., 1992; Makino, 2003), bypassing photorespiration (Kebeish et al., 2007; von Caemmerer et al., 2012), increasing mesophyll conductance (Flexas et al., 2013), improving Rubisco kinetic properties (Whitney et al., 2001), or redistribution of chlorophyll within the canopy (Ort et al., 2011). However, given that different photosynthetic processes may also limit CO₂ assimilation under fluctuating irradiance, additional targets can be identified that could contribute to further improvements of biomass production under natural conditions. From the literature review, experiment and models presented in this dissertation, six targets were identified that could aid in achieving improvements of CO₂ assimilation under fluctuating irradiance, ambient [CO₂], moderate temperatures, and absence of (a)biotic stress. In the next sub-sections, I discuss these possible targets. Emphasis is put on trade-offs that could offset benefits, as well as any published experiment using these targets to enhance photosynthesis. The potential technical limitations of using a particular target (e.g., difficulties in genetic transformations) are not discussed.

Rubisco activase

The results of the experiment (Chapter 3) and simulations (Chapters 4 and 5) indicate that the rate at which Rubisco is activated after an increase in irradiance can limit dynamic CO₂ assimilation. This rate is determined by the amount of Rca and its regulation. Increasing the ratio of Rca to Rubisco would have a positive effect on dynamic CO₂ assimilation, both at the leaf and canopy level. Yamori et al. (2012) observed increases in dynamic CO₂ assimilation when Rca was overexpressed in *Oryza sativa*, especially at high temperatures, although they did not measure biomass production. However, wildtype levels of Rca already represent a significant fraction of the total nitrogen at the leaf level available to photosynthesis (Mott and Woodrow, 2000), so the effect of such a transformation on leaf nitrogen partitioning should be carefully assessed. For example, Fukayama et al. (2012) observed a decrease in nitrogen partitioning towards Rubisco in Rca overexpressors of *O. sativa*.

The *rwt43* transformant tested in Chapter 3 shows that increases in dynamic CO₂ assimilation can be achieved by keeping Rubisco highly active at low irradiance. However, Carmo-Silva and Salvucci (2013) measured biomass production of *rwt43* grown under constant and fluctuating irradiance and obtained lower values than in the wildtype. The exact reasons for the lower performance at the plant level is not known, although the lack of regulation of Rubisco activity would affect the homeostasis of the Calvin cycle at low irradiances (Zhang et al., 2002), with unknown consequences.

Kinetics of stomatal conductance

In addition to the limitation on CO₂ assimilation by low g_s , the rate at which the stomata open imposes an additional diffusional limitation on photosynthesis. Therefore, faster

kinetics would result in transiently higher rates of CO₂ assimilation after increases in irradiance. However, this will also result in higher leaf transpiration that could adversely affect plant performance under conditions of limited water supply. The analysis of the experimental results (Chapter 3) indicated that the extent to which stomatal opening limits CO₂ assimilation also depends on the value of g_s at the beginning of the transient. Therefore, in addition to faster opening, it would also be beneficial to slow down stomatal closing after exposure to high irradiance, although this would also increase transpiration.

Finally, since the initial values of g_s affect the dynamic diffusional limitation, increasing the minimum and maximum values of g_s is also a plausible strategy to achieve faster induction, which would have the added benefit of also increasing steady-state CO₂ assimilation. This was indeed the case with the *aba2-1* mutant discussed in Chapter 3. However, such manipulation would also come at the expense of significant water losses. Although no biomass production was reported in Chapter 3, experiments on ABA mutants of *Solanum lycopersicum* (tomato) have shown a decrease in growth rates relative to wildtype (Nagel et al., 1994), due to lower rates of leaf area expansion, which was caused by the low water potentials in the leaf tissue created by the high transpiration rates.

The simulations at the canopy level (Chapter 4) suggested that the kinetics of g_s had a small effect on canopy CO₂ assimilation, even though the limitations at the leaf level were significant. This appears to be related to the fact that, in the canopy, irradiance levels were close to saturation for most leaves. However, it is expected that with different parameter values, such that g_s saturates at higher irradiance, the results may differ, although confirmation of this hypothesis requires further research.

H⁺ /ATP stoichiometry of ATP synthase

Current estimations of the amount of H⁺ transported per rotation of the F₀ subunit of the ATPase (HPR) indicate that the most likely values are either 12 or 14 (i.e., 4 and 4.67 H⁺ per ATP, respectively). The former value is obtained from biochemical assays, whereas the latter is derived from the structure of ATPase in *Spinacia oleracea* using different techniques (see Section 5.2.5 for details). Estimations from biochemical assays may be affected by some methodological artefact and discrepancies between these two methods have also been reported for the mitochondrial ATPase of other organisms (Steigmiller et al., 2008; Petersen et al., 2012). For this reason, I chose to perform the simulations in Chapter 5 with an HPR of 14. However, given the impact this ratio could have on alternative electron transport, a subset of the simulations was repeated assuming an HPR of 12.

The results of using an HPR of 12 was, as expected from previous studies (Yin et al., 2006; Walker et al., 2014), a decrease in the fraction of alternative electron transport, yielding a negligible cyclic electron flux around PSI and a low fraction of electrons allocated to alternative electron sinks. However, the model also predicted an increase in the flux of electrons consumed by the Calvin cycle. This indicates that alternative electron sinks were competing with CO₂ assimilation at an HPR of 14. Furthermore, because of the changes in the relationship between ATP production and pmf, the pH of the lumen was lower (leading to higher NPQ) when using a lower HPR, even if the alternative electron fluxes had been reduced significantly. This increase in the pmf when HPR is reduced has been confirmed experimentally by Pogoryelov et al. (2012), who modified the value of HPR for mitochondrial ATP synthase of *Escherichia coli*.

Targeting HPR has been proposed before (Kramer and Evans, 2011), although, to my knowledge, this is the first study that analyses in detail the potential benefits of reducing HPR. Evolutionary, an HPR of 14 seems sub-optimal, but it is important to remember that the energy consumed by alternative electron sinks is not necessarily wasted. Nitrogen assimilation in chloroplast is a physiological process fundamental to plant growth (although this will vary with species and the source of nitrogen in the soil), and export of redox power via the malate shuttle may support the metabolism in the cell that is derived from photosynthesis (e.g., synthesis of sucrose and aminoacids). Indeed, the metabolism of the chloroplasts and that of the mitochondria appear to be highly interrelated (Foyer et al., 2011).

Energy-dependent non-photochemical quenching (qE)

Non-photochemical quenching of excess energy absorbed by the antenna complexes of PSII is considered one of the most important forms of protection against photoinhibition (Avenson et al., 2004). Reducing qE can reduce CO₂ assimilation, through increases in photoinhibition (Li et al., 2002; Hubbart et al., 2012), and this reduces biomass production under fluctuating irradiance (Külheim et al., 2002; Krah and Logan, 2010). Increasing qE in *O. sativa* resulted in a decrease of CO₂ assimilation under fluctuating irradiance (Hubbart et al., 2012), although *A. thaliana* plants with higher levels of qE grown in greenhouses achieved higher biomass compared to the wildtype (Logan et al., 2008). The simulations with the model can shed light on this apparent contradiction: whereas qE can have a positive effect on CO₂ assimilation due to its photoprotective effect, it may also limit CO₂ assimilation when in excess, especially after a decrease in irradiance. Therefore, the effects of manipulating qE levels depend on the specific conditions under which the plants are grown, and whether measurements are performed at the leaf or the canopy level.

On the other hand, increasing the speed at which qE relaxes after a decrease in irradiance would minimize the negative effects on CO₂ assimilation, while maintaining the photoprotective effect. This effect was demonstrated by Kromdijk et al. (2016) by accelerating the relaxation of qE which resulted in an increase of biomass production in *Nicotiana tabacum*. The need to test whole plant performance under fluctuating irradiance is important: a rapid relaxation would result in a lower value of qE at the end of a cloudfleck or at the beginning of a sunfleck. Therefore, rapid relaxation without also rapid activation could result in transiently lower photoprotection at high irradiance. In addition to changing the kinetics of lumen pH, several mechanisms may exist for changing the kinetics of the xanthophyll cycle, including changes in the pool of xanthophylls, reductions in the activity of violaxanthin de-epoxidase (VDE), or increases in the activity of zeaxanthin epoxidase (EPO). However, the total amount of xanthophylls also affects the levels of qE (Demmig-Adams and William III, 1996), whereas the ratio of activities of VDE relative to EPO affects the apparent pH sensitivity of qE (Takizawa et al., 2007). Therefore, an optimal qE system may require multiple genetic transformations that affect different aspects of the system.

Chloroplast movements

In those species and/or growth conditions in which chloroplast movements are significant (Davis et al., 2011), these movements modify the amount of irradiance that reach the photosynthetic pigments, by creating a “sieve” effect that minimizes the area of

chloroplast exposed to irradiance. This would reduce the excess of energy reaching the reaction centres, reducing the rates of photoinhibition (Kasahara et al., 2002; Davis and Hangarter, 2012). However, based on the simulations from Chapter 4, the slow rate at which the chloroplasts return to their low-irradiance position limits CO₂ assimilation significantly. As with qE, removing chloroplast movements may incur in a net negative balance because of the enhanced rates of photoinhibition. Although the simulations at the canopy level resulted in an increase of canopy CO₂ assimilation, it is not likely that plants growing under field conditions with full exposure to the sun would display such high rates of chloroplast movement (Davis et al., 2011; Higa and Wada, 2016). On the other hand, this target could be relevant for the commercial growth of shade-adapted, ornamental plants (Li et al., 2014). In addition, it is clear that accelerating the movements of chloroplasts would have an overall positive effect, as it would still protect from photoinhibition, while minimizing transient limitations to CO₂ assimilation. However, little is yet known about the mechanisms of chloroplast movement (Banas et al., 2012), including the energy required for the movement, which could limit how fast these movements could be.

Photoinhibition

In addition to enhancing photoprotective mechanisms, a reduction of photoinhibition could also be achieved by increasing the rate of PSII repair, in particular the protein D1 of the reaction centre, upon which most research has focused. The process of PSII repair consists of several steps: (i) degradation of damaged protein D1, (ii) synthesis *de novo* of protein D1, and (iii) assembly of new PSII units (Aro et al., 1993). Several proteases participate in the degradation of protein D1, including two main families: Deg and FtsH proteases (Allahverdiyeva and Aro, 2012). Failure to slow down PSII repair in *A. thaliana* by knocking out a specific Deg protease has been interpreted as the coexistence of multiple pathways for protein D1 degradation (Huesgen et al., 2006), which would make identifying specific targets difficult. Another strategy would be to improve the protein translation machinery within the chloroplasts, which are sensitive to the oxidative stress associated with photoinhibition (Takahashi and Murata, 2008). The advantage of reducing photoinhibition by accelerating the repair is that it does not incur the trade-offs inherent to photoprotection discussed above.

6.2 Methodological limitations and future research

6.2.1 Need for a comprehensive quantification of photosynthesis

The parameterization of the models in Chapters 4 and 5 revealed that, despite the existence of model plants such as *A. thaliana*, a complete quantitative characterization of photosynthesis in a particular species grown under specific conditions does not exist. Although it is possible to combine information from different sources to parameterize a model, the results do not necessarily represent a real system and conclusions from simulations could be misleading. Whereas the behaviour of steady-state photosynthesis across different C3 plants may be similar, there are important differences that may affect dynamic photosynthesis. This includes differences in the importance of chloroplast movement (Davis et al., 2011), regulation of Rca (Carmo-Silva and Salvucci, 2013), or regulation of sucrose phosphate synthase (Huber et al., 1989).

Steps towards more comprehensive datasets on photosynthesis may be facilitated by the integration of different measurement techniques into a single instrument. Whereas the

combination of gas exchange and modulated chlorophyll fluorescence is commonplace among commercial photosynthesis measurements systems, additional information can be obtained from measurements of absorbance changes at specific wavelength. For example, measurements of the epoxidation state of xanthophylls (Gamon et al., 1992), redox states of P₇₀₀ (Harbinson and Hedley, 1989b), cyt f (Sacksteder and Kramer, 2000), Pc and Fd (Klughhammer and Schreiber, 2016), as well as the electrochromic shift in the absorbance spectra of carotenoids, which is proportional to the electrical field across the thylakoid membrane and has been used to study the regulation of pmf and ATPase (Cruz et al., 2001; Kanazawa and Kramer, 2002).

In Chapter 3, mutants and transformants were used to study the effects of specific processes on photosynthesis under fluctuating conditions. In the last two decades, genetic approaches have been extensively used in the study of the Calvin cycle and photorespiration (Raines, 2003; Stitt et al., 2010; Carmo-Silva et al., 2015), and the regulation of the electron transport chain (Horton, 2014; Pottosin and Shabala, 2016). This has, to a large extent, substituted the earlier work on the biochemistry and biophysics of photosynthesis. Although phenotyping of mutants is useful to construct a qualitative description of the system, this approach does not produce good quantitative analysis of photosynthesis. For example, it might appear that the difference in NPQ values between a wildtype and a PsbS mutant would provide a quantification of the contribution of PsbS to NPQ. However, other processes that contribute to NPQ are upregulated in the absence of PsbS (Nilkens et al., 2010; Dall'Osto et al., 2014), so the difference between the wildtype and the mutant would underestimate the true contribution of PsbS. This is not restricted to the study of NPQ: pleiotropic effects of mutations and genetic transformations may in general introduce artefacts in quantitative analyses that rely on comparing wildtypes to mutants.

The use of models in combination with measurements may provide better quantification of certain processes (e.g., see the quantification of NPQ components in Chapter 4), but such an analysis is always biased by the assumptions underlying the model. An example of such a bias is the quantification of Rubisco kinetic properties from gas exchange measurements, which relies on the assumption that Rubisco limits CO₂ assimilation under specific conditions, both in the steady-state (Sharkey et al., 2007), and during transients (Chapter 3). Even though these methodologies may be widely accepted by the community, their usage does not provide any evidence in favour of the implicit assumptions, and conclusions may suffer from circular logic.

Measurements of gas exchange, fluorescence and spectroscopy, combined with comparisons of mutants and transformants may not suffice to understand photosynthesis, as much information on the underlying processes would still not be accessible. For example, proper modelling of the kinetics of the Calvin cycle requires a complete profile of enzyme kinetics *in vivo*. Currently, most information on enzymes has been obtained from *in vitro* assays that were not performed under physiologically relevant conditions and thus may fail to describe the behaviour of the Calvin cycle *in vivo* (Harris and Königer, 1997). The use of new technology and automation of assays may facilitate measuring the properties of these enzymes under more relevant conditions (Stitt and Gibon, 2014). In addition, it would also be required to quantify the concentration of metabolites in the different subcellular compartments. Developments in metabolomics, combined with isotope labelling, may provide new opportunities to

measure metabolite concentrations and fluxes through the different pathways (Heise et al., 2014).

In the short term, progress may also be achieved by compiling published data into a database that would help identify knowledge gaps, facilitate modelling activities and comparisons across species and growth conditions. Chapters 4 and 5 contribute to this effort, by collecting values for more than 250 parameters. Given the wide scope that such a database would have, models like the one in Chapter 5 (and future extensions) would be helpful in its design, as it would aid in defining an ontology that standardizes the relevant terminology in photosynthesis. Given the multidisciplinary nature of photosynthesis research, such an ontology would not only be useful for the design of a comprehensive database, but would also facilitate communication across different areas of research. Examples in other communities include the use of ontologies in ecology (Madin et al., 2008) or systems biology (Malone et al., 2016). Some databases contain some information about photosynthesis, such as the leaf traits database TRY (Kattge et al., 2011), but they only include a limited number of parameters from the FvCB model.

6.2.2 Space in photosynthesis: are compartmental models good enough?

The models presented in Chapters 4 and 5 consist of systems of ordinary differential equations. Space is represented as well-mixed compartments. Compartments may not always be volumetric, and the thylakoid membrane in Chapter 5 represents a surface. Some of the potential issues associated with the lack of an explicit representation of space are discussed below, as well as the approaches that have been used in previous models of photosynthesis to represent space.

An important simplification is the assumption that a whole leaf may be represented as a single photosynthetic cell embedded in a homogeneous intercellular space. A recently reaction–diffusion model of CO₂ that takes into account the 3D structure of the leaf tissue, indicated that [CO₂] is uniform within the intercellular spaces (Ho et al., 2016). However, the results from the experiment by Parkhurst and Mott (1990), suggested a lack of uniform [CO₂] in the intercellular spaces, and this was confirmed by a 2D model of CO₂ diffusion (Ho et al., 2012). It is possible that the use of 2D models would enhance gradients in [CO₂] by isolating intercellular spaces, or perhaps the different leaf anatomies explained the discrepancy across studies. For example, [CO₂] gradients would be higher in hypostomatous leaves and/or heterobaric leaves (Evans and von Caemmerer, 1996). Further research is required to quantify how heterogeneous the intercellular [CO₂] for different leaf anatomies is.

Farquhar (1989) demonstrated that, if Rubisco content and maximum rate of electron transport (i.e., photosynthetic capacity) varied within the leaf in proportion to the distribution of irradiance, CO₂ assimilation would scale directly from the chloroplast to the leaf. The models in Chapters 4 and 5 make use of this result to justify the use of a single chloroplast compartment. There are two possible reasons why this result may not hold in general. Firstly, this result was obtained with the equations described by Farquhar et al. (1980), which did not include mesophyll conductance, regulation of the electron transport chain, chloroplast movements, or the different efficiencies of blue, green and red irradiance in driving photosynthesis. When these processes are taken into account, the equations may no longer scale between the chloroplast and the leaf levels. Secondly, the distribution of irradiance within the leaf depends on: (i) the angle of incidence

(Vogelmann and Martin, 1993), (ii) chloroplast movements (Davis and Hangarter, 2012), (iii) relative illumination on either side of the leaf (Buckley and Farquhar, 2004), and (iv) the wavelength (Terashima et al., 2009). This means that the distribution of irradiance within a leaf could change faster than the distribution of photosynthetic capacity. However, no detailed analysis exists of how the profile of irradiance within a leaf changes during the course of a day and hence it is not possible to quantify the importance of this phenomenon.

Progress has been made in adjusting the FvCB model to take into account the distribution of irradiance from the abaxial and adaxial sides (Buckley and Farquhar, 2004), but taking into account all the factors mentioned in the above would require the use of a multilayer model of leaf photosynthesis (Terashima and Saeki, 1985; Evans, 2009), or a ray-tracing algorithm coupled with a 3D representation of the leaf (Ustin et al., 2001; Ho et al., 2016). Adapting the models in Chapters 4 or 5 to a multilayer representation of the leaf would represent a major improvement. However, this would introduce the difficulty of having to determine the spatial distributions of all the parameters in the model. It is also possible to convert these models into systems of partial differential equations coupled with simulations of irradiance based on ray tracers, though this would require accurate descriptions of the leaf anatomy (Ho et al., 2016).

The models in Chapters 4 and 5 use a resistance approach to simulate CO₂ diffusion from the intercellular spaces to the chloroplast. Although this approach has been used successfully in the past, and can capture the effect of leaf anatomy (Berghuijs et al., 2015), models of this type rely on several assumptions that may limit their usefulness (Berghuijs et al., 2016). The use of a 2D or 3D reaction–diffusion model would help in further understanding the effect of chloroplast movements on CO₂ diffusion (Ho et al., 2016), reassimilation of (photo)respired CO₂ (Berghuijs et al., 2016), and the role of biochemical reactions that affect CO₂ diffusion, such as carbonic anhydrase and intracellular distribution of HCO₃⁻ (Tholen and Zhu, 2011).

Spatial effects may also be of relevance for the photosynthetic electron transport chain, especially as the diffusion of plastoquinone/ol (PQ/PQH₂) and plastocyanin (Pc) may affect the kinetics of the system (Tikhonov and Vershubskii, 2014). Diffusion of PQ and PQH₂ occurs within the thylakoid membrane, which is mostly occupied by protein complexes that affect molecular diffusion (Kirchhoff et al., 2002). It has been proposed that the structure of the thylakoid membrane produces microdomains containing a small number of PSII and cyt b₆f complexes within ca. 20 nm of each other (Tremmel et al., 2003), such that diffusion of PQ and PQH₂ is no longer rate-limiting within a microdomain (Lavergne et al., 1992; Kirchhoff et al., 2000). However, a direct validation of microdomains does not exist (Kirchhoff, 2014). Microdomains are expected to give PSII a higher control on the linear electron flux than a model where all PSII equilibrate with all cyt b₆f via a common pool of PQ/PQH₂ (Kirchhoff, 2014). The diffusion of PQ/PQH₂ can be simulated using percolation theory, which takes into account the effect of obstacles on the apparent diffusion coefficient (Tremmel et al., 2003; Tikhonov and Vershubskii, 2014).

The diffusion of Pc through the lumen may also become limiting, especially due to the small width of the lumen, at least in dark-adapted thylakoids (Kirchhoff, 2014). However, changes in the osmotic potential of the lumen due to ion transport (induced in the light) may result in a doubling of its width (Kirchhoff et al., 2011), which would facilitate faster

Pc diffusion. I hypothesize that changes of the lumen width with irradiance may be an additional form of regulation of the electron transport chain.

In summary, spatial effects may affect the dynamics and regulation of photosynthesis at different scales and are related to the anatomy of the leaf and the structure of the thylakoid membrane. In all cases, the models in Chapters 4 and 5 could be extended into a system of partial differential equations that would be applied on a 1D, 2D, or 3D mesh (i.e., a reaction-diffusion model). The main limitations to constructing such extensions would be: (i) knowledge on the anatomy/structure at a particular scale, and (ii) measurements of the diffusion coefficients of the relevant substances. The simulation itself would still be performed with an ODE solver, after discretization of the spatial component with a suitable numerical method, but the number of differential equations required to solve the problem would increase by several orders of magnitude. Hence, such a conversion would result in a significant increase of the computational time required for simulations.

6.3 Potential applications of the models

6.3.1 Parameterization of photosynthesis

The FvCB model (cited 3681 times, according to the database Scopus, consulted on 1st November 2016) and posterior extensions have been used for numerous thought experiments on photosynthesis (von Caemmerer, 2013), and have become the workhorse for state-of-the-art models of canopy photosynthesis (Duursma and Medlyn, 2012; Kobayashi et al., 2012) and plant growth (Yin and van Laar, 2005; Evers et al., 2010; Morales et al., 2016). However, Sharkey (2016) has argued that the success of the FvCB model cannot be explained without considering the fact that this model is most often used to interpret gas exchange measurements. Even though not all parameters of the FvCB model are routinely estimated from gas exchange parameters (Sharkey et al., 2007), it has become a powerful tool in photosynthesis research due to its ability to transform the complex behaviour of a leaf into a small number of parameters.

For example, the FvCB model has been used to study genetic variation in photosynthesis (Gu et al., 2012a; Driever et al., 2014) and some parameters of the FvCB model have become part of the ecological concept of leaf traits (Kattge et al., 2011). The benefit of using parameters, instead of measurements of CO₂ assimilation, is that the model corrects for the effect of the environment and allows extrapolation to other environments.

These attributes of the FvCB model were taken into account when designing the model in Chapter 4. Firstly, that model is an extension of the FvCB model, such that all the parameters available for the FvCB model may be used in the new model. Secondly, when designing the model, emphasis was placed on the ability to represent the phenomenology at the leaf level, as opposed to represent explicitly the underlying molecular mechanisms. Therefore, expressions are as simple as possible, and nearly all parameters can be determined from established experimental methods, as demonstrated in Sections 4.2 and 4.3.

The model proposed by Pearcy et al. (1997) has been used as a means to parameterize dynamic CO₂ assimilation in some occasions (Naumburg et al., 2001a; Montgomery and Givnish, 2008), which sets a good precedence for the model in Chapter 4. However, in many occasions, simpler models have been built to analyse specific effects, such as the

kinetics of stomatal conductance (Noe and Giersch, 2004; Vialet-Chabrand et al., 2016), Rubisco activation (Mott and Woodrow, 2000), or the effect of NPQ (Zhu et al., 2004). Although these models require fewer parameters to be estimated than the model in Chapter 4, the conclusions of analyses performed with such models can be misleading as they miss important processes that affect dynamic CO₂ assimilation. For example, if Rubisco activation is ignored (Noe and Giersch, 2004; Vialet-Chabrand et al., 2016), the role of stomatal conductance in limiting CO₂ assimilation would be overestimated. The fact that a model may adequately fit measurements is not enough reason to justify it, as this would reduce the model to a statistical tool, losing the ability to extrapolate to other environments (and correct for environmental effects), and parameters may lose their physiological meaning.

The phenotyping of dynamic photosynthesis as required by the model remains however a challenge. Although many parameters can be estimated with gas exchange systems if the correct protocols are used (see Section 4.3), these measurements can be more time-consuming than steady-state response curves. On the other hand, the protocols followed in Chapter 3 may be sub-optimal. The design of experiments can be improved with the use of dynamic models (Franceschini and Macchietto, 2008), though this requires making *a priori* assumptions about the most likely values of the different parameters.

A final challenge is the technical difficulty inherent to estimating parameters of a system of differential equations. Simulations of the model in Chapter 4 can only be achieved with numerical methods, and estimation of the parameters requires either the use of non-linear optimization algorithms (the choice made in Chapter 4) or a Markov Chain Monte Carlo algorithm (if a Bayesian approach is preferred). In both cases, the ODE solver needs to produce highly accurate numerical solutions in the minimum amount of time possible (Gábor and Banga, 2015). This can be achieved with the use of high performance programming languages and adaptive, implicit ODE solvers. The fact that parameters of the FvCB model are often estimated with a spreadsheet (Bellasio et al., 2016), illustrates the large difference in technical skills required to work with dynamic instead of steady-state models of CO₂ assimilation.

6.3.2 Exploring hypotheses *in silico*

Whereas the model in Chapter 4 was designed with the aim of describing the phenomenology of dynamic CO₂ assimilation at the leaf level, the model in Chapter 5 zooms in and provides a framework to analyse the regulation of the photosynthetic electron transport chain. This model was designed to represent an “average” C3 species, though *A. thaliana* was always used as a reference. As opposed to narrowing the application of the model to one particular research question, the model was built to take into account as many processes as possible. This has practical consequences for the parameterization of the model: despite only including the effects of irradiance and some of the effects of [CO₂] (i.e., no temperature or humidity effects), the model in Chapter 5 had twice the number of parameters than the model in Chapter 4 (i.e., 205 vs. 100), and many of them could not be determined by techniques commonly available (see Section 4.2 for details). Therefore, this model is not very useful for the kind of applications discussed in the previous section, but that does not mean that it is useless.

Its holistic approach and higher degree of realism makes it an attractive tool to explore *in silico* hypotheses concerning the regulation of electron transport. The practical limitations to experimentation and the lack of system-wide, quantitative

characterizations of photosynthesis (see Section 6.2.1 for details) make it difficult to test hypotheses regarding the behaviour of the electron transport chain as a system. Rather, experiments tend to focus on specific components, such as, for example, the effect of PsbS (Niyogi et al., 2005), stromal phosphate content (Takizawa et al., 2008), or the transport of Cl^- across the thylakoid membrane (Herdean et al., 2016). However, as the behaviour of a system is not the sum of its parts, this knowledge does not add up to a complete understanding of the regulation of the electron transport chain. Models like the one presented in Chapter 5 can be useful in this context. Such models allow to filter hypotheses that are physically impossible (e.g., due to conservation of energy and matter), define theoretical limits to the system's properties that would result in a particular behaviour (e.g., what range of enzyme activities would result in a high control coefficient), generate testable hypotheses that can provide indirect evidence on (practically) unmeasurable quantities (e.g., estimations of the pH of the lumen *in vivo*), and, most importantly, identify knowledge gaps that guide further research.

For example, the model in Chapter 5 may be used to test hypotheses on the role of alternative electron sinks in the regulation of the electron transport chain. The simulations presented in this dissertation were performed for a particular set of kinetic parameters describing these sinks, but further exploration could be used to address the large uncertainties regarding these values. For example, how would the system behave in plants fertilized with NH_4^+ instead of NO_3^- as nitrogen source? Given that all pathways for alternative electron transport were below their potential (see Section 6.1.3), it appears that the system should be capable of adjusting to this situation. However, other variables in the system are expected to change due to necessary changes on the redox state of ferredoxin, which could then propagate to the rest of the system. Such complex interactions cannot be captured with a simple stoichiometric analysis and thus require the use of a sufficiently complex simulation model.

In addition to “what-if” scenarios and sensitivity analyses, the model may also be extended to study additional processes. For example, the effect that changes in the volume of the lumen (Kirchhoff et al., 2011) could have on the regulation of electron transport chain could be tested by simply adding an equation describing the temporal dynamics of the variable V_L in Equation 5.59. Or, the detailed description of the PSII reaction centre means that, by adding one (or more) reactions the model could simulate acceptor-side photoinhibition (Aro et al., 1993), and explore the effects of the electrical field across the thylakoid membrane on photoinhibition of PSII (Davis et al., 2016). Other possible extensions would include more mechanistic treatments of the buffering of H^+ in the lumen (van Kooten et al., 1986), the transport of ions across the thylakoid membrane by different channels (Pottosin and Shabala, 2016), or state transitions regulated by the redox state of the PQ/PQH₂ pool and thioredoxin (Rintamäki et al., 2000). Regarding the stromal metabolism, many processes could be added, including the Calvin cycle, photorespiration and sucrose synthesis (Zhu et al., 2007; Laisk et al., 2009a). The model in Chapter 5 could also be combined with models of the metabolism in C₄ species (Wang et al., 2014), where cyclic electron transport plays an important role (Yin and Struik, 2012; Nakamura et al., 2013).

In order for such extensions to be materialised, the model needs to be shared and extended efficiently. The detailed description of the model (Section 5.2) is offered with this purpose but it may not be sufficient. Future developments in integration and sharing of models via a community platform (Zhu et al., 2016) may facilitate these tasks. Modelling

languages tailored to the description of biological systems (Hucka et al., 2003; Lloyd et al., 2004) could reduce the effort required to extend the model and its documentation. These modelling languages allow the user to focus on the description of the problem, while the code needed for the numerical algorithms is generated automatically, preferably in high performance programming language. Due to the complexity of the model in Chapter 5, I created an ad-hoc modelling language that generates the code required for simulations from high-level descriptions of the biological system. In addition, libraries to manage simulations are provided. With these tools, technical limitations to future adoption and extension of the model may be lessened.

References

- Albertsson P-A, Andreasson E, Svensson P, Yu S-G (1991) Localization of cytochrome f in the thylakoid membrane - evidence for multiple domains. *Biochimica et Biophysica Acta - Bioenergetics* 1098 (1):90-94. doi:10.1016/0005-2728(91)90012-D
- Alexandratos N, Bruinsma J (2012) World agriculture towards 2030/2050: the 2012 revision. ESA Working Paper. Food and Agriculture Organization of the United Nations, Rome, Italy
- Allahverdiyeva Y, Aro E-M (2012) Photosynthetic responses of plants to excess light: Mechanisms and conditions for photoinhibition, excess energy dissipation and repair. In: Eaton-Rye JJ, Tripathy BC, Sharkey TD (eds) *Photosynthesis: Plastid Biology, Energy Conversion and Carbon Assimilation*. Springer Netherlands, Dordrecht, pp 275-297. doi:10.1007/978-94-007-1579-0_13
- Allen MT, Pearcy RW (2000a) Stomatal versus biochemical limitations to dynamic photosynthetic performance in four tropical rainforest shrub species. *Oecologia* 122 (4):479-486. doi:10.1007/s004420050969
- Allen TM, Pearcy WR (2000b) Stomatal behavior and photosynthetic performance under dynamic light regimes in a seasonally dry tropical rain forest. *Oecologia* 122 (4):470-478. doi:10.1007/s004420050968
- Alonso JM, Stepanova AN, Leisse TJ, Kim CJ, Chen H, Shinn P, Stevenson DK, Zimmerman J *et al.* (2003) Genome-wide insertional mutagenesis of *Arabidopsis thaliana*. *Science* 301 (5633):653-657. doi:10.1126/science.1086391
- Andralojc Paul J, Madgwick Pippa J, Tao Y, Keys A, Ward Jane L, Beale Michael H, Loveland Jane E, Jackson Phil J *et al.* (2012) 2-Carboxy-D-arabinitol 1-phosphate (CA1P) phosphatase: evidence for a wider role in plant Rubisco regulation. *Biochemical Journal* 442:733-742. doi:10.1042/BJ20111443
- Arena C, Vitale L, Virzo De Santo A (2005) Photosynthetic response of *Quercus ilex* L. plants grown on compost and exposed to increasing photon flux densities and elevated CO₂. *Photosynthetica* 43 (4):615-619. doi:10.1007/s11099-005-0096-9
- Armbruster U, Carrillo LR, Venema K, Pavlovic L, Schmidtman E, Kornfeld A, Jahns P, Berry JA *et al.* (2014) Ion antiport accelerates photosynthetic acclimation in fluctuating light environments. *Nature Communications* 5:5439. doi:10.1038/ncomms6439
- Aro EM, Virgin I, Andersson B (1993) Photoinhibition of Photosystem II. Inactivation, protein damage and turnover. *Biochimica et Biophysica Acta - Bioenergetics* 1143 (2):113-134. doi:10.1016/0005-2728(93)90134-2
- Asada K (1999) The water-water cycle in chloroplasts: Scavenging of active oxygens and dissipation of excess photons. *Annual Review of Plant Physiology and Plant Molecular Biology* 50:601-639. doi:10.1146/annurev.arplant.50.1.601
- Asada K (2000) The water-water cycle as alternative photon and electron sinks. *Philosophical Transactions of the Royal Society B: Biological Sciences* 355 (1402):1419-1431. doi:10.1098/rstb.2000.0703
- Avenson TJ, Cruz JA, Kanazawa A, Kramer DM, Ryan CA (2005) Regulating the proton budget of higher plant photosynthesis. *Proceedings of the National Academy of Sciences* 102 (27):9709-9713. doi:10.1073/pnas.0503952102
- Avenson TJ, Cruz JA, Kramer DM, Croteau RB (2004) Modulation of energy-dependent quenching of excitons in antennae of higher plants. *Proceedings of the National Academy of Sciences* 101 (15):5530-5535. doi:10.1073/pnas.0401269101

References

- Avron M, Gibbs M (1974) Properties of phosphoribulokinase of whole chloroplasts. *Plant Physiology* 53 (2):136-139. doi:10.1104/pp.53.2.136
- Azcón-Bieto J, Lambers H, Day DA (1983) Effect of photosynthesis and carbohydrate status on respiratory rates and the involvement of the alternative pathway in leaf respiration. *Plant Physiology* 72 (3):598-603. doi:10.1104/pp.72.3.598
- Bailey S, Walters RG, Jansson S, Horton P (2001) Acclimation of *Arabidopsis thaliana* to the light environment: the existence of separate low light and high light responses. *Planta* 213 (5):794-801. doi:10.1007/s004250100556
- Baldocchi DD, Wilson KB, Gu L (2002) How the environment, canopy structure and canopy physiological functioning influence carbon, water and energy fluxes of a temperate broad-leaved deciduous forest - an assessment with the biophysical model CANOAK. *Tree physiology* 22:1065-1077. doi:10.1093/treephys/22.15-16.1065
- Ball JT, Woodrow IE, Berry JA (1987) A model predicting stomatal conductance and its contribution to the control of photosynthesis under different environmental conditions. *Progress in Photosynthesis Research* 4:221-224. doi:10.1007/978-94-017-0519-6_48
- Balmford A, Green RE, Scharlemann JPW (2005) Sparing land for nature: exploring the potential impact of changes in agricultural yield on the area needed for crop production. *Global Change Biology* 11 (10):1594-1605. doi:10.1111/j.1365-2486.2005.001035.x
- Banas AK, Aggarwal C, Labuz J, Sztatelman O, Gabrys H (2012) Blue light signalling in chloroplast movements. *Journal of Experimental Botany* 63:1559-1574. doi:10.1093/jxb/err429
- Bates GW, Rosenthal DM, Sun J, Chattopadhyay M, Peffer E, Yang J, Ort DR, Jones AM (2012) A comparative study of the *Arabidopsis thaliana* guard-cell transcriptome and its modulation by sucrose. *PLOS ONE* 7 (11):e49641. doi:10.1371/journal.pone.0049641
- Batie CJ, Kamin H (1984) Electron transfer by ferredoxin:NADP⁺ reductase. Rapid-reaction evidence for participation of a ternary complex. *Journal of Biological Chemistry* 259 (19):11976-11985
- Baumann DT, Bastiaans L, Goudriaan J, van Laar HH, Kropff MJ (2002) Analysing crop yield and plant quality in an intercropping system using an eco-physiological model for interplant competition. *Agricultural Systems* 73 (2):173-203. doi:10.1016/S0308-521X(01)00084-1
- Belgio E, Johnson Matthew P, Jurić S, Ruban Alexander V (2012) Higher plant Photosystem II light-harvesting antenna, not the reaction center, determines the excited-state lifetime - both the maximum and the nonphotochemically quenched. *Biophysical Journal* 102 (12):2761-2771. doi:10.1016/j.bpj.2012.05.004
- Bellasio C, Beerling DJ, Griffiths H (2016) An Excel tool for deriving key photosynthetic parameters from combined gas exchange and chlorophyll fluorescence: theory and practice. *Plant, Cell and Environment* 39 (6):1180-1197. doi:10.1111/pce.12560
- Belyaeva NE, Schmitt FJ, Steffen R, Paschenko VZ, Riznichenko GY, Chemeris YK, Renger G, Rubin AB (2008) PS II model-based simulations of single turnover flash-induced transients of fluorescence yield monitored within the time domain of 100 ns-10 s on dark-adapted *Chlorella pyrenoidosa* cells. *Photosynthesis Research* 98 (1):105-119. doi:10.1007/s11120-008-9374-2

- Berghuijs HNC, Yin X, Ho QT, Driever SM, Retta MA, Nicolai BM, Struik PC (2016) Mesophyll conductance and reaction-diffusion models for CO₂ transport in C₃ leaves; needs, opportunities and challenges. *Plant Science* 252:62-75. doi:10.1016/j.plantsci.2016.05.016
- Berghuijs HNC, Yin X, Tri Ho Q, van der Putten PEL, Verboven P, Retta MA, Nicolai BM, Struik PC (2015) Modelling the relationship between CO₂ assimilation and leaf anatomical properties in tomato leaves. *Plant Science* 238:297-311. doi:10.1016/j.plantsci.2015.06.022
- Bernacchi CJ, Bagley JE, Serbin SP, Ruiz-Vera UM, Rosenthal DM, Vanloocke A (2013) Modelling C₃ photosynthesis from the chloroplast to the ecosystem. *Plant, Cell and Environment* 36 (9):1641-1657. doi:10.1111/pce.12118
- Bernacchi CJ, Pimentel C, Long SP (2003) In vivo temperature response functions of parameters required to model RuBP-limited photosynthesis. *Plant, Cell and Environment* 26:1419-1430. doi:10.1046/j.0016-8025.2003.01050.x
- Berry S, Rumberg B (1996) H⁺/ATP coupling ratio at the unmodulated CF₀CF₁-ATP synthase determined by proton flux measurements. *Biochimica et Biophysica Acta - Bioenergetics* 1276 (1):51-56. doi:10.1016/0005-2728(96)00031-X
- Berry S, Rumberg B (2001) Kinetic modeling of the photosynthetic electron transport chain. *Bioelectrochemistry* 53:35-53. doi:10.1016/S0302-4598(00)00108-2
- Bilger W, Bj, xf, rkman O (1991) Temperature dependence of violaxanthin de-epoxidation and non-photochemical fluorescence quenching in intact leaves of *Gossypium hirsutum* L. and *Malva parviflora* L. *Planta* 184 (2):226-234. doi:10.1007/BF01102422
- Bird RE, Riordan C (1986) Simple solar spectral model for direct and diffuse irradiance on horizontal and tilted planes at the Earth's surface for cloudless atmospheres. *Journal of Climate and Applied Meteorology* 25 (1):87-97. doi:10.1175/1520-0450(1986)025<0087:SSSMFD>2.0.CO;2
- Blackman FF (1905) Optima and limiting factors. *Annals of Botany* 19 (2):281-296
- Bloom AJ, Richard MC, John F, Warner RL, Joseph W (1989) Oxygen and carbon dioxide fluxes from barley shoots depend on nitrate assimilation. *Plant Physiology* 91 (1):352-356. doi:10.1104/pp.91.1.352
- Bloom AJ, Smart DR, Nguyen DT, Searles PS (2002) Nitrogen assimilation and growth of wheat under elevated carbon dioxide. *Proceedings of the National Academy of Sciences* 99 (3):1730-1735. doi:10.1073/pnas.022627299
- Bohme H (1978) Quantitative determination of ferredoxin, ferredoxin-NADP⁺ reductase and plastocyanin in spinach chloroplasts. *European Journal of Biochemistry* 141:137-141
- Böhme H (1977) On the role of ferredoxin and ferredoxin-NADP⁺ reductase in cyclic electron transport of spinach chloroplasts. *European Journal of Biochemistry* 72:283-289. doi:10.1111/j.1432-1033.1977.tb11251.x
- Bonan GB (2008) Forests and climate change: forcings, feedbacks, and the climate benefits of forests. *Science* 320 (5882):1444-1449. doi:10.1126/science.1155121
- Booth BBB, Jones CD, Collins M, Totterdell IJ, Cox PM, Sitch S, Huntingford C, Betts Ra *et al.* (2012) High sensitivity of future global warming to land carbon cycle processes. *Environmental Research Letters* 7:024002. doi:10.1088/1748-9326/7/2/024002
- Boyer PD (1993) The binding change mechanism for ATP synthase - Some probabilities and possibilities. *Biochimica et Biophysica Acta - Bioenergetics* 1140 (3):215-250. doi:10.1016/0005-2728(93)90063-L

References

- Bratt CE, Arvidsson P-O, Carlsson M, Åkerlund H-E (1995) Regulation of violaxanthin de-epoxidase activity by pH and ascorbate concentration. *Photosynthesis Research* 45 (2):169-175. doi:10.1007/bf00032588
- Breitholtz HL, Srivastava R, Tyystjärvi E, Rintamäki E (2005) LHC II protein phosphorylation in leaves of *Arabidopsis thaliana* mutants deficient in non-photochemical quenching. *Photosynthesis Research* 84 (1-3):217-223. doi:10.1007/s11120-005-0998-1
- Brettel K (1997) Electron transfer and arrangement of the redox cofactors in Photosystem I. *Biochimica et Biophysica Acta - Bioenergetics* 1318 (3):322-373. doi:10.1016/S0005-2728(96)00112-0
- Brettel K, Schlodder E, Witt HT (1984) Nanosecond reduction kinetics of photooxidized chlorophyll-a_{II} (P-680) in single flashes as a probe for the electron pathway, H⁺-release and charge accumulation in the O₂-evolving complex. *Biochimica et Biophysica Acta - Bioenergetics* 766 (2):403-415. doi:10.1016/0005-2728(84)90256-1
- Brooks a, Portis aR, Sharkey TD (1988) Effects of irradiance and methyl viologen treatment on ATP, ADP, and activation of ribulose biphosphate carboxylase in spinach leaves. *Plant Physiology* 88:850-853. doi:10.1104/pp.88.3.850
- Brosche M, Merilo E, Mayer F, Pechter P, Puzorjova I, Brader G, Kangasjarvi J, Kollist H (2010) Natural variation in ozone sensitivity among *Arabidopsis thaliana* accessions and its relation to stomatal conductance. *Plant, Cell and Environment* 33 (6):914-925. doi:10.1111/j.1365-3040.2010.02116.x
- Brugnoli E, Björkman O (1992) Chloroplast movements in leaves: Influence on chlorophyll fluorescence and measurements of light-induced absorbance changes related to ΔpH and zeaxanthin formation. *Photosynthesis Research* 32 (1):23-35. doi:10.1007/bf00028795
- Buckley TN, Farquhar GD (2004) A new analytical model for whole-leaf potential electron transport rate. *Plant, Cell and Environment* 27:1487-1502. doi:10.1111/j.1365-3040.2004.01232.x
- Bunney TD, van Walraven HS, de Boer aH (2001) 14-3-3 protein is a regulator of the mitochondrial and chloroplast ATP synthase. *Proceedings of the National Academy of Sciences* 98:4249-4254. doi:10.1073/pnas.061437498
- Burkey KO (1993) Effect of growth irradiance on plastocyanin levels in barley. *Photosynthesis Research* 36:103-110. doi:10.1007/BF00016275
- Burkey KO, Gizlice Z, Carter TE (1996) Genetic variation in soybean photosynthetic electron transport capacity is related to plastocyanin concentration in the chloroplast. *Photosynthesis Research* 49 (2):141-149. doi:10.1007/BF00117664
- Burrows PA, Sazanov LA, Svab Z, Maliga P, Nixon PJ (1998) Identification of a functional respiratory complex in chloroplasts through analysis of tobacco mutants containing disrupted plastid *ndh* genes. *The EMBO Journal* 17 (4):868-876. doi:10.1093/emboj/17.4.868
- Busch A, Hippler M (2011) The structure and function of eukaryotic Photosystem I. *Biochimica et Biophysica Acta - Bioenergetics* 1807 (8):864-877. doi:10.1016/j.bbabi.2010.09.009
- Cadet F, Meunier JC (1988) pH and kinetic studies of chloroplast sedoheptulose-1,7-bisphosphatase from spinach (*Spinacia oleracea*). *Biochemical Journal* 253 (1):249-254. doi:10.1042/bj2530249
- Cafilisch RE (1998) Monte Carlo and quasi-Monte Carlo methods. *Acta Numerica* 7:1-49. doi:10.1017/s0962492900002804

- Cammack R, Rao KK, Barger CP, Hutson KG, Andrew PW, Rogers LJ (1977) Midpoint redox potentials of plant and algal ferredoxins. *Biochemical Journal* 168 (2):205-209. doi:10.1042/bj1680205
- Campbell DA, Tyystjärvi E (2012) Parameterization of Photosystem II photoinactivation and repair. *Biochimica et Biophysica Acta - Bioenergetics* 1817 (1):258-265. doi:10.1016/j.bbabi.2011.04.010
- Campbell GS (1986) Extinction coefficients for radiation in plant canopies calculated using an ellipsoidal inclination angle distribution. *Agricultural and Forest Meteorology* 36 (4):317-321. doi:10.1016/0168-1923(86)90010-9
- Carmo-Silva AE, Salvucci ME (2011) The activity of Rubisco's molecular chaperone, Rubisco activase, in leaf extracts. *Photosynthesis Research* 108:143-155. doi:10.1007/s11120-011-9667-8
- Carmo-Silva AE, Salvucci ME (2013) The regulatory properties of Rubisco activase differ among species and affect photosynthetic induction during light transitions. *Plant Physiology* 161 (4):1645-1655. doi:10.1104/pp.112.213348
- Carmo-Silva E, Scales JC, Madgwick PJ, Parry MAJ (2015) Optimizing Rubisco and its regulation for greater resource use efficiency. *Plant, Cell and Environment* 38 (9):1817-1832. doi:10.1111/pce.12425
- Carr PD, Verger D, Ashton AR, Ollis DL (1999) Chloroplast NADP-malate dehydrogenase: structural basis of light-dependent regulation of activity by thiol oxidation and reduction. *Structure* 7 (4):461-475. doi:10.1016/S0969-2126(99)80058-6
- Carrillo LR, Froehlich JE, Cruz JA, Savage LJ, Kramer DM (2016) Multi-level regulation of the chloroplast ATP synthase: the chloroplast NADPH thioredoxin reductase C (NTRC) is required for redox modulation specifically under low irradiance. *The Plant Journal*. doi:10.1111/tpj.13226
- Carrillo N, Ceccarelli EA (2003) Open questions in ferredoxin-NADP⁺ reductase catalytic mechanism. *The FEBS Journal* 270 (9):1900-1915. doi:10.1046/j.1432-1033.2003.03566.x
- Cescatti A (1997) Modelling the radiative transfer in discontinuous canopies of asymmetric crowns. I. Model structure and algorithms. *Ecological Modelling* 101:263-274. doi:10.1016/S0304-3800(97)00050-1
- Champigny M-L, Bismuth E (1976) Role of photosynthetic electron transfer in light activation of Calvin cycle enzymes. *Physiologia Plantarum* 36 (1):95-100. doi:10.1111/j.1399-3054.1976.tb05034.x
- Chazdon RL, Pearcy RW (1986) Photosynthetic responses to light variation in rainforest species. II. Carbon gain and photosynthetic efficiency during lightflecks. *Oecologia* 69 (4):524-531. doi:10.1007/BF00410357
- Chelle M, Andrieu B (2007) Modelling the light environment of virtual crop canopies. In: Vos J, Marcelis LFM, Visser PHB, Struik PC, Evers JB (eds) *Functional-Structural Plant Modelling in Crop Production*. Wageningen UR Frontis Series, vol 22. Springer Netherlands, The Netherlands, pp 75-89
- Chow W, Hope A (1987) The stoichiometries of supramolecular complexes in thylakoid membranes from spinach chloroplasts. *Australian Journal of Plant Physiology* 14:21-28. doi:10.1071/PP9870021
- Chow WS, Heather Y, Adamson HY, Anderson JM (1991) Photosynthetic acclimation of *Tradescantia albiflora* to growth irradiance: Lack of adjustment of light-harvesting components and its consequences. *Physiologia Plantarum* 81:175-182. doi:10.1111/j.1399-3054.1991.tb02126.x

References

- Chow WS, Qian L, Goodchild DJ, Anderson JM (1988) Photosynthetic acclimation of *Alocasia macrorrhiza* (L.) G. Don to growth irradiance: structure, function and composition of chloroplasts. *Australian Journal of Plant Physiology* 15 (2):107-122. doi:10.1071/PP9880107
- Clarke JE, Johnson GN (2001) In vivo temperature dependence of cyclic and pseudocyclic electron transport in barley. *Planta* 212 (5/6):808-816. doi:10.1007/s004250000432
- Cleland RE (1998) Voltammetric measurement of the plastoquinone redox state in isolated thylakoids. *Photosynthesis Research* 58:183-192. doi:10.1023/A:1006165501184
- Cleveland WS, Grosse E, Shyu WM (1992) Local regression models. In: Chambers JM, Hastie TJ (eds) *Statistical Models in S*, vol 2. Wadsworth & Brooks/Cole, pp 309-376
- Courteille A, Vesa S, Sanz-Barrio R, Cazalé A-C, Becuwe-Linka N, Farran I, Havaux M, Rey P *et al.* (2013) Thioredoxin m4 controls photosynthetic alternative electron pathways in *Arabidopsis*. *Plant Physiology* 161 (1):508-520. doi:10.1104/pp.112.207019
- Cousins AB, Pracharoenwattana I, Zhou W, Smith SM, Badger MR (2008) Peroxisomal malate dehydrogenase is not essential for photorespiration in *Arabidopsis* but its absence causes an increase in the stoichiometry of photorespiratory CO₂ release. *Plant Physiology* 148 (2):786-795. doi:10.1104/pp.108.122622
- Crews CE, Vines HM, Black CC (1975) Postillumination burst of carbon dioxide in Crassulacean acid metabolism plants. *Plant Physiology* 55 (4):652-657. doi:10.1104/pp.55.4.652
- Croce R, van Amerongen H (2013) Light-harvesting in Photosystem I. *Photosynthesis Research* 116 (2):153-166. doi:10.1007/s11120-013-9838-x
- Crofts AR, Wraight CA (1983) The electrochemical domain of photosynthesis. *Biochimica et Biophysica Acta - Reviews on Bioenergetics* 726 (3):149-185. doi:10.1016/0304-4173(83)90004-6
- Cruz-Gallardo I, Díaz-Moreno I, Díaz-Quintana A, De la Rosa MA (2012) The cytochrome f-plastocyanin complex as a model to study transient interactions between redox proteins. *FEBS Letters* 586 (5):646-652. doi:10.1016/j.febslet.2011.08.035
- Cruz JA, Sacksteder CA, Kanazawa A, Kramer DM (2001) Contribution of electric field ($\Delta\Psi$) to steady-state transthylakoid proton motive force (pmf) *in vitro* and *in vivo*. Control of pmf parsing into $\Delta\Psi$ and ΔpH by ionic strength. *Biochemistry* 40:1226-1237. doi:10.1021/bi0018741
- Dai Z, Edwards GE, Ku MSB (1992) Control of photosynthesis and stomatal conductance in *Ricinus communis* L. (Castor Bean) by leaf to air vapor pressure deficit. *Plant Physiology* 99 (4):1426-1434. doi:10.1104/pp.99.4.1426
- Dall'Osto L, Cazzaniga S, Wada M, Bassi R (2014) On the origin of a slowly reversible fluorescence decay component in the *Arabidopsis npq4* mutant. *Philosophical Transactions of the Royal Society B: Biological Sciences* 369 (1640):20130221. doi:10.1098/rstb.2013.0221
- Damour G, Simonneau T, Cochard H, Urban L (2010) An overview of models of stomatal conductance at the leaf level. *Plant, Cell and Environment* 33:1419-1438. doi:10.1111/j.1365-3040.2010.02181.x
- Davis GA, Kanazawa A, Schöttler MA, Kohzuma K, Froehlich JE, Rutherford AW, Satoh-Cruz M, Minhas D *et al.* (2016) Limitations to photosynthesis by proton motive

- force-induced Photosystem II photodamage. *eLife* 5:e16921. doi:10.7554/eLife.16921
- Davis PA, Caylor S, Whippo CW, Hangarter RP (2011) Changes in leaf optical properties associated with light-dependent chloroplast movements. *Plant, Cell and Environment* 34 (12):2047-2059. doi:10.1111/j.1365-3040.2011.02402.x
- Davis PA, Hangarter RP (2012) Chloroplast movement provides photoprotection to plants by redistributing PSII damage within leaves. *Photosynthesis Research* 112 (3):153-161. doi:10.1007/s11120-012-9755-4
- De Angeli A, Zhang J, Meyer S, Martinoia E (2013) AtALMT9 is a malate-activated vacuolar chloride channel required for stomatal opening in Arabidopsis. *Nature Communications* 4:1804. doi:10.1038/ncomms2815
- de la Torre A, Delgado B, Lara C (1991) Nitrate-dependent O₂ evolution in intact leaves. *Plant Physiology* 96 (3):898-901. doi:10.1104/pp.96.3.898
- De Pury DGG, Farquhar GD (1997) Simple scaling of photosynthesis from leaves to canopies without the errors of big-leaf models. *Plant, Cell and Environment* 20:537-557. doi:10.1111/j.1365-3040.1997.tb00466.x
- de Wijn R, van Gorkom HJ (2001) Kinetics of electron transfer from Q_A to Q_B in Photosystem II. *Biochemistry* 40:11912-11922. doi:10.1021/bi010852r
- de Wijn R, van Gorkom HJ (2002) The rate of charge recombination in Photosystem II. *Biochimica et Biophysica Acta - Bioenergetics* 1553 (3):302-308. doi:10.1016/S0005-2728(02)00183-4
- de Wit CT (1992) Resource use efficiency in agriculture. *Agricultural Systems* 40 (1-3):125-151. doi:10.1016/0308-521x(92)90018-j
- de Wit M, Kegge W, Evers JB, Vergeer-van Eijk MH, Gankema P, Voeselek LACJ, Pierik R (2012) Plant neighbor detection through touching leaf tips precedes phytochrome signals. *Proceedings of the National Academy of Sciences* 109 (36):14705-14710. doi:10.1073/pnas.1205437109
- Decker JP (1955) A rapid, postillumination deceleration of respiration in green leaves. *Plant Physiology* 30 (1):82-84. doi:10.1104/pp.30.1.82
- Dekker JP, Plijter JJ, Ouweland L, Van Gorkom HJ (1984) Kinetics of manganese redox transitions in the oxygen-evolving apparatus of photosynthesis. *Biochimica et Biophysica Acta - Bioenergetics* 767 (1):176-179. doi:10.1016/0005-2728(84)90093-8
- del Riego G, Casano LM, Martín M, Sabater B (2006) Multiple phosphorylation sites in the β subunit of thylakoid ATP synthase. *Photosynthesis Research* 89 (1):11-18. doi:10.1007/s11120-006-9078-4
- Demmig-Adams B, Adams WW, Winter K, Meyer A, Schreiber U, Pereira JS, Krüger A, Czygan F-C *et al.* (1989) Photochemical efficiency of photosystem II, photon yield of O₂ evolution, photosynthetic capacity, and carotenoid composition during the midday depression of net CO₂ uptake in *Arbutus unedo* growing in Portugal. *Planta* 177 (3):377-387. doi:10.1007/bf00403596
- Demmig-Adams B, Williams III WA (1996) Xanthophyll cycle and light stress in nature: Uniform response to excess direct sunlight among higher plant species. *Planta* 198 (3):460-470. doi:10.1007/BF00620064
- Denholm JV (1981) The influence of penumbra on canopy photosynthesis I. Theoretical considerations. *Agricultural Meteorology* 25:145-166. doi:10.1016/0002-1571(81)90070-4

References

- Dietz K-J, Heber U (1984) Rate-limiting factors in leaf photosynthesis. I. Carbon fluxes in the Calvin cycle. *Biochimica et Biophysica Acta - Bioenergetics* 767 (3):432-443. doi:10.1016/0005-2728(84)90041-0
- Dietzel L, Bräutigam K, Pfannschmidt T (2008) Photosynthetic acclimation: State transitions and adjustment of photosystem stoichiometry - functional relationships between short-term and long-term light quality acclimation in plants. *FEBS Journal* 275 (6):1080-1088. doi:10.1111/j.1742-4658.2008.06264.x
- Diner BA (1977) Dependence of the deactivation reactions of Photosystem II on the redox state of plastoquinone pool A varied under anaerobic conditions. Equilibria on the acceptor side of Photosystem II. *Biochimica et Biophysica Acta - Bioenergetics* 460 (2):247-258. doi:10.1016/0005-2728(77)90211-0
- Downton WJS (1970) Preferential C4-dicarboxylic acid synthesis, the postillumination CO₂ burst, carboxyl transfer step, and grana configurations in plants with C4-photosynthesis. *Canadian Journal of Botany* 48 (10):1795-1800. doi:10.1139/b70-263
- Drake PL, Froend RH, Franks PJ (2013) Smaller, faster stomata: scaling of stomatal size, rate of response, and stomatal conductance. *Journal of Experimental Botany* 64 (2):495-505. doi:10.1093/jxb/ers347
- Drepper F, Hippler M, Nitschke W, Haehnel W (1996) Binding dynamics and electron transfer between plastocyanin and Photosystem I. *Biochemistry* 35 (4):1282-1295. doi:10.1021/bi951471e
- Driever SM, Baker NR (2011) The water-water cycle in leaves is not a major alternative electron sink for dissipation of excess excitation energy when CO₂ assimilation is restricted. *Plant, Cell and Environment* 34 (5):837-846. doi:10.1111/j.1365-3040.2011.02288.x
- Driever SM, Lawson T, Andralojc PJ, Raines CA, Parry MAJ (2014) Natural variation in photosynthetic capacity, growth, and yield in 64 field-grown wheat genotypes. *Journal of Experimental Botany* 65 (17):4959-4973. doi:10.1093/jxb/eru253
- Duursma RA, Medlyn BE (2012) MAESPA: a model to study interactions between water limitation, environmental drivers and vegetation function at tree and stand levels, with an example application to [CO₂] x drought interactions. *Geoscientific Model Development* 5 (4):919-940. doi:10.5194/gmd-5-919-2012
- Duvick DN (2005) The contribution of breeding to yield advances in maize (*Zea mays* L.). In: *Advances in Agronomy*. vol 86. Academic Press, pp 83-145. doi:10.1016/S0065-2113(05)86002-X
- Ebenhöh O, Houwaart T, Lokstein H, Schlede S, Tirok K (2011) A minimal mathematical model of nonphotochemical quenching of chlorophyll fluorescence. *BioSystems* 103 (2):196-204. doi:10.1016/j.biosystems.2010.10.011
- Eberhard S, Finazzi G, Wollman F-A (2008) The dynamics of photosynthesis. *Annual Review of Genetics* 42:463-515. doi:10.1146/annurev.genet.42.110807.091452
- Eckardt Na, Snyder GW, Portis aR, Orgen WL (1997) Growth and photosynthesis under high and low irradiance of *Arabidopsis thaliana* antisense mutants with reduced ribulose-1,5-bisphosphate carboxylase/oxygenase activase content. *Plant Physiology* 113:575-586. doi:10.1104/pp.113.2.575
- Evans J (1993) Photosynthetic acclimation and nitrogen partitioning within a lucerne canopy. II. Stability through time and comparison with a theoretical optimum. *Functional Plant Biology* 20 (1):69-82. doi:10.1071/PP9930069
- Evans J (1995) Carbon fixation profiles do reflect light absorption profiles in leaves. *Functional Plant Biology* 22 (6):865-873. doi:10.1071/PP9950865

- Evans JR (1987) The relationship between electron transport components and photosynthetic capacity in pea leaves grown at different irradiances. *Functional Plant Biology* 14:157-170. doi:10.1071/PP9870157
- Evans JR (2009) Potential errors in electron transport rates calculated from chlorophyll fluorescence as revealed by a multilayer leaf model. *Plant and Cell Physiology* 50:698-706. doi:10.1093/pcp/pcp041
- Evans JR, Poorter H (2001) Photosynthetic acclimation of plants to growth irradiance: The relative importance of specific leaf area and nitrogen partitioning in maximizing carbon gain. *Plant, Cell and Environment* 24 (8):755-767. doi:10.1046/j.1365-3040.2001.00724.x
- Evans JR, von Caemmerer S (1996) Carbon dioxide diffusion inside leaves. *Plant Physiology* 110 (2):339-346. doi:10.1104/pp.110.2.339
- Evans JR, Von Caemmerer S (2013) Temperature response of carbon isotope discrimination and mesophyll conductance in tobacco. *Plant, Cell and Environment* 36 (4):745-756. doi:10.1111/j.1365-3040.2012.02591.x
- Evers JB, Vos J, Yin X, Romero P, van der Putten PEL, Struik PC (2010) Simulation of wheat growth and development based on organ-level photosynthesis and assimilate allocation. *Journal of Experimental Botany* 61 (8):2203-2216. doi:10.1093/jxb/erq025
- Falkenmark M (2013) Growing water scarcity in agriculture: future challenge to global water security. *Philosophical Transactions of the Royal Society A: Mathematical, Physical and Engineering Sciences* 371 (2002). doi:10.1098/rsta.2012.0410
- Fan D-Y, Fitzpatrick D, Oguchi R, Ma W, Kou J, Chow WS (2016) Obstacles in the quantification of the cyclic electron flux around Photosystem I in leaves of C3 plants. *Photosynthesis Research* 129 (3):239-251. doi:10.1007/s11120-016-0223-4
- Fan D-Y, Nie Q, Hope AB, Hillier W, Pogson BJ, Chow WS (2007) Quantification of cyclic electron flow around Photosystem I in spinach leaves during photosynthetic induction. *Photosynthesis Research* 94 (2):347. doi:10.1007/s11120-006-9127-z
- Farquhar GD (1979) Models describing the kinetics of ribulose biphosphate carboxylase-oxygenase. *Archives of Biochemistry and Biophysics* 193 (2):456-468. doi:10.1016/0003-9861(79)90052-3
- Farquhar GD (1989) Models of integrated photosynthesis of cells and leaves. *Philosophical Transactions of the Royal Society B: Biological Sciences* 323 (1216):357-367. doi:10.1098/rstb.1989.0016
- Farquhar GD, S vC, Berry JA (2001) Models of photosynthesis. *Plant Physiology* 125:42-45. doi:10.1104/pp.125.1.42
- Farquhar GD, Sharkey TD (1982) Stomatal conductance and photosynthesis. *Annual Review of Plant Physiology* 33:317-345. doi:10.1146/annurev.pp.33.060182.001533
- Farquhar GD, von Caemmerer S Electron transport limitations on the CO₂ assimilation rate of leaves: a model and some observations in *Phaseolus vulgaris* L. In: Akoyunoglou G (ed) *Proceedings Fifth International Congress of Photosynthesis*, Philadelphia, USA, 1981. pp 163-175
- Farquhar GD, von Caemmerer S, Berry JA (1980) A biochemical model of photosynthetic CO₂ assimilation in leaves of C3 species. *Planta* 149:78-90. doi:10.1007/BF00386231
- Farquhar GD, Wong SC (1984) An empirical model of stomatal conductance. *Australian Journal of Plant Physiology* 11:191-210. doi:10.1071/PP9840191

References

- Fato R, Estornell E, Di Bernardo S, Pallotti F, Parenti Castelli G, Lenaz G (1996) Steady-state kinetics of the reduction of coenzyme Q analogs by complex I (NADH:ubiquinone oxidoreductase) in bovine heart mitochondria and submitochondrial particles. *Biochemistry* 35 (8):2705-2716. doi:10.1021/bi9516034
- Fay PA, Knapp AK (1993) Photosynthetic and stomatal responses of *Avena sativa* (Poaceae) to a variable light environment. *American Journal of Botany* 80 (12):1369-1373. doi:10.2307/2445664
- Fay PA, Knapp AK (1995) Stomatal and photosynthetic responses to shade in sorghum, soybean and eastern gamagrass. *Physiologia Plantarum* 94 (4):613-620. doi:10.1034/j.1399-3054.1995.940411.x
- Feller U, Crafts-Brandner SJ, Salvucci ME (1998) Moderately high temperatures inhibit ribulose-1,5-bisphosphate carboxylase/oxygenase (Rubisco) activase-mediated activation of Rubisco. *Plant Physiology* 116 (2):539-546. doi:10.1104/pp.116.2.539
- Finazzi G, Petroustos D, Tomizioli M, Flori S, Sautron E, Villanova V, Rolland N, Seigneurin-Berny D (2015) Ions channels/transporters and chloroplast regulation. *Cell Calcium* 58 (1):86-97. doi:10.1016/j.ceca.2014.10.002
- Fisher N, Kramer DM (2014) Non-photochemical reduction of thylakoid photosynthetic redox carriers in vitro: Relevance to cyclic electron flow around photosystem I? *Biochimica et Biophysica Acta - Bioenergetics* 1837:1944-1954. doi:10.1016/j.bbabi.2014.09.005
- Flexas J, Barbour MM, Brendel O, Cabrera HM, Carriquí M, Díaz-Espejo A, Douthe C, Dreyer E *et al.* (2012) Mesophyll diffusion conductance to CO₂: An unappreciated central player in photosynthesis. *Plant Science* 193-194:70-84. doi:10.1016/j.plantsci.2012.05.009
- Flexas J, Diaz-Espejo A, Galmés J, Kaldenhoff R, Medrano H, Ribas-Carbo M (2007a) Rapid variations of mesophyll conductance in response to changes in CO₂ concentration around leaves. *Plant, Cell and Environment* 30:1284-1298. doi:10.1111/j.1365-3040.2007.01700.x
- Flexas J, Niinemets Ü, Gallé A, Barbour MM, Centritto M, Diaz-Espejo A, Douthe C, Galmés J *et al.* (2013) Diffusional conductances to CO₂ as a target for increasing photosynthesis and photosynthetic water-use efficiency. *Photosynthesis Research* 117 (1):45-59. doi:10.1007/s11120-013-9844-z
- Flexas J, Ortuño MF, Ribas-Carbo M, Diaz-Espejo A, Flórez-Sarasa ID, Medrano H (2007b) Mesophyll conductance to CO₂ in *Arabidopsis thaliana*. *New Phytologist* 175:501-511. doi:10.1111/j.1469-8137.2007.02111.x
- Flexas J, Ribas-Carbó M, Diaz-Espejo A, Galmés J, Medrano H (2008) Mesophyll conductance to CO₂: Current knowledge and future prospects. *Plant, Cell and Environment* 31:602-621. doi:10.1111/j.1365-3040.2007.01757.x
- Flood PJ, Harbinson J, Aarts MGM (2011) Natural genetic variation in plant photosynthesis. *Trends in Plant Science* 16 (6):327-335. doi:10.1016/j.tplants.2011.02.005
- Foley JA, Ramankutty N, Brauman KA, Cassidy ES, Gerber JS, Johnston M, Mueller ND, O'Connell C *et al.* (2011) Solutions for a cultivated planet. *Nature* 478 (7369):337-342. doi:10.1038/nature10452
- Foyer CH, Bloom AJ, Queval G, Noctor G (2009) Photorespiratory metabolism: genes, mutants, energetics, and redox signaling. *Annual Review of Plant Biology* 60 (1):455-484. doi:10.1146/annurev.arplant.043008.091948

- Foyer CH, Lelandais M, Harbinson J (1992) Control of the quantum efficiencies of photosystems I and II, electron flow, and enzyme activation following dark-to-light transitions in pea leaves: Relationship between NADP/NADPH Ratios and NADP-malate dehydrogenase activation state. *Plant Physiology* 99 (3):979-986. doi:10.1104/pp.99.3.979
- Foyer CH, Neukermans J, Queval G, Noctor G, Harbinson J (2012) Photosynthetic control of electron transport and the regulation of gene expression. *Journal of Experimental Botany* 63:1637-1661. doi:10.1093/jxb/ers013
- Foyer CH, Noctor G (2002) Photosynthetic nitrogen assimilation and associated carbon and respiratory metabolism. *Advances in Photosynthesis and Respiration*, vol 12. Springer Netherlands, The Netherlands. doi:10.1007/0-306-48138-3
- Foyer CH, Noctor G, Hodges M (2011) Respiration and nitrogen assimilation: targeting mitochondria-associated metabolism as a means to enhance nitrogen use efficiency. *Journal of Experimental Botany* 62 (4):1467-1482. doi:10.1093/jxb/erq453
- Foyer CH, Shigeoka S (2011) Understanding oxidative stress and antioxidant functions to enhance photosynthesis. *Plant Physiology* 155 (1):93-100. doi:10.1104/pp.110.166181
- Franceschini G, Macchietto S (2008) Model-based design of experiments for parameter precision: State of the art. *Chemical Engineering Science* 63 (19):4846-4872. doi:10.1016/j.ces.2007.11.034
- Fridlyand LE (1992) Enzymatic control of 3-phosphoglycerate reduction in chloroplasts. *Biochimica et Biophysica Acta - Bioenergetics* 1102 (1):115-118. doi:10.1016/0005-2728(92)90071-9
- Fridlyand LE, Backhausen JE, Scheibe R (1998) Flux control of the malate valve in leaf cells. *Archives of Biochemistry and Biophysics* 349 (2):290-298. doi:10.1006/abbi.1997.0482
- Fridlyand LE, Scheibe R (1999a) Controlled distribution of electrons between acceptors in chloroplasts: A theoretical consideration. *Biochimica et Biophysica Acta - Bioenergetics* 1413 (1):31-42. doi:10.1016/S0005-2728(99)00079-1
- Fridlyand LE, Scheibe R (1999b) Regulation of the Calvin cycle for CO₂ fixation as an example for general control mechanisms in metabolic cycles. *BioSystems* 51:79-93. doi:10.1016/S0303-2647(99)00017-9
- Frommolt R, Goss R, Wilhelm C (2001) The de-epoxidase and epoxidase reactions of *Mantoniella squamata* (Prasinophyceae) exhibit different substrate-specific reaction kinetics compared to spinach. *Planta* 213 (3):446-456. doi:10.1007/s004250100589
- Fukayama H, Ueguchi C, Nishikawa K, Katoh N, Ishikawa C, Masumoto C, Hatanaka T, Misoo S (2012) Overexpression of rubisco activase decreases the photosynthetic CO₂ assimilation rate by reducing rubisco content in rice leaves. *Plant and Cell Physiology* 53 (6):976-986. doi:10.1093/pcp/pcs042
- Furbank RT, Badger MR (1983) Oxygen exchange associated with electron transport and photophosphorylation in spinach thylakoids. *Biochimica et Biophysica Acta - Bioenergetics* 723 (3):400-409. doi:10.1016/0005-2728(83)90047-6
- Furbank RT, Jenkins CL, Hatch MD (1989) CO₂ concentrating mechanism of C₄ photosynthesis permeability of isolated bundle sheath cells to inorganic carbon. *Plant Physiology* 91 (4):1364-1371. doi:10.1104/pp.91.4.1364

References

- Gábor A, Banga JR (2015) Robust and efficient parameter estimation in dynamic models of biological systems. *BMC Systems Biology* 9:74. doi:10.1186/s12918-015-0219-2
- Gamon JA, Peñuelas J, Field CB (1992) A narrow-waveband spectral index that tracks diurnal changes in photosynthetic efficiency. *Remote Sensing of Environment* 41 (1):35-44. doi:10.1016/0034-4257(92)90059-S
- Gardemann A, Schimkat D, Heldt HW (1986) Control of CO₂ fixation regulation of stromal fructose-1,6-bisphosphatase in spinach by pH and Mg²⁺ concentration. *Planta* 168 (4):536-545. doi:10.1007/bf00392274
- Gardemann A, Stitt M, Heldt HW (1982) Regulation of spinach ribulose 5-phosphate kinase by 3-phosphoglycerate. *FEBS Letters* 137 (2):213-216. doi:10.1016/0014-5793(82)80352-9
- Gerhardt R, Heldt HW (1984) Measurement of subcellular metabolite levels in leaves by fractionation of freeze-stopped material in nonaqueous media. *Plant Physiology* 75 (3):542-547. doi:10.1104/pp.75.3.542
- Gibeaut DM, Hulett J, Cramer GR, Seemann JR (1997) Maximal biomass of *Arabidopsis thaliana* using a simple, low-maintenance hydroponic method and favorable environmental conditions. *Plant Physiology* 115 (2):317-319. doi:10.1104/pp.115.2.317
- Giersch C (1982) Capacity of the malate/oxaloacetate shuttle for transfer of reducing equivalents across the envelope of leaf chloroplasts. *Archives of Biochemistry and Biophysics* 219 (2):379-387. doi:10.1016/0003-9861(82)90169-2
- Giersch C, Heber U, Kobayashi Y, Inoue Y, Shibata K, Heldt HW (1980) Energy charge, phosphorylation potential and proton motive force in chloroplasts. *Biochimica et Biophysica Acta* 590:59-73. doi:10.1016/0005-2728(80)90146-2
- Giersch C, Robinson SP (1987) Regulation of photosynthetic carbon metabolism during phosphate limitation of photosynthesis in isolated spinach chloroplasts. *Photosynthesis Research* 14 (3):211-227. doi:10.1007/BF00032706
- Gijzen H, Goudriaan J (1989) A flexible and explanatory model of light distribution and photosynthesis in row crops. *Agricultural and Forest Meteorology* 48:1-20. doi:10.1016/0168-1923(89)90004-X
- Gilmore AM, Björkman O (1995) Temperature-sensitive coupling and uncoupling of ATPase-mediated, nonradiative energy dissipation: Similarities between chloroplasts and leaves. *Planta* 197 (4):646-654. doi:10.1007/bf00191573
- Gilmore AM, Hazlett TL, Debrunner PG, Govindjee (1996) Comparative time-resolved photosystem II chlorophyll a fluorescence analyses reveal distinctive differences between photoinhibitory reaction center damage and xanthophyll cycle-dependent energy dissipation. *Photochemistry and Photobiology* 64 (3):552-563. doi:10.1111/j.1751-1097.1996.tb03105.x
- Glauser DA, Bourquin F, Manieri W, Schürmann P (2004) Characterization of ferredoxin:thioredoxin reductase modified by site-directed mutagenesis. *Journal of Biological Chemistry* 279 (16):16662-16669. doi:10.1074/jbc.M313851200
- Goral TK, Johnson MP, Duffy CDP, Brain APR, Ruban AV, Mullineaux CW (2012) Light-harvesting antenna composition controls the macrostructure and dynamics of thylakoid membranes in *Arabidopsis*. *The Plant Journal* 69 (2):289-301. doi:10.1111/j.1365-313X.2011.04790.x
- Goudriaan J (1977) *Crop micrometeorology: a simulation study*. Simulation monographs. Pudoc, Center for Agricultural Publishing and Documentation, Wageningen, The Netherlands

- Goudriaan J, van Laar HH (1994) Modelling potential crop growth processes: textbook with exercises. 2 edn. Kluwer Academic Publisher, Dordrecht, The Netherlands
- Govindjee (1995) Sixty-three years since Kautsky: chlorophyll a fluorescence. *Functional Plant Biology* 22 (2):131-160. doi:10.1071/PP9950131
- Graan T, Ort DR (1984) Quantitation of the rapid electron donors to P₇₀₀, the functional plastoquinone pool, and the ratio of the photosystems in spinach chloroplasts. *Journal of Biological Chemistry* 259 (22):14003-14010
- Grant L (1987) Diffuse and specular characteristics of leaf reflectance. *Remote Sensing of Environment* 22 (2):309-322. doi:10.1016/0034-4257(87)90064-2
- Greer DH, Berry JA, Björkman O (1986) Photoinhibition of photosynthesis in intact bean leaves: role of light and temperature, and requirement for chloroplast-protein synthesis during recovery. *Planta* 168 (2):253-260. doi:10.1007/bf00402971
- Griffiths H, Helliker BR (2013) Mesophyll conductance: internal insights of leaf carbon exchange. *Plant, Cell and Environment* 36 (4):733-735. doi:10.1111/pce.12075
- Gross LJ (1982) Photosynthetic dynamics in varying light environments: A model and its application to whole leaf carbon gain. *Ecology* 63 (1):84-93. doi:10.2307/1937034
- Gross LJ, Kirschbaum MUF, Pearcy RW (1991) A dynamic model of photosynthesis in varying light taking account of stomatal conductance, C₃-cycle intermediates, photorespiration and Rubisco activation. *Plant, Cell and Environment* 14 (9):881-893. doi:10.1111/j.1365-3040.1991.tb00957.x
- Gu J, Yin X, Stomph TJ, Wang H, Struik PC (2012a) Physiological basis of genetic variation in leaf photosynthesis among rice (*Oryza sativa* L.) introgression lines under drought and well-watered conditions. *Journal of Experimental Botany* 63 (14):5137-5153. doi:10.1093/jxb/ers170
- Gu J, Yin X, Struik PC, Stomph TJ, Wang H (2012b) Using chromosome introgression lines to map quantitative trait loci for photosynthesis parameters in rice (*Oryza sativa* L.) leaves under drought and well-watered field conditions. *Journal of Experimental Botany* 63:455-469. doi:10.1093/jxb/err292
- Gu L, Sun Y (2014) Artefactual responses of mesophyll conductance to CO₂ and irradiance estimated with the variable J and online isotope discrimination methods. *Plant, Cell and Environment* 37 (5):1231-1249. doi:10.1111/pce.12232
- Gutschick VP (2016) Leaf energy balance: basics, and modeling from leaves to canopies. In: Hikosaka K, Niinemets Ü, Anten PRN (eds) *Canopy Photosynthesis: From Basics to Applications*. Springer Netherlands, Dordrecht, pp 23-58. doi:10.1007/978-94-017-7291-4_2
- Hald S, Pribil M, Leister D, Gallois P, Johnson GN (2008) Competition between linear and cyclic electron flow in plants deficient in Photosystem I. *Biochimica et Biophysica Acta - Bioenergetics* 1777 (9):1173-1183. doi:10.1016/j.bbabi.2008.04.041
- Hammond ET, John Andrews T, Mott Ka, Woodrow IE (1998) Regulation of rubisco activation is antisense plants of tobacco containing reduced levels of rubisco activase. *Plant Journal* 14 (1):101-110. doi:10.1046/j.1365-313X.1998.00103.x
- Hampp R, Goller M, Ziegler H (1982) Adenylate levels, energy charge, and phosphorylation potential during dark-light and light-dark transition in chloroplasts, mitochondria, and cytosol of mesophyll protoplasts from *Avena sativa* L. *Plant Physiology* 69:448-455. doi:10.1104/pp.69.2.448
- Harbinson J, Genty B, Baker NR (1989) Relationship between the quantum efficiencies of Photosystems I and II in pea leaves. *Plant Physiology* 90:1029-1034. doi:10.1104/pp.90.3.1029

References

- Harbinson J, Hedley CL (1989a) The kinetics of P-700⁺ reduction in leaves - a novel insitu probe of thylakoid functioning. *Plant Cell and Environment* 12:357-369
- Harbinson J, Hedley CL (1989b) The kinetics of P-700⁺ reduction in leaves: a novel insitu probe of thylakoid functioning. *Plant, Cell and Environment* 12 (4):357-369. doi:10.1111/j.1365-3040.1989.tb01952.x
- Harley PC, Loreto F, Di Marco G, Sharkey TD (1992a) Theoretical considerations when estimating the mesophyll conductance to CO₂ flux by analysis of the response of photosynthesis to CO₂. *Plant Physiology* 98 (4):1429-1436. doi:10.1104/pp.98.4.1429
- Harley PC, Sharkey TD (1991) An improved model of C₃ photosynthesis at high CO₂: Reversed O₂ sensitivity explained by lack of glycerate reentry into the chloroplast. *Photosynthesis Research* 27:169-178. doi:10.1007/BF00035838
- Harley PC, Thomas RB, Reynolds JF, Strain BR (1992b) Modeling photosynthesis of cotton grown in elevated CO₂. *Plant, Cell and Environment* 15:271-282. doi:10.1111/j.1365-3040.1992.tb00974.x
- Harris GC, Königer M (1997) The 'high' concentrations of enzymes within the chloroplast. *Photosynthesis Research* 54:5-23. doi:10.1023/A:1005895213775
- Härtel H, Lokstein H, Grimm B, Rank B (1996) Kinetic studies on the xanthophyll cycle in barley leaves: Influence of antenna size and relations to nonphotochemical chlorophyll fluorescence quenching. *Plant Physiology* 110 (2):471-482. doi:10.1104/pp.110.2.471
- Haslett BG, Cammack R, Whatley FR (1973) Quantitative studies on ferredoxin in greening bean leaves. *Biochemical Journal* 136 (3):697-703. doi:10.1042/bj1360697
- Haupt W, Scheuerlein R (1990) Chloroplast movement. *Plant, Cell and Environment* 13 (7):595-614. doi:10.1111/j.1365-3040.1990.tb01078.x
- Hauska G, Schütz M, Büttner M (1996) The cytochrome b₆f complex - composition, structure and function. In: Ort DR, Yocum CF (eds) *Oxygenic Photosynthesis: The Light Reactions*. *Advances in Photosynthesis and Respiration*, vol 4. Springer Netherlands, pp 377-398. doi:10.1007/0-306-48127-8_19
- Hay RKM (1995) Harvest index: a review of its use in plant breeding and crop physiology. *Annals of Applied Biology* 126 (1):197-216. doi:10.1111/j.1744-7348.1995.tb05015.x
- Hazra S, Henderson JN, Liles K, Hilton MT, Wachter RM (2015) Regulation of ribulose-1,5-bisphosphate carboxylase/oxygenase (Rubisco) activase: Product inhibition, cooperativity, and magnesium activation. *Journal of Biological Chemistry* 290 (40):24222-24236. doi:10.1074/jbc.M115.651745
- Heineke D, Riens B, Grosse H, Hoferichter P, Peter U, Flügge UI, Heldt HW (1991) Redox transfer across the inner chloroplast envelope membrane. *Plant Physiology* 95 (4):1131-1137. doi:10.1104/pp.95.4.1131
- Heinrich R, Rapoport TA (1974) A linear steady-state treatment of enzymatic chains. *European Journal of Biochemistry* 42 (1):89-95. doi:10.1111/j.1432-1033.1974.tb03318.x
- Heise R, Arrivault S, Szecowka M, Tohge T, Nunes-Nesi A, Stitt M, Nikoloski Z, Fernie AR (2014) Flux profiling of photosynthetic carbon metabolism in intact plants. *Nature Protocols* 9 (8):1803-1824. doi:10.1038/nprot.2014.115
- Herdean A, Teardo E, Nilsson AK, Pfeil BE, Johansson ON, Ünneper R, Nagy G, Zsiros O *et al.* (2016) A voltage-dependent chloride channel fine-tunes photosynthesis in plants. *Nature Communications* 7:11654. doi:10.1038/ncomms11654

- Hertle AP, Blunder T, Wunder T, Pesaresi P, Pribil M, Armbruster U, Leister D (2013) PGRL1 is the elusive ferredoxin-plastoquinone reductase in photosynthetic cyclic electron flow. *Molecular Cell* 49 (3):511-523. doi:10.1016/j.molcel.2012.11.030
- Higa T, Wada M (2016) Chloroplast avoidance movement is not functional in plants grown under strong sunlight. *Plant, Cell and Environment* 39 (4):871-882. doi:10.1111/pce.12681
- Hikosaka K, Ishikawa K, Borjigidai A, Muller O, Onoda Y (2006) Temperature acclimation of photosynthesis: mechanisms involved in the changes in temperature dependence of photosynthetic rate. *Journal of Experimental Botany* 57 (2):291-302. doi:10.1093/jxb/erj049
- Hikosaka K, Kato MC, Hirose T (2004) Photosynthetic rates and partitioning of absorbed light energy in photoinhibited leaves. *Physiologia Plantarum* 121:699-708. doi:10.1111/j.1399-3054.2004.00364.x
- Hindmarsh AC, Brown PN, Grant KE, Lee SL, Serban R, Shumaker DE, Woodward CS (2005) SUNDIALS: Suite of nonlinear and differential/algebraic equation solvers. *ACM Transactions on Mathematical Software* 31:363-396. doi:10.1145/1089014.1089020
- Hirasawa M, Droux M, Gray KA, Boyer JM, Davis DJ, Buchanan BB, Knaff DB (1988) Ferredoxin-thioredoxin reductase: Properties of its complex with ferredoxin. *Biochimica et Biophysica Acta - Bioenergetics* 935 (1):1-8. doi:10.1016/0005-2728(88)90101-6
- Hirasawa M, Tripathy JN, Somasundaram R, Johnson MK, Bhalla M, Allen JP, Knaff DB (2009) The interaction of spinach nitrite reductase with ferredoxin: A site-directed mutation study. *Molecular Plant* 2 (3):407-415. doi:10.1093/mp/ssn098
- Hirst J (2013) Mitochondrial complex I. *Annual Review of Biochemistry* 82 (1):551-575. doi:10.1146/annurev-biochem-070511-103700
- Ho QT, Berghuijs HNC, Watté R, Verboven P, Herremans E, Yin X, Retta MA, Aernouts B *et al.* (2016) Three-dimensional microscale modelling of CO₂ transport and light propagation in tomato leaves enlightens photosynthesis. *Plant, Cell and Environment* 39 (1):50-61. doi:10.1111/pce.12590
- Ho QT, Verboven P, Yin X, Struik PC, Nicolai BM (2012) A microscale model for combined CO₂ diffusion and photosynthesis in leaves. *PLOS ONE* 7 (11):e48376. doi:10.1371/journal.pone.0048376
- Hogewoning SW, Wientjes E, Douwstra P, Trouwborst G, van Ieperen W, Croce R, Harbinson J (2012) Photosynthetic quantum yield dynamics: from photosystems to leaves. *The Plant Cell* 24:1921-1935. doi:10.1105/tpc.112.097972
- Holišová P, Zitová M, Klem K, Urban O (2012) Effect of elevated carbon dioxide concentration on carbon assimilation under fluctuating light. *Journal of Environmental Quality* 41 (6):1931-1938. doi:10.2134/jeq2012.0113
- Holzwarth AR, Muller MG, Reus M, Nowaczyk M, Sander J, Rogner M (2006) Kinetics and mechanism of electron transfer in intact Photosystem II and in the isolated reaction center: Pheophytin is the primary electron acceptor. *Proceedings of the National Academy of Sciences* 103 (18):6895-6900. doi:10.1073/pnas.0505371103
- Hope AB, Valente P, Matthews DB (1994) Effects of pH on the kinetics of redox reactions in and around the cytochrome bf complex in an isolated system. *Photosynthesis Research* 42 (2):111-120. doi:10.1007/bf02187122
- Horton P (2014) Developments in research on non-photochemical fluorescence quenching: Emergence of key ideas, theories and experimental approaches. In:

References

- Demmig-Adams B, Garab G, Adams Iii W, Govindjee (eds) Non-Photochemical Quenching and Energy Dissipation in Plants, Algae and Cyanobacteria. Springer Netherlands, Dordrecht, pp 73-95. doi:10.1007/978-94-017-9032-1_3
- Horton P, Johnson MP, Perez-Bueno ML, Kiss AZ, Ruban AV (2008) Photosynthetic acclimation: Does the dynamic structure and macro-organisation of photosystem II in higher plant grana membranes regulate light harvesting states? FEBS Journal 275:1069-1079. doi:10.1111/j.1742-4658.2008.06263.x
- Howard TP, Lloyd JC, Raines CA (2011) Inter-species variation in the oligomeric states of the higher plant Calvin cycle enzymes glyceraldehyde-3-phosphate dehydrogenase and phosphoribulokinase. Journal of Experimental Botany 62 (11):3799-3805. doi:10.1093/jxb/err057
- Howard TP, Metodiev M, Lloyd JC, Raines CA (2008) Thioredoxin-mediated reversible dissociation of a stromal multiprotein complex in response to changes in light availability. Proceedings of the National Academy of Sciences 105 (10):4056-4061. doi:10.1073/pnas.0710518105
- Hu P, Lv J, Fu P, Hualing M (2013) Enzymatic characterization of an active NDH complex from *Thermosynechococcus elongatus*. FEBS Letters 587 (15):2340-2345. doi:10.1016/j.febslet.2013.05.040
- Hubbart S, Ajigboye OO, Horton P, Murchie EH (2012) The photoprotective protein PsbS exerts control over CO₂ assimilation rate in fluctuating light in rice. Plant Journal 71:402-412. doi:10.1111/j.1365-313X.2012.04995.x
- Huber SC, Nielsen TH, Huber JLA, Pharr DM (1989) Variation among species in light activation of sucrose-phosphate synthase. Plant and Cell Physiology 30 (2):277-285
- Hucka M, Finney A, Sauro HM, Bolouri H, Doyle JC, Kitano H, Forum: atrotS, Arkin AP *et al.* (2003) The systems biology markup language (SBML): a medium for representation and exchange of biochemical network models. Bioinformatics 19 (4):524-531. doi:10.1093/bioinformatics/btg015
- Huesgen PF, Schuhmann H, Adamska I (2006) Photodamaged D1 protein is degraded in Arabidopsis mutants lacking the Deg2 protease. FEBS Letters 580 (30):6929-6932. doi:10.1016/j.febslet.2006.11.058
- Igamberdiev AU, Bykova NV, Lea PJ, Gardeström P (2001) The role of photorespiration in redox and energy balance of photosynthetic plant cells: A study with a barley mutant deficient in glycine decarboxylase. Physiologia Plantarum 111 (4):427-438. doi:10.1034/j.1399-3054.2001.1110402.x
- Igamberdiev AU, Hurry V, Krömer S, Gardeström P (1998) The role of mitochondrial electron transport during photosynthetic induction. A study with barley (*Hordeum vulgare*) protoplasts incubated with rotenone and oligomycin. Physiologia Plantarum 104 (3):431-439. doi:10.1034/j.1399-3054.1998.1040319.x
- Ikeuchi M, Uebayashi N, Sato F, Endo T (2014) Physiological functions of PsbS-dependent and PsbS-independent NPQ under naturally fluctuating light conditions. Plant and Cell Physiology 55:1286-1295. doi:10.1093/pcp/pcu069
- Imsande J, Touraine B (1994) N demand and the regulation of nitrate uptake. Plant Physiology 105 (1):3-7. doi:10.1104/pp.105.1.3
- Ingenhousz J (1779) Experiments upon vegetables: Discovering their great power of purifying the common air in the sun-shine, and of injuring it in the shade and at night to which is joined, a new method of examining the accurate degree of salubrity of the atmosphere. London

- IPCC (2007) Climate Change 2007: Synthesis Report IPCC Fourth Assessment Report. Intergovernmental Panel on Climate Change, Geneva
- IPCC (2013) Climate change 2013: the physical science basis. Contribution of Working Group I to the Fifth Assessment Report of the Intergovernmental Panel on Climate Change. Cambridge University Press, Cambridge, U. K. & New York, U. S. A.
- Ishijima S, Uchibori A, Takagi H, Maki R, Ohnishi M (2003) Light-induced increase in free Mg^{2+} concentration in spinach chloroplasts: Measurement of free Mg^{2+} by using a fluorescent probe and necessity of stromal alkalinization. *Archives of Biochemistry and Biophysics* 412 (1):126-132. doi:10.1016/S0003-9861(03)00038-9
- Jacquemoud S, Ustin SL Leaf optical properties: a state of the art. In: 8th International Symposium Physical Measurements & Signatures in Remote Sensing, Aussois (France), 2001. CNES,
- Jahns P, Holzwarth AR (2012) The role of the xanthophyll cycle and of lutein in photoprotection of Photosystem II. *Biochimica et Biophysica Acta - Bioenergetics* 1817 (1):182-193. doi:10.1016/j.bbabi.2011.04.012
- Johnson GN (2011) Physiology of PSI cyclic electron transport in higher plants. *Biochimica et Biophysica Acta - Bioenergetics* 1807 (3):384-389. doi:10.1016/j.bbabi.2010.11.009
- Johnson MP, Goral TK, Duffy CDP, Brain APR, Mullineaux CW, Ruban AV (2011) Photoprotective energy dissipation involves the reorganization of Photosystem II light-harvesting complexes in the grana membranes of spinach chloroplasts. *The Plant Cell* 23 (4):1468-1479. doi:10.1105/tpc.110.081646
- Johnson MP, Ruban AV (2011) Restoration of rapidly reversible photoprotective energy dissipation in the absence of PsbS protein by enhanced ΔpH . *Journal of Biological Chemistry* 286:19973-19981. doi:10.1074/jbc.M111.237255
- Johnson MP, Zia A, Ruban AV (2012) Elevated ΔpH restores rapidly reversible photoprotective energy dissipation in Arabidopsis chloroplasts deficient in lutein and xanthophyll cycle activity. *Planta* 235:193-204. doi:10.1007/s00425-011-1502-0
- Johnson SG (2016) The NLOpt nonlinear-optimization package. <http://ab-initio.mit.edu/nlopt>
- Joliot P, Lavergne J, Béal D (1992) Plastoquinone compartmentation in chloroplasts. I. Evidence for domains with different rates of photo-reduction. *Biochimica et Biophysica Acta - Bioenergetics* 1101:1-12. doi:10.1016/0167-4838(92)90460-U
- Jones JW, Hoogenboom G, Porter CH, Boote KJ, Batchelor WD, Hunt LA, Wilkens PW, Singh U *et al.* (2003) The DSSAT cropping system model. *European Journal of Agronomy* 18 (3-4):235-265. doi:10.1016/S1161-0301(02)00107-7
- Junesch U, Gräber P (1985) The rate of ATP synthesis as a function of ΔpH in normal and dithiothreitol-modified chloroplasts. *Biochimica et Biophysica Acta - Bioenergetics* 809 (3):429-434. doi:10.1016/0005-2728(85)90194-X
- Junesch U, Gräber P (1987) Influence of the redox state and the activation of the chloroplast ATP synthase on proton-transport-coupled ATP synthesis/hydrolysis. *Biochimica et Biophysica Acta - Bioenergetics* 893 (2):275-288. doi:10.1016/0005-2728(87)90049-1
- Junesch U, Gräber P (1991) The rate of ATP-synthesis as a function of ΔpH and $\Delta \psi$ catalyzed by the active, reduced H^+ -ATPase from chloroplasts. *FEBS Letters* 294 (3):275-278. doi:10.1016/0014-5793(91)81447-g

References

- Junge W (2013) Half a century of molecular bioenergetics. *Biochemical Society Transactions* 41 (5):1207-1218. doi:10.1042/BST20130199
- Junge W, Ausländer W, McGeer AJ, Runge T (1979) The buffering capacity of the internal phase of thylakoids and the magnitude of the pH changes inside under flashing light. *Biochimica et Biophysica Acta - Bioenergetics* 546 (1):121-141. doi:10.1016/0005-2728(79)90175-0
- Kaiser E, Morales A, Harbinson J, Heuvelink E, Prinzenberg AE, Marcelis LFM (2016) Metabolic and diffusional limitations of photosynthesis in fluctuating irradiance in *Arabidopsis thaliana*. *Scientific Reports* 6:31252. doi:10.1038/srep31252
- Kaiser E, Morales A, Harbinson J, Kromdijk J, Heuvelink E, Marcelis LFM (2015) Dynamic photosynthesis in different environmental conditions. *Journal of Experimental Botany* 66 (9):2415-2426. doi:10.1093/jxb/eru406
- Kaiser H, Kappen L (2000) In situ observation of stomatal movements and gas exchange of *Aegopodium podagraria* L. in the understorey. *Journal of Experimental Botany* 51 (351):1741-1749. doi:10.1093/jexbot/51.351.1741
- Kaiser H, Kappen L (2001) Stomatal oscillations at small apertures: indications for a fundamental insufficiency of stomatal feedback-control inherent in the stomatal turgor mechanism. *Journal of Experimental Botany* 52 (359):1303-1313. doi:10.1093/jexbot/52.359.1303
- Kaiser WM, Stoimenova M, Man H-M (2002) What limits nitrate reduction in leaves? In: Foyer CH, Noctor G (eds) *Photosynthetic Nitrogen Assimilation and Associated Carbon and Respiratory Metabolism*, vol 12. Springer Netherlands, Dordrecht, pp 63-70. doi:10.1007/0-306-48138-3_5
- Kanazawa A, Kramer DM (2002) In vivo modulation of nonphotochemical exciton quenching (NPQ) by regulation of the chloroplast ATP synthase. *Proceedings of the National Academy of Sciences* 99 (20):12789-12794. doi:10.1073/pnas.182427499
- Kasahara M, Kagawa T, Oikawa K, Suetsugu N, Miyao M, Wada M (2002) Chloroplast avoidance movement reduces photodamage in plants. *Nature* 420 (6917):829-832. doi:10.1038/nature01213
- Kattge J, Díaz S, Lavorel S, Prentice IC, Leadley P, BÖNisch G, Garnier E, Westoby M *et al.* (2011) TRY – a global database of plant traits. *Global Change Biology* 17 (9):2905-2935. doi:10.1111/j.1365-2486.2011.02451.x
- Kautsky H, Hirsch A (1931) Neue Versuche zur Kohlensäureassimilation. *Naturwissenschaften* 19 (48):964-964. doi:10.1007/bf01516164
- Kebeish R, Niessen M, Thiruveedhi K, Bari R, Hirsch H-J, Rosenkranz R, Stabler N, Schonfeld B *et al.* (2007) Chloroplastic photorespiratory bypass increases photosynthesis and biomass production in *Arabidopsis thaliana*. *Nature Biotechnology* 25 (5):593-599. doi:10.1038/nbt1299
- Keurentjes JJB, Angenent GC, Dicke M, Martins dos Santos VAP, Molenaar J, van der Putten WH, de Rooter PC, Struik PC *et al.* (2011) Redefining plant systems biology: from cell to ecosystem. *Trends in Plant Science* 16 (4):183-190. doi:10.1016/j.tplants.2010.12.002
- Kiel S, Tyler PA (2010) Chemosynthetically-driven ecosystems in the deep sea. In: Kiel S (ed) *The Vent and Seep Biota: Aspects from Microbes to Ecosystems*. Springer Netherlands, Dordrecht, pp 1-14. doi:10.1007/978-90-481-9572-5_1
- Kirchhoff H (2014) Diffusion of molecules and macromolecules in thylakoid membranes. *Biochimica et Biophysica Acta - Bioenergetics* 1837 (4):495-502. doi:10.1016/j.bbabi.2013.11.003

- Kirchhoff H, Hall C, Wood M, Herbstová M, Tsabari O, Nevo R, Charuvi D, Shimoni E *et al.* (2011) Dynamic control of protein diffusion within the granal thylakoid lumen. *Proceedings of the National Academy of Sciences* 108 (50):20248-20253. doi:10.1073/pnas.1104141109
- Kirchhoff H, Horstmann S, Weis E (2000) Control of the photosynthetic electron transport by PQ diffusion microdomains in thylakoids of higher plants. *Biochimica et Biophysica Acta - Bioenergetics* 1459 (1):148-168. doi:10.1016/S0005-2728(00)00143-2
- Kirchhoff H, Mukherjee U, Galla HJ (2002) Molecular architecture of the thylakoid membrane: Lipid diffusion space for plastoquinone. *Biochemistry* 41 (15):4872-4882. doi:10.1021/bi011650y
- Kirchhoff WR, Hall AE, Thomson WW (1989) Gas exchange, carbon isotope discrimination, and chloroplast ultrastructure of a chlorophyll-deficient mutant of cowpea. *Crop Science* 29 (1):109-115. doi:10.2135/cropsci1989.0011183X002900010026x
- Kirschbaum MUF, Gross LJ, Pearcy RW (1988) Observed and modelled stomatal responses to dynamic light environments in the shade plant *Alocasia macrorrhiza*. *Plant, Cell and Environment* 11 (2):111-121. doi:10.1111/1365-3040.ep11604898
- Kirschbaum MUF, Küppers M, Schneider H, Giersch C, Noe S (1998) Modelling photosynthesis in fluctuating light with inclusion of stomatal conductance, biochemical activation and pools of key photosynthetic intermediates. *Planta* 204 (1):16-26. doi:10.1007/s004250050225
- Kirschbaum MUF, Oja V, Laik A (2005) The quantum yield of CO₂ fixation is reduced for several minutes after prior exposure to darkness. Exploration of the underlying causes. *Plant Biology* 7 (1):58-66. doi:10.1055/s-2004-830476
- Kitano H (2002) Systems biology: A brief overview. *Science* 295:1662-1664. doi:10.1126/science.1069492
- Klughammer C, Schreiber U (2016) Deconvolution of ferredoxin, plastocyanin, and P700 transmittance changes in intact leaves with a new type of kinetic LED array spectrophotometer. *Photosynthesis Research* 128 (2):195-214. doi:10.1007/s11120-016-0219-0
- Knapp AK, Smith WK (1988) Effect of water stress on stomatal and photosynthetic responses in subalpine plants to cloud patterns. *American Journal of Botany* 75 (6):851-858. doi:10.2307/2444004
- Kniemeyer O, Buck-Sorlin GH, Kurth W (2007) GroIMP as a platform for functional-structural modelling of plants. In: Vos J, Marcelis LFM, Visser PHB, Struik PC, Evers JB (eds) *Functional-Structural Plant Modelling in Crop Production*. pp 43-52
- Kobayashi H, Baldocchi DD, Ryu Y, Chen Q, Ma S, Osuna JL, Ustin SL (2012) Modeling energy and carbon fluxes in a heterogeneous oak woodland: A three-dimensional approach. *Agricultural and Forest Meteorology* 152:83-100. doi:10.1016/j.agrformet.2011.09.008
- Kobza J, Edwards GE (1987) The photosynthetic induction response in wheat leaves: net CO₂ uptake, enzyme activation, and leaf metabolites. *Planta* 171:549-559. doi:10.1007/BF00392305
- Kohzuma K, Dal Bosco C, Kanazawa A, Dhingra A, Nitschke W, Meurer J, Kramer DM (2012) Thioredoxin-insensitive plastid ATP synthase that performs moonlighting

References

- functions. Proceedings of the National Academy of Sciences 109 (9):3293-3298. doi:10.1073/pnas.1115728109
- Kok B (1956) On the inhibition of photosynthesis by intense light. *Biochimica et Biophysica Acta* 21 (2):234-244. doi:10.1016/0006-3002(56)90003-8
- Kok B, Forbush B, McGloin M (1970) Cooperation of charges in photosynthetic O₂ evolution - I. A linear four step mechanism. *Photochemistry and Photobiology* 11 (6):457-475. doi:10.1111/j.1751-1097.1970.tb06017.x
- Kono M, Terashima I (2014) Long-term and short-term responses of the photosynthetic electron transport to fluctuating light. *Journal of Photochemistry and Photobiology B: Biology* 137:89-99. doi:10.1016/j.jphotobiol.2014.02.016
- Köpke-Secundo E, Molnar I, Schnarrenberger C (1990) Isolation and characterization of the cytosolic and chloroplastic 3-phosphoglycerate kinase from spinach leaves. *Plant Physiology* 93 (1):40-47. doi:10.1104/pp.93.1.40
- Krah NM, Logan BA (2010) Loss of PsbS expression reduces vegetative growth, reproductive output, and light-limited, but not light-saturated, photosynthesis in *Arabidopsis thaliana* (Brassicaceae) grown in temperate light environments. *American Journal of Botany* 97:644-649. doi:10.3732/ajb.0900163
- Kramer D, Crofts a (1993) The concerted reduction of the high- and low-potential chains of the bf complex by plastoquinol. *Biochimica et Biophysica Acta - Bioenergetics* 1183:72-84. doi:10.1016/0005-2728(93)90006-2
- Kramer DM, Avenson TJ, Edwards GE (2004a) Dynamic flexibility in the light reactions of photosynthesis governed by both electron and proton transfer reactions. *Trends in Plant Science* 9 (7):349-357. doi:10.1016/j.tplants.2004.05.001
- Kramer DM, Evans JR (2011) The importance of energy balance in improving photosynthetic productivity. *Plant Physiology* 155 (1):70-78. doi:10.1104/pp.110.166652
- Kramer DM, Johnson G, Kiirats O, Edwards GE (2004b) New fluorescence parameters for the determination of Q_A redox state and excitation energy fluxes. *Photosynthesis Research* 79:209-218. doi:10.1023/B:PRES.0000015391.99477.0d
- Kramer DM, Sacksteder CA, Cruz JA (1999) How acidic is the lumen? *Photosynthesis Research* 60 (2):151-163. doi:10.1023/A:1006212014787
- Kramer DM, Wise RR, Frederick JR, Alm DM, Hesketh JD, Ort DR, Crofts AR (1990) Regulation of coupling factor in field-grown sunflower: A Redox model relating coupling factor activity to the activities of other thioredoxin-dependent chloroplast enzymes. *Photosynthesis Research* 26:213-222. doi:10.1007/BF00033134
- Krause GH (1988) Photoinhibition of photosynthesis. An evaluation of damaging and protective mechanisms. *Physiologia Plantarum* 74 (3):566-574. doi:10.1111/j.1399-3054.1988.tb02020.x
- Krieger-Liszkay A, Kós PB, Hideg É (2011) Superoxide anion radicals generated by methylviologen in photosystem I damage Photosystem II. *Physiologia Plantarum* 142 (1):17-25. doi:10.1111/j.1399-3054.2010.01416.x
- Krieger A, Rutherford AW, Johnson GN (1995) On the determination of redox midpoint potential of the primary quinone electron acceptor, Q_A, in Photosystem II. *Biochimica et Biophysica Acta - Bioenergetics* 1229 (2):193-201. doi:10.1016/0005-2728(95)00002-Z
- Kromdijk J, Głowacka K, Leonelli L, Gabilly ST, Iwai M, Niyogi KK, Long SP (2016) Improving photosynthesis and crop productivity by accelerating recovery from photoprotection. *Science* 354 (6314):857-861. doi:10.1126/science.aai8878

- Kromer S (1995) Respiration during photosynthesis. *Annual Review of Plant Physiology and Plant Molecular Biology* 46 (1):45-70. doi:10.1146/annurev.pp.46.060195.000401
- Külheim C, Agren J, Jansson S (2002) Rapid regulation of light harvesting and plant fitness in the field. *Science* 297:91-93. doi:10.1126/science.1072359
- Kunz H-H, Gierth M, Herdean A, Satoh-Cruz M, Kramer DM, Spetea C, Schroeder JI (2014) Plastidial transporters KEA1, -2, and -3 are essential for chloroplast osmoregulation, integrity, and pH regulation in *Arabidopsis*. *Proceedings of the National Academy of Sciences* 111 (20):7480-7485. doi:10.1073/pnas.1323899111
- Küppers M, Pfiz M (2009) Role of photosynthetic induction for daily and annual carbon gains of leaves and plant canopies. In: Laisk A, Nedbal L, Govindjee (eds) *Photosynthesis in silico : Understanding Complexity from Molecules to Ecosystems*. Springer Netherlands, Dordrecht, pp 417-440. doi:10.1007/978-1-4020-9237-4_18
- Küppers M, Schneider H (1993) Leaf gas exchange of beech (*Fagus sylvatica* L.) seedlings in lightflecks: effects of fleck length and leaf temperature in leaves grown in deep and partial shade. *Trees* 7 (3):160-168. doi:10.1007/bf00199617
- Łabuz J, Hermanowicz P, Gabryś H (2015) The impact of temperature on blue light induced chloroplast movements in *Arabidopsis thaliana*. *Plant Science* 239:238-249. doi:10.1016/j.plantsci.2015.07.013
- Laing WA, Stitt M, Heldt HW (1981) Control of CO₂ fixation: Changes in the activity of ribulosephosphate kinase and fructose- and sedoheptulose-bisphosphatase in chloroplasts. *Biochimica et Biophysica Acta - Bioenergetics* 637 (2):348-359. doi:10.1016/0005-2728(81)90174-2
- Laisk A, Eichelmann H, Oja V (2006) C₃ photosynthesis in silico. *Photosynthesis Research* 90 (1):45-66. doi:10.1007/s1120-006-9109-1
- Laisk A, Eichelmann H, Oja V (2009a) Leaf C₃ photosynthesis in silico: Integrated carbon/nitrogen metabolism. In: Laisk A, Nedbal L, Govindjee (eds) *Photosynthesis in silico : Understanding Complexity from Molecules to Ecosystems*. Springer Netherlands, Dordrecht, pp 295-322. doi:10.1007/978-1-4020-9237-4_13
- Laisk A, Eichelmann H, Oja V (2009b) Leaf C₃ Photosynthesis in silico: Integrated Carbon/Nitrogen Metabolism. *Photosynthesis in silico*:295-322. doi:10.1007/978-1-4020-9237-4_13
- Laisk A, Eichelmann H, Oja V, Eatherall A, Walker DA (1989) A mathematical model of the carbon metabolism in photosynthesis. Difficulties in explaining oscillations by fructose 2,6-bisphosphate regulation. *Philosophical Transactions of the Royal Society B: Biological Sciences* 237. doi:10.1098/rspb.1989.0057
- Laisk a, Kiirats O, Oja V (1984) Assimilatory power (postillumination CO₂ uptake) in leaves: measurement, environmental dependencies, and kinetic properties. *Plant Physiology* 76 (3):723-729. doi:10.1104/pp.76.3.723
- Laisk A, Oja V, Eichelmann H (2012) Oxygen evolution and chlorophyll fluorescence from multiple turnover light pulses: charge recombination in photosystem II in sunflower leaves. *Photosynthesis Research* 113 (1):145-155. doi:10.1007/s1120-012-9751-8
- Laisk A, Oja V, Eichelmann H, Dall'Osto L (2014) Action spectra of photosystems II and I and quantum yield of photosynthesis in leaves in State 1. *Biochimica et*

References

- Biophysica Acta - Bioenergetics 1837 (2):315-325. doi:10.1016/j.bbabi.2013.12.001
- Laisk A, Walker DA (1989) A mathematical model of electron transport. Thermodynamic necessity for Photosystem II regulation: 'light stomata'. *Philosophical Transactions of the Royal Society B: Biological Sciences* 237 (1289):417-444. doi:10.1098/rspb.1989.0058
- Lan Y, Woodrow IE, Mott KA (1992) Light-dependent changes in ribulose biphosphate carboxylase activase activity in leaves. *Plant Physiology* 99:304-309. doi:10.1104/pp.99.1.304
- Lavergne J, Bouchard J-P, Joliot P (1992) Plastoquinone compartmentation in chloroplasts. II. Theoretical aspects. *Biochimica et Biophysica Acta - Bioenergetics* 1101 (1):13-22. doi:10.1016/0167-4838(92)90461-L
- Lavergne J, Trissl HW (1995) Theory of fluorescence induction in photosystem II: derivation of analytical expressions in a model including exciton-radical-pair equilibrium and restricted energy transfer between photosynthetic units. *Biophysical Journal* 68 (6):2474-2492. doi:10.1016/s0006-3495(95)80429-7
- Lawlor DW (2001) *Photosynthesis*. 3 edn. BIOS Scientific Publishers, Oxford
- Lawson T, Blatt MR (2014) Stomatal size, speed, and responsiveness impact on photosynthesis and water use efficiency. *Plant Physiology* 164 (4):1556-1570. doi:10.1104/pp.114.237107
- Lawson T, Caemmerer S, Baroli I (2011) Photosynthesis and stomatal behaviour. In: Lüttge EU, Beyschlag W, Büdel B, Francis D (eds) *Progress in Botany*, vol 72. Springer Berlin Heidelberg, Berlin, Heidelberg, pp 265-304. doi:10.1007/978-3-642-13145-5_11
- Lawson T, Simkin AJ, Kelly G, Granot D (2014) Mesophyll photosynthesis and guard cell metabolism impacts on stomatal behaviour. *New Phytologist* 203:1064-1081. doi:10.1111/nph.12945
- Lazár D (1999) Chlorophyll a fluorescence induction. *Biochimica et Biophysica Acta - Bioenergetics* 1412 (1):1-28. doi:10.1016/S0005-2728(99)00047-X
- Lazár D (2003) Chlorophyll a fluorescence rise induced by high light illumination of dark-adapted plant tissue studied by means of a model of photosystem II and considering photosystem II heterogeneity. *Journal of Theoretical Biology* 220 (4):469-503. doi:10.1006/jtbi.2003.3140
- Leakey ADB, Press MC, Scholes JD (2003) High-temperature inhibition of photosynthesis is greater under sunflecks than uniform irradiance in a tropical rain forest tree seedling. *Plant, Cell and Environment* 26 (10):1681-1690. doi:10.1046/j.1365-3040.2003.01086.x
- Leakey ADB, Press MC, Scholes JD, Watling JR (2002) Relative enhancement of photosynthesis and growth at elevated CO₂ is greater under sunflecks than uniform irradiance in a tropical rain forest tree seedling. *Plant, Cell and Environment* 25 (12):1701-1714. doi:10.1046/j.1365-3040.2002.00944.x
- Lebedeva GV, Belyaeva NE, Demin OV, Rizinchenko GY, Rubin AB (2002) Kinetic model of primary photosynthetic processes in chloroplasts. Description of the fast phase of chlorophyll fluorescence induction under different light intensities. *Biophysics* 47 (6):968-980
- Lemaire M, Miginiac-Maslow M, Decottignies P (1996) The catalytic site of chloroplastic NADP-dependent malate dehydrogenase contains a His/Asp pair. *European Journal of Biochemistry* 236 (3):947-952. doi:10.1111/j.1432-1033.1996.00947.x

- Léon-Kloosterziel KM, Gil MA, Ruijs GJ, Jacobsen SE, Olszewski NE, Schwartz SH, Zeevaart JAD, Koornneef M (1996) Isolation and characterization of abscisic acid-deficient *Arabidopsis* mutants at two new loci. *Plant Journal* 10 (4):655-661. doi:10.1046/j.1365-313X.1996.10040655.x
- Leuning R, Kelliher FM, Pury DGG, Schulze E-D (1995) Leaf nitrogen, photosynthesis, conductance and transpiration: scaling from leaves to canopies. *Plant, Cell and Environment* 18:1183-1200. doi:10.1111/j.1365-3040.1995.tb00628.x
- Lever MA, Rouxel O, Alt JC, Shimizu N, Ono S, Coggon RM, Shanks WC, Lapham L *et al.* (2013) Evidence for microbial carbon and sulfur cycling in deeply buried ridge flank basalt. *Science* 339 (6125):1305-1308. doi:10.1126/science.1229240
- Li T, Heuvelink E, van Noort F, Kromdijk J, Marcelis LFM (2014) Responses of two *Anthurium* cultivars to high daily integrals of diffuse light. *Scientia Horticulturae* 179:306-313. doi:10.1016/j.scienta.2014.09.039
- Li X-P, Bjorkman O, Shih C, Grossman AR, Rosenquist M, Jansson S, Niyogi KK (2000a) A pigment-binding protein essential for regulation of photosynthetic light harvesting. *Nature* 403 (6768):391-395
- Li X-P, Gilmore AM, Caffarri S, Bassi R, Golan T, Kramer D, Niyogi KK (2004) Regulation of photosynthetic light harvesting involves intrathylakoid lumen pH sensing by the PsbS protein. *Journal of Biological Chemistry* 279 (22):22866-22874. doi:10.1074/jbc.M402461200
- Li X-P, Muller-Moule P, Gilmore AM, Niyogi KK (2002) PsbS-dependent enhancement of feedback de-excitation protects photosystem II from photoinhibition. *Proceedings of the National Academy of Sciences* 99:15222-15227. doi:10.1073/pnas.232447699
- Li XP, Bjorkman O, Shih C, Grossman AR, Rosenquist M, Jansson S, Niyogi KK (2000b) A pigment-binding protein essential for regulation of photosynthetic light harvesting. *Nature* 403 (6768):391-395. doi:10.1038/35000131
- Lin ZF, Ehleringer J (1982) Changes in spectral properties of leaves as related to chlorophyll content and age of papaya. *Photosynthetica* 16 (4):520-525
- Lloyd CM, Halstead MDB, Nielsen PF (2004) CellML: its future, present and past. *Progress in Biophysics and Molecular Biology* 85 (2-3):433-450. doi:10.1016/j.pbiomolbio.2004.01.004
- Lobell DB, Cassman KG, Field CB (2009) Crop yield gaps: Their importance, magnitudes, and causes. *Annual Review of Environment and Resources* 34 (1):179-204. doi:10.1146/annurev.enviro.041008.093740
- Logan B, xa, A, Terry S, xa, G, Niyogi K, xa *et al.* (2008) Genotypes with differing levels of psbS expression differ in photosystem II quantum yield, xanthophyll cycle pool size, and aboveground growth. *International Journal of Plant Sciences* 169 (5):597-604. doi:10.1086/533597
- Lohammar T, Larsson S, Linder S, Falk SO (1980) FAST: Simulation models of gaseous exchange in Scots pine. *Ecological Bulletins* (32):505-523
- Long SP, Ainsworth EA, Leakey ADB, Nösberger J, Ort DR (2006a) Food for thought: Lower-than-expected crop yield stimulation with rising CO₂ concentrations. *Science* 312 (5782):1918-1921. doi:10.1126/science.1114722
- Long SP, Bernacchi CJ (2003) Gas exchange measurements, what can they tell us about the underlying limitations to photosynthesis? Procedures and sources of error. *Journal of Experimental Botany* 54:2393-2401. doi:10.1093/jxb/erg262

References

- Long SP, Humphries S, Falkowski PG (1994) Photoinhibition of photosynthesis in nature. *Annual Review of Plant Physiology and Plant Molecular Biology* 45:633-662. doi:10.1146/annurev.pp.45.060194.003221
- Long SP, Zhu XG, Naidu SL, Ort DR (2006b) Can improvement in photosynthesis increase crop yields? *Plant, Cell and Environment* 29 (3):315-330. doi:10.1111/j.1365-3040.2005.01493.x
- Loriaux SD, Avenso TJ, Welles JM, Mcdermitt DK, Eckles RD, Riensche B, Genty B (2013) Closing in on maximum yield of chlorophyll fluorescence using a single multiphase flash of sub-saturating intensity. *Plant, Cell and Environment* 36:1755-1770. doi:10.1111/pce.12115
- Lunn JE, Douce R (1993) Transport of inorganic pyrophosphate across the spinach chloroplast envelope. *Biochemical Journal* 290 (Pt 2):375-379. doi:10.1042/bj2900375
- Madin JS, Bowers S, Schildhauer MP, Jones MB (2008) Advancing ecological research with ontologies. *Trends in Ecology and Evolution* 23 (3):159-168. doi:10.1016/j.tree.2007.11.007
- Makino A (2003) Rubisco and nitrogen relationships in rice: Leaf photosynthesis and plant growth. *Soil Science and Plant Nutrition* 49:319-327. doi:10.1080/00380768.2003.10410016
- Makino A, Miyake C, Yokota A (2002) Physiological functions of the water-water cycle (Mehler reaction) and the cyclic electron flow around PSI in rice leaves. *Plant and Cell Physiology* 43 (9):1017-1026. doi:10.1093/pcp/pcf124
- Makino A, Sato T, Nakano H, Mae T (1997) Leaf photosynthesis, plant growth and nitrogen allocation in rice under different irradiances. *Planta* 203:390-398. doi:10.1007/s004250050205
- Malone J, Stevens R, Jupp S, Hancocks T, Parkinson H, Brooksbank C (2016) Ten simple rules for selecting a bio-ontology. *PLOS Computational Biology* 12 (2):e1004743. doi:10.1371/journal.pcbi.1004743
- Mate CJ, Hudson GS, von Caemmerer S, Evans JR, Andrews TJ (1993) Reduction of ribulose biphosphate carboxylase activase levels in tobacco (*Nicotiana tabacum*) by antisense RNA reduces ribulose biphosphate carboxylase carbamylation and impairs photosynthesis. *Plant Physiology* 102:1119-1128. doi:10.1104/pp.102.4.1119
- Mate CJ, von Caemmerer S, Evans JR, Hudson GS, Andrews TJ (1996) The relationship between CO₂-assimilation rate, Rubisco carbamylation and Rubisco activase content in activase-deficient transgenic tobacco suggests a simple model of activase action. *Planta* 198 (4):604-613. doi:10.1007/BF00262648
- Matrosova A, Bogireddi H, Mateo-Peñas A, Hashimoto-Sugimoto M, Iba K, Schroeder JI, Israelsson-Nordström MC (2015) The HT1 protein kinase is essential for red light-induced stomatal opening and genetically interacts with OST1 in red light and CO₂-induced stomatal movement responses. *New Phytologist* 208 (4):1126-1137. doi:10.1111/nph.13566
- Matson RS, Kimura T (1975) Immunological quantitation of chloroplast ferredoxin. *Biochimica et Biophysica Acta - Bioenergetics* 396 (2):293-300. doi:10.1016/0005-2728(75)90042-0
- Matsubara S, Chow WS (2004) Populations of photoinactivated photosystem II reaction centers characterized by chlorophyll a fluorescence lifetime *in vivo*. *Proceedings of the National Academy of Sciences* 101 (52):18234-18239. doi:10.1073/pnas.0403857102

- Matuszyńska A, Heidari S, Jahns P, Ebenhöf O (2016) A mathematical model of non-photochemical quenching to study short-term light memory in plants. *Biochimica et Biophysica Acta - Bioenergetics* 1857 (12):1860-1869. doi:10.1016/j.bbabi.2016.09.003
- Maxwell K, Johnson GN (2000) Chlorophyll fluorescence - a practical guide. *Journal of experimental botany* 51:659-668. doi:10.1093/jexbot/51.345.659
- McAlister ED, Myers J (1940) The time course of photosynthesis and fluorescence observed simultaneously. *Smithsonian Miscellaneous Collections*, vol 99. Smithsonian Institution, Washington D. C., U. S. A.
- McAusland L, Davey PA, Kanwal N, Baker NR, Lawson T (2013) A novel system for spatial and temporal imaging of intrinsic plant water use efficiency. *Journal of Experimental Botany* 64 (16):4993-5007. doi:10.1093/jxb/ert288
- McAusland L, Vialet-Chabrand S, Davey P, Baker NR, Brendel O, Lawson TC (2016) Effects of kinetics of light-induced stomatal responses on photosynthesis and water-use efficiency. *New Phytologist* 211 (4):1209-1220. doi:10.1111/nph.14000
- McCree KJ (1972) The action spectrum, absorptance and quantum yield of photosynthesis in crop plants. *Agricultural Meteorology* 9:191-216. doi:10.1016/0002-1571(71)90022-7
- McCree KJ, Loomis RS (1969) Photosynthesis in fluctuating light. *Ecology* 50 (3):422-428. doi:10.2307/1933892
- McNevin D, Von Caemmerer S, Farquhar G (2006) Determining RuBisCO activation kinetics and other rate and equilibrium constants by simultaneous multiple non-linear regression of a kinetic model. *Journal of Experimental Botany* 57:3883-3900. doi:10.1093/jxb/erl156
- McTavish H (1988) A demonstration of photosynthetic state transitions in nature - Shading by photosynthetic tissue causes conversion to state 1. *Photosynthesis Research* 17 (3):247-254. doi:10.1007/bf00035451
- Medlyn BE, Badeck FW, De Pury DGG, Barton CVM, Broadmeadow M, Ceulemans R, De Angelis P, Forstreuter M *et al.* (1999) Effects of elevated [CO₂] on photosynthesis in European forest species: a meta-analysis of model parameters. *Plant, Cell and Environment* 22 (12):1475-1495. doi:10.1046/j.1365-3040.1999.00523.x
- Medlyn BE, Dreyer E, Ellsworth D (2002) Temperature response of parameters of a biochemically-based model of photosynthesis. II. A review of experimental data. *Plant, Cell and Environment* 25:1167-1179. doi:10.1046/j.1365-3040.2002.00891.x
- Mekala NR, Suorsa M, Rantala M, Aro E-M, Tikkanen M (2015) Plants actively avoid state transitions upon changes in light intensity: Role of light-harvesting complex II protein dephosphorylation in high light. *Plant Physiology* 168 (2):721-734. doi:10.1104/pp.15.00488
- Melillo JM, McGuire AD, Kicklighter DW, Moore B, Vorosmarty CJ, Schloss AL (1993) Global climate change and terrestrial net primary production. *Nature* 363 (6426):234-240. doi:10.1038/363234a0
- Merilo E, Jõesaar I, Brosché M, Kollist H (2014) To open or to close: Species-specific stomatal responses to simultaneously applied opposing environmental factors. *New Phytologist* 202:499-508. doi:10.1111/nph.12667
- Mishra RK, Singhal GS (1992) Function of photosynthetic apparatus of intact wheat leaves under high light and heat stress and its relationship with peroxidation of thylakoid lipids. *Plant Physiology* 98 (1):1-6. doi:10.1104/pp.98.1.1

References

- Mishra Y, Johansson Jänkänpää H, Kiss AZ, Funk C, Schröder WP, Jansson S (2012) Arabidopsis plants grown in the field and climate chambers significantly differ in leaf morphology and photosystem components. *BMC Plant Biology* 12 (1):1-18. doi:10.1186/1471-2229-12-6
- Mitchell P (2011) Chemiosmotic coupling in oxidative and photosynthetic phosphorylation. *Biochimica et Biophysica Acta - Bioenergetics* 1807 (12):1507-1538. doi:10.1016/j.bbabi.2011.09.018
- Mizokami Y, Noguchi K, Kojima M, Sakakibara H, Terashima I (2014) Mesophyll conductance decreases in the wild type but not in an ABA-deficient mutant (*aba1*) of *Nicotiana glauca* under drought conditions. *Plant, Cell and Environment* 38:388-398. doi:10.1111/pce.12394
- Monsi M, Saeki T (1953) Über den Lichtfaktor in den Pflanzengesellschaften und seine Bedeutung für die Stoffproduktion. *Japanese Journal of Botany* 14:22-52. doi:10.1093/aob/mci052
- Monteith JL (1995) A reinterpretation of stomatal responses to humidity. *Plant, Cell and Environment* 18 (4):357-364. doi:10.1111/j.1365-3040.1995.tb00371.x
- Monteith JL, Unsworth MH (2013) *Principles of Environmental Physics*. 4 edn. Academic Press, Oxford, UK
- Montgomery RA, Givnish TJ (2008) Adaptive radiation of photosynthetic physiology in the Hawaiian lobeliads: dynamic photosynthetic responses. *Oecologia* 155 (3):455-467. doi:10.1007/s00442-007-0936-3
- Morales A, Leffelaar PA, Testi L, Orgaz F, Villalobos FJ (2016) A dynamic model of potential growth of olive (*Olea europaea* L.) orchards. *European Journal of Agronomy* 74:93-102. doi:10.1016/j.eja.2015.12.006
- Mott KA (2009) Opinion: Stomatal responses to light and CO₂ depend on the mesophyll. *Plant, Cell and Environment* 32 (11):1479-1486. doi:10.1111/j.1365-3040.2009.02022.x
- Mott KA, Woodrow IE (2000) Modelling the role of Rubisco activase in limiting non-steady-state photosynthesis. *Journal of Experimental Botany* 51 Spec No:399-406. doi: 10.1093/jexbot/51.suppl_1.399
- Mubarakshina MM, Ivanov BN, Naydov IA, Hillier W, Badger MR, Krieger-Liszkay A (2010) Production and diffusion of chloroplastic H₂O₂ and its implication to signalling. *Journal of Experimental Botany* 61 (13):3577-3587. doi:10.1093/jxb/erq171
- Munekage Y, Hojo M, Meurer J, Endo T, Tasaka M, Shikanai T (2002) PGR5 is involved in cyclic electron flow around Photosystem I and is essential for photoprotection in Arabidopsis. *Cell* 110 (3):361-371. doi:10.1016/S0092-8674(02)00867-X
- Murchie EH, Chen Y-z, Hubbart S, Peng S, Horton P (1999) Interactions between senescence and leaf orientation determine in situ patterns of photosynthesis and photoinhibition in field-grown rice. *Plant Physiology* 119:553-564. doi:10.1104/pp.119.2.553
- Murchie EH, Niyogi KK (2011) Manipulation of photoprotection to improve plant photosynthesis. *Plant Physiology* 155 (1):86-92. doi:10.1104/pp.110.168831
- Murray FW (1967) On the computation of saturation vapor pressure. *Journal of Applied Meteorology* 6:203-204. doi:10.1175/1520-0450(1967)006<0203:OTCOSV>2.0.CO;2
- Nagel OW, Konings H, Lambers H (1994) Growth rate, plant development and water relations of the ABA-deficient tomato mutant *sitiens*. *Physiologia Plantarum* 92 (1):102-108. doi:10.1111/j.1399-3054.1994.tb06661.x

- Nakamura N, Iwano M, Havaux M, Yokota A, Munekage YN (2013) Promotion of cyclic electron transport around photosystem I during the evolution of NADP-malic enzyme-type C4 photosynthesis in the genus *Flaveria*. *New Phytologist* 199 (3):832-842. doi:10.1111/nph.12296
- Naumburg E, Ellsworth DS (2000) Photosynthetic sunfleck utilization potential of understory saplings growing under elevated CO₂ in FACE. *Oecologia* 122 (2):163-174. doi:10.1007/pl00008844
- Naumburg E, Ellsworth DS (2002) Short-term light and leaf photosynthetic dynamics affect estimates of daily understory photosynthesis in four tree species. *Tree Physiology* 22:393-401. doi:10.1093/treephys/22.6.393
- Naumburg E, Ellsworth DS, Katul GG (2001a) Modeling dynamic understory photosynthesis of contrasting species in ambient and elevated carbon dioxide. *Oecologia* 126:487-499. doi:10.1007/s004420000543
- Naumburg E, Ellsworth DS, Pearcy RW (2001b) Crown carbon gain and elevated [CO₂]. Responses of understorey saplings with differing allometry and architecture. *Functional Ecology* 15 (2):263-273. doi:10.1046/j.1365-2435.2001.00518.x
- Navarro JA, Gleason FK, Cusanovich MA, Fuchs JA, Meyer TE, Tollin G (1991) Kinetics of electron transfer from thioredoxin reductase to thioredoxin. *Biochemistry* 30 (8):2192-2195. doi:10.1021/bi00222a024
- Nikkanen L, Rintamäki E (2014) Thioredoxin-dependent regulatory networks in chloroplasts under fluctuating light conditions. *Philosophical Transactions of the Royal Society B: Biological Sciences* 369 (1640). doi:10.1098/rstb.2013.0224
- Nilkens M, Kress E, Lambrev P, Miloslavina Y, Müller M, Holzwarth AR, Jahns P (2010) Identification of a slowly inducible zeaxanthin-dependent component of non-photochemical quenching of chlorophyll fluorescence generated under steady-state conditions in *Arabidopsis*. *Biochimica et Biophysica Acta - Bioenergetics* 1797:466-475. doi:10.1016/j.bbabi.2010.01.001
- Nishio JN, Whitmarsh J (1993) Dissipation of the proton electrochemical potential in intact chloroplasts II. The pH gradient monitored by cytochrome f reduction kinetics. *Plant Physiology* 101 (1):89-96. doi:10.1104/pp.101.1.89
- Niyogi KK, Grossman AR, Björkman O (1998) *Arabidopsis* mutants define a central role for the xanthophyll cycle in the regulation of photosynthetic energy conversion. *The Plant cell* 10:1121-1134. doi:10.1105/tpc.10.7.1121
- Niyogi KK, Li XP, Rosenberg V, Jung HS (2005) Is PsbS the site of non-photochemical quenching in photosynthesis? *Journal of Experimental Botany* 56:375-382. doi:10.1093/jxb/eri056
- Noctor G, Foyer CH (1998) A re-evaluation of the ATP:NADPH budget during C3 photosynthesis: a contribution from nitrate assimilation and its associated respiratory activity? *Journal of Experimental Botany* 49 (329):1895-1908. doi:10.1093/jxb/49.329.1895
- Noctor G, Foyer CH (2000) Homeostasis of adenylate status during photosynthesis in a fluctuating environment. *Journal of Experimental Botany* 51 Spec No:347-356. doi:10.1093/jexbot/51.suppl_1.347
- Noe SM, Giersch C (2004) A simple dynamic model of photosynthesis in oak leaves: Coupling leaf conductance and photosynthetic carbon fixation by a variable intracellular CO₂ pool. *Functional Plant Biology* 31:1195-1204. doi:10.1071/FP03251

References

- Norman JM, Jarvis PG (1975) Photosynthesis in Sitka spruce (*Picea sitchensis* (Bong.) Carr.): V. Radiation penetration theory and a test case. *Journal of Applied Ecology* 12 (3):839-878. doi:10.2307/2402094
- Norman JM, Welles JM (1983) Radiative transfer in an array of canopies. *Agronomy Journal* 75 (3):481-488. doi:10.2134/agronj1983.00021962007500030016x
- Ögren E, Sundin U (1996) Photosynthetic responses to variable light: a comparison of species from contrasting habitats. *Oecologia* 106 (1):18-27. doi:10.1007/bf00334403
- Oja V, Eichelmann H, Laisk A (2011) The size of the lumenal proton pool in leaves during induction and steady-state photosynthesis. *Photosynthesis Research* 110 (2):73-88. doi:10.1007/s11120-011-9697-2
- Ono T, Inoue Y (1988) Discrete extraction of the Ca atom functional for O₂ evolution in higher plant Photosystem II by a simple low pH treatment. *FEBS Letters* 227 (2):147-152. doi:10.1016/0014-5793(88)80886-x
- Ooba M, Takahashi H (2003) Effect of asymmetric stomatal response on gas-exchange dynamics. *Ecological Modelling* 164:65-82. doi:10.1016/S0304-3800(03)00012-7
- Ort DR, Zhu X, Melis A (2011) Optimizing antenna size to maximize photosynthetic efficiency. *Plant Physiology* 155 (1):79-85. doi:10.1104/pp.110.165886
- Osmond C, Oja V, Laisk A (1988) Regulation of carboxylation and photosynthetic oscillations during sun-shade acclimation in *Helianthus annuus* measured with a rapid-response gas exchange system. *Functional Plant Biology* 15 (2):239-251. doi:10.1071/PP9880239
- Osmond CB, Björkman O, Anderson DJ (1980) Photosynthesis. In: *Physiological Processes in Plant Ecology: Toward a Synthesis with Atriplex*. Ecological Studies, vol 36. Springer Berlin Heidelberg, Berlin, Heidelberg, pp 291-377. doi:10.1007/978-3-642-67637-6_9
- Osterhout WJV, Haas ARCC (1918) Dynamical aspects of photosynthesis. *Proceedings of the National Academy of Sciences* 4 (4):85-91. doi:10.1073/pnas.4.4.85
- Osyczka A, Moser CC, Dutton PL (2005) Fixing the Q cycle. *Trends in Biochemical Sciences* 30 (4):176-182. doi:10.1016/j.tibs.2005.02.001
- Ozturk I, Holst N, Ottosen C-O (2012) Simulation of leaf photosynthesis of C3 plants under fluctuating light and different temperatures. *Acta Physiologiae Plantarum* 34 (6):2319-2329. doi:10.1007/s11738-012-1033-8
- Pan Y, Birdsey RA, Fang J, Houghton R, Kauppi PE, Kurz WA, Phillips OL, Shvidenko A *et al.* (2011) A large and persistent carbon sink in the world's forests. *Science* 333 (6045):988-993. doi:10.1126/science.1201609
- Pänke O, Rumberg B (1996) Kinetic modelling of the proton translocating CF₀CF₁-ATP synthase from spinach. *FEBS Letters* 383:196-200. doi:10.1016/0014-5793(96)00246-3
- Pänke O, Rumberg B (1999) Kinetic modeling of rotary CF₀CF₁-ATP synthase: storage of elastic energy during energy transduction. *Biochimica et Biophysica Acta - Bioenergetics* 1412:118-128. doi:10.1016/S0005-2728(99)00059-6
- Papageorgiou GC, Govindjee (2014) The non-photochemical quenching of the electronically excited state of chlorophyll a in plants: definitions, timelines, viewpoints, open questions. In: Demmig-Adams B, Garab G, Adams III W, Govindjee (eds) *Non-Photochemical Quenching and Energy Dissipation in Plants, Algae and Cyanobacteria*. Springer Netherlands, Dordrecht, pp 1-44. doi:10.1007/978-94-017-9032-1_1

- Parkhurst DF, Mott KA (1990) Intercellular diffusion limits to CO₂ uptake in leaves: Studies in air and helox. *Plant Physiology* 94 (3):1024-1032. doi:10.1104/pp.94.3.1024
- Parry MAJ, Andralojc PJ, Scales JC, Salvucci ME, Carmo-Silva AE, Alonso H, Whitney SM (2013) Rubisco activity and regulation as targets for crop improvement. *Journal of Experimental Botany* 64 (3):717-730. doi:10.1093/jxb/ers336
- Peak D, Mott KA (2011) A new, vapour-phase mechanism for stomatal responses to humidity and temperature. *Plant, Cell and Environment* 34 (1):162-178. doi:10.1111/j.1365-3040.2010.02234.x
- Pearcy RW (1990) Sunflecks and photosynthesis in plant canopies. *Annual Review of Plant Biology* 41:421-453. doi:10.1146/annurev.arplant.41.1.421
- Pearcy RW, Gross LJ, He D (1997) An improved dynamic model of photosynthesis for estimation of carbon gain in sunfleck light regimes. *Plant, Cell and Environment* 20 (4):411-424. doi:10.1046/j.1365-3040.1997.d01-88.x
- Pearcy RW, Krall JP, Sassenrath-Cole GF (1996) Photosynthesis in fluctuating light environments. In: Baker NR (ed) *Photosynthesis and the Environment. Advances in Photosynthesis and Respiration*, vol 5. Kluwer Academic Publishers, Dordrecht, pp 321-346. doi:10.1007/0-306-48135-9_13
- Pearcy RW, Osteryoung K, Calkin HW (1985) Photosynthetic responses to dynamic light environments by Hawaiian trees: Time course of CO₂ uptake and carbon gain during sunflecks. *Plant Physiology* 79:896-902. doi:10.1104/pp.79.3.896
- Pearcy RW, Roden JS, Gamon JA (1990) Sunfleck dynamics in relation to canopy structure in a soybean (*Glycine max* (L.) Merr.) canopy. *Agricultural and Forest Meteorology* 52 (3):359-372. doi:10.1016/0168-1923(90)90092-K
- Pearcy RW, Way DA (2012) Two decades of sunfleck research: looking back to move forward. *Tree Physiology* 32 (9):1059-1061. doi:10.1093/treephys/tps084
- Pearcy RW, Yang W (1996) A three-dimensional crown architecture model for assessment of light capture and carbon gain by understory plants. *Oecologia* 108 (1):1-12. doi:10.1007/bf00333208
- Peguero-Pina JJ, Gil-Pelegrín E, Morales F (2013) Three pools of zeaxanthin in *Quercus coccifera* leaves during light transitions with different roles in rapidly reversible photoprotective energy dissipation and photoprotection. *Journal of Experimental Botany* 64 (6):1649-1661. doi:10.1093/jxb/ert024
- Peng L, Shimizu H, Shikanai T (2008) The chloroplast NAD(P)H dehydrogenase complex interacts with Photosystem I in Arabidopsis. *Journal of Biological Chemistry* 283 (50):34873-34879. doi:10.1074/jbc.M803207200
- Pepin S, Livingston NJ (1997) Rates of stomatal opening in conifer seedlings in relation to air temperature and daily carbon gain. *Plant, Cell and Environment* 20 (12):1462-1472. doi:10.1046/j.1365-3040.1997.d01-40.x
- Petersen J, Forster K, Turina P, Graber P (2012) Comparison of the H⁺/ATP ratios of the H⁺-ATP synthases from yeast and from chloroplast. *Proceedings of the National Academy of Sciences* 109 (28):11150-11155. doi:10.1073/pnas.1202799109
- Peterson RB (1983) Estimation of photorespiration based on the initial rate of postillumination CO₂ release: II. Effects of O₂, CO₂ and temperature. *Plant Physiology* 73 (4):983-988. doi:10.1104/pp.73.4.978
- Pettersson G, Ryde-Pettersson U (1988) A mathematical model of the Calvin photosynthesis cycle. *FEBS Journal* 175 (3):661-672. doi:10.1111/j.1432-1033.1988.tb14242.x

References

- Pfündel EE, Dilley RA (1993) The pH dependence of violaxanthin deepoxidation in isolated pea chloroplasts. *Plant Physiology* 101 (1):65-71. doi:10.1104/pp.101.1.65
- Pfündel EE, Klughammer C, Meister A, Cerovic ZG (2013) Deriving fluorometer-specific values of relative PSI fluorescence intensity from quenching of F_0 fluorescence in leaves of *Arabidopsis thaliana* and *Zea mays*. *Photosynthesis Research* 114 (3):189-206. doi:10.1007/s11120-012-9788-8
- Pogoryelov D, Klyszejko AL, Krasnoselska GO, Heller E-M, Leone V, Langer JD, Vonck J, Müller DJ *et al.* (2012) Engineering rotor ring stoichiometries in the ATP synthase. *Proceedings of the National Academy of Sciences* 109 (25):E1599-E1608. doi:10.1073/pnas.1120027109
- Pons TL, Pearcy RW, Seemann JR (1992) Photosynthesis in flashing light in soybean leaves grown in different conditions. I. Photosynthetic induction state and regulation of Ribulose-1,5-bisphosphate carboxylase activity. *Plant, Cell and Environment* 15:569-576. doi:10.1111/j.1365-3040.1992.tb01490.x
- Poolman MG, Fell DA, Thomas S (2000) Modelling photosynthesis and its control. *Journal of Experimental Botany* 51 Spec No (1):319-328. doi:10.1093/jexbot/51.suppl_1.319
- Portis AR (2003) Rubisco activase - Rubisco's catalytic chaperone. *Photosynthesis Research* 75:11-27. doi:10.1023/A:1022458108678
- Portis AR, Salvucci ME, Ogren WL (1986) Activation of ribulosebisphosphate carboxylase/oxygenase at physiological CO₂ and ribulosebisphosphate concentrations by Rubisco activase. *Plant Physiology* 82 (4):967-971. doi:10.1104/pp.82.4.967
- Pottosin I, Shabala S (2016) Transport across chloroplast membranes: Optimizing photosynthesis for adverse environmental conditions. *Molecular Plant* 9 (3):356-370. doi:10.1016/j.molp.2015.10.006
- Powell MJD (2009) The BOBYQA algorithm for bound constrained optimization without derivatives. NA Report NA2009/06:39
- Pradhan P, Fischer G, van Velthuizen H, Reusser DE, Kropp JP (2015) Closing yield gaps: How sustainable can we be? *PLOS ONE* 10 (6):e0129487. doi:10.1371/journal.pone.0129487
- Price GD, Evans JR, Caemmerer S, Yu J-W, Badger MR (1995) Specific reduction of chloroplast glyceraldehyde-3-phosphate dehydrogenase activity by antisense RNA reduces CO₂ assimilation via a reduction in ribulose bisphosphate regeneration in transgenic tobacco plants. *Planta* 195 (3):369-378. doi:10.1007/bf00202594
- Prinsley RT, Dietz K-J, Leegood RC (1986a) Regulation of photosynthetic carbon assimilation in spinach leaves after a decrease in irradiance. *Biochimica et Biophysica Acta - Bioenergetics* 849 (2):254-263. doi:10.1016/0005-2728(86)90032-0
- Prinsley RT, Hunt S, Smith AM, Leegood RC (1986b) The influence of a decrease in irradiance on photosynthetic carbon assimilation in leaves of *Spinacia oleracea* L. *Planta* 167 (3):414-420. doi:10.1007/bf00391348
- Quick WP, Fichtner K, Schulze E-D, Wendler R, Leegood RC, Mooney H, Rodermeil SR, Bogorad L *et al.* (1992) Decreased ribulose-1,5-bisphosphate carboxylase-oxygenase in transgenic tobacco transformed with "antisense" rbcS. *Planta* 188 (4):522-531. doi:10.1007/bf00197044

- R Core Team (2016) R: A language and environment for statistical computing. R Foundation for Statistical Computing, Vienna, Austria
- Raines CA (2003) The Calvin cycle revisited. *Photosynthesis Research* 75:1-10. doi:10.1023/A:1022421515027
- Raines CA (2011) Increasing photosynthetic carbon assimilation in C3 plants to improve crop yield: Current and future strategies. *Plant Physiology* 155 (1):36-42. doi:10.1104/pp.110.168559
- Raines CA, Lloyd JC, Dyer TA (1999) New insights into the structure and function of sedoheptulose-1,7-bisphosphatase; an important but neglected Calvin cycle enzyme. *50:1-8*. doi:10.1093/jxb/50.330.1
- Rappaport F, Guergova-Kuras M, Nixon PJ, Diner BA, Lavergne J (2002) Kinetics and pathways of charge recombination in Photosystem II. *Biochemistry* 41 (26):8518-8527. doi:10.1021/bi025725p
- Rawsthorne S, Hylton CM (1991) The relationship between the post-illumination CO₂ burst and glycine metabolism in leaves of C3 and C3-C4 intermediate species of *Moricandia*. *Planta* 186 (1):122-126. doi:10.1007/bf00201507
- Ray DK, Mueller ND, West PC, Foley JA (2013) Yield trends are insufficient to double global crop production by 2050. *PLOS ONE* 8 (6):e66428. doi:10.1371/journal.pone.0066428
- Razeghifard MR, Klughammer C, Pace RJ (1997) Electron paramagnetic resonance kinetic studies of the S states in spinach thylakoids. *Biochemistry* 36 (1):86-92. doi:10.1021/bi9614287
- Reed AJ, Canvin DT, Sherrard JH, Hageman RH (1983) Assimilation of [¹⁵N]nitrate and [¹⁵N]nitrite in leaves of five plant species under light and dark conditions. *Plant Physiology* 71 (2):291-294. doi:10.1104/pp.71.2.291
- Reinman S, Mathis P (1981) Influence of temperature on Photosystem II electron transfer reactions. *Biochimica et Biophysica Acta - Bioenergetics* 635 (2):249-258. doi:10.1016/0005-2728(81)90024-4
- Renger G, Eckert HJ, Bergmann A, Bernarding J, Liu B, Napiwotzki A, Reifarth F, Eichler HJ (1995) Fluorescence and spectroscopic studies of exciton trapping and electron transfer in Photosystem II of higher plants. *Australian Journal of Plant Physiology* 22 (2):167-181. doi:10.1071/PP9950167
- Retkute R, Smith-Unna SE, Smith RW, Burgess AJ, Jensen OE, Johnson GN, Preston SP, Murchie EH (2015) Exploiting heterogeneous environments: does photosynthetic acclimation optimize carbon gain in fluctuating light? *Journal of Experimental Botany* 66 (9):2437-2447. doi:10.1093/jxb/erv055
- Riikonen J, Holopainen T, Oksanen E, Vapaavuori E (2005) Leaf photosynthetic characteristics of silver birch during three years of exposure to elevated concentrations of CO₂ and O₃ in the field. *Tree Physiology* 25 (5):621-632. doi:10.1093/treephys/25.5.621
- Rintamäki E, Martinsuo P, Pursiheimo S, Aro EM (2000) Cooperative regulation of light-harvesting complex II phosphorylation via the plastoquinol and ferredoxin-thioredoxin system in chloroplasts. *Proceedings of the National Academy of Sciences* 97 (21):11644-11649. doi:10.1073/pnas.180054297
- Riznichenko GY, Belyaeva NE, Kovalenko IB, Rubin AB (2009) Mathematical and computer modeling of primary photosynthetic processes. *Biophysics* 54 (1):10-22. doi:10.1134/s0006350909010035
- Robinson JM (1988) Does O₂ photoreduction occur within chloroplasts in vivo? *Physiologia Plantarum* 72 (3):666-680. doi:10.1111/j.1399-3054.1988.tb09181.x

References

- Robinson SP (1985) Osmotic adjustment by intact isolated chloroplasts in response to osmotic stress and its effect on photosynthesis and chloroplast volume. *Plant Physiology* 79 (4):996-1002. doi:10.1104/pp.79.4.996
- Roden JS (2003) Modeling the light interception and carbon gain of individual fluttering aspen (*Populus tremuloides* Michx) leaves. *Trees* 17 (2):117-126. doi:10.1007/s00468-002-0213-3
- Roden JS, Pearcy RW (1993) Photosynthetic gas exchange response of poplars to steady-state and dynamic light environments. *Oecologia* 93 (2):208-214. doi:10.1007/BF00317673
- Roelofs TA, Lee CH, Holzwarth AR (1992) Global target analysis of picosecond chlorophyll fluorescence kinetics from pea chloroplasts: A new approach to the characterization of the primary processes in photosystem II α - and β -units. *Biophysical Journal* 61 (5):1147-1163. doi:10.1016/S0006-3495(92)81924-0
- Rogers A, Medlyn BE, Dukes JSC (2014) Improving representation of photosynthesis in Earth System Models. *New Phytologist* 204 (1):12-14. doi:10.1111/nph.12972
- Rojas-Pierce M, Whippe CW, Davis PA, Hangarter RP, Springer PS (2014) PLASTID MOVEMENT IMPAIRED1 mediates ABA sensitivity during germination and implicates ABA in light-mediated chloroplast movements. *Plant Physiology and Biochemistry* 83:185-193. doi:10.1016/j.plaphy.2014.07.014
- Rosenthal DM, Locke AM, Khozaei M, Raines CA, Long SP, Ort DR (2011) Over-expressing the C3 photosynthesis cycle enzyme Sedoheptulose-1-7 Bisphosphatase improves photosynthetic carbon gain and yield under fully open air CO₂ fumigation (FACE). *BMC Plant Biology* 11 (1):123. doi:10.1186/1471-2229-11-123
- Ruban AV, Belgio E (2014) The relationship between maximum tolerated light intensity and photoprotective energy dissipation in the photosynthetic antenna: chloroplast gains and losses. *Philosophical Transactions of the Royal Society B: Biological Sciences* 369 (1640):20130222. doi:10.1098/rstb.2013.0222
- Ruban AV, Johnson MP (2009) Dynamics of higher plant photosystem cross-section associated with state transitions. *Photosynthesis Research* 99 (3):173-183. doi:10.1007/s11120-008-9387-x
- Ruban AV, Johnson MP, Duffy CDP (2012) The photoprotective molecular switch in the Photosystem II antenna. *Biochimica et Biophysica Acta - Bioenergetics* 1817 (1):167-181. doi:10.1016/j.bbabi.2011.04.007
- Ruelland E, Miginiac-Maslow M (1999) Regulation of chloroplast enzyme activities by thioredoxins: activation or relief from inhibition? *Trends in Plant Science* 4 (4):136-141. doi:10.1016/S1360-1385(99)01391-6
- Rutherford AW, Osyczka A, Rappaport F (2012) Back-reactions, short-circuits, leaks and other energy wasteful reactions in biological electron transfer: Redox tuning to survive life in O₂. *FEBS Letters* 586 (5):603-616. doi:10.1016/j.febslet.2011.12.039
- Ruuska S, Andrews TJ, Badger MR, Hudson GS, Laisk A, Price GD, Caemmerer Sv (1999) The interplay between limiting processes in C₃ photosynthesis studied by rapid-response gas exchange using transgenic tobacco impaired in photosynthesis. *Functional Plant Biology* 25 (8):859-870. doi:10.1071/PP98079
- Ruuska SA, Badger MR, Andrews TJ, von Caemmerer S (2000) Photosynthetic electron sinks in transgenic tobacco with reduced amounts of Rubisco: little evidence for significant Mehler reaction. *Journal of Experimental Botany* 51 (suppl 1):357-368. doi:10.1093/jexbot/51.suppl_1.357

- Sacksteder CA, Jacoby ME, Kramer DM (2001) A portable, non-focusing optics spectrophotometer (NoFOSpec) for measurements of steady-state absorbance changes in intact plants. *Photosynthesis Research* 70:231-240. doi:10.1023/A:1017906626288
- Sacksteder CA, Kanazawa A, Jacoby ME, Kramer DM (2000) The proton to electron stoichiometry of steady-state photosynthesis in living plants: A proton-pumping Q cycle is continuously engaged. *Proceedings of the National Academy of Sciences* 97 (26):14283-14288. doi:10.1073/pnas.97.26.14283
- Sacksteder CA, Kramer DM (2000) Dark-interval relaxation kinetics (DIRK) of absorbance changes as a quantitative probe of steady-state electron transfer. *Photosynthesis Research* 66:145-158. doi:10.1023/A:1010785912271
- Sage RF, Kubien DS (2007) The temperature response of C3 and C4 photosynthesis. *Plant, Cell and Environment* 30 (9):1086-1106. doi:10.1111/j.1365-3040.2007.01682.x
- Sage RF, Stata M (2015) Photosynthetic diversity meets biodiversity: The C4 plant example. *Journal of Plant Physiology* 172:104-119. doi:10.1016/j.jplph.2014.07.024
- Salvucci ME, Crafts-Brandner SJ (2004) Inhibition of photosynthesis by heat stress: the activation state of Rubisco as a limiting factor in photosynthesis. *Physiologia Plantarum* 120 (2):179-186. doi:10.1111/j.0031-9317.2004.0173.x
- Salvucci ME, Portis AR, Ogren WL (1985) A soluble chloroplast protein catalyzes ribulosebisphosphate carboxylase/oxygenase activation *in vivo*. *Photosynthesis Research* 7 (2):193-201. doi:10.1007/bf00037012
- Salvucci ME, Werneke JM, Ogren WL, Portis AR (1987) Purification and species distribution of Rubisco activase. *Plant Physiology* 84 (3):930-936. doi:10.1104/pp.84.3.930
- Sassenrath-Cole GF, Pearcy RW (1992) The role of ribulose-1,5-bisphosphate regeneration in the induction requirement of photosynthetic CO₂ exchange under transient light conditions. *Plant Physiology* 99:227-234. doi:10.1104/pp.99.1.227
- Sassenrath-Cole GF, Pearcy RW (1994a) Regulation of photosynthetic induction state by the magnitude and duration of low light exposure. *Plant Physiology* 105 (4):1115-1123. doi:10.1104/pp.105.4.1115
- Sassenrath-Cole GF, Pearcy RW (1994b) Regulation of photosynthetic induction state by the magnitude and duration of low light exposure. *Plant Physiology* 105:1115-1123. doi:10.1104/pp.105.4.1115
- Sassenrath-Cole GF, Pearcy RW, Steinmaus S (1994) The role of enzyme activation state in limiting carbon assimilation under variable light conditions. *Photosynthesis Research* 41 (2):295-302. doi:10.1007/BF00019407
- Savikhin S (2006) Ultrafast optical spectroscopy of Photosystem I. In: Golbeck JH (ed) *Photosystem I: The Light-Driven Plastocyanin:Ferredoxin Oxidoreductase*, vol 24. *Advances in Photosynthesis and Respiration*. Springer Netherlands, Dordrecht, pp 155-175. doi:10.1007/978-1-4020-4256-0_12
- Scales JC, Parry MaJ, Salvucci ME (2014) A non-radioactive method for measuring Rubisco activase activity in the presence of variable ATP: ADP ratios, including modifications for measuring the activity and activation state of Rubisco. *Photosynthesis Research* 119:355-365. doi:10.1007/s11120-013-9964-5
- Scheibe R (1981) Thioredoxin_m in pea chloroplasts: concentration and redox state under light and dark conditions. *FEBS Letters* 133 (2):301-304. doi:10.1016/0014-5793(81)80529-7

References

- Schimkat D, Heineke D, Heldt HW (1990) Regulation of sedoheptulose-1,7-bisphosphatase by sedoheptulose-7-phosphate and glycerate, and of fructose-1,6-bisphosphatase by glycerate in spinach chloroplasts. *Planta* 181 (1):97-103. doi:10.1007/BF00202330
- Scholl RL, May ST, Ware DH (2000) Seed and molecular resources for Arabidopsis. *Plant Physiology* 124 (4):1477-1480. doi:10.1104/pp.124.4.1477
- Schöttler MA, Tóth SZ (2014) Photosynthetic complex stoichiometry dynamics in higher plants: environmental acclimation and photosynthetic flux control. *Frontiers in Plant Science* 5:188. doi:10.3389/fpls.2014.00188
- Schumaker MF, Kramer DM (2011) Comparison of Monte Carlo simulations of cytochrome b₆f with experiment using latin hypercube sampling. *Bulletin of Mathematical Biology* 73 (9):2152-2174. doi:10.1007/s11538-010-9616-2
- Schurmann P (2003) Redox signaling in the chloroplast: the ferredoxin/thioredoxin system. *Antioxidants & Redox Signaling* 5 (1):69-78. doi:10.1089/152308603321223559
- Schürmann P (2002) Ferredoxin-dependent thioredoxin reductase: A unique iron-sulfur protein. In: Helmut S, Lester P (eds) *Methods in enzymology*, vol 347. Academic Press, pp 403-411. doi:10.1016/S0076-6879(02)47040-1
- Schürmann P, Buchanan BB (2008) The ferredoxin/thioredoxin system of oxygenic photosynthesis. *Antioxidants & Redox Signaling* 10 (7):1235-1274. doi:10.1089/ars.2007.1931
- Schwarz O, Schurmann P, Strotmann H (1997) Kinetics and thioredoxin specificity of thiol modulation of the chloroplast H⁺-ATPase. *Journal of Biological Chemistry* 272:16924-16927. doi:10.1074/jbc.272.27.16924
- Schymanski SJ, Or D, Zwieniecki M (2013) Stomatal control and leaf thermal and hydraulic capacitances under rapid environmental fluctuations. *PLOS ONE* 8 (1):e54231. doi:10.1371/journal.pone.0054231
- Seelert H, Poetsch A, Dencher NA, Engel A, Stahlberg H, Müller DJ (2000) Structural biology. Proton-powered turbine of a plant motor. *Nature* 405:418-419. doi:10.1038/35013148
- Seemann JR, Miko UFK, Sharkey TD, Pearcy RW (1988) Regulation of ribulose-1,5-bisphosphate carboxylase activity in *Alocasia macrorrhiza* in response to step changes in irradiance. *Plant Physiology* 88 (1):148-152. doi:10.1104/pp.88.1.148
- Servaites JC, Shieh W-J, Geiger DR (1991) Regulation of photosynthetic carbon reduction cycle by ribulose bisphosphate and phosphoglyceric acid. *Plant Physiology* 97 (3):1115-1121. doi:10.1104/pp.97.3.1115
- Sétif P (2001) Ferredoxin and flavodoxin reduction by Photosystem I. *Biochimica et Biophysica Acta - Bioenergetics* 1507 (1-3):161-179. doi:10.1016/S0005-2728(01)00205-5
- Šetlík I, Suleyman A, Nedbal L, Setlikova E, Klimov VV (1990) Three types of Photosystem II photoinactivation. 1. Damaging processes on the acceptor side. *Photosynthesis Research* 23 (1):39-48. doi:10.1007/BF00030061
- Shan X, Wang J, Chua L, Jiang D, Peng W, Xie D (2011) The role of Arabidopsis Rubisco activase in jasmonate-induced leaf senescence. *Plant Physiology* 155 (2):751-764. doi:10.1104/pp.110.166595
- Sharkey TD (1985) O₂-insensitive photosynthesis in C₃ plants. *Plant Physiology* 78:71-75. doi:10.1104/pp.78.1.71

- Sharkey TD (1989) Evaluating the role of Rubisco regulation in photosynthesis of C3 plants. *Philosophical Transactions of the Royal Society B: Biological Sciences* 323:435-448. doi:10.1098/rstb.1989.0022
- Sharkey TD (2015) What gas exchange data can tell us about photosynthesis. *Plant, Cell & Environment*:n/a-n/a. doi:10.1111/pce.12641
- Sharkey TD (2016) What gas exchange data can tell us about photosynthesis. *Plant, Cell and Environment* 39 (6):1161-1163. doi:10.1111/pce.12641
- Sharkey TD, Bernacchi CJ, Farquhar GD, Singsaas EL (2007) Fitting photosynthetic carbon dioxide response curves for C3 leaves. *Plant, Cell and Environment* 30:1035-1040. doi:10.1111/j.1365-3040.2007.01710.x
- Sharkey TD, Seemann JR, Berry JA (1986a) Regulation of ribulose-1,5-bisphosphate carboxylase activity in response to changing partial pressure of O₂ and light in *Phaseolus vulgaris*. *Plant Physiology* 81 (3):788-791. doi:10.1104/pp.81.3.788
- Sharkey TD, Seemann JR, Percy RW (1986b) Contribution of metabolites of photosynthesis to postillumination CO₂ assimilation in response to lightflecks. *Plant Physiology* 82:1063-1068. doi:10.1104/pp.82.4.1063
- Sharkey TD, Vanderveer PJ (1989) Stromal phosphate concentration is low during feedback limited photosynthesis. *Plant Physiology* 91:679-684. doi:10.1104/pp.91.2.679
- Shikanai T (2014) Central role of cyclic electron transport around photosystem I in the regulation of photosynthesis. *Current Opinion in Biotechnology* 26:25-30. doi:10.1016/j.copbio.2013.08.012
- Shikanai T (2016) Chloroplast NDH: A different enzyme with a structure similar to that of respiratory NADH dehydrogenase. *Biochimica et Biophysica Acta - Bioenergetics* 1857 (7):1015-1022. doi:10.1016/j.bbabi.2015.10.013
- Shinkarev VP, Zybailov B, Vassiliev IR, Golbeck JH (2002) Modeling of the P700⁺ charge recombination kinetics with phylloquinone and plastoquinone-9 in the A₁ site of Photosystem I. *Biophysical Journal* 83 (6):2885-2897. doi:10.1016/S0006-3495(02)75298-3
- Siebbe K, Laisk A, Oja V, Kiirats O, Raschke K, Heber U (1990) Control of photosynthesis in leaves as revealed by rapid gas exchange and measurements of the assimilatory force F_A. *Planta* 182 (4):513-522. doi:10.1007/bf02341026
- Simkin AJ, McAusland L, Headland LR, Lawson T, Raines CA (2015) Multigene manipulation of photosynthetic carbon assimilation increases CO₂ fixation and biomass yield in tobacco. *Journal of Experimental Botany*:1-16. doi:10.1093/jxb/erv204
- Smith WK, Berry ZC (2013) Sunflecks? *Tree Physiology* 33 (3):233-237. doi:10.1093/treephys/tpt005
- Soetaert K, Cash J, Mazzia F (2012) Initial Value Problems. In: *Solving Differential Equations in R*. Springer Berlin Heidelberg, Berlin, Heidelberg, pp 15-40. doi:10.1007/978-3-642-28070-2_2
- Solovchenko A (2010) Optical screening as a photoprotective mechanism. In: *Photoprotection in Plants: Optical Screening-Based Mechanisms*. Springer Berlin Heidelberg, Berlin, Heidelberg. doi:10.1007/978-3-642-13887-4_1
- Somersalo S, Krause GH (1989) Photoinhibition at chilling temperature. *Planta* 177 (3):409-416. doi:10.1007/bf00403600
- Spitters CJT, Toussaint HAJM, Goudriaan J (1986) Separating the diffuse and direct component of global radiation and its implications for modeling canopy

References

- photosynthesis. Part I. Components of incoming radiation. *Agricultural and Forest Meteorology* 38:217-229. doi:10.1016/0168-1923(86)90060-2
- Stec B (2012) Structural mechanism of RuBisCO activation by carbamylation of the active site lysine. *Proceedings of the National Academy of Sciences* 109 (46):18785-18790. doi:10.1073/pnas.1210754109
- Stegemann J, Timm H-C, Küppers M (1999) Simulation of photosynthetic plasticity in response to highly fluctuating light: an empirical model integrating dynamic photosynthetic induction and capacity. *Trees* 14:0145. doi:10.1007/s004680050219
- Steigmiller S, Turina P, Gräber P (2008) The thermodynamic H⁺/ATP ratios of the H⁺-ATP synthases from chloroplasts and *Escherichia coli*. *Proceedings of the National Academy of Sciences* 105 (10):3745-3750. doi:10.1073/pnas.0708356105
- Stirbet A, Govindjee (2011) On the relation between the Kautsky effect (chlorophyll a fluorescence induction) and Photosystem II: Basics and applications of the OJIP fluorescence transient. *Journal of Photochemistry and Photobiology B: Biology* 104 (1-2):236-257. doi:10.1016/j.jphotobiol.2010.12.010
- Stirbet A, Govindjee, Strasser BJ, Strasser RJ (1998) Chlorophyll a fluorescence induction in higher plants: modelling and numerical simulation. *Journal of Theoretical Biology* 193 (1):131-151. doi:10.1006/jtbi.1998.0692
- Stitt M, Gibon Y (2014) Why measure enzyme activities in the era of systems biology? *Trends in Plant Science* 19:256-265. doi:10.1016/j.tplants.2013.11.003
- Stitt M, Grosse H (1988) Interactions between sucrose synthesis and CO₂ fixation I. Secondary kinetics during photosynthetic induction are related to a delayed activation of sucrose synthesis. *Journal of Plant Physiology* 133:129-137. doi:10.1016/S0176-1617(88)80127-5
- Stitt M, Lunn J, Usadel B (2010) Arabidopsis and primary photosynthetic metabolism - More than the icing on the cake. *Plant Journal* 61:1067-1091. doi:10.1111/j.1365-313X.2010.04142.x
- Stitt M, Wirtz W, Heldt HW (1980) Metabolite levels during induction in the chloroplast and extrachloroplast compartments of spinach protoplasts. *Biochimica et Biophysica Acta* 593 (1):85-102. doi:10.1016/0005-2728(80)90010-9
- Strand DD, Fisher N, Davis GA, Kramer DM (2016a) Redox regulation of the antimycin A sensitive pathway of cyclic electron flow around photosystem I in higher plant thylakoids. *Biochimica et Biophysica Acta - Bioenergetics* 1857 (1):1-6. doi:10.1016/j.bbabi.2015.07.012
- Strand DD, Fisher N, Kramer DM (2016b) The higher plant plastid complex I (NDH) is a reversible proton pump that increases ATP production by cyclic electron flow around Photosystem I. *bioRxiv*. doi:10.1101/049759
- Strand DD, Kramer DM (2014) Control of non-photochemical exciton quenching by the proton circuit of photosynthesis. In: Demmig-Adams B, Garab G, Adams III W, Govindjee (eds) *Non-photochemical quenching and energy dissipation in plants, algae and cyanobacteria*, vol 40. *Advances in Photosynthesis and Respiration*. Springer Netherlands, Dordrecht, pp 387-408. doi:10.1007/978-94-017-9032-1_18
- Strand DD, Livingston AK, Satoh-Cruz M, Froehlich JE, Maurino VG, Kramer DM (2015) Activation of cyclic electron flow by hydrogen peroxide in vivo. *Proceedings of the National Academy of Sciences* 112 (17):5539-5544. doi:10.1073/pnas.1418223112

- Strelow F, Rumberg B (1993) Kinetics and energetics of redox regulation of ATP synthase from chloroplasts. *FEBS Letters* 323 (1-2):19-22. doi:10.1016/0014-5793(93)81439-7
- Sun J, Edwards GE, Okita TW (1999) Feedback inhibition of photosynthesis in rice measured by O₂ dependent transients. *Photosynthesis Research* 59 (2):187-200. doi:10.1023/a:1006180102395
- Sun J, Zhang J, Larue CT, Huber SC (2011) Decrease in leaf sucrose synthesis leads to increased leaf starch turnover and decreased RuBP regeneration-limited photosynthesis but not Rubisco-limited photosynthesis in Arabidopsis null mutants of SPSA1. *Plant, Cell and Environment* 34 (4):592-604. doi:10.1111/j.1365-3040.2010.02265.x
- Suorsa M, Järvi S, Grieco M, Nurmi M, Pietrzykowska M, Rantala M, Kangasjärvi S, Paakkari V *et al.* (2012) PROTON GRADIENT REGULATION5 Is essential for proper acclimation of Arabidopsis Photosystem I to naturally and artificially fluctuating light conditions. *The Plant Cell* 24 (7):2934-2948. doi:10.1105/tpc.112.097162
- Sylak-Glassman EJ, Zaks J, Amarnath K, Leuenberger M, Fleming GR (2016) Characterizing non-photochemical quenching in leaves through fluorescence lifetime snapshots. *Photosynthesis Research* 127 (1):69-76. doi:10.1007/s11120-015-0104-2
- Szeicz G (1974) Solar radiation for plant growth. *Journal of Applied Ecology* 11 (2):617-636. doi:10.2307/2402214
- Tagawa K, Arnon DI (1962) Ferredoxins as electron carriers in photosynthesis and in the biological production and consumption of hydrogen gas. *Nature* 195 (4841):537-543. doi:10.1038/195537a0
- Takahama U, Shimizu-Takahama M, Heber U (1981) The redox state of the NADP system in illuminated chloroplasts. *Biochimica et Biophysica Acta - Bioenergetics* 637 (3):530-539. doi:10.1016/0005-2728(81)90060-8
- Takahashi H, Kopriva S, Giordano M, Saito K, Hell R (2011) Sulfur assimilation in photosynthetic organisms: Molecular functions and regulations of transporters and assimilatory enzymes. *Annual Review of Plant Biology* 62 (1):157-184. doi:10.1146/annurev-arplant-042110-103921
- Takahashi S, Murata N (2008) How do environmental stresses accelerate photoinhibition? *Trends in Plant Science* 13 (4):178-182. doi:10.1016/j.tplants.2008.01.005
- Takizawa K, Cruz JA, Kanazawa A, Kramer DM (2007) The thylakoid proton motive force in vivo. Quantitative, non-invasive probes, energetics, and regulatory consequences of light-induced pmf. *Biochimica et Biophysica Acta - Bioenergetics* 1767 (10):1233-1244. doi:10.1016/j.bbabi.2007.07.006
- Takizawa K, Kanazawa A, Kramer DM (2008) Depletion of stromal Pi induces high 'energy-dependent' antenna exciton quenching (q_E) by decreasing proton conductivity at CF₀-CF₁ ATP synthase. *Plant, Cell and Environment* 31 (2):235-243. doi:10.1111/j.1365-3040.2007.01753.x
- Tanaka A, Makino A (2009) Photosynthetic research in plant science. *Plant and Cell Physiology* 50 (4):681-683. doi:10.1093/pcp/pcp040
- Taniguchi M, Miyake H (2012) Redox-shuttling between chloroplast and cytosol: Integration of intra-chloroplast and extra-chloroplast metabolism. *Current Opinion in Plant Biology* 15:252-260. doi:10.1016/j.pbi.2012.01.014

References

- Tausz M, Warren CR, Adams MA (2005) Dynamic light use and protection from excess light in upper canopy and coppice leaves of *Nothofagus cunninghamii* in an old growth, cool temperate rainforest in Victoria, Australia. *New Phytologist* 165 (1):143-155. doi:10.1111/j.1469-8137.2004.01232.x
- Tcherkez G (2013) Modelling the reaction mechanism of ribulose-1,5-bisphosphate carboxylase/oxygenase and consequences for kinetic parameters. *Plant, Cell and Environment* 36:1586-1596. doi:10.1111/pce.12066
- Terashima I, Fujita T, Inoue T, Chow WS, Oguchi R (2009) Green light drives leaf photosynthesis more efficiently than red light in strong white light: Revisiting the enigmatic question of why leaves are green. *Plant and Cell Physiology* 50:684-697. doi:10.1093/pcp/pcp034
- Terashima I, Saeki T (1985) A new model for leaf photosynthesis incorporating the gradients of light environment and of photosynthetic properties of chloroplasts within a leaf. *Annals of Botany* 56 (4):489-499
- Tholen D, Boom C, Noguchi KO, Ueda S, Katase T, Terashima I (2008) The chloroplast avoidance response decreases internal conductance to CO₂ diffusion in *Arabidopsis thaliana* leaves. *Plant, Cell and Environment* 31 (11):1688-1700. doi:10.1111/j.1365-3040.2008.01875.x
- Tholen D, Ethier G, Genty B, Pepin S, Zhu X-G (2012) Variable mesophyll conductance revisited: theoretical background and experimental implications. *Plant, Cell and Environment* 35:2087-2103. doi:10.1111/j.1365-3040.2012.02538.x
- Tholen D, Zhu XG (2011) The mechanistic basis of internal conductance: A theoretical analysis of mesophyll cell photosynthesis and CO₂ diffusion. *Plant Physiology* 156 (1):90-105. doi:10.1104/pp.111.172346
- Tikhonov AN, Vershubskii AV (2014) Computer modeling of electron and proton transport in chloroplasts. *BioSystems* 121:1-21. doi:10.1016/j.biosystems.2014.04.007
- Tikkanen M, Grieco M, Nurmi M, Rantala M, Suorsa M, Aro EM (2012) Regulation of the photosynthetic apparatus under fluctuating growth light. *Philosophical Transactions of the Royal Society B: Biological Sciences* 367 (1608):3486-3493. doi:10.1098/rstb.2012.0067
- Tilman D, Cassman KG, Matson Pa, Naylor R, Polasky S (2002) Agricultural sustainability and intensive production practices. *Nature* 418:671-677. doi:10.1038/nature01014
- Tilman D, Socolow R, Foley JA, Hill J, Larson E, Lynd L, Pacala S, Reilly J *et al.* (2009) Beneficial biofuels - the food, energy, and environment trilemma. *Science* 325 (5938):270-271. doi:10.1126/science.1177970
- Timm H-C, Küppers M, Stegemann J (2004) Non-destructive analysis of architectural expansion and assimilate allocation in different tropical tree saplings: consequences of using steady-state and dynamic photosynthesis models. *Ecotropa* 10 (2):101-121
- Tinoco-Ojanguren C, Pearcy RW (1993a) Stomatal dynamics and its importance to carbon gain in two rainforest *Piper* species. I. VPD effects on the transient stomatal response to lightflecks. *Oecologia* 94 (3):388-394. doi:10.1007/BF00317115
- Tinoco-Ojanguren C, Pearcy RW (1993b) Stomatal dynamics and its importance to carbon gain in two rainforest *Piper* species. II. Stomatal versus biochemical limitations during photosynthetic induction. *Oecologia* 94:395-402. doi:10.1007/BF00317115

- Tomimatsu H, Iio A, Adachi M, Saw LG, Fletcher C, Tang Y (2014) High CO₂ concentration increases relative leaf carbon gain under dynamic light in *Dipterocarpus sublamellatus* seedlings in a tropical rain forest, Malaysia. *Tree Physiology* 34 (9):944-954. doi:10.1093/treephys/tpu066
- Tomimatsu H, Tang Y (2012) Elevated CO₂ differentially affects photosynthetic induction response in two *Populus* species with different stomatal behavior. *Oecologia* 169 (4):869-878. doi:10.1007/s00442-012-2256-5
- Tremmel IG, Kirchhoff H, Weis E, Farquhar GD (2003) Dependence of plastoquinol diffusion on the shape, size, and density of integral thylakoid proteins. *Biochimica et Biophysica Acta - Bioenergetics* 1607 (2-3):97-109. doi:10.1016/j.bbabi.2003.09.004
- Turina P, Samoray D, Gräber P (2003) H⁺/ATP ratio of proton transport-coupled ATP synthesis and hydrolysis catalysed by CF₀F₁-liposomes. *The EMBO Journal* 22 (3):418-426. doi:10.1093/emboj/cdg073
- Tyystjärvi E, Hakala M, Sarvikas P (2005) Mathematical modelling of the light response curve of photoinhibition of Photosystem II. *Photosynthesis Research* 84:21-27. doi:10.1007/s11120-004-7174-x
- U.N. (2015) World Population Prospects: The 2015 Revision, Key Findings and Advance Tables. Working Paper No. ESA/P/WP.241. United Nations, Department of Economic and Social Affairs, Population Division New York, U. S. A.
- Ueda T, Nomoto N, Koga M, Ogasa H, Ogawa Y, Matsumoto M, Stampoulis P, Sode K *et al.* (2012) Structural basis of efficient electron transport between photosynthetic membrane proteins and plastocyanin in spinach revealed using nuclear magnetic resonance. *The Plant Cell* 24 (10):4173-4186. doi:10.1105/tpc.112.102517
- Ustin SL, Jacquemoud S, Govaerts Y (2001) Simulation of photon transport in a three-dimensional leaf: Implications for photosynthesis. *Plant, Cell and Environment* 24 (10):1095-1103. doi:10.1046/j.0016-8025.2001.00762.x
- Valladares F, Allen MT, Pearcy RW (1997) Photosynthetic responses to dynamic light under field conditions in six tropical rainforest shrubs occurring along a light gradient. *Oecologia* 111 (4):505-514. doi:10.1007/s004420050264
- van Amerongen H, Croce R (2013) Light harvesting in Photosystem II. *Photosynthesis Research* 116 (2):251-263. doi:10.1007/s11120-013-9824-3
- van der Veen R (1949) Induction phenomena in photosynthesis. *Physiologia Plantarum* 2 (3):217-234. doi:10.1111/j.1399-3054.1949.tb07482.x
- van Ittersum MK, Cassman KG, Grassini P, Wolf J, Tittonell P, Hochman Z (2013) Yield gap analysis with local to global relevance - A review. *Field Crops Research* 143:4-17. doi:10.1016/j.fcr.2012.09.009
- van Kooten O, Snel JF, Vredenberg WJ (1986) Photosynthetic free energy transduction related to the electric potential changes across the thylakoid membrane. *Photosynthesis Research* 9 (1):211-227. doi:10.1007/BF00029745
- van Leeuwen PJ, Heimann C, Gast P, Dekker JP, van Gorkom HJ (1993) Flash-induced redox changes in oxygen-evolving spinach Photosystem II core particles. *Photosynthesis Research* 38 (2):169-176. doi:10.1007/bf00146416
- van Rooijen R, Aarts MGM, Harbinson J (2015) Natural genetic variation for acclimation of photosynthetic light use efficiency to growth irradiance in *Arabidopsis thaliana*. *Plant Physiology*. doi:10.1104/pp.114.252239
- Varco-Merth B, Fromme R, Wang M, Fromme P (2008) Crystallization of the c₁₄-rotor of the chloroplast ATP synthase reveals that it contains pigments. *Biochimica et*

References

- Biophysica Acta - Bioenergetics 1777 (7-8):605-612. doi:10.1016/j.bbabi.2008.05.009
- Veljovic-Jovanovic SD, Pignocchi C, Noctor G, Foyer CH (2001) Low ascorbic acid in the *vtc-1* mutant of *Arabidopsis* is associated with decreased growth and intracellular redistribution of the antioxidant system. *Plant Physiology* 127 (2):426-435. doi:10.1104/pp.010141
- Velthuys BR, Amesz J (1974) Charge accumulation at the reducing side of system 2 of photosynthesis. *Biochimica et Biophysica Acta - Bioenergetics* 333 (1):85-94. doi:10.1016/0005-2728(74)90165-0
- Violet-Chabrand S, Dreyer E, Brendel O (2013) Performance of a new dynamic model for predicting diurnal time courses of stomatal conductance at the leaf level. *Plant, Cell and Environment* 36:1529-1546. doi:10.1111/pce.12086
- Violet-Chabrand S, Matthews JSA, Brendel O, Blatt MR, Wang Y, Hills A, Griffiths H, Rogers S *et al.* (2016) Modelling water use efficiency in a dynamic environment: An example using *Arabidopsis thaliana*. *Plant Science* 251:65-74. doi:10.1016/j.plantsci.2016.06.016
- Vico G, Manzoni S, Palmroth S, Katul G (2011) Effects of stomatal delays on the economics of leaf gas exchange under intermittent light regimes. *New Phytologist* 192:640-652. doi:10.1111/j.1469-8137.2011.03847.x
- Vines HM, Armitage AM, Chen S-S, Tu Z-P, Black CC (1982) A transient burst of CO₂ from geranium leaves during illumination at various light intensities as a measure of photorespiration. *Plant Physiology* 70 (2):629-631. doi:10.1104/pp.70.2.629
- Vines HM, Tu Z-P, Armitage AM, Chen S-S, Black CC (1983) Environmental responses of the post-lower illumination CO₂ burst as related to leaf photorespiration. *Plant Physiology* 73 (1):25-30. doi:10.1104/pp.73.1.25
- Vogelmann TC, Evans JR (2002) Profiles of light absorption and chlorophyll within spinach leaves from chlorophyll fluorescence. *Plant, Cell and Environment* 25:1313-1323. doi:10.1046/j.1365-3040.2002.00910.x
- Vogelmann TC, Martin G (1993) The functional significance of palisade tissue: penetration of directional versus diffuse light. *Plant, Cell and Environment* 16 (1):65-72. doi:10.1111/j.1365-3040.1993.tb00845.x
- Vollmar M, Schlieper D, Winn M, Buchner C, Groth G (2009) Structure of the c₁₄ rotor ring of the proton translocating chloroplast ATP synthase. *Journal of Biological Chemistry* 284 (27):18228-18235. doi:10.1074/jbc.M109.006916
- von Caemmerer S (2000) *Biochemical Models of Leaf Photosynthesis*. CSIRO Publishing, Collingwood, Australia
- von Caemmerer S (2013) Steady-state models of photosynthesis. *Plant, Cell and Environment* 36:1617-1630. doi:10.1111/pce.12098
- von Caemmerer S, Edmondson DL (1986) Relationship between steady-state gas exchange, *in vivo* ribulose biphosphate carboxylase activity and some carbon reduction cycle intermediates in *Raphanus sativus*. *Australian Journal of Plant Physiology* 13 (5):669-688. doi:10.1071/PP9860669
- von Caemmerer S, Evans J (1991) Determination of the average partial pressure of CO₂ in chloroplasts from leaves of several C₃ plants. *Functional Plant Biology* 18 (3):287-305. doi:10.1071/PP9910287
- von Caemmerer S, Evans JR (2015) Temperature responses of mesophyll conductance differ greatly between species. *Plant, Cell and Environment* 38 (4):629-637. doi:10.1111/pce.12449

- von Caemmerer S, Quick WP, Furbank RT (2012) The development of C4 rice: Current progress and future challenges. *Science* 336 (6089):1671-1672. doi:10.1126/science.1220177
- Vredenberg WJ, Tonk WJM (1975) On the steady-state electrical potential difference across the thylakoid membranes of chloroplasts in illuminated plant cells. *Biochimica et Biophysica Acta - Bioenergetics* 387 (3):580-587. doi:10.1016/0005-2728(75)90095-X
- Walker B, Ariza LS, Kaines S, Badger MR, Cousins AB (2013) Temperature response of *in vivo* Rubisco kinetics and mesophyll conductance in *Arabidopsis thaliana*: Comparisons to *Nicotiana tabacum*. *Plant, Cell and Environment* 36 (12):2108-2119. doi:10.1111/pce.12166
- Walker BJ, Strand DD, Kramer DM, Cousins AB (2014) The response of cyclic electron flow around photosystem I to changes in photorespiration and nitrate assimilation. *Plant Physiology* 165:453-462. doi:10.1104/pp.114.238238
- Walker DA (1973) Photosynthetic induction phenomena and the light activation of Ribulose diphosphate carboxylase. *New Phytologist* 72 (2):209-235. doi:10.1111/j.1469-8137.1973.tb02027.x
- Walters RG, Horton P (1991) Resolution of components of non-photochemical chlorophyll fluorescence quenching in barley leaves. *Photosynthesis Research* 27 (2):121-133. doi:10.1007/bf00033251
- Walters RG, Horton P (1995) Acclimation of *Arabidopsis thaliana* to the light environment: regulation of chloroplast composition. *Planta* 197 (3):475-481. doi:10.1007/bf00196669
- Walters RG, Rogers JJM, Shephard F, Horton P (1999) Acclimation of *Arabidopsis thaliana* to the light environment: the role of photoreceptors. *Planta* 209 (4):517-527. doi:10.1007/s004250050756
- Wang Y, Bräutigam A, Weber APM, Zhu X-G (2014) Three distinct biochemical subtypes of C4 photosynthesis? A modelling analysis. *Journal of Experimental Botany* 65 (13):3567-3578. doi:10.1093/jxb/eru058
- Wang YP, Jarvis PG (1990) Description and validation of an array model MAESTRO. *Agricultural and Forest Meteorology* 51:257-280. doi:10.1016/0168-1923(90)90112-J
- Warburg O (1920) Über die Geschwindigkeit der photochemischen Kohlensäurezersetzung in lebenden Zellen. II. *Biochemische Zeitschrift* 103:188-217
- Way DA, Pearcy RW (2012) Sunflecks in trees and forests: From photosynthetic physiology to global change biology. *Tree Physiology* 32:1066-1081. doi:10.1093/treephys/tps064
- WEC (2016) World Energy Resources - 2016. World Energy Council, London, U. K.
- Wedel N, Soll J, Paap BK (1997) CP12 provides a new mode of light regulation of Calvin cycle activity in higher plants. *Proceedings of the National Academy of Sciences* 94 (19):10479-10484
- Wen F, Xing D, Zhang L (2008) Hydrogen peroxide is involved in high blue light-induced chloroplast avoidance movements in *Arabidopsis*. *Journal of Experimental Botany* 59 (10):2891-2901. doi:10.1093/jxb/ern147
- Weraduwege SM, Chen J, Anozie FC, Morales A, Weise SE, Sharkey TD (2015) The relationship between leaf area growth and biomass accumulation in *Arabidopsis thaliana*. *Frontiers in Plant Science* 6:1-21. doi:10.3389/fpls.2015.00167

References

- Werner C, Ryel RJ, Correia O, Beyschlag W (2001) Effects of photoinhibition on whole-plant carbon gain assessed with a photosynthesis model. *Plant, Cell and Environment* 24 (1):27-40. doi:10.1046/j.1365-3040.2001.00651.x
- Whitney SM, Baldet P, Hudson GS, Andrews TJ (2001) Form I Rubiscos from non-green algae are expressed abundantly but not assembled in tobacco chloroplasts. *The Plant Journal* 26 (5):535-547. doi:10.1046/j.1365-313x.2001.01056.x
- Wientjes E, van Amerongen H, Croce R (2013) LHCII is an antenna of both photosystems after long-term acclimation. *Biochimica et Biophysica Acta - Bioenergetics* 1827 (3):420-426. doi:10.1016/j.bbabi.2012.12.009
- Willmer C, Fricker M (1996) *Stomata*. 2 edn. Chapman & Hall, London, U. K.
- Winter H, Robinson DG, Heldt HW (1993) Subcellular volumes and metabolite concentration in barley leaves. *Planta* 191 (2):180-190. doi:10.1007/BF02411558
- Winter H, Robinson DG, Heldt HW (1994) Subcellular volumes and metabolite concentrations in spinach leaves. *Planta* 193 (4):530-535. doi:10.1007/bf02411558
- Woodrow I, Mott K (1989) Rate limitation of non-steady-state photosynthesis by ribulose-1,5-bisphosphate carboxylase in spinach. *Functional Plant Biology* 16 (6):487-500. doi:10.1071/PP9890487
- Woodrow IE (2009) Flux control analysis of the rate of photosynthetic CO₂ assimilation. In: Laik A, Nedbal L, Govindjee (eds) *Photosynthesis in silico : Understanding Complexity from Molecules to Ecosystems*. Springer Netherlands, Dordrecht, pp 349-360. doi:10.1007/978-1-4020-9237-4_15
- Woodrow IE, Kelly ME, Mott KA (1996) Limitation of the rate of ribulosebisphosphate carboxylase activation by carbamylation and ribulosebisphosphate carboxylase activase activity: Development and tests of a mechanistic model. *Australian Journal of Plant Physiology* 23 (2):141-149. doi:10.1071/PP9960141
- Woodrow IE, Mott KA (1993) Modelling C₃ photosynthesis: A sensitivity analysis of the photosynthetic carbon-reduction cycle. *Planta* 191 (4):421-432. doi:10.1007/BF00195743
- Wu G, Ortiz-Flores G, Ortiz-Lopez A, Ort DR (2007) A point mutation in *atpC1* raises the redox potential of the Arabidopsis chloroplast ATP synthase γ -subunit regulatory disulfide above the range of thioredoxin modulation. *Journal of Biological Chemistry* 282 (51):36782-36789. doi:10.1074/jbc.M707007200
- Wullschleger SD (1993) Biochemical limitations to carbon assimilation in C₃ plants - A retrospective analysis of the A/C_i curves from 109 species. *Journal of Experimental Botany* 44 (262):907-920. doi:10.1093/jxb/44.5.907
- Xin CP, Yang J, Zhu XG (2013) A model of chlorophyll a fluorescence induction kinetics with explicit description of structural constraints of individual Photosystem II units. *Photosynthesis Research* 117 (1):339-354. doi:10.1007/s11120-013-9894-2
- Xing HT, Guo P, Xia XL, Yin WL (2011) PdERECTA, a leucine-rich repeat receptor-like kinase of poplar, confers enhanced water use efficiency in Arabidopsis. *Planta* 234 (2):229-241. doi:10.1007/s00425-011-1389-9
- Yamamoto H, Shikanai T (2013) In planta mutagenesis of Src homology 3 domain-like fold of NdhS, a ferredoxin-binding subunit of the chloroplast NADH dehydrogenase-like complex in Arabidopsis: a conserved arg-193 plays a critical role in ferredoxin binding. *Journal of Biological Chemistry* 288 (51):36328-36337. doi:10.1074/jbc.M113.511584

- Yamori W, Hikosaka K, Way DA (2014) Temperature response of photosynthesis in C3, C4, and CAM plants: temperature acclimation and temperature adaptation. *Photosynthesis Research* 119 (1):101-117. doi:10.1007/s11120-013-9874-6
- Yamori W, Masumoto C, Fukayama H, Makino A (2012) Rubisco activase is a key regulator of non-steady-state photosynthesis at any leaf temperature and, to a lesser extent, of steady-state photosynthesis at high temperature. *Plant Journal* 71:871-880. doi:10.1111/j.1365-313X.2012.05041.x
- Yamori W, Noguchi K, Kashino Y, Terashima I (2008) The role of electron transport in determining the temperature dependence of the photosynthetic rate in spinach leaves grown at contrasting temperatures. *Plant and Cell Physiology* 49 (4):583-591. doi:10.1093/pcp/pcn030
- Yamori W, Shikanai T (2016) Physiological functions of cyclic electron transport around Photosystem I in sustaining photosynthesis and plant growth. *Annual Review of Plant Biology* 67 (1):81-106. doi:10.1146/annurev-arplant-043015-112002
- Yamori W, Suzuki K, Noguchi KO, Nakai M, Terashima I (2006) Effects of Rubisco kinetics and Rubisco activation state on the temperature dependence of the photosynthetic rate in spinach leaves from contrasting growth temperatures. *Plant, Cell and Environment* 29 (8):1659-1670. doi:10.1111/j.1365-3040.2006.01550.x
- Yin X, Harbinson J, Struik PC (2006) Mathematical review of literature to assess alternative electron transports and interphotosystem excitation partitioning of steady-state C3 photosynthesis under limiting light. *Plant, Cell and Environment* 29:1771-1782. doi:10.1111/j.1365-3040.2006.01554.x
- Yin X, Struik PC (2009) C3 and C4 photosynthesis models: An overview from the perspective of crop modelling. *NJAS - Wageningen Journal of Life Sciences* 57:27-38. doi:10.1016/j.njas.2009.07.001
- Yin X, Struik PC (2010) Modelling the crop: from system dynamics to systems biology. *Journal of Experimental Botany* 61 (8):2171-2183. doi:10.1093/jxb/erp375
- Yin X, Struik PC (2012) Mathematical review of the energy transduction stoichiometries of C4 leaf photosynthesis under limiting light. *Plant, Cell and Environment* 35:1299-1312. doi:10.1111/j.1365-3040.2012.02490.x
- Yin X, Struik PC (2015) Constraints to the potential efficiency of converting solar radiation into phytoenergy in annual crops: from leaf biochemistry to canopy physiology and crop ecology. *Journal of Experimental Botany* 66 (21):6535-6549. doi:10.1093/jxb/erv371
- Yin X, Sun Z, Struik PC, Gu J (2011) Evaluating a new method to estimate the rate of leaf respiration in the light by analysis of combined gas exchange and chlorophyll fluorescence measurements. *Journal of Experimental Botany* 62 (10):3489-3499. doi:10.1093/jxb/err038
- Yin X, van Laar HH (2005) *Crop Systems Dynamics: an ecophysiological simulation model for genotype-by-environment interactions*. Wageningen Academic Publishers, Wageningen
- Yoon HS, Hackett JD, Ciniglia C, Pinto G, Bhattacharya D (2004) A molecular timeline for the origin of photosynthetic eukaryotes. *Molecular Biology and Evolution* 21 (5):809-818. doi:10.1093/molbev/msh075
- Yu O, Goudriaan J, Wang T-D (2001) Modelling diurnal courses of photosynthesis and transpiration of leaves on the basis of stomatal and non-stomatal responses, including photoinhibition. *Photosynthetica* 39 (1):43-51. doi:10.1023/a:1012435717205

References

- Zaks J, Amarnath K, Kramer DM, Niyogi KK, Fleming GR (2012) A kinetic model of rapidly reversible nonphotochemical quenching. *Proceedings of the National Academy of Sciences* 109 (39):15757-15762. doi:10.1073/pnas.1211017109
- Zaks J, Amarnath K, Sylak-Glassman EJ, Fleming GR (2013) Models and measurements of energy-dependent quenching. *Photosynthesis Research* 116 (2-3):389-409. doi:10.1007/s11120-013-9857-7
- Zhang N, Kallis RP, Ewy RG, Portis AR (2002) Light modulation of Rubisco in Arabidopsis requires a capacity for redox regulation of the larger Rubisco activase isoform. *Proceedings of the National Academy of Sciences* 99:3330-3334. doi:10.1073/pnas.042529999
- Zhang N, Portis AR (1999) Mechanism of light regulation of Rubisco: a specific role for the larger Rubisco activase isoform involving reductive activation by thioredoxin-f. *Proceedings of the National Academy of Sciences* 96:9438-9443. doi:10.1073/pnas.96.16.9438
- Zhu X-G, de Sturler E, Long SP (2007) Optimizing the distribution of resources between enzymes of carbon metabolism can dramatically increase photosynthetic rate: a numerical simulation using an evolutionary algorithm. *Plant Physiology* 145 (2):513-526. doi:10.1104/pp.107.103713
- Zhu X-G, Long SP, Ort DR (2010) Improving photosynthetic efficiency for greater yield. *Annual Review of Plant Biology* 61 (1):235-261. doi:10.1146/annurev-arplant-042809-112206
- Zhu X-G, Lynch JP, LeBauer DS, Millar AJ, Stitt M, Long SP (2016) Plants in silico: why, why now and what?—an integrative platform for plant systems biology research. *Plant, Cell and Environment* 39 (5):1049-1057. doi:10.1111/pce.12673
- Zhu XG, Govindjee, Baker NR, DeSturler E, Ort DR, Long SP (2005) Chlorophyll a fluorescence induction kinetics in leaves predicted from a model describing each discrete step of excitation energy and electron transfer associated with Photosystem II. *Planta* 223 (1):114-133. doi:10.1007/s00425-005-0064-4
- Zhu XG, Ort DR, Whitmarsh J, Long SP (2004) The slow reversibility of Photosystem II thermal energy dissipation on transfer from high to low light may cause large losses in carbon gain by crop canopies: A theoretical analysis. *Journal of Experimental Botany* 55:1167-1175. doi:10.1093/jxb/erh141
- Zhu XG, Song Q, Ort DR (2012) Elements of a dynamic systems model of canopy photosynthesis. *Current Opinion in Plant Biology* 15:237-244. doi:10.1016/j.pbi.2012.01.010
- Zhu XG, Wang Y, Ort DR, Long SP (2013) e-photosynthesis: A comprehensive dynamic mechanistic model of C3 photosynthesis: From light capture to sucrose synthesis. *Plant, Cell and Environment* 36:1711-1727. doi:10.1111/pce.12025

Summary

In their natural environment, leaves are exposed to rapid fluctuations of irradiance. Research on CO₂ assimilation under fluctuating irradiance (dynamic CO₂ assimilation) often relies on measurements of gas exchange during transients where irradiance is rapidly increased or decreased, after the leaf has adapted to a particular set of environmental conditions. In the field, such increases and decreases occur mostly because of sunflecks (rapid increases in irradiance on a low irradiance background) created by gaps in the canopy and plant movement by wind, and cloudflecks (rapid decreases in irradiance on a high irradiance background) generated by clouds that transiently block the sun.

For a given set of environmental conditions, CO₂ assimilation depends on the activity of the different photosynthetic enzymes and protein complexes, as well as CO₂ diffusion from the surrounding air into the chloroplasts, determined by conductances. These activities and conductances are themselves dependent on environmental conditions and, collectively, define the “induction state” of the leaf. When the irradiance incident on a leaf increases, the induction state of the leaf increases (photosynthetic induction) and the speed at which it changes determines the time required to reach the new rate of CO₂ assimilation. The rate at which the induction state is decreased at low irradiance is also relevant, as it will determine the induction state of the leaf at the beginning of a sunfleck and may also result in transient reductions of CO₂ assimilation at low irradiance.

The rates of photosynthetic induction are affected by temperature, CO₂ mole fraction ([CO₂]) and air humidity, depending on the environmental sensitivity of the different photosynthetic processes affecting the induction state of a leaf. Understanding the interactions among these processes requires the use of models that integrate knowledge acquired with experiments. In addition, the complex spatio-temporal distribution of irradiance within canopies means that proper scaling from the leaf to the plant or community level requires the use of dynamic models with high predictive power and ease of calibration.

In this dissertation, the metabolic regulation of photosynthesis and how this may limit dynamic CO₂ assimilation is studied *in silico* with the development and application of simulation models. In order to support the development of the models, a review of the literature was performed as well as an experiment designed to generate data on dynamic CO₂ assimilation for different photosynthetic mutants of *Arabidopsis thaliana*. In addition to providing these models to the research community, this dissertation also identifies multiple targets that may be used for improving dynamic CO₂ assimilation in plants. It further demonstrates that the dynamic responses of CO₂ assimilation to changes in irradiance has a significant effect on canopy CO₂ assimilation, even for dense canopies exposed to open skies, resembling the conditions of commercial crops.

In **Chapter 1**, the context of this dissertation is presented. The societal relevance of this research is argued, making reference to the role that photosynthesis could play in addressing global problems such as food and energy security. The necessary background on the physiology of photosynthesis is provided, with special emphasis on the terminology and concepts required to understand the rest of the dissertation, with the aim of making the contents more accessible to a wider audience. Then, prior literature on the specific topics of this dissertation (i.e., photosynthesis in a dynamic environment

Summary

and its mathematical modelling) is presented, with a chronological approach that analyses the evolution of ideas and methodologies up to the present. The chapter concludes with the formulation of four specific research questions that are addressed by Chapters 2–5. These research questions may be summarized into (i) the effect of environmental conditions on dynamic CO₂ assimilation through responses of the different photosynthetic processes, (ii) the limitations to dynamic CO₂ assimilation imposed by different photosynthetic processes, (iii) the metabolic regulation of the electron transport chain when coupled to the Calvin cycle, and (iv) the identification of targets for improvement of dynamic CO₂ assimilation.

In **Chapter 2**, the current literature on dynamic CO₂ assimilation is reviewed, with an emphasis on the effects of environmental conditions ([CO₂], temperature, and air humidity) on the rates of photosynthetic induction and loss of induction. This review reveals major knowledge gaps, especially on the loss of induction. Also, experimental evidence from different sources is sometimes contradictory and the origin of these discrepancies is unknown. Overall, the availability of data on the effects of environmental conditions on dynamic CO₂ assimilation is low, especially when compared with studies on steady-state CO₂ assimilation. The little data available indicates that rates of photosynthetic induction increase with [CO₂], which could be explained by a weak effect on Rubisco activation and a strong effect on stomatal opening. Increases in temperature also increase the rates of photosynthetic induction, up to an optimum, beyond which a strong negative effect can be observed, which could be attributed to deactivation of Rubisco activase. Although other small effects of [CO₂], temperature and air humidity have been reported in the literature and are described in the chapter, much more research is required to better quantify these effects and resolve the apparent contradictions among different sources.

In **Chapter 3**, an experiment is presented that makes use of several photosynthetic mutants of *A. thaliana*. The aim of the experiment is to test hypotheses regarding the limitations imposed on dynamic CO₂ assimilation by different photosynthetic processes (non-photochemical quenching, sucrose synthesis, regulation of Rubisco activity, and CO₂ diffusion). A secondary objective is to provide data for calibrating and validating the models presented in Chapters 4 and 5. Downregulating non-photochemical quenching and sucrose synthesis did not have any significant effect on dynamic CO₂ assimilation, whereas CO₂ diffusion and Rubisco activation exerted stronger limitations.

Further analysis revealed that whether stomatal opening limited CO₂ assimilation after an increase in irradiance depended on the stomatal conductance prior to the change in irradiance. A threshold value of 0.12 mol m⁻² s⁻¹ (defined for fluxes of water vapour) could be defined, above which stomata did not affect the rates of photosynthetic induction. The comparison of measurements across irradiance levels also indicated that the apparent rate constant of Rubisco activation was irradiance-dependent, at least for irradiance levels below 150 μmol m⁻² s⁻¹.

In **Chapter 4**, a phenomenological model of leaf-level CO₂ assimilation is presented. The model is described in detail and all the parameters are first estimated with published data, and later refined by fitting the model to the data from Chapter 3. Additional data from the experiment in Chapter 3 is used to validate predictions of CO₂ assimilation under lightflecks for the different photosynthetic mutants. The model predicts accurately dynamic CO₂ assimilation for the different photosynthetic mutants by only

modifying those parameters that are affected by the mutation. This demonstrates that the model has a high predictive power and that the equations, although phenomenological in nature, have a solid physiological basis.

The model is further used to analyse, *in silico*, the limitations imposed by different photosynthetic processes on dynamic CO₂ assimilation at the leaf and canopy level, allowing a more in depth analysis than in Chapter 3. The analysis demonstrates that results obtained at the leaf level should not be extrapolated directly to the canopy level, as the spatial and temporal distribution of irradiance within a canopy is more complex than what is achieved in experimental protocols. Both at the leaf and canopy level, CO₂ diffusion is strongly limiting, followed by photoinhibition, chloroplast movements and Rubisco activation.

The predictions at the canopy level indicate that if the regulation of the electron transport chain and enzymes in the Calvin cycle, as well as the kinetics of stomatal conductance, are ignored, canopy CO₂ assimilation would be overestimated by 5.0% to 9.2%, depending on the environmental conditions. This puts into question the accuracy of current models of canopy CO₂ assimilation and photosynthesis-based plant growth models.

In **Chapter 5**, a mechanistic model of the dynamic, metabolic regulation of the electron transport chain is presented. The model is described in detail and all the parameters are estimated from published literature, using measurements on *A. thaliana* when available. Predictions of the model are tested with steady-state and dynamic measurements of gas exchange, chlorophyll fluorescence and absorbance spectroscopy on *A. thaliana*, with success.

The analysis *in silico* indicates that a significant amount of alternative electron transport is required to couple ATP and NADPH production and demand, and most of it is associated with nitrogen assimilation and export of redox power through the malate shuttle. The fractions of electrons allocated to the different alternative electron transport pathways increases at low [CO₂] and during photosynthetic induction. The analysis also reveals that the relationship between ATP synthesis and the proton motive force is highly regulated by the concentrations of substrates (ADP, ATP and inorganic phosphate), and this regulation facilitates an increase in non-photochemical quenching under conditions of low metabolic activity in the stroma. Thus, flexibility in alternative electron transport and regulation of ATP synthase fine-tune the electron transport chain in response to a wide range of environmental conditions, both in the steady-state and during dynamic transients.

In **Chapter 6**, the findings of Chapters 2–5 are summarised and employed to answer in detail the four research questions formulated in Chapter 1. Of great interest is the identification of six potential targets that may be used to improve dynamic CO₂ assimilation. These targets are: (i) regulation of Rubisco activity through changes in the amount or regulation of Rubisco activase, (ii) acceleration of stomatal opening and closure, (iii) a lower H⁺/ATP for ATP synthesis, (iv) faster relaxation of non-photochemical quenching, (v) reduced chloroplast movements, and (vi) reduced photoinhibition by increased rates of repair of Photosystem II.

The methodology followed in this dissertation is also discussed in detail in this chapter. Firstly, there is a need for better quantification of different aspects of photosynthesis, as

Summary

opposed to qualitative knowledge based on identification of genes and proteins. In the short term, progress may be achieved by the creation of a multidisciplinary database on photosynthesis. Secondly, whereas this dissertation has focused on photosynthesis as a function of time, spatial variation within chloroplasts, leaves and canopies may play an important role. The different ways in which spatial issues may be of relevance are discussed, and suggestions are made on how the models from Chapters 4 and 5 may be extended to include space in a more explicit manner. Finally, the potential applications of the models from Chapters 4 and 5 are presented, with suggestions for further research.

Acknowledgements

I am very grateful to my supervisors (Paul Struik, Jaap Molenaar, Xinyou Yin and Jeremy Harbinson) for their patience, guidance and unconditional trust in my work. Paul, your constant support and belief in my project and my abilities goes beyond your responsibilities. I have been very lucky to have you as promotor and I thank you for always having time for me. Jaap, your analytical skills and clarity of mind have always been very useful, as well as your ability to solve problems calmly and effectively, both in terms of scientific content and process. Xinyou, not only have I learnt much about photosynthesis modelling from you, but your attention to detail and uncanny ability to detect errors is a privilege and a safeguard for a PhD candidate. Jeremy, without you, this thesis would have been poorer in quality, your knowledge of photosynthesis is unique and you can always cite the key publications in any photosynthesis topic.

Although many people have helped me to arrive at this point, I must make a special mention of a colleague without whom I doubt I would have succeeded. Elias Kaiser, you have played a fundamental role in my PhD (you are co-author of almost every chapter!) and I believe we have reached a level of synergy that is seldom seen in academic research. Of course, part of the success in our collaboration was due to the fact that our theses are largely complementary (what are the odds?), but this would not have been possible without the respect and trust that we have developed throughout these years. In the old days, a paranympth could act as backup for the doctoral candidate when answering the committee's questions and, although this is no longer the norm, I am sure you could have performed that role perfectly. I know that we will continue to collaborate in the future and I am sure our "dynamic duo" is going to rock the photosynthesis world.

I am grateful to David Kramer and Jin Chen for hosting me at Michigan State University. I learnt a lot during that time and enjoy the interaction with the different lab members. Their research on photosynthesis is at the highest level and they are constructing a complete new paradigm on regulation of the electron transport chain. Chapter 5 of this thesis is in part the result of that visit and my discussions with David M Kramer and members of his lab, especially Jeffrey Cruz, Geoffry Davis, Deserah Strand and Nicholas Fisher. I always felt welcome among you. Dave, your energy and enthusiasm have been very motivating and kept me fighting against the hardest bits of my work and I also appreciate enormously your interest in the more technical aspects of modelling.

Herman Berghuijs and Steven Driever, you have always been available to discuss any photosynthesis topic and our chats have been most valuable. I learnt much during the CSA Photosynthesis Discussion meetings and I have to thank Herman for his initiative and effort to set it up. Only now that I have to organise them myself I realise that it is not trivial to arrange such meetings. Steven, not only have you contributed to one of the chapters, but you are always making an effort to promote my work within the photosynthesis community. I just hope I can live up to the expectations.

I am grateful to Laurens Krah for doing his internship with me on such a complex topic as modelling NPQ on cyanobacteria. Not only did I learn much about photosynthesis in cyanobacteria, but you also helped me understand better my own model of the electron transport chain. Your sharp intellect and analytical skills were very useful.

Even though they may not have contributed directly to my thesis, I have to recognize the influence in my work of Francisco Villalobos, Luca Testi and Francisco Orgaz, who trained me as a scientist during my early research years in Spain. They taught the meaning of good science and the need to connect the lab with the field. While parts of this thesis took a long detour into the molecular world, I still consider myself close to the fields of “ecophysiology” and “environmental physics” as a result of their training.

I am most grateful to my colleagues at the Centre for Crop Systems Analysis, where I have spent most of my awake time of the last four years. I cannot imagine a better group in which I could do my research and I am so lucky that I can continue work in this group for the next years. The variety of research topics in CSA is amazing and, although this can sometimes be a weakness, it is also a strength, especially because everyone is so open minded and willing to collaborate. I appreciate very much your feedback, even when my presentations were full of photosynthesis jargon. The research staff members have always been very helpful and kind and, although in Wageningen we take it for granted, it is nonetheless amazing that an entire room of Dutch people would decide to discuss complex topics for an hour in English because the Spanish guy has not managed to learn Dutch after six years in The Netherlands... So thank you Niels, Bob, Peter (both!), Willemien (both!), Tjeerd Jan, Alex-Jan, Lammert, Jochem, Wopke, Ans, Jet, Marjolein, Pepijn, Cor, Aad and Jan. A very special thanks to Sjanie and Nicole, you make every problem look so easy and you are always so patient!

I feel grateful to the group of PhD candidates at CSA, especially for making my life more enjoyable in the last, stressful months of the PhD trajectory. I very much enjoyed the lunch breaks, there is always so much variety on the table! And the Thursday drinks, especially the ones that somehow got extended into the wee hours of the night... And for the PhD meetings. And for the fun on Whatsapp. And for everything else! So thanks, Wenjing, Uta, Niteen, Luuk, Martin, Kailei, Herman, Jorad, Franca, Marcelo, Ioannis, Ali, Adugna, Dennis, Shenghao, Tianyao, Huanhe, Cesar, Andre and everyone that I shamefully forgot to mention.

Despite the help I received from everyone named in the above, the truth is that, without Pulu I would not have been able to write this thesis. Doing a PhD is a lonely activity, very often stressful and frustrating. Therefore, skills and knowledge are not sufficient: a strong emotional support is required to keep pushing forward in the face of adversity. I am lucky to have met Pulu right before starting my PhD and she has always been an anchor to which I could hold myself.

Last but not least, I am very grateful to my parents. Without them I would not be here... literally! Not just for the obvious biological reasons... but also for the tremendous effort they made to raise me (my mother became an expert on first aid) and educate me beyond the (rather low) level that was expected of me by the educational system.

If anyone thinks that I have forgotten to include his/her name here, that is very likely, and I can only apologize for my terrible memory.

PE&RC Training and Education Statement

With the training and education activities listed below the PhD candidate has complied with the requirements set by the C.T. de Wit Graduate School for Production Ecology and Resource Conservation (PE&RC) which comprises of a minimum total of 32 ECTS (= 22 weeks of activities).



Review of literature (4.5 ECTS)

- Dynamic C3 photosynthesis from leaf to canopy (2016)

Writing of project proposal (2.5 ECTS)

- Modelling dynamic rice adaptation to drought: from the chloroplast to the canopy using the 'Crop Systems Biology' approach

Post-graduate courses (5.4 ECTS)

- Photosynthesis, climate and change; PE&RC (2013)
- NCSB Tutorial: basics of parameter estimation; SB@NL (2013)
- Measuring the photosynthetic phenome; PE&RC (2014)
- Uncertainty analysis of dynamic models; PE&RC (2015)
- Modelling plant form and function using GroIMP; PE&RC (2016)

Laboratory training and working visits (4.5 ECTS)

- Regulation of electron transport chain; Michigan State University, USA (2014)

Invited review of (unpublished) journal manuscript (1 ECTS)

- Remote Sensing of Environment: photosynthesis: measurement and modelling (2016)

Deficiency, refresh, brush-up courses (6 ECTS)

- Ecological modelling in R; CSA (2012)

Competence strengthening / skills courses (1.8 ECTS)

- Project & time management; PE&RC (2015)
- PhD Carrousel; PE&RC (2015)

PE&RC Annual meetings, seminars and the PE&RC weekend (1.8 ECTS)

- PE&RC First year weekend (2012)
- PE&RC Last year weekend (2016)
- PE&RC Day (2016)

Discussion groups / local seminars / other scientific meetings (10 ECTS)

- Wageningen centre for systems biology meeting (2013-2016)
- CSA Photosynthesis discussion group (2013-2016)
- R-users group (2014-2016)
- Modelling and Statistics Network (MSN) (2014-2016)

International symposia, workshops and conferences (9.1 ECTS)

- 16th International congress on photosynthesis research (2013)
- 17th International congress on photosynthesis research (2016)
- Plant environmental physiology group techniques workshop (2016)
- BioSB conference (2016)

Lecturing / supervision of practicals / tutorials (0.6 ECTS)

- Advanced methods for plant-climate research in controlled environments (2016)
- Plant plasticity and adaptation (2016)

Supervision of MSc students

- Database of dynamic photosynthesis
- Modelling state transitions in cyanobacteria

Curriculum Vitae

Alejandro was born in San Fernando, Spain, on the 18th July 1986. He received his primary and secondary education in Spain, except the 2001-2002 course, which he spent in Memphis (Tennessee, USA) as part of an international student exchange program. Between 2004 and 2010, Alejandro studied simultaneously two degrees at the University of Cordoba (Spain): Agricultural Engineering and Forestry Engineering. He received awards for best academic results in both degrees. Each engineering consisted of 5 academic years (300 ECTS) and can be considered equivalent to a Master in Engineering (MEng).

A professional project or a thesis was required to obtain each of these degrees, so Alejandro wrote a thesis on measuring and modelling the carbon balance of olive orchards and a second one where the same techniques were applied to the carbon balance of holm oak plantations in reforestation. This research work required several field experiments, as well as computer modelling. This work was the result of collaborations between the Institute for Sustainable Agriculture (IAS) of the Spanish National Research Council, and the University of Cordoba (UCO). During this time, Alejandro enjoyed two undergraduate research scholarships, at IAS and UCO, respectively.

Alejandro continued his studies in Wageningen University (with a postgraduate scholarship from Caja Madrid Foundation) where he graduated with distinction from the MSc Plant Science programme. He did his MSc thesis (and a minor MSc thesis) in the Plant Production Systems chairgroup, in collaboration with IAS. In these theses, he continued his research on olive orchards, with an emphasis on photosynthesis and its scaling from the leaf to the canopy level. This research also included field work (with an emphasis on micrometeorological techniques) and computer modelling.

In the second year of the MSc program, Alejandro wrote a PhD project proposal submitted to the ALW Open Call by NWO, in collaboration with the research staff at the Centre for Crop Systems Analysis (CSA) at Wageningen University. Despite favourable reviews, the proposal was not granted, though a revised version of this proposal was submitted a year later to the same program and granted. After the rejection of the proposal, Alejandro decided to accept a PhD position at CSA on modelling of photosynthesis, which has led to this PhD thesis.

Alejandro is bilingual in Spanish and English and has basic knowledge of French. In the virtual world, he “speaks” several programming languages, especially R, C++ and Julia. When he is not doing research, Alejandro enjoys reading and watching science fiction and e-sports, listening to non-pop music and learning about programming.

List of Publications

- Kaiser E, **Morales A**, Harbinson J, Heuvelink E, Prinzenberg AE, Marcelis LFM (2016) Metabolic and diffusional limitations of photosynthesis in fluctuating irradiance in *Arabidopsis thaliana*. Scientific Reports 6:31252. doi: 10.1038/srep31252
- Morales A**, Leffelaar PA, Testi L, Orgaz F, Villalobos FJ (2016) A dynamic model of potential growth of olive (*Olea europaea* L.) orchards. European Journal of Agronomy 74:93-102. doi: 10.1016/j.eja.2015.12.006
- Kaiser E, **Morales A**, Harbinson J, Kromdijk J, Heuvelink E, Marcelis LFM (2015) Dynamic photosynthesis in different environmental conditions. Journal of Experimental Botany 66 (9):2415-2426. doi: 10.1093/jxb/eru406
- Weraduwege SM, Chen J, Anozie FC, **Morales A**, Weise SE, Sharkey TD (2015) The relationship between leaf area growth and biomass accumulation in *Arabidopsis thaliana*. Frontiers in Plant Science 6:1-21. doi: 10.3389/fpls.2015.00167
- Zarco-Tejada PJ, **Morales A**, Testi L, Villalobos FJ (2013) Spatio-temporal patterns of chlorophyll fluorescence and physiological and structural indices acquired from hyperspectral imagery as compared with carbon fluxes measured with eddy covariance. Remote Sensing of Environment 133:102-115. doi: 10.1016/j.rse.2013.02.003
- Villalobos FJ, Perez-Priego O, Testi L, **Morales A**, Orgaz F (2012) Effects of water supply on carbon and water exchange of olive trees. European Journal of Agronomy 40:1-7. doi: 10.1016/j.eja.2012.02.004

Funding

This project was part of the IP/OP Systems Biology WUR 2012-2015 programme. This work was also carried out within the research programme of Biosolar Cells, co-financed by the Dutch Ministry of Economic Affairs.

